Synthesis, MCD- and Raman- Spectroscopic, and Quantum Chemical Investigation of Ferric Heme Model Complexes and their Reaction with NO

Dissertation
zur Erlangung des Doktorgrades
der Mathematisch-Naturwissenschaftlichen Fakultät
der Christian-Albrechts-Universität
zu Kiel

vorgelegt von

Florian Paulat

geboren in Köln

Kiel, 2007

Referent/in:	Prof. Dr. F. Tuczek
Korreferent/in:	PD Dr. N. Lehnert
	Prof. Dr. M. Bröring, Marburg
Tag der mündlichen Prüfung:	11.12.2007
Zum Druck genehmigt:	11.12.2007

Prof. Dr. J. Grotemeyer, Dekan

Abstract

In this thesis, a detailed spectroscopic investigation of ferric heme model complexes and their nitric oxide adducts is presented. To this end, two magnetic circular dichroism (MCD) and one resonance Raman (rRaman) spectrometer have been built. These techniques are powerful tools for the investigation of the electronic structures and vibrational properties of transition metal complexes. In combination with TD-DFT calculations, the complicated MCD and UV-Vis absorption spectra of five-coordinate ferric [Fe(TPP)(Cl)] have been completely assigned for the first time. This provides detailed insight into the electronic structures of five-coordinate ferric hemes, which was not available so far. These assignments obtained from MCD spectroscopy have been confirmed by other methods, especially rRaman measurements. In addition, ferric heme nitrosyls with *trans* thiolate coordination have been investigated using *in-situ* UV-Vis and rRaman spectroscopies, and DFT calculations. The DFT results show that the difference between axial N- and S-donor-coordinated ferric heme nitrosyls is due to a σ-*trans* effect of the coordinated thiolate on the bound NO, mediated by an NO σ* orbital. This way, the Fe-N and N-O bonds are weakened, and the Fe-N-O unit is bent in the S-coordinated case. The Fe-N stretching vibration in [Fe(OEP)(SR')(NO)] has been identified in the rRaman spectrum at 550 cm^{-1} via isotope labeling, and force constants of 3.56 and 14.51 mdyn $Å^{-1}$ for the Fe-NO and N-O bonds, respectively, have been determined using Normal Coordinate Analysis. Potential energy surface (PES) calculations on six-coordinate ferric heme NO model systems in different electronic states show that the elusive ls-Fe(III)-NO(radical) state does in fact exist as an energy minimum, and that this state is surprisingly close in energy to the Fe(II)-NO^+ ground state. This is especially relevant for the thiolate-bound ferric nitrosyls, where this state could be the ground state. Further investigations are necessary in this case. These results reveal an unexpectedly complex energy landscape for binding of NO to ferric heme.

In addition to these investigations, the synthesis of the anthracene bridged cofacial porphyrin H_4DPA, which is relevant as model complex for bacterial nitric oxide reductase, has been carried out. This way, the complex [Co_2(DPA)$(NO)_2$] has been synthesized and characterized using UV-Vis, IR and rRaman spectroscopies. Vibrational spectra show the ν(N-O) stretch 1685 cm^{-1} for this compound. Finally, DFT calculations have been used to investigate potential intermediates in the reduction of NO to N_2O using these cofacial porphyrins as platform.

Kurzzusammenfassung

Die vorliegende Arbeit beschäftigt sich mit der detailierten spektroskopischen Untersuchung von Modellsystemen für Fe(III) Hämproteine und deren NO-Addukte. Zu diesem Zweck wurden zwei Magnetische Zirkulardichroismus (MCD) und ein Resonanz-Raman (rRaman) Spektrometer aufgebaut. Diese Methoden sind extrem hilfreich bei der Untersuchung von elektronischen Strukturen und schwingungspektroskopischen Eigenschaften von Übergangsmetallkomplexen. In Kombination mit TD-DFT Rechnungen wurden die komplizierten MCD und UV-Vis Spektren von [Fe(TPP)(Cl)] zum ersten Mal vollständig zugeordnet. Hierbei handelt es sich um den ersten detailierten Einblick in die elektronische Struktur von fünffach-koordinierten Fe(III) Hämsystemen. Die so erzielten Zuordnungen wurden durch weitere Methoden verifiziert, wobei insbesondere die rRaman Spektroskopie zu nennen ist. Darueber hinaus wurden Fe(III)-Porphyrin NO-Addukte mit *trans* Thiolat-Koordination mit Hilfe von DFT Rechnungen, und *in-situ* UV-Vis Absorptions- und rRaman-Messungen untersucht. Die DFT Rechnungen zeigen, dass ein σ^* Orbital des NO für die Unterschiede zwischen Fe(III)-NO Hämsystemen mit *trans* N- und S-Donorliganden verantwortlich ist. Fe(III)-NO Hämkomplexe mit *trans* Thiolat-Liganden haben aufgrund dieser Wechselwirkung schwächere Fe-N sowie N-O Bindungen. Mit Hilfe einer Normal Koordinaten Analyse wurden Kraftkonstanten von 3.56 mdyn/Å (Fe-N) und 14.51 mdyn/Å (N-O) für das Modellsystem [Fe(OEP)(SR')(NO)] (**2H-NO**) bestimmt. Ausserdem ist die Fe-N-O Einheit gewinkelt. Die Fe-NO Streckschwingung in **2H-NO** wird bei 550 cm^{-1} beobachtet und verschiebt sich zu 535 cm^{-1} im entsprechenden $^{15}N^{18}O$-isotopensubstituierten Komplex. Berechnungen der Potentialhyperflächen von Fe(III)-NO Komplexen in verschiedenen elektonischen Zuständen haben gezeigt, dass der ls-Fe(III)-NO(Radikal) Zustand tatsächlich als Energieminimum existiert und überraschend nah zum Fe(II)-NO^+ Grundzustand ist. Dies ist besonders relevant für Thiolat koordinierte Fe(III)-NO Addukte, da in diesem Fall dieser Zustand der Grundzustand sein könnte. In diesem Zusammenhang sind jedoch weitere Untersuchungen notwendig. Die Rechnungen zeigen eine unerwartet komplizierte Energie-Landschaft für die Bindung von NO an Fe(III)-Hämsysteme.

Weiterhin wurde die Synthese von dem bifacialen Porphyrinliganden H_4DPA ausgearbeitet, einem Modellsystem für die bakterielle Stickstoffmonoxidreduktase. Der Komplex [Co_2(DPA)$(NO)_2$] wurde synthetisiert und spektroskopisch mit Hilfe der UV-Vis-, IR- und rRaman-Spektroskopie charakterisiert. Die N-O Streckschwingung wird bei 1685 cm^{-1} beobachtet. Darueber hinaus wurden potentielle Intermediate der Reduktion von NO zu N_2O mit diesem bifacialen Modellsystemen mittels DFT untersucht. Die Ergebnisse deuten darauf hin, dass cofaciale Porphyrinkomplexe für die Reduktion von NO zu N_2O verwendet werden können.

Table of Contents

1 Introduction

1.1 Nitric Oxide

It was a sensation in the 1980's that nitric oxide (NO), a poisonous gas and a common air pollutant, which is formed when nitrogen burns (for example in automobile exhaust fumes), could exert important functions in the human body. NO is present in most living creatures and made by many different types of cells. In 1992, nitric oxide was therefore voted as 'the molecule of the year' by the magazine Science.[1] It is known that NO plays a key role in nerve signal transduction, vasodilation, blood clotting, and immune response by white blood cells.[2] White blood cells use the poisonous property of NO to kill infectious agents such as bacteria, fungi and parasites. Robert F. Furchgott, Louis J. Ignarro and Ferid Murad, the discoverers of NO as a signal molecule were awarded with the Nobel Prize in Medicine in 1998. NO plays also an important role in medicine today, for example: In atherosclerosis, the endothelium has a reduced capacity to produce NO. However, NO can be introduced by treatment with nitroglycerin, which was invented by Ascanio Sobrero. Nitroglycerine can be synthesized by mixing glycerine with sulfuric and nitric acid. Dynamite, which was invented by Alfred Nobel in 1866 in Krümmel (Schleswig-Holstein, Germany) is an explosive based on the explosive nitroglycerin using kieselguhr (diatomaceous earth) as an adsorbent. When Nobel was ill with heart disease, his doctor prescribed nitroglycerin. In a letter to his friend, Nobel wrote:[3] "It is ironical that I am now ordered by my physician to eat nitroglycerin." Bacterial infections can lead to sepsis and circulatory shock. In this condition, NO plays a harmful role. White blood cells react to bacterial products by releasing large amounts of NO that dilate the blood vessels. The blood pressure drops and the patient may become unconscious. In this situation, inhibitors of NO synthase may be useful in intensive care treatment. NO can initiate erection of the penis by dilating the blood vessels to the erectile bodies. This knowledge has led to the development of drugs against impotence (for example Viagra). Of course, the dosage is critical since the gas can be toxic at high concentrations. Paracelsus: „Alle Ding' sind Gift und nichts ohn' Gift; allein die Dosis macht, dass ein Ding kein Gift ist." ("All things are poison and nothing is without poison, only the dose permits something not to be poisonous.") For example, sodium nitroprusside, which corresponds to the iron complex $Na_2[Fe(CN)_5NO]x2H_2O$, is a NO donor used to lower blood pressure.

1.2 Heme Proteins

Heme Proteins include all proteins that contain a heme moiety as a prosthetic group. This class of enzymes show impressively varied biological functions. For example, heme proteins play a dominant role throughout the chemistry of nitric oxide in biology. NO is produced in vivo from arginine performed by the nitric oxide synthase (NOS) family of enzymes.[4] The cardiovascular regulation by NO (produced by endothelial(e-) NOS) is then mediated by soluble guanylate cyclase (sGC), which is activated by coordination of NO to its ferrous heme active site.[5] Nitrophorins (Np's) are hemoproteins found in the saliva of blood-sucking insects, which act as NO-carriers.[6] Histamine, which is released by the host in response to tissue damage, binds to Np and this way, facilitates the release of NO into the tissue where it induces vasodilatation. In addition, *the biological reduction of NO to N_2O (cf. equation 1) is mediated by heme proteins, the so-called nitric oxide reductases (NOR's)*.

$$2\ NO + 2\ H^+ + 2\ e^- \rightarrow N_2O + H_2O \quad (1)$$

Nitric oxide reductases (NOR) are found in either bacteria or fungi. The bacterial NOR (NorBC) is part of the dissimilatory denitrification, whereas the fungal nitric oxide reductase (P450nor) is part of a similar process that is observed in fungi (fungal denitrification). NorBC consists of a binuclear active site with one heme (axial histidine coordination) and one non-heme center, whereas P450nor consists of a single heme center with axial cysteine coordination. This suggests that the individual mechanisms for the NO reduction are completely different in these complexes. However, not much is known about the mechanisms of NorBC and P450nor (vide infra).

Dissimilatory Denitrification. Nitrate can be used by bacteria as an energy source in a process called *dissimilatory denitrification, which corresponds to the stepwise reduction of nitrate to dinitrogen* following equation 2.

$$NO_3^- \rightarrow NO_2^- \rightarrow \mathbf{NO \rightarrow N_2O} \rightarrow N_2 \quad (2)$$

Here, nitrate is reduced to nitrite by nitrate reductase (NAR), nitrite is then reduced to nitric oxide by nitrite reductase (NIR). This is *followed by NO reduction to nitrous oxide mediated by nitric oxide reductase (NOR)*, and finally, N_2O is further reduced to dinitrogen catalyzed by nitrous oxide reductase (N_2OR).

1.3 Bacterial Nitric Oxide Reductase (NorBC)

Denitrifying NO reductases (NOR) are integral membrane protein complexes in case of which there are no crystal structures available yet. However, careful analysis of the protein sequences of bacterial NORs from different organisms has shown that these enzymes are closely related to the respiratory heme-copper oxidases, the so-called cytochrome c oxidases (CCO).[7] Spectroscopic investigations further supported this proposal.[8] For example, Cheesman and coworkers used magnetic circular dichroism (MCD) and EPR spectroscopy to show that *Pseudomonas stutzeri* NorBC is structurally related to the CCO's.[8a] Therefore, the CCO's serve as structural models for the NorBC enzymes. Note that it is known that CCO's can reduce NO to N_2O, but at rates several orders of magnitude lower than for NorBC's.[9] It has also been reported that NorBC from P. *denitrificans* is able to reduce dioxygen to water.[9c] Several crystal structures are known for CCO's. The mitochondrial cytochrom c oxidase structure is shown in Figure 1.1, which consists of a binuclear active site.[10] The heme a_3 center is five-coordinate with axial histidine coordination, and the so-called Cu_B center is coordinated by three histidines. Correspondingly, the NorB subunit of NorBC comprises one high-spin heme b with axial histidine coordination, and one non-heme iron with three histidines coordinated, which is known as Fe_B in analogy to Cu_B in CCO.

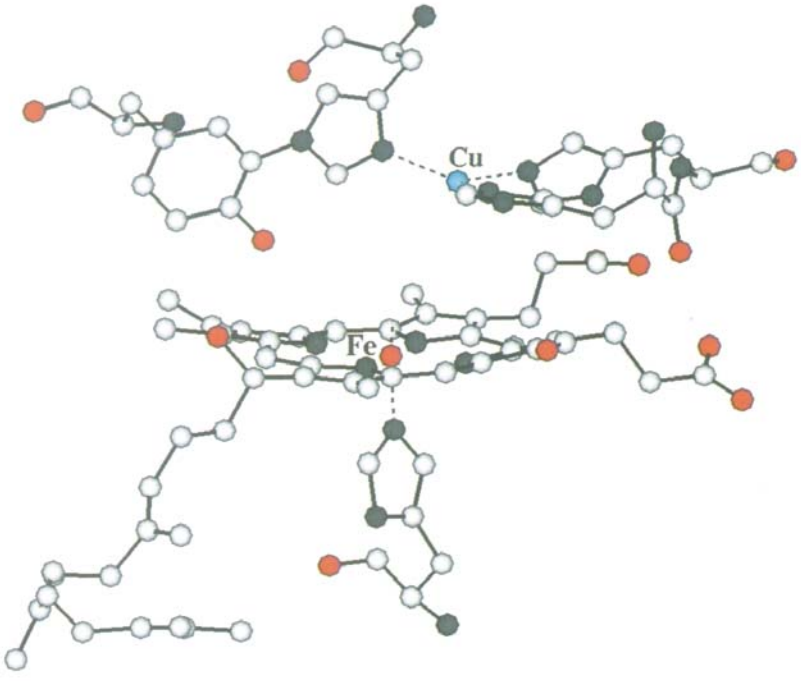

Figure 1.1. Crystal structure of the active site of mitochondrial cytochrom c oxidase (from ref[10]).

In order to model the NorBC active site, the distance between the heme b and Fe_B center is of critical importance. The distance between the Fe a_3 and the Cu_B center in oxidized bovine heart cytochrome c oxidase is 4.5 Å from crystal structure determinations.[11] The distance between the ferric iron atoms in NorBC has been estimated at 3.5 Å in the resting state of the enzyme, due to a μ-oxo bridge between the iron centers.[12]

The mechanism of NO reduction by NorBC can be divided into four steps: the initial coordination of NO at the diiron site, the formation of the N-N bond, the cleavage of the N-O bond and the release of nitrous oxide. In the catalytically active state of NorBC, both the heme and the non-heme iron are in the ferrous oxidation state. For the coordination of NO and the formation of the N-N bond, three possible mechanisms have been proposed: (a) the *trans* mechanism, (b) the *cis*-Fe_B mechanism and (c) the *cis*-heme b_3 mechanism:

(a) *trans* mechanism: Figure 1.2 shows the important steps of NO reduction proposed for the *trans* mechanism by deVries and coworkers from steady-state kinetic data of NorBC.[17] In the first step, the binding of two NO molecules to both the ferrous heme b_3 and the non-heme center are proposed to form an iron-nitrosyl dimer intermediate. EPR signals that can be interpreted as $Fe(II)_B$-NO as well as Fe(II)-heme b_3-NO have been reported for the enzyme under turnover.[8c,13] In addition, the characterization of an $(FeCO)_2$ heme/non-heme dicarbonyl complex from binding studies of ferrous NorBC suggests a binding of NO to both the heme and the non-heme center in the first step.[14] In the next step, radical coupling of the two nitrogen atoms of NO leads to a metal bound hyponitrite ($N_2O_2^{2-}$) species (Fe-N_2O_2-Fe), which decomposes yielding N_2O and the ferric μ-oxo bridged dimer. Note that the only intermediate of this mechanism, which has been identified so far, is the ferric μ-oxo bridged dimer.[15]

However, the biggest problem with this *trans* mechanism is the large stability of the Fe(II)-heme b_3-NO complex. Ferrous heme nitrosyls are known as 'dead-end' of enzyme activity due to the high affinity of NO for ferrous hemes, which is reflected by both a fast on and a slow off rate (vide infra).[16]

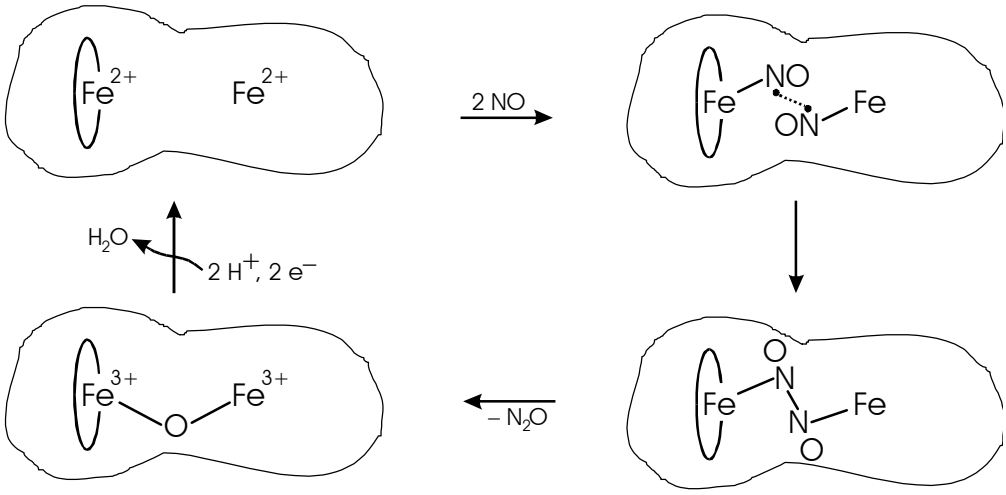

Figure 1.2. Proposed *trans* mechanism of NorBC by deVries and coworkers.[17]

(b) *cis*-Fe_B mechanism: Here, NO is reduced exclusively at the Fe_B center. Therefore, the role of the heme iron would be limited to electron transfer and to stabilize the resting state of the enzyme, which corresponds to the μ-oxo dimer complex (vide supra). A corresponding mechanism was proposed for the reaction of NO with catalytically active CCO, where two molecules of NO seem to bind to the Cu_B center.[18] Note that this mechanism does not include the formation of a stable ferrous heme nitrosyl species (vide infra).

(c) *cis*-heme b_3 mechanism: In this case, the transformation of NO to N_2O is proposed to be performed only by the heme iron b_3. An example for this mechanism is P450nor (vide infra). Note that the *cis*-heme b_3 mechanism includes again the formation of stable Fe(II)-NO species (vide infra).

However, these three mechanisms have to be considered speculative and more studies on both enzymes and model complexes are necessary to understand the complicated mechanism of the reduction of NO to N_2O catalyzed by NorBC.

1.4 Fungal Nitric Oxide Reductase (P450nor)

Nitric oxide reductase (P450nor) is involved in the fungal denitrification process and catalyzes the reduction of NO to N_2O according to equation 3. Note that P450nor uses NADH directly for the reduction of NO.

$$2\ NO + NADH + H^+ \rightarrow N_2O + NAD^+ + H_2O \quad (3)$$

For P450nor, crystal structures were determined for the enzyme from the fungus *Fusarium oxysporum*. The ferric NO form of wild type (WT) fungal NOR (cf. Figure 1.3) shows a single heme center with axial cysteine coordination.[19] The crystal structure shows a bent Fe-N-O unit with an angle of 161 °. Importantly, ferric heme nitrosyls with *trans* imidazole or pyridine donor ligands have linear Fe-N-O units,[20] whereas thiolate coordination leads to a bent structure. It was not clear whether this is due to electronic or steric effects.[21] Recently, Xu et al. published the first X-ray structural characterization of the ferric nitrosyl heme thiolate model complex [Fe(OEP)(NO){S-2,6-$(CF_3CONH)_2C_6H_3$}] (**1**) (OEP = octaethylporphyrin).[22] Importantly, the Fe-N-O unit is again bent with an angle of 160°, which demonstrates an intrinsic bending of the Fe-N-O moiety *due to electronic effects*. Therefore, we explored the effect of the *trans* thiolate coordination on the Fe-N-O moiety, which is of critical importance for the role of thiolate for the function of the proteins. These results are comprised in Chapter 6 of this thesis.

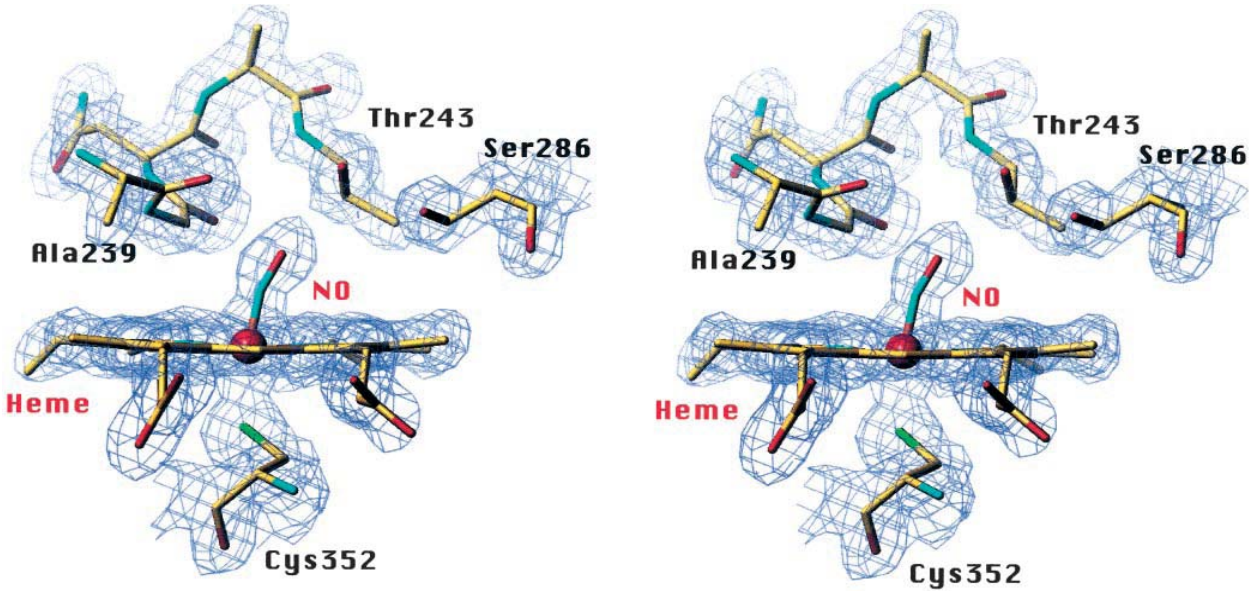

Figure 1.3. Stereo view of the heme iron-NO coordination geometry of the WT fungal NOR in the ferric NO state (from ref[19b]).

It has been shown that the ferric form of P450nor is catalytically active.[23] In addition, EPR studies by Shiro and coworkers showed that a mixture of a low-spin form, which is six-coordinate due to coordination of water, and a five-coordinate high-spin form coexist in the active form of P450nor.[24] However, the coordination of NO leads to a diamagnetic, low-spin Fe(III)-NO adduct. Then, two-electron reduction by NADH follows, leading to the so-called intermediate *I*, which was initially identified by Shiro and coworkers based on stopped-flow kinetic data.[25] After addition of NADH to the ferric P450nor-NO adduct, the 431nm band of the Fe(III)-NO complex decreases and at the same time, a new band at 444 nm occurs, which has been assigned to intermediate *I*. Shiro and coworkers proposed that intermediate *I* corresponds to an Fe(I)-NO or Fe(II)-NO^- complex,[25] which does not seem to undergo deuterium exchange indicating that intermediate *I* is not protonated.[26] Intermediate *I* reacts then with a second molecule of NO to form N_2O and water. However, there is some doubt about how the electron transfer from NADH to the active site takes place. Therefore, another mechanism was proposed by Daiber et al.,[27] which is schematically shown in Figure 1.4. In this case, hydride transfer to the NO group bound to the ferric heme is postulated generating an Fe(II)-(HNO) species. For the hydride transfer, it is expected that NADH binds close to the Fe(III)-NO at the distal side with respect to the thiolate.

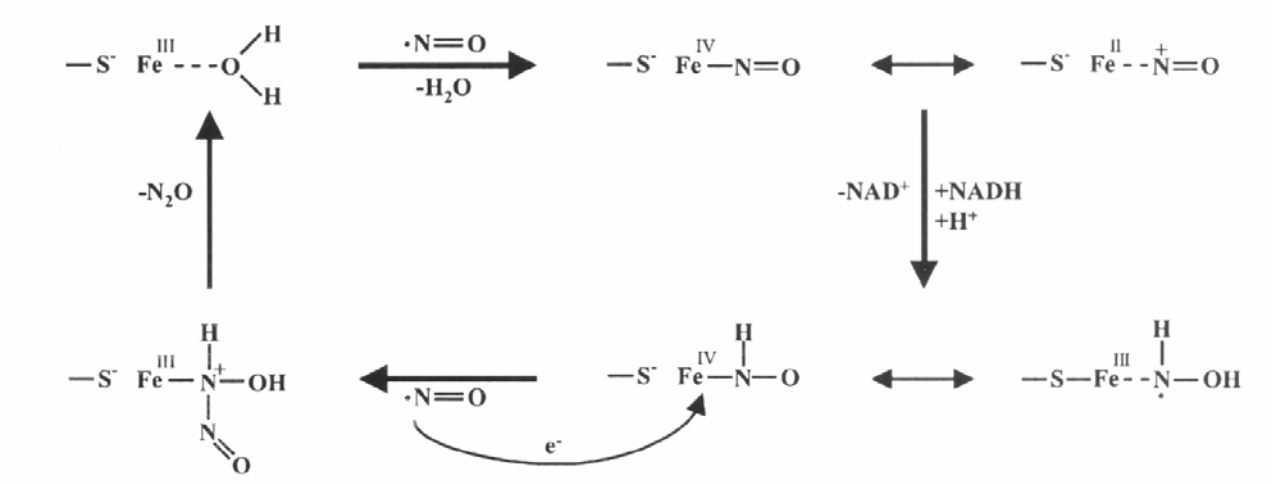

Figure 1.4. Mechanism of P450nor by Daiber et al.[27]

In a chemical approach, NADH has been replaced by sodium borohydride forming an intermediate again absorbing around 444 nm, which indicates that a hydride transfer takes place during the formation of this species.[27a] In addition, our results from DFT calculations on corresponding model complexes, comprised in Chapter 7, further support the direct hydride transfer.[28] The electronic structure of this intermediate has been proposed as either Fe(III) with a bound N(H)-OH radical (doubly protonated) or Fe(IV) with bound HNO and a cysteinyl radical (singly protonated). However, not much is known about intermediate *I*. Finally, another molecule of NO reacts with intermediate *I* leading to N_2O and water.

1.5 Comparison of Ferric and Ferrous Heme NO Adducts

As mentioned earlier in this Chapter, various functions in the chemistry of nitric oxide in biology are mediated by heme proteins. Importantly, the individual functions are highly dependent on the oxidation state of iron. In the Enemark and Feltham notation, ferrous heme NO adducts are denoted $\{FeNO\}^7$ and ferric heme NO adducts $\{FeNO\}^6$, respectively.[29] This electron counting system has been used to predict MNO (M = metal) geometries in general ($\{MNO\}^n$).[30] In mononitrosyls, the number of electrons *n* is simply the sum of metal d-electrons plus the electron in the π* orbital of NO. For $\{MNO\}^6$ systems the M-N-O unit is predicted to be linear, whereas for $\{MNO\}^7$ a bent structure is predicted.

Ferrous and ferric hemes have very different properties. The occurrence of ferric or ferrous hemes is closely related to the individual functions of the enzymes, due to the much smaller affinity to NO of ferric hemes compared to ferrous hemes. Note that the rates of NO loss are approximately 4-8 orders of magnitude smaller in ferrous hemes.[31] For example, for hemoglobin in the ferrous state (R-state), the on rate is $2 \cdot 10^7$ M^{-1} s^{-1} and the off rate is $1.8 \cdot 10^{-5}$ s^{-1},[32a] whereas in the ferric state the on rate is $4 \cdot 10^3$ M^{-1} s^{-1} and the off rate is 1 s^{-1}, respectively.[32b] This is also the reason why ferrous heme NO adducts have been referred to as a 'dead end' of protein activity. Note that non-heme iron complexes have a significantly lower affinity for NO than heme proteins.[31a] In addition, NO has a strong *trans* effect. For example, NO can dissociate the *trans* ligand in heme proteins and therefore, can destabilize the binding of the heme to the protein. Hence, in guanylate cyclase, binding of NO displaces the proximal histidine ligand and is therefore frequently purified without the heme cofactor.[31a] The effect that NO binding leads to the dissociation of the *trans* axial ligand forming the 5-coordinate heme-NO adduct is also known

in the literature as negative *trans* effect.[33] Correspondingly, coordination of a ligand (L) *trans* to NO can lead to NO loss forming the corresponding five-coordinate NO free species with L in axial position. Binding studies on ferrous heme model complexes performed in our group lead to the same result.[34] In this case, excess base (pyridine or imidazole) lead to denitrosylation, forming the six-coordinate bis-base complex. In biology, this mechanism constitutes one possibility how NO can be removed from ferrous hemes. Changing the protein structure can force a ligand (for example histidine) to bind *trans* to NO and therefore, induce the loss of NO from the active site.

Ferric heme nitrosyl adducts are very important and occur as intermediates or as enzyme-product complexes in a number of enzymes, such as Nitrophorins (Np), cytochrome cd_1 nitrite reductase, nitric oxide synthase (NOS) and fungal nitric oxide reductase (P450nor). However, the synthesis and spectroscopic characterization of ferric heme nitrosyl model complexes is challenging due to the low affinity of Fe(III) towards NO and the high instability of the corresponding Fe(III)-NO adducts. In particular, *trans* thiolate coordinated ferric heme nitrosyls are extremely unstable, which is reflected by the small number of publications on these systems (see also Chapter 6). Due to the importance of ferric hemes and their NO adducts in biology, and the lack of model complex studies on these systems, this thesis focuses mostly on ferric heme model complexes and their reaction with nitric oxide.

References

[1] Culotta, E.; Koshland, D. E. *Science* **1992**, *258*, 1862-1865.
[2] (a) Moncada, S.; Palmer, R. M.; Higgs, E. A. *Pharmacol. Rev.* **1991**, *43*, 109-142. (b) Snyder, S. H. *Science* **1992**, *257*, 494-496. (c) Butler, A. R.; Williams, D. L. H. *Chem. Soc. Revs.* **1993**, 233-241. (d) Bredt, D. S.; Snyder, S. H. *Annu. Rev. Biochem.* **1994**, *63*, 175-195. (e) Lancaster, J. R., Jr.; in: Encyclopedia of Inorganic Chemistry, Bruce, R. B., Ed., Wiley: Chichester, 1994. (f) *Methods in Nitric Oxide Research*; Feelisch, M.; Stamler, J. S., Eds.; Wiley: Chichester, 1996. (g) Cooper, C. E. *Biochim. Biophys. Acta* **1999**, *1411*, 290-309.
[3] Snyder, S. H.; Bredt, D. S. *Spektrum der Wissenschaft* **1992**, *Juli*, 72-80.
[4] (a) Stuehr, D. J. *Annu. Rev. Pharmacol. Toxicol.* **1997**, *37*, 339-359. (b) Poulos, T. L.; Li, H.; Raman, C. S. *Curr. Opin. Chem. Biol.* **1999**, *3*, 131-137. (c) Li, H.; Poulos, T. L. *J. Inorg. Biochem.* **2005**, *99*, 293-305. (d) Rousseau, D. L.; Li, D.; Couture, M.; Yeh, S.-R. *J. Inorg. Biochem.* **2005**, *99*, 306-323.
[5] (a) Garbers, D. L.; Lowe, D. G. *J. Biol. Chem.* **1994**, *269*, 30741-30744. (b) Zhao, Y.; Hoganson, C.; Babcock, G. T.; Marletta, M. A. *Biochemistry* **1998**, *37*, 12458-12464. (c) Karow, D. S.; Pan, D.; Tran, R.; Pellicena, P.; Presley, A.; Mathies, R. A.; Marletta, M. A. *Biochemistry* **2004**, *43*, 10203-10211. (d) Gilles-Gonzalez, M.-A.; Gonzales, G. *J. Inorg. Biochem.* **2005**, *99*, 1-22. (e) Ballou, D. P.; Zhao, Y.; Brandish, P. E.; Marletta, M. A. *Proc. Natl. Acad. Sci. USA* **2002**, *99*, 12097-12101.
[6] (a) Ribeiro, J. M. C.; Hazzard, J. M. H.; Nussenzveig, R. H.; Champagne, D. E.; Walker, F. A. *Science* **1993**, *260*, 539-541. (b) Ding, X. D.; Weichsel, A.; Andersen, J. F.; Shokhireva, T. K.; Balfour, C.; Pierik, A. J.; Averill, B. A.;

Montfort, W. R.; Walker, F. A. *J. Am. Chem. Soc.* **1999**, *121*, 128-138. (c) Walker, F. A. *J. Inorg. Biochem.* **2005**, *99*, 216-236.
[7] (a) van der Oost, J.; de Boer, A. P. N.; de Gier, J.-W. L.; Zumft, W. G.; Stouthamer, A. H.; van Spanning, R. J. M. *FEMS Microbiol. Lett.* **1994**, *121*, 1-10. (b) Saraste, M.; Castresana, J. *FEBS Lett.* **1994**, *341*, 1-4. (c) Arai, H.; Igarashi, Y.; Kodama, T. *Biochim. Biophys. Acta* **1995**, *1261*, 279-284. (d) de Boer, A. P. N.; van der Oost, J.; Reijnders, W. N. M.; Westerhoff, H. V.; Stouthamer, A. H.; van Spanning, R. J. M. *Eur. J. Biochem.* **1996**, *242*, 592-600.
[8] (a) Cheesman, M. R.; Zumft, W. G.; Thomson, A. J. *Biochemistry* **1998**, *37*, 3994-4000. (b) Moënne-Loccoz, P.; de Vries, S. *J. Am. Chem. Soc.* **1998**, *120*, 5147-5152. (c) Hendriks, J.; Warne, A.; Gohlke, U.; Haltia, T.; Ludovici, C.; Lübben, M.; Saraste, M. *Biochemistry* **1998**, *37*, 13102-13109.
[9] (a) Heiss, B.; Frunzke, K; Zumft, W. G. *J. Bacteriol.* **1989**, *171*, 3288-3297. (b) Kastrau, D. H.; Heiss, B.; Kroneck, P. M. H.; Zumft, W. G. *Eur. J. Biochem.* **1994**, *222*, 293-303. (c) Fujiwara, T.; Fukumori, Y. *J. Bacteriol.* **1996**, *178*, 1866-1871. (d) Brudvig, G. W.; Stevens, T. H.; Chan, S. I. *Biochemistry* **1980**, *19*, 5275-5285.
[10] Yoshikawa, S.; Shinzawa-Itoh, K.; Yamashita, E.; Tsukihara, T. *Mitochondrial cytochrome c oxidase*; Wiley: Chichester, England, 2001; Vol. 1.
[11] Tsukihara, T.; Aoyama, H.; Yamashita, E.; Tomizaki, T.; Yamaguchi, H.; Shinzawa-Itoh, K.; Nakashima, R.; Yaono, R.; Yoshikawa, S. *Science* **1995**, *269*, 1069-1074.
[12] Zumft, W. G. *J. Inorg. Biochem.* **2005**, *99*, 194-215.
[13] Sakurai, T.; Sakurai, N.; Matsumoto, H.; Hirota, S.; Yamauchi, O. *Biochem. Biophys. Res. Commun.* **1998**, *251*, 248-251.
[14] Lu Suharti, S.; de Vries, S.; Moënne-Loccoz, P. *J. Am. Chem. Soc.* **2004**, *126*, 15332-15333.
[15] (a) Martens, C. F.; Murthy, N. N.; Obias, H. V.; Karlin, K. D. *Chem. Commun.* **1996**, 629-630. (b) Moënne-Loccoz, P.; Richter, O.-M. H.; Huang, H.; Wasser, I. M.; Ghiladi, R. A.; Karlin, K. D.; de Vries, S. *J. Am. Chem. Soc.* **2000**, *122*, 9344-9345.
[16] Cooper, C. E. *Biochim. Biophys. Acta* **1999**, *1411*, 290-309.
[17] Girsch, P.; de Vries, S. *Biochim. Biophys. Acta* **1997**, *1318*, 202-216.
[18] (a) Butler, C. S.; Seward, H. E.; Greenwood, C.; Thomson, A. J. *Biochemistry* **1997**, *36*, 16259-16266. (b) Watmough, N. J.; Cheesman, M. R.; Butler, C. S.; Little, R. H.; Greenwood, C.; Thomson, A. J. *J. Bioenerg. Biomemb.* **1998**, *30*, 55-62.
[19] (a) Park, S.-Y.; Shimizu, H.; Adachi, S.; Nagagawa, A.; Tanaka, I.; Nakahara, K.; Shoun, H.; Obayashi, E.; Nakamura, H.; Iizuka, T.; Shiro, Y. *Nat. Struct. Biol.* **1997**, *4*, 827-832. (b) Shimizu, H.; Park, S.-Y.; Gomi, Y.; Arakawa, H.; Nakamura, H.; Adachi, S.-I.; Obayashi, E.; Iizuka, T.; Shoun, H.; Shiro, Y. *J. Biol. Chem.* **2000**, *275*, 4816-4826. (c) Shimizu, H.; Park, S.-Y.; Shiro, Y.; Adachi, S.-I. *Acta Crystallogr. D* **2002**, *D58*, 81-89.
[20] Linder, D. P.; Rodgers, K. R. *Inorg. Chem.* **2005**, *44*, 1367.
[21] (a) Pant, K.; Crane, B. R. *Biochemistry* **2006**, *45*, 2537-2544. (b) Shimizu, H.; Obayashi, E.; Gomi, Y.; Arakawa, H.; Park, S.-Y.; Nakamura, H.;Adachi, S.-i.; Shoun, H.; Shiro, Y. *J. Biol. Chem.* **2000**, *275*, 4816-4826.
[22] Xu, N.; Powell, D. R.; Cheng, L.; Richter-Addo, G. B. *Chem. Comm.* **2006**, 2030-2032.
[23] (a) Nakahara, K.; Tanimoto, T.; Hatano, K.; Usuda, K.; Shoun, H. *J. Biol. Chem.* **1993**, *268*, 8350-8355. (b) Shiro, Y.; Fujii, M.; Iizuka, T.; Adachi, S.; Tsukamoto, K.; Nakahara, K.; Shoun, H. *J. Biol. Chem.* **1995**, *270*, 1617-1623.
[24] (a) Shiro, Y.; Fujii, M.; Isogai, Y.; Adachi, S.; Iizuka, T.; Obayashi, E.; Makino, R.; Nakahara, K.; Shoun, H. *Biochemistry* **1995**, *34*, 9052-9058. (b) Obayashi, E.; Tsukamoto, K.; Adachi, S.; Takahashi, S.; Nomura, M.; Iizuka, T.; Shoun, H.; Shiro, Y. *J. Am. Chem. Soc.* **1997**, *119*, 7807-7816.
[25] Shiro, Y.; Fujii, M.; Iizuka, T.; Adachi, S.; Tsukamoto, K.; Nakahara, K.; Shoun, H. *J. Biol. Chem.* **1995**, *270*, 1617-1623.
[26] Farmer, P. J.; Sulc, F. *J. Inorg. Biochem.* **2005**, *99*, 166-184.
[27] (a) Daiber, A.; Nauser, T.; Takaya, N.; Kudo, P.; Weber, P.; Hultschig, C.; Shoun, H.; Ullrich, V. *J. Inorg. Biol. Chem.* **2002**, *88*, 343-352. (b) Daiber, A.; Shoun, H.; Ulrich, V. *J. Inorg. Biochem.* **2005**, *99*, 185-193.
[28] Lehnert, N.; Praneeth, V. K. K.; Paulat, F. *J. Comput. Chem.* **2006**, *27*, 1338-1351.
[29] Enemark, J. H.; Feltham, R. D. *Coord. Chem. Rev.* **1974**, *13*, 339.
[30] Wyllie, G. R. A.; Scheidt, W. R. *Chem. Rev.* **2002**, *102*, 1067-1089.
[31] (a) Cooper, C. E. *Biochim. Biophys. Acta* **1999**, *1411*, 290-309. (b) Ford, P. C.; Laverman, L. E. *Coord. Chem. Rev.* **2005**, *249*, 391-403.
[32] (a) Cassoly, R.; Gibson, Q. H. *J. Mol. Biol.* **1975**, *91*, 301-313. (b) Sharma, V. S.; Traylor, T. G.; Gardiner, R.; Mizukami, H. *Biochemistry* **1987**, *26*, 3837-3843.
[33] Ohta, T.; Kitagawa, T. *Inorg. Chem.* **2005**, *44*, 758-769.
[34] Praneeth, V. K. K.; Näther, C.; Peters, G.; Lehnert, N. *Inorg. Chem.* **2006**, *45*, 2795-2811.

2 Overview

In this thesis, ferric heme model complexes and their reaction with nitric oxide (NO) are investigated. The results presented here are important for the understanding of the individual mechanisms of the corresponding enzymes, but also for the in-depth characterization of these transition metal complexes themselves. These model complexes are relevant for a number of enzymes, such as fungal nitric oxide reductase, nitric oxide synthase, cytochrome cd_1 nitrite reductase, nitrophorins, horseradish peroxidase, myoglobin and chloroperoxidase, and will be further introduced in the individual chapters, when applicable. These investigations comprise about 75 % of the work presented here. In addition, the syntheses of cofacial metalloporphyrin NO complexes, which serve as model complexes for the bacterial nitric oxide reductase, are developed. Finally, a variety of spectroscopic and theoretical investigations have been performed in collaborative projects, which are summarized at the end of this thesis.

Magnetic circular dichroism and resonance Raman spectroscopies are introduced in Chapter 3. In order to have unrestricted instrument time for measurements with these important techniques, we have built one MCD spectrometer in Kiel (C.A.U.) and another one in Ann Arbor (UM). In addition, one rRaman spectrometer has been built in Ann Arbor. Note that the MCD spectrometer in Kiel is only the third instrument in Germany in the area of chemistry. The first part of Chapter 3 gives a brief introduction of the theoretical backgrounds of these methods, and then presents details about the design and construction of the MCD instruments. In addition, important test results are also included in this chapter.

Magnetic circular dichroism (MCD) and resonance Raman (rRaman) are extremely powerful techniques to explore the properties of heme active sites in enzymes and of corresponding model complexes. However, the detailed interpretation of the obtained data is very complicated. Therefore, in order to explore the Raman and MCD spectroscopic properties of heme-nitrosyls, I have investigated five-coordinate model complexes of type [M(TPP)(Cl)] (M = Fe^{III}, Mn^{III} and Co^{III}; TPP = tetraphenylporphyrin) first using these techniques. The first part of Chapter 4 comprises the vibrational investigations, including rRaman spectroscopy, on these model complexes. The assignments of the nonresonance Raman and IR spectra of [M(TPP)(Cl)]

obtained from DFT calculations presented in my diploma thesis could be verified using polarized Raman spectroscopy. In addition, assignments of anomalous polarized bands, which correspond to A_{2g} vibrations (forbidden in nonresonance Raman in D_{4h}), were obtained from polarized rRaman spectroscopy. Note that ferric heme proteins and the corresponding model complex [Fe(TPP)(Cl)] exhibit similar UV-Vis and MCD spectra. Therefore, this complex is an excellent model for the five-coordinate high-spin ferric state of hemes. Since MCD is an extremely powerful method to investigate the electronic structures and spectra of paramagnetic transition metal complexes, MCD has been widely applied as a "fingerprinting" technique to a variety of ferric heme proteins. However, detailed assignments of the spectra are missing. Hence, complete assignments for the high-spin (hs) ferric [Fe(TPP)(Cl)] complex are reported for the first time in the second half of Chapter 4. These assignments are based on MCD data and their detailed analysis correlated to TD-DFT calculations. Importantly, polarizations of the electronic transitions observed in [Fe(TPP)(Cl)] have been obtained from fitting the VTVH magnetization isotherms. The assignments obtained form MCD are confirmed by other methods, especially rRaman (vide supra).

Chapter 5 deals with model systems for the bacterial nitric oxide reductase (NorBC). The active site of this enzyme consists of a mixed heme/non-heme center. Therefore, binuclear iron complexes are necessary to model NorBC. Besides model systems of the heme/non-heme type, binuclear porphyrin systems are of interest. Therefore, the synthesis of bis-porphyrin ligands in a cofacial geometry is elaborated here. In addition, the corresponding cobalt NO complex has been synthesized and investigated using IR, UV-Vis absortion and rRaman spectroscopy. The driving force behind this project is the question whether it is possible to reduce NO to N_2O using two hemes in a close geometry instead of a heme/non-heme type model complex. However, in order to investigate these systems in more detail, quantum-chemical calculations have been performed first. These calculations are summarized at the end of Chapter 5.

As mentioned in the Introduction, ferric heme nitrosyl adducts occur as intermediates or as enzyme-product complexes in a number of proteins, such as Nitrophorins (Np), cytochrome cd_1 nitrite reductase, nitric oxide synthase (NOS), and fungal nitric oxide reductase (P450nor), and therefore, play an important role in enzymology. The first part of Chapter 6 comprises the quantum-chemical investigations performed on model complexes for P450nor. The second part

of the Chapter (Section 6.3) deals with the synthesis and spectroscopic investigations on [Fe(OEP)(NO){S-2,6-$(CF_3CONH)_2C_6H_3$}] (**2H-NO**, OEP = octaethylporphyrin). This work has been conducted in collaboration with Prof. George B. Richter-Addo, Department of Chemistry and Biochemistry, University of Oklahoma, USA. In addition, I have performed a normal coordinate analysis (QCC-NCA) for **2H-NO**. These model complex studies are performed to explore (a) the electronic effect of the thiolate on the Fe-NO unit, (b) the effect of the NH---S hydrogen bond strength on the coordinated nitric oxide, (c) the instability of **2H-NO** and **1H-NO** (one NH---S hydrogen bond) in solution, (d) to determine the missing vibrational data, especially, the Fe-N(O) stretching vibration, and (e) to determine the N-O and Fe-N(O) force constants of the Fe-N-O unit. Finally, I have investigated the binding of NO to ferric hemes using potential energy surface (PES) calculations. These calculations are presented in the last section of Chapter 6. For this investigation, ferric heme model systems with axial 1-methylimidazole (MI) were used, because more experimental data for the N-donor coordinated systems compared to corresponding thiolate-bound species are available from the literature. These results provide insight into (a) the relative stabilities of Fe(II)-NO^+ vs. Fe(III)-NO(radical) electronic structures, (b) the NO to Fe(III) electron transfer upon coordination of NO, and (c) the surprisingly large Fe-NO force constant in ferric hemes.

In addition to these studies on ferric heme model complexes, a variety of collaborative investigations focusing on spectroscopic and theoretical studies of transition metal complexes have been performed during my Ph.D. The systems investigated include mononuclear and binuclear copper-diazene complexes (Raman measurements) and copper nitrosyl complexes (Raman and MCD measurements) in collaboration with Prof. Dr. Kiyoshi Fujisawa (University of Tsukuba, Japan), the twist-boat/half-chair conformer ratio in $[Fe^{III}(tmdta)]^-$ (Raman measurements) in collaboration with Dr. Roland Meier (Friedrich-Alexander Universität Erlangen-Nürnberg, Germany), and the N-N cleavage in Mo/W hydrazidium complexes with diphosphine coligands (PES calculations) in collaboration with Prof. Dr. Felix Tuczek (Christian-Albrechts-Universität zu Kiel, Germany). In addition, I have performed DFT calculations in order to investigate key intermediates of the catalytic cycle of P450nor. Most of the results have been published by our group recently, or are currently submitted for publication. These results are summarized in Chapter 7.

Finally, the key results obtained during my graduate research (Promotion) conducted between August, 2004 and September, 2007 are summarized in Chapter 8.

3 Material and Methods

Two MCD as well as one rRaman spectrometer have been built by myself and my supervisor, Prof. Dr. Nicolai Lehnert, during my graduation ("Promotion"). The first MCD spectrometer has been build for Prof. Dr. Felix Tuczek at the University of Kiel, Germany. Note that the construction plan for the MCD table has been elaborated during my diploma work and in addition, the installation of the cryostat was performed during that time.[1] The second MCD and the rRaman spectrometer have been built for Prof. Dr. Nicolai Lehnert at the University of Michigan, Ann Arbor, USA. Importantly, most of the MCD and rRaman data, presented in this thesis, have been obtained by using these instruments. As already mentioned above, rRaman and MCD spectroscopies are key techniques to explore the properties of heme active sites and of corresponding model complexes. The theoretical background of these spectroscopic techniques is summarized in the following.

3.1 Theoretical Background

This Section summarizes the theoretical background of both low-temperature Magnetic Circular Dichroism (MCD) and resonance Raman spectroscopies (rRaman), which are the key methods applied in this thesis.

3.1.1 Magnetic Circular Dichroism Spectroscopy

Magnetic Circular Dichroism (MCD) is an extremely powerful technique to investigate the electronic structures and spectra of paramagnetic transition metal complexes.[2] This technique has clear advantages compared to UV-Vis absorption spectroscopy, because of the much better resolution of electronic transitions, or EPR, because MCD is not restricted to non-integer spin systems.[3] In addition, the polarizations of the electronic bands are accessible by MCD in samples of randomly oriented molecules.

The theoretical background of MCD spectroscopy was developed by P. J. Stephens in the 1970's and has been summarized in a number of reviews and articles.[2a-d,2f,4] Recently, a review by Mack et al. has been published that summarizes the background of MCD spectroscopy and the application of this technique to porphyrinoids.[5] MCD spectroscopy measures the difference in

intensity of left (lcp) and right (rcp) circular polarized light. MCD intensity is proportional to three different contributions, designated as MCD **A**-, **B**- and **C**-terms (cf. equation 1).

$$I \sim \left[A_1 \left(\frac{-\partial f(E)}{\partial E} \right) + \left(B_0 + \frac{C_0}{kT} \right) f(E) \right] \cdot B \quad (1)$$

Here, I is the MCD intensity, T the temperature, B the magnetic field, and the function *f(E)* represents the band shape of an absorption band. Hence, **B**- and **C**-terms both show an absorption band shape in MCD, whereas the **A**-term corresponds to a signal with a derivative band shape. Importantly, the **A**- and **B**-terms are temperature independent, whereas MCD **C**-term intensity is temperature dependent. Therefore, the most important mechanism at low temperature is the **C**-term. From eqn. 1, MCD intensity increases linearly with the strength of the magnetic field. This strictly applies to the **A**- and **B**-terms.

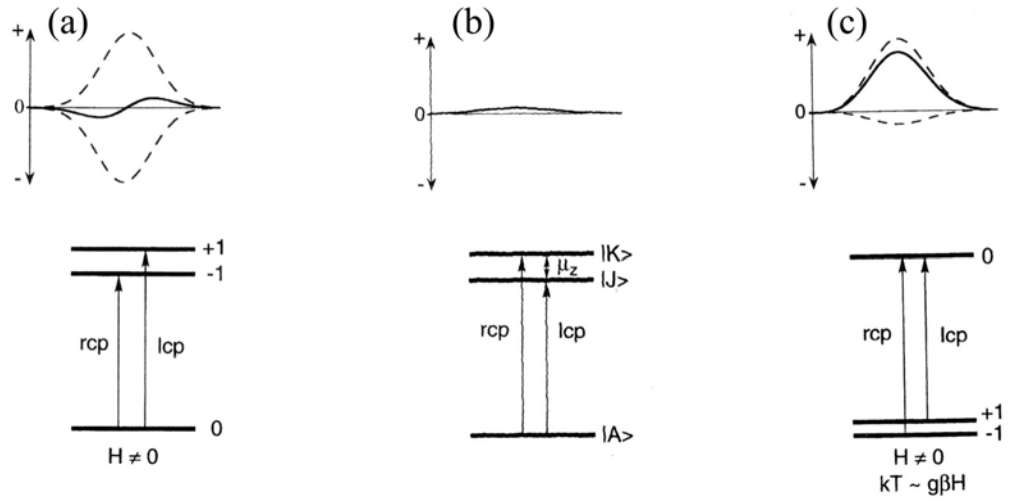

Figure 3.1. MCD mechanisms: (a) **A**-term, (b) **B**-term, and (c) **C**-term. Taken from ref.[6].

In order for **A**-term intensity to arise, the molecule must have degenerate excited states as shown in Figure 3.1. In the presence of a magnetic field the excited state is split due to the Zeeman effect. Since the Zeeman splitting is usually only of a few wavenumbers, the oppositely signed transitions for rcp and lcp light will almost cancel leading to a derivative band shape (cf. Figure 3.1a). Figure 3.1, b shows the origin of **B**-term MCD intensity. In this case, magnetic field induced mixing of the excited state |J> with an energetically close intermediate state |K> occurs. Alternatively, field-induced mixing is also possible between the ground state |A> and an intermediate state |K>. However, in both cases significant **B**-term intensity does only arise if |K>

is close in energy to either the excited state |J> or the ground state |A>. On the other hand, in the second case it is required that the energetic separation between |A> and |K> is large enough such that |K> is not thermally populated. Otherwise, this leads to **C**-term intensity. As already stated, **B**-term signals have an absorption band shape. Finally, the most important mechanism at low temperatures is the **C**-term. **C**-term intensity arises from a degenerate ground state, which is split in the magnetic field due to the Zeeman effect. In general, degenerate ground states are due to spin degeneracy and hence, *only paramagnetic compounds exhibit **C**-term signals*. Thus, **A**- and **C**-term MCD intensity requires either a degenerate excited state or a degenerate ground state. However, in the **C**-term case, a saturation of the signal is observed at very low temperature and high field (vide infra). At low temperatures, kT is in the order of the Zeeman splitting in the presence of a strong magnetic field, which leads to a larger population of the lower energy compared to the higher energy Zeeman sublevels of the ground state corresponding to the Boltzmann distribution. Hence, the intensities of the rcp and lcp transitions do not cancel anymore leading to an absorption band shape for the **C**-term. A further decrease of the temperature or an increase of the magnetic field results in an increase in the population of the lowest-energy sublevel and therefore, the **C**-term MCD intensity also increases. If the higher energy sublevels are completely depopulated, the **C**-term intensity reaches its maximum value (saturation limit). Importantly, *the temperature and magnetic field dependent **C**-term intensity contains the complete information of the properties of the ground state including g values and zero-field splitting (zfs) parameters as well as the polarizations of the electronic transitions*. The dependence of the MCD intensity on temperature and field is explored by the variable temperature variable field (VTVH) experiment. Here, the MCD **C**-term intensity at a given wavelength is plotted against βB/2kT (β_B the Bohr magneton, B the magnetic field, T the temperature, k the Boltzmann constant).

The VTVH data (cf. Chapter 4) can be fitted using the general method developed by Neese and Solomon.[2f] The analysis is based on the following equation (2):

$$\frac{\Delta\varepsilon}{E} = -\frac{\gamma}{4\cdot\pi}\int_{\theta}\int_{\phi}\tanh\left(\frac{g\beta_B B}{2kT}\right)\frac{\sin\theta}{g}\left(l_x^2 g_x M_{yz}^{eff} + l_y^2 g_y M_{xz}^{eff} + l_z^2 g_z M_{xy}^{eff}\right)d\theta d\phi \quad (2)$$

where $\Delta\varepsilon/E$ is the MCD intensity, M^{eff} are the effective transition dipole moment products (cf. equation 3), l the angular momentum, β_B the Bohr magneton, B the magnetic field, T the temperature, k the Boltzmann constant and g the ground-state g-values. Therefore, the shape of

the isotherms is related to the g-values of the system and the products of the relative polarizations. Note that spin-orbit coupling (SOC) must exist in the system in order for MCD **C**-term intensity to occur.[2f,7] SOC of the excited state |J> to another intermediate excited state |K> leads to mixing of the transition moment m_x^{AJ} of the excitation from the ground state |A> to the excited state |J> (x polarized) with the transition moment m_y^{AK} of the excitation from the ground state |A> to the excited state |K> (y polarized). This leads to equation 3 for the effective transition dipole moment products:

$$M_{xy}^{eff} = m_x^{AJ} \cdot m_y^{AK} \cdot \overline{L}_z^{KJ} \cdot \Delta_{KJ}^{-1} \quad (3),$$

where $\overline{L}_z^{KJ}$ corresponds to the matrix element for the SOC between |J> and |K> and $\Delta_{KJ}^{-1} = E_K - E_J$ is the energetic difference between |K> and |J>. Hence, for non-zero MCD intensity, two perpendicular transition dipole moments are needed and SOC coupling between the excited states has to be effective in the direction orthogonal to the plane formed by the two transition dipole moments (cf. equation 3). The SOC will be more efficient when the excited states are close in energy (Δ_{KJ}^{-1} small) and the SOC matrix elements are large. The individual polarizations of MCD bands can then be calculated using the M^{eff} values obtained from the fit of the VTVH saturation curves, using equation 4:

$$\%x = 100 \cdot \frac{\left(M_{xy}^{eff} \cdot M_{xz}^{eff}\right)^2}{\left(M_{xy}^{eff} \cdot M_{xz}^{eff}\right)^2 + \left(M_{xy}^{eff} \cdot M_{yz}^{eff}\right)^2 + \left(M_{xz}^{eff} \cdot M_{yz}^{eff}\right)^2} \quad (4)$$

The calculation of the y- and z-polarizations can be performed correspondingly.

MCD spectra are usually measured in [θ] = mdeg and can be converted to Δε [M^{-1} T^{-1} cm^{-1}] using the conversion factor Δε = θ / (32980*c*d), where c is the concentration and d the thickness of the sample (path length). Importantly, the product c*d can be substituted by $A_{MCD}/\varepsilon_{UV\text{-}Vis}$, where A is the absorbance of the sample measured by the CD spectrometer. This is of particular importance, since it is difficult to determine d for polymer films, which were used here (cf. Chapter 4).

3.1.2 Resonance Raman Spectroscopy

Vibrational spectroscopy is a very valuable method to gain insight into the electronic structures of metalloporphyrins. Especially heme proteins which contain iron porphyrins as prosthetic groups have been studied in detail and information about the properties of their heme cofactors have been obtained due to the sensitivity of vibrational frequencies to changes in oxidation state, coordination number, and spin state.[8,9] Hemes occur in many different proteins as active sites and have been characterized by all kinds of spectroscopic methods. Among these, Resonance Raman (rRaman) spectroscopy has always played a key role. Resonance Raman selectively enhances vibrational modes of the absorbing chromophore whereas the remaining vibrational modes in the molecule (protein) are suppressed.[10,11,12] This way, rRaman spectra of a heme chromophore can selectively be obtained even in a large molecule (protein) where many other vibrations are present. From the vibrational energies as well as the nature of the enhanced modes, information about the geometric and electronic properties of the heme as well as its environment can be obtained.[8,12] Besides the investigation of metalloporphyrins in biological systems, synthetic porphyrin model complexes have widely been studied to gain insight into the catalytic reactions or functions performed by heme proteins.[13]

A resonance Raman spectrometer was built by myself and my supervisor, Prof. Dr. Nicolai Lehnert, at the University of Michigan, Ann Arbor, USA. A schematic drawing of the setup is shown in Figure 3.2. The original design was elaborated by Dr. Renée Dillinger and Prof. Dr. Felix Tuczek.[14]

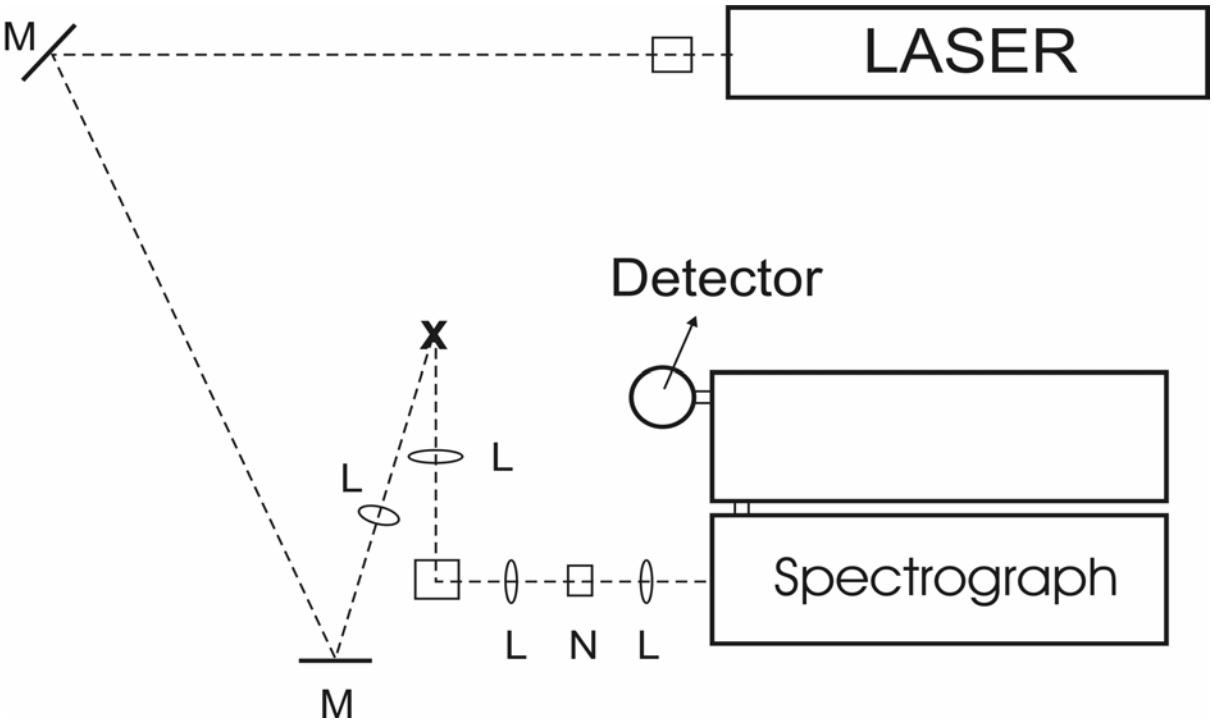

Figure 3.2. Resonance Raman assembly built in Ann Arbor, USA (M = mirror, L = lens, N = notch filter).

The laser light source of the rRaman spectrometer in the Lehnert laboratory corresponds to the Argon/Krypton ion mixed gas laser BeamLok 2060 from Spectra-Physics. The main excitation energies (power > 100 mW) accessible with the BeamLok 2060 are 647.1, 568.2, (530.9), 514.5, 488.0, (476.5), 457.9, 413.1, (406.7) and 351.0 nm. Both Notch and interference filters are available in the Lehnert laboratory for all lines except the ones in parentheses. After passing through mirrors, the interference filter, etc. the beam is focussed on the sample, the position of which is indicated as 'x' in Figure 3.2. The sample is placed in a dewar (EPR cold-finger dewar), which is cooled with liquid nitrogen. The scattered light is then collected by another lens and redirected in a 90° geometry using a beam stirrer (square box in Figure 3.2). The scattered light is then collimated, the Raleigh light is blocked using a Notch filter ('N' in Figure 3.2) and finally, the remaining light is focussed on the monochromator entrance slit. The monochromator corresponds to a PI Acton TriVista DM55 double monochromator with an attached SPEC 10 400B LN CCD detector (1340x400 pixel, back-illuminated CCD, liquid nitrogen cooled) from Princeton Instruments (now PI Acton).

The first experimental study of inelastic light scattering was reported in 1928 by Raman and Krishnan.[15] Raman and Krishnan observed the inelastic light scattering in water and alcohol vapors. Until the 1960s Raman spectroscopy did not play an important role in science, simply because no intense monochromatic light source was available. But with the invention of the laser as an intense, monochromatic light source, Raman spectroscopy became an important spectroscopic method. Today, powerful, sensitive CCD cameras (CCD = charge coupled device), better monochromators, and holographic notch filter are also available.

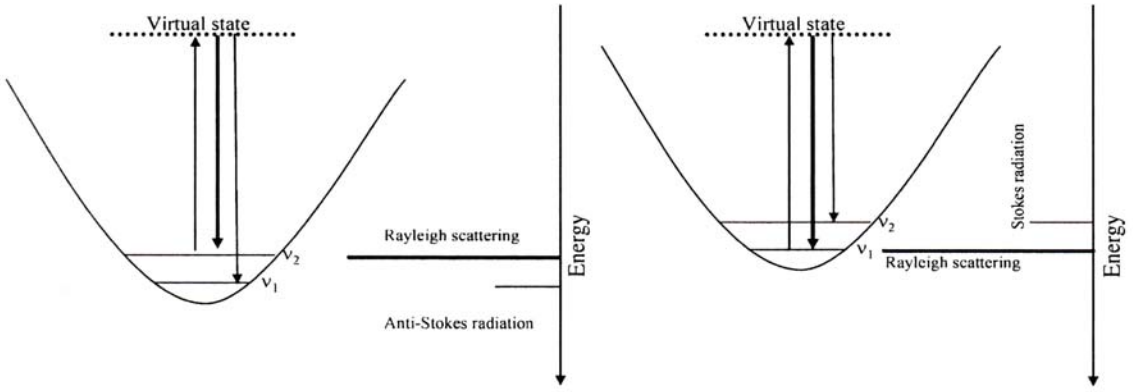

Figure 3.3. Nonresonance Raman spectroscopy: Anti-Stokes, Rayleigh- and Stokes scattering

As already mentioned above, inelastic light scattering is of very weak intensity. Most of the incident light either passes through the sample unscattered, or is absorbed by the sample. A small fraction is elastically scattered, which means that the scattered light has the same energy (frequency) as the incident light (Rayleigh scattering). A much smaller fraction is inelastically scattered (Raman scattering). The principles of nonresonance Raman scattering are illustrated in Figure 3.3. Note that Raman scattering corresponds to a two-photon process. The molecules are excited from the ground state into a virtual excited state and then return into lower (Anti-Stokes) or higher vibrational states (Stokes) of the ground state accompanied by light emission (cf. Figure 3.3). As evident from Figure 3.3, the energy difference between the incident light (Rayleigh) and the inelastically scattered light corresponds to the vibrational frequencies of the molecule. In general, Stokes scattering is more intense than Anti-Stokes scattering due to a Boltzmann population over the vibrational states of the electronic ground state. At very low temperatures, where all molecules occupy the vibrational ground state, the Anti-Stokes scattering disappears.

If the wavelength of the incident light is resonant (of the same energy) with an electronic transition of the molecule, then the Raman scattering may be enhanced by several orders of magnitude, depending on the nature of the excited state and the individual vibrations. The molecular origin of the resonance Raman phenomenon is illustrated in Figure 3.4 for Stokes scattering.

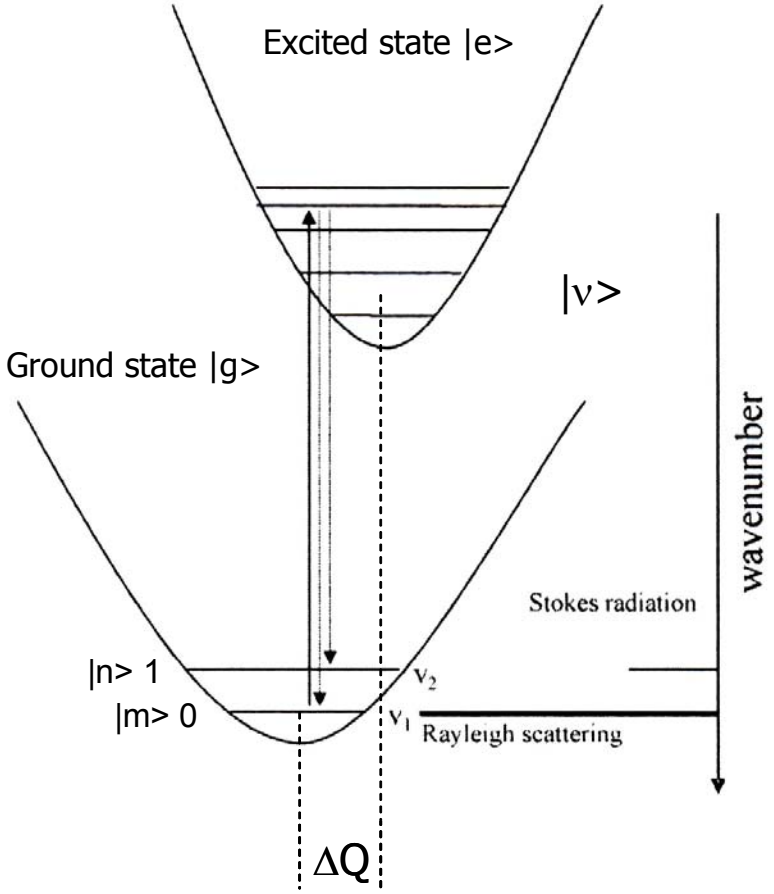

Figure 3.4. Illustration of the resonance Raman effect. ΔQ is the excited state displacement.

In this case, molecules are enhanced from the vibronic ground state |i> (|i> = |g> |m>) into the excited vibronic state |f> (|f> = |e> |ν>) of the resonant excited electronic state |e>. The de-excitation leads to Rayleigh, Stokes or Anti-Stokes scattering (vide supra). Note that the intensity of Raman light is proportional to α^2 (α: polarizability). The following equations were derived by Andreas C. Albrecht using the Herzberg-Teller formalism of vibronic coupling.[16] Albrecht derived equations for the three mechanisms for Raman intensity, the so-called ***A***-, ***B***- and ***C***-terms. Here, the essential results are given and their application to metalloporphyrins is explained. The ***A***-term is given by equation 5:

$$A = \sum_{\upsilon} \frac{\langle e|\mu|g\rangle^2 \cdot \langle m|\upsilon\rangle \cdot \langle \upsilon|n\rangle}{E_{e,\upsilon} - E_{g,m} - E_0 + i\Gamma} \qquad (5),$$

where E_0 is the energy of the incident light, $E_{e,n} - E_{g,m}$ is the energy separation of the vibronic ground state |i> and the resonant excited state |f>, and $i\Gamma$ a damping factor. The ***A***-term intensity is large if $E_{e,n} - E_{g,m} \approx E_0$, which means that the incident light is resonant with the vibronic transition (vide supra). From equation 5, ***A***-term intensity is proportional to the square of the transition dipole moment $\langle e|\mu|g\rangle$ and linearly dependent on the vibrational overlap integrals $\langle m|\upsilon\rangle$ and $\langle \upsilon|n\rangle$, the so-called Franck-Condon factors. Therefore, ***A***-term enhancement is dominant in the case of intense electronic transitions (dipole allowed). Importantly, for the Franck-Condon factors to be non-zero, a displacement of the potential curves along the normal coordinate Q ($\Delta Q > 0$) has to be present, which in general only occurs for totally-symmetric modes.

The ***B***-term enhancement mechanism is given by equation 6:

$$B = \sum_{\upsilon} \left[D_{\upsilon} \cdot \sum_{s} \sum_{j} \frac{\langle e|h_j|s\rangle}{\Delta E_{e,s}} \cdot \left(\begin{array}{l} \langle e|\mu|g\rangle \cdot \langle s|\mu|g\rangle \cdot \langle n|\upsilon\rangle \cdot \langle \upsilon|Q_j|m\rangle \\ + \langle e|\mu|g\rangle \cdot \langle s|\mu|g\rangle \cdot \langle m|\upsilon\rangle \cdot \langle \upsilon|Q_j|n\rangle \end{array} \right) \right] \qquad (6),$$

$$\text{with } D_{\upsilon} = \left(\frac{1}{E_{e,\upsilon} - E_{g,m} - E_0 + i\Gamma} \right).$$

As evident from equation 6, ***B***-term enhancement arises from vibronic coupling of the resonant excited state |e> to another excited state |s> via the vibronic coupling integral $\langle e|h_j|s\rangle$. Another consequence of equation 6 is that both electric dipole moments for the transitions from the ground state to the resonant excited state |e> and to the other excited state |s> must be nonvanishing. Therefore, the corresponding excited states must belong to allowed electronic transitions. The $\langle \nu|Q_j|m,n\rangle$ integrals connect the vibrational levels of the electronic ground state |g> and the resonant excited state |e> that differ by one quantum number (see Scheme 3.1). If these integrals are multiplied with Franck-Condon factors having the same quantum numbers, the nominator does not vanish even if there is no excited state displacement. Hence, in general totally and non-totally symmetric modes are enhanced via the ***B***-term mechanism. But importantly, only

vibrations are enhanced that are effective in mixing the two excited states. Hence, since totally symmetric modes do not lead to a distortion of the molecule, they are ineffective in mixing these states, and therefore, only non-totally symmetric modes are enhanced via the ***B***-term mechanism.

Finally, the ***C***-term intensity is proportional to the $\langle m|Q|\upsilon\rangle$ and $\langle \upsilon|Q|n\rangle$ integrals (vide supra), as shown in equation 7:

$$C = \sum_{\upsilon}\left[D_{\upsilon} \cdot \sum_{s}\sum_{j} \frac{\langle s|h_j|e\rangle^2}{\Delta E_{e,s}^2} \cdot \langle s|\mu|g\rangle^2 \cdot \langle m|Q_j|\upsilon\rangle \cdot \langle \upsilon|Q_j|n\rangle \right] \qquad (7)$$

$$\text{with } D_{\upsilon} = \left(\frac{1}{E_{e,\upsilon} - E_{g,m} - E_0 + i\Gamma} \right)$$

As evident from Scheme 3.1, overtones are enhanced via the ***C***-term enhancement mechanism.

Scheme 3.1

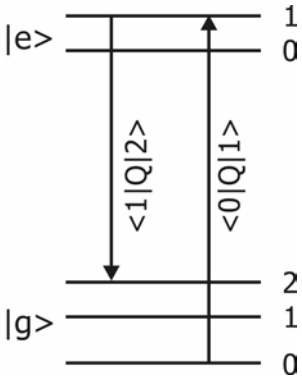

Application to metalloporphyrins (cf. Chapter 4): For the rRaman spectra of metalloporphyrins, ***A***-, ***B***- and ***C***-term enhancement mechanisms are important.[17] A-term enhancement is caused by a displacement of the excited state relative to the ground state and is in general only relevant for totally symmetric modes (vide supra). Since A-term intensity is proportional to the square of the electric dipole transition moment of the excited electronic state, this mechanism is dominant in the region of the Soret transition. B-term enhancement is caused by vibronic coupling between the excited state |e> and another excited state |s>, which leads to resonance enhancement of the vibrations which are effective in coupling these states (vide supra). Hence, this mechanism applies to the Q band, where vibrations of A_{2g}, B_{1g} and B_{2g} symmetry are

enhanced. Additional A-term enhancement of A_{1g} modes in the Q region is also expected. Importantly, resonance enhancement of non-totally symmetric modes is therefore indicative for the presence of vibronic bands in the absorption spectra. However, B_{1g} and B_{2g} enhancement could theoretically also be induced by a Jahn-Teller distortion of the excited states with E_u symmetry.[18] Hence, *enhancement of A_{2g} modes is most diagnostic for the presence of vibronic coupling*. A_{2g} modes are easily identified in the Raman spectra due to their anomalous polarisation (ap; $\rho > ¾$, vide infra), which relates to the scattering tensor being antisymmetric.[19,20,21] Finally, C-Term enhancement is observed upon excitation into a vibronic side band of a forbidden or weakly allowed 0-0 electronic transition,[17] which leads to enhancement of overtones and combination modes. This applies to the Q_v region of the absorption spectra of metalloporphyrins.

Importantly, *polarized Raman measurements allow for the determination of the symmetry of a mode*, which can be used to explore the nature of the excited electronic transition in rRaman spectroscopy as shown above (cf. Chapter 4), and in general to support Raman assignments (cf. Chapter 4). The depolarization ratio ρ is defined as: $\rho = I_{perpendicular}/I_{parallel}$. In D_{4h} symmetry, one obtains:[8]

1) $0 < \rho < 0.75$ for polarized bands (A_{1g} vibrations),
2) $\rho = 0.75$ for depolarized bands (B_{1g} or B_{2g} vibrations) and
3) $\rho > 0.75$ for anomalous polarized bands (A_{2g} vibrations (only RR spectroscopy)).

Importantly, A_{2g} vibrations are forbidden in nonresonance Raman spectroscopy (in D_{4h}) and hence, are only observed in the rRaman spectra of metalloporphyrins as anomalous polarized bands (cf. Chapter 4).

3.2 Assembly of Low-Temperature Magnetic Circular Dichroism Spectrometer in Kiel and in Ann Arbor

Both CD and MCD spectroscopies measure the difference in intensity between left and right circular polarized light (vide supra). However, in contrast to CD, MCD spectroscopy is performed in a strong magnetic field parallel to the direction of propagation of the circular polarized light. Figure 3.5 shows the setup of the MCD spectrometer that we have built at the University of Kiel, Germany. The MCD spectrometer consists of a JASCO J-810 CD spectropolarimeter, a Spectromag^{4000} cryostat (OXFORD) with incorporated superconducting magnet, and the detector as indicated in Figure 3.5. A schematic drawing of the MCD setup is shown in Figure 3.6. The complete MCD spectrometer built in Kiel is 4.7 m long and 70 cm wide. The frame is manufactured from square type stainless steel tubes (30 x 30 x 2 cm) and aluminum plates.

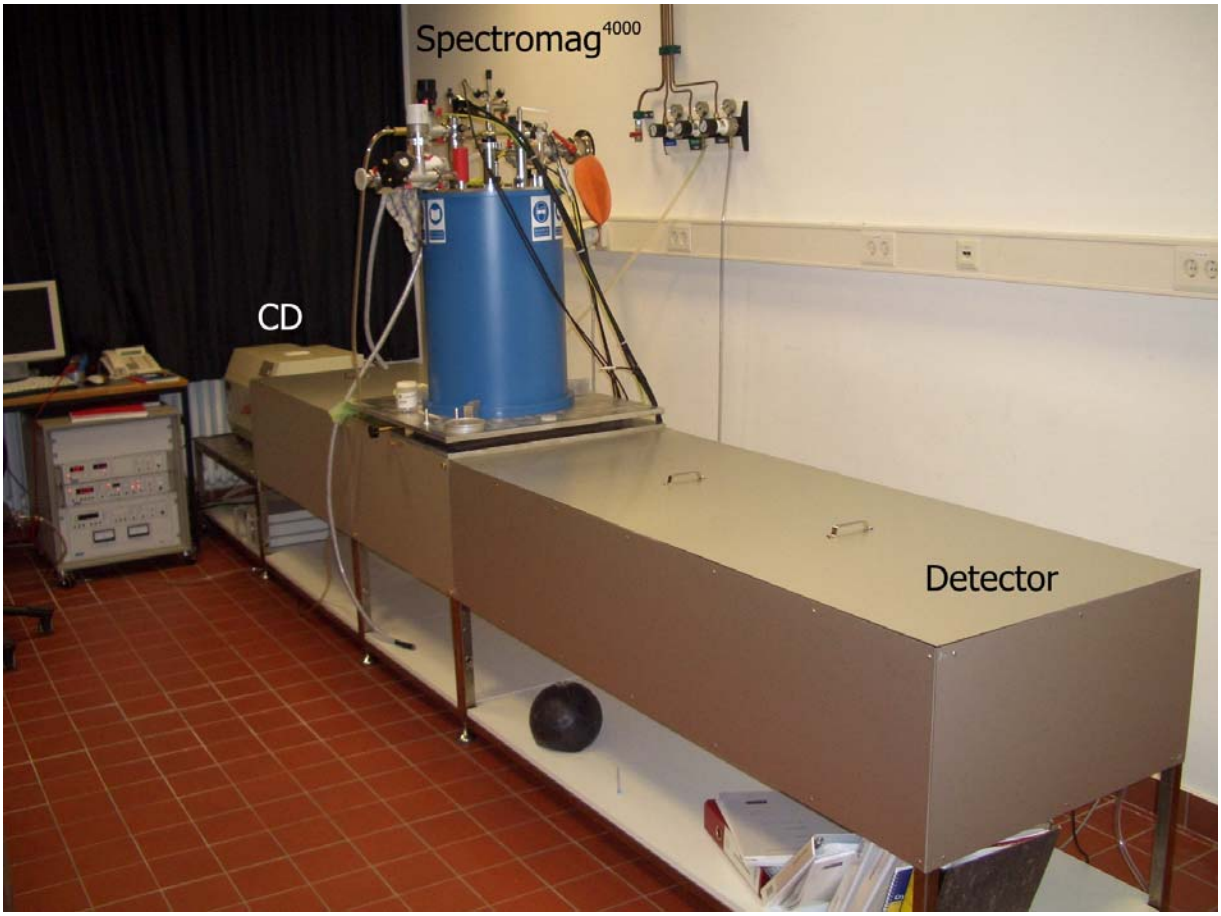

Figure 3.5: Picture of the low-temperature MCD spectrometer built at the University of Kiel.

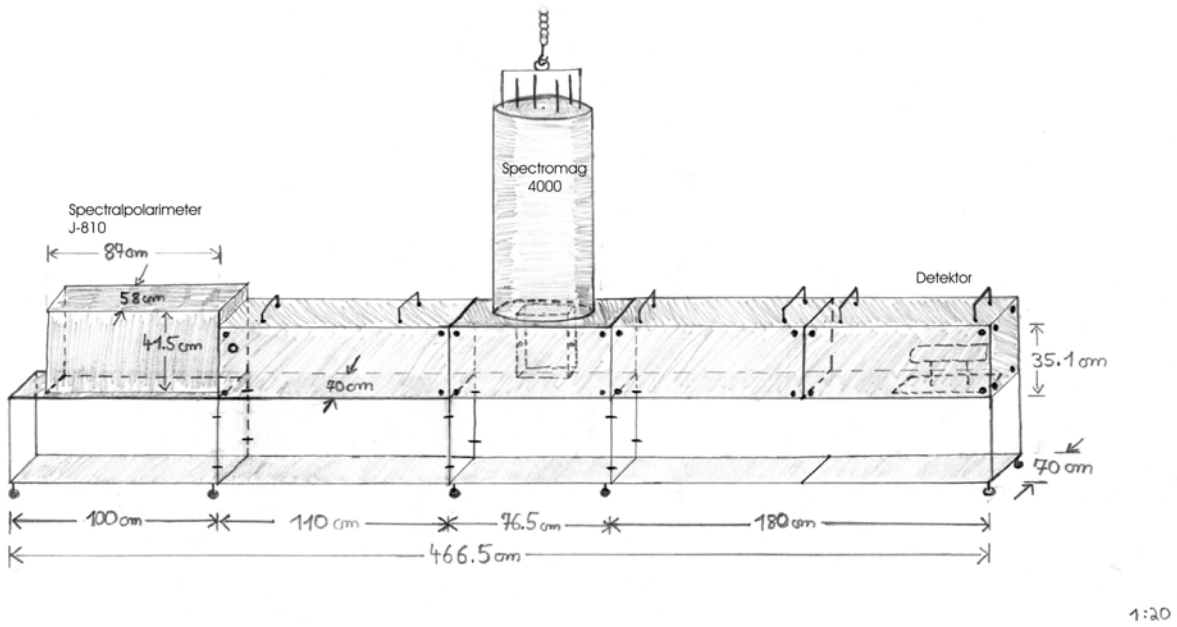

Figure 3.6: Schematic drawing of the MCD spectrometer.

Figure 3.7. Picture of the low-temperature MCD spectrometer built at the University of Michigan, USA.

Figure 3.7 shows the setup of the MCD spectrometer that we have built at the University of Michigan, USA. In contrast to the instrument built in Kiel, the CD spectrometer corresponds to the JASCO J-815 spectropolarimeter and the frame is manufactured from square type aluminum tubes (1.5 x 1.5 inch ≈ 3.8 x 3.8 cm).

Typical experimental conditions for low-temperature (LT) MCD measurements are temperatures between 1.5 - 30 K (liquid helium) and magnetic fields of 0 - 7 T. The Spectromag^{4000} cryostat comprises a horizontal field split pair superconducting magnet in a low boil-off helium cryostat. The magnet is also able to operate at 8 T, but this requires cooling of the magnet coil to 2.2 K. For the 2.2 K operation of the magnet, a lambda point refrigerator is included in the Spectromag^{4000} system. Samples are loaded into a 1.5 - 300 K variable temperature insert (VTI), which offers access to the sample by four optical windows in the tail piece of the cryostat made from Spectrosil B quartz. Two of these windows are oriented parallel to the field, two are perpendicular (cf. Figure 3.8). The inner liquid helium bath (20 L volume) is surrounded by a liquid nitrogen bath (24 L volume) and a vacuum jacket, which is designated as the outer vacuum chamber (OVC; 41 L volume). Both baths are fitted with a liquid level probe. The VTI and the helium bath are connected via an automatic needle valve. The helium flows via the needle valve from the main reservoir into the VTI. The sample is located at the bottom of the VTI and this way, directly cooled by the helium stream. The needle valve is fitted with a heater to allow blockades to be cleared without the necessity to warm up the entire system. The circular polarized light is generated by a JASCO J-815 CD spectropolarimeter (cf. Figure 3.5). The light source is a 150 W air cooled xenon lamp and the detector system corresponds to two interchangeable head-on photomultiplier tubes with a combined wavelength range of 163-1100 nm.

OXFORD Spectromag^{4000}

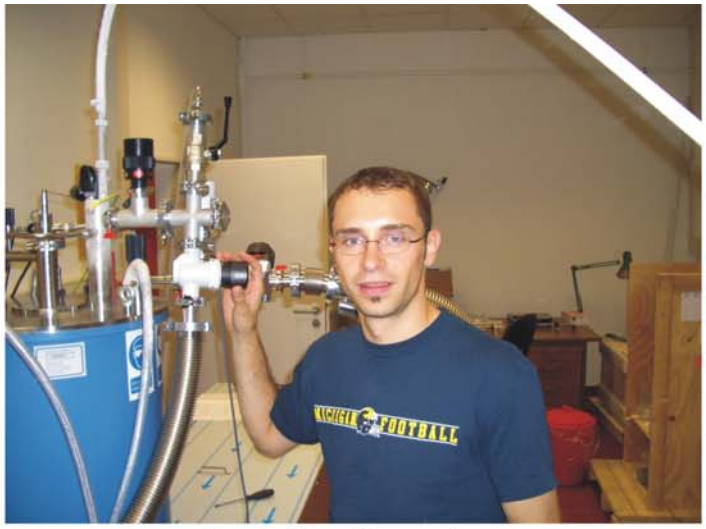

Operating the system

Helium cooling

Cooling the system down to liquid Helium temperature

MCD measurement at 1.75 K and + 7T

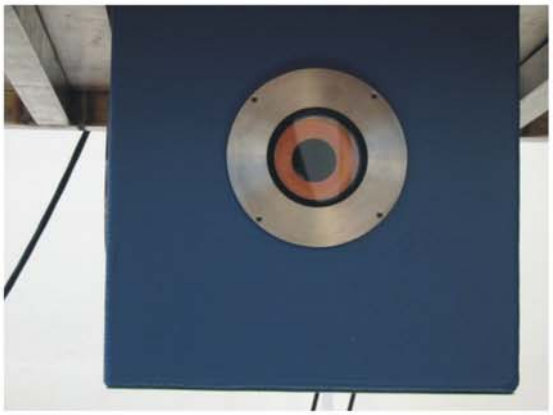

Spectrosil B quartz windows

Figure 3.8: Selected photos taken during the operation of the MCD instrument.

3.2.1 Test results

Due to the strong magnetic fields, the magnet can influence both the detector and the CD spectrometer resulting in artifacts in the spectra at high magnetic fields. In order to prevent this from happening, the table is constructed to separate the magnet from the other components as shown in Figures 3.5-3.7. Apart from the elements that hold the CD spectrometer and the cryostat, the other elements of the table are almost empty; they only contain two lenses in front and behind the cryostat, and the detector. It is therefore necessary to run test measurements before taking actual data to ensure that there are no artifacts in the MCD data. The best test experiment for this purpose is the above described variable temperature variable field (VTVH) measurement, in the case of which the intensity at a given wavelength is plotted against βH/2*k*T (VTVH saturation isotherms, vide supra). In the absence of zero field splitting (zfs), the VTVH isotherms overlay.[6,7] Since copper(II) complexes have an S = 1/2 ground state, no zfs splitting is present in these systems. Figure 3.9 shows the VTVH isotherms (2, 5 and 10 K) measured for [Cu{HB(3,5-*i*-Pr_2pz)$_3$}NO] with the setup built in Kiel (Panel A) and for [Cu(EDTA)] with the setup built in Ann Arbor (Panel B). As evident from this Figure, the VTVH isotherms overlay and hence, the magnet has in both cases no influence on the detector. Note that the data obtained from the MCD measurements on the [Cu{HB(3,5-*i*-Pr_2pz)$_3$}NO] complex are of excellent quality and are further analyzed in Section 7.4.

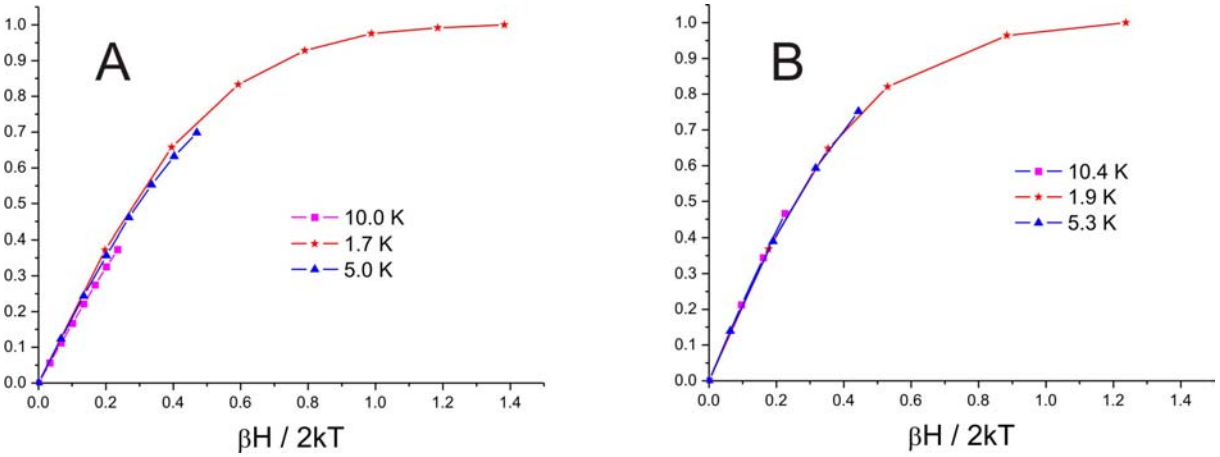

Figure 3.9. VTVH saturation isotherms for the copper(II) (S=1/2) [Cu{HB(3,5-*i*-Pr_2pz)$_3$}NO] complex (A, left) measured with the Kiel setup and the [Cu(EDTA)] (B) complex measured with the Ann Arbor setup.

Magnetic field direction: The results obtained for [Fe(TPP)(Cl)] (S = 5/2), comprised in Chapter 4, have been compared with earlier results obtained by Stephens and coworkers.[22] Importantly, this comparison shows that the magnetic field direction in Kiel is actually inversed. Hence, in order to obtain the correct signs of the individual bands, the spectra measured in Kiel simply have to be inverted.

3.3 Experimental Section

3.3.1 Syntheses

For some of the syntheses (for example, the nitrosylation reactions presented in Chapters 5 and 6) performed in this work, Schlenk techniques were applied using Argon (≥ 4.6) as inert gas. The NO gas was carefully purified before usage to remove higher NO_x impurities such as N_2O_3 and NO_2. For this purpose, the NO gas was passed through an ascarite II column (sodium hydroxide on silica gel) and then through a cold trap at -60 to -70 °C using dry ice and acetone. The $^{15}N^{18}O$ isotopically labeled gas was not further purified, and was taken directly from the lecture bottles. Sample preparation and storage of oxygen sensitive compounds was performed in an inert atmosphere using a MBraun dry box (Glovebox). Oxygen sensitive samples for MCD and rRaman spectroscopies were prepared in the dry box and immediately frozen in liquid nitrogen after removing from the dry box.

3.3.2 Spectrocopic Instrumentation

3.3.2.1 MCD and rRaman Spectroscopy

MCD and rRaman spectra were recorded using the above described instruments (vide supra), or otherwise as indicated (cf. Chapter 4).

3.3.2.2 Nonresonance Raman Spectroscopy (FT Raman)

FT-Raman (nonresonance) spectra were recorded on a Bruker IFS 66 interferometer with a Bruker FRA 106 Raman attachment using a NdYAG laser for excitation (λ = 1064 nm). Measurements were performed on pure compounds.

3.3.2.3 Infrared Spectroscopy

Middle- and Far Infrared spectra (MIR & FIR) were recorded on a Bruker IFS 66v vacuum instrument at room temperature. For the MIR region, KBr disks were used and the spectra were

recorded at a resolution of 1 cm^{-1}. FIR spectra were obtained on PE pellets at a resolution of 2 cm^{-1}.

3.3.2.4 UV-Vis Spectroscopy

Absorption spectra were recorded at room temperature using a Varian CARY 5 UV/Vis-NIR spectrophotometer. The in-situ UV-Vis absorption spectroscopy was performed using an Analytik Jena Specord S600 diode array spectrophotometer and a dip probe. In this case, the operating range of the optical fibers is from 220 nm to1100 nm.

3.3.2.5 ^{1}H-NMR spectroscopy

^{1}H-NMR spectra in Kiel were recorded on a Bruker Avance 400 pulse Fourier transform spectrometer operating at a ^{1}H frequency of 400 MHz. ^{1}H-NMR spectra in Ann Arbor were recorded on both a Varian Inova 400 spectrometer operating at 400 MHz (9.4 Tesla; Oxford Magnet) and a Varian Mercury 300 spectrometer operating at 300 MHz (7.0 Tesla; Oxford Magnet). Spectra were recorded at 300 K.

3.3.2.6 Mass Spectrometry

Mass spectra were recorded on a Micromass Ultima spectrometer, which is a high resolution magnetic sector mass spectrometer using EI, CI or Electrospray ionization techniques.

3.3.3 Density Functional Calculations

In general, density functional calculations were performed using the B3LYP and BP86 functionals, and the LanL2DZ and TZVP basis sets, respectively, as implemented in the program package Gaussian 03.[23] In addition, the LanL2DZ* basis set was used, which consists of LanL2DZ plus polarization functions (from TZVP) on all heavy atoms.[24] Details for the calculations are given in the individual chapters, when applicable. In all calculations, convergence was reached when the relative change in the density matrix between subsequent iterations was less than 1×10^{-8}. Semi-empirical calculations of absorption spectra were performed using the INDO/S-CI method as implemented in ORCA.[25] Molecular and electronic structures as well as vibrations were visualized using the program packages GaussView [23] and Molden [26].

3.3.4 Normal Coordinate Analysis (NCA)

Normal coordinate calculations were performed using the QCPE computer program 576 by M.R. Peterson and D.F. McIntosh. The calculations are based on a general valence force field; force constants are refined with a non-linear simplex algorithm. The simplex optimization was used to refine only *selected* force constants according to the quantum-chemistry centered normal coordinate analysis (QCC-NCA) scheme.[24,27] Here, a force field from DFT calculations is used as a starting point to generate initial force constants and a subset of these is fit to reproduce the known experimental frequencies. Force constants were obtained from the Gaussian output using a modified version of the program Redong [28](QCPE 628). Details for the NCA's are given in the corresponding chapters, when applicable.

References

[1] Paulat, F. *Diploma thesis (Diplomarbeit)*, Christian-Albrechts-Universität zu Kiel, Germany, 2004.
[2] (a) Solomon, E. I.; Pavel, E. G.; Loeb, K. E.; Campochiaro, C. *Coord. Chem. Rev.* **1995**, *144*, 369-460. (b) Stephens, P. J. Ann. Rev. Phys. Chem. **1974**, 25, 201-232. (c) Stephens, P. J. Adv. Chem. Phys. **1975**, 35, 197-264. (d) Oganesyan, V. S.; George, S. J.; Cheesman, M. R.; Thomson, A. J. J. Chem. Phys. **1999**, 110, 762-777. (e) Cheek, J.; Dawson, J. H. In *Handbook of Porphyrins and Related Macrocycles*, Vol. 7, edited by K. Kadish, K. Smith, R. Guilard, 339-369. New York: Academic Press, (2000). (f) Neese, F.; Solomon, E. I. *Inorg. Chem.* **1999**, *38*, 1847-1865.
[3] Neese, F.; Solomon, E. I. *Inorg. Chem.* **1999**, *38*, 1847-1865.
[4] (a) Stephens, P. J. *J. Chem. Phys.* **1970**, *52*, 3489-3516. (b) Piepho, S. B.; Schatz, P. N. *Group Theory in Spectroscopy with Applications to Magnetic Circular Dichroism;* John Wiley & Sons: New York, Chichester, Brisbane, Toronto, Singapore, 1983.
[5] Mack, J. Stillman, M.J., Kobayashi, N. *Coord. Chem. Rev.* **2007**, *251*429-453.
[6] Solomon, E. I.; Pavel, E. G.; Loeb, K. E.; Campochiaro, C. *Coord. Chem. Rev.* **1995**, *144*, 369-460.
[7] Lehnert, N.; DeBeer George, S.; Solomon, E. I. *Curr. Op. Chem. Biol.* **2001**, *5*, 176-187.
[8] Spiro, T. G. in *Iron porphyrins*; Lever, A. B. P.; Gray, H. B., Eds.; Addison-Wesley: Massachusetts, 1983, part two, pp 89-159.
[9] Spiro, T. G.; Li, X.-Y. in *Resonance raman spectra of heme and metalloproteins*; Spiro, T. G., Ed.; Wiley: New York, 1988, pp 1-37.
[10] Spiro, T. G.; Czernuszewicz, R. S. *Physical Methods in Bioinorganic Chemistry*; Que, L., Jr., Ed.; University Science Books: Sausalito, 2000, pp. 59-120.
[11] Loehr, T. M. in *Spectroscopic Methods in Bioinorganic Chemistry*; Solomon, E. I.; Hodgson, K. O., Eds.; American Chemical Society: Washington, DC, 1998, pp. 136-153.
[12] Czernuszewicz, R. S.; Spiro, T. G. in *Inorganic electronic structure and spectroscopy*; Solomon, E. I., Lever, A. B. P., Eds.; John Wiley & Sons: New York, 1999, Vol. I, pp 353-441.
[13] Walker, F. A. in *Encyclopedia of Inorganic Chemistry*; King, R. B., Ed.; John Wiley & Sons, 1994, Volume 4, pp. 1785-1846.
[14] Renée Dillinger, *Dissertation*, Johannes Gutenberg Universität Mainz, 2000.
[15] Raman, C. V.; Krishnan, R. S. *Nature* **1928**, *121*, 501-502.
[16] (a) Albrecht, A. C. *J. Chem. Phys.* **1960**, *33*, 156-169. (b) Albrecht, A. C. *J. Chem. Phys.* **1961**, *34*, 1476-1484.
[17] Czernuszewicz, R. S.; Spiro, T. G. in *Inorganic electronic structure and spectroscopy*; Solomon, E. I., Lever, A. B. P., Eds.; John Wiley & Sons: New York, 1999, Vol. I, pp 353-441.
[18] Egawa, T.; Suzuki, N.; Dokoh, T.; Higuchi, T.; Shimada, H.; Kitagawa, T.; Ishimura, Y. *J. Phys. Chem. A* **2004**, *108*, 568-577.

[19] Spiro, T. G. *Current Science* **1998**, *74*, 304-307.
[20] Placzek, G. *Handbuch der Radiologie*; Marx, E., Ed.; Akademische Verlagsgesellschaft: Leipzig, 1934, Vol. 6, Part 2, p. 205.
[21] Spiro, T. G.; Strekas, T. C. *Proc. Nat. Acad. Sci. USA* **1972**, *69*, 2622-2626.
[22] Browett, W. R.; Fucaloro, A. F.; Morgan, T. V.; Stephens, P. J. *J. Am. Chem. Soc.* **1983**, *105*, 1868-1872.
[23] Frisch, M. J.; Trucks, G. W.; Schlegel, H. B.; Scuseria, G. E.; Robb, M. A.; Cheeseman, J. R.; Montgomery, J. A.; Vreven, Jr., T.; Kudin, K. N.; Burant, J. C.; Millam, J. M.; Iyengar, S. S.; Tomasi, J.; Barone, V.; Mennucci, B.; Cossi, M.; Scalmani, G.; Rega, N.; Petersson, G. A.; Nakatsuji, H.; Hada, M.; Ehara, M.; Toyota, K.; Fukuda, R.; Hasegawa, J.; Ishida, M.; Nakajima, T.; Honda, Y.; Kitao, O.; Nakai, H.; Klene, M.; Li, X.; Knox, J. E.; Hratchian, H. P.; Cross, J. B.; Adamo, C.; Jaramillo, J.; Gomperts, R.; Stratmann, R. E.; Yazyev, O.; Austin, A. J.; Cammi, R.; Pomelli, C.; Ochterski, J. W.; Ayala, P. Y.; Morokuma, K.; Voth, G. A.; Salvador, P.; Dannenberg, J. J.; Zakrzewski, V. G.; Dapprich, S.; Daniels, A. D.; Strain, M. C.; Farkas, O.; Malick, D. K.; Rabuck, A. D.; Raghavachari, K.; Foresman, J. B.; Ortiz, J. V.; Cui, Q.; Baboul, A. G.; Clifford, S.; Cioslowski, J.; Stefanov, B. B.; Liu, G.; Liashenko, A.; Piskorz, P.; Komaromi, I.; Martin, R. L.; Fox, D. J.; Keith, T.; Al-Laham, M. A.; Peng, C. Y.; Nanayakkara, A.; Challacombe, M.; Gill, P. M. W.; Johnson, B.; Chen, W.; Wong, M. W.; Gonzalez, C.; Pople, J. A. Gaussian, Inc., Pittsburgh PA, 2003.
[24] Praneeth, V. K. K.; Näther, C.; Peters, G.; Lehnert, N. *Inorg. Chem.* **2005**, *45*, 2795-2811.
[25] Neese, F. *ORCA*, version 2.2; Max-Planck Institut fuer Bioanorganische Chemie, Muelheim/Ruhr, Germany, 2004.
[26] Schaftenaar, G.; Noordik, J.H. *J. Comput.-Aided Mol. Design* **2000**, *14*, 123-134.
[27] Lehnert, N.; Tuczek, F. *Inorg. Chem.* **1999**, *38*, 1659-1670.
[28] Allouche, A.; Pourcin, J. *Spectrochim. Acta* **1993**, *49A*, 571.

4 MCD and Vibrational Spectroscopy of Metalloporphyrins

4.1 Scope of this project

Magnetic Circular Dichroism (MCD) and resonance Raman (rRaman) spectroscopies are extremely powerful techniques to investigate the electronic structures and spectra of transition metal complexes. Hence, these methods have been applied to both heme proteins and corresponding model complexes.[1,2] However, the detailed interpretation of the obtained data is very complicated. Therefore, in order to explore the Raman and MCD spectroscopic properties of heme-nitrosyls, I have investigated the five-coordinate model complexes of the type [M(TPP)(Cl)] (M = Fe^{III}, Mn^{III} and Co^{III}; TPP = tetraphenylporphyrin) first using these techniques. These investigations are especially focused on [Fe(TPP)(Cl)], because of the great significance of five-coordinate high-spin (hs) ferric hemes in biology. First, the vibrational data of these compounds have been analyzed in detail. These results are summarized in Section 4.2, and have been published recently in Inorganic Chemistry.[3] Note that the crystal structure of [Mn(TPP)(Cl)] (chloroform solvate) was contributed by two co-authors on this paper: the single crystals were grown by my colleague Praneeth V. K. K., and Priv.-Doz. Dr. Christian Näther solved the crystal structure. The assignments of the nonresonance Raman and IR spectra of [M(TPP)(Cl)] obtained from DFT calculations are part of my diploma thesis.[4] These assignments could now be verified using polarized Raman spectroscopy. In addition, assignments of anomalous polarized bands, which correspond to A_{2g} vibrations (forbidden in nonresonance Raman in D_{4h} symmetry) were obtained from polarized rRaman spectroscopy. Besides its use for the determination of vibrational energies, rRaman spectroscopy offers detailed insight into the nature of the electronically excited state. This relates to the mechanism of resonance enhancement and the actual nature of the enhanced vibrations. The optical spectra of metalloporphyrins are in general dominated by π to π^* transitions of the porphyrin core, which give rise to the Soret, Q and Q_v features in the absorption spectra.[5] Resonance Raman spectroscopy is a powerful method to identify the Soret, Q and Q_v bands in the spectra of heme proteins and corresponding model complexes. Here, rRaman has been used to identify these transitions in the spectra of the complexes [M(TPP)(Cl)] (M = Fe, Mn and Co). Additional

features in the absorption spectra of metalloporphyrins are often masked by these intense bands. This includes d-d transitions as well as charge transfer (CT) transitions between the metal (M) and axially coordinated ligands (L), both of which are diagnostic for the properties of the metal ion and the electronic structure of the M-L bond. Hence, it is very important to identify these additional transitions, which, in the case of paramagnetic complexes, is possible with the help of magnetic circular dichroism (MCD) spectroscopy. To this end, I have performed low-temperature MCD measurements on the five-coordinate model complex [Fe(TPP)(Cl)], which has very complex electronic spectra, and hence, is a very good system to develop an MCD methodology to analyze the spectra of high-spin ferric heme complexes in models and proteins. Variable temperature and variable field (VTVH) measurements have been used to determine the polarizations of most of the electronic bands observed in the MCD spectra of this compound. In correlation to resonance Raman (vide supra) results and TD-DFT calculations, this allows for a detailed assignment of the optical spectra of [Fe(TPP)(Cl)] for the first time and this way, provides detailed insight into the electronic structure of five-coordinate ferric hemes. In addition, these results are also used for a calibration of the theoretical methods. In future studies, the methodology developed here can be applied to ferric P450 and corresponding model complexes [Fe(TPP)(SR)].

Reference

[1] (a) Spiro, T. G.; Li, X.-Y. in *Resonance raman spectra of heme and metalloproteins*; Spiro, T. G., Ed.; Wiley: New York, 1988, pp 1-37. (b) Spiro, T. G. in *Iron porphyrins*; Lever, A. B. P.; Gray, H. B., Eds.; Addison-Wesley: Massachusetts, 1983, part 2, pp 89-159.

[2] (a) Cheesman, M. R.; Greenwood, C.; Thomson, A. J. *Adv. Inorg. Chem.* **1991**, *36*, 201-255. (b) Cheek, J.; Dawson, J. H. In *Handbook of Porphyrins and Related Macrocycles*, Vol. 7, edited by K. Kadish, K. Smith, R. Guilard, 339-369.

[3] Paulat, F.; Praneeth, V. K. K., Naether, C.; Lehnert, N. *Inorg. Chem.* **2006**, *45*, 2835-2856.

[4] Paulat, F. *Diploma thesis (Diplomarbeit)*, Christian-Albrechts-Universität zu Kiel, 2004.

[5] Gouterman, M. in *The Porphyrins*; Dolphin, D., Ed.; Academic: New York, 1979, Vol. III, Part A, pp 1-156.

4.2. Quantum Chemistry-Based Analysis of the Vibrational Spectra of Five-Coordinate Metalloporphyrins [M(TPP)(Cl)]

Florian Paulat, V. K. K. Praneeth, Christian Näther, and Nicolai Lehnert*

Published in: *Inorg. Chem.* **2006**, 45, 2835-2856.

Inorg. Chem. **2006**, *45*, 2835–2856

Quantum Chemistry-Based Analysis of the Vibrational Spectra of Five-Coordinate Metalloporphyrins [M(TPP)Cl]

Florian Paulat, V. K. K. Praneeth, Christian Näther, and Nicolai Lehnert*

Institut für Anorganische Chemie, Christian-Albrechts-Universität Kiel, Olshausenstrasse 40, D-24098 Kiel, Germany

Received June 30, 2005

Vibrational properties of the five-coordinate porphyrin complexes [M(TPP)(Cl)] (M = Fe, Mn, Co) are analyzed in detail. For [Fe(TPP)(Cl)] (**1**), a complete vibrational data set is obtained, including nonresonance (NR) Raman, and resonance Raman (RR) spectra at multiple excitation wavelengths as well as IR spectra. These data are completely assigned using density functional (DFT) calculations and polarization measurements. Compared to earlier works, a number of bands are reassigned in this one. These include the important, structure-sensitive band at 390 cm^{-1}, which is reassigned here to the totally symmetric $\nu_{breathing}$(Fe–N) vibration for complex **1**. This is in agreement with the assignments for [Ni(TPP)]. In general, the assignments are on the basis of an idealized $[M(TPP)]^+$ core with D_{4h} symmetry. In this Work, small deviations from D_{4h} are observed in the vibrational spectra and analyzed in detail. On the basis of the assignments of the vibrational spectra of **1**, [Mn(TPP)(Cl)] (**2**), and diamagnetic [Co(TPP)(Cl)] (**3**), eight metal-sensitive bands are identified. Two of them correspond to the ν(M–N) stretching modes with B_{1g} and E_u symmetries and are assigned here for the first time. The shifts of the metal sensitive modes are interpreted on the basis of differences in the porphyrin C–C, C–N, and M–N distances. Besides the porphyrin core vibrations, the M–Cl stretching modes also show strong metal sensitivity. The strength of the M–Cl bond in **1**–**3** is further investigated. From normal coordinate analysis (NCA), force constants of 1.796 (Fe), 0.932 (Mn), and 1.717 (Co) mdyn/Å are obtained for **1**–**3**, respectively. The weakness of the Mn–Cl bond is attributed to the fact that it only corresponds to half a σ bond. Finally, RR spectroscopy is used to gain detailed insight into the nature of the electronically excited states. This relates to the mechanism of resonance enhancement and the actual nature of the enhanced vibrations. It is of importance that anomalous polarized bands (A_{2g} vibrations), which are diagnostic for vibronic mixing, are especially useful for this purpose.

Introduction

Vibrational spectroscopy is a very valuable method that is used to gain insight into the electronic structures of metalloporphyrins. Especially, heme proteins that contain iron porphyrins as prosthetic groups have been studied in detail, and information about the properties of their heme cofactors have been obtained because of the sensitivity of the vibrational frequencies to the changes in oxidation state, coordination number, and spin state.[1,2] Hemes occur as active sites in many different proteins and have been characterized by all types of spectroscopic methods. Among these, resonance Raman (RR) spectroscopy has always played a key role. RR spectroscopy selectively enhances the vibrational modes of the absorbing chromophore, whereas the remaining vibrational modes in the molecule (protein) are suppressed.[3−5] In this way, RR spectra of a heme chromophore can be obtained selectively even in a large molecule (protein) where many other vibrations are present. From the vibrational energies as well as the nature of the enhanced modes, information about the geometric and electronic

* To whom correspondence should be addressed. E-mail: nlehnert@ac.uni-kiel.de.

(1) Spiro, T. G. In *Iron Porphyrins;* Lever, A. B. P., Gray, H. B., Eds.; Addison-Wesley: Reading, MA, 1983; Part 2, pp 89−159.
(2) Spiro, T. G.; Li, X.-Y. In *Resonance Raman Spectra of Heme and Metalloproteins;* Spiro, T. G., Ed.; Wiley: New York, 1988; pp 1−37.
(3) Spiro, T. G.; Czernuszewicz, R. S. In *Physical Methods in Bioinorganic Chemistry;* Que, L., Jr., Ed.; University Science Books: Sausalito, CA, 2000; pp 59−120.
(4) Loehr, T. M. In *Spectroscopic Methods in Bioinorganic Chemistry;* Solomon, E. I., Hodgson, K. O., Eds.; American Chemical Society: Washington, DC, 1998; pp 136−153.
(5) Czernuszewicz, R. S.; Spiro, T. G. In *Inorganic Electronic Structure and Spectroscopy;* Solomon, E. I., Lever, A. B. P., Eds.; John Wiley & Sons: New York, 1999; Vol. 1, pp 353−441.

10.1021/ic0510866 CCC: $33.50
Published on Web 02/28/2006

Scheme 1

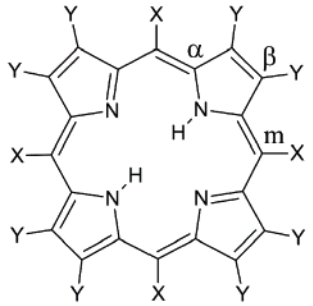

Porphine: X = H ; Y = H

OEP: X = H ; Y = Et

TPP: X = Ph ; Y = H

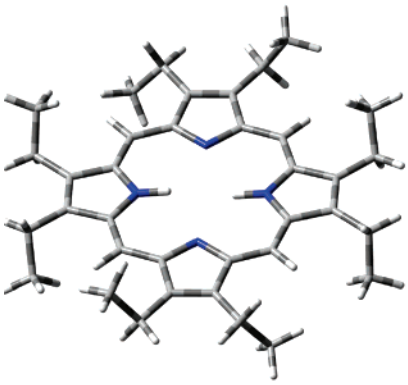

OEP

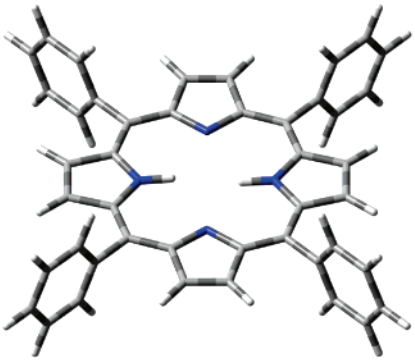

TPP

properties of the heme as well as its environment can be obtained.[1,5] Besides the investigation of metalloporphyrins in biological systems, synthetic porphyrin model complexes have been studied widely to gain insight into the catalytic reactions or functions performed by heme proteins.[6] In many cases, tetraphenylporphyrin (TPP) and octaethylporphyrin (OEP) ligands have been used for such model systems. Scheme 1 shows the OEP and TPP ligands, which are based on simple porphine P, where the meso (X) and β substituents (Y) are hydrogen atoms. OEP has ethyl groups in the β position (Y = Et), whereas TPP has phenyl groups in the meso position (X = Ph). The RR spectra of such metalloporphyrin model complexes have been intensely studied, and spectral assignments have been obtained.[1] For the vibrational assignments, four-coordinate Nickel complexes have, in general, been used because they are stable and nonfluorescent. In addition, there are no complications due to axial ligands when using the four-coordinate species. Correspondingly, much effort has been spent to investigate the RR and IR spectra of the Ni(II) complexes [Ni(OEP)] and [Ni(TPP)]. On the basis of multiple isotope substitution, multiple-wavelength RR spectroscopy, and IR measurements, the spectra of [Ni(OEP)] and [Ni(TPP)] have been assigned by different groups. Kitagawa and co-workers assigned most of the infrared and RR in-plane modes of [Ni(OEP)] using variable excitation RR spectra, ^{15}N and C_m-D isotope shifts, and a normal-coordinate analysis (NCA).[7,8] In-plane as well as out-of-plane modes for general metalloporphines [M(P)] were calculated by Warshel and Lappicirella[9] using a semiempirical force field (QCFF/PI). This study provides the first analysis of the out-of-plane vibrations of the porphyrin core. Spiro and co-workers[10] later developed a consistent empirical force field for nickel porphyrins with different substituents, including porphine, OEP, and TPP. The RR spectra of [Ni(TPP)] were completely assigned using pyrrole-$^{15}N_4$, pyrrole-d_8, $^{13}C_4$-meso and phenyl-d_{20} isotopomers, and NCA.[10] Other simple [M(TPP)] complexes (M = Cu(II), Zn(II), and Co(II)) were studied by other groups.[11,12] However, until now, no detailed vibrational assignments of five-coordinate complexes of type [M(P)(X)] existed.

In contrast to the RR spectra, the IR spectra of TPP complexes remained unassigned for a long time because of their complexity. The first complete assignment of an infrared spectrum of a TPP complex was performed by Rush III et al.[13] in 2000 for [Ni(TPP)] using DFT−SQM calculations. RR intensities were also calculated using the semiempirical INDO method, which led to the reassignment of several RR bands. Hence, these new assignments are on the basis of quantum chemical calculations, which only became available

(6) Walker, F. A. In *Encyclopedia of Inorganic Chemistry;* King, R. B., Ed.; John Wiley & Sons: New York, 1994; Vol. 4, pp 1785−1846.
(7) Kitagawa, T.; Abe, M.; Ogoshi, H. *J. Chem. Phys.* **1978**, *69*, 4516−4525.
(8) Abe, M.; Kitagawa, T.; Kyogoku, Y. *J. Chem. Phys.* **1978**, *69*, 4526−4534.
(9) Warshel, A.; Lappicirella, A. *J. Am. Chem. Soc.* **1981**, *103*, 4664−4673.
(10) Li, X.-Y.; Czernuszewicz, R. S.; Kincaid, J. R.; Su, Y. O.; Spiro, T. G. *J. Phys. Chem.* **1990**, *94*, 31−47. (b) Li, X.-Y.; Czernuszewicz, R. S.; Kincaid, J. R.; Stein, P.; Spiro, T. G. *J. Phys. Chem.* **1990**, *94*, 47−61. (c) Li, X.-Y.; Czernuszewicz, R. S.; Kincaid, J. R.; Spiro, T. G. *J. Am. Chem. Soc.* **1989**, *111*, 7012−7023.
(11) Atamian, M.; Donohoe, R. J.; Lindsey, J. S.; Bocian, D. F. *J. Phys. Chem.* **1989**, *93*, 2236−2243.
(12) Kozuka, M.; Iwaizumi M. *Bull. Chem. Soc. Jpn.* **1983**, *56*, 3165−3166.
(13) Rush, T. S., III; Kozlowski, P. M.; Piffat, C. A.; Kumble, R.; Zgierski, M. Z.; Spiro, T. G. *J. Phys. Chem. B* **2000**, *104*, 5020−5034.

recently for the routine treatment of large molecules such as [Ni(TPP)]. These theoretical methods provide a new tool to researchers that enables them to analyze the missing puzzle pieces of the vibrational assignments of porphyrin complexes, as will be further demonstrated in this study.

Besides the detailed assignments of nickel porphyrin complexes including [Ni(TPP)],[10,14,15] the Spiro group has also analyzed the effects of oxidation- and spin-state changes on the RR spectra of heme proteins.[15b,d−f,42,44] It was concluded that the oxidation-state sensitivity largely depends on the back-bonding between the metal and the porphyrin ring. In the case of iron, back-bonding is greatly reduced for Fe(III) compared to Fe(II) because of a lowering in energy of the d orbitals, which induces shifts in certain porphyrin vibrations. In agreement with this analysis, axial ligands of increasing π-acceptor strength increase the frequencies of the oxidation-state sensitive bands[15e] by competing with the porphyrin ring for the iron d_π electrons. Correspondingly, using the strong π donor ligand cysteine, these oxidation-state sensitive bands shift to energies below the typical range associated with nonacceptor ligands.[16] Spin-sensitivity, on the other hand, has been attributed to ring conformation.[15b] Doming of the porphyrin ring occurs as a consequence of out-of-plane displacement of iron,[15b] which is due to the fact that high-spin iron(II) and iron(III) are too large to fit into the center of the porphyrin ring. In this way, the high-spin state of iron causes doming that then induces band shifts. On the other hand, Spaulding et al.[17] suggested that the core size is the dominant parameter for spin-state sensitivity. Because of the out-of-plane displacement of the iron atom, the pyrrole rings are expected to tilt to maintain the overlap with the metal orbitals. This leads to a lowering of certain vibrational frequencies because of the loss of π conjugation at the methine bridges of the porphyrin ring. Hence, both core expansion and pyrrole tilting are expected to contribute to the lowering of vibrational frequencies, where core expansion is dominant at moderate tilt angles.[15f] Altogether, five structure sensitive RR signals were described in the literature and designated as bands A−E. These oxidation- and spin-state sensitive bands are also expected to be sensitive to the nature of the metal ion because of the variable occupation and energies of the d orbitals of different metals.[18] Oshio et al.[18b] observed metal-sensitivity in the IR spectra of [M(TPP)] complexes. The frequencies of these bands I−III were found to decrease as the metal−porphyrinato nitrogen distances increased (Ni(II) > Co(II) > Cu(II) > Zn(II)).

In this study, density functional theory (DFT) is used to calculate the IR and Raman spectra of the five-coordinate complexes [M(TPP)(Cl)] with M = Fe (**1**), Mn (**2**), and Co (**3**). On the basis of these results, the experimental nonresonance Raman (NR Raman), resonance Raman, and IR spectra of compound **1** are assigned in detail for the first time. The calculated Raman spectra cannot be compared to resonance Raman measurements because of the difference in the selection rules for resonance and nonresonance Raman scattering.[19] Therefore, using an excitation wavelength of 1064 nm, the nonresonance Raman spectra of **1**, including polarized measurements are presented for the first time. Resonance Raman spectra at multiple excitation wavelengths have also been obtained for **1**, which, together with polarized measurements, allow for the assignments of additional bands. Altogether, a complete assignment of all available experimental data has been achieved for compound **1**. These results are then compared to an earlier assignment[20] of a few RR bands of **1** in the 1000−1600 cm^{-1} range. Results of Burke et al.,[14] who roughly classified the vibrations of compound **1** on the basis of RR isotope shifts and polarization measurements, are also taken into consideration. The vibrational assignments obtained for **1** are then compared to the assignments of the Raman and IR spectra of **2** and **3** to identify the metal-sensitive bands. Not surprisingly, one of the most metal-sensitive bands in these complexes is the metal−chloride stretching vibration. These are identified in the IR spectra of **1**−**3**, and the corresponding force constants are determined using the quantum-chemistry centered normal coordinate analysis (QCC−NCA).[21] Finally, the correlation of our results to the detailed assignments for [Ni(TPP)] is also included.[13] Going from [Ni(TPP)] to [M(TPP)(Cl)] type complexes adds the complexity of having (a) open shells, (b) larger distortions of the porphyrin ring, and (c) axial ligands. The influence of these electronic and structural differences on the vibrational spectra of metalloporphyrins is analyzed.

Experimental and Computational Procedures

Syntheses. The complexes [Fe(TPP)(Cl)] (**1**) and [Mn(TPP)(Cl)] (**2**) were synthesized using published procedures[22] and isolated as microcrystalline solids. Complex [Co(TPP)Cl] (**3**) was synthesized using the procedure by Mahmood et al.[23] Single Crystals of **2** were obtained by slow diffusion of *n*-hexane into a solution of **2** in

(14) Burke, J. M.; Kincaid, J. R.; Spiro, T. G. *J. Am. Chem. Soc.* **1978**, *100*, 6077−6083. (b) Burke, J. M.; Kincaid, J. R.; Peters, S.; Gagne, R. R.; Collman, J. P.; Spiro, T. G. *J. Am. Chem. Soc.* **1978**, *100*, 6083−6088.

(15) Spiro, T. G. In *Iron Porphyrins*; Lever, A. B. P., Gray, H. B., Eds.; Addison-Wesley: Reading, MA, 1983; Part 2, pp 89−159. (b) Spiro, T. G.; Strekas, T. C. *J. Am. Chem. Soc.* **1974**, *96*, 338−345. (c) Spiro, T. G.; Strekas, T. C. *Proc. Natl. Acad. Sci. U.S.A.* **1972**, *69*, 2622−2626. (d) Burke, J. M.; Kincaid, J. R.; Peters, S.; Gagne, R. R.; Collman, J. P.; Spiro, T. G. *J. Am. Chem. Soc.* **1978**, *100*, 6083−6088. (e) Spiro, T. G.; Burke, J. M. *J. Am. Chem. Soc.* **1976**, *98*, 5482−5489. (f) Spiro, T. G.; Stong, J. D.; Stein, P. *J. Am. Chem. Soc.* **1979**, *101*, 2648−2655.

(16) Champion, P. M.; Gunsalus, I. C. *J. Am. Chem. Soc.* **1977**, *99*, 2000−2002. (b) Champion, P. M.; Gunsalus, I. C.; Wagner, G. C. *J. Am. Chem. Soc.* **1978**, *100*, 3743−3751.

(17) Spaulding, L. D.; Chang, C. C.; Yu, N.-T.; Felton, R. H. *J. Am. Chem. Soc.* **1975**, *97*, 2517−2525.

(18) Kincaid, J.; Nakamoto, K. *J. Inorg. Nucl. Chem.* **1975**, *37*, 85. (b) Oshio, H.; Ama, T.; Watanabe, T.; Kincaid, J.; Nakamoto, K. *Spectrochim. Acta, Part A* **1984**, *40*, 863−870.

(19) Tang, J.; Albrecht, A. C. In *Raman Spectroscopy;* Szymanski, H. A., Ed.; Plenum Press: New York, 1970; Vol. 2. (b) Albrecht, A. C. *J. Chem. Phys.* **1961**, *34*, 1476.

(20) Czernuszewicz, R. S.; Macor, K. A.; Li, X.-Y.; Kincaid, J. R.; Spiro, T. G. *J. Am. Chem. Soc.* **1989**, *111*, 3860−3869.

(21) Lehnert, N.; Tuczek, F. *Inorg. Chem.* **1999**, *38*, 1659−1670. (b) Praneeth, V. K. K.; Näther, C.; Peters, G.; Lehnert, N. *Inorg. Chem.*, in press.

(22) Adler, A. D.; Longo, F. R.; Kampas, F.; Kim, J. *J. Inorg. Nucl. Chem.* **1970**, *32*, 2443−2445.

(23) Mahmood, A.; Liu, H.-I.; Jones, J. G.; Edwards, J. O.; Sweigart, D. A. *Inorg. Chem.* **1988**, *27*, 2149−2154.

$CHCl_3$. The identity of the compounds was established using ^1H NMR and UV−vis absorption spectroscopy and mass spectrometry (for compound **2**).

Crystal Structure Determination. The data were collected using an STOE imaging plate diffraction system (IPDS). The structure was solved with direct methods using SHELXS-97 and was refined against F^2 using SHELXL-97. All non-H atoms were refined anisotropically, except for some of the chlorine atoms of the disordered chloroform molecule. The H atoms were positioned with idealized geometry and refined using a riding model. The chloroform molecule is disordered and was refined using a split model.

Vibrational Spectroscopy. FT-Raman spectra were recorded on a Bruker IFS 66 interferometer with a Bruker FRA 106 Raman attachment using an Nd:YAG laser for excitation ($\lambda = 1064$ nm). Measurements were performed on pure compounds. The polarized FT-Raman spectra of **1** were measured in CH_2Cl_2. Resolution was set to 2 cm^{-1}. Resonance Raman spectra were measured on a Dilor XY Raman spectrograph with a triple monochromator and a CCD detector. An Ar/Kr mixed-gas laser with a maximum power of 5 W was used for excitation. The spectra were measured on KBr disks cooled to 10 K with a helium cryostat. The spectral band pass was set to 2 cm^{-1}. Middle- and far-infrared spectra (MIR and FIR) were recorded on a Bruker IFS 66v vacuum instrument at room temperature. For the MIR region, KBr disks were used, and the spectra were recorded at a resolution of 1 cm^{-1}. FIR spectra were obtained on PE pellets at a resolution of 2 cm^{-1}.

UV−Vis Spectroscopy. Absorption spectra were recorded in chloroform for **1**, in a 1/1 mixture of butyronitrile and propionitrile for **2**, and in methanol solution for **3** at room temperature using a Varian Cary 5 UV−vis NIR spectrometer. The absorption data were scaled using literature extinction coefficients as indicated in Figure 7.

Density Functional Calculations. DFT calculations using Becke's three parameter hybrid functional with the correlation functional of Lee, Yang, and Parr (B3LYP[24]) were performed using the program package Gaussian 03.[25] The structures of the compounds [Fe(TPP)(Cl)] ($S = {}^5/_2$), [Mn(TPP)(Cl)] ($S = 2$), and [Co(TPP)(Cl)] ($S = 0$) were fully optimized without simplifications using the LanL2DZ basis set. Calculated vibrational frequencies for **1** show that the obtained geometry represents a true minimum because no imaginary frequency is obtained. For compounds **2** and **3**, one imaginary frequency ($<6i$ cm^{-1}) is calculated, which corresponds to the out-of-plane deformation mode of the ruffling type[26] (B_{1u}) at low energy. Infrared and Raman intensities were calculated as well. In all calculations, convergence was reached when the relative change in the density matrix between subsequent iterations was less than 1×10^{-8}. The structures of the models [Fe(P)(Cl)] (P = porphine; $\tilde{\mathbf{1}}$, $S = {}^5/_2$), [Mn(P)(Cl)] ($\tilde{\mathbf{2}}$, $S = 2$), and [Co(P)(Cl] ($\tilde{\mathbf{3}}$, $S = 0$) have also been fully optimized using B3LYP/LanL2DZ. For these calculations, the TPP ligand has been simplified to porphine (Scheme 1). The illustrations of the local coordinates of bromobenzene (cf. Figure 3) were obtained using the program GaussView.

Normal Coordinate Analysis (NCA). Normal coordinate calculations were performed using the QCPE computer program 576 by M. R. Peterson and D. F. McIntosh. The calculations are on the basis of a general valence force field and the force constants are refined with a nonlinear simplex algorithm. The simplex optimization was used to refine only selected force constants according to the quantum-chemistry centered normal coordinate analysis (QCC−NCA) scheme.[21] Here, a force field from DFT calculations is used as a starting point to generate initial force constants, and a subset of these is fitted to reproduce the known experimental frequencies. Force constants were obtained from the Gaussian output using a modified version of the program Redong[27] (QCPE 628). For the normal coordinate analysis, model complexes $\tilde{\mathbf{1}}-\tilde{\mathbf{3}}$ were modified by using a mass of 77 corresponding to a phenyl group for the hydrogens of the meso carbon atoms. This leads to models [Fe(P*)Cl] ($\tilde{\mathbf{1}}$**a**), [Mn(P*)Cl] ($\tilde{\mathbf{2}}$**a**), and [Co(P*)Cl] ($\tilde{\mathbf{3}}$**a**).

Results and Analysis

A. Crystal and DFT-optimized Structures of [Fe(TPP)(Cl)] (1), [Mn(TPP)(Cl)] (2), and [Co(TPP)Cl] (3). To calculate the vibrational spectra of **1**−**3**, their geometric structures have to be fully optimized first. In this section, the calculated structures are compared to the experimental ones, and in addition, a new crystal structure of the chloroform solvate of complex **2** is presented. Altogether, satisfactory agreement between the DFT calculations and experiment is obtained. Considering the porphyrin core bond lengths, excellent agreement with experiment is achieved in this study, as shown in Table S6.

A.1. Crystal and DFT Structures of Compound 1. The crystal structure of the tetragonal form of compound **1** has been determined by Hoard et al.[28] Later, Scheidt and Finnegan[29] obtained the structure of a monoclinic form of this complex. The monoclinic form differs significantly from the tetragonal form. It shows a small C_{4v} doming and a displacement of the iron from the N_4 plane by $\Delta Fe-Ct = 0.49$ Å. In contrast, the tetragonal form has an almost planar porphyrin core. Because of the conditions applied to the preparation of the compound (solvent used for recrystallization), it can be assumed that our compound corresponded to the tetragonal form. In this structure, the axial Fe−Cl bond is 2.192 Å, the averaged Fe−N distance is 2.049 Å, and the out-of-plane displacement of the iron atom is $\Delta Fe-Ct = 0.383$ Å. Figure 1A shows the DFT-optimized structure of **1**, which shows an overall good agreement with the crystal structure. In both cases, the porphyrin ring is almost planar

(24) Becke, A. D. *Phys. Rev. A: At., Mol., Opt. Phys.* **1988**, *38*, 3098. (b) Becke, A. D. *J. Chem. Phys.* **1993**, *98*, 1372. (c) Becke, A. D. *J. Chem. Phys.* **1993**, *98*, 5648.

(25) Frisch, M. J.; Trucks, G. W.; Schlegel, H. B.; Scuseria, G. E.; Robb, M. A.; Cheeseman, J. R.; Montgomery, J. A., Jr.; Vreven, T.; Kudin, K. N.; Burant, J. C.; Millam, J. M.; Iyengar, S. S.; Tomasi, J.; Barone, V.; Mennucci, B.; Cossi, M.; Scalmani, G.; Rega, N.; Petersson, G. A.; Nakatsuji, H.; Hada, M.; Ehara, M.; Toyota, K.; Fukuda, R.; Hasegawa, J.; Ishida, M.; Nakajima, T.; Honda, Y.; Kitao, O.; Nakai, H.; Klene, M.; Li, X.; Knox, J. E.; Hratchian, H. P.; Cross, J. B.; Bakken, V.; Adamo, C.; Jaramillo, J.; Gomperts, R.; Stratmann, R. E.; Yazyev, O.; Austin, A. J.; Cammi, R.; Pomelli, C.; Ochterski, J. W.; Ayala, P. Y.; Morokuma, K.; Voth, G. A.; Salvador, P.; Dannenberg, J. J.; Zakrzewski, V. G.; Dapprich, S.; Daniels, A. D.; Strain, M. C.; Farkas, O.; Malick, D. K.; Rabuck, A. D.; Raghavachari, K.; Foresman, J. B.; Ortiz, J. V.; Cui, Q.; Baboul, A. G.; Clifford, S.; Cioslowski, J.; Stefanov, B. B.; Liu, G.; Liashenko, A.; Piskorz, P.; Komaromi, I.; Martin, R. L.; Fox, D. J.; Keith, T.; Al-Laham, M. A.; Peng, C. Y.; Nanayakkara, A.; Challacombe, M.; Gill, P. M. W.; Johnson, B.; Chen, W.; Wong, M. W.; Gonzalez, C.; Pople, J. A. *Gaussian 03*, revision C.02; Gaussian, Inc.: Wallingford, CT, 2004.

(26) Jentzen, W.; Song, X.-Z.; Shelnutt, A. *J. Phys. Chem. B* **1997**, *101*, 1684−1699.

(27) Allouche, A.; Pourcin, J. *Spectrochim. Acta, Part A* **1993**, *49*, 571.

(28) Hoard, J. L.; Cohen, G. H.; Glick, M. D. *J. Am. Chem. Soc.* **1967**, *89*, 1992−1996.

(29) Scheidt, W. R.; Finnegan, M. G. *Acta Crystallogr., Sect. C* **1989**, *45*, 1214−1216.

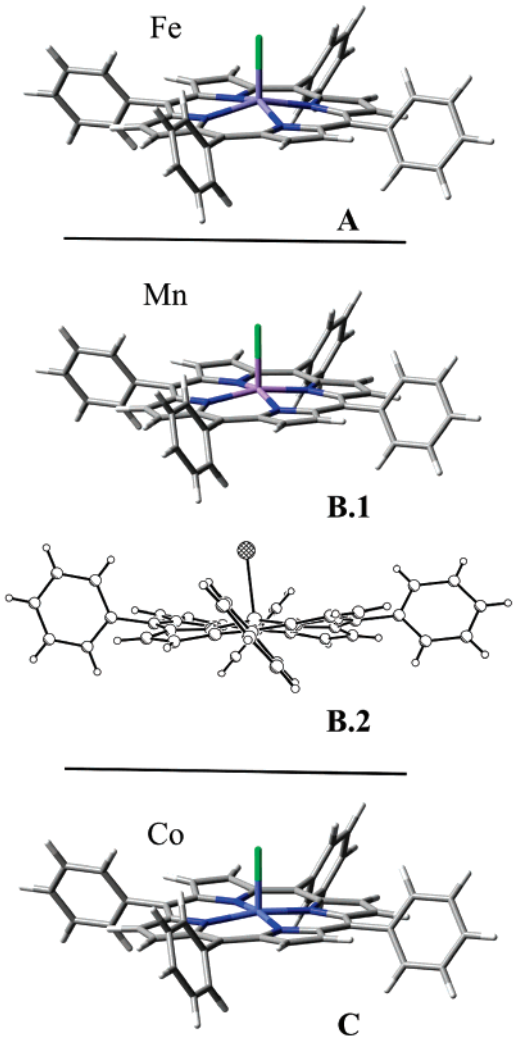

Figure 1. DFT optimized structure of **1** (A); DFT optimized structure of **2** (B.1); the crystal structure of **2** in side view (B.2); and DFT optimized structure of **3** (C).

and the phenyl rings are slightly tilted. The DFT structure also shows a very small amount of saddling of the porphyrin ring, which is not observed experimentally. The calculated Fe−N distance of 2.09 Å and the obtained Fe−Ct distance of 0.45 Å are in very good agreement with experiment. Therefore, a good theoretical description of the $[Fe(TPP)]^+$ core of **1** has been obtained. The largest deviation in the calculated structure is observed for the Fe−Cl bond distance of 2.32 Å, which is too long.

A.2. Crystal and DFT Structures of Compound 2. In the new crystal structure presented here, compound **2** crystallizes in the monoclinic space group $P2_1/n$ with four formula units in the unit cell and all atoms located in general positions. The porphyrin moiety is saddled and shows a deviation of the atoms from the best least-squares plane of about 0.29 Å. The manganese atom is located 0.258 Å above the plane formed by the four nitrogen atoms. The averaged manganese nitrogen distance is 2.019 Å, and hence it is between the values for **1** and **3** (vide infra). The obtained manganese chloride distance is 2.389 Å. Note that the crystal structures of **2** as toluene[30] or acetone[31] solvate are very similar. Larger deviations are observed for the solvate's free

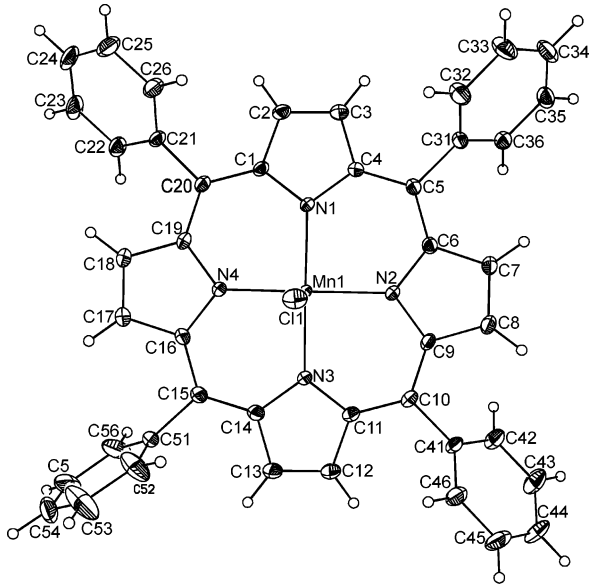

Figure 2. Crystal structure of compound **2** with labeling. Displacement ellipsoids are drawn at the 50% probability level.

crystal structure,[32] which shows an almost planar porphyrin core. The DFT-optimized and the crystal structures of **2** (chloroform solvate) are shown in Figures 1B and 2. In contrast to the crystal structure, the optimized structure shows an almost planar porphyrin core with a small amount of saddling present. The averaged manganese nitrogen distance of 2.036 Å and the Mn−Cl distance of 2.420 Å, however, are both in very good agreement with experiment. In addition, the calculated displacement of the manganese atom from the nitrogen N_4 plane of the porphyrin is 0.28 Å and hence, close to the experimental value. Therefore, in this case, the largest deviation of the calculated structure is observed for the ring conformation of the TPP ligand.

A.3. Crystal and DFT Structures of Compound 3. The crystal structure of [Co(TPP)(Cl)] shows a body-centered tetragonal unit cell.[33] The coordination geometry of the Co(III) ion corresponds to a pyramid, where the cobalt atom is displaced from the porphyrin plane by only 0.05 Å. The porphyrin ring itself is almost planar. Bond distances of 1.985 Å for Co−N and 2.145 Å for Co−Cl are observed. The DFT-optimized structure of **2** is shown in Figure 1C. The optimized structure shows an almost planar porphyrin core in agreement with experiment, with a small amount of saddling present. The calculated Co−N distance of 1.99 Å is in excellent agreement with the crystal structure, whereas the out-of-plane displacement of ΔCo−Ct = 0.17 Å is somewhat overestimated. As in the case of **1**, the largest deviation is observed for the Co−Cl distance, which is calculated to be 2.25 Å.

B. Vibrational Spectra and Assignment of Compound 1. As mentioned in the Introduction, earlier vibrational

(30) Armstrong, R. S.; Foran, G. J.; Hambley, T. W. *Acta Crystallogr., Sect. C* **1993**, *49*, 236−238.
(31) Tulinsky, A.; Chen, B. M. L. *J. Am. Chem. Soc.* **1977**, *99*, 3647−3651.
(32) Cheng, B.; Scheidt, W. R. *Acta Crystallogr., Sect. C* **1996**, *52*, 361−363.
(33) Sakurai, T.; Yamamoto, K.; Naito, H.; Nakamoto, N. *Bull. Chem. Soc. Jpn.* **1976**, *49*, 3042−3046.

analyses of [Fe(TPP)(Cl)] were restricted to the RR spectrum obtained for the Soret excitation.[20] Additionally, three IR bands of **1** were assigned, which are considered to be structure-sensitive.[18b] Here, we report the nonresonance Raman (NR Raman) spectrum of **1**, including polarized measurements for the first time. Complete assignments of these data are achieved using DFT calculations. In addition, RR data measured at variable wavelengths including new polarized data are presented and used to assign additional bands. Finally, the IR spectrum of **1** is assigned.

B.1. Classification of the TPP Vibrations Using Group Theory. To assign the vibrational spectra of **1**, an effective D_{4h} symmetry was applied. The analysis of the polarized data (cf. section B.5) shows that this approach is justified even for five-coordinate compounds such as **1**−**3**. D_{4h} symmetry is obtained for a planar porphyrin core with the metal being located in the plane with no axial ligand present. The phenyl rings are exactly perpendicular to the porphyrin plane. In this D_{4h} model system [M(TPP)] (idealized metalloporphyrin), the planar porphyrin core has 71 in-plane modes:[10a]

$$\Gamma_{\text{in plane}} = 9A_{1g}(R) + 8A_{2g}(RR) + 9B_{1g}(R) + 9B_{2g}(R) + 18E_u(IR) \quad (1)$$

In the NR Raman spectrum, 27 in-plane vibrations are therefore expected, 9 of them polarized (A_{1g}) and 18 of them depolarized (B_{1g} and B_{2g}). The infrared spectrum shows a maximum of 18 modes with E_u symmetry. In addition, the porphyrin core of the D_{4h} model system has 34 out-of-plane vibrations:[10a]

$$\Gamma_{\text{out of plane}} = 3A_{1u} + 6A_{2u}(IR) + 4B_{2u} + 5B_{1u} + 8E_g(R) \quad (2)$$

The eight E_g modes are Raman-active, and the six A_{2u} modes are infrared-active. Therefore, on the basis of a purely statistical consideration, many more in-plane than out-of-plane modes can be expected in the NR Raman and IR spectra of metalloporphyrins. To classify the different porphyrin core vibrations, the local coordinates defined by Li et al.[10] are used (cf. Figures S6 and S7) in the following analysis of these spectra.

Besides the porphyrin core modes, a large number of phenyl vibrations are also present in TPP complexes. Different approaches can be taken in the classification of these vibrations. For example, Stein et al.[34] identified several phenyl modes in [(FeTPP)$_2$O] using biphenyl as the model system.[35] To give an intuitive assignment of the phenyl modes of TPP, we use bromobenzene as the model. Table 2 provides a complete list of all normal modes of bromobenzene together with calculated energies and assignments using local coordinates. Figure 3 shows the important phenyl vibrations in bromobenzene that are also observed in the spectra of **1**−**3**. The TPP ligand itself has four phenyl groups that are bound to the meso carbon atoms of the porphyrin core. Hence, for every local phenyl coordinate, there are four symmetry-adapted combinations in TPP. Because the interactions of the local vibrations of different phenyl rings are small, the obtained splittings between the resulting four combinations are also small (usually 5−10 cm^{-1}). Hence, the four resulting symmetry-adapted linear combinations are also designated as a symmetry block because they are close in energy. Because there are four different irreducible representations in C_{2v} (the point group of bromobenzene), four different symmetry blocks exist:

$$\text{out-of-plane: } B_1 \rightarrow B_{1g}(R) + A_{2g}(RR) + E_u(IR) \quad (\pi, \pi', \text{and } \pi'') \quad (3)$$

$$\text{out-of-plane: } A_2 \rightarrow A_{1u} + B_{2u} + E_g(R) \quad (\sigma, \sigma', \text{and } \sigma'') \quad (4)$$

$$\text{in-plane: } B_2 \rightarrow B_{1u} + A_{2u}(IR) + E_g(R) \quad (\psi, \psi', \text{and } \psi'') \quad (5)$$

$$\text{in-plane: } A_1 \rightarrow A_{1g}(R) + B_{2g}(R) + E_u(IR) \quad (\phi, \phi', \text{and } \phi'') \quad (6)$$

The nomenclature (π, σ, ψ, and ϕ) is taken from ref 10. To classify the different porphyrin core and phenyl modes in D_{4h} symmetry, we used the idealized model [Zn(TPP)] and calculated the vibrations of this model in D_{4h} symmetry. [Zn(TPP)] has 169 normal modes (56 of them are degenerate), where 44% are Raman- and 27% are IR-active.

B.2. NR Raman Spectrum and Assignment of 1. The experimental and calculated NR Raman spectra of **1** are shown in the top panel of Figure 4. Corresponding polarized data are included in the lower panel. The calculated spectrum is, in general, shifted to a somewhat higher energy (the average deviation in vibrational energies is about 2 to 3%) compared to experiment, which is further evaluated in the discussion. Besides the good agreement in vibrational frequencies, very good agreement with experiment is obtained for the calculated NR Raman intensities, as shown in Figure 4 (top). This allows for a detailed assignment of the data. Importantly, additional information to support the Raman assignments is available from polarization measurements. The depolarization ratio ρ is defined as $\rho = I_{\text{perpendicular}}/I_{\text{parallel}}$. In D_{4h} symmetry, one obtains[1]

Table 1. Crystal Data and Results of Structure Refinement for Compound **2**

cmpd	**2**
chemical formula	$C_{44}H_{28}N_4MnCl \cdot CHCl_3$
fw	822.46
$T =$	150 K
$\lambda =$	0.71073
crystal system	monoclinic
space group	$P2_1/n$
$a =$	12.157 (1) Å
$b =$	21.899 (2) Å
$c =$	14.479 (1) Å
$\beta =$	102.05 (1)
$V =$	3769.7 (4) Å^3
Z	4
$D_{\text{calcd}} =$	1.449 g·cm^{-3}
$\mu =$	0.67 mm^{-1}
R1[a] [$I > 2\sigma(I)$]	0.0392
wR2[b] [all data]	0.1053

[a] $R1 = \Sigma ||Fo| - |Fc||/\Sigma|Fo|$. [b] $wR2 = [\Sigma[w(F_o^2 - F_c^2)^2]/\Sigma[w(F_o^2)^2]]^{1/2}$.

(34) Stein, P.; Ulman, A.; Spiro, T. G. *J. Phys. Chem.* **1984**, *88*, 369−374.
(35) Zerbi, G.; Sandioni, S. *Spectrochim. Acta, Part A* **1968**, *24*, 511.

Table 2. Calculated Vibrational Energies (cm^{-1}) of Bromobenzene and Assignments Using Local Coordinates

	frequencies				frequencies		
$\nu(Ph)_i$	calcd[a]	assignment[b]	sym.[c]	$\nu(Ph)_i$	calcd[a]	assignment[b]	sym.[c]
1	167	γ(Br)	B_1	16	1082	ν_1(C−C)	A_1
2	242	δ(C−C−Br)	B_2	17	1098	ν_{asym1}(C−C) + δ(C−C−H)	B_2
3	301	ν(C−Br)	A_1	18	1206	δ_{asym}(C−C−H)	B_2
4	419	τ(ringtwist)	A_2	19	1216	δ_{sym}(C−C−H)	A_1
5	475	γ_1(C)	B_1	20	1344	δ(C−C−H) + ν_2(C−C)	B_2
6	627	δ_1(C−C−C)	B_2	21	1364	ν_{asym2}(C−C)	B_2
7	669	δ_2(C−C−C)	A_1	22	1468	ν_{asym3}(C−C) + δ(C−C−H)	B_2
8	712	γ_2(C)	B_1	23	1499	δ(C−C−H) + ν_{asym4}(C−C)	A_1
9	773	γ_1(H)	B_1	24	1621	ν_{sym}(C−C)	A_1
10	870	γ_2(H)	A_2	25	1629	ν_3(C−C)	B_2
11	952	γ_3(H)	B_1	26	3198	ν(C−H)	A_1
12	1009	δ_{sym}(C−C−C)	A_1	27	3209	ν(C−H)	B_2
13	1014	τ_1	A_2	28	3224	ν(C−H)	A_1
14	1032	$\nu_{breathing}$(C−C)	A_1	29	3235	ν(C−H)	B_2
15	1038	τ_2	B_1	30	3242	ν(C−H)	A_1

[a] Calculated with B3LYP/LanL2DZ; see the Experimental section. [b] Assignments using local coordinates; see Figure 3. [c] Symmetries in the point group C_{2v}.

(1) $0 < \rho < 0.75$ for polarized bands (A_{1g} vibrations),

(2) $\rho = 0.75$ for depolarized bands (B_{1g} or B_{2g} vibrations), and

(3) $\rho > 0.75$ for anomalous polarized bands (A_{2g} vibrations (only RR spectroscopy)).

Hence, *the polarized measurements allow for the determination of the symmetry of a particular mode.*[36] The complete assignments obtained in this manner are listed in Table 3. Additionally, the d_8 isotope shifts available for a number of bands from the RR measurements[14b] are used for comparison with calculated isotope shifts to further confirm our assignments. For a better comparison with the literature, the notation established by Spiro and co-workers for [Ni(TPP)] is used in Table 3. Correspondingly, the porphyrin in-plane modes (both stretching and deformation modes) are labeled ν_i and the porphyrin out-of-plane modes are designated as γ_i.[13] The phenyl mode notation is on the basis of the different symmetry blocks (eqs 3−6). For the oxidation- and spin-state sensitive modes, the common notation from the literature is included in Table 3, where bands A(p), B(dp), C(ap), D(p), and E(p)[18b] are observed in the RR spectra and bands I, II, and III are found in the IR spectra.[18b,42]

The NR Raman spectrum of **1** in Figure 4 can be divided into four regions showing different kinds of vibrations. In the low-energy region between 200 and 500 cm^{-1}, two phenyl out-of-plane vibrations, one porphyrin out-of-plane deformation, and three in-plane porphyrin vibrations are observed (cf. Table 3). The mode at 199 cm^{-1} (calcd: 202 cm^{-1}) corresponds to the Fe−N stetching vibration of B_{1g} symmetry (ν_{18}) and is therefore depolarized. The mode at 390 cm^{-1} (calcd: 388 cm^{-1}) is known to be oxidation-state-sensitive (band E(p)[18b]) and was assigned previously to a porphyrin core deformation mode.[14,18b] However, on the basis of the calculations and the fact that this mode shows strong Soret resonance enhancement, it is assigned to the totally symmetric $\nu_{breathing}$(Fe−N) vibration (ν_8). This is in agreement with the assignments for [Ni(TPP)].[10a,13] The calculated d_8 isotope shift for this mode of 8 cm^{-1} is in very good agreement with the experimental value of 10 cm^{-1}.[14b] The weak band at 379 cm^{-1} (calcd: 336 cm^{-1}) corresponds to the Fe−Cl stretching vibration, which is strongly IR-active (vide infra). The very weak band at 257 cm^{-1} (calcd: 251 cm^{-1}) belongs to the Raman-forbidden γ(Pyr. tilting) vibration of B_{2u} symmetry, which gains intensity through coupling with the Raman allowed γ(Phenylrot.) phenyl vibration of B_{1g} symmetry. Hence, the fact that this mode appears in the Raman spectra is a true effect of the symmetry lowering in **1**. Correspondingly, the very weak feature at 247 cm^{-1} (calcd: 241 cm^{-1}) is assigned to the γ(Phenylrot.) phenyl vibration with B_{1g} symmetry, which is mixed with the γ(Pyr. tilting) porphyrin core vibration with A_{2u} symmetry.

In the energy range from 800 to 1050 cm^{-1}, two weak bands are observed that are assigned to porphyrin core modes. The feature at 994 cm^{-1} (calcd: 1008 cm^{-1}) corresponds to ν(Pyr. breathing) with phenyl contribution (ν_6; cf. Table 3), and the band at 886 cm^{-1} (calcd: 898 cm^{-1}) corresponds to a totally symmetric in-plane deformation mode. This latter vibration was originally assigned to a phenyl vibration,[14] which, based on our calculations is described as a mixed δ_{sym}(Pyr. deformation) and phenyl mode (ν_7). The calculated d_8 isotope shift is 5 cm^{-1}, which is in

(36) Depolarization ratios for some of the weaker bands are difficult to determine from the polarized NR Raman spectrum in Figure 4. In these cases, the depolarization ratios from RR measurements were used. For example, the band at 1364 cm^{-1} is strongly enhanced in Soret resonance, where the depolarized band at 1371 cm^{-1} is not observed. Hence, from the Soret resonance spectrum, the depolarization ratio of this band can be determined.

(37) For the two weak bands at 1275 and 1467 cm^{-1}, depolarization ratios that are slightly larger than 0.75 have been obtained. However, these bands are enhanced in Q and Q_v resonance and are depolarized in these spectra. In addition, anomalous polarized bands (A_{2g}), where $\rho > 0.75$, are forbidden in NR Raman. Hence, the bands at 1275 and 1467 cm^{-1} are classified as dp.

(38) Gouterman, M. In *The Porphyrins*; Dolphin, D., Ed.; Academic Press: New York, 1979; Vol. 3, Part A, pp 1−156.

(39) According to group theory, A_{1g} vibrations could also induce vibronic mixing. However, A_{1g} modes are ineffective because they do not induce a distortion of the molecule.

(40) Czernuszewicz, R. S.; Spiro, T. G. In *Inorganic Electronic Structure and Spectroscopy;* Solomon, E. I., Lever, A. B. P., Eds.; John Wiley & Sons: New York, 1999; Vol. 1, pp 353−441.

(41) Egawa, T.; Suzuki, N.; Dokoh, T.; Higuchi, T.; Shimada, H.; Kitagawa, T.; Ishimura, Y. *J. Phys. Chem. A* **2004**, *108*, 568−577.

(42) Spiro, T. G. *Curr. Sci.* **1998**, *74*, 304−307.

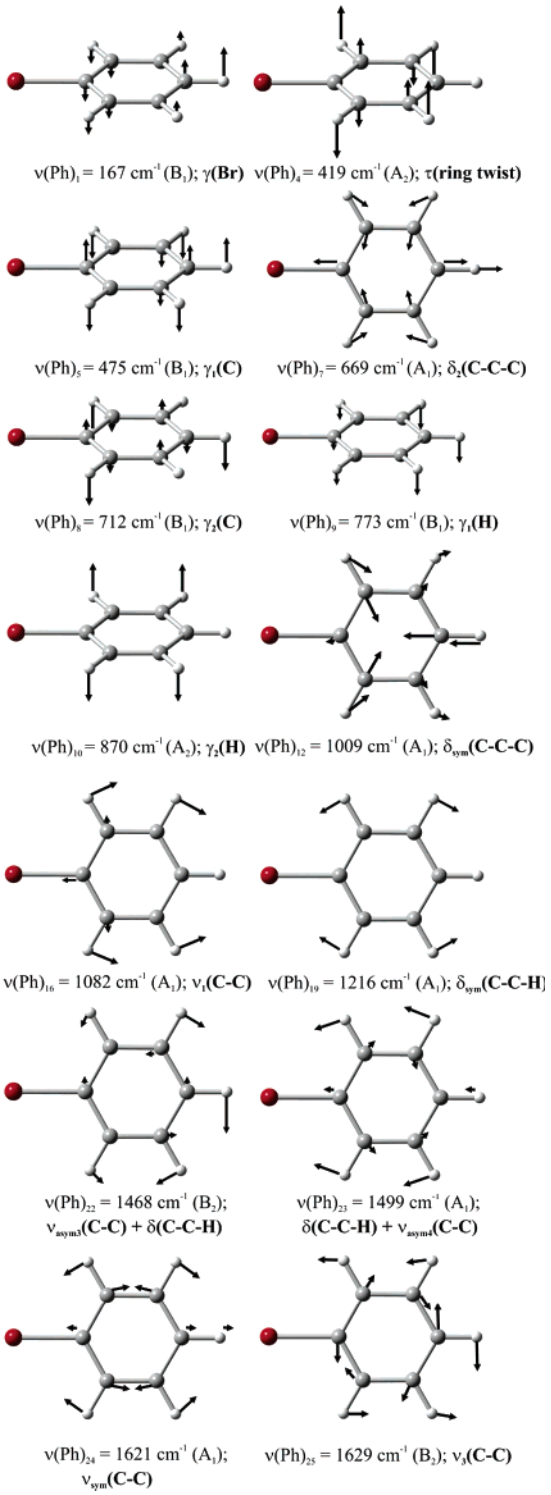

Figure 3. Illustration of the local coordinates of bromobenzene used for classification of in-plane and out-of plane phenyl modes in complexes **1**−**3** (γ(Br) = γ(Phenylrot.)).

contrast to the experiment, where no shift was detected.[14b] This indicates that the calculations overestimate the δ_{sym}(Pyr. deformation) contribution to this mode (Discussion). The most intense band in this spectral region is located at 1006 cm^{-1} (calcd: 1018 cm^{-1}). This feature is assigned to a polarized (totally symmetric) phenyl in-plane vibration (ϕ_8). It was originally assigned to a ν(C$_\alpha$−C$_m$) vibration[14] and later reassigned to a ν(Pyr. breathing) mode.[20] However, on the basis of the calculated intensities, this band has to be assigned to the mixed phenyl δ_{sym}(C−C−C) and ν(Pyr. breathing) porphyrin vibration (calcd: 1018 cm^{-1}), which is more in agreement with ref 20. The calculated d_8 isotope shift of 1 cm^{-1} is in the correct range compared to the experimental value of 6 cm^{-1}.[14b] The observed discrepancies indicate that in this case the calculations underestimate the admixture of the porphyrin core vibration (Discussion). Finally, a weak band is found at 1030 cm^{-1} (calcd: 1054 cm^{-1}), which corresponds to an in-plane phenyl vibration (ϕ_7).

The region between 1050 and 1550 cm^{-1} contains only in-plane porphyrin core vibrations with the exception of the highly intense band at 1495 cm^{-1}, which is of the in-plane phenyl type (ϕ_5') but also has some porphyrin C−C stretching character (ν_{sym}(C$_\alpha$−C$_m$)). With the exception of the totally symmetric vibration at 1072 cm^{-1} (calcd: 1124 cm^{-1}), which is a C$_\beta$−H deformation mode (ν_9), all of the other porphyrin core vibrations are of the stretching type. The calculated frequency of ν_9 is 52 cm^{-1}, 4.9% higher in energy compared to the experimental value, which reflects the neglect of anharmonicity in the calculation (Discussion). Two totally symmetric vibrations in this region are known to be structure sensitive. The ν_{sym}(Pyr. half-ring) vibration at 1363 cm^{-1} (calcd: 1379 cm^{-1}) is both oxidation- and spin-state sensitive (band A(p) [18b]). The calculated d_8 isotope shift of 12 cm^{-1} of this mode is in excellent agreement with experiment (13 cm^{-1}).[14b] The polarized band at 1554 cm^{-1} (calcd: 1598 cm^{-1}) is assigned to a combined ν(C$_\beta$−C$_\beta$) + ν_{sym}(C$_\alpha$−C$_m$) + δ_{sym}(C$_\beta$−H) spin-state-sensitive vibration (band D(p) [18b]). The calculated d_8 isotope shift of 21 cm^{-1} is identical to the experimental value.[14b] These assignments are in agreement with the literature.[14b] One additional polarized (totally symmetric) band is found at 1233 cm^{-1} (calcd: 1260 cm^{-1}), which is assigned to ν(Pyr. breathing) + ν(C$_m$−Ph) (ν_1) with a calculated d_8 isotope shift of 3 cm^{-1}, which is again in excellent agreement with experiment (3 cm^{-1}).[14b] This assignment is partially in agreement with the literature, where this band was assigned to a pure ν(C$_m$−Ph).[20] Finally, four depolarized bands are observed in this region. Only the ν_{sym}(Pyr. half-ring) (ν_{12}) vibration at 1275 cm^{-1} (calcd: 1274 cm^{-1}) has B$_{1g}$ symmetry,[37] whereas the others at 1495, 1371, and 1467 cm^{-1} have B$_{2g}$ symmetry. Detailed assignments of these features are given in Table 3.

Finally, the two bands at the highest energy are both assigned to purely symmetric C−C stretching modes of the phenyl rings. From the polarized measurements, these have different symmetries: the band at 1597 cm^{-1} (calcd: 1650 cm^{-1}) is polarized (A$_{1g}$) and the feature at 1574 cm^{-1} (calcd 1649 cm^{-1}) is depolarized (B$_{2g}$). The larger deviations observed between the calculated and experimental frequencies for these modes (∼4%) are partly due to an intrinsic inaccuracy in the calculations (Discussion). The assignment of the band at 1597 cm^{-1} is in agreement with earlier work.[20] No d_8 isotope shift is calculated for these features. In comparison, the experimental value for the A$_{1g}$ mode is 5 cm^{-1}, [14b] indicating the presence of a small admixture of porphyrin core modes.

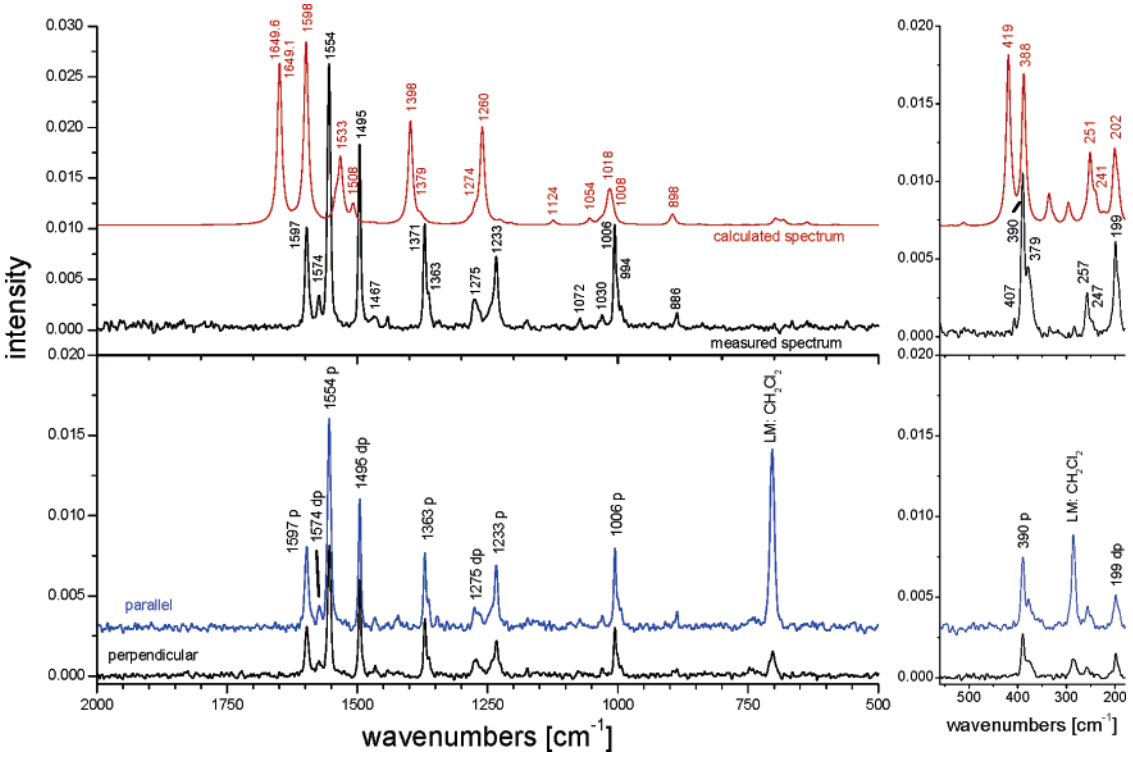

Figure 4. Comparison of the calculated and measured NR Raman spectra of **1** (top) and the polarization measurement in dichloromethane (bottom). The low energy part (560−180 cm^{-1}) of the calculated spectrum (top right) is enlarged in the Figure.

B.3. Infared Spectrum and Assignment of 1. Figure 5 shows the experimental and calculated IR spectra of **1**. As in the NR Raman case, the calculated vibrational energies are in good agreement and the IR intensities are in very good agreement with the experimental data, reproducing the overall appearance of the experimental spectrum very well. The calculated frequencies for a number of modes are too high in energy, as analyzed below. The assignments of the infrared spectrum of **1** are on the basis of the calculated energies and intensities, and the results are summarized in Table 3. In addition, calculated d_8 isotope shifts for the structure-sensitive bands I, II, and III can be compared to the experimental data[18b] reported for [Co(TPP)] and [{Fe(TPP)}$_2$O]. The IR spectrum can be divided into five regions of different types of vibrational modes.

In the far-IR region between 350 and 450 cm^{-1}, only in-plane porphyrin core vibrations are observed. The only exception is the strong band at 378 cm^{-1} (calcd: 336 cm^{-1}), which corresponds to the ν(Fe−Cl) stretching mode. More importantly, the totally symmetric Fe−N breathing vibration (ν_8) at 390 cm^{-1} (calcd: 388 cm^{-1}; vide supra) is also observed in the IR spectrum as a weak band. This is another indication of the lowered symmetry in **1** because this band is IR forbidden in D_{4h}. Two E_u symmetric vibrations are observed in this region: the feature at 402 cm^{-1} (calcd: 407 cm^{-1}) corresponds to a mixed ν(Fe−N) + δ(Pyr. translation) (ν_{50}) mode, whereas the band at 434 cm^{-1} (calcd: 444 cm^{-1}) is assigned to a Pyrrol rotation δ(Pyr. rotation) (ν_{49}). This latter feature corresponds to the spin-state sensitive band III, as defined by Oshio et al.[18b] and was identified as a low-energy porphyrin core deformation mode [18b] in agreement with our assignment. The calculated d_8 isotopic shift of 16 cm^{-1} of this feature is in excellent agreement with the observed shifts for [Co(TPP)] and [{Fe(TPP)}$_2$O] of 16 and 17 cm^{-1}.[18b]

The second region between 500 and 810 cm^{-1} mostly comprises out-of-plane vibrations. The two features at 528 (calcd: 537) and 703 cm^{-1} (calcd: 730 cm^{-1}) correspond to out-of-plane phenyl modes with E_u symmetry (π_5'' and π_4''), whereas the phenyl mode at 661 cm^{-1} (calcd: 675 cm^{-1}) is of the in-plane deformation type. Besides these highly intense bands, a very weak feature is observed at 570 cm^{-1} (calcd: 582 cm^{-1}) and assigned as shown in Table 3. The four bands between 710 and 810 cm^{-1} are all of the out-of-plane type. The intense feature at 750 cm^{-1} (calcd: 790 cm^{-1}) corresponds to a phenyl mode (π_3'') of E_u symmetry. Two out-of-plane porphyrin modes of A_{2u} symmetry are found at 720 (calcd: 750 cm^{-1}; γ_8) and 806 cm^{-1} (calcd: 847 cm^{-1}; γ_5), the latter one being the oxidation-state-sensitive band II.[18b] It was originally assigned to an in-plane deformation mode with δ(C$_\beta$−H) character,[18b] on the basis of an observed pyrrole-d_8 isotope shift. However, from the calculations, this band is associated with the intense band calculated at 847 cm^{-1} that corresponds to a γ(H$_\beta$) + γ_{sym}(Pyr. folding) vibration. This mode shows a calculated-d_8 isotope shift of 40 cm^{-1}, which is in excellent agreement with the observed shift of 35 cm^{-1} for [Co(TPP)].[18b] On the basis of these results, band II is reassigned. Finally, the very weak band at 727 cm^{-1} (calcd: 758 cm^{-1}) is assigned to an E_g vibration (γ_{20}; cf. Table 3), which gains in IR intensity via coupling with a phenyl vibration with E_u symmetry. This is another indication of the lowered symmetry in **1** because these two vibrations cannot mix in D_{4h}. The deviations in energy of about 4 to 5% between calculated and experimental

Table 3. Assignment of the Infrared (IR), NR Raman (λ_{exc} = 1064 nm), and Resonance Raman (Soret: λ_{exc} = 454.5 nm; Q_v: λ_{exc} = 514.5 nm; Q: λ_{exc} = 568.2 nm) Spectra of [Fe(TPP)(Cl)] (**1**)[a]

	mode		experimental[d] (cm^{-1})			
ν_i [h]	assignment[b]	symmetry[c]	IR	NR R[e]	RR[e]	calcd[d,f] (cm^{-1})
ϕ_4	ν_{sym}(C−C)	A_{1g}		1597 m (p)	1597 (Soret: 1598 w,p; Q_v: 1595 vw,p; Q: shoulder)	1650 s
ϕ_4''	ν_{sym}(C−C)	E_u	1597 m			1649 m
ϕ_4'	ν_{sym}(C−C)	B_{2g}		1574 w (dp)	~1572/1577 (Soret: -; Q_v: 1571 m,dp/1576 s,dp; Q: 1573 s,dp/1578 vs,dp)	1649 m
ψ_3'	ν_3(C−C) + **ν_{asym}(C$_\alpha$−C$_m$)**	$A_{2u} + B_{1g}$	1574 vw			1618 vw
ν_2	**$\underline{\nu(C_\beta-C_\beta)}$ + ν_{sym}(C$_\alpha$−C$_m$) + δ_{sym}(C$_\beta$−H)**	A_{1g}		1554 vs (p)	~1556 (Soret: 1557 vs,p; Q_v: 1555 s,p; Q: 1557 s,p)	1598 vs
ν_{19}	**$\underline{\nu_{asym}(C_\alpha-C_m)}$ + ν_{asym}(C$_\alpha$−C$_\beta$) + δ_{asym}(C$_\beta$−H)**	A_{2g}			~1522/1516 (Soret: 1523/1517 vw; Q_v: 1523/1517 w,ap; Q: 1521/1515 m,ap)	1560
ϕ_5'	δ(C−C−H) + ν_{asym4}(C−C) + **ν_{sym}(C$_\alpha$−C$_m$)**	B_{2g}		1495 m (dp)	~1495 (Soret: 1494 vw,-; Q_v: 1494 s,dp; Q: 1496 vs,dp)	1533 m
ϕ_5''	δ(C−C−H) + ν_{asym4}(C−C) + **ν(C$_\beta$−C$_\beta$) + ν_{asym}(C$_\alpha$−C$_m$) + ν_{sym}(C$_\alpha$−C$_m$)**	E_u	1486 w			1521 s
ν_{28}	**$\underline{\nu_{sym}(C_\alpha-C_m)}$ + ν_{asym}(Pyr. half-ring)**	B_{2g}		1467 vw (dp)	1467 (Soret: -; Q_v: 1467 vw,dp; Q: 1467 vw,dp)	1508 w
ν_3	**$\underline{\nu_{sym}(C_\alpha-C_m)}$ + ν(C$_\beta$−C$_\beta$)**	A_{1g}			1452 (Soret: 1452 m,p; Q_v: 1450 vw,p; Q: -)	1489
ψ_4'	ν_{asym3}(C−C) + δ(C−C−H)	A_{2u}	1440 m			1470 m
ν_{29}	**$\underline{\nu(Pyr.\ quarter\text{-}ring)}$ + ν(C$_m$−Ph)**	B_{2g}		1371 m (dp)	~1371 (Soret: -; Q_v: 1370 s,dp; Q: 1372 m,dp)	1398 m
ν_4	**$\underline{\nu_{sym}(Pyr.\ half\text{-}ring)}$**	A_{1g}		1363 w	~1363 (Soret: 1364 s,p; Q_v: 1361 m,p; Q: 1365 m,p)	1379 vw
ν_{20}	**$\underline{\nu(Pyr.\ quarter\text{-}ring)}$ + δ_{sym}(C$_\beta$−H)** + δ(C−C−H) + ν_2(C−C)	A_{2g}			~1335 (Soret: -; Q_v: 1334 m,ap; Q: 1336 m,ap)	1373
ν_{41}	**δ_{asym}(C$_\beta$−H) + ν(C$_m$−Ph) + $\underline{\nu_{sym}(Pyr.\ half\text{-}ring)}$ ν_{asym}(C$_\alpha$−C$_\beta$)**	E_u	1340 m 1334 m			1369 s
ν_{12}	**$\underline{\nu_{sym}(Pyr.\ half\text{-}ring)}$**	B_{1g}		1275 w (dp)	1278 (Soret: 1278 vw,-; Q_v: 1278 w,dp; Q: 1278 m,dp)	1274 vw
ν_{27}	**ν(Pyr. quarter-ring) + $\underline{\nu(C_m-Ph)}$** + ν_1(C−C)	B_{2g}			~1266 (Soret: 1266 vw,dp; Q_v: 1265 w,dp; Q: 1266 m,dp)	1286 vvw
ν_1	**ν(Pyr. breathing) + $\underline{\nu(C_m-Ph)}$**	A_{1g}		1233 m (p)	~1233 (Soret: 1235 m,p; Q_v: 1230 w,p; Q: 1232 w,p)	1260 m
ν_{26}	**$\underline{\delta_{asym}(C_\beta-H)}$ + ν_{sym}(Pyr. quarter-ring)**	A_{2g}			~1225 (Soret: -; Q_v: 1225 w,ap; Q: 1226 vw,ap)	1248
ν_{36}	**ν_{sym}(Pyr. half-ring) + ν(Pyr. quarter-ring) + $\underline{\nu(C_m-Ph)}$**	E_u	1200 w			1250 w
ν_{34}	**$\underline{\delta_{asym}(C_\beta-H)}$ + ν_{asym}(C$_\alpha$−C$_\beta$)**	B_{2g}			1182 (Soret: -; Q_v: 1181 w,dp; Q: 1182 w,dp)	1226

Table 3 (Continued)

	mode		experimental[d] (cm^{-1})			
ν_i [h]	assignment[b]	symmetry[c]	IR	NR R[e]	RR[e]	calcd[d,f] (cm^{-1})
ν_{51}	**ν(Pyr. quarter-ring) + ν(Pyr. breathing)**	E_u	1175 m			1236 m
ϕ_6''	δ_{sym}(C−C−H)	E_u	1158 w			1223 w
ν_{17}	**δ_{sym}(C$_\beta$−H)**	B_{1g}			1080 (Soret: -; Q_v: 1081 w,dp; Q: 1080 m,dp)	1125
ν_9	**δ_{sym}(C$_\beta$−H)**	A_{1g}		1072 vw	~1072 (Soret: 1073 m,p; Q_v: 1070 m,p; Q: 1073 m,p)	1124 vw
ψ_8'	ν_{asym1}(C−C) + δ(C−C−H)	A_{2u}	1070 m			1106 m
ν_{52}	**δ_{sym}(C$_\beta$−H)**	E_u				1117 w
ϕ_7	ν_1(C−C)	A_{1g}		1030 vw	~1029 (Soret: -; Q_v: 1028 vw,p; Q: 1030 vw,p)	1054 w
ν_{30}	**ν_{asym}(Pyr. half-ring)**	B_{2g}			~1017 (Soret: -; Q_v:1015 w,dp; Q:1018 s,dp)	1035
ν_{15}	**ν(Pyr. breathing)**	B_{1g}				1030
ϕ_8	δ_{sym}(C−C−C) + **ν(Pyr. breathing)**	A_{1g}		1006 m (p)	1006 (Soret: 1006 w,p; Q_v: 1006 w,p; Q: 1006 m,p)	1018 w
ϕ_8''	δ_{sym}(C−C−C) + **ν(Pyr. breathing) + ν_{asym}(Pyr. half-ring)**	E_u	1002 vs			1017 s
ν_{47}	**ν(Pyr. breathing) + δ_{asym}(Pyr. deformation)** + $\nu_{breathing}$(C−C)	E_u	995 vs			1005 s
ν_6	**ν(Pyr. breathing)** + $\nu_{breathing}$(C−C)	A_{1g}		994 vw (p)	994 (Soret: -; Q_v: 993 w,p; Q: 994 m,p)	1008 w
ν_7	**δ_{sym}(Pyr. deformation)** + γ_2(H)	A_{1g}		886 vw (p)	887 (Soret: 887 w,p; Q_v: 887 vw,p; Q: 887 vw,p)	898 w
ν_{32}	**δ_{asym}(Pyr. deformation)**	B_{2g}			851 (Soret: -; Q_v: 850 vw,dp; Q: 851 w,dp)	890
ν_{16}	**δ_{sym}(Pyr. deformation)** + γ_1(H)	B_{1g}				874
γ_5	**γ(H$_\beta$) + γ_{sym}(Pyr. folding)**	A_{2u}	806 s			847 s
core	overtone 390 cm^{-1}	A_{1g}			779 (Soret: -; Q_v: 779 m,p; Q: 778 vw,p)	
π_3''	γ_1(H)	E_u	750 s			790 vs
π_3	γ_1(H)	B_{1g}			744 (Soret: -; Q_v: -; Q: 744 w,dp)	781
		A_{1g}			723 (Soret: 723 vw,p; Q_v: 723 vw,p; Q: -)	
γ_{20}	**γ_{sym}(Pyr. folding) + γ_{asym}(Pyr. folding) + γ(H$_\beta$)** + γ_1(H)	$E_g + E_u$	727 vw			758
γ_8	**γ_{sym}(Pyr. folding) + γ(H$_\beta$)** + γ_1(H)	A_{2u}	720 m			750
π_4''	γ_2(C)	E_u	703 s			730 s
ϕ_9''	δ_2(C−C−C) + **δ(Pyr. rotation)**	E_u	661 m			675 m
ϕ_9	δ_2(C−C−C)	A_{1g}			639 (Soret: 639 vw,p; Q_v: -; Q: -)	652
	combination band (184 + 391 cm^{-1})	A_{1g}			572 (Soret: 572 vw,p; Q_v: 570 w,p; Q: -)	
γ_7	**γ(C$_\alpha$−C$_m$) + γ_{asym}(Pyr. folding) + γ_{sym}(Pyr. folding)**	A_{2u}	570 vw			582 vw

Table 3 (Continued)

	mode		experimental[d] (cm^{-1})			
ν_i [h]	assignment[b]	symmetry[c]	IR	NR R[e]	RR[e]	calcd[d,f] (cm^{-1})
π_5''	γ_1(C) + **δ(Pyr. translation)**	E_u	528 m			537 m
ν_{49}	**δ(Pyr. rotation)**	E_u	434 s			444 m
σ_{13}''	τ(ring twist)	E_g		407 vw	408 (Soret: -; Q_v: -; Q: 408 vw,-)	419 w
ν_{50}	**ν(Fe−N)** + **δ(Pyr. translation)**	E_u	402 m			407 m
ν_8	**$\nu_{breathing}$(Fe−N)**	A_{1g}	390 m	390 m (p)	391 (Soret: 392 s,p; Q_v: 390 vs,p; Q: 390 w,p)	388 w
Fe−Cl	**ν(Fe−Cl)**		378 s	379 w		336
		A_{1g}			257 (Soret: 258 vw,p; Q_v: 257 w,p; Q: 258 vw,p)	
γ_{16}	**γ(Pyr. tilting)** + γ(Phenylrot.)[g]	$B_{2u} + B_{1g}$		257 vw	258 (Soret: -; Q_v: -; Q: -; $\lambda_{exc.}$= 647.1 nm: 258 vw,dp)	251 vw
Ph	γ(Phenylrot.)[g] + **γ(Pyr. tilting)**	$B_{1g} + A_{2u}$		247 vw	247 (Soret: -; Q_v: -; Q: 247 vw, dp; 647.1 nm: 247 vw,dp)	241 vw
	porphyrin breathing				203 (Soret: 204 vw,p; Q_v: 202 w,p; Q: 202 vw,p)	200 vw
ν_{18}	**ν(Fe−N)**	B_{1g}		199 w (dp)	199 (Soret: -; Q_v: -; Q: -; 647.1 nm: 199 vw,dp)	202 vw

[a] For notations of in-plane and out-of-plane core modes see Li et al.[10a,10c] and Figures S6 and S7. [b] Assignment in local coordinates: see Table 2 and Figure 3 for the phenyl coordinates and ref 10a and c (Figures S6 and S7) for the in-plane and out-of-plane porphyrin coordinates. Porphyrin coordinates are printed in bold. Assignments for [Ni(TPP)] by Rush III et al.[13] are underlined. [c] Effective D_{4h} symmetry: see the Results and Analysis section. [d] Calculated (DFT) and experimental intensity (vs = very strong, s = strong, m = middle, w = weak, and vw = very weak). [e] Depolarization ratio: p = polarized, dp = depolarized and ap = anomalous polarized band. [f] Calculated with B3LYP/LanL2DZ: see Experimental section. [g] γ(Phenylrot.) corresponds to $\nu(Ph)_1$ = γ(Br) in bromobenzene. [h] Labeling used by Spiro and co-workers (cf. ref 13).

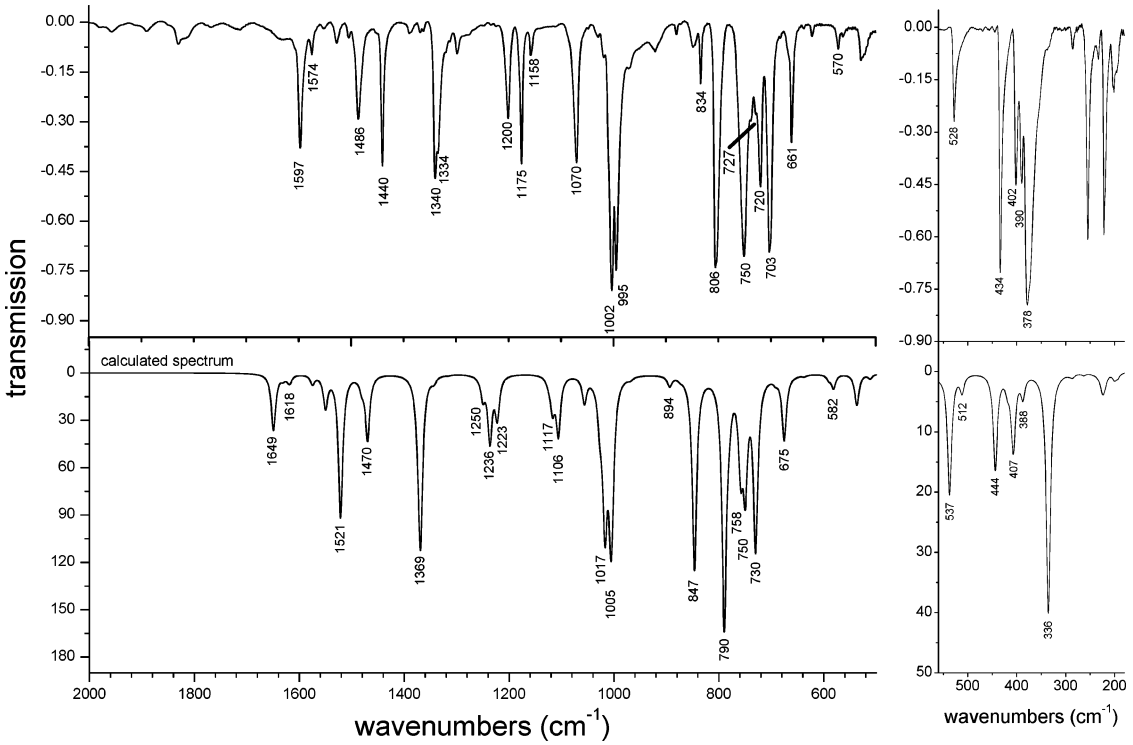

Figure 5. IR spectrum of **1**: the measured spectrum (top) and the calculated spectrum (bottom).

frequencies observed for the phenyl C−H deformation (π_4'', π_3 and π_3'') and the $\gamma(H_\beta)$ porphyrin vibrations in this region are due to the neglect of anharmonicity in the calculations (cf. Discussion).

The third region between 990 and 1160 cm^{-1} mostly comprises in-plane vibrations. The strong band at 995 cm^{-1} (calcd: 1005 cm^{-1}) is assigned to a ν(Pyr. breathing) + δ_{asym}(Pyr. deformation) porphyrin core vibration with $\nu_{breathing}$(C−C) phenyl contribution (ν_{47}), whereas the intense feature at 1002 cm^{-1} (calc.: 1017 cm^{-1}) corresponds to the mixed δ_{sym}(C−C−C) + ν(Pyr. breathing) + ν_{asym}(Pyr. half-ring) mode with mostly phenyl character (ϕ_8''). Both have E_u symmetry. The assignment of the strong band at 1070 cm^{-1} is not entirely clear. One possibility is a $\delta_{sym}(C_\beta-H)$ core mode with E_u symmetry, which is calculated at 1117 cm^{-1} (ν_{52}). Alternatively, this feature could be identified as the ν_{asym1}(C−C) + δ(C−C−H) phenyl vibration (ψ_8') with A_{2u} symmetry, calculated at 1106 cm^{-1}. A d_8 isotope substitution would be necessary to distinguish between these possibilities. Finally, the band at 1158 cm^{-1} is assigned to a phenyl vibration as shown in Table 3.

The following region between 1160 and 1350 cm^{-1} mostly consists of E_u symmetric in-plane porphyrin vibrations. The two bands at 1175 (calcd: 1236 cm^{-1}) and 1200 cm^{-1} (calcd: 1250 cm^{-1}) are both in-plane porphyrin stretching modes, which show deviations in energy of 4 to 5% between calculation and experiment (cf. Discussion) and are assigned as shown in Table 3. The band at 1340 cm^{-1} (calcd: 1369 cm^{-1}) is assigned to a mixed $\delta_{asym}(C_\beta-H)$ + $\nu(C_m-Ph)$ + ν_{sym}(Pyr. half-ring) + $\nu_{asym}(C_\alpha-C_\beta)$ vibration and is known to be spin-state-sensitive (band I [18b]). It appears split into two components in **1**, where a shoulder at 1334 cm^{-1} is present. Previously, this band was assigned to a $\nu(C_\alpha-C_m)$ + $\nu(C_m-Ph)$ by Oshio et al.[18b] The calculated d_8 isotope shift for this band of 19 cm^{-1} shows some deviation from the experimental value (8 cm^{-1}) obtained for [Co(TPP)].[18b] However, this is most probably due to the highly mixed nature of this mode, where, depending on the actual complex, changes in the contributions of individual local coordinates can be expected to occur.

The region at the highest energy between 1400 and 1600 cm^{-1} consists only of phenyl-type vibrations, which are assigned as shown in Table 3. For ϕ_4'', the frequency is obtained 52 cm^{-1} higher in energy compared to experiment. The reason for this is discussed in section B.2 for the corresponding modes ϕ_4 and ϕ_4', which are combinations of the same local coordinate but with different symmetries (cf. Table 3). The weak band at 1574 cm^{-1} (calcd: 1618 cm^{-1}) corresponds to the ν_3(C−C) phenyl vibration of A_{2u} symmetry, which is mixed with the IR forbidden $\nu_{asym}(C_\alpha-C_m)$ porphyrin vibration with B_{1g} symmetry. Hence, this is another indication of the symmetry lowering in **1**. The band at 1486 cm^{-1} (calcd: 1521 cm^{-1}) is assigned to a strongly mixed in-plane vibration (ϕ_5'') of the δ(C−C−H) + ν_{asym4}(C−C) phenyl and $\nu(C_\beta-C_\beta)$ + $\nu_{asym}(C_\alpha-C_m)$ + $\nu_{sym}(C_\alpha-C_m)$ porphyrin type. From the calculations, we have classified this band as a phenyl type mode, but the individual contributions might vary experimentally depending on the actual complex investigated.

B.4. Resonance Raman Spectra of 1 and Assignment. The electronic spectra of metalloporphyrins have been explained on the basis of the four-orbital model of Gouterman.[38] They are dominated by the two $\pi \rightarrow \pi^*$ transitions from the a_{1u} and a_{2u} HOMOs to the e_g LUMO of the porphyrin dianion. Both resulting excited states have E_u symmetry and show a strong configuration interaction (CI). This leads to two well-separated bands in the absorption spectra, the intense Soret band (where the individual transition moments are additive), and the weak Q band (where they nearly cancel). In addition, a third band is observed on the higher energy side of Q. This band, Q_v, is a result of vibronic mixing between the Soret and the Q band. Because both excited states are of E_u symmetry, vibronic mixing is enabled by the vibrations of A_{2g}, B_{1g}, and B_{2g} symmetries.[39] For the resonance Raman spectra of metalloporphyrins, A-, B-, and C-term enhancement mechanisms are important.[40] A-term enhancement is caused by a displacement of the excited state relative to the ground state and is in general only relevant for totally symmetric modes. Because A-term intensity is proportional to the square of the electric dipole transition moment of the excited electronic state, this mechanism is dominant in the region of the Soret transition. B-term enhancement is caused by the vibronic coupling between the excited state $|e\rangle$ and another excited state $|s\rangle$, which leads to the resonance enhancement of the vibrations that are effective in coupling these states. Hence, this mechanism applies to the Q band, where vibrations of A_{2g}, B_{1g}, and B_{2g} symmetries are enhanced. Additional A-term enhancement of A_{1g} modes in the Q region is also expected. Thus, resonance enhancement of nontotally symmetric modes is therefore indicative of the presence of vibronic bands in the absorption spectra. However, B_{1g} and B_{2g} enhancements could theoretically also be induced by a Jahn−Teller distortion of the excited states with E_u symmetry.[41] Hence, *the enhancement of A_{2g} modes is the most diagnostic for the presence of vibronic coupling.* A_{2g} modes are easily identified in the Raman spectra because of their anomalous polarization (ap; $\rho > 3/4$), which relates to the scattering tensor being antisymmetric.[42−44] Finally, C-term enhancement is observed upon the excitation to a vibronic sideband of a forbidden or weakly allowed 0−0 electronic transition[40] that leads to the enhancement of overtones and combination modes. This applies to the Q_v region of the absorption spectra. These different types of resonance enhancement are indeed observed for complex **1**, as shown in Figure S2. Figures 8−10 present the RR spectra of **1** including the polarized data in Q (λ_{exc} = 568.2 nm), Q_v (λ_{exc} = 514.5 nm), and Soret (λ_{exc} = 454.5 nm) resonance. Figure 7 shows the absorption spectrum of **1** indicating the different excitation wavelengths. The RR data in the Soret region are dominated by polarized (A_{1g}) bands, which can therefore easily be identified from the Soret spectrum. The Q and Q_v spectra of **1** contain depolarized, polarized, and anomalous polarized bands. The presence of A_{2g} vibrations in the Q and Q_v spectra confirms well the presence of vibronic coupling as already discussed. The Q_v RR spectra also show overtones and

(43) Placzek, G. In *Handbuch der Radiologie;* Marx, E., Ed.; Akademische Verlagsgesellschaft: Leipzig, Germany, 1934; Vol. 6, Part 2, p 205.
(44) Spiro, T. G.; Strekas, T. C. *Proc. Natl. Acad. Sci. U.S.A.* **1972**, *69*, 2622−2626.

combination bands above 1600 cm^{-1} corresponding to C-term enhancement, which confirms that Q_v is the vibronic sideband of Q.

A number of new bands are observed in the RR spectra compared to the NR Raman spectra. The assignments of the RR data included in Table 3 are on the basis of the energies of the bands in correlation to the DFT results as well as the symmetries determined from the polarized experiments. In some cases, calculated d_8 isotope shifts for **1** in comparison to experimental shifts obtained for [Ni(TPP)][13] are used to further confirm the assignments. The ν(Fe−N) breathing mode at 390 cm^{-1} is strongly enhanced in the Q_v region of compound **1**, which is surprising because this band has A_{1g} symmetry; therefore, one would anticipate its maximum enhancement in the Soret region (Figure S3).[45] The band at 639 cm^{-1} (calcd: 652 cm^{-1}) in Soret resonance is assigned to an in-plane δ_2(C−C−C) phenyl vibration (ϕ_9) with A_{1g} symmetry. This feature shows no d_8 isotope shift in the calculations and is in agreement with results for [Ni(TPP)].[13] The depolarized band at 744 cm^{-1} (calcd: 781 cm^{-1}) observed in Q resonance corresponds to an out-of-plane γ_1(H) phenyl vibration (π_3) with B_{1g} symmetry. The calculated d_8 isotope shift of 10 cm^{-1} for this mode is in good agreement with the value of 7 cm^{-1} observed for [Ni(TPP)].[13] Two new depolarized bands are observed at 851 and 1017 cm^{-1} in Q and Q_v resonances, respectively. In both cases, two possible features with B_{1g} and B_{2g} symmetries are present in the calculations as well as in the RR spectra of [Ni(TPP)]. Hence, no assignments of these bands are possible. The depolarized band at 1080 cm^{-1} observed in Q and Q_v resonances is assigned as shown in Table 3. The depolarized band observed at 1182 cm^{-1} in Q_v and Q resonances corresponds to either the calculated vibration at 1226 cm^{-1} (a $\delta_{asym}(C_\beta-H) + \nu_{asym}(C_\alpha-C_\beta)$ core mode) or the feature predicted at 1222 cm^{-1} (a phenyl vibration); both have B_{2g} symmetry. In [Ni(TPP)],[13] a band at 1190 cm^{-1} with a small phenyl-d_{20} shift is observed and assigned to the $\delta(C_\beta-H)$ vibration calculated at 1226 cm^{-1}. Because a larger d_{20} isotope shift is expected for the phenyl vibration, the band at 1182 cm^{-1} is tentatively assigned to this feature. The modes at 744 cm^{-1} (phenyl vibration), ν_{17}, and ν_{34} (both $C_\beta-H$ in-plane porphyrin vibrations) show larger deviations in energy between calculation and experiment compared to those of the other porphyrin modes, which are due to the neglect of anharmonicity (Discussion). The weak, anomalous polarized bands at 1225 and 1335 cm^{-1} in Q and Q_v resonances are assigned as shown in Table 3. The depolarized band at 1266 cm^{-1} (calcd: 1286 cm^{-1}) is observed in all RR spectra. It is assigned to a mixed ν(Pyr. quarter-ring) + $\nu(C_m-Ph)$ porphyrin core vibration with phenyl contribution (ν_1(C−C)) with B_{2g} symmetry (ν_{27}). The calculated d_8 isotope shift of 2 cm^{-1} is in very good agreement with experiment (1 cm^{-1} for [Ni(TPP)][13]). The band at 1452 cm^{-1} in Soret and Q_v resonances is assigned to the mixed in-plane $\nu_{sym}(C_\alpha-C_m) + \nu(C_\beta-C_\beta)$ porphyrin vibration (ν_3) with A_{1g} symmetry. The split, anomalous polarized band [46] at 1522/1516 cm^{-1} (calcd: 1560 cm^{-1}) is assigned to the mixed $\nu_{asym}(C_\alpha-C_m) + \nu_{asym}(C_\alpha-C_\beta) + \delta_{asym}(C_\beta-H)$ in-plane porphyrin core vibration and is known to be spin-state sensitive (band C(ap)[47,18b]). It was originally assigned to only $\nu(C_\alpha-C_m)$.[14b] The predicted d_8 isotope shift of this feature is 6 cm^{-1}. All of these assignments are listed in Table 3.

B.5. Effects of Symmetry Lowering. There are three major effects resulting from the symmetry lowering from idealized D_{4h} to the actual symmetry of [Fe(TPP)(Cl)]. Because of the fact that the phenyl rings are no longer perpendicular to the porphyrin core, the coupling between the core and the phenyl vibrations becomes stronger. The second effect is that modes with different symmetries in D_{4h} appear mixed in **1**. Several examples are observed in the NR Raman and IR spectra as discussed above, where even (g) and odd (u) vibrations are combined. This applies, for example, to the NR Raman bands at 247 and 257 cm^{-1} and the IR bands at 390, 727, and 1574 cm^{-1}. Of importance though is the fact that all of these symmetry-breaking modes obtain only very small intensities because of this intensity-stealing mechanism. This together with the observation of polarized, depolarized, and anomalous polarized bands clearly shows that the $[Fe(TPP)]^+$ core of **1** still behaves as if it has D_{4h} symmetry. The third effect of symmetry lowering beyond C_{4v} in **1** is that degenerate E_u vibrations appear to be split in the IR spectra. However, the observed splittings are very small (about 5 cm^{-1}). Hence, this again indicates that an effective D_{4h} symmetry is present in **1**.

C. Vibrational Spectra and Assignments of Compounds 2 and 3 in Comparison with Those of 1. The crystal as well as the DFT optimized structures of complexes **1**−**3** are very similar overall, as discussed in section A. Correspondingly, the averaged metal−nitrogen distances are similar and increase in the order of Co (1.985 Å) < Mn (2.019 Å) < Fe (2.049 Å). The most pronounced difference among **1**, **2**, and **3** occurs for the metal−chloride bond distances, which increase in the order of Co (2.145 Å) < Fe (2.192 Å) ≪ Mn (2.389 Å). Another important difference is observed for the out-of-plane displacement of the metal atom from the N_4 plane of the porphyrin, which increases in the order of Co (0.05 Å) < Mn (0.258 Å) < Fe (0.383 Å). On the basis of the large structural similarities of complexes **1**−**3**, it can be expected that the overall vibrational properties of the corresponding $[M(TPP)]^+$ units are quite similar. The only exception is the metal−chloride stretching vibration, where larger differences should be observed.

Figure 6 shows the NR Raman data of **2** together with the calculated spectrum. In this case, exceptional agreement is obtained between theory and experiment. The corresponding spectra of **3** are presented in Figure S1. The agreement between the calculated and experimental data is also very good in this case. As already discussed for **1**, small shifts of certain bands to higher energy (average deviation in energy of about 2 to 3%) are also observed in the calculations for

(45) The excitation profile is a plot of the Raman intensity versus the Raman excitation energy.

(46) The origin of the splitting is not known. It might relate to the fact that the spectrum was recorded in a KBr disk.

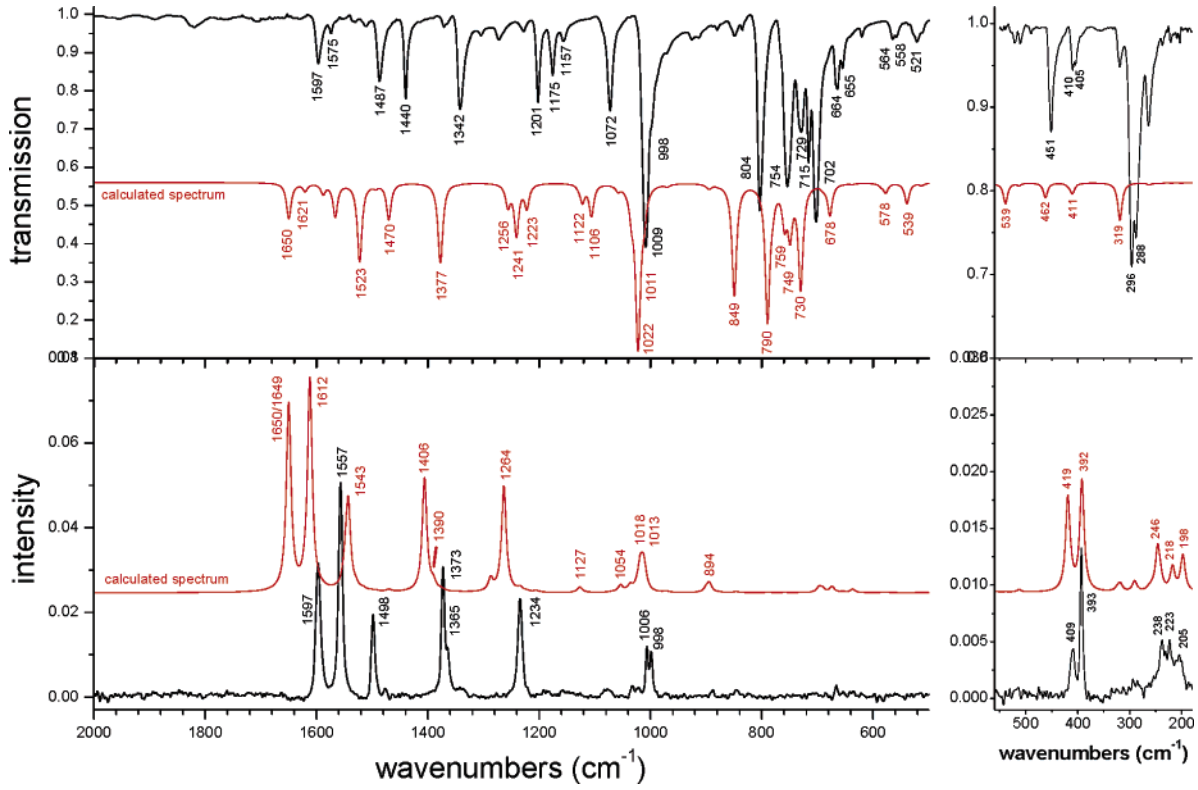

Figure 6. IR spectrum of **2** (top) and the NR Raman spectrum of **2** (bottom). The corresponding calculated spectra are included in the two panels as indicated. The low energy part (560−180 cm^{-1}) of the calculated spectra is enlarged.

Table 4. Comparison of Metal−Chloride Stretching Frequencies (cm^{-1}) and QCC-NCA as well as Calculated (DFT) Force Constants *f*(M−Cl) (mdyn/Å) for [M(TPP)Cl] (**1**, **2**, and **3**) and Model Systems [M(P*)Cl] (**1̃a**, **2̃a**, and **3̃a**)

	ν(M−Cl)				ν(M−Cl)	*f*(M−Cl)	
compound	calcd[b,f]	exptl[c]	lit.	model	PED[a,f]	calcd[b]	QCC-NCA
1	263/*336*	378	360[2] 364[57] [d]	**1̃a**	225 (9%)/*339* (86%)	1.419	1.796
2	263/*319*	296	299[57] [e]	**2̃a**	235 (39%)/*318* (74%)	1.160	0.932
3	286/*398*	397		**3̃a**	262 (40%)/*396* (82%)	1.704	1.717

[a] PED = potential energy distribution; the numbers in parentheses correspond to the % contribution of the M−Cl coordinate to this mode. [b] Calculated with B3LYP/LanL2DZ; see Experimental section. [c] Experimental infrared frequencies. [d] Determined from Raman data of [Fe(OEP)(Cl)]. [e] Determined from Raman data. [f] The ν(M−Cl) vibration is mixed with a porphyrin mode, and hence there are two vibrations that carry ν(M−Cl) contributions. As shown in the PED, the mode at higher energy has more M−Cl stretching character.

2 and **3** (Discussion). Because of the structural similarities of **1**−**3**, it is not surprising that the NR Raman spectra of these compounds show large similarities as evidenced by a comparison of Figures 4, 6, and S1. Hence, the assignments of the NR Raman spectra of **2** and **3** listed in Tables S1 and S2, respectively, largely parallel the assignments for **1**. Only a few differences are observed. The band at 1574 cm^{-1} in the experimental NR Raman spectrum of **1** is not observed in the spectra of compounds **2** and **3**. This band corresponds to the phenyl in-plane vibration ν_{sym}(C−C) (ϕ_4') with B_{2g} symmetry. However, complex **3** shows an additional small band at 1540 cm^{-1} that could not be unambiguously assigned. The metal−chloride stretching vibration only appears in the NR Raman spectrum of **1**. Otherwise, the same vibrations are observed in the NR Raman spectra of **1**−**3**. Some of them show small characteristic shifts, which are discussed in section E.

Figure 6 shows the IR data of **2** together with the calculated spectrum. Again, in this case, the most exceptional agreement is obtained between theory and experiment. The corresponding spectra of **3** are presented in Figure S1. A good agreement between theory and experiment is also achieved in this case. The IR spectra of all three compounds **1**−**3** basically show the same normal modes. Correspondingly, the appearances of the MIR spectra are very similar. However, the far-IR spectra look clearly different because the metal−chloride and the metal−nitrogen stretching vibrations are located in this region, which show the strongest metal sensitivity (cf. section E).

D. Metal−Chloride Bonding. For compounds **1** and **3**, the experimental frequency of the metal−chloride stretching vibration is similar with ν(Fe−Cl) = 378 cm^{-1} and ν(Co−Cl) = 397 cm^{-1} (cf. Table 4). In contrast, the Mn−Cl stretching vibration of 296 cm^{-1} is located at a significantly lower energy. This trend is in agreement with the metal−chloride distances with **3** (2.145 Å) < **1** (2.192 Å) ≪ **2** (2.389 Å). As mentioned in section A, the metal−chloride bond lengths are overestimated in the calculations, especially for compound **1**. Correspondingly, the calculated frequency obtained for **1** of 336 cm^{-1} is significantly lower than the

experimental value, whereas for **2** (319 cm^{-1}) and **3** (398 cm^{-1}) a very good agreement is observed. To compare the M−Cl bond strengths in these compounds rigorously, accurate M−Cl force constants are necessary and require a normal coordinate analysis (NCA). For this purpose, simple model systems [Fe(P)(Cl)] (**$\tilde{1}$**), [Mn(P)(Cl)] (**$\tilde{2}$**), and [Co(P)(Cl)] (**$\tilde{3}$**; P = porphine) were fully optimized, and the force constants were calculated as listed in Table 4. In the next step, a mass of 77 was used for the meso hydrogens of these models corresponding to the phenyl groups. This leads to models **$\tilde{1}$a**, **$\tilde{2}$a**, and **$\tilde{3}$a**, which accurately reproduce the M−Cl frequencies of full model systems **1**−**3** applying TPP (cf. Table 4). This is an important result because it shows that the simple porphine ligand is a good approximation for TPP when only the properties of the central M−Cl unit are considered. Finally, using the QCC-NCA procedure,[21] the M−Cl force constants were fitted to reproduce the experimental M−Cl stretching frequencies. In this way, experimental force constants for compounds **1**, **2**, and **3** of 1.796, 0.932, and 1.717 mdyn/Å, respectively, were obtained. The NCA force constants show that the Fe−Cl and Co−Cl bonds are twice as strong as the Mn−Cl bond. The reason for this rather surprising result is evidenced by an analysis of the MO diagrams of these complexes. For this purpose, models **$\tilde{1}$**−**$\tilde{3}$** were used because porphine has proven to be a good model for TPP, considering the presence of the M−Cl bond. The coordinate system is chosen such that the *z* axis is aligned with the M−Cl bond, whereas the *x* and *y* axes are oriented along the M−N bonds of the porphyrin ligand. Hence, the $d_{x^2-y^2}$ orbital of the metal undergoes a strong σ bond with the pyrrole nitrogens of the porphyrin, whereas d_{xy} is partially nonbonding. However, the metal−chloride σ bond is mediated by the orbital d_{z^2}, whereas d_{xz} and d_{yz} are potentially involved in π bonds with the chloride ligand. Note that the principal bonding scheme of [Fe(TPP)(Cl)] has been analyzed before; however, the main focus was the metal−porphyrin interaction.[48]

[Co(TPP)(Cl)] (**3**) has the simplest electronic structure due to the low-spin d^6 configuration of Co(III) ($S = 0$), which corresponds to a $[d_{xy},d_{xz},d_{yz}]^6 \equiv [t_2]^6$ configuration of the metal. Hence, the unoccupied d_{z^2} orbital undergoes a strong σ bond with the filled p_z orbital of the chloro ligand, where the corresponding bonding combination has 29% d_{z^2} and 58% chloro p_z character. Because the d_{xz} and d_{yz} orbitals of the metal are fully occupied, no π bond with the p_x and p_y orbitals of chloride is possible. In summary, the metal−Cl bond in **3** can be described as a strong (pure) σ bond. In comparison, compound **1** is a high-spin d^5 complex with $S = {}^5/_2$ ground state. In the spin-unrestricted scheme, this means that all α-d orbitals are fully occupied and hence, do not contribute to the bonding with σ- or π-donor ligands. Therefore, all metal−ligand bonding comprises unoccupied β-d orbitals. The Fe−Cl σ bond is mediated by the interaction of d_{z^2} and p_z of the chloro ligand. The corresponding bonding combination has 26% iron d_{z^2} and 60% chloro p_z orbital contributions, which corresponds to a strong σ bond. Additional π bonds between the d_{xz} and d_{yz} orbitals of iron and the p_x and p_y orbitals of the chloro ligand, respectively, are also present. The corresponding bonding combinations have about 10% metal and about 45% chloride character indicative of a medium-strength interaction. Therefore, complex **1** formally has one-half of a σ bond and one π bond. Compared to **3**, the σ bond is reduced by 50%, whereas an additional π bond is present. These effects seem to cancel, giving almost identical M−Cl force constants in these complexes.

Compound **2** is a high-spin d^4 complex with $S = 2$ ground state and a $[d_{xz},d_{yz},d_{xy},d_{z^2}]^4$ electron configuration. Compared to complex **1**, the α-$d_{x^2-y^2}$ orbital is unoccupied and therefore, similar M−Cl interactions would be expected in **1** and **2**. However, the force constants show that this is not the case. The Mn−Cl σ bond between d_{z^2} and the p_z orbital of chloride is somewhat weaker compared to that in **1** as evidenced by the 16% metal d_{z^2} and 57% chloro p_z character of the corresponding bonding combination. The largest difference occurs for the M−Cl π bond. The corresponding bonding combinations between d_{xz} and d_{yz} of Mn(III) and p_x and p_y of chloride only have about 2% metal and 75% chloro character, respectively, which corresponds to a very weak interaction. Therefore, the M−Cl bond in complex **2** corresponds only to half a σ bond. This is the reason for the much smaller M−Cl force constant of only 0.932 mdyn/Å in **2** compared to 1.796 mdyn/Å for **1**.

E. Metal-Sensitive Bands in the Raman and IR Spectra of 1−3. Boucher and Katz[49] measured the IR spectra of several divalent metal complexes of protoporphyrin IX and hematoporphyrin IX dimethyl ester and identified three metal-sensitive bands at 920−980, 500−525, and 350−365 cm^{-1}, but no definitive assignments could be made. The skeletal stretching and breathing modes were found to only have small shifts within the experimental uncertainty. Nakamoto and co-workers assigned the metal−nitrogen stretching bands of a series of OEP and TPP complexes on an empirical basis.[50,18a] The observed shifts were attributed to the variable occupation of the σ-antibonding $d_{x^2-y^2}$ orbital in these complexes. Hence, vibrations that contain a direct contribution of the M−N stretching coordinate should be the most affected. However, the oxidation- and spin-state sensitive IR bands I−III and Raman bands A, C, D, and E (band B is characteristic for penta coordination) as described in the Introduction should also be sensitive to the metal ion.[18] The frequency shifts of bands I and III were correlated to the metal−porphyrinato nitrogen distances[18b] in agreement with Nakamoto's analysis.

In the IR and NR Raman spectra of **1**, 50 and 36% of the observed modes, respectively, are of the phenyl type, which show no shifts or show only small frequency shifts.[51] In contrast, frequency shifts are observed for most porphyrin

(47) Chottard, G.; Battioni, P.; Battioni, J.-P.; Lange, M.; Mansuy, D. *Inorg. Chem.* **1981**, *20*, 1718−1722.
(48) Cheng, R.-J.; Chen, P.-Y.; Lovell, T.; Liu, T.; Noodleman, L.; Case, D. A. *J. Am. Chem. Soc.* **2003**, *125*, 6774−6783.
(49) Boucher, L. J.; Katz, J. J. *J. Am. Chem. Soc.* **1967**, *89*, 1340−1345.
(50) Ogoshi, H.; Masai, N.; Yoshida, Z.; Takemoto, J.; Nakamoto, K. *Bull. Chem. Soc. Jpn.* **1971**, *44*, 49.
(51) Very small shifts of some of these bands that were observed can be traced back to small admixtures of porphyrin core vibrations.

Table 5. Metal-Sensitive Bands (Also Oxidation- and Spin-State-Sensitive) in the Infrared, NR Raman, and RR Spectra of **1**−**3**[a]

		FeTPPCl (**1**)		MnTPPCl (**2**)		CoTPPCl (**3**)	
		experimental	calcd[b]	experimental	calcd[b]	experimental	calcd[b]
	M−N (Å), averaged	2.049	2.09	2.019	1.99	1.985	1.99
IR[18b]	band I, spin (cm^{-1})	1340/1334	1369	1342	1377	1351	1387
	band II, ox. (cm^{-1})	806	847	804	849	795	848
	band III, spin (cm^{-1})	434	444	451	462	465	475
R[18b]	band A, ox., and spin (cm^{-1})	1363	1379	1365	1390	1359	1393
	band B[c] (cm^{-1})	1371	1398	1373	1406	1372	1408
	band C, spin (cm^{-1})	1522/1516	1560	1538/1532	1588		1588
	band D, spin (cm^{-1})	1554	1598	1557	1612	1563	1626
	band E, ox. (cm^{-1})	390	388	393	392	403	390
IR	ν(M−Cl)	378	336	296	319	397	399
	ν_{50} (cm^{-1})	402	407	410/405	411	?	411
R	ν_{18} (cm^{-1})	199	202	223	218	255 ?	238

[a] Frequencies are given in cm^{-1}. [b] Calculated with B3LYP/LanL2DZ. [c] Band B is a marker band for five-coordinate porphyrin complexes.[47,18b]

Table 6. Selected Crystallographic Distances (Å) for Compound **1** (cf. Ref 28), **2** (This Article), and **3** (cf. Ref 33) that are Important for the Structure-Sensitive Bands[a]

compound	d(M−N)	d(C_m−Ph)	d(C_β−C_β)	d(C_α−C_β)	d(C_α-N)	d(M−Ct)	d(C_α−C_m)
[Fe(TPP)(Cl)] (**1**)	2.04(9)	1.50(8)	1.38(0)	1.44(6)	1.38(4)	0.383	1.39(9)
[Mn(TPP)(Cl)] (**2**)	2.019	1.496	1.357	1.440	1.385	0.258	1.399
[Co(TPP)(Cl)] (**3**)	1.985	1.518	1.360	1.446	1.372	0.05	1.391

[a] Distances are averaged over chemically equivalent bonds.

core vibrations in the [M(TPP)(Cl)] complexes, but only a few of them are of considerable size as already correctly stated by Boucher and Katz. The bands with large shifts are mostly vibrations with a large M−N stretching contribution as proposed before.[18,50] Hence, frequency shifts are mostly expected for bands below 500 cm^{-1}. Table 5 lists the experimental and calculated frequencies of the eight spin- and oxidation-state-sensitive bands known from the literature for complexes **1**−**3**. In the IR spectra, the three porphyrin vibrations I−III show metal sensitivity. In the NR Raman spectra, three modes show significant shifts for complexes **1**−**3** (band A, D, and E). Hence, only six of the eight structurally sensitive bands from the literature are metal-sensitive in the [M(TPP)(Cl)] series studied here. Three additional metal sensitive bands are identified here. These are ν_{18} (from NR Raman), ν_{50} (IR), and the M−Cl stretching vibration as discussed in section D (cf. Table 4). Corresponding to the relatively small frequency shifts observed for **1**−**3** as shown in Table 5, the underlying differences in complex geometries must be small. Therefore, to analyze the reasons for the appearance of the shifts, detailed assignments of the corresponding vibrations as obtained in this study are necessary. For the stretching vibrations, the differences in the vibrational frequencies can be correlated with the differences in bond lengths. However, the interpretation of the metal sensitivity of the deformation modes is not straightforward.

Vibrations with a considerable M−N contribution are observed in the low-energy region of the spectra. The metal−nitrogen distances decrease in the order of Fe (2.049 Å) > Mn (2.019 Å) > Co (1.985 Å), and hence the frequencies of vibrations with ν(M−N) character are expected to increase in the order of Fe < Mn < Co. There are three vibrations with a pure or mostly M−N stretching contribution observed in complexes **1**−**3**. The most intense band corresponds to the totally symmetric $\nu_{breathing}$(M−N) vibration (band E, ν_8), which increases in the order of 390 cm^{-1} (Fe) < 393 cm^{-1} (Mn) < 403 cm^{-1} (Co) in agreement with this trend. The ν(M−N) vibrations with B_{1g} symmetry (ν_{18}) observed in the NR Raman spectra of **1**−**3** also strongly follows this trend as shown in Table 5. Finally, the ν(M−N) vibrations with E_u symmetry (ν_{50}) observed in the IR spectra of **1** and **2** are mixed with the δ(Pyr. translation) porphyrin deformation mode. Nevertheless, the correlation also applies here where this feature appears at 402 cm^{-1} in **1** and at 410/405 cm^{-1} in **2**. The fact that this band is split in **2** reflects a small degree of symmetry lowering from ideal D_{4h} symmetry (cf. section B.5).

Bands A, C, and D in the Raman and band I in the IR spectra of **1**−**3** correspond to in-plane porphyrin stretching vibrations (cf. Table 3); therefore, their frequencies can be correlated with C−C, C−N, and M−N distances as observed in the crystal structures of **1**−**3** (cf. Table 6). Band A corresponds to the in-plane ν_{sym}(Pyr. half-ring) porphyrin vibration. Hence, the frequency of this mode relates to changes in the metal−nitrogen, the C_α−C_β and the C_α−N distances. However, because the observed frequency shifts are very small, a quantitative interpretation of the observed behavior of this mode is not possible. For band C, the observed frequency is larger for the Mn than for the Fe complex. This mode has considerable ν_{asym}(C_α−C_m) character; however, the C_α−C_m distance is comparable in the two complexes, as shown in Table 6. However, this mode also has some C_α−C_β contribution, and the corresponding C_α−C_β distance is slightly larger for **1** compared to that for **2**, which is consistent with the observed trend in frequencies (cf. Table 5). The totally symmetric metal-sensitive band D, which is assigned to a ν(C_β−C_β) + ν_{sym}(C_α−C_m) porphyrin vibration with a small amount of δ_{asym}(C_β−H) contribution, is observed in both the NR Raman and RR spectra of **1**−**3**.

The frequency of this mode increases in the order of **1** < **2** < **3**, as shown in Table 5. This can be traced back to differences in the C−C bond lengths of the porphyrin core. First, the $C_\beta-C_\beta$ distances are almost identical for **2** and **3**, whereas they are elongated in **1**. However, complexes **1** and **2** have almost identical $C_\alpha-C_m$ distances, whereas this bond is shorter in complex **3**. These trends are consistent, leading to the observed frequency shifts of this band. Finally, band I corresponds to the mixed $\delta_{asym}(C_\beta-H) + \nu(C_m-Ph) + \nu_{sym}$(Pyr. half-ring) $+ \nu_{asym}(C_\alpha-C_\beta)$ in-plane porphyrin vibration. The frequency shift of this band cannot be analyzed because of a large number of different contributions. For example, the C_m-Ph distances behave inversely to the M−N distances. Besides these stretching vibrations, two deformation modes (bands II and III; cf. Table 5) are also found to be metal-sensitive. Band II corresponds to the out-of-plane $\gamma(H_\beta) + \gamma_{sym}$(Pyr. folding) porphyrin deformation mode and hence, the frequency shift of this vibration is difficult to interpret. The energy increases in the order of Co ≪ Mn < Fe. The frequency shift of band III, which is an in-plane δ(Pyr. rotation) porphyrin deformation mode, seems to be correlated to the out-of-plane displacement of the metal, which increases in the order of Co < Mn < Fe. Correspondingly, the observed trend in the vibrational energies is Co > Mn > Fe.

Discussion

In this study, the vibrational properties of the five-coordinate porphyrin complexes [M(TPP)(Cl)] (M = Fe, Mn, and Co) are analyzed in detail. For complex [Fe(TPP)(Cl)] (**1**), nonresonance Raman (NR Raman) spectra including polarized data are presented for the first time. Resonance Raman (RR) spectra of this compound are also reported, including Soret, Q, and Q_v resonance data together with polarized measurements. In addition, MIR and FIR spectra of **1** are presented. Hence, a complete vibrational data set for complex **1** is obtained in this study. These data are then assigned in detail using calculated vibrational energies as well as calculated NR Raman and IR intensities, which show very good agreement with experiment overall (vide infra). Additional information that assists in assigning the spectra is available from (a) the polarized measurements that allow for the determination of the symmetries of the different vibrations and (b) d_8 isotope data reported in the literature for a number of complexes.[13,14b,18b] The assignments are based on an idealized model system [M(TPP)] with D_{4h} symmetry. For the phenyl mode assignment, local internal coordinates derived from bromobenzene are used. On the basis of all this information, a complete and consistent assignment of all of the spectroscopic data obtained for **1** has been achieved. So far, no detailed vibrational assignments for five-coordinate porphyrin complexes such as [Fe(TPP)(Cl)] are available from the literature, where most of the research has been focused on four-coordinate complexes. For compound **1**, only a small number of totally symmetric modes from the Soret RR spectrum (λ_{exc} = 457.9 nm) have been assigned before,[20] on the basis of a simple comparison of the obtained spectra with those of [Ni(TPP)]. Additional bands in the Raman and IR spectra of **1** were identified and classified, but no further analysis was performed.[14,18b] The assignments obtained in this study are in general consistent with recent work by Rush III et al., who assigned the RR and IR spectra of [Ni(TPP)] based on a DFT-SQM analysis.[13] In some cases, large deviations in vibrational frequencies (for example, ν_2 is located at 1554 cm^{-1} in **1** and at 1572 cm^{-1} in [Ni(TPP)]) are observed. In addition, because of very good agreement between the calculated and experimental NR Raman and IR spectra obtained here, more sophisticated assignments of the observed vibrations were possible in this study, as indicated in Table 3. The complete analysis of the vibrational spectra of **1** performed here also leads to the reassignment of a number of bands. These include features at 1233, 1006, and 886 cm^{-1} in the Raman spectra of **1** (cf. Table 3). The prominent band at 390 cm^{-1}, which is one of the structure-sensitive bands identified by Burke et al.,[14b] is reassigned to the totally symmetric $\nu_{breathing}$(Fe−N) vibration on the basis of the calculated NR Raman spectra and the excellent agreement between its calculated and experimental pyrrole-d_8 isotope shift. This is in agreement with the assignments for [Ni(TPP)].[10a,13] The IR spectra of complex **1** are assigned here for the first time with the exception of structure-sensitive bands I−III. However, band II at 806 cm^{-1} is reassigned in this work to the out-of-plane $\gamma(H_\beta) + \gamma_{sym}$(Pyr. folding) porphyrin core vibration on the basis of the calculated IR spectra and the excellent agreement between its calculated and experimental pyrrole-d_8 isotope shift. In addition, a number of new bands are assigned in this study. These include the important bands at 402 cm^{-1} in the IR (ν_{50}) and 199 cm^{-1} in the Raman spectrum (ν_{18}) of **1**, which correspond to the Fe−N stretching vibrations with E_u and B_{1g} symmetries. These modes have not been assigned yet. Similar to the corresponding A_{1g} mode at 390 cm^{-1}, these are also strongly metal-sensitive and probably oxidation- and spin-state-sensitive.

A general shift of the vibrational frequencies of **1**−**3** to somewhat higher energy (average deviation: about 2 to 3%) is observed in the calculations compared to experiment. However, in some cases, larger deviations (up to 5%) are observed. These can be traced back to different effects depending on the nature of the respective modes. First, large shifts (about 5%) are observed for the three combinations of the ν_{sym}(C−C) stretching mode of the phenyl rings (ϕ_4, ϕ_4', ϕ_4'' in Table 3), which occur just below 1600 cm^{-1}. In this case, the deviations are partly due to an intrinsic inaccuracy of the B3LYP/LanL2DZ method. This is evident from frequency calculations on benzene. As shown in Table S7, ν_{sym}(C−C) is calculated at 1641 and observed at 1594 cm^{-1} (average), which corresponds to a deviation of 2.9%. Interestingly, using the much more time consuming B3LYP/TZVP method does not lead to an improvement for this mode. The second class of vibrations in which larger deviations of the frequencies are observed correspond to in-plane and out-of-plane C−H deformation modes. This especially includes the $\delta(C_\beta-H)$ and $\gamma(H_\beta)$ core vibrations and the δ(C−C−H) bends of the phenyl rings. (See, for example, $\delta(C_\beta-H)$ at about 1100 cm^{-1}, $\gamma(H_\beta)$ at about 800

cm^{-1}, and δ(C−C−H) at about 1100 cm^{-1}, as listed in Table 3.) These deviations are due to the neglect of anharmonicity effects in the theoretical treatment. Calculations on benzene show that C−H vibrations usually show significant degrees of anharmonicity (cf. Table S7). These calculations indicate that ν_{sym}(C−C) is also affected by deviations due to anharmonicity. Finally, differences are observed for the amount of mixing between phenyl and porphyrin core vibrations, which applies to a small number of modes (Results and Analysis). This is evident from a comparison of calculated and experimental d_8 isotope shifts, which reflect the porphyrin core mode contribution. In the case of **1**, the calculated structure shows smaller dihedral angles between the phenyl substituents and the porphyrin core compared to the crystal structure. Hence, this rotation of the phenyl rings toward the porphyrin plane introduces changes in mode mixing of phenyl and porphyrin core vibrations. This most probably explains the observed deviations.

Three major effects of symmetry lowering from the idealized D_{4h} symmetry of the $[M(TPP)]^+$ core are observed for complexes **1**−**3**. Compared to four-coordinate [Ni(TPP)] and corresponding systems, the chloro complexes studied here show the additional complexity of having open shells, a larger distortion of the porphyrin core, and axial ligands. From vibrational spectra, these deviations from D_{4h} are manifested in (i) enhanced coupling between porphyrin core and phenyl vibrations, (ii) the combination of even (g) and odd (u) vibrations, and (iii) small splittings of the degenerate E_u vibrations. However, these effects are very small and therefore, together with the observation of polarized, depolarized, and anomalous polarized bands in the Raman spectra, this clearly shows that the $[M(TPP)]^+$ cores of **1**−**3** still behave as if they have D_{4h} symmetry. As discussed above, the assignments of the vibrational spectra of complexes **1**−**3** are therefore carried out in an effective D_{4h} symmetry. The overall vibrational properties of the $[M(TPP)]^+$ units in complexes **1**−**3** are quite similar, which relates to the large structural similarities of the metalloporphyrin cores of these systems. The largest differences are observed in the low-energy region of the spectra, where the M−Cl and the M−N stretching vibrations are observed. On the basis of our analysis, it is possible to give more precise assignments of the metal-sensitive modes than before, as inferred by Oshio et al.[18b] in 1984: "In order to understand the structure-sensitivity of these bands on a quantitative basis, it is necessary to carry out theoretical calculations [...]." Not surprisingly, it is found that modes with mostly phenyl character do not show noticeable shifts. In the case of porphyrin core vibrations, frequency shifts are in general observed for most vibrations; however, only a few of them are of considerable size. Of the eight oxidation and spin-state-sensitive bands known from the literature,[18] five are found to be metal-sensitive in the [M(TPP)(Cl)] series studied here. These are bands A, D, and E (RR) and bands I−III (IR). In addition, two more metal-sensitive porphyrin core vibrations are identified here (ν_{50} and ν_{18}, vide supra). Bands with large M−N stretching contributions are sensitive because of the differences in the M−N bond lengths in **1**−**3**,

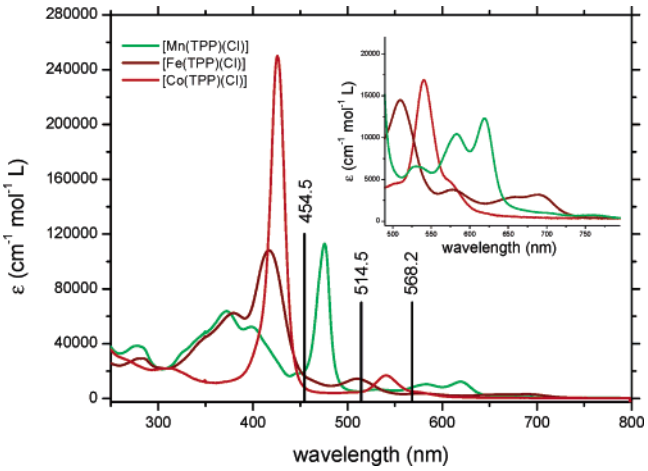

Figure 7. Solution absorption spectra of compound **1** (brown) measured in chloroform, of compound **2** (green) in a 1/1 mixture of butyronitrile and propionitrile, and of compound **3** (red) in methanol. The spectra are scaled with absorption coefficients taken from the literature.[58,59,33]

Table 7. Absorption Bands Observed in the UV−Vis Absorption Spectra of Complexes **1**−**3** (in nm)

[Fe(TPP)Cl] (**1**)		[Mn(TPP)(Cl)] (**2**)		[Co(TPP)(Cl)] (**3**)	
position	assignment	position	assignment	position	assignment
379	Cl → M CT	390	Soret		
417	Soret	476	P → M CT	426	Soret
510	Q_v	530	?	540	Q_v
578	?	583	Q_v	574	Q
654	P → M CT	620	Q		
690	P → M CT ?				

Scheme 2

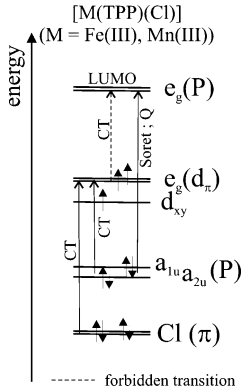

which applies to bands E, ν_{50}, and ν_{18}. These occur in the low-energy region of the spectra. Bands I, A, C, and D correspond to porphyrin core stretching modes. In this Article, we have developed a model where the shifts of these bands are interpreted on the basis of differences in the porphyrin C−C and C−N and the metal−N distances. The interpretation of the frequency shifts of remaining vibrations I and II is not straightforward because of the fact that these are deformation modes.

Besides the analysis of the metal-sensitive modes, we have investigated the strength of the metal−chloride interaction in complexes **1**−**3**. To this end, the M−Cl stretching vibrations have been assigned, and from normal coordinate analysis (NCA), M−Cl force constants of 1.796 (Fe−Cl), 0.932 (Mn−Cl), and 1.717 mdyn/Å (Co−Cl) have been determined. These large differences in M−Cl bond strengths

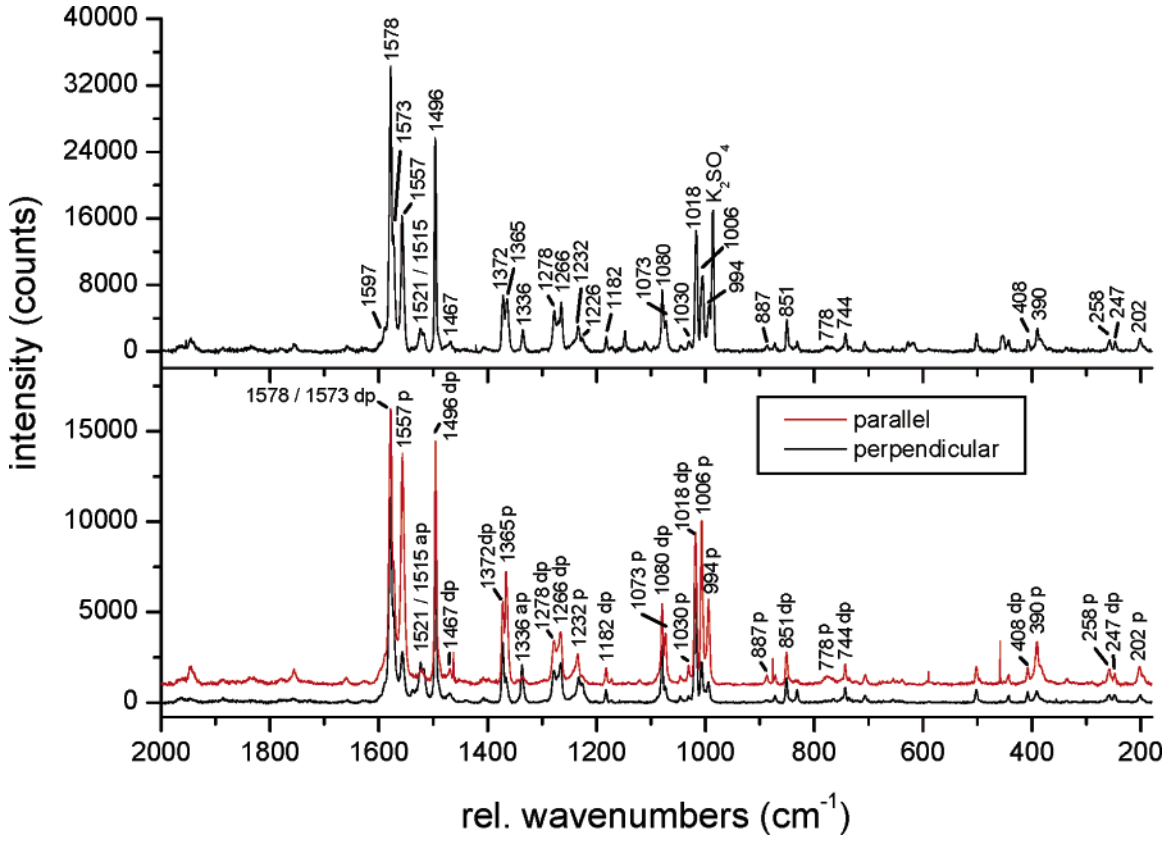

Figure 8. Resonance Raman spectra of **1**, excited at 568.2 nm (Q resonance). The RR spectra were measured with potassium sulfate as the internal standard (top). The polarized measurement is shown on the bottom.

are reflected by the M−Cl bond distances of 2.192 Å in **1**, 2.389 Å in **2** and 2.145 Å in **3**. For **2**, this value is obtained from a new crystal structure presented here. An analysis of the MO diagrams of **1**−**3** allows for a determination of the electronic structural reasons for these differences. In the case of compound **1**, the Fe−Cl bond can roughly be classified as one-half of a σ bond and one π bond. In comparison, the Co−Cl bond in **3** corresponds to one σ bond. The similar M−Cl force constants obtained for **1** and **3** indicate that the enhanced σ and the reduced π interaction in **3** compared to those in **1** seem to compensate and lead to comparable bond strengths. The strongly reduced M−Cl bond strength in **2** compared to that in **1** (and **3**) is mostly due to a lack of the M−Cl π bond in this complex. Correspondingly, the Mn−Cl bond only corresponds to half a σ bond in agreement with the observed reduction of the force constant by half in **2** (0.932 mdyn/Å) compared to that in **1** (1.796 mdyn/Å).

Besides its use for the determination of vibrational energies, RR spectroscopy offers detailed insight into the nature of electronically excited states. This relates to the mechanism of resonance enhancement and the actual nature of enhanced vibrations. For metalloporphyrins, A-, B- and C-term enhancements are important,[40] as described in section B.4. The A-term mechanism is dominant in the region of the intense Soret transition and leads to the enhancement of totally symmetric modes. B-term enhancement is found in the region of Q and Q_v bands and relates to vibronic coupling, which is manifested in the enhancement of anomalous polarized A_{2g} modes. Complex **3** shows the simplest absorption spectrum of compounds **1**−**3**, investigated here (cf. Figure 7). In this case, the Soret transition is located at 426 nm (cf. Table 7). At lower energy, the band at 540 nm is assigned to Q_v and the shoulder at 574 nm to the Q band, which is in agreement with the assignments for [Co(TPP)] from the literature.[38] These assignments are further confirmed using RR spectroscopy. Excitation at 514.5 and 568.2 nm leads to the enhancement of the anomalous polarized vibration ν_{20} at 1335 cm^{-1} (cf. Table S2). This indicates that the band at 540 nm is the Q_v band and the shoulder at about 574 nm must then correspond to Q. The separation of these features of about 1100 cm^{-1} supports this assignment.[38] The fact that no other bands are observed in the absorption spectrum of **3** relates to the low-spin d^6 electron configuration of the metal, which prohibits low-energy porphyrin → metal or chloride → metal charge-transfer transitions.

The absorption spectrum of compound **1** is more complicated and shows at least six bands at 379, 417, 510, 578, 654, and 690 nm (cf. Table 7). Because of the high-spin d^5 configuration of iron in this complex, porphyrin to metal charge-transfer (P → M CT) transitions can now occur (cf. Scheme 2). These $a_{1u}(\pi)$, $a_{2u}(\pi) \rightarrow e_g(d_\pi)$ CT transitions have been assigned to bands near 600 nm for high-spin Fe^{III} porphyrin complexes.[15a] Because the corresponding excited states have E_u symmetry in idealized D_{4h} symmetry, strong CI mixing with the nearby Q excited state might also occur. In addition, chloro to iron charge-transfer transitions (Cl → M CT) might also be present in the spectra. The Soret band in complex **1** appears split with its components located at

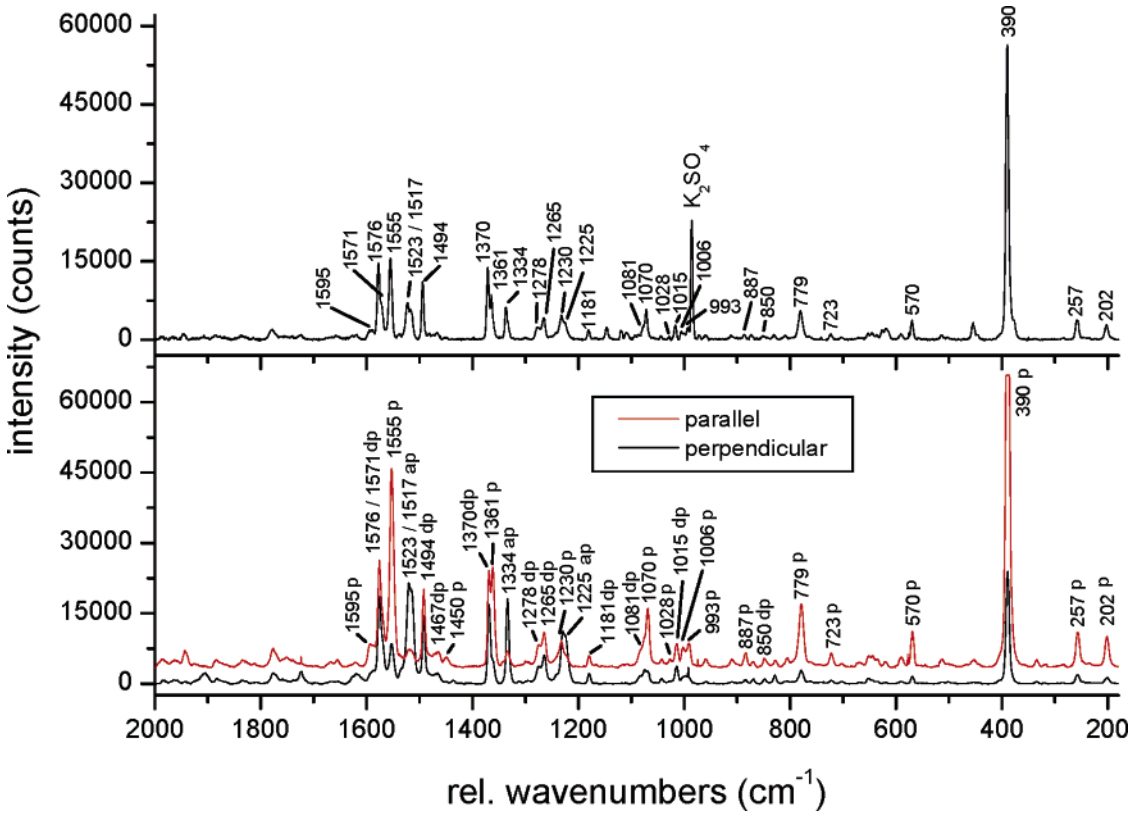

Figure 9. Resonance Raman spectra of **1**, excited at 514.5 nm (Q_v resonance). The RR spectra were measured with potassium sulfate as the internal standard (top). The polarized measurement is shown on the bottom. In the perpendicular measurement, the 390 cm^{-1} band is cut off because of its large intensity.

about 379 and 417 nm (cf. Figure 7). Further insight into these band assignments can be gained from RR measurements. The RR spectrum of **1**, excited at 454.5 nm shows mostly totally symmetric vibrations (cf. Figure 10); therefore, the absorption band at 417 nm is assigned to the Soret band. From the literature, the 379 nm band has been assigned to a chloride → Fe^{III} charge-transfer transition.[52,53] However, the large intensity of this band indicates that the corresponding excited state might steal some intensity from the Soret band. The remaining four absorption bands are located in the Q region of **1**. The RR spectrum of **1**, excited at 568.2 nm (cf. Figure 8) shows a weak band, and the data obtained at 514.5 nm (cf. Figure 9) show medium-intensity anomalous polarized bands, indicating vibronic coupling (anomalous polarized bands that are typically observed are located at about 1520 and 1335 cm^{-1}). In addition, overtones are enhanced with excitation into the absorption band at 510 nm (cf. Figure S2), which indicates that this band is actually the Q_v band (see Section B.4). Hence, a possible assignment might be that Q and Q_v correspond to the bands at about 578 and 510 nm, respectively. However, the separation of these absorption bands of about 2350 cm^{-1} is too large. It should only be about 1250 cm^{-1}, as determined by Gouterman.[38] Hence, the Q band is probably weak in **1** and masked by the feature at 578 nm, the nature of which is not known. The RR spectrum, excited at 647.1 nm (cf. Figure S5), shows not only the usually observed porphyrin A_{2g} modes at 1335 and 1522 cm^{-1} but also the low-energy anomalous polarized bands (Figure S5) that are not observed at any other excitation wavelength. These low-energy bands correspond to in-plane porphyrin deformation modes with some phenyl out-of-plane mode contribution. Hence, the band at 654 nm shows a completely different excitation behavior than the usual Q and Q_v band enhancements. This indicates that the band at 654 nm might correspond to the P → Fe CT transition in agreement with the prediction from the literature.[1] Because this transition leads to two excited states with E_u symmetries (cf. Scheme 2), the second component could correspond to the band at 690 nm, but this is only speculative.

In the case of **2**, the absorption spectrum shows two strong bands in the Soret region at 476 (band V[54]) and 390 nm (band VI)[55] (cf. Table 7). This has been attributed to a CI mixing of the Soret excited state with the porphyrin to metal $a_{1u}(\pi)$, $a_{2u}(\pi)$ → $e_g(d_\pi)$ charge-transfer states with E_u symmetry[38] (cf. Scheme 2). Note that this requires a shift of the P → M CT states from the visible to the UV region compared to that in **1**. Because of the stronger RR enhancement of low-energy vibrations observed, including Mn−X (X = halide) and Mn−N stretching modes in the region of band V in [Mn(ETP)(Cl)] (ETP = etioporphyrin I), this feature

(52) Spiro, T. G.; Li, X.-Y. In *Resonance Raman Spectra of Heme and Metalloproteins;* Spiro, T. G., Ed.; Wiley: New York, 1988; pp 1−37.
(53) Hendrickson, D. N.; Kinnaird, M. G.; Suslick, K. S. *J. Am. Chem. Soc.* **1987**, *109*, 1243−1244.
(54) Boucher, L. J. *Coord. Chem. Rev.* **1972**, *7*, 289−329.
(55) Parthasarathi, N.; Hansen, C.; Yamaguchi, S.; Spiro, T. G. *J. Am. Chem. Soc.* **1987**, *109*, 3865−3871. (b) Gaughan, R. R.; Shriver, D. F.; Boucher, L. J. *Proc. Natl. Acad. Sci. U.S.A.* **1975**, *72*, 433.

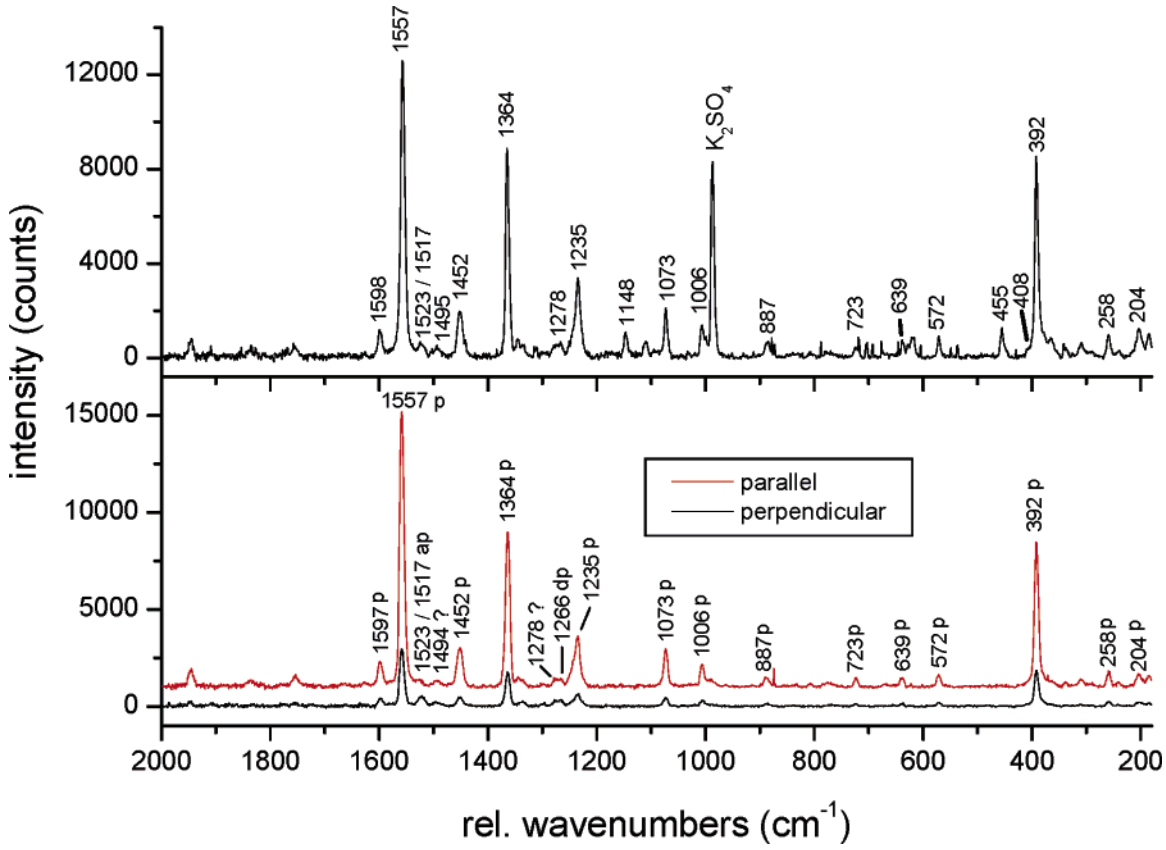

Figure 10. Resonance Raman spectra of **1**, excited at 454.5 nm (Soret resonance). The RR spectra were measured with potassium sulfate as the internal standard (top). The polarized measurement is shown on the bottom.

has been assigned to the predominant CT transition.[56] Note that Soret excitation in general leads to the enhancement of higher-energy porphyrin core vibrations. A stronger enhancement of the low-energy bands in the RR spectrum upon excitation at 488 nm is also found for compound **2** compared to that in the Soret RR spectra of **1** and **3**, indicating that this analysis is correct. It is important to note that the most intense band in this spectrum for **2** is the feature at 393 cm^{-1}, which corresponds to the totally symmetric $\nu_{breathing}$(Mn−N) vibration. The RR excitation profiles of this mode differ significantly for compounds **2** and **1**, as shown in Figures S3 and S4. For complex **1**, the maximum enhancement appears in Q_v resonance, whereas complex **2** shows the maximum upon excitation into band V. More importantly, the RR spectrum of **2**, excited at 454.5 nm shows anomalous polarized bands indicating the vibronic character of band VI, which is centered around 390 nm. This has also been observed by Parthasarathi et al.,[55] who obtained two anomalous polarized bands at 1339 and 1529 cm^{-1} upon excitation at 406.7 nm in **2**. This indicates that the simple hyperporphyrin model by Gouterman[38] might not be sufficient to explain the occurrence of bands V and VI in [Mn(TPP)(Cl)]. In the lower-energy region, the RR spectrum obtained at an excitation wavelength of 568 nm again shows anomalous polarized bands that indicate vibronic coupling. Therefore, the band at about 583 nm is assigned to the vibronic band, Q_v, and the band at 620 nm to Q (cf. Table 7). The separation of these bands of about 1020 cm^{-1} is in agreement with this assignment. In addition, corresponding bands at 560 and 592 nm in [Mn(ETP)(Cl)] have also been attributed to these features.[56] Finally, the nature of the band at about 530 nm is not clear. Anomalous polarized bands are present in the RR spectra but only with low intensity upon excitation at 514.5 nm.

Acknowledgment. We gratefully acknowledge the financial support provided by the Deutsche Forschungsgemeinschaft (DFG; grant LE 1393/1). F.P. acknowledges the Fonds der Chemischen Industrie (FCI) for a Chemiefonds-fellowship. We acknowledge Mrs. U. Cornelissen for recording the Raman spectra of compounds **1**−**3**.

Supporting Information Available: IR and Raman spectra of **3**, RR spectra of **1**, excitation profiles of $\nu_{breathing}$(M−N) for **1** and **2**, and illustrations of the local coordinates used for the classification of in- and out-of-plane porphyrin core modes by Li et al. Assignments of the vibrational data of complexes **2** and **3**, and details of the crystal structure determination of **2**, including atomic coordinates, anisotropic displacement parameters, and geometric parameters. Coordinates of the DFT fully optimized structures of **1**−**3** are also included. This material is available free of charge via the Internet at http://pubs.acs.org.

IC0510866

(56) Asher, S.; Sauer, K. *J. Chem. Phys.* **1976**, *64*, 4115−4125.
(57) Kitagawa, T.; Abe, M.; Kyogoku, Y.; Ogoshi, H.; Watanabe, E.; Yoshida, Z. *J. Phys. Chem.* **1976**, *80*, 1181−1186.
(58) Browett, W. R.; Fucaloro, A. F.; Morgan, T. V.; Stephens, P. J. *J. Am. Chem. Soc.* **1983**, *105*, 1868−1872.
(59) Mu, X. H.; Schultz, F. A. *Inorg. Chem.* **1992**, *31*, 3351−3357.

4.3. First Detailed Assignment of the Magnetic Circular Dichroism and UV-Vis Spectra of Five-Coordinate High-Spin Ferric [Fe(TPP)(Cl)]

Florian Paulat, and Nicolai Lehnert*

Submitted for Publication

First Detailed Assignment of the Magnetic Circular Dichroism and UV-Vis Spectra of Five-Coordinate High-Spin Ferric [Fe(TPP)(Cl)]

Florian Paulat, and Nicolai Lehnert*

Department of Chemistry, The University of Michigan, 930 N. University, Ann Arbor, Michigan 48109-1055, USA.

Abstract:

Five-coordinate high-spin (hs) ferric heme centers occur in the catalytic or redox cycles of many metalloproteins, and therefore, play an important role in enzymology. However, hs ferric hemes exhibit very complicated MCD and UV-Vis absorption spectra and therefore, detailed assignments of the MCD spectra of these species are missing. In this study, the electronic spectra (MCD and UV-Vis) of the five-coordinate hs ferric model complex [Fe(TPP)(Cl)] are analyzed in detail. A correlated fit of the absorption and low-temperature MCD spectra of [Fe(TPP)(Cl)] lead to the identification of at least 20 different electronic transitions. The detailed assignments of these spectra are based on: (a) VTVH saturation data, which allow for the determination of the polarizations of the MCD bands, (b) TD-DFT calculations, to identify the important transitions and their relative energies and intensities with good accuracy, (c) MCD pseudo **A**-terms, to locate E_u excited states, split in the lower symmetry of [Fe(TPP)(Cl)], and (d) correlation to rRaman data to validate the assignments. From the assignments, a number of puzzling questions about the electronic spectra of [Fe(TPP)(Cl)] are addressed. The Soret band in [Fe(TPP)(Cl)] is split into three components, which is due to the fact that one component of the Soret band is mixed with the porphyrin A_{2u}<72> → E_g<82/83> ($\pi \rightarrow \pi^{*(1)}$) transition. The broad, intense feature at higher energy from the Soret band is due to the band at 25577 cm^{-1} in MCD, which shows z-polarization and is therefore, assigned to the mixed σ and π chloro to iron CT transition ($CT^{(Cl,\pi,\sigma)}$). The high-temperature MCD data allow for the identification of Q_v at 20202 cm^{-1}, which corresponds to the **C**-term feature at 20150 cm^{-1}. Q is not observed, but can be localized by correlation to rRaman data published before.[22] The low energy band around 650 nm is due to two P → Fe CT transitions, one being the long thought $A_{1u} \rightarrow d_\pi$ transition ($CT^{(1)}$).

Introduction

Magnetic Circular Dichroism (MCD) is an extremely powerful technique to investigate the electronic structures and spectra of paramagnetic transition metal complexes.[1,2] This technique has clear advantages compared to UV-Vis absorption spectroscopy, because of the much better resolution of electronic transitions, or EPR, because MCD is not restricted to non-integer spin systems. In addition, the polarizations of the electronic bands are accessible by MCD in samples of randomly oriented molecules. Correspondingly, MCD spectroscopy has frequently been applied to heme proteins.[1f,3] Heme active sites occur in many different proteins and are extremely important for numerous biological processes.[4] Detailed information about the spin state, geometry, oxidation state (ferrous, ferric and ferryl) and axial ligand (identity, number and type) of the heme(s) in many different proteins has been obtained by comparison of their MCD data with those of standards, including porphyrin model complexes and heme proteins with known spectra. Hence, MCD has been widely used as a powerful "fingerprinting" technique to classify newly discovered heme proteins.[1f,5] For example, Dawson and Sono have used MCD spectroscopy to provide evidence for axial cysteine ligation to the hs ferric state in Cytochrome P-450 and Chloroperoxidase (CPO) by comparing the MCD spectra of these enzymes to those of synthetic model compounds.[5] In addition, the MCD spectra of newly discovered heme proteins are often compared to those of horseradish peroxidase (HRP) and myoglobin (Mb) to determine the nature of the prosthetic group and its ligation state, because these systems have been studied extensively by MCD spectroscopy.[1f] *Importantly, however, in almost all of these cases, detailed assignments of the MCD spectra are missing, and the nature of the different transitions of the different transitions observed is thus unknown.* In particular, high-spin (hs) ferric hemes exhibit very complicated MCD and UV-Vis absorption spectra.[5] Five-coordinate hs ferric heme centers occur in the catalytic or redox cycles of many proteins, and therefore, play an important role in enzymology. Important axial ligands to hs ferric hemes are cysteinate in P450 type enzymes, and histidine in HRP, hemoglobin (Hb), Mb, and in nitrophorins from Rhodinus prolixus[6]. In addition, catalase enzymes contain a five-coordinate hs ferric heme b with tyrosinate ligation, which is also evident from MCD spectroscopy.[7] It is therefore of critical importance to explore the electronic structures of five-coordinate hs ferric heme active sites in order to understand their functions in these different proteins. One important step toward this goal is the actual assignment of their UV-Vis and MCD spectra. Besides the investigation of metalloporphyrins in biological

systems, synthetic porphyrin model complexes have widely been studied to gain insight into the catalytic reactions or functions performed by heme proteins.[8] In many cases, tetraphenylporphyrin (TPP^{2-}) and octaethylporphyrin (OEP^{2-}) ligands have been used for such model systems.

The theoretical background of MCD spectroscopy was developed by P. J. Stephens in the 1970's and has been summarized in a number of reviews and articles.[1a,b,d,e,2,9] Recently, a review by Mack et al. has been published that summarizes the background of MCD spectroscopy and its applications to porphyrinoids.[10] MCD spectroscopy measures the difference in intensity of left (lcp) and right (rcp) circular polarized light in an applied, longitudinal field. MCD intensity is proportional to three different contributions, designated as MCD **A**-, **B**- and **C**-terms (cf. equation 1).

$$I \sim \left[A_1 \left(\frac{-\partial f(E)}{\partial E} \right) + \left(B_0 + \frac{C_0}{kT} \right) f(E) \right] \cdot B \quad (1)$$

Here, I is the MCD intensity, T the temperature, B the magnetic field and the function *f(E)* represents the band shape of an absorption band. Importantly, the **A**- and **B**-terms are temperature independent, whereas MCD **C**-term intensity is temperature dependent. Therefore, the most important mechanism at low temperature is the **C**-term. From eqn. 1, MCD intensity increases linearly with the strength of the magnetic field (B). This strictly applies to the **A**- and **B**-terms. **C**-term intensity arises from a degenerate ground state, which is split in the magnetic field due to the Zeeman effect as shown in Scheme 1. In general, degenerate ground states are due to spin degeneracy and hence, *only paramagnetic compounds exhibit **C**-term signals*. At low temperatures, kT is in the order of the Zeeman splitting in the presence of a strong magnetic field, which leads to a larger population of the lower energy compared to the higher energy Zeeman sublevels of the ground state corresponding to the Boltzmann distribution. Hence, the intensities of the rcp and lcp transitions do not cancel anymore leading to an absorption band shape for the **C**-term. A further decrease of the temperature or an increase of the magnetic field results in an increase in the population of the lowest-energy sublevel and therefore, the **C**-term MCD intensity also increases. If the higher energy sublevels are completely depopulated, the **C**-term intensity reaches its maximum value, it saturates. Importantly, *the temperature and magnetic field dependent **C**-term intensity contains the complete information of the ground state properties including g values and zero-field splitting (zfs) parameters as well as the polarizations of the*

electronic transitions. All this information can be extracted by fitting these **C**-term saturation magnetization curves.

In order to establish detailed assignments for the electronic spectra of a hs ferric heme for the first time in the literature, we have studied the five-coordinate model complex [Fe(TPP)(Cl)], which exhibits very complex MCD and UV-Vis absorption spectra similar to those of the hs ferric heme centers in the above mentioned enzymes. Therefore, this complex is an excellent model for the five-coordinate high-spin ferric state. So far, no assignments of the MCD spectra of [Fe(TPP)(Cl)] have been made. Browett et al., who determined the zfs parameter D for [Fe(TPP)(Cl)] by analysing MCD saturation curves, stated in 1983:[11] "The analysis of the MCD [data] of FeCl(TPP) is therefore a substantial challenge. […] It remains to be demonstrated that this analysis successfully predicts the temperature dependence of the MCD to liquid helium temperatures, which is a sine qua non of a viable theory." This explicit theoretical description of MCD intensity is now available via a general method developed by Neese and Solomon,[2,12] which we have applied in this study. Up to this day, the only effort to assign parts of the MCD spectra of [Fe(TPP)(Cl)] was performed by Kobayashi and coworker, who evaluated the MCD data of this compound in benzene solution, and at liquid nitrogen temperatures (77 K) in a polymethyl methacrylate matrix.[13] Simple calculations were then performed to investigate the effect of CI mixing the charge transfer states that are due to the excitation of an electron from the porphyrin HOMOs (a_{1u} and a_{2u}) to the singly occupied d_π ($d_{xz,yz}$) orbitals of iron with the $\pi \rightarrow \pi^*$ Soret/Q excited states (singlet and triplet) of the porphyrin. However, as we will show in this work, this interpretation is highly questionable, and in particular cannot account for the experimentally observed polarizations of many electronic transitions.

In summary, despite the large significance of five-coordinate hs ferric heme in biology, detailed assignments of MCD and UV-Vis data of corresponding species are not available to this date. To this end, we have performed low-temperature MCD measurements on the five-coordinate model complex [Fe(TPP)(Cl)], which has very complex electronic spectra, and hence, is a very good system to develop an MCD methodology to analyze the spectra of high-spin ferric heme complexes in models and proteins. Variable temperature and variable field (VTVH) measurements have been used to determine the polarizations of most of the electronic bands observed in the MCD spectra of this compound. In correlation to resonance Raman (rRaman)

results and TD-DFT calculations, this allows for a detailed assignment of the optical spectra of [Fe(TPP)(Cl)] for the first time and this way, provides detailed insight into the electronic structure of five-coordinate ferric hemes. In future studies, the methodology developed here will be applied to ferric P450 and corresponding model complexes [Fe(TPP)(SR)].

Experimental and Computational Procedures

Syntheses. The complex [Fe(TPP)(Cl)] was synthesized using published procedures [14] and isolated as microcrystalline solid. The identity of the compound was established using ^{1}H-NMR, UV-Vis absorption, IR, and MCD spectroscopy.
^{1}H-NMR(400 MHz, $CDCl_3$): 81.6 (s, Pyrrole-H), 13.6 and 12.4 (s, meso-H), 6.45 (s, para-H) and ~5.3 (broad, ortho-H).

UV-Vis Spectroscopy. Absorption spectra were recorded in chloroform at room temperature using an Analytik Jena Specord S600 spectrophotometer. The absorption data were scaled using literature extinction coefficients (λ_{max} (ε in cm^{-1} M^{-1}) = 372 nm (4.71×10^4), 418 (1.08×10^5), 507 (1.18×10^4), 572 (5.0×10^3) and 685 (3.1×10^3)).[15]

MCD Spectroscopy. MCD spectra have been obtained on thin polystyrene films. The films were prepared by dissolving [Fe(TPP)(Cl)] and polystyrene in benzene, followed by slow evaporation of the solvent. The polystyrene films were placed between two quartz plates (Suprasil 1), which were mounted on a copper sample holder. MCD spectra were recorded using a setup that consists of an OXFORD spectromag^{4000} cryostat and a JASCO J810 CD spectropolarimeter. The SM^{4000} consists of a split pair superconducting magnet providing horizontal magnetic fields of 0-7 T in a low boil-off helium cryostat. The light source of the J810 is an air cooled xenon lamp. The detector system corresponds to two interchangeable head-on photomultiplier tubes. Samples are loaded into a 1.5 – 300K variable temperature insert (VTI), which offers access to the sample by four optical windows made from Spectrosil B quartz. The obtained MCD spectra were measured in [θ] = mdeg and converted to $\Delta\varepsilon$ [M^{-1} T^{-1} cm^{-1}] using the conversion factor $\Delta\varepsilon = \theta / (32980*c*d)$, where c is the concentration and d the thickness of the sample (path length). Importantly, the product c*d can be substituted by $A_{MCD}/\varepsilon_{UV\text{-}Vis}$, where A is the absorbance of the sample measured by the CD spectrometer. This is of particular importance, since it is difficult to

determine d for the polymer films used here. The extinction coefficient $\varepsilon_{UV\text{-}Vis}$ has been determined by Browett et al.[11] We have used $\varepsilon_{UV\text{-}Vis}$ and A determined from the Soret band for the calculation of the molar MCD intensity. For each temperature and field, the complete spectrum was recorded to obtain the VTVH data for every MCD band, and also to examine the quality of the spectra (baseline shifts, etc.).

Density Functional Calculations. DFT calculations using Becke's three parameter hybrid functional with the correlation functional of Lee, Yang and Parr (B3LYP)[16] were performed using the program package Gaussian 03.[17] The structure of [Fe(TPP)(Cl)] (S = 5/2) was fully optimized without simplifications using the LanL2DZ* basis set. The LanL2DZ* basis set consists of LanL2DZ plus polarization functions (from TZVP) on all heavy atoms.[18] TD-DFT calculations for [Fe(TPP)(Cl)], [Zn(P)] and [Zn(TPP)] applying B3LYP/LanL2DZ* were performed using G03. Calculations for [Fe(TPP)(Cl)] were performed both on the fully optimized structure, and on a corresponding structure where the Fe-Cl distance has been set to the crystallographically obtained value of 2.192 Å, determined by Hoard et al.[19] In all calculations, convergence was reached when the relative change in the density matrix between subsequent iterations was less than 1×10^{-8}. The absorption spectra of [Zn(P)] and [Zn(TPP)] were also calculated using the semi-empirical INDO/S-CI method as implemented in ORCA[20]. In the case of [Fe(TPP)(Cl)], however, this method could not be applied, since the wrong ground state is predicted by INDO/S for this compound. Note that the number of states for the TD-DFT calculations on [Fe(TPP)(Cl)] was limited to 70, because of the complexity of the problem, which makes these calculations very time consuming (keeping in mind the size of the molecule). Hence, the calculations cover the range up to 27964 cm^{-1} (358 nm) and accordingly, higher energy states are not included in the calculations.

Fitting of the VTVH data. The VTVH data were fitted using the general method developed by Neese and Solomon.[2] The analysis is based on the following equation (2):

$$\frac{\Delta\varepsilon}{E} = -\frac{\gamma}{4\cdot\pi}\int_{\theta}\int_{\phi}\tanh\left(\frac{g\beta_B B}{2kT}\right)\frac{\sin\theta}{g}\left(l_x^2 g_x M_{yz}^{eff} + l_y^2 g_y M_{xz}^{eff} + l_z^2 g_z M_{xy}^{eff}\right)d\theta d\phi \quad (2)$$

where $\Delta\varepsilon/E$ is the MCD intensity, M^{eff} are the effective transition dipole moment products, l is the angular momentum, β_B is the Bohr magneton, B is the magnetic field, T is the temperature, k is the Boltzmann constant, and g are the ground-state g-values. The individual polarizations of

MCD bands can then be calculated using the M^{eff} values obtained from the fit of the VTVH saturation curves, using the equation (3):

$$\%x = 100 \cdot \frac{\left(M_{xy}^{eff} \cdot M_{xz}^{eff}\right)^2}{\left(M_{xy}^{eff} \cdot M_{xz}^{eff}\right)^2 + \left(M_{xy}^{eff} \cdot M_{yz}^{eff}\right)^2 + \left(M_{xz}^{eff} \cdot M_{yz}^{eff}\right)^2} \quad (3)$$

The calculation of the y- and z-polarizations is performed correspondingly.

Results and Analysis

A. TD-DFT calculations and classification of the electronic transitions.

A.1 Method calibration for quantum-chemical excited state calculations using four-coordinate zinc porphyrins: [Zn(P)] and [Zn(TPP)].

In order to assign the UV-Vis absorption and MCD spectra of [Fe(TPP)(Cl)], quantum-chemical excited state calculations were performed. To explore the performance of TD-DFT and semiempirical INDO/S-CI calculations on metalloporphyrins, we have calculated the absorption spectra of the simple [Zn(P)] (P^{2-} = porphine) and [Zn(TPP)] (TPP^{2-} = tetraphenylporphyrin) complexes first, and compared the results to the experimental spectra of [Zn(TPP)][21], which shows a very simple absorption spectrum. The results are summarized in Table S1 in the Supporting Information. $Zinc^{2+}$ is a good choice for these method calibration studies, because it has a d^{10} electron configuration and therefore, no charge transfer (CT) transitions from the porphyrin to the metal are possible, and no d-d transitions are present. Correspondingly, [Zn(TPP)] shows a very simple absorption spectrum, which allows for the straight-forward identification of the Soret and Q bands at 23880 and 17080 cm^{-1}, respectively. The Soret and Q transitions are also easy to identify in the calculations. As shown in Table S1, the calculations clearly indicate that the simple porphine ligand is not a good model for TPP in both the TD-DFT and INDO/S-CI calculations producing significant errors in comparison with the experimental data for [Zn(TPP)]. This is not surprising, because the phenyl substituents have a critical influence on the geometric and electronic structure of the porphyrin core. These effects cannot be neglected if the calculation of porphyrin $\pi \rightarrow \pi^*$ transitions is desired. Hence, the complete TPP ligand has to be used in the theoretical treatment. The TD-DFT calculations on simple [Zn(P)] also show that more accurate results are obtained by adding polarization functions (from TZVP) to the LanL2DZ basis set on all heavy atoms (LanL2DZ* basis set)[18]. A further extension of the

basis set to TZVP does not lead to a noticeable improvement, which indicates that LanL2DZ* is sufficient for the TD-DFT calculations (cf. Table S1). However, there are still considerable deviations to experiment, and therefore, the TD-DFT results by themselves are not sufficient for a quantitative interpretation of the complicated electronic spectra of high-spin (hs) ferric hemes. This requires further experimental input. Nevertheless, the calculations can be used to define the "active space" of electronic transitions, which need to be considered for the analysis, and their relative energies. This is very useful for the assignment of the spectra.

A.2 Classification of the electronic transitions of [Fe(TPP)(Cl)].

A good theoretical description of the $[Fe(TPP)]^+$ core of [Fe(TPP)(Cl)] has been obtained using B3LYP with both LanL2DZ (cf. ref. [22]) and LanL2DZ* (this work). However, both methods show large deviations from experiment with respect to the Fe-Cl bond length. From X-ray crystallography, d(Fe-Cl) = 2.192 Å[19] has been determined. In comparison, using B3LYP/LanL2DZ, d(Fe-Cl) = 2.32 Å is calculated. A better description of the Fe-Cl bond is obtained by adding polarization functions on all heavy atoms, which leads to d(Fe-Cl) = 2.26 Å. Therefore, we used the B3LYP/LanL2DZ* fully optimized structure for the TD-DFT calculations, but adjusted the Fe-Cl distance to the experimental value. For the evaluation of the TD-DFT results, it is first necessary to consider the MO diagram of [Fe(TPP)(Cl)]. Since this complex is high-spin (S = 5/2), all α-d orbitals are fully occupied, whereas the β-d orbitals are empty, leading to a $^6A_1$ ground state. Correspondingly, no CT transitions of porphyrin → Fe-d type are possible for α-electrons, and hence, only the β-orbitals are considered in the following analysis. Figure 1 shows the molecular orbital scheme for [Fe(TPP)(Cl)]. The corresponding charge contributions of the β spin molecular orbitals are given in Table 1. Contour plots of important orbitals are shown in Figure 2. Note that the labels of the porphyrin π and π* orbitals refer to the MO diagram of free porphine^{2-}, which is shown in Figure S1. In the applied coordinate system, the z axis is aligned with the Fe-Cl bond, whereas the x and y axes are located along the Fe-N bonds of the porphyrin ligand (cf. Figure 1, top). Correspondingly, the $d_{x^2-y^2}$ orbital of the metal forms a strong σ-bond with the pyrrole nitrogens of the porphyrin, whereas d_{xy} is practically non-bonding (LUMO: β<170>). The E_g<82/83> LUMOs of the free porphyrin ligand are mixed with d_{xz} and d_{yz} (labeled d_π) in [Fe(TPP)(Cl)], and have about 18 % d_π contribution (β<174/175>; cf. Table 1). The metal-chloride σ-bond is mediated by the d_{z^2} orbital of iron and the p_z orbital of the chloro ligand. The corresponding bonding combination,

p_z _ d_{z2} (β<148>), has 24 % iron d_{z2} and 60 % chloro p_z character, which corresponds to a strong σ bond.[22] Additional π-bonds between the d_{xz} and d_{yz} orbitals of iron and the p_x and p_y orbitals of the chloro ligand, respectively, are also present. The corresponding bonding combinations, p_y _ d_{yz} and p_x _ d_{xz} (β<152/153>), have about 8 % metal and 46 % chloride character (cf. Table 1), indicative of a medium strong interaction. The HOMOs of [Fe(TPP)(Cl)] are the A_{1u}<79> and A_{2u}<81> orbitals of the porphyrin core. Note that the A_{1u} orbital is mixed with the empty d_{z2} _ p_z orbital (the antibonding combination of d_{z2} and p_z of chloride). Other important molecular orbitals for the interpretation of the electronic spectra of [Fe(TPP)(Cl)] are low lying porphyrin π orbitals, i.e. B_{2u}<74> (β<167>) and A_{2u}<72> (β<156>). Note that the principal bonding scheme of [Fe(TPP)(Cl)], focusing on the metal-porphyrin interaction, has been analyzed before by Cheng et al.[23] A more detailed description of the Fe-Cl bond has recently been published by our group.[22] By using polarized rRaman spectroscopy, we have shown in this publication that the $[Fe(TPP)]^+$ core of [Fe(TPP)(Cl)] still behaves as if it has D_{4h} symmetry. Therefore, an effective D_{4h} symmetry is applied in the following analysis of the TD-DFT results.

The absorption and MCD spectra of [Fe(TPP)(Cl)] presented in Figure 3 are significantly more complex than those of [Zn(TPP)][21]. This is due to the high-spin d^5 configuration of iron(III), which leads to a $[d_{xz}, d_{yz}, d_{xy}, d_{z2}, d_{x2-y2}]^5$ electron configuration as described above. Hence, all five d orbitals are singly occupied, which allows for a magnitude of CT transitions of porphyrin → Fe(III) and Cl^- → Fe(III) type. These are not present in Zn(II) with a d^{10} electron configuration. Scheme 2 shows all important electric dipole allowed transitions identified from TD-DFT. In the following, transitions are classified as inner porphyrin, porphyrin to iron CT (P → Fe CT), and chloro to iron CT transitions (Cl → Fe CT) for their further evaluation. Considering d-d transitions, these are all spin forbidden due to the $^6A_1$ ground state of hs iron(III) and hence, are not further considered. The following one-electron transitions are important:

1) Inner porphyrin transitions (cf. Scheme 2 and Figure S1 for porphyrin orbital labels):

a) π → π* $^{(0)}$: A_{1u}, A_{2u} <79,81> → E_g <82,83> (Soret and Q band)

b) π → π* $^{(1)}$: A_{2u} <72> → E_g <82,83>

c) π → π* $^{(2)}$: B_{2u} <74> → E_g <82,83>

2) Porphyrin to iron charge-transfer transitions (P → Fe CT; cf. Scheme 2):

a) $CT^{(1)}$: A_{1u} <79> → d_{xz},d_{yz} = d_π

b) $CT^{(2)}$: A_{2u} <81> → $d_{xz},d_{yz} = d_\pi$

c) $CT^{(3)}$: B_{2u} <74> → $d_{xz},d_{yz} = d_\pi$

d) $CT^{(4)}$: A_{2u} <72> → $d_{xz},d_{yz} = d_\pi$

e) $CT^{(5)}$: A_{2u}<81> _ d_{z^2} _ p_z → d_{z^2} _ p_z _ A_{2u}<81> (z-polarized)

f) $CT^{(6)}$: B_{2u} <74> → d_{z^2} _ p_z _ A_{2u}<81> (z-polarized)

Note that the overlap of the porphyrin orbital A_{1u} <79> with the d_π orbitals of iron(III) is poor, since the nitrogen p orbitals of the porphyrin do not contribute to A_{1u}<79>. Therefore, one would expect that $CT^{(1)}$ has no or little intensity. However, the d_π orbitals show mixing with the E_g <82/83> LUMO of the porphyrin dianion (~18%, cf. Table 1), and therefore, $CT^{(1)}$ steals intensity from the intense π → π* transition through this mixing.

3) Chloro to iron CT transitions (Cl → Fe CT; cf. Scheme 2):

a) $CT^{(Cl,\pi)}$: p_x,p_y → d_π (z-polarized)

b) $CT^{(Cl,\sigma)}$: p_z → d_{z^2} (z-polarized)

Importantly, all of the listed π → π* inner porphyrin and P → Fe CT excited states with the exception of $CT^{(5,6)}$ have E_u symmetry, are x,y-polarized, and are potentially subject to strong configuration interaction. In addition, note that the iron d_π orbitals and the LUMO orbitals of the porphyrin are of the same symmetry, and are therefore mixed (cf. Table 1). Correspondingly, the electronic transitions observed in [Fe(TPP)(Cl)] are also highly mixed as evident from the TD-DFT results, which renders the quantitative analysis of these spectra highly challenging. Table S2 lists all important excited states obtained from the TD-DFT calculations and their individual contributions. Scheme 2 summarizes the most important transitions.

A.3 Principal trends in the electronic spectra of [Fe(TPP)(Cl)].

The TD-DFT calculations show out-of-plane (z-polarized) transitions at 11945, 12325, 20740, 22455, 22605 and 25008 cm^{-1} originating from the z-polarized excited states $CT^{(Cl,\pi,\sigma)}$ and $CT^{(5,6)}$ (cf. Table S2), respectively. Note that both $CT^{(5,6)}$ are z-polarized, because of the out-of-plane displacement of the iron center towards the axial chloro ligand in [Fe(TPP)(Cl)]. Importantly, the z-polarized bands are all calculated to lower energy of the Soret band. Eaton and Hochstrasser observed a weak z-polarized band (ε = 800 M^{-1} cm^{-1}) at 14388 cm^{-1} (695 nm) in the polarized single crystal UV-Vis absorption spectrum of ferricytochrome c, which contains low-spin Fe(III) and has an S = ½ ground state. They assigned this band to $CT^{(5)}$.[24] The TD-DFT calculations predict $CT^{(5)}$ in [Fe(TPP)(Cl)] at 11945 cm^{-1} (837 nm), which is an almost pure excited state

(82 % $CT^{(5)}$ character). The transition at 12325 cm^{-1} (811 nm) corresponds to A_{1u}<79> → d_{xy} (90 % contribution), and has about 10 % $CT^{(5)}$ character. Correspondingly, this feature has almost no absorption intensity due to poor orbital overlap of A_{1u}<79> and d_{xy}. The next z-polarized bands to higher energy are found at 20740 cm^{-1} and 22455 cm^{-1}. Both correspond to Laporte forbidden E_g → d_π transitions (about 90 % contribution; cf. Table S2). Their weak intensity and z-polarization is due to admixture of 7 % chloro to iron π charge transfer ($CT^{(Cl,\pi)}$), 4 % chloro to iron σ charge transfer $CT^{(Cl,\sigma)}$ (4 %) and 6 % $CT^{(6)}$, respectively. The corresponding, almost pure $CT^{(6)}$ transition (90 %) is predicted very close in energy at 22605 cm^{-1}. Finally, the z-polarized transition calculated at highest energy is located at 25008 cm^{-1}. This feature corresponds to a mixed chloro to iron and porphyrin to iron CT transition with about 39 % $CT^{(Cl,\pi)}$, 13 % $CT^{(Cl,\sigma)}$ and 28 % $CT^{(5)}$ contribution.

Importantly, all other excited states below 20000 cm^{-1} (500 nm) derive from mixing of π → $\pi^{*(0)}$ (Q/Soret band) with either $CT^{(1)}$ or $CT^{(2)}$. Mixing of π → $\pi^{*(0)}$ with $CT^{(2)}$ leads to two low energy transitions at 8342 cm^{-1} (1199 nm) and 8800 cm^{-1} (1136 nm, cf. Table S2), which have mostly $CT^{(2)}$ (87 %) character with 5 % π → $\pi^{*(0)}$ contribution (cf. Table S2). Accordingly, the two corresponding transitions at 18988 cm^{-1} (527 nm) and 18990 cm^{-1} (527 nm) have 97 % π → $\pi^{*(0)}$ character. Interestingly, $CT^{(2)}$ is almost exclusively mixed with the A_{2u} → E_g component of π → $\pi^{*(0)}$, whereas $CT^{(1)}$ mixes with both the A_{1u} and A_{2u} → E_g transitions of π → $\pi^{*(0)}$. The latter interaction gives rise to bands at 12329 cm^{-1}, 12910 cm^{-1}, 13893 cm^{-1}, 14185 cm^{-1}, 16783 cm^{-1} and 16921 cm^{-1} as listed in Table S2. Note that the features at 13893 and 14185 cm^{-1} are predicted to have zero electric dipole transition strength.

The region above 20000 cm^{-1} contains a number of new electronic transitions. $CT^{(3)}$ is observed at 21631 cm^{-1} (462 nm) and 22341 cm^{-1} (448 nm), where both states have about 89 % $CT^{(3)}$ character. Both features are mixed with π → $\pi^{*(0)}$ (~5 %) and π → $\pi^{*(2)}$ (2 %). $CT^{(4)}$, which originates from the low lying A_{2u}<72> porphyrin orbital, is predicted at 25202 cm^{-1} (397 nm). Further excited states with $CT^{(4)}$ contribution are calculated at 24410 cm^{-1} (410 nm) and 24446 cm^{-1} (409 nm). These two excited states have mainly $p_{x,y}$(Cl) → d_{z2} character (53 %; cf. Table S2), which, however, are overlap forbidden transitions that do not contribute to the oscillator strengths of these features. The calculated relatively large intensities of these transitions

are actually due to substantial admixture of the allowed $\pi \rightarrow \pi^{*(0)}$ (21 %) and $\pi \rightarrow \pi^{*(2)}$ (6 %) transitions. Four excited states with significant $\pi \rightarrow \pi^{*(2)}$ character are located at 25475, 25718, 27164 and 27250 cm^{-1} (cf. Table S2). The two transitions around 25000 cm^{-1} show mixing with $CT^{(2,3)}$.

The prediction of TD-DFT for the Soret band region in [Fe(TPP)(Cl)] is very interesting, and explains unusual observations in the MCD and UV-Vis spectra as discussed below. In the Soret region, four intense transitions are calculated within 300 cm^{-1} (transitions 24-27 in Table S2). State 24 at 25843 cm^{-1} corresponds to a $\pi \rightarrow \pi^{*(1)}$ transition (31 %) with about 6 % $\pi \rightarrow \pi^{*(0)}$ (Soret) contribution. Transitions 25 and 26 (at 26071 and 26109 cm^{-1}), corresponding to the Soret components 1 and 2 with 14 and 11 % $\pi \rightarrow \pi^{*(0)}$ character, respectively, show significant admixtures of $\pi \rightarrow \pi^{*(2)}$ (about 20 %) and $CT^{(4)}$ (11 and 34 %, respectively). Finally, the third Soret component at 26143 cm^{-1} is again mixed with $\pi \rightarrow \pi^{*(2)}$,but does not show any $CT^{(4)}$ contribution (cf. Table S2).

Figure 5 shows a comparison of the observed and calculated absorption spectrum of [Fe(TPP)(Cl)]. As evident from this Figure, the TD-DFT calculations show surprisingly good agreement with experiment, but the alignment of the observed features is not close enough for a quantitatively assignment of the electronic spectra. However, as exercised above, the calculations help to classify the possible excited states, define their relative energies and intensities, and this way, provide very important input for the spectral assignments. In addition, the calculations afford a theoretical description of the z-polarized bands, which can experimentally be determined from fitting the VTVH data (vide infra). Hence, the TD-DFT results presented above serve as a basis for the interpretation of the experimental UV-Vis and MCD data of [Fe(TPP)(Cl)].

B. Analysis of the MCD and UV-Vis spectra.

B.1 Absolute A- and C-Term MCD Intensities.

Figure 3 presents the UV-Vis (top) and MCD **C**-term (bottom) spectra of [Fe(TPP)(Cl)] in molar units (ε / M^{-1} cm^{-1} and $\Delta\varepsilon$ / M^{-1} cm^{-1} T^{-1}, respectively). Both spectra are complicated, showing at least six bands in the UV-Vis and 20 bands in the MCD spectrum, which again emphasizes the impact of MCD compared to absorption spectroscopy for the resolution of electronic spectra. In a

classic study, Browett et al. determined the axial zfs parameter for [Fe(TPP)(Cl)] (D = 6.9 cm^{-1}) by analysing MCD saturation curves using low-temperature MCD spectroscopy (at liquid helium temperature).[11] The obtained value for D is in good agreement with D = 6 cm^{-1} as determined from single crystal magnetic susceptibility measurements,[25] and D values from far IR (6.5 cm^{-1})[26a] and Mössbauer (7.0 cm^{-1})[26b] experiments. The fit of the temperature-dependent MCD data also demonstrates that the ground state is S = 5/2,[11] because contributions of the six ground-state sublevels are required to simulate the data of [Fe(TPP)(Cl)]. This is further in agreement with EPR results, which show an axial spectrum with g values of $g_{\perp} \approx 6.06$ and $g_{\parallel} \approx 2.01$.[11] Hence, E/D is zero. The low-temperature MCD data of [Fe(TPP)(Cl)] presented in Figure 3 are in agreement with the data obtained by Browett et al.[11] The MCD spectrum shows one temperature independent B-term feature at 19084 cm^{-1}, and five sign changes at about 15340, 23530, 26630, 29500 and 31740 cm^{-1}, respectively (cf. Figure 3). The latter two sign changes were not observed by Browett et al.[11] indicating that the data set presented here has a better resolution in the higher energy region. The saturation intensity (peak-to-trough intensity of the Soret band) obtained from the MCD spectrum measured at 1.8 K and +7 T is 3.4 * 10^3 M^{-1} cm^{-1}, which is significantly lower than saturation limits observed for low-spin ferric heme proteins with S = ½ ground states. As shown in Table 3, the saturation intensity observed for the low-spin compounds is in the range of 25 * 10^3 to 61 * 10^3 M^{-1} cm^{-1}. For example, horse heart cytochrome c shows a value of 40.5 * 10^3 M^{-1} cm^{-1}.[27]

Figure 4 presents high-temperature MCD spectra of [Fe(TPP)(Cl)] measured at 290 K, which have been determined in order to quantify temperature-independent **A**- and **B**-term contributions to the total MCD intensity. The two Soret components are observed as a derivative shaped band at 24272 and 23121 cm^{-1}. Due to the nearly degenerate E_g<82/83> (LUMO) orbitals of the TPP^{2-} ligand, the Soret band shows intense **A**-term features with 15 and -11 M^{-1} cm^{-1} T^{-1}, respectively. Q_v is observed as a derivative shaped band at 20202 cm^{-1}, whereas Q is not observed in the spectrum. The molar intensity at 290 K for Q_v is about 0.4 M^{-1} cm^{-1} T^{-1}. Subtraction of the molar 290 K spectrum from the low temperature data yields the corresponding pure **C**-term spectrum shown in Figure 4 and Figure 3, bottom. Based on these data, the molar **C**-term intensity of the two major Soret components of [Fe(TPP)(Cl)] is 477 and -182 M^{-1} cm^{-1} T^{-1}, respectively. In order to perform a reliable analysis of the VTVH **C**-term data, it is of critical importance to subtract the temperature independent **A**- and **B**- term contributions. This especially applies to the Soret band,

because significant **A**-term contributions are present in this case as discussed above. Nevertheless, the paramagnetic **C**-term contributions are dominant at low temperature, especially for the other features as evident from the high-temperature MCD spectrum shown in Figure 4.

B.2 Assignments

Figures 6, 7 and 8 show the VTVH saturation curves for the Soret$^{(1)}$ component located at 23266 cm^{-1} (band 12), band 4 at 15015 cm^{-1} (CT$^{(1)}$), and band 6 at 16444 cm^{-1} (CT$^{(Cl,\pi)}$), respectively. For the fitting of these data, the zero field splitting parameter D determined by Browett et al. (D = 6.9 cm^{-1})[11] from MCD data was used and E/D was set to zero in agreement with EPR (vide supra). Since the MCD **C**-term spectrum of [Fe(TPP)(Cl)] is very crowded with many overlapping bands, the individual band positions were determined first from a correlated fit of the absorption and **C**-term spectra as shown in Figure 3. In the next step, the VTVH curves were determined for every band at an energy that minimizes overlap with the neighboring bands (for example: cf. Figures 6-8). Because of this, the specified positions used to obtain the VTVH curves do not necessarily correspond to the particular band maxima. Importantly, *the obtained VTVH curves show two different types of saturation behavior indicating different polarizations*. In-plane (x,y) polarizations induce a nesting behavior of the corresponding saturation isotherms ("N" behavior: bands 4, 10, 12, 13 and 15; cf. Figures 6 and 7), whereas out-of-plane (z) polarization generates overlaying saturation isotherms ("O" behavior: bands 3, 6, 7, 8, 11 and 14; cf. Figure 8). *This means that the saturation curves allow to clearly distinguish between in-plane and out-of-plane polarized transitions, which is a corner stone for the assignments of all the observed bands* that we identified from the fit shown in Figure 3. For bands 5 and 16, VTVH curves were difficult to obtain due to the low MCD intensities of these transitions. Hence, their magnetization behavior could not be clearly determined.

Based on the experimentally determined polarizations of the electronic transitions, and the TD-DFT results, the electronic spectra of [Fe(TPP)(Cl)] can now be assigned for the first time. The UV-Vis spectrum in Figure 3 shows the Soret band at about 23980 cm^{-1}, and an unusual, broad band to higher energy at 26385 cm^{-1}, which could correspond to a second Soret component. A much better resolution of this spectral region is available from the MCD spectrum, which shows three Soret components at 23266, 24270 and 27017 cm^{-1} (bands 12, 13 and 15), which all exhibit in-plane polarizations. This observation is in agreement with the TD-DFT results, which also

show three Soret components (bands 25-27 in Table S2). The appearance of three Soret components instead of the expected two in form of a pseudo-**A** (cf. Discussion) is due to admixture of the $CT^{(4)}$ excited state, which corresponds to the transition from the low-lying A_{2u}<72> porphyrin orbital (β<156>; cf. Figures 1 and 2) to the d_π orbitals (d_{xz}, d_{yz}) of iron. In the case of [Fe(TPP)(Cl)], $CT^{(4)}$ is close in energy to the Soret excited state, which induces a CI mixing of these states (both excited states have E_u symmetry in D_{4h}). Hence, the Soret band splits into three components. In the calculation, the band in the middle (band 26 at 27017 cm^{-1}) has most $CT^{(4)}$ character. Experimentally, the assignment is different. As further elaborated in the Discussion, the Soret band usually gives rise to a pseudo-**A** in the MCD, where each MCD band corresponds to one component of the low-symmetry split Soret E_u excited state. Importantly, since $CT^{(4)}$ does only have the $A_{2u} \rightarrow E_g$ component, it only mixes with one component of the Soret band, either the positive or negative **C**-term feature. A quick inspection of Figure 3, bottom shows that in this case, the negative feature is split into two bands (bands 12 and 15), which are therefore assigned to the mixed Soret/$CT^{(4)}$ transitions. Correspondingly, the combined integral intensity of bands 12 and 15 should be roughly equivalent to the other Soret component, band 13. In this respect, please note that the UV-Vis and **C**-term intensity ratios of bands 14 and 15 are not well defined from the spectra. In any case, the fact that band 14 does not correspond to another Soret component is evident from its out-of-plane (z-) polarization, experimentally determined from the VTVH data of this band. The fit shown in Figure 3 places band 14 at 26181 cm^{-1}. This feature is assigned to the $CT^{(Cl,\pi,\sigma)}$ transition mixed with $CT^{(5)}$. This is in agreement with photoreduction experiments of Hendrickson et al. (see Discussion).[28]

To higher energy of the Soret transition, bands 16 and 17 are assigned to two components of the $\pi \rightarrow \pi^{*(2)}$ transition, which correspond to the excitation of an electron from B_{2u}<74> into the E_g <82/83> orbitals of the porphyrin. The corresponding excited state has E_u symmetry (in D_{4h}) and hence, generates a pseudo **A**-term in the lower symmetry environment of [Fe(TPP)(Cl)] (see Discussion). Correspondingly, bands 16 and 17 have opposite signs in MCD (cf. Figure 3), in agreement with this assignment. To lower energy of the Soret transition, a number of z-polarized bands are observed. Band 11 corresponds to the A_{2u}<81> $\rightarrow$ B_{1u}<84> transition, which is Laporte forbidden and hence, does not offer oscillator strength. The intensity of this band is actually due to 7 % $CT^{(Cl,\pi)}$ character (z-polarized) and 6 % $\pi \rightarrow \pi^{*(1)}$ admixture (x,y-polarized; cf. Table S2), which combined give rise to the mixed magnetization saturation behaviour (O_N) observed

experimentally for this feature. Three additional out-of-plane polarized bands are observed at 18336, 17700 and 16444 cm^{-1} (bands 6-8; cf. Table 2), respectively. Band 8 corresponds to the z-polarized B_{2u}<74> → d_{z^2} transition (90 % $CT^{(6)}$; cf. Table S2). Note that this feature is z-polarized, because the iron is located above the porphyrin plane towards the axial chloro ligand.[22] Band 6 is assigned to the mixed $CT^{(Cl,\pi)}$ transition, and band 7 to an excitation with mixed $CT^{(6)}$ and $CT^{(Cl,\sigma)}$ character, based on the energy sequence of these transitions in the TD-DFT calculations. Note that for both bands 6 and 7, the main contribution to the excited states comes from the forbidden E_g → d_π transition (cf. Table S2). $CT^{(5)}$, which shows z-polarization due to the out-of-plane displacement of the iron, is assigned to band 3 at 14512 cm^{-1} in agreement with the TD-DFT result. The nature of bands 1 and 2 at 11584 and 13542 cm^{-1} in MCD and in UV-Vis, respectively, is not entirely clear. Both bands are very weak, so no polarizations could have been determined experimentally. We believe that these two features correspond to the spin-forbidden $^6A_1$ → $^4T_1$ + $^4T_2$ ligand field transitions of hs Fe(III), which are usually observed in the 10000-15000 cm^{-1} region.

Finally, Q_v is observed at 19950 cm^{-1} (band 10) showing in-plane polarization in the MCD spectrum, and at 20150 cm^{-1} in UV-Vis. This feature should give rise to a pseudo-**A** in MCD, but no derivative band shape is observed in this case. This is most likely due to the fact that Q_v is really weak in the MCD spectrum of [Fe(TPP)(Cl)], and hence, the other component is likely hidden by excitations with larger **C**-term intensity at low-temperature. On the other hand, Q_v can be identified from the high-temperature data, where a corresponding **A**-term signal is observed at 20202 cm^{-1} (vide supra), indicating that this assignment is correct. This assignment is further supported by resonance Raman (rRaman) spectroscopy (cf. Discussion). The Q band is neither observed in MCD nor UV-Vis, and therefore, must be of very low intensity in [Fe(TPP)(Cl)]. Importantly, this is also observed for a number of other metalloporphyrins.[21] For example, four-coordinate low-spin [Co(TPP)] does not show the Q band either in MCD or in UV-Vis.[29] [Fe(TPP)(NO)] is another example for very weak Q and Q_v bands.[18] Transitions 4 and 5 at 15000 and 15600 cm^{-1}, respectively, are in-plane polarized and therefore, assigned to $CT^{(1)}$. Since this excited state has E_u symmetry in D_{4h}, corresponding to the A_{1u} → d_π excitation, it shows a pseudo **A**-term in the lower symmetry environment of [Fe(TPP)(Cl)] (see Discussion). Note that from the TD-DFT calculations, this band has also π → $\pi^{*(0)}$ character (cf. Figure S2). This assignment is further supported by rRaman spectroscopy (see Discussion). The related transition

$CT^{(2)}$, corresponding to the $A_{2u} \rightarrow d_\pi$ excitation, is predicted below 9000 cm^{-1}. We were not able to observe this transition within the energy range of our equipment (cut off: 9090 cm^{-1}).

Discussion.

In this study, the electronic spectra (MCD and UV-Vis) of five-coordinate [Fe(TPP)(Cl)] are analyzed in detail. As evident from Figure 3, and explicitely noticed in the preceding literature before, the electronic spectra of high-spin ferric hemes, especially [Fe(TPP)(Cl)], are very complicated, and hence, could not have been assigned before to analyse the electronic spectra a correlated fit of the absorption and low-temperature MCD data of [Fe(TPP)(Cl)] was performed first, which allows for the identification of at least 20 electronic transitions. Therefore, it is not surprising that an assignment of these data was not possible so far. Since iron has a high-spin d^5 configuration in [Fe(TPP)(Cl)], d-d transitions are in general spin forbidden. Hence, three different types of electronic transitions are in general expected for hs ferric porphyrins: porphyrin to metal charge-transfer (P → M CT) transitions, axial ligand to iron charge transfer transitions (here: Cl → M CT), and porphyrin $\pi \rightarrow \pi^*$ transitions (cf. Scheme 2). In order to obtain further insight into the nature of the different transitions, we measured VTVH **C**-term saturation curves, which allow for the determination of the polarizations of the MCD bands. In order to obtain reliable VTVH data for all bands, and to deal with overlapping features, the complete MCD spectrum has been measured at each temperature and field, and was then deconvoluted into individual transitions using Gaussian fitting. The VTVH saturation curves obtained this way were then simulated.[2] [Fe(TPP)(Cl)] shows axial zero field splitting (zfs) as evident from EPR (E/D = 0). The axial zfs parameter has been determined to 6.9 cm^{-1} from MCD spectroscopy.[11] Importantly, due to this strong axial zfs of the complex, a large magnetic anisotropy is obtained, and correspondingly, the magnetization saturation behavior of in-plane and out-of-plane polarized transitions is dramatically different. In fact, two different types of saturation behavior are found experimentally. The VTVH isotherms for in-plane polarized bands are nested as shown for the Soret band (band 12) in Figure 6. In contrast, for out-of-plane polarized bands, the isotherms are overlaying as shown for $CT^{(Cl,\pi)}$ (band 6) in Figure 7. With the polarizations of all the individual transitions thus known *experimentally*, TD-DFT calculations have been used to completely assign the spectra. An accurate theoretical description of [Fe(TPP)(Cl)] was obtained from TD-DFT calculations on the B3LYP/LanL2DZ* level. These calculations are not sufficient enough by themselves to assign the spectra, but they supply a number of important pieces to

solve the puzzle. The TD-DFT results provide a list of important transitions and their relative energies and intensities with good accuracy, and this way, define the "active space" of electronic transitions that are relevant. Finally, the occurrence of pseudo **A**-terms in the MCD **C**-term spectra is very useful to locate E_u excited states, split in the lower symmetry of [Fe(TPP)(Cl)] (vide infra).[30]

The complete assignments of the UV-Vis and MCD spectra of [Fe(TPP)(Cl)] are listed in Table 3. Based on these results, we are now able to explain a number of puzzling observations in the absorption spectra of [Fe(TPP)(Cl)], which have gained much interest and caused much confusion in the literature in the past.[2,13,11,21,28,31,32] This includes (a) the nature of the intense, broad band to higher energy of the Soret band, (b) the broad appearance of the Soret band, (c) the position of Q and Q_v, (d) the assignment of the ~640 nm feature, (e) the position of Cl → Fe CT transitions, and (f) the energy of porphyrin → d_π CT transitions.

As described by Gouterman,[21] the electronic absorption spectra of "normal" metalloporphyrins are quite simple and show the intense Soret, Q and Q_v bands. Note that Q_v is a vibronic band due to vibronic coupling of the Soret and Q states. As evident from Figure 3, top, a much more complicated situation is encountered for [Fe(TPP)(Cl)]. In the case of the Soret and Q transitions, we have derived theoretically that these features should give rise to a pseudo-**A** signal in the low-temperature MCD **C**-term spectrum.[18,30] This is due to the fact that the corresponding excited Soret and Q states have E_u symmetry, but the degeneracy is slightly lifted due to the lower symmetry of the metalloporphyrins.[33] Both resulting components of these E_u states then spin-orbit couple, leading to the appearance of the pseudo-**A** signal.[30] As shown in Figure 3, bottom, the MCD **C**-term spectrum of [Fe(TPP)(Cl)] does <u>*not*</u> show the predicted pseudo-**A** term for the Soret band. In contrast, four different features (bands 12-15) are observed in the Soret region by MCD. What is the assignment of these features? First, analysis of the VTVH saturation behavior of these bands shows that band 14 is z polarized, and hence, cannot correspond to a Soret component (vide infra). From the saturation behavior and the TD-DFT results, the remaining bands 12, 13 and 15 are in fact Soret components. But why are there three instead of the expected two features? This is due to the fact that in [Fe(TPP)(Cl)], the Soret band is mixed with the porphyrin A_{2u}<72> → E_g<82/83> ($\pi \rightarrow \pi^{*(1)}$) transition, which also gives rise to an E_u excited state. However, there is one important difference to the Soret state: whereas the Soret excited

state has both A_{1u}<79> → E_g<82/83> and A_{2u}<81> → E_g<82/83> contributions, there is no additional A_{1u} → E_g<82/83> transition present in the porphyrin that corresponds to $\pi \rightarrow \pi^{*(1)}$. Hence, $\pi \rightarrow \pi^{*(1)}$ mixes selectively with *one component* of the Soret band, in this case the negative MCD feature, which is split into two negative components giving rise to bands 12 and 15. The positive Soret component is unaffected, giving rise to band 13. This is in agreement with the TD-DFT results. Additional information that confirms these assignments is available from resonance Raman spectroscopy. In a recent publication by our group, the resonance Raman (rRaman) spectra of [Fe(TPP)(Cl)] have been investigated.[22] The rRaman spectrum of [Fe(TPP)(Cl)] excited at 454.5 nm shows mostly totally symmetric (A_{1g}) vibrations corresponding to Raman **A**-term enhancement,[34] and therefore, the absorption band at 417 nm has been assigned to the Soret band. This is in agreement with the assignments from MCD presented here.

Researchers have been speculating for a long time about the nature of the band at 379 nm. Our results show that one component (band 15) corresponds to the split Soret band, whereas band 14 is assigned to a chloride to iron CT. This is in agreement with work by Hendrickson et al.[28], who observed that irradiation into the near-ultraviolet band at ~379 nm in [Fe(TPP)(X)] (X = F^-, Cl^-, Br^-, I^- and N_3^-) leads to rapid photoreduction of the iron atom and dissociation of a halid radical and therefore, assigned this band as a halide ligand to Fe CT. As shown above, the MCD VTVH isotherms for band 14 at 25577 cm^{-1} indeed show z-polarization. This band is therefore assigned here to the $CT^{(Cl,\pi,\sigma)}$ transition mixed with $CT^{(5)}$ (cf. Table 2), in agreement with Hendrickson et al. This finding leads to another interesting question: do the Cl to Fe CT transitions give rise to other distinct features besides band 14? This question is easy to address by MCD, because these transitions are z polarized. Analysis of the data shows that there are additional bands (bands 6, 7 and 11; cf. Table 2) observed with $CT^{(Cl,\pi,\sigma)}$ character, evident from MCD and TD-DFT. Correspondingly, the absorption band at 578 nm has distinct chloro to Fe CT character.

As mentioned above, the Q and Q_v excited states also have E_u symmetry in D_{4h}, and correspondingly, these should also generate pseudo **A**-terms in the low-temperature MCD spectra. However, no such features are observed. Since Q and Q_v usually give rise to weak features in the MCD **C**-term spectra, this result is not surprising, considering the additional intense bands observed for [Fe(TPP)(Cl)] in this energy region. However, Q_v is readily identified

in the high-temperature MCD spectrum of [Fe(TPP)(Cl)], where Q_v gives rise to an **A**-term at 20202 cm^{-1}. A closer inspection of the **C**-term MCD spectrum then reveals one component of Q_v at 20150 cm^{-1} (band 10, cf. Table 2), showing the expected in-plane polarization. Due to the very low intensity of Q in [Fe(TPP)(Cl)], this band is neither observed in MCD nor UV-Vis. On the other hand, rRaman spectroscopy is a powerful tool to identify Q and Q_v in metalloporphyrins. Both Q and Q_v lead to Raman **B**-term enhancement related to vibronic coupling, which is manifested in the enhancement of anomalous polarized A_{2g} modes, as well as B_{1g} and B_{2g} vibrations.[22,31,32] The rRaman spectrum of [Fe(TPP)(Cl)] excited at 568.2 nm shows weak, and the data obtained at 514.5 nm show medium intense anomalous polarized bands indicating vibronic coupling.[22] In addition, overtones are enhanced upon excitation into the absorption band at 510 nm, which indicates that this band actually corresponds to Q_v. This latter assignment is in very good agreement with the high-temperature MCD data, which reveal Q_v at 20202 cm^{-1}. Based on these results, Q must be located in the 18000-19000 cm^{-1} range from the rRaman results. However, this would lead to an energy separation of Q and Q_v of about 2350 cm^{-1}, which is too large. It should only be about 1250 cm^{-1} as determined by Gouterman.[21] Hence, the Q band is very weak in [Fe(TPP)(Cl)] both in absorption and MCD, and not observed spectroscopically. This feature is likely masked by the intense band at 578 nm (band 7; cf. Figure 3), which, however, is z polarized and therefore, cannot correspond to Q (vide infra).

Another interesting feature in the electronic spectra of [Fe(TPP)(Cl)] is the low-energy band at 654 nm, which is quite intense in absorption. The nature of this band has led to much discussion in the literature in the past.[13,21,31,32] In earlier work, we found that rRaman excitation at 647.1 nm not only shows the usually observed porphyrin A_{2g} modes at 1335 and 1522 cm^{-1} indicative of vibronic coupling, but also low-energy anomalous polarized bands that are not observed at any other excitation wavelength. *These low-energy bands correspond to in-plane and out-of-plane porphyrin deformation modes* with some phenyl out-of-plane mode contribution. Hence, the absorption band at 654 nm (15291 cm^{-1}) shows a completely different excitation behavior as usually observed for Q and Q_v band enhancements. Based on this, we concluded that this absorption band should correspond to a P → Fe CT transition.[22] This result is now confirmed by MCD spectroscopy, which allows to assign the corresponding bands 4 and 5 (cf. Figure 3) to the A_{1u} <79> → d_π transition ($CT^{(1)}$). Since this excitation leads to an excited state with E_u symmetry, a pseudo-**A** signal is observed for bands 4 and 5 in agreement with this assignment. We believe

that the enhancement of out-of-plane deformation modes of A_{2g} symmetry relates to the fact that $CT^{(1)}$ corresponds to a one electron transition from the A_{1u}<79> HOMO of the porphyrin into the d_π orbitals of iron. This generates a porphyrin π-cation radical electronic structure in the excited state. In fact, crystallographic data for the π-cation radical complex [Zn(TPP)(ClO_4)] show a strongly ruffled porphyrin core with large out of plane distortions.[35] Hence, the observed enhancement of porphyrin deformation modes is indicative of large structural changes of the porphyrin core following the $CT^{(1)}$ excitation (vibronic coupling to the geometry-relaxed state?). Taken together, these results therefore allow us to unambiguously assign the 654 nm absorption band of [Fe(TPP)(Cl)] to porphyrin to iron CT transitions. One component, bands 4 and 5, correspond to the $A_{1u} \rightarrow d_\pi$ transition, the exact location of which has therefore finally been classified. A second component, band 3, is z-polarized and of $A_{2u} \rightarrow d_{z^2}$ type.

Based on the detailed analysis of the MCD data of [Fe(TPP)(Cl)] presented here, we were therefore able to address all open questions about the electronic spectra of this complex. As mentioned in the Introduction, the only other effort to assign parts of the MCD spectra of [Fe(TPP)(Cl)] was performed by Kobayashi and coworker.[13] In this study, the lowest excited sextet state energies of [Fe(TPP)(Cl)] were calculated from empirical molecular parameters. These molecular parameters were mostly derived from spectral data of related metalloporphyrins with simple spectra, for example [Co(TPP)(Cl)] in pyridine. The electronic spectra of [Fe(TPP)(Cl)] were then explained based on the configuration interactions of the porphyrin excited triplet and singlet states ($\pi \rightarrow \pi^*$) and $CT^{(1,2)}$. First, the strong contribution of triplet states in the chosen model, which means that they are a main contributor to the complicated electronic spectra of [Fe(TPP)(Cl)], is very doubtful. No corresponding transitions are observed for [Co(TPP)] and other simple metalloporphyrins. Second, the transitions generated this way are all xy polarized, whereas the experimental data show many z-polarized bands in the low energy region, which this model cannot account for. Finally, the number of transitions involved is much too small, in particular, no chloro to Fe CT has been considered. This interpretation is therefore very unsatisfactorily, whereas the assignments presented here are in agreement with all available experimental data.

Interestingly, the observed MCD saturation intensity for hs [Fe(TPP)(Cl)] is one order of magnitude smaller compared to ls ferric heme. Table 3 summarizes the peak to trough saturation

limits for a number of ferric hemes in different spin-states. For example, horse heart cytochrome c shows 40.5 * 10^3 M^{-1} cm^{-1} (ls → S = 1/2),[27] whereas [Fe(TPP)(Cl)] shows only 3.4 * 10^3 M^{-1} cm^{-1}. This is due to dramatic differences in the SOC of the ground state with low-lying excited states. Scheme 3 shows the two different mechanisms for **C**-term intensity, based on SOC between two excited states, or the ground state and a low lying excited state. Whereas mechanism 1 is valid for all iron(III) porphyrins, the ls state also has contributions from mechanism 2 because of the low lying t_2 excited states that do not exist in the hs state. For ls ferric hemes with the normal ground state as indicated in Scheme 3, very strong SOC exists between the ground state and the first excited state corresponding to the SOC matrix element $\left\langle d_{xz} \middle| l_z \middle| d_{yz} \right\rangle$. This leads to a dramatic increase in MCD intensity compared to the hs state. The fact that mechanism 2 is in fact responsible for this increase in MCD intensity of xy polarized transitions is evident from MCD data of ls ferric heme with the alternative "d_{xy}" ground state ($[d_{xz},d_{yz}]^4$ $[d_{xy}]^1$). In this case, no SOC effective in z direction is present, and hence, mechanism 2 cannot contribute. Correspondingly, the MCD spectra obtained by Cheesman et al. for a complex with "d_{xy}" ground state show a dramatic decrease in total MCD intensity compared to "normal" ls ferric heme.[36] The differences in SOC are also reflected by the fact that ls-Fe(III) shows large g shifts, whereas hs Fe(III) has practically no shifts at all.[37]

Conclusions. Altogether, reliable assignments of the electronic spectra of [Fe(TPP)(Cl)] have been obtained in this work, based on MCD data and their detailed analysis correlated to TD-DFT calculations. These assignments are confirmed by other methods, especially rRaman. Based on these data, an accurate theoretical description of the ground and excited states of [Fe(TPP)(Cl)] has been obtained for the first time. This study nicely demonstrates the impact of low-temperature MCD spectroscopy for the analysis and assignment of electronic spectra of paramagnetic transition metal complexes. In future studies, we will apply this methodology to hs ferric hemes in proteins, especially P450 type enzymes.

Acknowledgment. Financial support of this work was provided by the Deutsche Forschungsgemeinschaft (DFG; Grant LE 1393/1-2) which is gratefully acknowledged. F. P. acknowledges the Fonds der Chemischen Industrie (FCI) for a Chemiefonds fellowship.

Supporting Information Available: Tables of the calculated (TD-DFT, INDO/S-CI) energies for the Soret and Q bands of [Zn(P)] and [Zn(TPP)], assignments of the calculated spectra (TD-DFT) for [Fe(TPP)(Cl)], and Coordinates and Figures of the fully optimized structure of [Fe(TPP)(Cl)]. This material is available free of charge via the internet at http://pubs.acs.org.

Scheme 1.

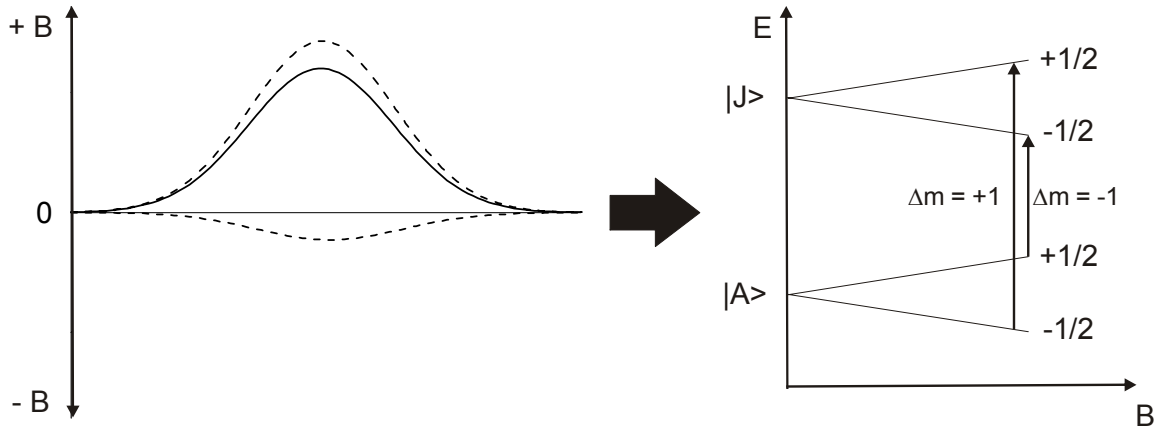

Scheme 2.

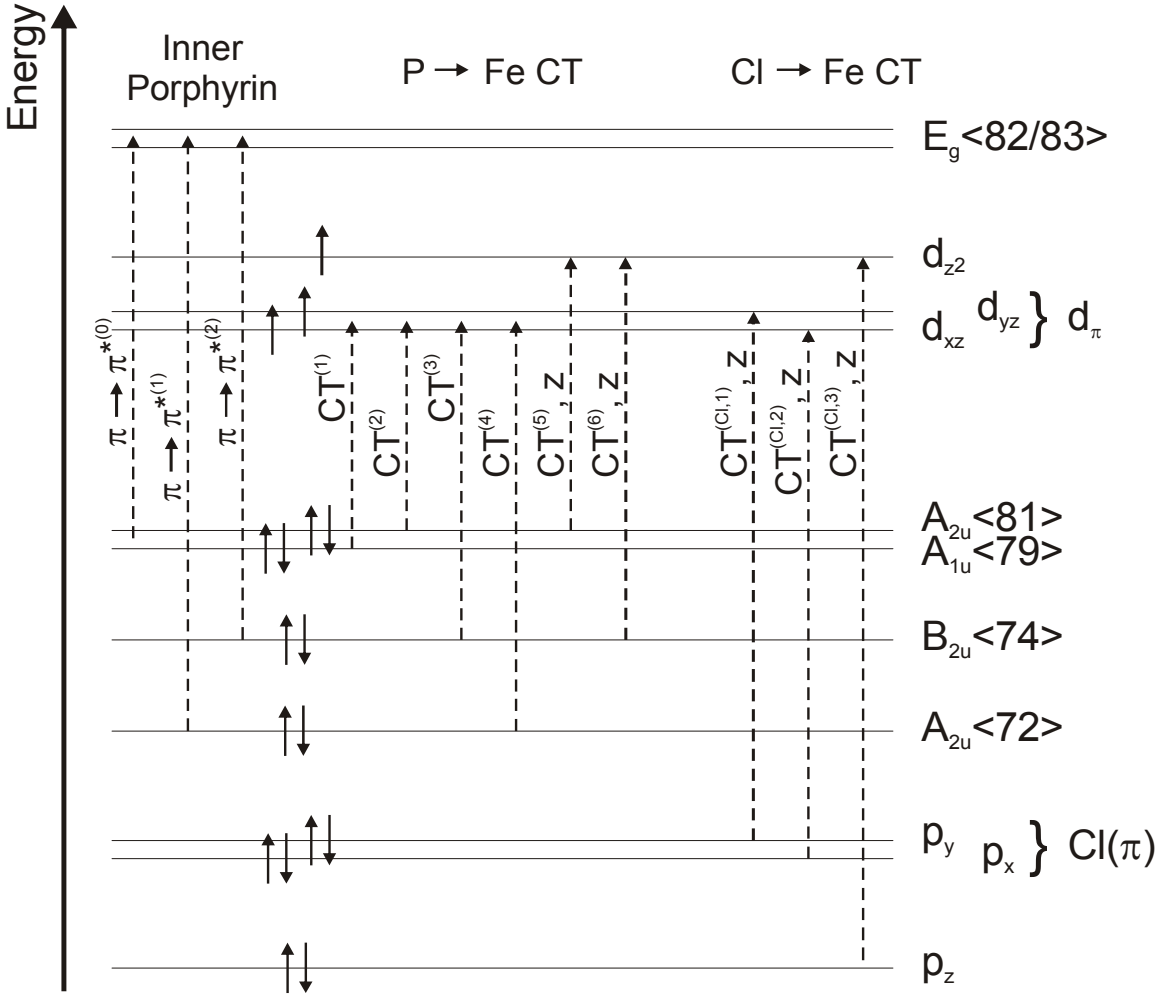

Scheme 3.

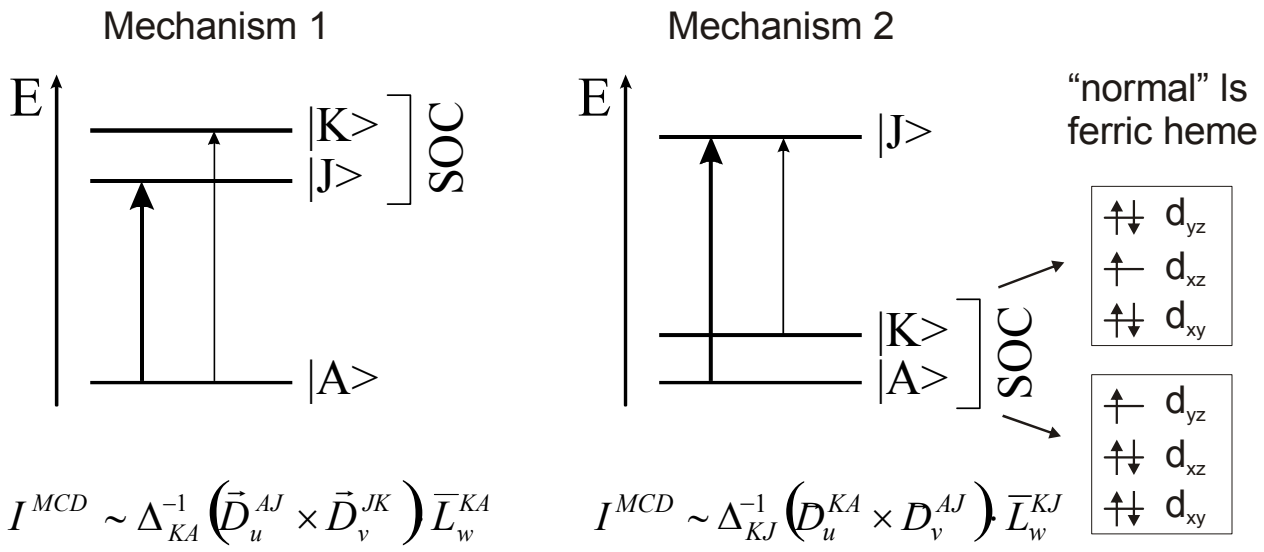
Mechanism 1
E
|K>
|J>
SOC
|A>
$I^{MCD} \sim \Delta_{KA}^{-1}\left(\vec{D}_u^{AJ} \times \vec{D}_v^{JK}\right)\overline{L}_w^{KA}$
Mechanism 2
E
|J>
|K>
|A>
SOC
"normal" ls
ferric heme
d_{yz}
d_{xz}
d_{xy}
d_{yz}
d_{xz}
d_{xy}
$I^{MCD} \sim \Delta_{KJ}^{-1}\left(\vec{D}_u^{KA} \times \vec{D}_v^{AJ}\right)\overline{L}_w^{KJ}$

Table 1. Charge contributions to the β spin molecular orbitals of [Fe(TPP)(Cl)] calculated with B3LYP/LanL2DZ* (d(Fe-Cl) is taken from the crystal structure; ref[19]).

No.	Label [a]	Energy	Fe	Cl	Porphyrin
		[Hartree]	d	p	
β<177>	B_{1u}<84>	-0.03459	0	0	100
β<176>	d_{x2-y2} _ B_{1g}<80>	-0.06626	53	0	47
β<175>	E_g<82/83> _ d_{xz} _ p_x	-0.08372	17	1	82
β<174>	E_g<82/83> _ d_{yz} _ p_y	-0.08563	18	1	81
β<173>	d_{z2} _ p_z _ A_{2u}<81>	-0.10595	57	14	27
β<172>	d_{yz} _ p_y _ E_g<82/83>	-0.11024	57	6	35
β<171>	d_{xz} _ p_x _ E_g<82/83>	-0.11373	59	8	32
β<170> LUMO	d_{xy}	-0.11496	93	0	6
β<169> HOMO	A_{2u}<81> _ d_{z2} _ p_z	-0.19876	9	2	87
β<168>	A_{1u}<79>	-0.20181	0	0	100
β<167>	B_{2u}<74>	-0.24501	0	0	100
β<166>	E_g<75/76> _ p_x	-0.24520	0	14	85
β<165>	E_g<75/76> _ p_y	-0.24535	0	12	86
β<157-164>	Ph(π)	-0.25168 to -0.26025			
β<156>	A_{2u}<72> _ d_{z2}	-0.26481	4	0	94
β<155>	E_g<75/76> _ p_y _ d_{yz}	-0.28322	2	10	84
β<154>	E_g<75/76> _ p_x _ d_{xz}	-0.28349	3	14	82
β<153>	p_y _ d_{yz}	-0.28512	8	48	40
β<152>	p_x _ d_{xz}	-0.28606	8	43	46
β<151>	B_{1u}<69>	-0.31854	0	0	100
β<150>	E_u _ d_{yz}	-0.32385	3	0	97
β<149>	E_u _ d_{xz}	-0.32412	2	0	98
β<148>	p_z _d_{z2}	-0.32644	24	60	12

[a] p_x, p_y and p_z are the chloride 3P orbitals. The labels of the porphyrin orbitals, for example A_{2u}<81>, refers to Figure S1.

Table 2. Correlated Fit of the UV-Vis absorption and MCD spectra of [Fe(TPP)(Cl)]

No.	MCD		UV-Vis		Calcd. [c]	Assignment	Polarization from MCD [d]
	position	Δε [a]	Position	ε [b]			
1	11584	13	11584	680	12329 (5)	$^6A_1 \rightarrow {}^4T_1$	
2	13542	7	13542	312	12910 (6)	$^6A_1 \rightarrow {}^4T_2$	
3	14512	49	14450	3156	11945 (3)	$CT^{(5)}$	z
4	15000	24	15100	1696	12329 (5)	$CT^{(1)}$ $\pi \rightarrow \pi^{*(0)}$	x,y
5	15600	-13	15570	1563	12910 (6)	$CT^{(1)}$ $\pi \rightarrow \pi^{*(0)}$	x,y
6	16444	-28	16450	1859	20740 (11)	$CT^{(Cl,\pi)}$	z
7	17700	-38	17500	3084	22455 (15)	$CT^{(6)}$ $CT^{(Cl,\sigma)}$	z
8	18336	-18	18440	2253	22605 (16)	$CT^{(6)}$	z
9	(19129)	-9	19250	9163		B-Term signal	
10	20150	-22	19950	8782		Q_v	x,y
11	22232	-101	22400	16099	25203 (21)	$\pi \rightarrow \pi^{*(1)}$ $CT^{(Cl,\pi)}$	x,y and z
12	23266	-226	23266	37833	26071 (25)	$\pi \rightarrow \pi^{*(2)}$ $\pi \rightarrow \pi^{*(0)}$ **Soret** $CT^{(4)}$	x,y
13	24269	479	24270	95604	26143 (27)	$\pi \rightarrow \pi^{*(0)}$ **Soret** $\pi \rightarrow \pi^{*(2)}$	x,y
14	26181	214	26181	21665	25008 (19)	$CT^{(Cl,\pi,\sigma)}$ $CT^{(5)}$	Z
15	26472	-162	26472	35635	26109 (26)	$\pi \rightarrow \pi^{*(0)}$ **Soret** $\pi \rightarrow \pi^{*(2)}$ $CT^{(4)}$	x,y
16	28098	-48	28150	42029	27164 (28)	$\pi \rightarrow \pi^{*(2)}$	
17	29819	5	29819	13963	27250 (29)	$\pi \rightarrow \pi^{*(2)}$	
18	30704	18	30705	18511			
19	32402	-3	32402	19582			
20	33365	-22	33365	8148			

[a] Δε is given in [M^{-1} cm^{-1} T^{-1}], measured at 5.8 K for bands 11-20 and 5.6 K for bands 1-10. [b] ε is given in [M^{-1} cm^{-1}], measured at room temperature in $CHCl_3$. [c] Calculated with B3LYP/LanL2DZ* (vide supra) using the full TPP ligand without any simplifications (d(Fe-Cl) taken from the crystal structure; ref[19]). Numbers in parentheses correspond to the numbering of

the excited states in Table S2 from TD-DFT. [d] Polarizations were determined from fitting the experimental VTVH data (Examples are shown in Figures 6-8).

Table 3. Peak to trough saturation limits for [Fe(TPP)(Cl)] compared with limits observed in different enzymes

Compound	Spin-State	Peak to trough saturation limit [a]	Ref.
[Fe(TPP)(Cl)	5/2	$3.4 * 10^3$	This work
Horse heart cytochrome c	1/2	$40.5 * 10^3$	Ref[27]
Metmyoglobin CN^-	1/2	$60.5 * 10^3$	Ref[27]
Cytochrome c oxidase	1/2	$25 * 10^3$	Ref[38]
Cytochrome c oxidase CN^-	1/2	$54 * 10^3$	Ref[38]
Ferric horseradish peroxidase (HRP) compound I	3/2	$1.9 * 10^3$	Ref[39]

[a] Peak to trough saturation limits are given in $M^{-1} cm^{-1}$.

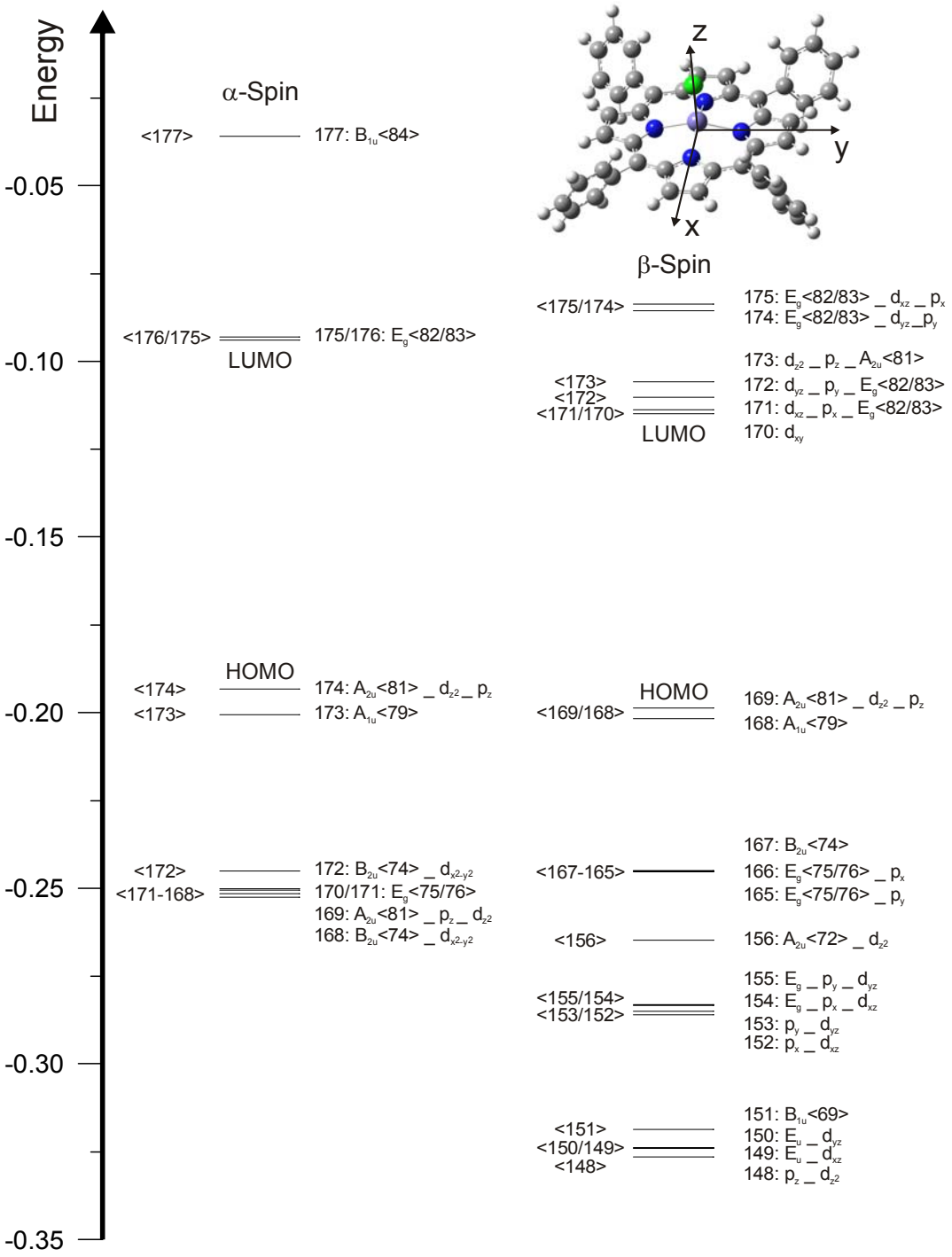

Figure 1. Molecular orbital diagram of [Fe(TPP)(Cl)] calculated with B3LYP/LanL2DZ* (d(Fe-Cl) is taken from the crystal structure; ref[19]). Note that p_x, p_y and p_z are chloride 3P orbitals. The labels of the porphyrin orbitals, i.e. A_{2u}<81>, refer to Figure S1. Molecular orbital labels *a* _ *b* indicate that orbital *a* interacts with *b*, and that *a* has a larger contribution to the resulting MO.

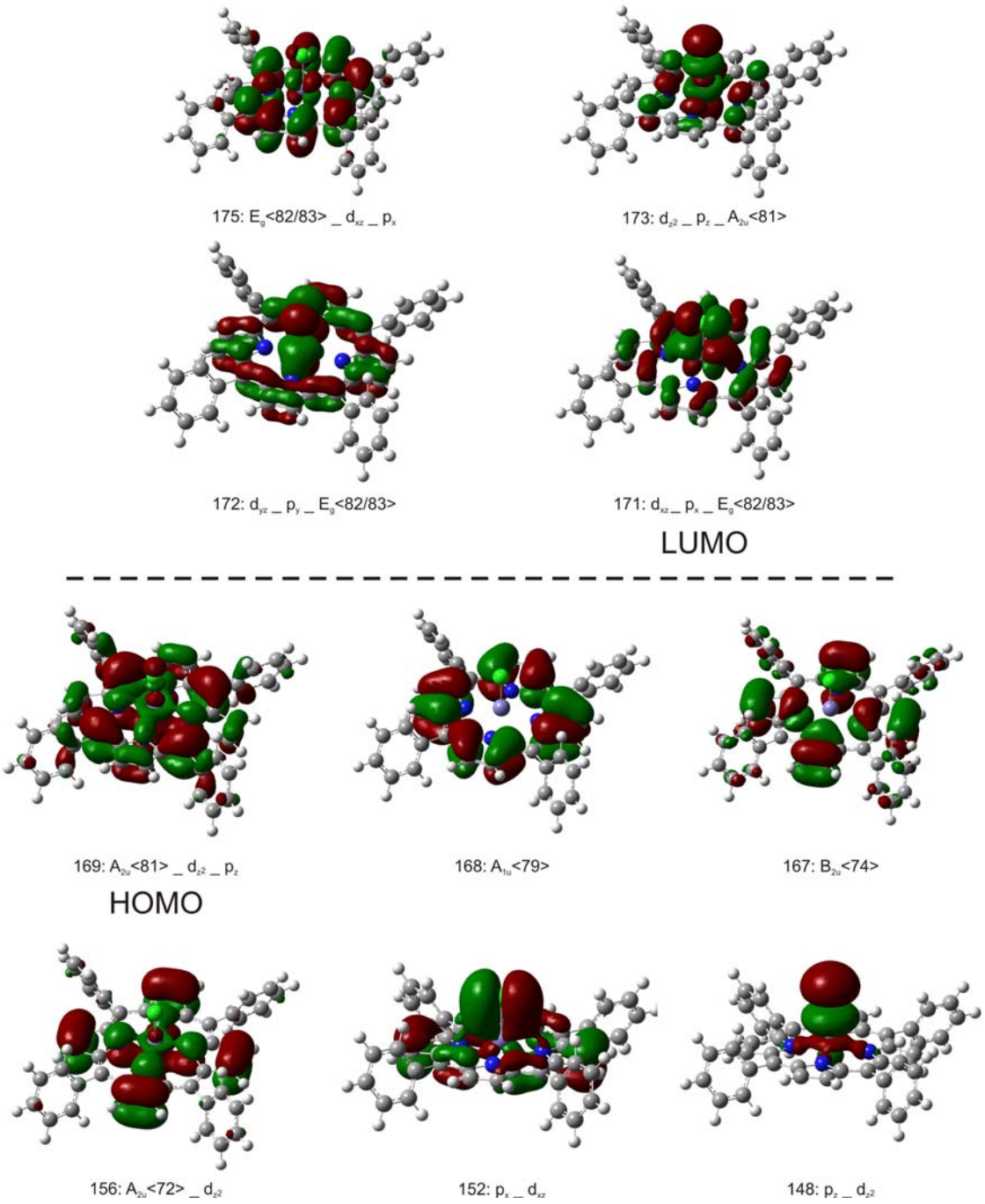

Figure 2. Contour Plots of important molecular orbitals of [Fe(TPP)(Cl)] (B3LYP/LanL2DZ*, d(Fe-Cl) is taken from the crystal structure; ref[19]). For the labels see Figure 1.

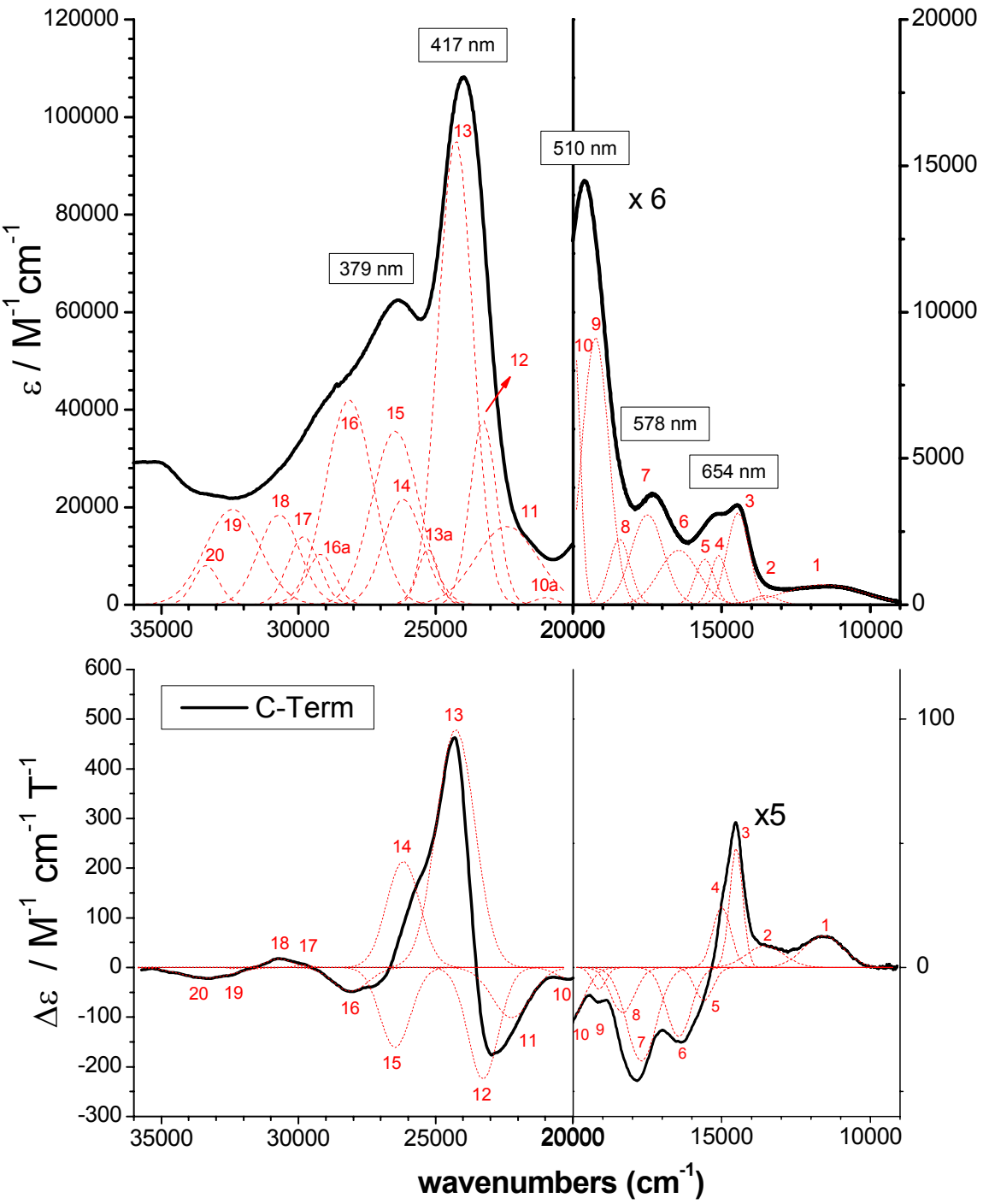

Figure 3. Electronic Spectra of [Fe(TPP)(Cl)]. Top: UV-Vis absorption spectrum measured in $CHCl_3$ at room temperature. Bottom: MCD C-term spectrum measured in polystyrene at 5.8 K (lower concentration for 36000 – 21000 cm^{-1} region) and 5.6 K (higher concentration for 21000 – 9000 cm^{-1}), respectively. The dashed red lines represent a correlated gaussian fit of these data (cf. Table 2).

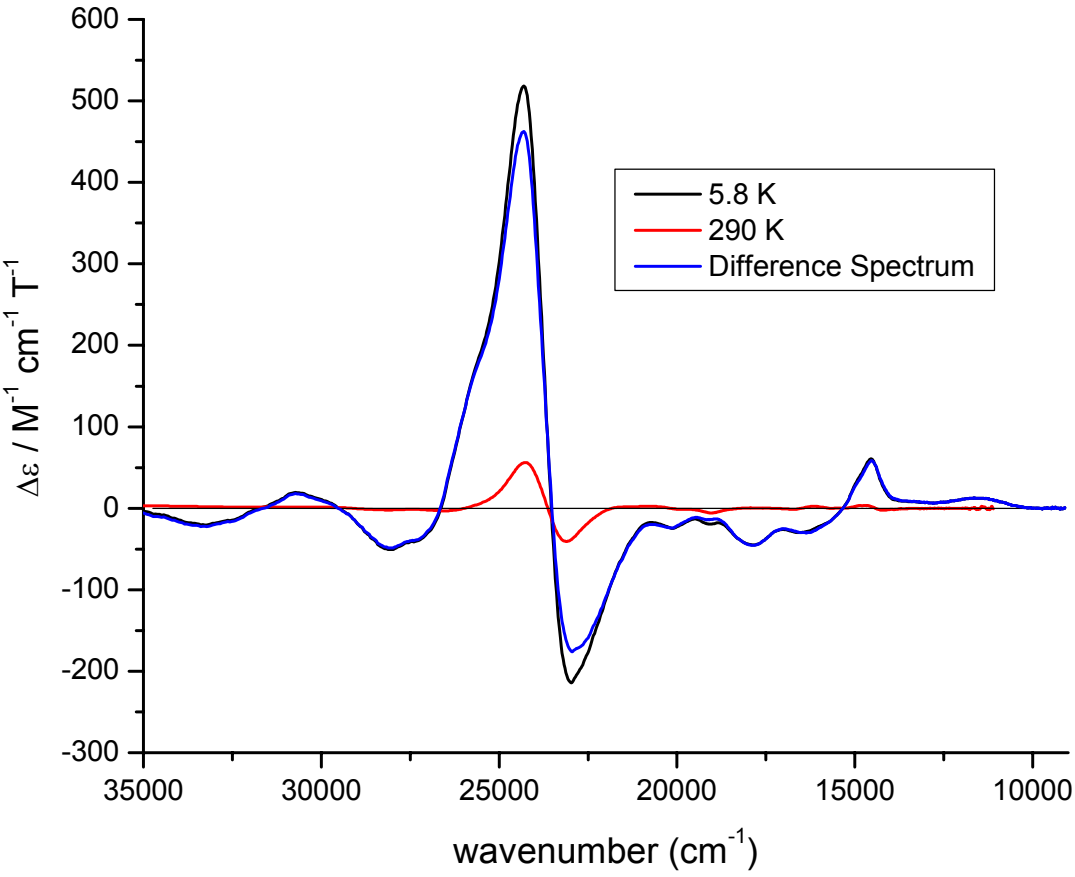

Figure 4. MCD spectrum of [Fe(TPP)(Cl)]: The black line represents the MCD spectrum measured at 5.8 K, and the red line shows the spectrum measured at 290 K. The **C**-term spectrum in blue results from subtraction of the 290 K from the low-temperature data.

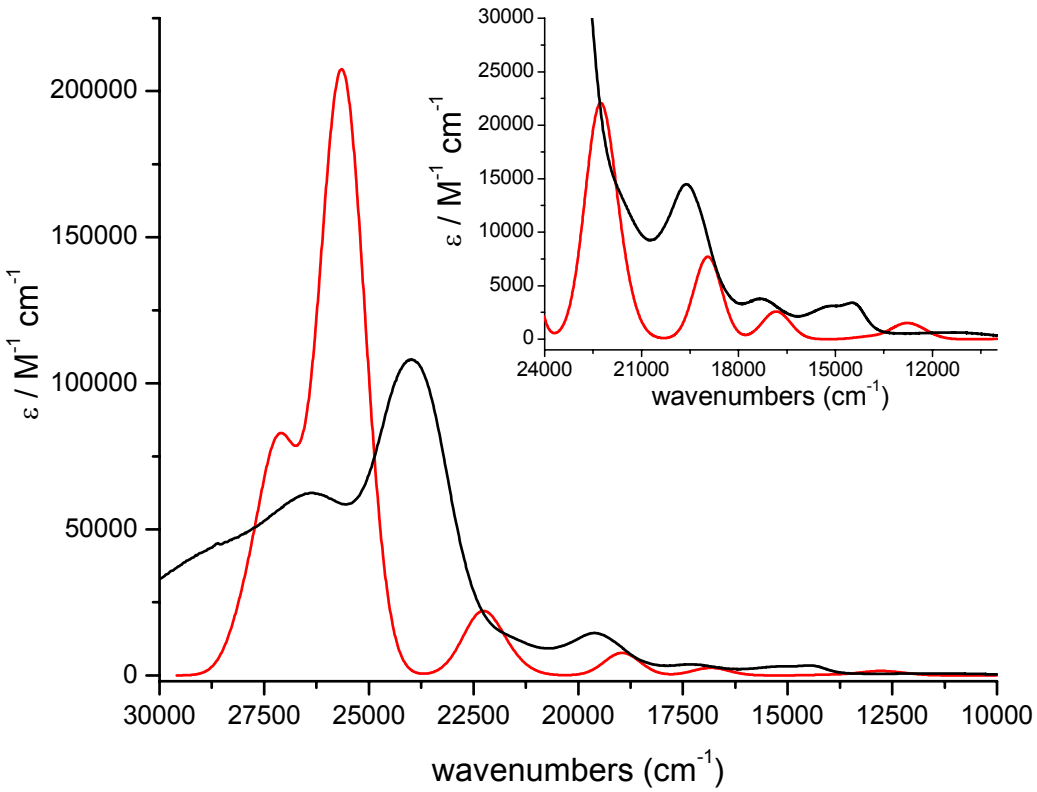

Figure 5. UV-Vis absorption spectrum of [Fe(TPP)(Cl)] measured in $CHCl_3$ at room temperature shown in black, and the calculated (B3LYP/LanL2DZ*) spectrum is shown in red. The calculated spectrum was obtained using the SWizard program.[40] The bandwidths at half height were set to 2000 cm^{-1} for the plot.

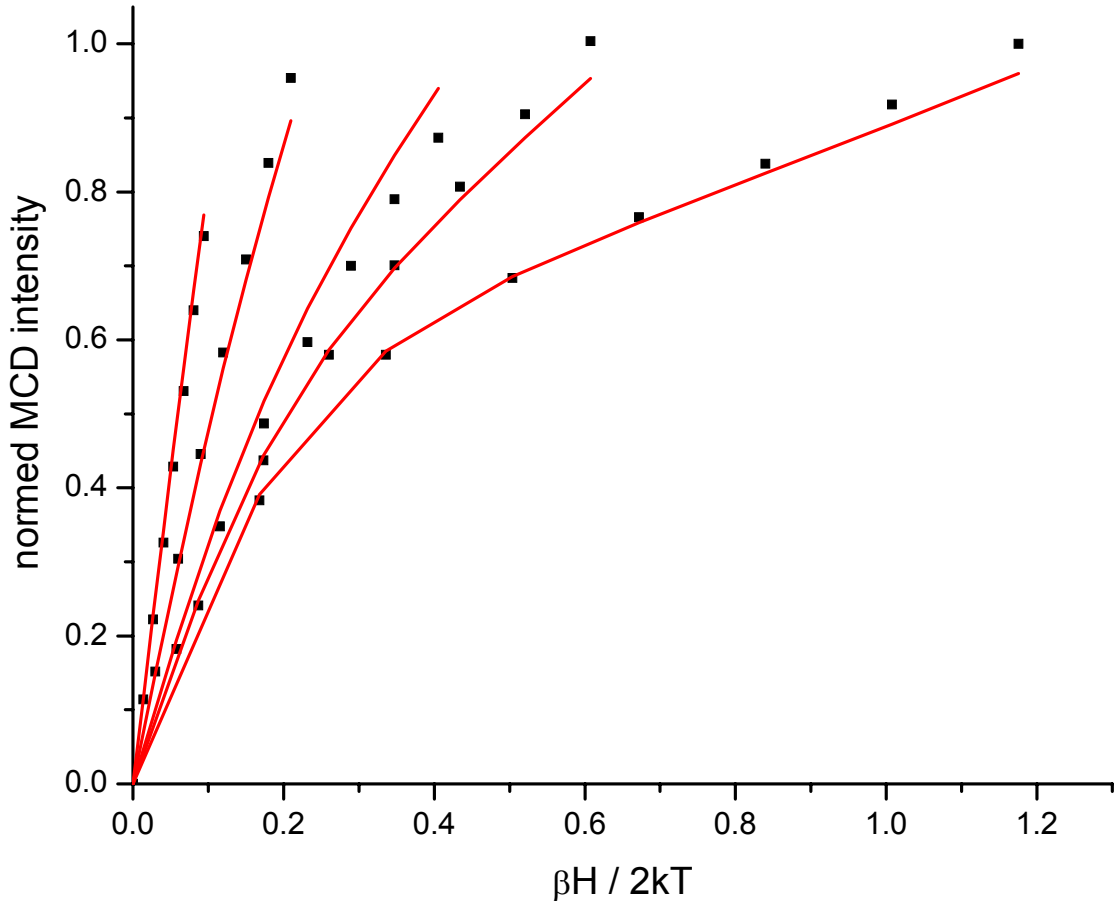

Figure 6. MCD saturation magnetization curves (VTVH) for band 12 (Soret) at 23266 cm^{-1} (red lines: fit; black dots: experimental data points) showing x,y-polarization.

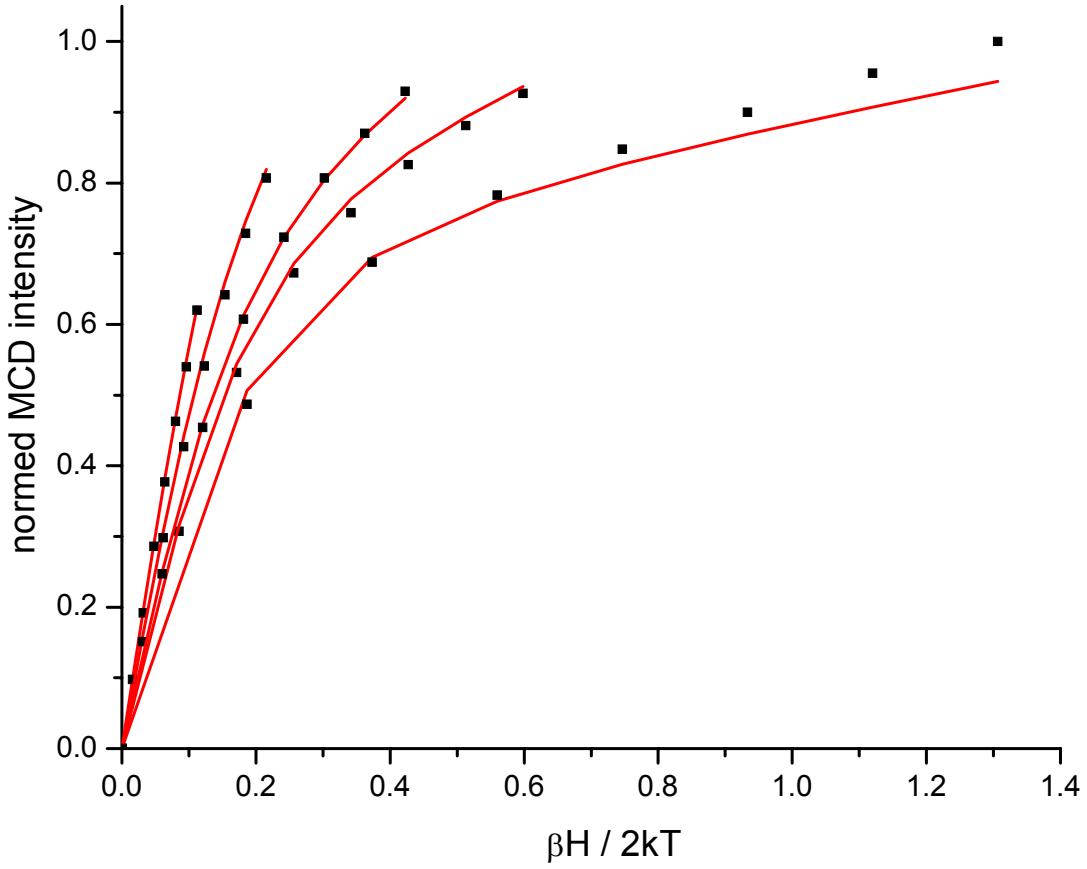

Figure 7. MCD saturation magnetization curves (VTVH) for band 4 ($CT^{(1)}$) at 15015 cm^{-1} (red lines: fit; black dots: experimental data points) showing x,y-polarization with about 2 % z-polarization.

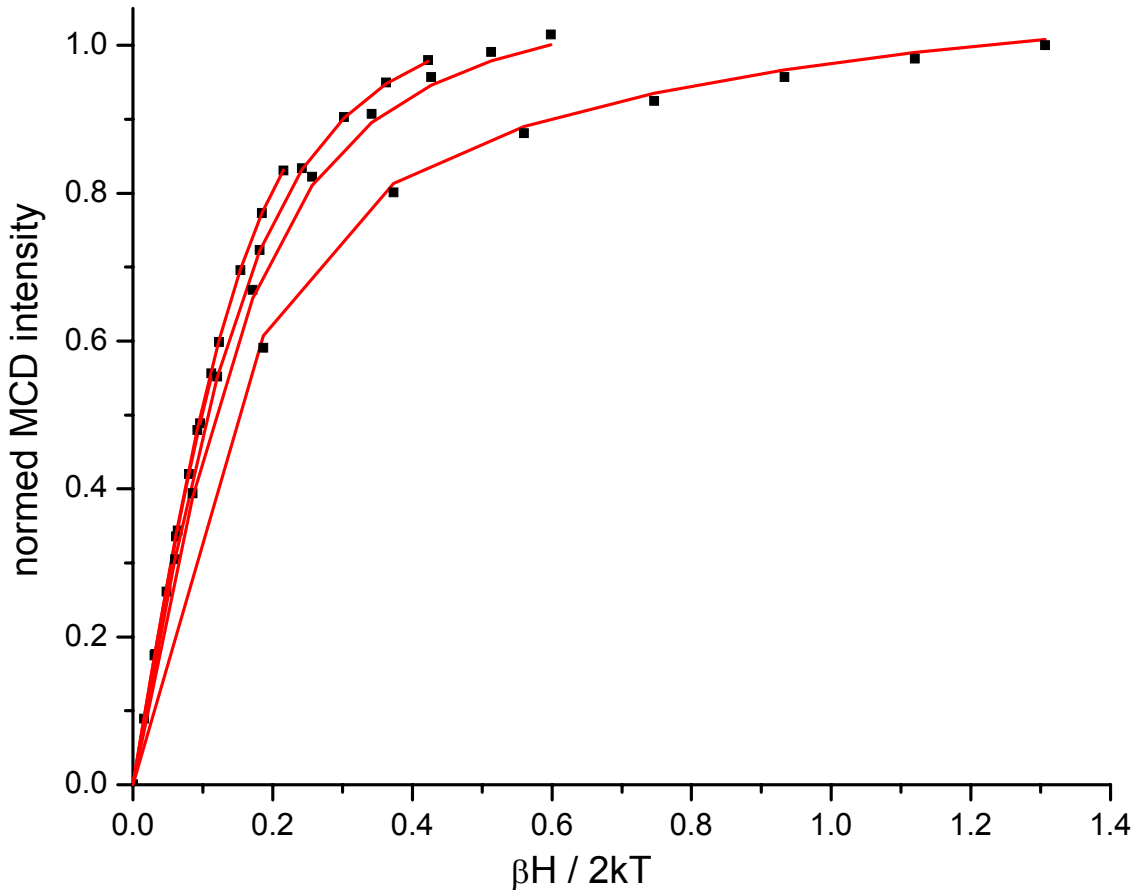

Figure 8. MCD saturation magnetization curves (VTVH) for band 6 ($CT^{(Cl,1,2)}$) at 16444 cm^{-1} (red lines: fit; black dots: experimental data points) showing 77% z-polarization with about 23 % x,y-polarization.

[1] (a) Stephens, P. J. Ann. Rev. Phys. Chem. **1974**, 25, 201-232. (b) Stephens, P. J. Adv. Chem. Phys. **1975**, 35, 197-264. (c) Cheesman, M. R.; Greenwood, C.; Thomson, A. J. *Adv. Inorg. Chem.* **1991**, *36*, 201-255. (d) Solomon, E. I.; Pavel, E. G.; Loeb, K. E.; Campochiaro, C. *Coord. Chem. Rev.* **1995**, *144*, 369-460. (e) Oganesyan, V. S.; George, S. J.; Cheesman, M. R.; Thomson, A. J. J. Chem. Phys. **1999**, 110, 762-777. (f) Cheek, J.; Dawson, J. H. In *Handbook of Porphyrins and Related Macrocycles*, Vol. 7, edited by K. Kadish, K. Smith, R. Guilard, 339-369. New York: Academic Press, 2000. (g) Lehnert, N.; DeBeer George, S.; Solomon, E. I. *Curr. Op. Chem. Biol.* **2001**, *5*, 176-187.
[2] Neese, F.; Solomon, E. I. *Inorg. Chem.* **1999**, *38*, 1847-1865.
[3] (a) Thomson, A. J.; Brittain, T.; Greenwood, C.; Springall, J. *FEBS Lett.* **1976**, *67*, 94-98. (b) Thomson, A. J., Brittain, T.; Greenwood, C.; Springall, J. P. *Biochem. J.* **1977**, *165*, 327-336. (c) Thomson, A. J.; Johnson, M. K.; Greenwood, C.; Gooding, P. E. *Biochem. J.* **1981**, *193*, 687-697. (d) Roach, M. P.; Pond, A. E.; Thomas, M. R.; Boxer, S. G.; Dawson, J. H. *J. Am. Chem. Soc.* **1999**, *121*, 12088-12093. (e) Maranon, M. J., R.; Mercier, D.; van Huystee, R. B.; Stillman, M. J. *Biochem. J.* **1994**, *301*, 335.
[4] *Advances in Inorganic Biochemistry*, Vol. 7: Heme Proteins. Eichhorn, Gunther L.; Marzilli, Luigi G.; Editors. New York: Elsevier. (1988).
[5] Dawson, J. H.; Sono, M. *Chem. Rev.* **1987**, *87*, 1255-1276.
[6] (a) Stuehr, D. J. *Annu. Rev. Pharmacol. Toxicol.* **1997**, *37*, 339-359. (b) Li, H.; Poulos, T. L. *J. Inorg. Biochem.* **2005**, *99*, 293-305.
[7] Andersson, L. A.; Johnson, A. K.; Simms, M. D.; Willingham, T. R. *FEBS Lett.* **1995**, *370*, 97-100.
[8] Walker, F. A. in *Encyclopedia of Inorganic Chemistry*; King, R. B., Ed.; John Wiley & Sons, 1994, Volume 4, pp. 1785-1846.
[9] (a) Stephens, P. J. *J. Chem. Phys.* **1970**, *52*, 3489-3516. (b) Piepho, S. B.; Schatz, P. N. *Group Theory in Spectroscopy with Applications to Magnetic Circular Dichroism;* John Wiley & Sons: New York, Chichester, Brisbane, Toronto, Singapore, 1983.
[10] Mack, J. Stillman, M.J., Kobayashi, N. *Coord. Chem. Rev.* **2007**, 25, 1429-453.
[11] Browett, W. R.; Fucaloro, A. F.; Morgan, T. V.; Stephens, P. J. *J. Am. Chem. Soc.* **1983**, *105*, 1868-1872.
[12] Neese, F.; Solomon, E. I. *J. Am. Chem. Soc.* **1998**, *120*, 12829-12848.
[13] (a) Kobayashi, H. *Adv. Biophys.* **1975**, *8*, 191-222. (b) Kobayashi, H.; Higuchi, T.; Eguchi, K. *Bull. Chem. Soc. Jpn.* **1976**, *49*, 457-463. (c) Kobayashi, H.; Yanagawa, Y.; Osada, H.; Minami, S.; Shimizu, M. *Bull. Chem. Soc. Jpn.* **1973**, *46*, 1471-1479.
[14] Adler, A. D.; Longo, F. R.; Kampas, F.; Kim J. *J. Inorg. Nucl. Chem.* **1970**, *Vol. 32*, 2443-2445.
[15] Browett, W. R.; Fucaloro, A. F.; Morgan, T. V.; Stephens, P. J. *J. Am. Chem. Soc.* **1983**, *105*, 1868-1872.
[16] (a) Becke, A. D. *Phys. Rev. A* **1988**, *38*, 3098. (b) Becke, A. D. *J. Chem. Phys.* **1993**, *98*, 1372. (c) Becke, A. D. *J. Chem. Phys.* **1993**, *98*, 5648.
[17] Frisch, M. J.; Trucks, G. W.; Schlegel, H. B.; Scuseria, G. E.; Robb, M. A.; Cheeseman, J. R.; Montgomery, J. A.; Vreven, Jr., T.; Kudin, K. N.; Burant, J. C.; Millam, J. M.; Iyengar, S. S.; Tomasi, J.; Barone, V.; Mennucci, B.; Cossi, M.; Scalmani, G.; Rega, N.; Petersson, G. A.; Nakatsuji, H.; Hada, M.; Ehara, M.; Toyota, K.; Fukuda, R.; Hasegawa, J.; Ishida, M.; Nakajima, T.; Honda, Y.; Kitao, O.; Nakai, H.; Klene, M.; Li, X.; Knox, J. E.; Hratchian, H. P.; Cross, J. B.; Adamo, C.; Jaramillo, J.; Gomperts, R.; Stratmann, R. E.; Yazyev, O.; Austin, A. J.; Cammi, R.; Pomelli, C.; Ochterski, J. W.; Ayala, P. Y.; Morokuma, K.; Voth, G. A.; Salvador, P.; Dannenberg, J. J.; Zakrzewski, V. G.; Dapprich, S.; Daniels, A. D.; Strain, M. C.; Farkas, O.; Malick, D. K.; Rabuck, A. D.; Raghavachari, K.; Foresman, J. B.; Ortiz, J. V.; Cui, Q.; Baboul, A. G.; Clifford, S.; Cioslowski, J.; Stefanov, B. B.; Liu, G.; Liashenko, A.; Piskorz, P.; Komaromi, I.; Martin, R. L.; Fox, D. J.; Keith, T.; Al-Laham, M. A.; Peng, C. Y.; Nanayakkara, A.; Challacombe, M.; Gill, P. M. W.; Johnson, B.; Chen, W.; Wong, M. W.; Gonzalez, C.; Pople, J. A. Gaussian, Inc., Pittsburgh PA, 2003.
[18] Praneeth, V. K. K.; Näther, C.; Peters, G.; Lehnert, N. *Inorg. Chem.* **2005**, *45*, 2795-2811.
[19] Hoard, J. L.; Cohen, G. H.; Glick, M. D. *J. Am. Chem. Soc.* **1967**, *89*, 1992-1996.
[20] Neese, F. *ORCA*, version 2.2; Max-Planck Institut fuer Bioanorganische Chemie, Muelheim/Ruhr, Germany, 2004.
[21] Gouterman, M. in *The Porphyrins*; Dolphin, D., Ed.; Academic: New York, 1979, Vol. III, Part A, pp 1-156.
[22] Paulat, F.; Praneeth, V. K. K., Naether, C.; Lehnert, N. *Inorg. Chem.* **2006**, *45*, 2835-2856.
[23] Cheng, R.-J.; Chen, P.Y.; Novell, T.; Liu, T.; Noddleman, L.; Case, D. A. *J. Am. Chem. Soc.* **2003**, *125*, 6774-6783.
[24] Eaton, W. A.; Hochstrasser, R. M. *J. Chem. Phys.* **1967**, *46*, 2533-2539.
[25] Behere, D. V.; Mitra, S. *Inorg. Chem.* **1979**, *18*, 1723-1724.
[26] (a) Uenoyama, H. *Biochim. Biophys. Acta* **1971**, *230*, 479. (b) Dolphin, D. H.; Sams, J. R.; Tsin, T. B.; Wong, K. L. *J. Am. Chem. Soc.* **1978**, *100*, 1711.
[27] Thomson, A. J.; Johnson, M. K. *Biochem. J.* **1980**, *191*, 411-420.

[28] Hendrickson, D. N.; Kinnaird, M. G.; Suslick, K. S. *J. Am. Chem. Soc.* **1987**, *109*, 1243-1244.
[29] Paulat, F.; Lehnert, N. manuscript in preparation.
[30] Lehnert, N. In *The Smallest Biomolecules: Diatomics and their interactions with heme proteins*; Ghosh, A., Ed.; Elsevier, 2008; in press.
[31] Spiro, T. G.; Li, X.-Y. In *Resonance Raman Spectra of Heme and Metalloproteins*; Spiro, T. G., Ed.; Wiley: New York, 1988; pp 1-37.
[32] Spiro, T. G.; In *Iron Porphyrins*; Lever, A. B. P., Gray, H. B., Eds.; Addison-Wesley: Reading, MA, 1983; Part 2. pp 89-159.
[33] The splitting of the Soret E_u state can only be determined from MCD, and is is usually in the range of 311 and 1404 cm^{-1}.
[34] Czernuszewicz, R. S.; Spiro, T. G. In *Inorganic Electronic Structure and Spectroscopy*; Solomon, E. I., Lever, A.B. P., Eds.; John Wiley & Sons: New York, 1999; Vol. 1, pp 353-441.
[35] (a) Spaulding, L. D.; Eller, P. G.; Bertrand, J. A.; Felton, R. H. *J. Am. Chem. Soc.* **1974**, *96,* 982-987. (b) Song, H.; Rath, N. P.; Reed, C. A.; Scheidt, W. R. *Inorg. Chem.* **1989**, *28*, 1839-1847. (c) Vangberg, T.; Lie, R.; Ghosh, A. *J. Am. Chem.. Soc.* **2002**, *124*, 8122-8130.
[36] Cheesman, M. R.; Walker, F. A. *J. Am. Chem. Soc.* **1996**, *118*, 7373-7380.
[37] Walker, F. A. *Coord. Chem. Rev.* **1999**, *185-186*, 471-534.
[38] Thomson, A. J.; Johnson, M. K.; Greenwood, C.; Gooding, P. E. *Biochem. J.* **1981**, *193*, 687-697.
[39] Browett, W. R.; Gasyna, Z.; Stillman, M. J. *J. Am. Chem. Soc.* **1988**, *110*, 3633-3640.
[40] S. I. Gorelsky, SWizard program, http://www.sg-chem.net/, University Of Ottawa, Canada, 2007.

Supporting Information

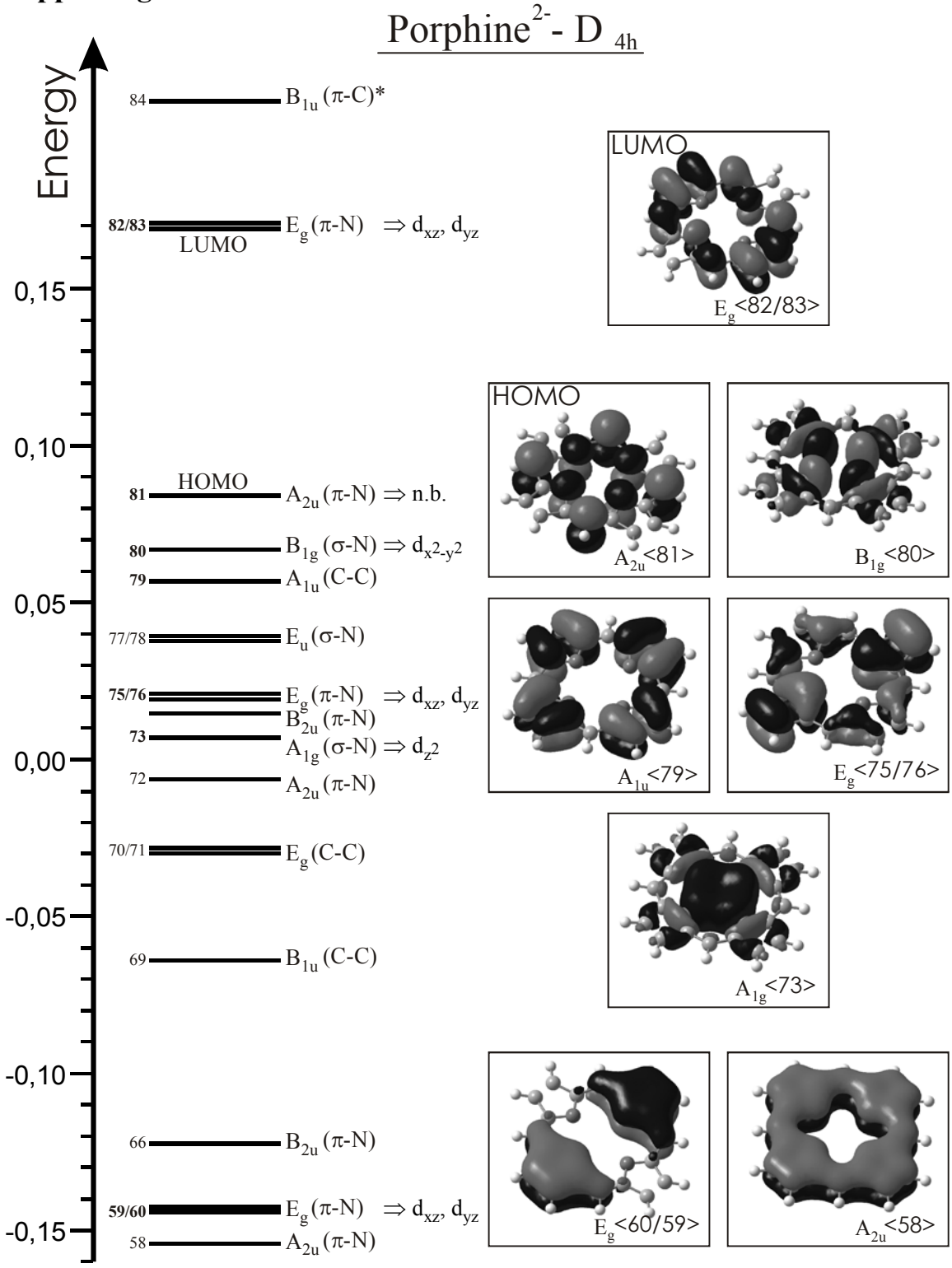

Figure S1. MO diagram of the free porphine(2-) ligand and contour plots. Energies are given in Hartree. Metal d orbitals that potentially interact with these MOs are indicated (labels are based on the coordinate system given in Figure 1).

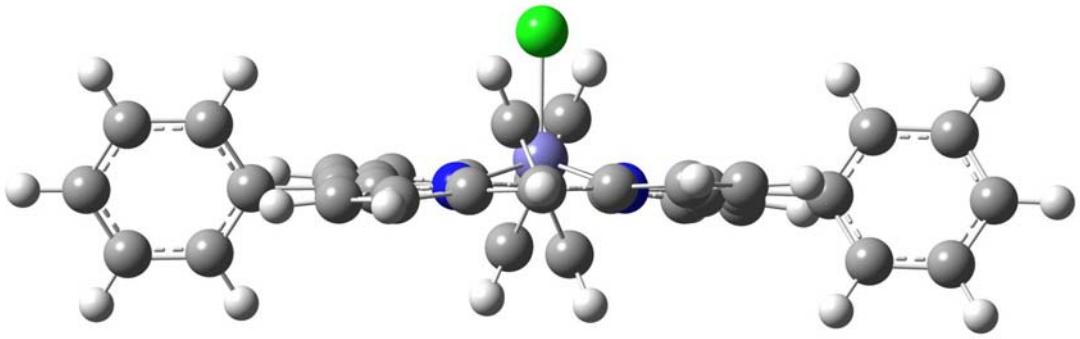

Figure S1. Side-View of the optimized (B3LYP/LanL2DZ*) structure of [Fe(TPP)(Cl)] with d(Fe-Cl) = 2.192 Å (taken from crystal structure; see: Hoard, J. L.; Cohen, G. H.; Glick, M. D. *J. Am. Chem. Soc.* **1967**, *89*, 1992-1996.).

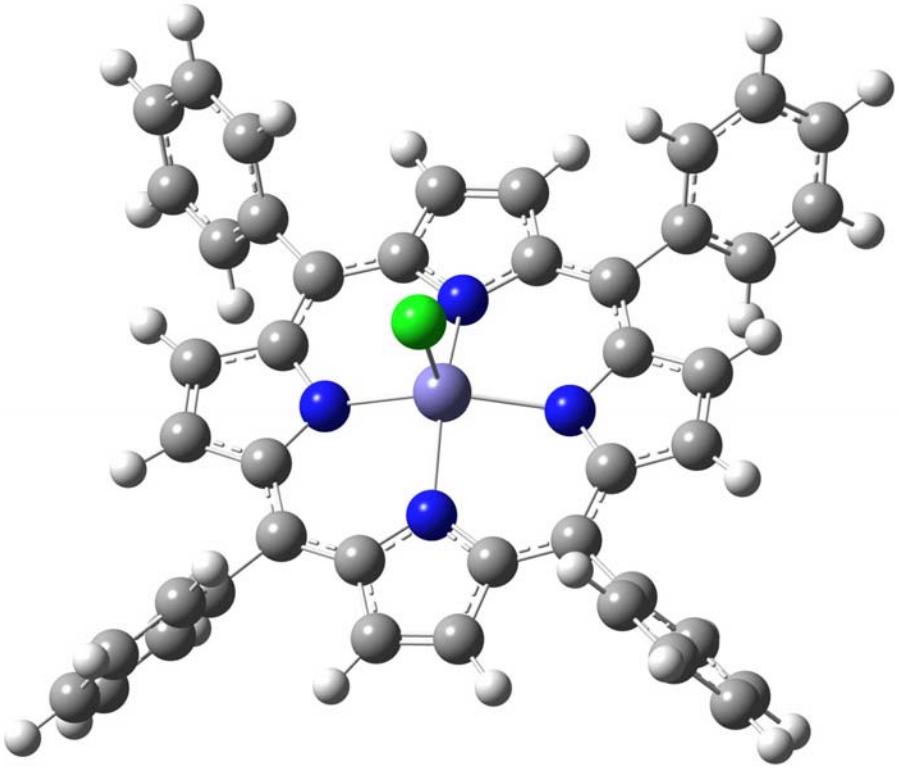

Figure S2. Top-View of the optimized (B3LYP/LanL2DZ*) structure of [Fe(TPP)(Cl)] with d(Fe-Cl) = 2.192 Å (taken from crystal structure; see: Hoard, J. L.; Cohen, G. H.; Glick, M. D. *J. Am. Chem. Soc.* **1967**, *89*, 1992-1996.).

Table S1. TD-DFT and INDO/S calculations on [Zn(P)] and [Zn(TPP)].

Assignment	[Zn(P)]				[Zn(TPP)]		
	B3LYP LanL2DZ	B3LYP LanL2DZ*	B3LYP TZVP	INDO/S-CI	B3LYP LanL2DZ	INDO/S-CI	Exp.[a]
Soret	28190	27700	27620	26952	26810	25008	23880
Q	19281	18940	18980	14546	18660	14250	17080

[a] Gouterman, M. in *The Porphyrins*; Dolphin, D., Ed.; Academic: New York, 1979, Vol. III, Part A, pp 1-156.

Table S2. TD-DFT (B3LYP/LanL2DZ*) results (Contributions are given in %).

No.	1	2	3	4	5	6
Excitation energy, cm^{-1} (nm, f)	8342 (1199, 0.0010)	8800 (1136, 0.0009)	11945 (837, 0.0023)	12325 (811, 0.0004)	12329 (811, 0.0029)	12910 (775, 0.0026)
Inner Porphyrin Excitations:						
$\pi \rightarrow \pi^{*(0)}$	4	6	-	-	27	45
$\pi \rightarrow \pi^{*(1)}$	-	-	-	-	-	-
$\pi \rightarrow \pi^{*(2)}$	-	-	-	-	-	-
Porphyrin to Fe Excitations:						
$CT^{(1)}$	-	-	-	-	**73**	55
$CT^{(2)}$	**88**	**86**	-	-	-	-
$CT^{(3)}$	-	-	-	-	-	-
$CT^{(4)}$	3	3	-	-	-	-
$CT^{(5)}$, z	-	-	**82**	10	-	-
Chloro to Fe Excitations:						
$CT^{(Cl,1)}$, z	-	-	2	-	-	-
$CT^{(Cl,2)}$, z	-	-	2	-	-	-
$CT^{(Cl,3)}$, z	-	-	1	-	-	-
Other contributions				A_{1u} <168> $\rightarrow$ d_{xy}: **90**		

Table S2. TD-DFT (B3LYP/LanL2DZ*) results (continued).

No.	7	8	9	10	11	12
Excitation energy, cm^{-1} (nm, f)	16783 (596, 0.0072)	16921 (591, 0.0053)	18988 (527, 0.0214)	18990 (527, 0.0146)	20740 (482, 0.0011)	21025/21115 (476/474, 0.0089/0.0071)
	$Q^{\alpha\,a}$	$Q^{\alpha\,a}$	$Q^{\beta\,a}$	$Q^{\beta\,a}$		
Inner Porphyrin Excitations:						
$\pi \rightarrow \pi^{*(0)}$	**96**	**97**	**97**	**98**	-	8
$\pi \rightarrow \pi^{*(1)}$	-	-	-	-	-	-
$\pi \rightarrow \pi^{*(2)}$	-	-	-	-	-	-
Porphyrin to Fe Excitations:						
$CT^{(1)}$	4	3	-	-	-	-
$CT^{(2)}$	-	-	3	2	-	-
$CT^{(3)}$	-	-	-	-	-	-
$CT^{(4)}$	-	-	-	-	-	-
$CT^{(5)}$, z	-	-	-	-	-	-
Chloro to Fe Excitations:						
$CT^{(Cl,1)}$, z	-	-	-	-	3	-
$CT^{(Cl,2)}$, z	-	-	-	-	4	-
$CT^{(Cl,3)}$, z	-	-	-	-	-	-
Other contributions					$E_g \rightarrow d_\pi$: **92**	$E_g \rightarrow d_{z2}$: **82**

[a] Two sets of Q bands are predicted (four bands) due to spin polarization. Bands 7 and 8 have more α-spin $\pi \rightarrow \pi^{*(0),\alpha}$, whereas bands 9 and 10 have more β-spin $\pi \rightarrow \pi^{*(0),\beta}$ character.

Table S2. TD-DFT (B3LYP/LanL2DZ*) results (continued).

No.	13	14	15	16	17	18
Excitation energy, cm^{-1} (nm, f)	21631 (462, 0.0118)	22341 (448, 0.0219)	22455 (445, 0.0134)	22605 (442, 0.0007)	24410 (410, 0.1310)	24446 (409, 0.1364)
Inner Porphyrin Excitations:						
$\pi \rightarrow \pi^{*(0)}$	5	6	-	-	21	21
$\pi \rightarrow \pi^{*(1)}$	-	-	-	-	-	-
$\pi \rightarrow \pi^{*(2)}$	2	2	-	-	5	6
Porphyrin to Fe Excitations:						
$CT^{(1)}$	-	-	-	-	-	-
$CT^{(2)}$	-	-	-	-	-	-
$CT^{(3)}$	**89**	**89**	-	-	-	-
$CT^{(4)}$	-	-	-	-	10	8
$CT^{(5)}$, z	-	-	-	-	-	-
$CT^{(6)}$, z	-		6	**90**		
Chloro to Fe Excitations:						
$CT^{(Cl,1)}$, z	-	-	-	-	-	-
$CT^{(Cl,2)}$, z	-	-	-	-	-	-
$CT^{(Cl,3)}$, z	-	-	4	-	-	-
Other contributions			$E_g \rightarrow d_\pi$: **88**		$p_{x,y} \rightarrow d_{z2}$: **52**	$p_{x,y} \rightarrow d_{z2}$ **53** %

Table S2. TD-DFT (B3LYP/LanL2DZ*) results (continued).

No.	19	20	21	22	23	24
Excitation energy, cm^{-1} (nm, f)	25008 (400, 0.0009)	25202 (397, 0.0323)	25203 (397, 0.0041)	25475 (393, 0.0024)	25718 (389, 0.0333)	25843 (387, 0.1016)
Inner Porphyrin Excitations:						
$\pi \rightarrow \pi^{*(0)}$	-	2	-	-	-	6
$\pi \rightarrow \pi^{*(1)}$	-	-	6	2	-	31
$\pi \rightarrow \pi^{*(2)}$	-	6	-	**41**	24	
Porphyrin to Fe Excitations:						
$CT^{(1)}$	-	-	-	-	-	
$CT^{(2)}$	-	3	-	20	5	4
$CT^{(3)}$	-	-	-	2	1	2
$CT^{(4)}$	-	**49**	-	-	-	
$CT^{(5)}$, z	28	-	-	-	-	
$CT^{(Cl,1)}$, z	**38**	-	1	-	-	
$CT^{(Cl,2)}$, z	1	-	6	-	-	
$CT^{(Cl,3)}$, z	13	-	-	-	-	
Other contributions			$A_{2u} \rightarrow B_{1u}$: **35**		Ph → d_{xy}: **54**	Ph → d_{xy}: **41**

Table S2. TD-DFT (B3LYP/LanL2DZ*) results (continued).

No.	25	26	27	28	29
Excitation energy, cm^{-1} (nm, f)	26071 (384, 0.3805)	26109 (383, 0.1539)	26143 (383, 0.5366)	27164 (368, 0.0967)	27250 (367, 0.0098)
	Soret	Soret	Soret		
Inner Porphyrin Excitations:					
$\pi \rightarrow \pi^{*(0)}$	14	11	23	1	-
$\pi \rightarrow \pi^{*(1)}$	-	1	3	2	2
$\pi \rightarrow \pi^{*(2)}$	20	23	24	**83**	**77**
Porphyrin to Fe Excitations:					
$CT^{(1)}$	-	-	2	-	-
$CT^{(2)}$	2	-	-	2	-
$CT^{(3)}$	2	4	2	-	-
$CT^{(4)}$	11	34	-	-	-
$CT^{(5)}$, z	-	-	-	-	-
Chloro to Fe Excitations:					
$CT^{(Cl,1)}$, z	-	-	-	-	-
$CT^{(Cl,2)}$, z	-	-	-	-	-
$CT^{(Cl,3)}$, z	-	-	-	-	-
Other contributions	Ph → d_{π,z^2}: 19	Ph → d_{π,z^2}: 11	Ph → d_{π,z^2}: 16		

Table S3. Optimized (B3LYP/LanL2DZ*) structure of [Fe(TPP)(Cl)] with d(Fe-Cl) set to 2.192 Å. Coordinates are given in Å

Atom type	x	Y	z
C	4.26625300	0.46927500	-0.34561900
C	4.19585000	-0.89774300	-0.36234900
C	2.91436200	0.95902400	-0.18383000
H	5.14690000	1.09118800	-0.45766400
C	2.80108400	-1.25003500	-0.20620900
N	2.03456500	-0.10400400	-0.11587200
C	2.57356400	2.32428100	-0.13266700
H	5.00838600	-1.60357700	-0.49019400
C	1.25124900	2.80423200	-0.09720600
C	2.32238200	-2.57346400	-0.17321500
C	3.69076400	3.32436000	-0.12305800
C	0.89893500	4.20536800	-0.01869300
N	0.10473600	2.03205100	-0.13986700
C	0.95836500	-2.91623800	-0.11908300
C	3.32804300	-3.68532900	-0.20600900
C	3.91412600	4.17212300	-1.22583400
C	4.54224200	3.42931500	0.99451600
C	-0.46796200	4.27465800	-0.03424400
C	-0.95834900	2.91616400	-0.11965400
C	0.46788600	-4.27475400	-0.03425800
N	-0.10466900	-2.03208300	-0.13933400
H	1.60465100	5.02475200	0.05404600
C	3.43566500	-4.52572300	-1.33159600
C	4.18530600	-3.90863500	0.88950500
C	4.96629700	5.10036300	-1.21377900
C	5.58854600	4.36374900	1.01220200
H	3.26868300	4.09250600	-2.10111200
H	4.37289900	2.78395300	1.85689500
C	-2.32236400	2.57338700	-0.17380500
C	-1.25121400	-2.80422100	-0.09699700
C	-0.89899700	-4.20535200	-0.01807500
H	-1.08920000	5.16088800	0.02416200
H	1.08906900	-5.16103500	0.02389900
C	4.38062300	-5.56229400	-1.36401100
C	5.12408900	-4.95104000	0.86272800
H	2.78375400	-4.35667900	-2.18916300
H	4.10364500	-3.27097100	1.77022100
C	5.80641200	5.20143800	-0.09334900
H	5.12994400	5.74222600	-2.08005300
H	6.23166000	4.43708200	1.88975900
C	-2.80109900	1.24997800	-0.20660500
C	-2.57349800	-2.32427700	-0.13271700
C	-3.32798500	3.68530500	-0.20646100
H	-1.60480100	-5.02466900	0.05465200
C	5.22709100	-5.78071400	-0.26528100
H	4.45544200	-6.19742800	-2.24730900
H	5.77263000	-5.11512900	1.72385400
H	6.62215200	5.92501500	-0.08210200
C	-4.19596500	0.89766000	-0.36187300
C	-2.91434200	-0.95906600	-0.18400300
C	-3.69066000	-3.32444100	-0.12310200
N	-2.03451400	0.10396700	-0.11656000
C	-4.18429500	3.90940000	0.88963200

C	-3.43652400	4.52491400	-1.33254000
H	5.95881800	-6.58891800	-0.28772900
C	-4.26629400	-0.46936500	-0.34541300
H	-5.00859000	1.60349100	-0.48916100
C	-3.91660700	-4.16915200	-1.22767700
C	-4.53948900	-3.43240700	0.99617800
C	-5.12305100	4.95183400	0.86293600
C	-4.38145700	5.56151300	-1.36486300
H	-4.10192800	3.27232200	1.77070600
H	-2.78533700	4.35525100	-2.19053500
H	-5.14696600	-1.09133200	-0.45699000
C	-4.96873400	-5.09745300	-1.21567100
C	-5.58573900	-4.36691600	1.01378400
C	-5.22697300	5.78073400	-0.26555900
H	-3.27316200	-4.08717700	-2.10421000
H	-4.36818000	-2.78930500	1.85985900
H	-5.77085700	5.11654700	1.72449700
H	-4.45699700	6.19604600	-2.24853000
C	-5.80618600	-5.20159800	-0.09352900
H	-5.13441200	-5.73697500	-2.08328800
H	-6.22681200	-4.44263300	1.89263000
H	-5.95868200	6.58895600	-0.28794200
H	-6.62188900	-5.92521700	-0.08232800
Fe	-0.00006400	0.00007800	0.35440800
Cl	-0.00046340	0.00035138	2.54640795

5 Model Systems for NorBC (Cofacial Porphyrins)

5.1 Scope of this project

As already mentioned in the Introduction (cf. Chapter 1), no crystal structure for bacterial nitric oxide reductase (NorBC) is available to this date, but it is known from spectroscopic investigations that the active site of NorBC is closely related to the respiratory heme-copper oxidases, the so-called cytochrome c oxidases (CCO). Thus, it consists of a five-coordinate heme a_3 with axial histidine coordination and a non-heme Fe_B center in close proximity with three histidine ligands coordinated. In order to model the active site of NorBCs, it is therefore necessary to synthesize binuclear complexes. Model systems that closely mimic the active site of the CCOs consist of a porphyrin, which is covalently attached to a multidentate N-donor ligand (based on pyridine, benzimidazole, amine, etc.). These ligands were developed in a number of different groups.[1] Corresponding heme/non-heme model systems are also currently investigated in our laboratory.[2] Alternatively, binuclear porphyrin systems are of interest for modeling NorBCs. Figure 5.1.1 shows binuclear porphyrin ligands, developed by different groups.[3]

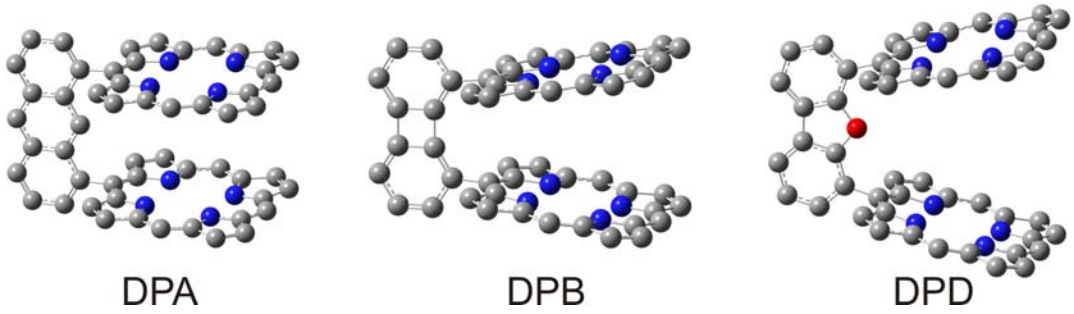

Figure 5.1.1 Optimized cofacial ligands using the semiempirical PM3 method (hydrogen atoms are excluded in this figure).

In this case, two porphyrin units are fixed by a rigid spacer in a cofacial geometry. Two arrangements are possible: The anthracene (H_4DPA) and biphenylene (H_4DPB) linked porphyrins show a parallel orientation of the porphyrins cores, whereas the dibenzofuran (H_4DPD) linked cofacial porphyrin shows an angulate geometry. Importantly, the metal to metal distance can be adjusted this way, as shown in Figure 5.1.2.

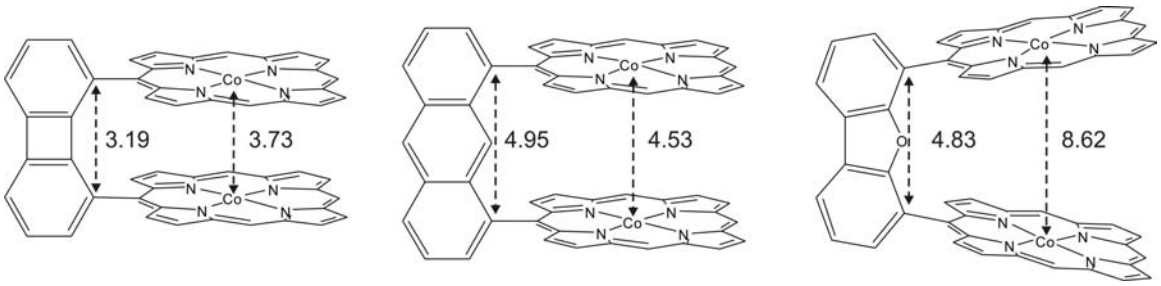

Figure 5.1.2. Selected crystallographic distances (in Å) in [Co_2DPB],[4a] [Co_2(DPA)],[4b] and [Co_2(DPD)$(MeOH)_2$].[4c,d]

Figure 5.1.2 shows the porphyrin to porphyrin and metal to metal distances of [Co_2DPB], [Co_2(DPA)] and [Co_2(DPD)$(MeOH)_2$], respectively, determined from reported crystal structures.[4] By using different linker units, the Co-Co distance can be varied from 3.73 Å in [Co_2DPB] to 8.62 Å in [Co_2(DPD)$(MeOH)_2$]. The Fe_{a_3} to Cu_B distance (from a crystal structure) in oxidized bovine heart cytochrome c oxidase is 4.5 Å and therefore, similar to the metal-metal distance in [Co_2(DPA)] (4.53 Å). Hence, the anthracene linked cofacial geometry might be best for modeling NorBC, whereas the metal-metal distance in [Co_2DPB] is too short (3.73 Å), and in [Co_2(DPD)$(MeOH)_2$] is too long (8.62 Å). From this and simple calculations (HF/3-21G and molecular modeling) on cofacial ruthenium porphyrin complexes, I decided to use the anthracene linked cofacial (DPA) system for modeling the active site of NorBC.

Note that more cofacial porphyrins with additional spacer units have been synthesized.[5] These systems were almost exclusively used for the investigation of the reduction of oxygen to water (cytochrome c oxidases). Hence, the scope of this project is to use these ligand systems for the investigation of the reaction mechanism of NorBCs. No nitrosyl coordinated anthracene linked metalloporphyrin is available from the literature to this date. It is known from the literature that ruthenium(III) porphyrin NO complexes are very stable compared to the corresponding iron complexes. In a first attempt, ruthenium complexes of TPP (tetraphenylporphyrin) and TMP (tetramesitylporphyrin) were synthesized. These investigations showed that the ruthenium insertion into porphyrins is difficult leading to low yields.[6] In contrast, my earlier investigations on corresponding [Co(P)(NO)] (P = TPP and TMP) complexes showed that these compounds are stable

and importantly, lead to high yields.[7] In addition, since a complete set of spectroscopic data for the [Co(P)(NO)] (P = TPP and TMP) complexes has been obtained, these spectroscopic data can be compared to the spectra of the corresponding cofacial systems. Therefore, the $[Co_2(DPA)(NO)_2]$ complex was synthesized first and spectroscopically characterized. In order to investigate the mechanism of the reduction of NO to N_2O using cofacial porphyrins, quantum-chemical calculations on the anthracene and biphenylene systems have been performed. These DFT results are summarized in Section 5.3.

5.2 Syntheses of Cofacial Porphyrins

5.2.1 Preface

The cofacial porphyrins can either be synthesized in a single-step synthesis based on the bisaldehyde of the rigid spacer ('direct synthesis'), which is schematically shown in Figure 5.2.2, or in a multi-step synthesis ('rational synthesis') following Lindsey's approach, which is shown in Figure 5.2.3 (see below).

Chang et al. synthesized the H_4DPA and H_4DPB ligands in 1983 for the first time in a multi-step synthesis with low yield.[3a] Then Collman and coworker developed a new synthetic stategy in 1995, which includes four steps based on the bisaldehyde.[8] One of the two aldehyde groups in 1,8-diformylanthracene is protected using 1,3-propanethiol and the unprotected aldehyde group is then reacted with pyrrole and the corresponding aromatic aldehyde in a mixed condensation to form the corresponding porphyrin (under Lindsey conditions)[9]. Next, the other aldehyde group is deprotected using DDQ and $BF_3{\cdot}(OEt)_2$, and another porphyrin condensation yields the cofacial porphyrin. This way, different porphyrin rings (cofacial heteroporphyrin) and metals can be introduced into the system. Note that heme/non-heme model systems could potentially also be synthesized this way. Collman and coworker mentioned in their article that the cofacial homoporphyrin can also be synthesized in one step by allowing the bisaldehyde to react with pyrrole and the corresponding aldehyde, but leads to more difficulties in the separation. This synthetic route will be denoted as 'direct synthesis' in the following. The direct synthetic route has several disadvantages: (a) very low yields (~3 %; vide infra), (b) a limitation to small scale reactions due to the highly diluted conditions necessary,

and (c) the difficult separation (purification) procedure, which includes several column chromatographic separation steps. Hence, the direct synthesis leads to only small quantities of the cofacial porphyrin (80-100 mg from each synthesis; vide infra). Due to these disadvantages, we decided to use another synthetic route with better yields for the final step (porphyrin condensation), which can be performed on a reasonable scale with less separation steps. Lindsey and coworker described a rational synthetic route for *meso*-substituted porphyrins, which allows large scale reactions with minimal chromatography.[10] This way, they were able to synthesize a number of monoporphyrins with different *meso*-substituents in large scales (~ 1 g). The final step in this synthesis is the acid-catalyzed condensation of a dipyrromethane-dicarbinol and a dipyrromethane. We have applied this method to the synthesis of cofacial porphyrins and the synthetic route for synthesizing H_4DPA is shown in Figure 5.2.3. Advantages of the rational synthetic route are: (a) better yields, (b) large scales (up to approximately 1 g) and (c) minimal column chromatography. In addition, the rational synthesis is more flexible. For example, different *meso*-substituents can easily be introduced into the system.

Metallation and nitrosylation of the cofacial porphyrins have been achieved by common literature methods (cf. Figure 5.2.4). The metallation of porphyrins in boiling DMF using MCl_2 (M = metal) was developed by Adler et al.[11] Correspondingly, H_4DPA was reacted with $CoCl_2$ and $FeCl_2$ to form $[Co_2(DPA)]$ and $[Fe_2(DPA)(Cl)_2]$, respectively. The reaction of the cofacial metalloporphyrins with NO yielded the corresponding nitrosylated $[Co_2(DPA)(NO)_2]$ and $[Fe_2(DPA)(NO)_2]$ species. For $[Fe_2(DPA)(NO)_2]$, methanol was added to the reaction mixture in order to obtain the corresponding Fe(II)-NO complex (vide infra) via autoreduction (cf. Figure 5.2.4).

The starting point for both synthetic routes is the synthesis of the bisaldehyde of the rigid linker. Therefore, the first part of this chapter (Section 5.2.2) deals with the synthesis of 1,8-diformylanthracene, which can be synthesized in three steps from 1,8-dichloroanthraquinone.

5.2.2 Synthesis of 1,8-Diformylanthracene (Rigid Linker)

1,8-Diformylanthracene was synthesized in a three-step synthesis (Steps A, B and C shown in Figure 5.2.2) starting from the commercially available 1,8-dichloroanthraquinone (Aldrich: D56403). In Step A, 1,8-dichloroanthraquinone is reduced to 1,8-dichloroanthracene using zinc powder. The chloro substituents were then substituted by nitrile using copper(I) cyanide in a Kolbe nitrile type reaction (Step B). Finally, the nitrile was reduced using diisobutylaluminum hydride (DIBAL-H), and then hydrolyzed yielding 1,8-diformylanthracene.

5.2.2.1 Synthesis of 1,8-Dichloroanthracene.[12]

1,8-Dichloroanthracene was synthesized using the literature methods by Guilard et al.[12] and House et al.[13] Note that both reactions lead to a further reduction of the product to anthracene. Fine tuning of the reaction conditions lead to 4 % anthracene impurity.

Method by Guilard et al.[12] 40.0 g zinc dust (612 mmol) were added in small portions to a stirred suspension of 10.0 g (36.1 mmol) 1,8-dichloroanthraquinone in aqueous ammonia (20 %, 400 mL), and then 0.17 g (1.07 mmol) cupric sulfate were added over a few minutes. The suspension turned red-brown and gas evolution was observed. The mixture was gently heated until the gas evolution diminished. Note that, because of the fine zinc dust, big bubbles occur. Therefore, it is necessary to heat gently. Also, the use of a mechanical stirrer is recommended for a large scale reaction. The mixture was heated carefully to 80 °C for 4.5 h. The hot mixture was then filtered yielding a grey solid containing the product and unreacted zinc. The solid was washed several times with water and then dried by suction. The crude product was extracted three times with 80 mL acetone, respectively. The combined, yellow organic extracts were evaporated in vacuum to dryness to give a lightly yellow solid. The crude solid was dissolved in hot 1-propanol and then precipitated by adding a few drops of concentrated hydrochloric acid. Yellow needles rapidly formed and the mixture was allowed to slowly cool to room temperature. Then the product was filtered, washed with cold methanol and dried in vacuum over phosphorus pentoxide. UV-Vis and ^{1}H-NMR spectroscopies showed about 30 % anthracene impurity.

Method by House et al.[13] This synthesis is very similar to the synthesis described by Guilard et al. The only difference is that House et al. did not add $CuSO_4$. Following the exact procedure from the literature, again approximately 30 % anthracene impurity has been obtained. In order to prevent the reduction to anthracene, the reaction temperature was lowered, which lead to 4 % anthracene impurity.

10.0 g zinc dust (153 mmol) were added in small portions to an ice cold suspension of 2.00 g (7.22 mmol) 1,8-dichloroanthraquinone in 42 mL aqueous ammonia (16 %). The suspension turned red-brown and the mixture was allowed to warm up to room temperature, then heated for 3 h to 60 °C and finally another 15 min. to 65 °C. The grey solid was filtered, washed three times with water, dried by suction, and then extracted with hot dichloromethane (three times). The dichloromethane was evaporated in vacuum to yield a yellow solid. The crude product was refluxed in a mixture of 88 mL 2-propanol and 8 mL concentrated HCl and then allowed to slowly cool down to room temperature. In order to achieve a complete precipitation of the product, the mixture was stored over night in the refrigerator. The yellow, crystalline product was filtered off and dried in vacuum over phosphorus pentoxide. 0.99 g (4.01 mmol; 56 % yield) 1,8-dichloanthracene was obtained, which contained about 4 % anthacene (^{1}H-NMR).

Yield: 0.99 g (4.01 mmol, 56 %; Lit.[12]: 88 %)

Analysis: UV-Vis (CH_2Cl_2; 275-450 nm region): 319, 335, 352, 370 and 391 nm. 1,8-Dichloroanthracene shows a red shift of the bands in UV-Vis compared to anthracene. The corresponding spectra are shown in Figure 5.2.1. ^{1}H-NMR (400 MHz, $CDCl_3$): 9.25 (s, 1 H, 9-anth), 8.45 (s, 1 H, 10-anth), 7.92 (d, 2 H, J = 8.55 Hz, 2,7-anth), 7.61 (dd, 2 H, J = 7.18 Hz, J = 0.99 Hz, 4,5-anth), 7.39 ppm (dd, 2 H, J = 8.53 Hz, J = 7.20 Hz, 3,6-anth).

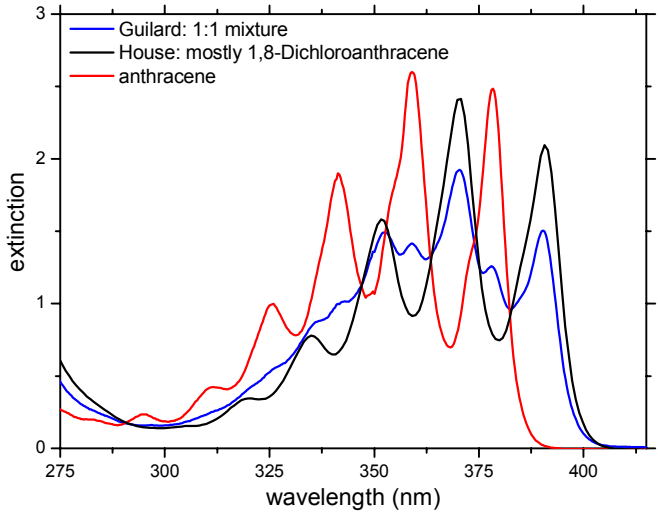

Figure 5.2.1. UV-Vis absorption spectra of 1,8-dichloroanthracene (black), anthracene (red) and a mixture (blue) obtained by different reaction procedures (vide supra).

5.2.2.2 Synthesis of 1,8-Dicyanoanthracene.[12]

5.64 g (22.8 mmol) 1,8-Dichloroanthracene and 9 g (100 mmol) copper(I) cyanide were dissolved in 61 mL *N*-methyl-2-pyrrolidinone and refluxed (about 220 °C) for 37 h. Then 1 g (11 mmol) CuCN were added and refluxed for another 52 h. The reaction mixture was cooled in an ice bath and then poured into 122 mL of stirred water. 122 mL aqueous NH_3 solution (20 %) were then added and the mixture stirred for 7 d. After filtration a brown-grey solid was obtained and a blue eluate indicating that the $[Cu(NH_3)_4]^{2+}$ complex had formed. The solid was washed three times with water and then suspensed in 25 mL aqueous NH_3 solution (20 %). The solid was filtered off and washed once with water. In order to dissolve the rest of the CuCN, the solid was washed twice with about 12.5 mL 0.6 M (aq.) potassium cyanide solution to form the water soluble tetracyanocuprat(I) complex ($[Cu(CN)_4]^{3-}$). Since not all of the CuCN was dissolved at this point, the solid was stirred for 1 h in 75 mL 0.6 M KCN aqueous solution, filtered off, and washed three times with water. The raw product was then dried in vacuum over phosphorus pentoxide and recrystallized from *N,N*-dimethylformamide yielding 1,8-dicyanoanthracene as brown, crystalline needles.

Yield: 3.52 g (13.8 mmol, 60 %; Lit.[12]: 68.4 %)

Analysis: IR (KBr disk): ν(CN) = 2224 cm^{-1}. ^{1}H-NMR (400 MHz, DMF-d_7): 9.25 (s, 1 H, 9-anth), 9.16 (s, 1 H, 10-anth), 8.77 (d, 2 H, J = 8.73 Hz, 2,7-anth), 8.55 (dd, 2H, J = 6.96 Hz, J = 0.97 Hz, 4,5-anth), 7.97 ppm (dd, 2H, J = 8.61 Hz, J = 6.98 Hz, 3,6-anth).

5.2.2.3 Synthesis of 1,8-Diformylanthracene.[12]

5.0 g (21.9 mmol) 1,8-dicyanoanthracene were placed in a Schlenk flask and purged with argon gas (three times). Then 210 mL freshly distilled dichloromethane (over CaH_2 in argon atmosphere) were added. Most of the solid was dissolved using an ultrasonic bath (for 10 min). The reaction mixture was cooled in an ice bath and 44 mL diisobutylaluminum hydride (1 M CH_2Cl_2 solution) were added, stirred for 15 min at 0 ˚C and then additional 20 mL DIBAL-H solution were added. The solution was stirred for 15 min at 0 ˚C, warmed up to room temperature and stirred for another 35 min. The colour of the reaction mixture changed from brown to yellow during the reaction. The mixture was then poured into 175 mL ice cooled aqueous sulphuric acid (50 %). The formation of large quantities of aluminum salts was observed. Therefore, 2 L water were added and the aqueous phase was extracted four times with technical dichloromethane. The combined organic extracts were washed twice with water, dried over sodium sulphate and filtered. The solvent was completely removed in vacuum. The raw product was purified using column chromatography (silica gel with CH_2Cl_2 : CH_3OH = 30:1). The first fraction yielded the 1,8-diformylanthracene, and after removal of the solvent, pure 1,8-diformylanthracene was obtained as yellow crystals.

Yield: 2.97 g (12.7 mmol, 58 %; Lit.[12]: 81 %)

Analysis: ^{1}H-NMR (400 MHz, $CDCl_3$): 11.11 (s, 1 H, 9-anth), 10.57 (s, 2 H, CHO), 8.54 (s, 1 H, 10-anth), 8.25 (d, 2 H, J = 8.61 Hz, 2,7-anth), 8.08 (dd, 2 H, J = 6.83, J = 1.23 Hz, 4,5-anth), 7.65 ppm (dd, 2 H, J = 8.47 Hz, J = 6.81 Hz, 3,6-anth).

5.2.3 Direct Synthesis of H_4DPA.

Figure 5.2.2 shows the reaction scheme for the direct synthesis of H_4DPA, which can be synthesized in one-step starting from 1,8-diformylanthracene.

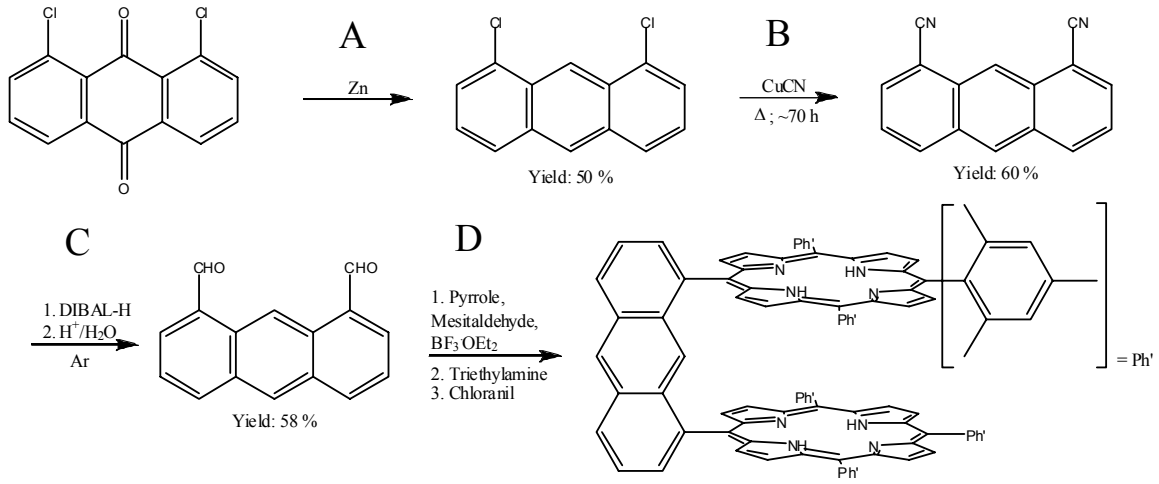

Figure 5.2.2 Reaction scheme for the direct synthesis of H_4DPA.

The direct synthesis of H_4DPA is a mixed condensation reaction, which leads to multiple porphyrin products. The main product is tetramesitylporphyrin (H_2TMP), whereas the yield in H_4DPA is only 3 % based on the bisaldehyde (vide infra). The yield in H_4DPA can be increased by increasing the bisaldehyde : pyrrole : mesitaldehyde ratio, but this also leads to a disproportional increase in H_2TMP. Collman and coworker stated that:[8] "[…] Larger scale reactions tend to give lower yields - again, we believe this to result from the difficulty in purification. […]". The main problem is the poor solubility of H_2TMP. In large quantities H_2TMP tends to partially precipitate on top of the column. Due to the higher R_f value of H_2TMP compared to H_4DPA, H_2TMP leaches continuously into the column during the column separation. Hence, pure H_4DPA could only be obtained after additional column chromatographic separations. The yield is therefore somehow limited. Using a 1 : 26 : 24 ratio, 80-90 mg H_4DPA could be isolated from one reaction (vide infra).

Solvent dependency of porphyrin condensations.[14] Note that porphyrin condensations are highly solvent dependent. This was intensively investigated by Lindsey and coworker.[14] Interestingly, the synthesis of H_2TMP fails in absolute $CHCl_3$, whereas the synthesis in commercial $CHCl_3$, which is stabilized by 0.75 % (v/v) ethanol, yields 30 % H_2TMP. Correspondingly, the reaction also fails in absolute CH_2Cl_2. The addition of 0.75 % (v/v) ethanol to the dichloromethane increased the yield of the reaction to 25 %. The best yield

(30 %) was obtained using $CHCl_3$ with 0.75 % ethanol. The reason for this observation is still not fully understood.

5.2.3.1 Synthesis of 1,8-Bis(5-tris(10,15,20-mesitylporphyrinyl))anthracene (H_4DPA).

440 mg (1.95 mmol) 1,8-Diformylanthracene were dissolved in 3 L $CHCl_3$, and then argon was bubbled through the solution for about 1 h, and continued to be bubbled throughout the reaction. Then, 6.6 mL (45 mmol) mesitaldehyde and 3.4 mL (49 mmol) pyrrole were added via a syringe. Approximately 4 mL (Lindsey conditions: $3.3 \cdot 10^{-3}$ M)[14] $BF_3 \cdot OEt_2$ were added and the reaction mixture was stirred at room temperature for 90 min (in the dark). In order to oxidize the formed porphyrinogens to the corresponding porphyrins, 11.09 g chloranil were added and the mixture was stirred for another 60 min. The acid catalyst was neutralized using 1.51 mL (10.9 mmol) triethylamine and the solvent was then completely removed in vacuum. The residue was dissolved in CH_2Cl_2 and loaded on a neutral alumina column. The mixed porphyrins were eluted using CH_2Cl_2, and the CH_2Cl_2 was then evaporated in vacuum. The raw product obtained this way was purified using silica gel column chromatography. The column was packed with a 4:1 mixture of *n*-Hexan/CH_2Cl_2. H_4DPA was eluted as fourth fraction. The first fraction was yellow-brown, the second and third fractions purple. After the elution of the first few drops of the first fraction, the polarity was increased using a 2:1 mixture of *n*-Hexan/CH_2Cl_2. Importantly, only after the third fraction was completely eluted, the polarity was again increased to a 1:2 mixture of *n*-Hexan/CH_2Cl_2. The color of H_4DPA in solution is brown. Additional column chromatographic separations were needed to yield pure H_4DPA, which has been analyzed using mass spectrometry, UV-Vis and ^{1}H-NMR spectroscopy.

Yield: 84 mg (0.0559 mmol; 2.9 % based on the bisaldehyde; Lit.[8]: 3.2 %)

Analysis: ESI-MS (MeOH/DCM): m/z = 1504.77 (M^+); UV-Vis (CH_2Cl_2), λ_{max} (nm): 416 (Soret), 516, 550, 592, 647 (In comparison: H_2TMP (CH_2Cl_2): 418 (Soret), 515, 547, 591, 647 nm and 1-(5-Tris(10,15,20-mesitylporphyrinyl))-8-formylanthracene (CH_2Cl_2):[8]

422 (Soret), 516, 550, 590, 646); ^{1}H-NMR (400 MHz, C_6D_6):[8] 9.33 (s, 1H), 8.92 (s, 1H), 8.63 (d, 4H, J = 4.65 Hz), 8.49 (d, 4H, J= 4.65 Hz), 8.34 (d, 2H, J = 4.72 Hz), 8.27 (d, 4H, J = 4.74 Hz), 8.03 (d, 4H, J = 4.73 Hz), 7.43-7.54 (m, 4H), 7.17 (s, 2H), 7.08 (s, 2H), 7.01 (s, 4H), 6.72 (s, 4H), 2.46 (s, 6H), 2.44 (s, 12H), 1.99 (s, 6H), 1.71 (s, 12H), 1.68 (s, 6H), 0.26 (s, 12H), -2.63 ppm (broad s, 4H, NH).

5.2.4 Rational Synthesis of H_4DPA.

The rational synthetic route is schematically shown in Figure 5.2.3. In this case, the porphyrin is synthesized step by step starting from pyrrole and the corresponding aldehydes. The crucial step is the condensation of the dipyrromethane-dicarbinol and the bis-dipyrromethane of the anthracene bridge. The dipyrromethane-dicarbinol can be synthesized from 5-mesithyldipyrromethane and 3,5-dimethylbenzoyl chloride. The 5-mesithyldipyrromethane can be synthesized from pyrrole and mesitaldehyde, and 3,5-dimethylbenzoyl chloride is obtained from 3,5-dimethylbenzoic acid and thionylchloride. The bis-dipyrromethane of the anthracene bridge can be synthesized using two different approaches. It can either be synthesized directly from 1,8-diformylanthracene and pyrrole, or through hydrogenolysis of the corresponding benzyloxycarbonyl protected bis-dipyrromethane, which in turn can be synthesized from 1,8-diformylanthracene and benzyl 2-pyrrolecarboxylate. Benzyl 2-pyrrolecarboxylate is obtained from 2-pyrrolecarboxylate and benzyl bromide (phase transfer catalysis, PTC). As already shown above, the 1,8-diformylanthracene can be synthesized in a three-step synthesis starting from 1,8-dichloroanthraquinone (cf. Figure 5.2.2, top).

5.2.4.1 Synthesis of 5-Mesityldipyrromethane.[15]

5.4 mL (5.52 g; 37.2 mmol) mesitaldehyde were mixed with 260 mL freshly distilled (dried over CaH_2) pyrrole and degassed with a stream of argon for 15-20 min. Note that argon was bubbled through the solution throughout the whole reaction. 3.42 g (18.6 mmol) $MgBr_2$ were added, and the solution was stirred for 1.5 h at room temperature. Then, 7.44 g (0.19 mol) NaOH were added to the mixture, which was stirred for another hour at room temperature and then filtered. The color of the reaction mixture changed from yellow to red-brown. The excess pyrrole was removed from the filtrate by

vacuum distillation (65 °C) and recovered. The obtained solid was extracted five times using 20 % ethyl acetate in hexanes. The combined organic extracts were filtered through a pad of silica (about 85 g), and the solvent was then removed in vacuum. The crude product was recrystallized from a 4:1 mixture of ethanol/water. 5.83 g (22.1 mmol) 5-mesityldipyrromethane were obtained as yellow crystals.

Yield: 5.83 g (22.1 mmol; 59 %; Lit.[15]: 53 %)

Analysis: Elemental analysis, Anal. Calcd. for $C_{18}H_{20}N_2$: C, 81.78; H, 7.62; N, 10.60; Found: C, 80.79; H, 7.57; N, 10.12. ^{1}H-NMR (400 MHz, $CDCl_3$): 7.93 (s, 2 H, N-H), 6.87 (s, 2 H, Ph-H), 6.66 (m, 2H, C_α-H), 6.18 (q, 2H, J = 2.99 Hz, J = 2.85 Hz, C_β-H), 6.01 (m, 2H, C_β-H close to Methyl-H), 5.92 (s, 1H, Methyl-H), 2.28 (s, 3H, p-Mesityl-H), 2.06 ppm (s, 6 H, o-Mesityl-H).

5.2.4.2 Synthesis of 3,5-Dimethylbenzoyl chloride.

25 g (166 mmol) 3,5-dimethylbenzoic acid were placed in a 250 mL schlenk flask and then 250 mL thionyl chloride were added. The reaction mixture was refluxed for 3 h and the excess thionyl chloride was distilled off. The product was then distilled and analyzed by ^{1}H-NMR spectroscopy.

Analysis: ^{1}H-NMR (300 MHz, $CDCl_3$): 7.69 (s, 2 H, o-Ph), 7.27 (s, 1 H, p-Ph), 2.35 ppm (s, 6 H, Methyl-H)

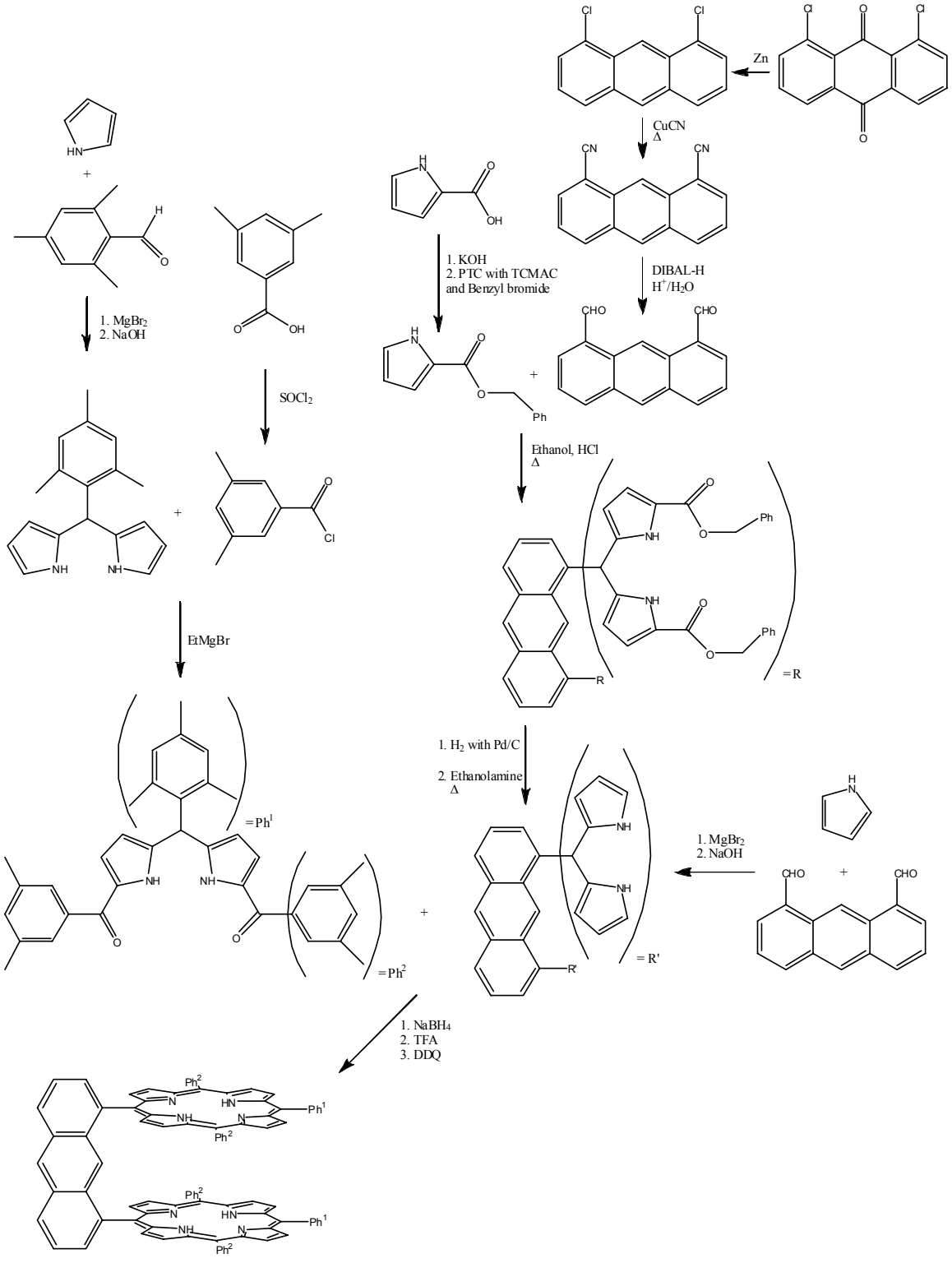

Figure 5.2.3. Reaction scheme for the rational synthesis of H_4DPA starting from pyrrole and the corresponding aldehydes.

5.2.4.3 Synthesis of 1,9-Bis(3,5-dimethylbenzoyl)-5-mesityldipyrromethane.[10]

Note that 1,9-bis(3,5-dimethylbenzoyl)-5-mesityldipyrromethane was not prepared by Lindsey and coworkers, but the general procedure for diacylation, exemplified for 1,9-Bis(4-methylbenzoyl)-5-phenyldipyrromethane in ref. 10, was applied here. 5.29 g (20.0 mmol) 5-mesithyldipyrromethane were dissolved in 400 mL toluene, stirred, and tap-water cooled. Then, 100 mL ethyl magnesium bromide were slowly added to the solution under an argon atmosphere, and gas evolution was observed. The reaction mixture was stirred for 30 min at room temperature, and then a solution of 8.43 g (50.0 mmol) 3,5-dibenzoylchloride in 50 mL toluene was added slowly over 10 min. The mixture was stirred for another 10 min, and the reaction was then quenched by adding 300 mL saturated NH_4Cl solution. Afterwards, 400 mL ethyl acetate were added, the organic phase was then washed with water, and then dried over sodium sulfate. The solvent was removed in vacuum. The product was separated using silica gel column chromatography. The initial TLC showed a lot of spots, but the column separation works actually pretty good using a 99:1 CH_2Cl_2/ethyl acetate mixture as eluant. The first fraction was yellow, the second orange, and the third brown. Note that these fractions were of small quantity and not the desired product. Then, the polarity was increased to 95:5 CH_2Cl_2/ethyl acetate, and the product was eluted as brown solution. The solvent was removed in vacuum and the remaining solid was analyzed by ^{1}H-NMR spectroscopy. 5.26 g (9.97 mmol) 1,9-Bis(3,5-dimethylbenzoyl)-5-mesityldipyrromethane were obtained this way.

Yield: 5.26 g (9.97 mmol; 50 %)

Analysis: ESI-MS: m/z = 528.4 (M^+), 395.3 ([M-C_9H_9O]$^+$), 328.3 ([M-$C_{13}H_{14}ON$]$^+$), 196.2 ([M-$C_{22}H_{22}O_2N$]$^+$), 133.1 ($C_9H_9O^+$); ^{1}H-NMR (400 MHz, $CDCl_3$): 9.79 (s, 2 H, N-H), 9.41 (s, 4 H, o-Ph), 7.16 (s, 2 H, p-Ph), 6.92 (s, 2 H, m-Ph), 6.79 (m, 2 H, C_β-H close to Methyl-H), 6.12 (m, 2H, C_β-H), 6.06 (s, 1 H, Methyl-H), 2.36 (s, 12 H, m-Methyl), 2.31 (s, 3 H, p-Methyl), 2.17 ppm (s, 6 H, o-Methyl).

5.2.4.4 Synthesis of Benzyl 2-pyrrolecarboxylate.

0.94 g KOH (15mmol) were dissolved 10 mL H_2O and added to 1.67 g pyrrole-2-carboxylic acid (15mmol) in a round bottom flask. Then, 250 mL of H_2O were added, and the mixture was heated to 40 °C until all of the pyrrole-2-carboxylic acid was dissolved, forming pyrrole-2-carboxylate. The water was then removed in vacuum. The pyrrole-2-carboxylate was placed in a 25 mL round bottom flask, and 1.7 mL of benzyl bromide (15 mmol) and 0.46 mL Aliquat® 366 (trioctylmethylammonium chloride, 1 mmol) were added, and the mixture was shaken for 15 min. After shaking, the flask was heated to 45 °C for 12 h. Then, 20 mL of diethyl ether were added and the solution was filtered through a pad of Florisil® (activated magnesium silicate). The ether was removed in vacuum, and the obtained raw product was purified by column chromatography (silica gel) using a 4:1 mixture of hexane/ethyl acetate as eluant. 2.96 g pure, white benzyl 2-pyrrolecarboxylate were obtained this way.

Yield: 2.96 g (14.7 mmol, 98 %; Lit.:[16] 87 %)

Analysis: ^{1}H-NMR (300 MHz,$CDCl_3$): 9.13ppm (br s, 1H, NH), 7.33ppm (m, 5H, Benzyl-H's), 6.96 (m, 2H, $H_{pyrrole}$-3,5), 6.25 (m, 1H, $H_{pyrrole}$-5), 5.29 ppm (s, 2H, CH_2-Benzyl).

5.2.4.5 Synthesis of 1,8-Bis[5,5'-bis(benzyloxycarbonyl)-2,2'-dipyrrolemethyl]anthracene.

10 mL absolute ethanol and 0.094 mL concentrated HCl were degassed with argon for 30 min. To this solution, 100 mg 1,8-diformylanthracene (0.45mmol) and 344 mg benzyl-2-pyrrolecarboxylate (1.8mmol) were added, and heated to reflux under argon for 5 h. The solution was allowed to cool down and placed in the freezer overnight, then filtered, and washed with cold methanol. After drying in vacuum, 324 mg 1,8-bis[5,5'-bis(benzyloxycarbonyl)-2,2'-dipyrrolemethyl]anthracene were obtained. The product was confirmed by mass spectrometry (m/z of $[M+Na]^+$ at 1025.5 with the correct isotope pattern). However, the ^{1}H-NMR spectrum showed impurities and in addition, the mass

spectrum showed species with a higher mass than the product (for example at m/z = 1442.6).

Yield: 324 mg

Analysis: ESI-MS (with Na^+ added): m/z = 1025.5 $[M+Na]^+$.

5.2.4.6 Synthesis of 1,8-Bis(-2,2'-dipyrrolemethyl)anthracene (Hydrogenation)

The hydrogenolysis of 600 mg 1,8-bis[5,5'-bis(benzyloxycarbonyl)-2,2'-dipyrrolemethyl]anthracene (0.59 mmol) was carried out in an Erlenmeyer flask containing 25 mL methanol, 0.24 mL triethylamine, and 119 mg 10% Pd/C under H_2 at normal pressure. The reaction mixture was slightly heated to approximately 40 °C, and stirred for 6 h in an H_2 atmosphere. The mixture was then filtered through Celite to remove the catalyst. The solvent was removed in vacuum to yield 346 mg product (92 %). The product was confirmed by mass spectrometry to be 1,8-bis(5,5'-dicarboxy-2,2'-dipyrrolemethyl)anthracene (the tetracarboxylate). However, the ^{1}H-NMR spectrum of the crude product showed impurities and was not conclusive. The tetracarboxylate was then refluxed in ethanolamine for 5 h. The hot solution was poured into ice water, but no 1,8-bis(-2,2'-dipyrrolemethyl)anthracene was obtained this way. The product obtained after the hydrogenation seemed to be the tetracarboxylate, based on the mass spectrum and the low solubility in organic solvents. Therefore, it seems that the problem with the synthesis was actually the decarboxylation. In order to further clarify this point, we decided to synthesize the desired 1,8-bis(-2,2'-dipyrrolemethyl)anthracene product in a different way (direct synthesis; cf. Section 5.2.4.7) and then to use the analytic results for the product to improve the synthetic procedure for the hydrogenolysis/decarboxylation, which is supposed to give approximately 99 % yield.

5.2.4.7 Synthesis of 1,8-Bis(-2,2'-dipyrrolemethyl)anthracene (direct synthesis).

In a Schlenk flask, 350 mL chloroform and 2.6 mL absolute ethanol were degassed for 40 min. Then, 0.89 mL pyrrole (12.9 mmol) and 40 mg $MgBr_2$ (215 mmol) were added. Finally, 100 mg 1,8-diformylanthracene (0.43 mmol) in 20 mL degassed chloroform were

added over 1 h to the pyrrole solution using an addition funnel. After complete addition of the 1,8-diformylanthracene, the reaction mixture was stirred for 1.5 h. The reaction was then quenched by adding 9 mg NaOH (0.22 mmol) to the solution, then stirred for 1 h, filtered, and finally dried in vacuum. The obtained raw product was purified by column chromatography (silica gel) using a 12:1 mixture of chloroform/ethyl acetate as eluant. 81.3 mg pure 1,8-bis(-2,2'-dipyrrolemethyl)anthracene were obtained this way.

Yield: 81.3 mg (0.174 mmol, 40 %)

5.2.5 Metallation of H_4DPA and Nitrosylation of the corresponding Metalloporphyrin.

Metallation was achieved by adding the corresponding MCl_2 (M = Co, Fe) salt to a boiling solution of H_4DPA in DMF. The metalloporphyrin was purified using column chromatography. $[Co_2(DPA)(NO)_2]$ was synthesized by dissolving $[Co_2(DPA)]$ in $CHCl_3$, followed by stirring the solution in an NO atmosphere. In order to obtain the Fe(II)-NO complex, autoreduction was achieved by adding methanol to the reaction mixture.

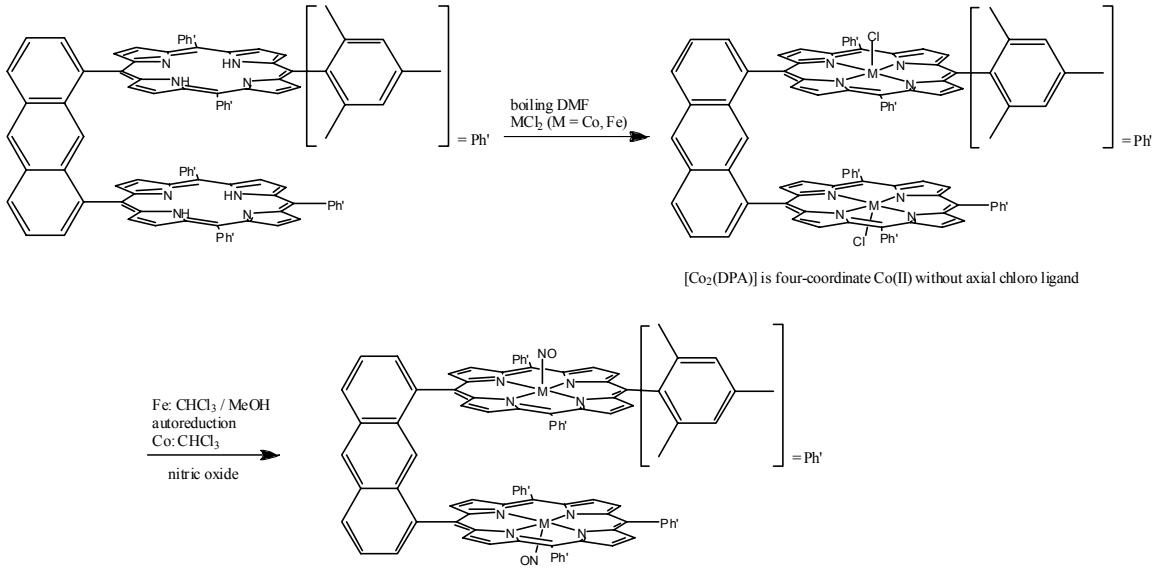

Figure 5.2.4. Metallation and Nitrosylation of cofacial porphyrins.

5.2.5.1 Synthesis of (1,8-Bis(5-tris(10,15,20-mesitylporphyrinyl))anthracene)bis-cobalt(II) [Co_2(DPA)]).

About 200 mg (0.133 mmol) H_4DPA were dissolved in 150 mL freshly distilled DMF (dried over CaH_2) and refluxed under an argon atmosphere. Then, about 520 mg (30 equivalent, 3.99 mmol) $CoCl_2$ were added to the boiling solution. After 45 min, another 210 mg (12 equivalents, 1.62 mmol) $CoCl_2$ were added, and refluxed for an additional 45 min. The reaction mixture was then cooled in an ice bath. Then, 150 mL H_2O were added, and the solution became cloudy orange-red. The reaction mixture was placed for 2 d in the refrigerator and filtered, but no precipitate could be obtained. Extraction with dichloromethane (4x) yielded a red-brown solution, which was washed once with water, dried over sodium sulfate, and filtered. The solvent was evaporated in vacuum. The raw product was then purified using column chromatography (silica gel, CH_2Cl_2), which lead to 158 mg (0.098 mmol) pure [Co(DPA)]. The product was then characterized using UV-Vis absorption spectroscopy and ESI-MS spectrometry.

Yield: 158 mg (0.098 mmol; 73 %)

Analysis: ESI-MS: m/z = 1617.6 (M^+); UV-Vis (CH_2Cl_2), λ_{max} (nm): 409 (Soret), 531 (Q_v), about 565 (Shoulder, Q).

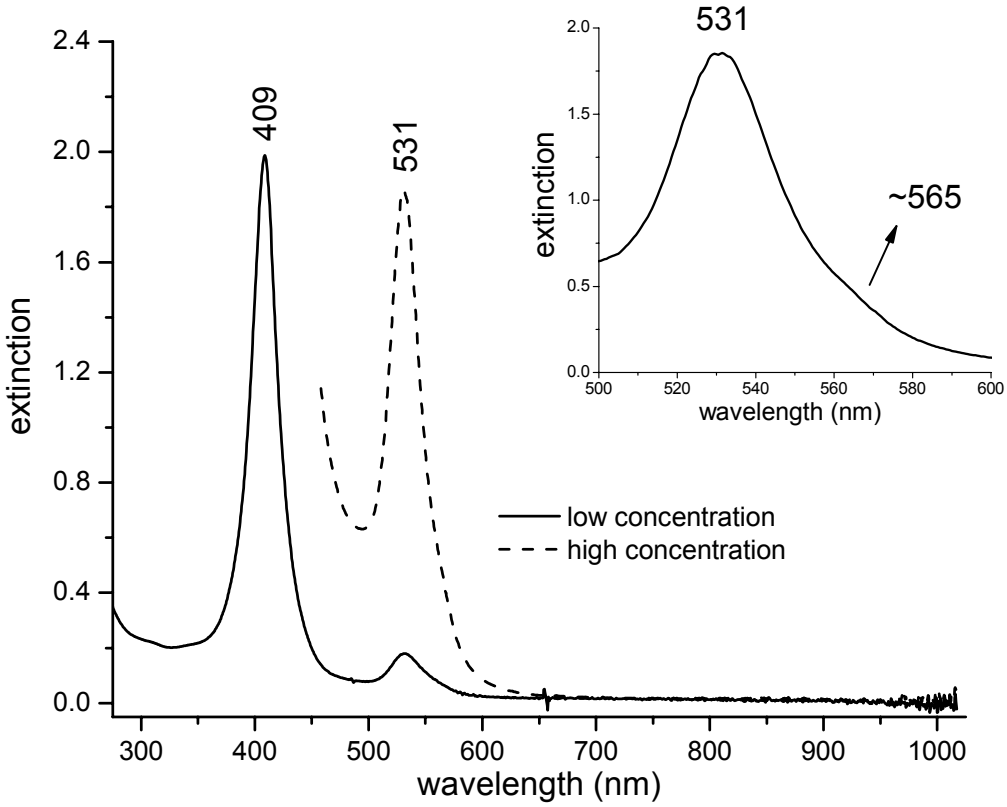

Figure 5.2.5. UV-Vis absorption spectrum of [Co_2(DPA)] measured in dichloromethane at room temperature.

5.2.5.2 Synthesis of Bis-chloro-(1,8-Bis(5-tris(10,15,20-mesitylporphyrinyl))-anthracene)bis-iron(III) [Fe_2(DPA)$(Cl)_2$]).

43.8 mg (0.029 mmol) H_4DPA were dissolved in 30 mL freshly distilled DMF (dried over CaH_2), and heated to reflux in an argon atmosphere. 115 mg (31 equivalent, 0.91 mmol) $FeCl_2$ (anhydrous) were added to the boiling solution, refluxed for 90 min, and then cooled in an ice bath. The reaction mixture changed its color from brown to yellow-brown. Then, 30 mL 0.1 M HCl were added and the mixture was placed in the refrigerator. After 1.5 d, a brown precipitate formed, which was filtered off. The raw product was purified using column chromatography (silica gel, CH_2Cl_2). Note that [Fe_2(DPA)$(Cl)_2$] reacts slowly with moisture during column chromatography to form the very stable, green μ-oxo dimer [{Fe_2(DPA)}$_2$O]. The combined [Fe_2(DPA)$(Cl)_2$] and [{Fe_2(DPA)}$_2$O] ractions were then shaken with 1 M HCl in a separation funnel in order

to convert the μ-oxo dimer back to $[Fe_2(DPA)(Cl)_2]$. The product was characterized using UV-Vis absorption spectroscopy and ESI-MS spectrometry.

Analysis: ESI-MS (in methanol) ; The ESI-MS was recorded in methanol, which coordinates to iron and replaces the two chloro ligands in $[Fe_2(DPA)(Cl)_2]$ to form $[Fe_2(DPA)(OMe)_2]$ (M = 1673.72 g mol^{-1}): m/z = 1674.6 (MH^+), 1659.6 (MH^+-Me) 1642.6 (M^+-OMe), 1628.5 (MH^+-OMe_2), 1612.5 (MH^+-$(OMe)_2$); UV-Vis (CH_2Cl_2), λ_{max} (nm): 371, 417(Soret), 510 (Q_v), 579, 603 and 691.

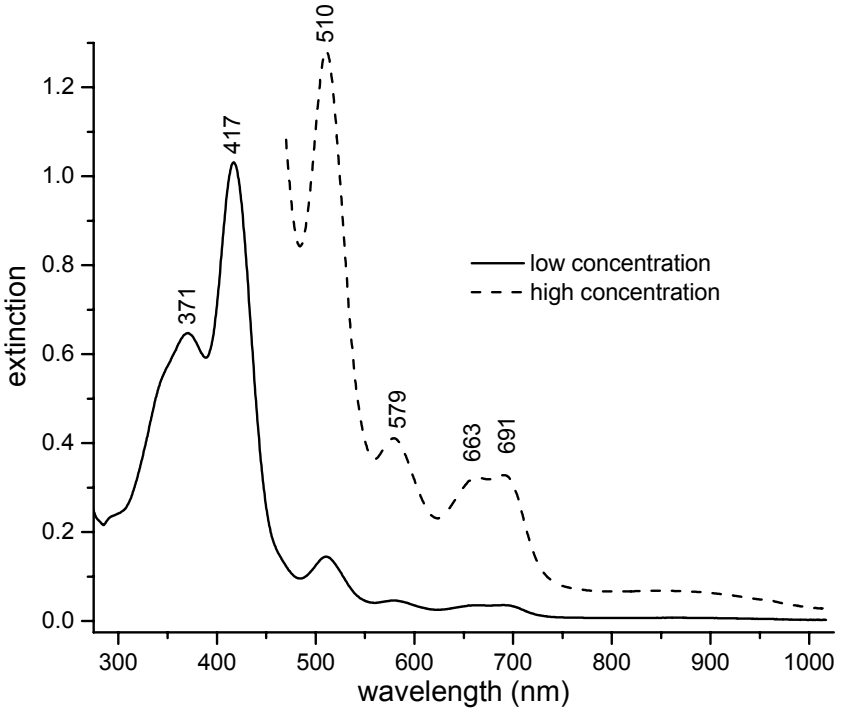

Figure 5.2.6. UV-Vis absorption spectrum of $[Fe_2(DPA)(Cl)_2]$ measured in dichloromethane at room temperature.

5.2.5.3 Synthesis of $[Co_2(DPA)(NO)_2]$.

155 mg (0.096 mmol) $[Co_2(DPA)]$ were dissolved in 20 mL dichloromethane in a schlenk flask. Nitric oxide was bubbled through the solution for 40 min, and the solution was then stirred for another 3 h 40 min in an NO atmosphere. In order to precipitate the corresponding nitrosyl complex, approximately 20 mL *n*-hexane were added via a

syringe, and the solution was then placed in the freezer at -30 °C for 3 d, but no precipitate was observed. Therefore, more *n*-hexane was added and the mixture was again placed in the freezer. Finally, a small amount of solid was formed and filtered off. The filtrate was collected and gently evaporated to dryness. The product was characterized using UV-Vis absorption, IR, and resonance Raman spectroscopy.

Analysis: IR (KBr disk): ν(N-O) = 1685 cm^{-1}; Raman ($\lambda_{exc.}$ = 457.9 nm); ν(N-O) = 1686 cm^{-1}; UV-Vis (CH_2Cl_2), λ_{max} (nm): 414 (Soret, broad), 545 (Q_v) and 594 (Q, shoulder).

Other cobalt porphyrins in comparison: (a) [Co(TMP)(NO)]: IR (KBr disk): ν(N-O) = 1682 cm^{-1}. (b) Co(TPP)(NO): IR (KBr disk): ν(N-O) = 1698/1683 cm^{-1};[7] Raman (pure solid, $\lambda_{exc.}$ = 1064 nm): ν(N-O) = 1698 cm^{-1};[7] Raman (KBr disk, $\lambda_{exc.}$ = 488 nm): ν(N-O) = 1696 cm^{-1};[7] UV-Vis: 414 (Soret, broad) and 540 (Q_v).[7]

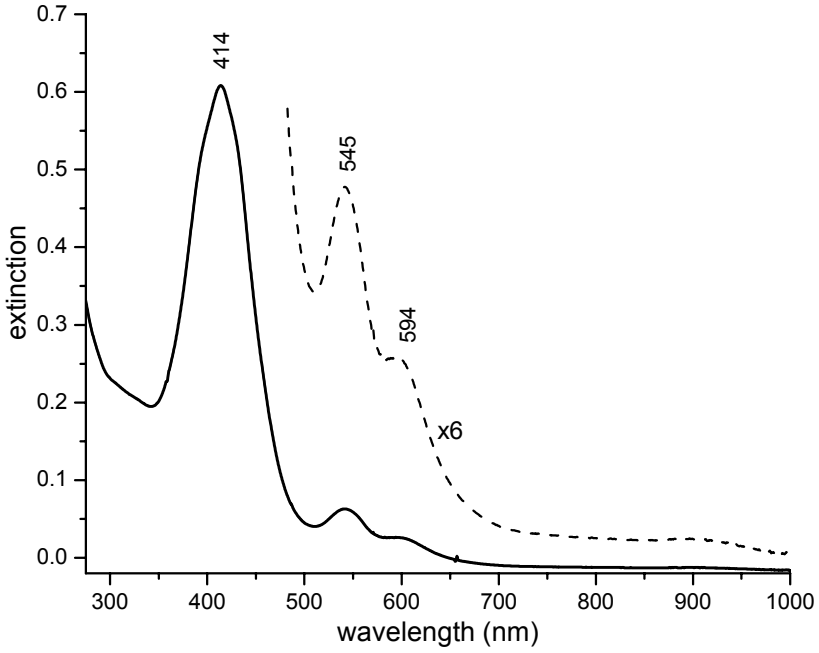

Figure 5.2.7. UV-Vis absorption spectrum of [Co_2(DPA)$(NO)_2$] measured in CH_2Cl_2 at room temperature.

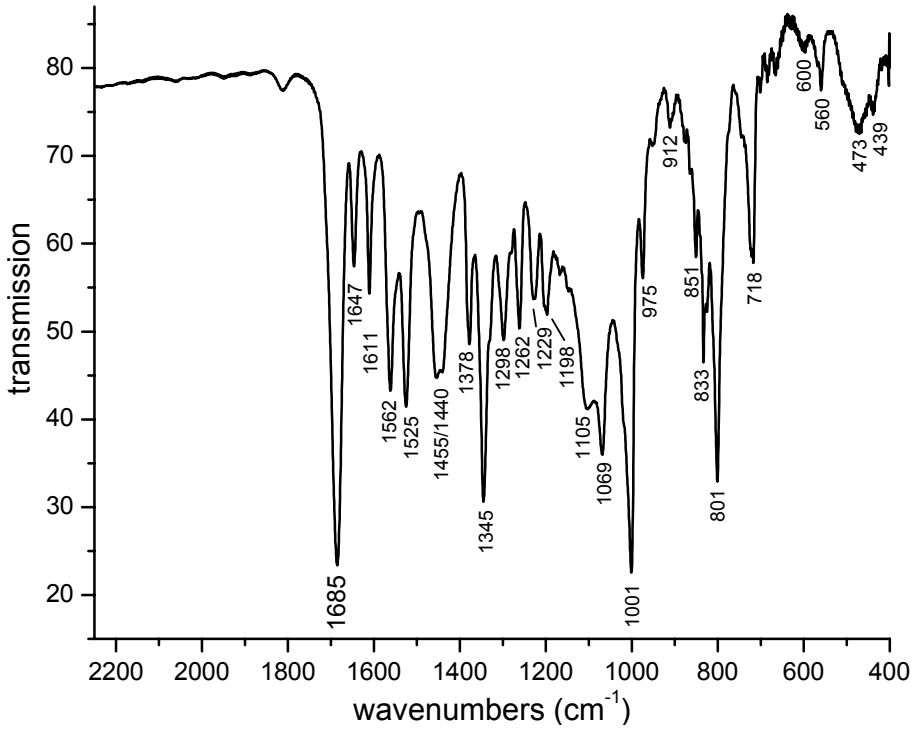

Figure 5.2.8. MIR spectrum of $[Co_2(DPA)(NO)_2]$ measured in KBr at room temperature.

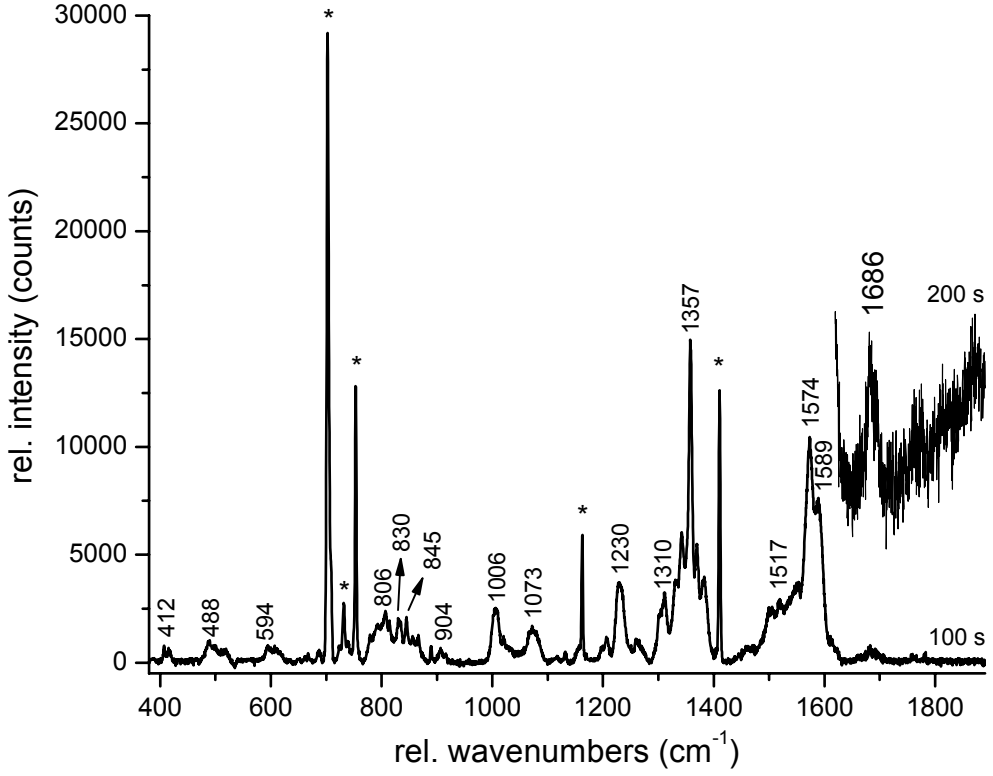

Figure 5.2.9. Resonance Raman spectrum of $[Co_2(DPA)(NO)_2]$ in frozen CH_2Cl_2 solution recorded at an excitation wavelength of 457.9 nm (pre-Soret resonance). Solvent peaks are marked as '*'.

5.2.5.4 Synthesis of $[Fe_2(DPA)(NO)_2]$

$[Fe_2(DPA)(Cl)_2]$ was dissolved in 1.5 mL chloroform and 0.15 mL methanol under an argon atmosphere using a schlenk flask. Then, gaseous nitric oxide was bubbled through the solution for 45 min, and the mixture was stirred for additional 3 h in an NO atmosphere. The color of the solution changed immediately from yellow-brown to red-brown. In order to precipitate the corresponding nitric oxide complex, about 3 mL *n*-hexane were added via a syringe, and the solution was placed in the freezer at -30 °C for 5 d. No precipitation occurred. The solvent was then gently evaporated yielding a dark oil. The IR spectrum obtained from the oil was not conclusive. Therefore, the oil was again dissolved in $CHCl_3$/methanol and stirred in nitric oxide for 3-4 h. Then, *n*-hexane was added and the reaction mixture was placed again in the freezer for three weeks. Unfortunately, again no precipitate could be obtained.

5.3 DFT Calculations

Besides the synthetic and spectroscopic work presented above, quantum chemical calculations were also performed in order to theoretically investigate the cofacial porphyrins in more detail. Importantly, these calculations provide information about the possibility of NO reduction by cofacial porphyrins, and also help to identify the most suitable linker for this purpose. This is very helpful for the design and synthesis of the optimal model system. These calculations have been performed on the B3LYP/LanL2DZ theoretical level (unless indicated otherwise). Note that geometry optimizations on metalloporphyrins using B3LYP/LanL2DZ lead to structures which are in good agreement with experiment (cf. Chapter 4: [M(TPP)(Cl)] with M = Fe, Co and Mn). This has been shown for five-coordinate [Fe(TPP)(NO)].**Fehler! Textmarke nicht definiert.**

5.3.1 Isomers of $[M_2(DPA)(NO)_2]$.

The N-N coupling step, which is necessary for the reduction of nitric oxide to nitrous oxide, requires that the two NO molecules have to be close at some point of the mechanistic cycle. Of course, this would require that the NO molecules bind inside the pocket formed by the two cofacial porphyrins. However, three different isomers for $[M_2(DPA)(NO)_2]$ exist theoretically as shown in Figure 3.1. In $[M_2(DPA)(NO)_2]_{o/o}$ both

NO molecules are bound outside (o/o) the pocket, whereas in $[M_2(DPA)(NO)_2]_{i/o}$ one NO is bound outside (o) and the other one inside (i) the pocket. The third isomer $[M_2(DPA)(NO)_2]_{i/i}$ corresponds to the complex where both NO molecules are located inside the pocket. In order to explore the relative energies of the individual isomers, the three different structures of the $[Co_2(DPA)(NO)_2]$ isomers have been fully optimized. In this case, Co(II) has the advantage over Fe(III) that the corresponding NO complexes are diamagnetic and therefore, spin restricted calculations can be applied. This makes the calculations much faster. The geometries were optimized using B3LYP/LanL2DZ, and then single point calculations (SP) on the optimized geometries were performed using the more "expensive" TZVP basis set, which leads to more accurate energies. These results are summarized in Table 3.1 and Figure 3.1.

From Figure 3.1, the o/o isomer is lowest in energy. Note that the energy of this isomer was set to zero, and all the other energies are therefore given relative to the o/o isomer. The i/o isomer is only 0.32 kcal/mol higher in energy (cf. Table 3.1), whereas the i/i isomer is 1.8 kcal/mol higher in energy. In general, these calculations show that the o/o isomer is favored, which is not surprising. This leads to the conclusion that the reaction of $[M_2(DPA)]$ with nitric oxide most likely generates the o/o isomer with NO bound outside the pocket. On the other hand, the calculations clearly show that the other isomers are relatively close in energy. This is important, because it implies that not much driving force is needed to make the NO molecules bind inside the porphyrin pocket.

For $[Fe_2(DPA)(NO)_2]$ two isomers have been optimized using B3LYP/LanL2DZ. In this case, iron is in the ferrous state and ls, and correspondingly, every Fe(II)-NO unit caries one unpaired electron. For simplicity, I have assumed ferromagnetical coupling for the calculations leading to an S = 1 total spin of the system. Since in this case the unrestricted approach has to be used for the calculations, the time consumption of these calculations dramatically increases. Therefore, only the i/i and the o/o isomers have been optimized. The calculated energy difference between these isomers is 1.56 kcal mol^{-1}, which is close to the value obtained for the $[Co_2(DPA)(NO)_2]$ isomers (vide supra). Important geometric parameters of $[Fe_2(DPA)(NO)_2]$ are given in Table 3.1.

Table 3.1. Comparison of Calculated Geometric Parameters (B3LYP/LanL2DZ) and Energies (SP with B3LYP/TZVP) for the isomers of $[M_2(DPA)(NO)_2]$ (M = Co, Fe).

Compound	E [kcal mol^{-1}] [a]	d(Co-Co) [Å]	$\angle(M_1\text{-}C_{anth,10}\text{-}M_2)$ [°] [b]	Dihed($C_{anth,4}$-$C_{anth,1}$-M-$C_{meso,90°}$) [°] [c]
$[Co_2(DPA)(NO)_2]_{o/o}$	0	5.9	61	93
$[Co_2(DPA)(NO)_2]_{i/o}$	0.32	6.2	64	94
$[Co_2(DPA)(NO)_2]_{i/i}$	1.79	6.5	67	126
$[Fe_2(DPA)(NO)_2]_{o/o}$ (S = 1)	0	6.1	63	102
$[Fe_2(DPA)(NO)_2]_{i/i}$ (S = 1)	1.56	6.2	64	123

[a] Energies are given relative to the o/o isomer. [b] $\angle(M_1\text{-}C_{anth,10}\text{-}M_2)$ gives the degree of parallel orientation of the porphyrin units. [c] Dihed($C_{anth,4}$-$C_{anth,1}$-M-$C_{meso,90°}$) is the dihedral angle between the anthracene and individual porphyrin planes, which measures the degree of twisting of the porphyrin planes with respect to the anthracene plane.

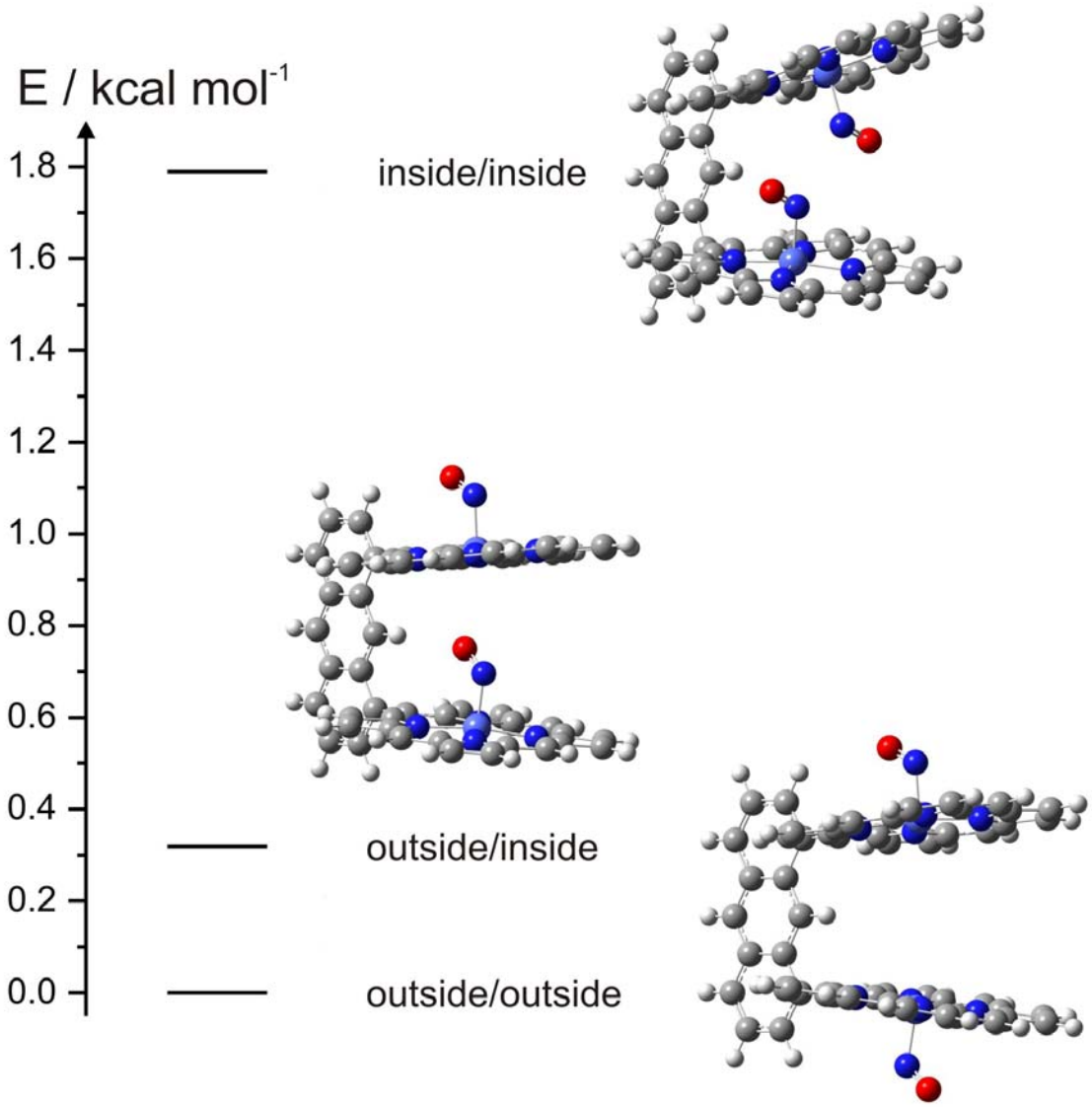

Figure 3.1. Energy diagram for the three isomers of $[Co_2(DPA)(NO)_2]$ obtained from SP calculations with B3LYP/TZVP on the B3LYP/LanL2DZ optimized structures.

5.3.2 Comparison of Intermediates in the Catalytic Cycle of NorBC using Different Spacer Units (i.e. DPA and DPB).

As described in the Introduction (Chapter 1), the mechanism of NO reduction by NorBC can be divided into four steps: a) initial coordination of NO, b) the formation of the N-N bond, c) cleavage of the N-O bond and d) release of nitrous oxide forming the μ-oxo dimer complex. Due to the high affinity of Fe(II) to NO, as described in Chapter 1, I assume that in the first step two molecules of NO are coordinated to each metal center in the cofacial porphyrin systems. Therefore, the *trans* mechanism proposed by de Vries and coworkers[17] (cf. Chapter 1) applies most likely to cofacial porphyrins, assuming that these systems are able to mediate the reduction of NO. The most important intermediate in the *trans* mechanism is the N-N coupled Fe-N_2O_2-Fe species, which corresponds to a bridged hyponitrite complex. In this study, calculations are used to investigate corresponding intermediates of the catalytic cycle applied to cofacial porphyrin model systems. From the initial calculations presented in Section 5.1 of this Chapter, the conclusion has been reached that the anthracene linked system (DPA) models the active site of NorBC best, based on the M-M distance. As shown above (Section 5.3.1), however, the cofacial porphyrins are quite flexible in their relative orientation by changing the bite angle ($\angle$(M-$C_{anth,10}$-M); cf. Table 3.1) and by twisting their planes with respect to the anthracene plane (Dihed($C_{anth,4}$-$C_{anth,1}$-M-$C_{meso,90°}$); cf. Table 3.1). Hence, the biphenylene bridged DPB cofacial system is also a reasonable platform and therefore, investigated here. The results obtained from the calculations for the different species involved in the coupling of two coordinated NO molecules are summarized in Table 3.2.

Table 3.2. Comparison of Calculated Geometries for different Co and Fe Complexes that are potentially relevant for the Mechanism of NorBC (B3LYP/LanL2DZ).

Compound	Distances in Å					Angles in degrees	
	d(M-M)	d(N_{NO}-N_{NO})	d(M-N_{NO})	d(N_{NO}-O)	d(M-N_{IM})	∠(M_1-$C_{anth,10}$-M_2)	Dihed($C_{anth,4}$-$C_{anth,1}$-M-$C_{meso,90°}$)
$[Co_2(DPA)(NO)_2]_{i/i}$ (S = 0)	6.47	3.37	1.85	1.21	-	67	126
$[Co_2(DPA)(N_2O_2)]$ (S = 0)	4.72	1.27	1.95	1.31	-	51	100
$[Co_2(DPA)(IM)_2(N_2O_2)]$ (S = 0)	4.91	1.33	2.01	1.31	2.03	52	109
$[Fe_2(DPA)(NO)_2]_{i/i}$ (S = 1)	6.17	3.43	1.74	1.21	-	64	123
$[Fe_2(DPA)(N_2O_2)]$ (S = 0)	4.77	1.79	1.79	1.23	-	51	112
$[Fe_2(DPA)(IM)_2(N_2O_2)]$ (S = 0)	5.03	1.74	1.90	1.23	2.03	53	130
$[Fe_2(DPA)(N_2O_2H)]^+$ (S = 0)	4.66	1.42	1.79/1.88 [b]	1.37/1.27 [b]	-	50	n.a. [c]
$[Fe_2(DPB)(IM)_2(N_2O_2)]$ (S = 0)	4.97	1.71	1.90	1.23	2.03	50[a]	104
$[Fe_2(DPB)(N_2O_2H)]$ (S = 0)	4.71	1.36	1.85/1.90 [b]	1.41/1.28 [b]	-	44[a]	100
$[Fe_2(DPB)(IM)_2(\mu$-oxo)] (S = 0)	3.57				2.05	35[a]	109

[a] In DPB this angle corresponds to ∠(M-C_1-M). [b] The first distance given corresponds to the one obtained for the protonated M-N-O-H unit. [c] In this case the porphyrin core is strongly deformed (doming).

Important conclusions resulting from the calculations shown in Table 3.2 are as follows:

1. As evident from the N-N distance (d(N_{NO}-N_{NO}); cf. Table 3.2) obtained for $[Co_2(DPA)(NO)_2]_{i/i}$ and $[Fe_2(DPA)(NO)_2]_{i/i}$, no interaction between the nitrogen atoms of the NO molecules exist. Instead, the nitrosyl molecules are repelling

each other, as evident from the distortion of the DPA ligand in the i/i isomers (d(M-M), d(N_{NO}-N_{NO}), ∠(M_1-$C_{anth,10}$-M_2) and Dihed($C_{anth,4}$-$C_{anth,1}$-M-$C_{meso,90°}$; cf. Table 3.2). Therefore, no spontaneous formation of the N-N bond takes place in the five-coordinate cases.

2. For the calculations on the hyponitrite intermediates, the input structures were obtained by placing $N_2O_2^{2-}$ (hyponitrite) between the metal centers in the $[M_2(DPA)]^{3+}$ fragment (M^{3+}-$N_2O_2^{2-}$-M^{3+}). The species obtained this way were fully optimized. Note that the hyponitrite intermediate $[M_2(DPA)(N_2O_2)]$ is 8.8 kcal/mol higher in energy compared to the corresponding i/i nitrosyl isomer $[M_2(DPA)(NO)_2]_{i/i}$ for cobalt and 15.7 kcal/mol for iron, respectively. In this case, the formation of an N-N bond is observed. This indicates a kinetic barrier for the N-N bond formation starting from two coordinated nitrosyls. Interestingly, binding of imidazole does not induce a decrease of the d(N_{NO}-N_{NO}) distance in $[M_2(DPA)(IM)_2(N_2O_2)]$ for both Co and Fe (cf. Table 3.2). Importantly, cobalt stabilizes the hyponitrite intermediate better than iron as reflected by the shorter N_{NO}-N_{NO} distances of 1.27 and 1.33 Å obtained for $[Co_2(DPA)(N_2O_2)]$ and $[Co_2(DPA)(IM)_2(N_2O_2)]$, respectively. This distance is in fact close to an N-N double bond (double bond: d(N=N) ≈ 1.25 Å and single bond: d(N-N) = 1.46 Å; from ref[18]). In contrast, d(N_{NO}-N_{NO}) in $[Fe_2(DPA)(N_2O_2)]$ (cf. Table 3.2) is 1.79 Å, which is due to the lower reduction potential of cobalt compared to iron. Therefore, in order to stabilize and study the $N_2O_2^{2-}$ intermediate, cobalt seems to be the better choice.
3. The formation of the N-N bond in the iron case can be enforced by protonation of $[Fe_2(DPA)(N_2O_2)]$, which leads to an N_{NO}-N_{NO} distance of 1.42 Å in $[Fe_2(DPA)(N_2O_2H)]^+$. This is close to the value of an N-N single bond (vide supra).
4. In the case of DPA as ligand the structure of the ferric μ-oxo dimer could not be optimized due to the large Fe-Fe distance in DPA. In contrast, using the biphenylene DPB ligand, the corresponding structure of the μ-oxo dimer could be obtained, and these results are shown in Table 3.2.

Outlook. The results obtained from the calculations suggest that the biphenylene system is actually the better platform to reduce NO to N_2O. In order to investigate the M-N_2O_2-M intermediate, however, the DPA system might be better. This intermediate can potentially be synthesized by reaction of $[M_2(DPA)]X$ (M = Co, Fe; X can, for example, be ClO_4^-, etc.) with HNO.

References

[1] (a) Collman, J. P.; Rapta, M.; Bröring, M.; Raptova, L.; Schwenninger, R.; Boitrel, B.; Fu, L.; L'Her, M. *J. Am. Chem. Soc.* **1999**, *121*, 1387-1388; (b) Collman, J. P.; Fu, L.; Herrmann, P. C.; Wang, Z.; Rapta, M.; Bröring, M.; Schwenninger, R.; Boitrel, B. *Angew. Chem.* **1998**, *110*, 3592-3595; (c) Obias, H. V.; van Strijdonck, G. P. F.; Lee, D.-H.; Ralle, M.; Blackburn, N. J.; Karlin, K. D. *J. Am. Chem. Soc.* **1998**, *120*, 9696-9697; (d) Kopf, M.-A.; Karlin, K. D. *Inorg. Chem.* **1999**, *38*, 4922-4923; (e) Franceschi, F.; Gullotti, M.; Monzani, E.; Casella, L.; Papaefthymiou, V. *Chem. Commun.* **1996**, 1645-1646; (f) Chishiro, T.; Shimazaki, Y.; Tani, F.; Tachi, Y.; Naruta, Y.; Karasawa, S.; Hayami, S.; Maeda, Y. *Angew. Chem.Int. Ed.* **2003**, *42*, 2788-2791

[2] Praneeth, V. K. K. *Dissertation*, Christian-Albrechts-Universität zu Kiel, Germany, *in preparation*.

[3] (a) Chang, C. K.; Abdalmuhdi, I. *J. Org. Chem.* **1983**, *48*, 5388-5390. (b) Naruta, Y.; Maruyama, K. *J. Am. Chem. Soc.* **1991**, *113*, 3595-3596. (c) Collman, J. P.; Hutchison, J. E.; Lopez, M. A.; Guilard, R. *J. Am. Chem. Soc.* **1992**, *114*, 8066-8073. (d) Naruta, Y.; Sasayama, M. *Chem. Commun.* **1994**, 2667-2668. (e) Deng, Y.; Chang, C. J.; Nocera, D. G. *J. Am. Chem. Soc.* **2000**, *122*, 410-411. (f) Cui, W.; Zhang, X. P.; Wayland, B. B. *J. Am. Chem. Soc.* **2003**, *125*, 4994-4995.

[4] (a) Collman, J. P.; Hutchison, J. E.; Lopez, M. A.; Tabard, A.; Guilard, R.; Seok, W. K.; Ibers, J. A.; L'Her, M. *J. Am. Chem. Soc.* **1992**, *114*, 9869. (b) Bolze, F.; Gros, C. P.; Drouin, M.; Espinosa, E.; Harvey, P. D.; Guilard, R. *J. Organomet. Chem.* **2002**, *89*, 643-644. (c) Chang, C. J.; Deng, Y.; Shi, C.; Chang, C. K.; Anson, F. C.; Nocera, D. G. *Chem. Commun.* **2000**, 1355. (d) Chang, C. J.; Baker, E. A.; Pistorio, B. J.; Deng, Y.; Loh, Z.-H.; Miller, S. E.; Carpenter, S. D.; Nocera, D. G. *Inorg. Chem.* **2002**, *41*, 3102.

[5] Fukuzumi, S.; Okamoto, K.; Gros, C. P.; Guilard, R. *J. Am. Chem. Soc.* **2004**, *126*, 10441-10449.

[6] (a) Nicken, H.; *ACF-2 Praktikum*, Universität Kiel, **2006**. (b) Meier, C.; *ACF-3 Praktikum*, Universität Kiel, **2006**.

[7] Paulat, F. *Diploma thesis (Diplomarbeit)*, Christian-Albrechts-Universität zu Kiel, Germany, 2004.

[8] Collman, J. P.; Tyvoll D. A.; Chng, L. L.; Fish, H. T. *J. Org. Chem.* **1995**, *60*, 1926-1931.

[9] (a) Lindsey, J. S.; Schreiman, I. C.; Hsu, H. C.; Kearney, P. C.; Marguerettaz, A. M. *J. Org. Chem.* **1987**, *52*, 827-836; (b) Lindsey, J. S.; Wagner, R. W. *J. Org. Chem.* **1989**, *54*, 828-836.

[10] Rao, P. D.; Dhanalekshmi, S.; Littler, B. J.; Lindsey, J. S. *J. Org. Chem.* **2000**, *65*, 7323-7344. (b) Rao, P. D.; Littler, B. J.; Geier III, G. R.; Lindsey, J. S. *J. Org. Chem.*, **2000**, *65*, 1084-1092.

[11] Adler, A. D.; Longo, F. R.; Kampas, F.; Kim, J. *J. inorg.nucl. Chem.* **1970**, *Vol.32,* 2443-2445.

[12] Guilard, R.; Lopez, M. A.; Tabard, A.; Richard, P.; Lecomte, C.; Brandes, S.; Hutchison, J. E.; Collman, J. P. *J. Am. Chem. Soc.* **1992**, *114*, 9877-9889.

[13] House, H. O.; Hrabie, J. A.; VanDerveer, D. *J. Org. Chem.* **1986**, *51*, 921-929.

[14] Lindsey, J. S.; Wagner, R. W. *J. Org. Chem.* **1989**, *54*, 828-836.

[15] Laha, J. K.; Dhanalekshmi, S.; Taniguchi, M.; Ambroise, A.; Linsey, J. S. *Org. Process Res. Dev.* **2003**, *7*, 799-812.

[16] Barry, J.; Bram, G.; Petit, A. *Heterocycles* **1985**, *23*, 875-880.

[17] Girsch, P.; de Vries, S. *Biochim. Biophys. Acta* **1997**, *1318*, 202-216.

[18] Aylward, G. H.; Findlay, T. J. V. in *Datensammlung Chemie in SI Einheiten* (1998), 4th edition, Wiley-VCH, Weinheim, Germany.

6 Ferric Heme Nitrosyls

6.1 Scope of this Project

Ferric heme nitrosyl adducts occur as intermediates or as enzyme-product complexes in a number of proteins, such as nitrophorins (Np), cytochrome cd_1 nitrite reductase, nitric oxide synthase (NOS), and fungal nitric oxide reductase (P450nor). The observed biological Fe(III)-porphyrin NO adducts can be divided into two classes depending on the nature of the axial ligand coordinated in *trans* position to NO, which is either histidine or cysteine. The Np's (Np1-4 from *Rhodinus prolixus*) and the cytochrome cd_1 nitrite reductase have histidine bound *trans* to NO, whereas NOS, cNp (from *Cimex lectularius*) and P450nor have cysteine coordinated *trans* to NO. The occurrence of ferric instead of ferrous hemes is closely related to the individual functions of the proteins due to the much smaller affinity of NO to ferric compared to ferrous hemes. Note that the rates of NO loss are approximately 4-8 orders of magnitude smaller in ferrous hemes.[1] This is also the reason why ferrous heme NO adducts have been referred to as a 'dead end' of protein activity. However, the synthesis and spectroscopic characterization of ferric heme nitrosyls is challenging due to the low affinity of Fe(III) towards NO, and the high instability of the corresponding Fe(III)-NO adducts. Especially the *trans* thiolate coordinated ferric heme nitrosyls are extremely unstable. Hence, besides the model studies of Suzuki et al.[2] and Xu et al.[3], no other investigation on ferric heme nitrosyl model complexes with axial thiolate coordination are available in the literature. Suzuki et al. have synthesized a ferric NO picket fence porphyrin with axial benzthiolate ligation, which binds NO as evident by in-situ IR spectroscopy showing ν(N-O) at 1828 cm^{-1}. However, this complex could not be isolated and decomposes readily as evidenced by kinetic investigations.[4] Recently, Richter-Addo and coworkers were able to determine the first crystal structure of a model complex for the above mentioned *trans* thiolate coordinated ferric heme proteins.[3] They synthesized and structurally characterized the complex [Fe(OEP)(NO){S-2,6-$(CF_3CONH)_2C_6H_3$}] (**2H-NO**, OEP = octaethylporphyrin and S-2,6-$(CF_3CONH)_2C_6H_3$ = SR'; cf. Figure 6.1.1, left).

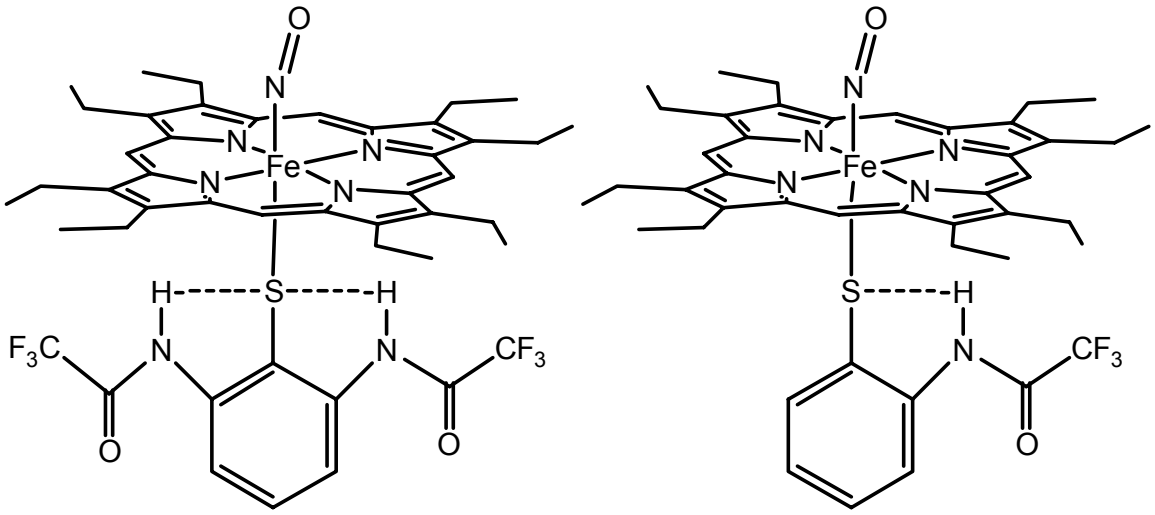

[Fe(OEP)(SR')(NO)] [Fe(OEP)(SR")(NO)]

Figure 6.1.1. Schematical illustration of [Fe(OEP)(SR')(NO)] (**2H-NO**) with two NH---S hydrogen bonds (left), and [Fe(OEP)(SR'')(NO)] (**1H-NO**) with one hydrogen NH---S bond (right).

Importantly, ferric heme nitrosyls with *trans* imidazole or pyridine coordination have linear Fe-N-O units, whereas thiolate coordination leads to a bent structure. Prior to the publication of the crystal structure of the model complex mentioned above, it was not clear whether this bending is due to electronic or steric effects induced by the protein. The crystal structure of **2H-NO** shows a bent Fe-N-O unit with an angle of 160°, which demonstrates an intrinsic bending of the Fe-N-O moiety due to electronic effects. The *trans* thiolate bound ferric heme nitrosyls in proteins and model complexes show low ν(N-O) stretching frequencies of 1800-1850 cm^{-1}, whereas *trans* imidazole or pyridine coordination leads to N-O stretching frequencies above 1900 cm^{-1}. Note that **2H-NO** could not be isolated from solution. The single crystals of [Fe(OEP)(SR')] (**2H**) were grown form CH_2Cl_2/hexane at room temperature and then reacted in a heterogeneous reaction with NO gas to give single crystals of **2H-NO**. Further investigations of **2H-NO** and related complexes are necessary to explore (a) the electronic effect of the thiolate on the Fe-NO unit, (b) the effect of the NH---S hydrogen bond strength on the coordinated nitric oxide, (c) the instability of **2H-NO** and **1H-NO** in solution, (d) to determine the missing vibrational data, importantly, the Fe-N(O) stretching vibration, and (e) to determine the N-O and Fe-N(O) force constants of the Fe-N-O unit.

These interesting points are addressed in this chapter. This work was partially conducted in collaboration with Prof. George B. Richter-Addo, Department of Chemistry and Biochemistry, University of Oklahoma, USA. Section 6.2 comprises the results from quantum chemical calculations on the effect of *trans* thiolate ligation on the coordinated nitric oxide in ferric heme nitrosyl complexes as a function of the thiolate donor strength, induced by variation of NH---S(thiolate) hydrogen bonds. Note that these results have been published recently in Inorganic Chemistry (2007). The results elaborated in collaboration with Prof. Richter-Addo are presented in Section 6.3. Here, the syntheses of the precursor compounds have been performed in the laboratory of Prof. Richter-Addo. The two precursor complexes, [Fe(OEP)(SR'] with two NH---S hydrogen bonds (**2H**; cf. left panel of Figure 6.1.1), and [Fe(OEP)(SR'')] with one NH---S hydrogen bond (**1H**; cf. right panel of Figure 6.1.1), were provided by the Richter-Addo group. I have synthesized the NO complexes **2H-NO** and **1H-NO** and in the case of **2H-NO**, the corresponding $^{15}N^{18}O$ isotope labeled complex (**2H-^{15}N^{18}O**). I have further spectroscopically characterized these complexes using in-situ UV-Vis absorption and resonance Raman (rRaman) spectroscopy. In order to substantiate the vibrational assignments, I have also performed a Normal Coordinate Analysis (QCC-NCA) on the **2H-NO** complex (cf. Section 6.3).

In addition to the studies on thiolate-bound ferric heme nitrosyls described above, I have also investigated the binding of NO to ferric hemes using potential energy surface (PES) calculations. These results are comprised in Section 6.4. For this investigation, ferric heme model systems with axial 1-methylimidazole (MI) coordination were used, because more experimental data are available from the literature in this case (vide supra), which can be compared to the quantum chemical results. Insight into the electronic structure of $[Fe(P)(MI)(NO)]^+$ is necessary to understand the PES results. Therefore, this electronic structure is included as Appendix (Section 6.4.5). The results presented in the Appendix were not elaborated by myself, and they are reproduced in this thesis with permission from Praneeth V. K. K. and my supervisor Prof. Dr. Nicolai Lehnert.[11]

6.2 Electronic Structure of Ferric Heme Nitrosyl Complexes with Thiolate Coordination

Florian Paulat and Nicolai Lehnert*

Published in: *Inorg. Chem.* **2007**, 46, 1547-1549.

Inorg. Chem. **2007**, *46*, 1547–1549

Electronic Structure of Ferric Heme Nitrosyl Complexes with Thiolate Coordination

Florian Paulat and Nicolai Lehnert*

Department of Chemistry, The University of Michigan, 930 N. University, Ann Arbor, Michigan 48109-1055

Received January 5, 2007

The effect of trans thiolate ligation on the coordinated nitric oxide in ferric heme nitrosyl complexes as a function of the thiolate donor strength, induced by variation of NH–S(thiolate) hydrogen bonds, is explored. Density functional theory (DFT) calculations (BP86/TZVP) are used to define the electronic structures of corresponding six-coordinate ferric [Fe(P)(SR)(NO)] complexes. In contrast to N-donor-coordinated ferric heme nitrosyls, an additional Fe–N(O) σ interaction that is mediated by the d_{z^2}/d_{xz} orbital of Fe and a σ^*-type orbital of NO is observed in the corresponding complexes with S-donor ligands. Experimentally, this is reflected by lower ν(N–O) and ν(Fe–N) stretching frequencies and a bent Fe–N–O moiety in the thiolate-bound case.

It is of great biological importance to explore the effect of trans thiolate coordination to heme nitrosyls in proteins and their corresponding model complexes. Nitric oxide (NO)-bound heme centers with axial cysteinate ligands are present in NO synthase (NOS),[1,2] the Cimex lectularius (bedbug) nitrophorin,[3] and the fungal nitric oxide reductase (P450nor).[4] Comparison of nitrosylation (on/off) rates shows that the thiolate ligand has a profound effect on the Fe^{III}−NO unit, but the electronic structural reasons for this finding are not clear.[5] In terms of other properties, it is known for a long time that ferric heme nitrosyls with trans imidazole or pyridine donors have linear Fe−N−O units and ν(N−O) of >1900 cm^{-1}. This has been observed in proteins and model complexes.[6] In contrast, thiolate coordination leads to a bent structure [$\angle$(Fe−N−O) = 161−165°], but it was not clear whether this is due to electronic or steric effects.[2,4] Recently, Xu et al. published the first X-ray structural characterization of the ferric nitrosyl heme thiolate model complex [Fe(OEP)(NO){S-2,6-$(CF_3CONH)_2C_6H_3$}] (**1**; OEP = octaethylporphyrin).[7] Importantly, the Fe−N−O unit is again bent with an angle of 160°, which demonstrates an intrinsic bending of the Fe−N−O moiety *due to electronic effects*. Another interesting feature of thiolate-coordinated ferric heme nitrosyls is the low ν(N−O) stretching frequency of 1800−1850 cm^{-1}. In order to determine the role of thiolate for the functions of the above-mentioned proteins, it is therefore of critical importance to explore the electronic effect of the thiolate on the Fe−NO unit.[8]

In this study, the effect of trans thiolate coordination on the coordinated NO as a function of the thiolate donor strength [induced by variation of NH−S(thiolate) hydrogen bonds] is explored for the first time. For this purpose, density functional theory (DFT) calculations (BP86/TZVP) have been performed on six-coordinate ferric [Fe(P)(SR)(NO)] (P = porphine^{2-}) complexes using benzene[2,6-bis(trifluoroacetamido)]thiolate (S-2,6-$(CF_3CONH)_2C_6H_3$ = **S1**) with *two hydrogen bonds* (**2**), benzene(2-trifluoroacetamido)thiolate (**S2**) with *one hydrogen bond* (**3**), thiophenolate (**S3**) with *no hydrogen bonds* (**4**), and, additionally, the strong donor methylthiolate (**5**) (cf. Chart 1).

The optimized geometric parameters for model **2** (cf. Figure 1) shown in Table 1 are in very good agreement with the crystal structure of compound **1**. Most notably, in all optimized structures, the Fe−N−O geometry is bent. In contrast, semiempirical SAM1 calculations by Scherlis et al. on the nitrosylated active site of ferric cytochrome P450 show a linear Fe−N−O group for the singlet ground state,[11] indicating that this method does not correctly describe the Fe−N−O geometry.

* To whom correspondence should be addressed. E-mail: lehnertn@umich.edu.

(1) Poulos, T. L.; Li, H.; Raman, C. S. *Curr. Opin. Chem. Biol.* **1999**, *3*, 131.
(2) Pant, K.; Crane, B. R. *Biochemistry* **2006**, *45*, 2537.
(3) (a) Walker, F. A. *J. Inorg. Biochem.* **2005**, *99*, 216. (b) Weichsel, A.; Maes, E. M.; Andersen, J. F.; Valenzuela, J. G.; Shokhireva, T. K.; Walker, F. A.; Montfort, W. R. *Proc. Natl. Acad. Sci. U.S.A.* **2005**, *102*, 594.
(4) Shimizu, H.; Obayashi, E.; Gomi, Y.; Arakawa, H.; Park, S.-Y.; Nakamura, H.; Adachi, S.-i.; Shoun, H.; Shiro, Y. *J. Biol. Chem.* **2000**, *275*, 4816.
(5) Cooper, C. E. *Biochim. Biophys. Acta* **1999**, *1411*, 290.
(6) Linder, D. P.; Rodgers, K. R. *Inorg. Chem.* **2005**, *44*, 1367.
(7) Xu, N.; Powell, D. R.; Cheng, L.; Richter-Addo, G. B. *Chem. Commun.* **2006**, 2030.
(8) Praneeth, V. K. K.; Haupt, E.; Lehnert, N. *J. Inorg. Biochem.* **2005**, *99*, 940.
(9) Allouche, A.; Pourcin, J. *Spectrochim. Acta A* **1993**, *49*, 571.
(10) Praneeth, V. K. K.; Naether, C.; Peters, G.; Lehnert, N. *Inorg. Chem.* **2006**, *45*, 2795.
(11) Scherlis, D. A.; Cymeryng, C. B.; Estrin, D. A. *Inorg. Chem.* **2000**, *39*, 2352.

10.1021/ic070023f CCC: $37.00
Published on Web 02/08/2007

Chart 1

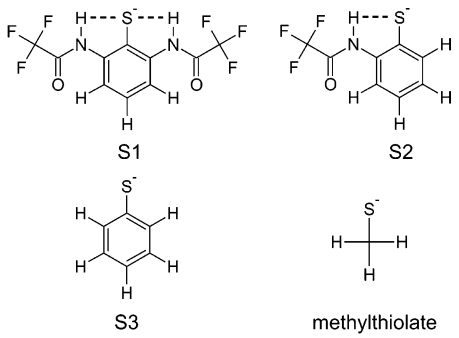

Chart 2

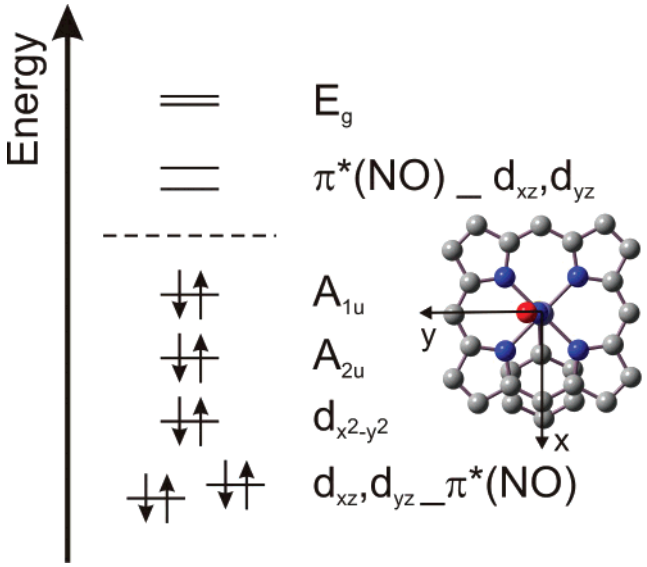

Ligands **S1** and **S2** show two and one hydrogen bond(s) between the thiophenolate S atom and the amido H atom(s), respectively [calcd Δ(S−H) ≈ 2.37 Å]. Corresponding hydrogen-bonding interactions in P450 enzymes are mediated by the cysteinate S atom and the protein backbone NH groups. Using sulfur K-edge X-ray absorption spectroscopy (XAS) and DFT calculations, Dey et al. showed that hydrogen bonding reduces the Fe−S bond covalency and the electron-donating power of the S atom.[12] This is in agreement with the shortening of the Fe−S bond and the increase of the *f*(Fe−S) force constant upon stepwise removal of the hydrogen bonds in the series **2** → **3** → **4** (cf. Table 1). Interestingly, this stepwise strengthening of the Fe−S bond goes along with a simultaneous weakening of the Fe−N(O) bond, giving the first evidence for a σ-trans effect of the coordinated thiolate on the Fe−N−O moiety.

To understand the σ-trans effect of the thiolate ligand in detail, the electronic structure of model complex **4** is analyzed. Figure S1 in the Supporting Information shows the obtained molecular orbital (MO) diagram for complex **4**, and charge contributions are given in Table S1 in the Supporting Information. In general, iron(III) heme nitrosyl complexes are known to have an $Fe^{II}NO^+$ electronic structure, and this also applies to complex **4**.[6,13] This electronic structure corresponds to an oxidation of NO upon binding to Fe^{III}. This is also observed for ruthenium(III) nitrosyls and has been extensively studied for these systems.[14] Therefore, in the case of **4**, Fe has a [d_{xz}, d_{yz}, $d_{x^2-y^2}$]^6 ≈ [t_2]^6 electronic configuration using the coordinate system shown in Chart 2. Both π^* orbitals of NO^+ are empty and undergo π-back-bonding interactions with d_{xz} and d_{yz} of Fe. The strength of this interaction is evident from the corresponding antibonding combinations π_h*_d_{yz}_p_z(S) ⟨129⟩ and π_v*_d_{z^2}/d_{xz} ⟨130⟩. MO ⟨130⟩ has 67% π_v* and 26% d orbital character, which corresponds to a very strong interaction. These very strong π back-bonds lead to a transfer of a significant amount of electron density from the d_{xz} and d_{yz} orbitals of Fe to the π^* orbitals of NO. Contour plots of these orbitals are shown in Figure S2 in the Supporting Information. The third t_2-type orbital of Fe, $d_{x^2-y^2}$ ⟨125⟩, is practically nonbonding (cf. Table S1 in the Supporting Information). This bonding situation is schematically shown in Chart 2. A weak σ interaction between σ_{nb} of NO and d_{z^2}/d_{xz} is also observed. The bonding combination σ_{nb}_d_{z^2}/d_{xz} ⟨76⟩ has 48% σ_{nb} and 9% d character. This electronic structure description is comparable to iron(III) heme nitrosyl complexes with trans N donors.[15] But, then why does the Fe−N−O unit bend in the presence of an axial thiolate? This is due to an additional Fe−N(O) σ interaction that is

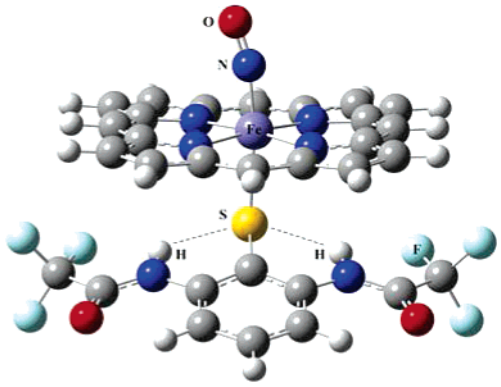

Figure 1. DFT (BP86/TZVP)-optimized structure of [Fe(P)(NO){S-2,6-$(CF_3CONH)_2C_6H_3$}] (**2**) showing two NH−S hydrogen bonds.

Table 1. Comparison of Calculated Geometries and Force Constants for Ferric [Fe(P)(SR)(NO)] Using BP86/TZVP

	geometric parameters (Å)			force constants[a]		
molecule	Δ(Fe−N)	Δ(Fe−S)	∠(Fe−N−O)	Fe−N	Fe−S	N−O
1 exp.[7]	1.672	2.356	159.7			
2 (2 HB)[b]	1.668	2.434	167	4.31	0.94	14.43
3 (1 HB)[b]	1.679	2.377	164	4.10	1.03	14.21
4 (0 HB)[b]	1.685	2.343	164	3.99	1.16	14.03
5[b]	1.691	2.300	164	3.87	1.40	13.96

[a] Force constants (in mdyn/Å) in internal coordinates were extracted from the Gaussian output using a modified version of the program Redong[9,10] (QCPE 628). [b] HB = hydrogen bond(s); calculated.

(12) Dey, A.; Okamura, T.; Ueyama, N.; Hedman, B.; Hodgson, K. O.; Solomon, E. I. *J. Am. Chem. Soc.* **2005**, *127*, 12046.

(13) (a) Averill, B. A. *Chem. Rev.* **1996**, *96*, 2951. (b) Enemark, J. H.; Feltham, R. D. *Coord. Chem. Rev.* **1974**, *13*, 339.

(14) (a) Bottomley, F. *Coord. Chem. Rev.* **1978**, *26*, 7. (b) Paulat, F.; Kuschel, T.; Näther, C.; Praneeth, V. K. K.; Sander, O.; Lehnert, N. *Inorg. Chem.* **2004**, *43*, 6979.

(15) Praneeth, V. K. K.; Naether, C.; Paulat, F.; Lehnert, N., in preparation.

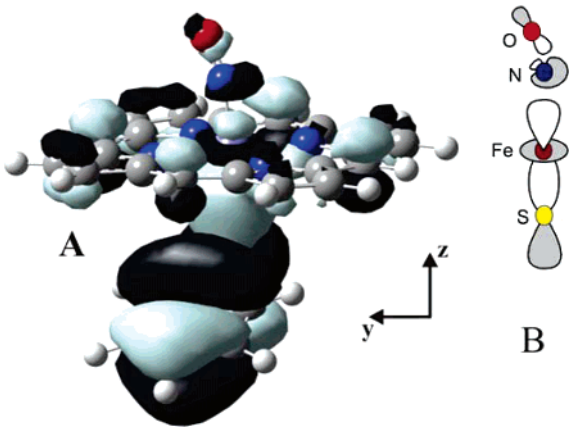

Figure 2. Contour plot of A_{2u} + $p_z(S)$_d_{z^2}/d_{xz}_σ^* ⟨124⟩ of compound **4** (A). Illustration of the contributions from the Fe−N−O moiety (B).

Table 2. Charge Contributions of the A_{2u} + $p_z(S)$_d_{z^2}/d_{xz}_σ^* MOs (⟨124⟩ and ⟨127⟩) Calculated with BP86/TZVP (in %)

	Fe	N		O		S
molecule	d	s	p	s	p	Σs
4[a] (optimized)	14.6	1.5	1.3	0	1.1	26.6
4a[a] (linearized **4**)	16.1	1.5	0.9	0	0.8	28.5
$[Fe(P)(MI)(NO)]^+$ (**6a**)[b]	1	0.2	0.1	0	0	2

[a] The values for compounds **4** and **4a** are the sums over the contributions from orbitals ⟨124⟩ and ⟨127⟩. [b] Reference 15 (MI = 1-methylimidazole); model complex **6a**, vide infra.

mediated by the d_{z^2}/d_{xz} orbital of Fe and a σ^*-type orbital of NO (MOs ⟨124⟩ and ⟨127⟩; cf. Figure S1 in the Supporting Information). The contour plot of MO ⟨124⟩ is shown in Figure 2A. Importantly, this orbital is *antibonding* with respect to both the Fe−N(O) and N−O bonds!

Charge contributions are 15% d and 4% σ^* (cf. Table 2), which corresponds to a weak antibonding interaction. This orbital is Fe−S σ bonding and also has porphyrin A_{2u} character.

Figure 2B illustrates schematically the orbital interactions for the Fe−N−O unit. In the case of complex **4a**, which is obtained by linearization of the Fe−N−O unit in **4**, no change to the composition of this orbital is observed. However, because of the increased overlap of d_{z^2} and σ^* in this case, it is effectively stronger Fe−N(O) antibonding than in the bent case. Hence, the bending of the Fe−N−O moiety slightly decreases the unfavorable Fe−N antibonding interaction and, hence, the bent structure **4** is about 1.6 kcal/mol lower in energy than the corresponding linear structure **4a**. Further evidence that this unfavorable orbital interaction is, in fact, responsible for the bending comes from a comparison with $[Fe(P)(MI)(NO)]^+$ [**6a**; MI = 1-methylimidazole; *f*(Fe−N) = 4.82 mdyn/Å],[15] which is the corresponding complex with *trans*-MI coordination. In this case, no such antibonding Fe−N(O) interaction is found, as shown in Table 2, and the complex is, in fact, linear (both experimentally and theoretically).

Table 3. Experimental and Calculated Vibrational Properties of Ferric Heme Nitrosyl Adducts in Proteins and Model Complexes[a]

molecule	ν(N−O), cm^{-1}	ν(Fe−N), cm^{-1}	ref
1	1850, 1839	n.o.	7
2 (calcd)	1859	604	this work
SR(III)[b]	1828	510	16a
P450nor(III)−NO	1853	530	16b
N-donor trans ligand:			
Mb(III)−NO[b]	1927	595	16c,d
$[Fe(TPP)(MI)(NO)]BF_4$ (**6**)	1911		15
$[Fe(OEP)(MI)(NO)]ClO_4$ (**7**)	1921		17

[a] Complete table: Table S2 in the Supporting Information. [b] SR = picket fence porphyrin model complex with an axial thiolate ligand; Mb = myoglobin.

Another consequence of the σ-trans effect of the thiolate ligand is the low ν(N−O) stretching frequency, as was already mentioned above (cf. Table 3). The ν(N−O) mode of complex **1** is ∼1850 cm^{-1} in solution (CH_2Cl_2) and 1839 cm^{-1} in solid state (reaction of [Fe(OEP)(S3)] powder with NO).[7] The calculated frequency for compound **2** is 1859 cm^{-1}, which is in excellent agreement with the experiment (calculated frequencies and force constants for N−O in models **2**−**5** are listed in Tables 1 and S2 in the Supporting Information). For P450nor, ν(N−O) is observed at 1853 cm^{-1} and ν(Fe−N) at 530 cm^{-1}. In comparison, ferric heme nitrosyls with trans N-donor coordination show ν(N−O) and ν(Fe−N) at 1927 cm^{-1} and 595 cm^{-1} ($Mb^{III}NO$), respectively. Model complex data are in agreement with this (cf. Table 3). Importantly, this shows that upon exchange of the trans N donor in ferric heme nitrosyls against a thiolate *both the Fe−N(O) and N−O vibrations decrease, implying that both bonds become weaker*. This direct correlation of Fe−N(O) and N−O bond strengths again shows that this must be related to a weakening of a σ bond[10] (a change in π backbonding would lead to an inverse correlation). This is another direct experimental proof that thiolate mediates a σ-trans effect on the coordinated NO. The reason for the lower ν(N−O) and ν(Fe−N) frequencies again relates to the interaction of d_{z^2} with σ^* of NO shown in Figure 2, which weakens *both* the Fe−N and N−O bonds relative to the ferric heme nitrosyls with trans N-donor coordination.

The difference between axial N- and S-donor-coordinated ferric heme nitrosyls is due to a σ-trans effect of the coordinated S on the bound NO mediated by an NO σ^* orbital. In this way, the Fe−N and N−O bonds are weakened, and Fe−N−O is bent in the S-coordinated case. This is reflected by lower ν(N−O) and ν(Fe−N) stretching frequencies in the presence of thiolate coordination.

Acknowledgment. F.P. acknowledges the Fonds der Chemischen Industrie (FCI) for a Chemiefonds fellowship.

Supporting Information Available: MO diagram for compound **4**, complete table of vibrational properties of ferric heme NO complexes, figures and tables of Cartesian coordinates of the optimized structures of **2**−**4**. This material is available free of charge via the Internet at http://pubs.acs.org.

IC070023F

(16) (a) Suzuki, N.; Higuchi, T.; Urano, Y.; Kikuchi, K.; Uchida, T.; Mukai, M.; Kitagawa, T.; Nagano, T. *J. Am. Chem. Soc.* **2000**, *122*, 12059. (b) Obayashi, E.; Tsukamoto, K.; Adachi, S.; Takahashi, S.; Nomura, M.; Iizuka, T.; Shoun, H.; Shiro, Y. *J. Am. Chem. Soc.* **1997**, *119*, 7807. (c) Benko, B.; Yu, N.-T. *Proc. Natl. Acad. Sci. U.S.A.* **1983**, *80*, 7042. (d) Miller, L. M.; Pedraza, A. J.; Chance, M. R. *Biochemistry* **1997**, *36*, 12199.

(17) Ellison, M. K.; Scheidt, W. R. *J. Am. Chem. Soc.* **1999**, *121*, 5210.

6.3 UV-Vis Absorption and Resonance Raman Spectroscopic Investigation of Thiolate Coordinated Ferric Heme Nitrosyls. (Collaboration with Prof. George B. Richter-Addo)

In this project the nitrosyl complexes of [Fe(OEP)(SR')] (two NH---S hydrogen bonds: **2H-NO**) and [Fe(OEP)(SR'')] (one NH---S hydrogen bond: **1H-NO**) were synthesized (cf. Figure 6.1.1). The reactions were monitored *in-situ* using UV-Vis absorption spectroscopy. In addition, resonance Raman (rRaman) spectra for **2H-NO** and the corresponding isotopically labeled complex **2H-^{15}N^{18}O** were recorded. Since the reaction of [Fe(OEP)(SR'')] (**1H)** with one equivalent of NO did not lead to a sufficient amount of nitrosyl complex for rRaman spectroscopy, no rRaman data are presented for **1H-NO**. Only mixtures of mostly **1H** with a small amount of **1H-NO** could be obtained. Note that this reaction was performed several times and hence, the results shown in Figure 6.4.4 represent the best data set obtained for this compound.

6.3.1 Syntheses of [Fe(OEP)(SR')(NO)] (2H-NO) and [Fe(OEP)(SR'')(NO)] (1H-NO) Followed by *in-situ* UV-Vis Spectroscopy.

The formation of [Fe(OEP)(SR')(NO)] (**2H-NO**) was monitored in CH_2Cl_2 solution at -40 °C using in-situ UV-Vis absorption spectroscopy. A solution of approximately 1.2 x 10^{-5} M **2H** in CH_2Cl_2 was placed in a 100 mL Schlenk tube and cooled to -40 ˚C using a acetone/dry ice bath. Then, approximately 1 equivalent of NO gas was injected via a microliter syringe. Figure 6.3.1 shows the spectral changes observed after NO addition. The absorption spectra were recorded every 2 min. The Soret band of the starting material at 380 nm decreases in intensity, and at the same time, a new Soret band appears at 430 nm. In addition, bands at 506, 534 and 636 nm of **2H** decrease in intensity, whereas new bands are observed at 536 nm and 567 nm. This corresponds to the formation of **2H-NO**. Moreover, isosbestic points at 407, 488, 513, 611 and 657 nm suggest a clean conversion of the starting material to the nitrosyl complex without further intermediates. After completion of the reaction, the mixture was stirred for an additional 40 min at -40 °C and importantly, no decomposition of **2H-NO** was observed. Then, a second equivalent of NO was added. The observed spectral changes are shown in Figure

6.3.2 (spectra were recorded every 2 min). Interestingly, in the presence of an additional equivalent of NO, a decomposition of the nitrosyl complex is observed. The Soret band of **2H-NO** at 430 nm decreases in intensity and at the same time, a new Soret band appears at 413 nm. In addition, bands at 536 nm and 667 nm of **2H-NO** decrease in intensity, whereas new bands are observed at 526 and 558 nm. The absorption spectrum of the new species is identical with that of [Fe(OEP)(NO_2)(NO)], which has been characterized by Scheidt and coworker (λ_{max} = 415, 528 and 560 nm).[5] Figure 6.3.3 summarizes the spectroscopic results obtained by the addition of one and two (or more) equivalents of NO to the starting material with two NH---S hydrogen bonds.

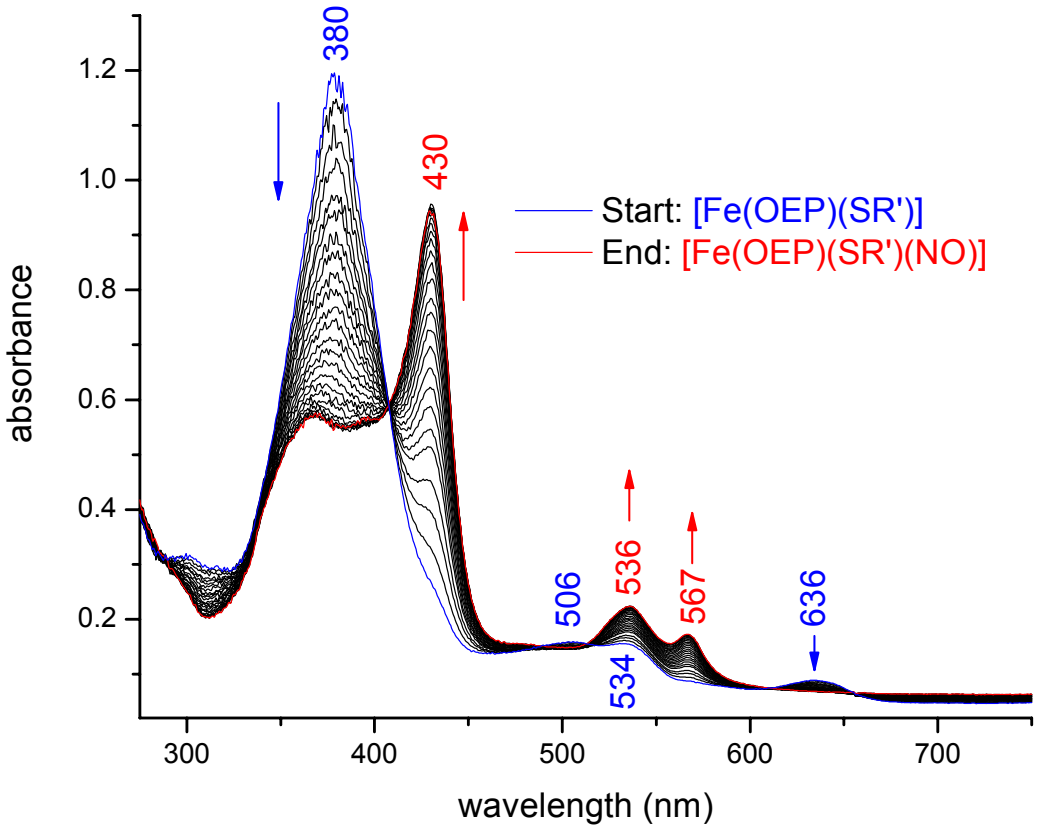

Figure 6.3.1. UV-Vis spectral changes for the reaction of **2H** (two H bonds, blue line) with approximately one equivalent of nitric oxide at -40 °C in CH_2Cl_2, forming the corresponding six-coordinate NO complex (430, 536 and 567 nm).

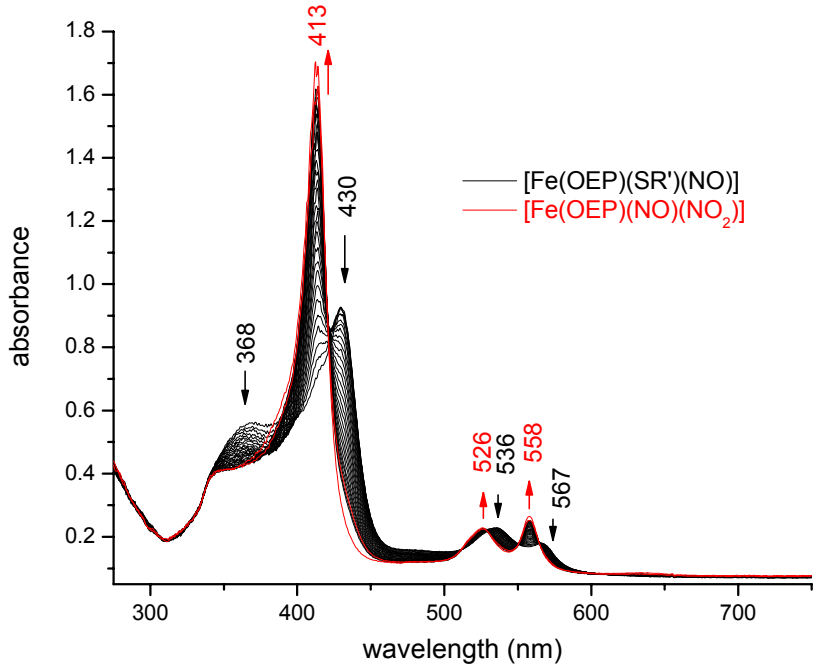

Figure 6.3.2: UV-Vis spectral changes for the reaction of **2H** (two H bonds) with ~2 equivalents and excess (15 equivalent) of nitric oxide at -40 °C in CH_2Cl_2, forming the six-coordinate complex [Fe(OEP)(NO_2)(NO)] (red line; 413, 526 and 558 nm).

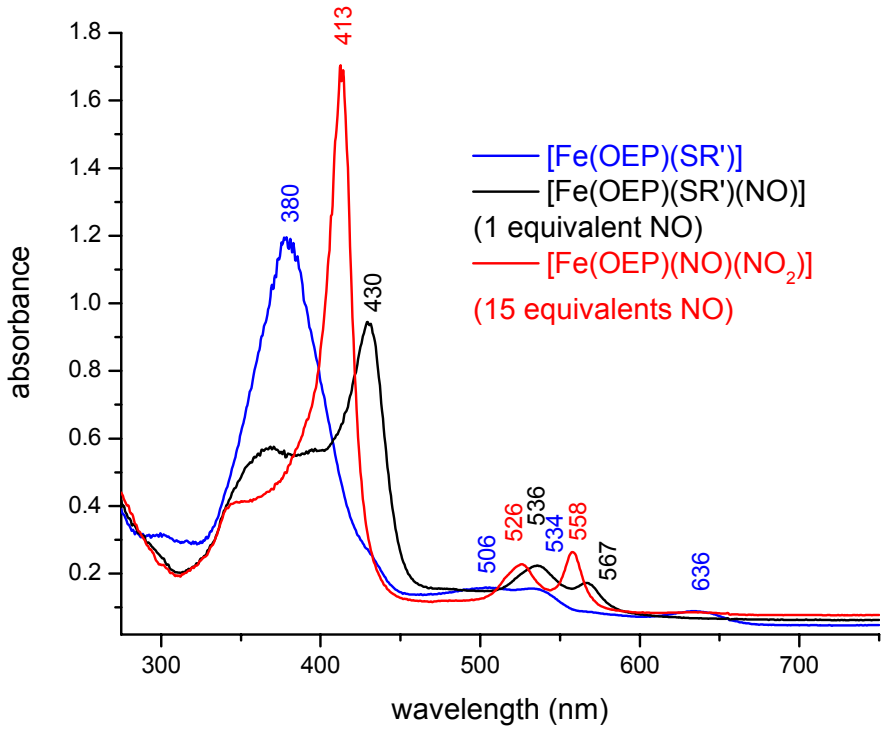

Figure 6.3.3. UV-Vis spectra (overview) of **2H** (SR' = two H bonds, XN-2-271, blue), [Fe(OEP)(SR')(NO)] (black), and [Fe(OEP)(NO)(NO_2)] (red).

In order to investigate how the stability of the NO complex changes upon the removal of one hydrogen bond, the complex [Fe(OEP)(SR'')] (**1H**), which only has one hydrogen bond (cf. Figure 6.1.1, right panel), was reacted with one equivalent of NO at -40 °C. Figure 6.3.4 shows the absorption spectrum of the starting material in black, which is similar to the spectrum obtained for complex **2H** with two hydrogen bonds, and the spectrum obtained after reacting **1H** with one equivalent of NO (shown in red). The Soret band of the starting material at 380 nm decreases after addition of NO and at the same time, a new band appears as a shoulder at 430 nm. In addition, new bands appear at 553 and 567 nm. The new species corresponds to the six-coordinate nitrosyl complex **1H-NO** in accordance to the experiments with **2H**. Importantly, in the case of **1H,** only weak spectral changes are observed and hence, the nitrosylation is not complete due to a lower stability of **1H-NO** as compared to **2H-NO**. Upon addition of a second equivalent of NO, the formation of [Fe(OEP)(NO_2)(NO)] (**3**) has been observed. Unfortunately, only a few percent of **1H** were actually nitrosylated in these experiments, which is insufficient for Raman measurements and therefore, ν(Fe-NO) could not be obtained for complex **1H-NO**.

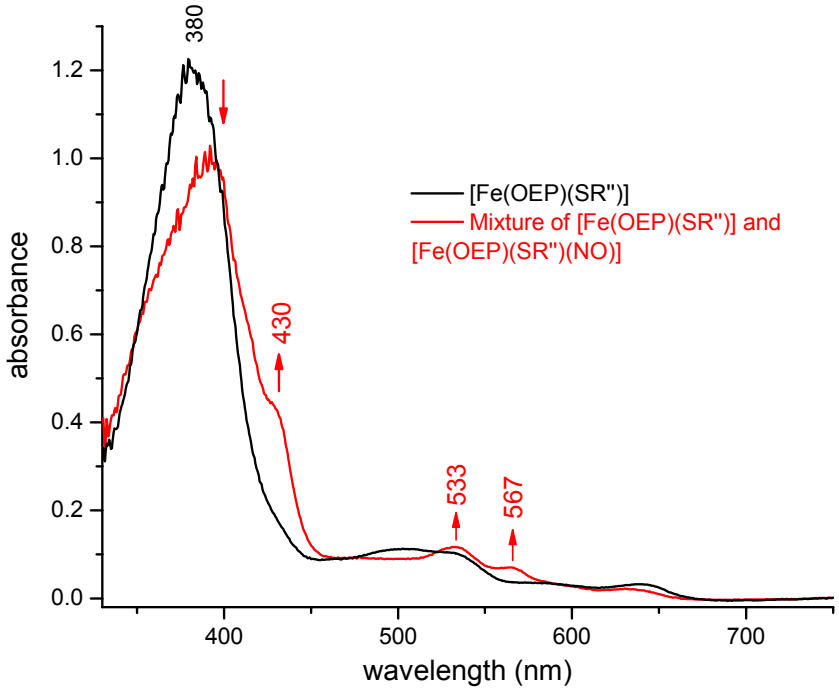

Figure 6.3.4. UV-Vis spectral changes for the reaction of **1H** (black line) with approximately one equivalent of NO at -40 °C in CH_2Cl_2, forming a mixture of **1H** and the corresponding six-coordinate NO complex (430, 533 and 567 nm, red line).

Mechanism of the Formation of [Fe(OEP)(SR')(NO)]. The formation of the nitrosyl complexes **2H-NO** and **1H-NO** corresponds to a simple binding of NO to **2H** and **1H**, respectively (cf. Scheme 6.3.1). The corresponding UV-Vis absorption spectra show a shift of the Soret band from 380 to 430 nm and importantly, several isosbestic points are observed indicating a clean conversion.

Scheme 6.3.1

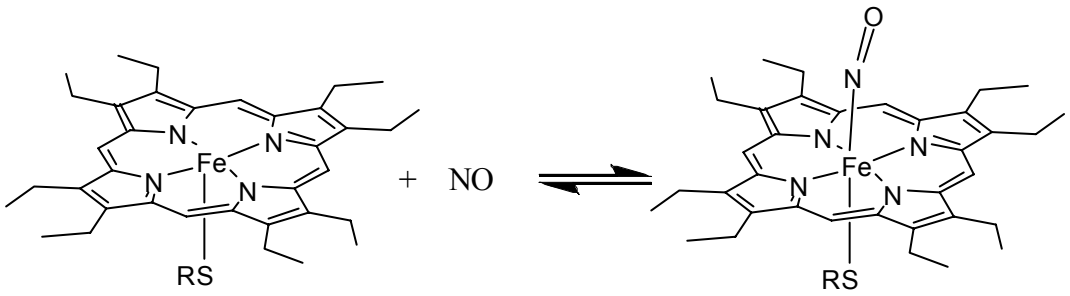

The binding of NO is reversible, which has been analyzed by the following procedure. First, **2H** was nitrosylated using approximately one equivalent of NO at -40 °C. The formation of **2H-NO** was monitored using *in-situ* UV-Vis spectroscopy. The solution was then warmed to room temperature causing the UV-Vis spectrum to change immediately back to the **2H** spectrum with the Soret band at 380 nm. The NO gas was removed from the reaction mixture by passing a stream of argon over the solution until the chloroform was completely evaporated. Then, a vacuum was applied for 15 min. The obtained residue was re-dissolved in $CHCl_3$ and then reacted with one equivalent of nitric oxide at -40 °C. The formation of **2H-NO** was again observed as evident from the characteristic shift of the Sort band.

Mechanism of the Decomposition of [Fe(OEP)(SR')(NO)]. In the presence of either a second equivalent or excess NO, the nitrosyl complexes of **2H** and **1H** decompose readily yielding [Fe(OEP)(NO)(NO_2)] (**3;** vide supra).

Mechanism A. A possible mechanistic scenario for this observation has been discussed recently.[6] Based on this, it is likely that the second molecule NO attacks the sulfur atom of benzene[2,6-bis(trifluoroacetamido)]thiolate (**S1**) and benzene(2-trifluoroacetamido)-

thiolate (**S2**), respectively. This leads to homolytic cleavage of the Fe-S bond yielding [Fe^{II}(OEP)(NO)] (**4**) and the corresponding S-nitrosothiol RS-NO. Complex **4** then reacts with N_2O_3 (or NO_2), which is always present in nitric oxide gas even after rigorous purification procedures,[6,7] to form the corresponding nitro-nitrosyl complex **3**.

Scheme 6.3.2

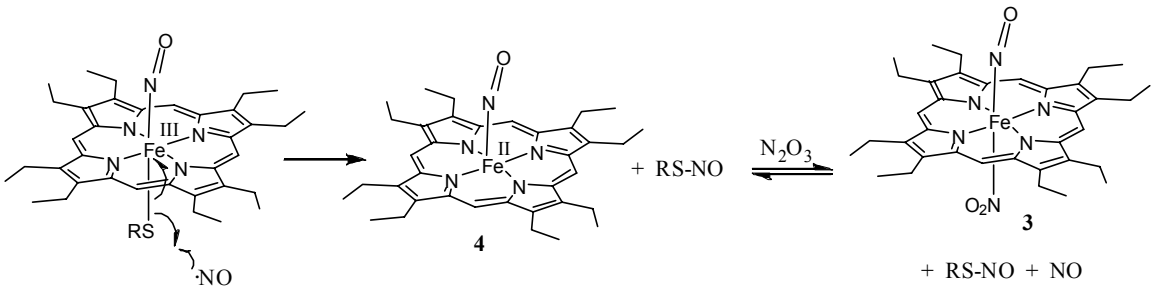

Mechanism B. In this case, homolytic cleavage of the Fe-S bond is independent of nitric oxide, forming a thiyl radical and the one-electron reduced ferrous complex [Fe(OEP)(NO)] (**4;** cf. Scheme 6.3.3). Subsequent radical coupling of the thiyl radical with excess NO leads to the formation of **3** and the S-nitrosothiol.

Scheme 6.3.3

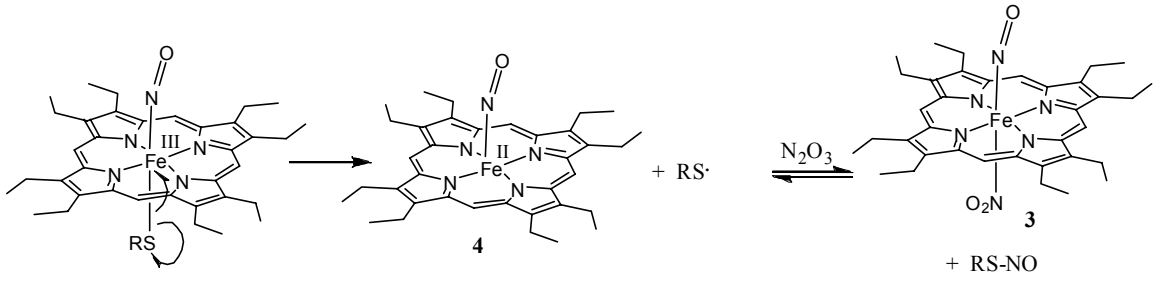

Mechanism B implies that the ferric NO adducts with *trans* thiolate coordination are unstable even in the absence of excess NO. Complex **2H-NO** was stable for at least 40 min after the addition of the first equivalent NO and therefore, no spontaneous decomposition was observed. This indicates that mechanism B is not applicable in this case. Since mechanism B was ruled out and considering the experimental evidence, the decomposition of **2H** and **1H** most likely follows mechanism A.

6.3.2 Resonance Raman Spectroscopy on 2H-NO. Ferric heme nitrosyls with *trans* thiolate coordination are extremely unstable. **2H-NO** and **1H-NO** react with traces of dioxygen under formation of complex **3**. Upon warming up, these complexes immediately lose NO (reversible binding of NO: vide supra). Therefore, the preparation of samples suitable for rRaman spectroscopy is challenging.

Sample preparations:

*Procedure for the preparation of the **2H-NO** rRaman sample*: 2.9 mg (3.15 x 10^{-3} mmol) of **2H** were dissolved in 4 mL CH_2Cl_2 and reacted with one equivalent of carefully purified NO gas, which was added using a microliter syringe. The complete conversion of the reaction was insured by stirring the reaction mixture for 1 h and 5 min. The solution was then transferred into an EPR tube using a syringe. Importantly, both the EPR tube and the syringe were cooled using dry ice before transferring the solution. After transferring the solution, the EPR tube was immediately frozen in liquid nitrogen. The concentration of **2H-NO** was 788 μM.

*Procedure for the preparation of the isotopically labeled **2H-^{15}N^{18}O** rRaman sample*: For the preparation of the isotopically labeled **2H-^{15}N^{18}O** complex, the same procedure as described above was used. In this case, $^{15}N^{18}O$ isotopically labeled nitric oxide was used. The concentration of the **2H-^{15}N^{18}O** sample was approximately 815 μM (3.0 mg **2H** in 4 mL CH_2Cl_2).

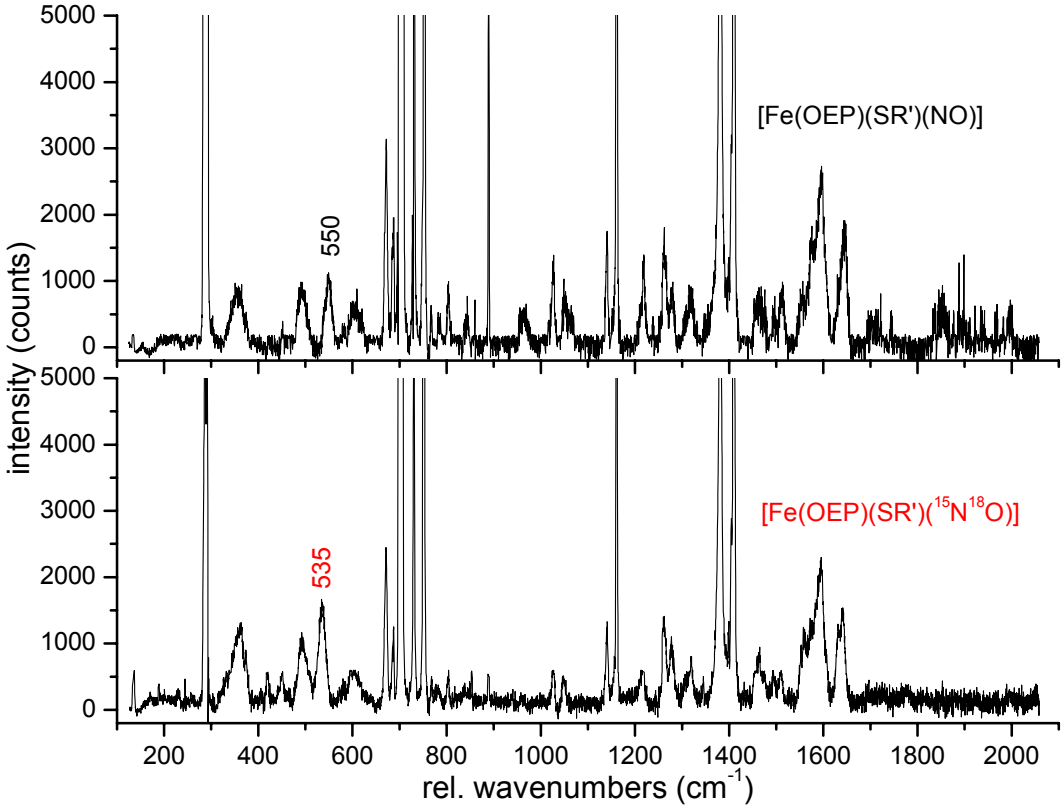

Figure 6.3.5. Resonance Raman spectra ($\lambda_{exc.}$ = 457.9 nm) of **2H-NO** (two NH---S hydrogen bonds) (top), and of the corresponding $^{15}N^{18}O$ isotopically labeled complex (bottom).

Figure 6.3.5 shows the rRaman spectra of **2H-NO** (top), and of the corresponding isotopically labeled complex **2H-^{15}N^{18}O** (bottom). The spectra were measured at liquid nitrogen temperature as frozen CH_2Cl_2 solutions. The excitation wavelength was 457.9 nm, which is in pre-resonance with the intense Soret band. The metal-ligand region of the spectra is shown in Figure 6.3.6. A strong band at 550 cm^{-1} is observed for **2H-NO** (black line), which shifts to 535 cm^{-1} in **2H-^{15}N^{18}O** (red line). This band is therefore assigned to the Fe-N(O) stretching vibration ν(Fe-NO). The observed isotopic shift of Δ = 15 cm^{-1} is in excellent agreement with the calculated shift of Δ = 17 cm^{-1}, which has been calculated using G03 and a modified version of the program redong[8,9] for the analysis of the Gaussian output (cf. Table 6.3.1). Note that for ν(N-O), an isotopic shift of 80 cm^{-1} is predicted (cf. Table 6.3.1). However, no infrared spectroscopic (IR) data of the isotopically labeled complex are available to date, and the determination of ν(N-O)

using resonance Raman spectroscopy is difficult due to the very low intensity of this mode in the Raman spectrum. This also applies to δ(Fe-N-O).

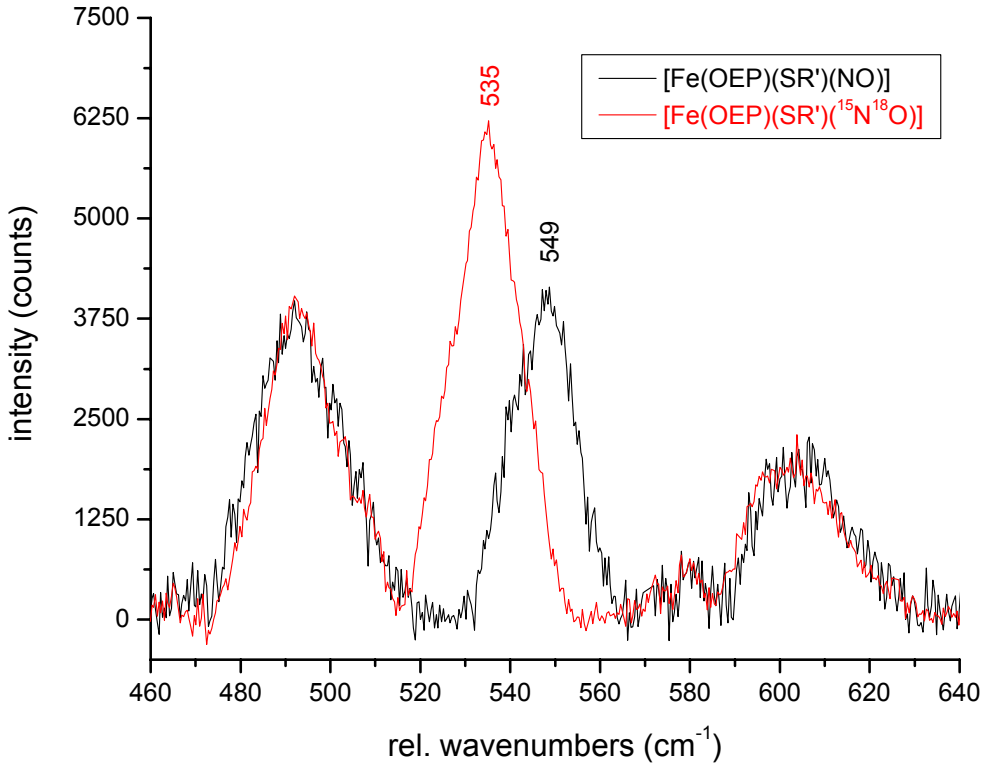

Figure 6.3.6. Resonance Raman (ν(Fe-$N_{(NO)}$) region) spectra ($\lambda_{exc.}$ = 457.9 nm) of **2H-NO** (two NH---S hydrogen bonds) (black), and of the corresponding isotopically labeled complex **2H-^{15}N^{18}O** (red).

6.3.3 Quantum-Chemistry Centered Normal Coordinate Analysis (QCC-NCA). The vibrational assignments presented above are further investigated using Normal Coordinate Analysis (NCA). Due to the size of the molecule, the initial force field was generated from the quantum chemical calculations. The OEP porphyrin ligand of the complex was substituted by porphine (P^{2-}) for the calculations. This simplification leads to a reasonable description of the Fe-NO subunit as has been shown for the TPP ligand in [Fe(TPP)(NO)].[6,10] The calculated force field of model [Fe(P)(SR'')(NO)] was therefore used for the NCA without further simplifications following the QCC-NCA approach. The results of the QCC-NCA are summarized in Table 6.3.2, which show excellent agreement with experiment.

Table 6.3.1. Comparison of Experimental and Calculated Vibrational Energies (in cm^{-1}) and Calculated Force Constants (in mdyn/Å) for Ferric [Fe(P)(SR)(NO)] (n.d. = not determined; n.a. = not available)

Compound	Vibrational energies						Calcd. force constants [a]		
	NO	$^{15}N^{18}O$	Δ	Fe-N	Fe-$^{15}N^{18}O$	Δ	Fe-N	Fe-S	N-N
2H-NO Exp.	1850, 1839 [b]	n.d.	n.a.	550	535	15	-	-	-
2H-NO	1859	1779 [c]	80	604	587 [c]	17	4.31	0.94	14.43
1H-NO	1840	n.d.	n.d.	591	n.d.	n.d.	4.10	1.03	14.21

[a] Force constants in internal coordinates were extracted from the Gaussian output using a modified version of the program Redong[8,9]. [b] ν(N-O) = 1850 cm^{-1} in CH_2Cl_2 solution and 1839 cm^{-1} in the solid state (reaction of **2H** powder with NO). Values for ν(N-O) are taken from ref[3]. [c] The vibrational energies for the isotopically labeled complex **2H-NO** were calculated using a modified version of the program Redong[8,9].

The mode at 550 cm^{-1} is a pure Fe-N(O) stretching vibration with 80 % ν(Fe-NO), 3 % ν(N-O) and 2 % δ_{ip}(Fe-N-O) character. The in-plane (δ_{ip}) and out-of-plane (δ_{oop}) Fe-N-O bending modes have not been identified experimentally to this date (vide supra). From the QCC-NCA approach, the δ_{ip}(Fe-N-O) mode is predicted to be at 584 cm^{-1}, and the out-of-plane mode is calculated at 596 cm^{-1}. Note that in the IR spectrum of [Fe(TPP)(1-MI) (NO)](BF_4) (1-MI = 1-methylimidazole), the band at 588 cm^{-1} has been assigned to δ(Fe-N-O) by our group due to an isotopic shift of this band to 572 cm^{-1} in the complex labeled with $^{15}N^{18}O$.[11] Since iron in [Fe(TPP)(1-MI) (NO)](BF_4) is also in the ferric oxidation state, the result for **2H-NO** obtained from the QCC-NCA treatment seems reasonable.

The N-O and Fe-NO force constants in [Fe(OEP)(SR')(NO)] obtained from QCC-NCA are 14.51 and 3.56 mdyn/Å, respectively (cf. Table 6.3.2). The calculated N-O force constant from DFT is in very good agreement with the NCA result, whereas the Fe-NO force constant is calculated too large (cf. Table 6.3.2). Correspondingly, the Fe-NO stretching frequency is obtained at too high energy from DFT. Importantly, this has also been observed for five-coordinate and six-coordinate ferrous heme nitrosyls[9] and

Copper(I) nitrosyls (cf. Section 7.4) indicating that DFT calculations using BP86/TZVP tend to overestimate the metal-NO bond strengths. In general, iron(III) heme nitrosyl complexes are known to have an $Fe^{II}NO^{+}$ electronic structure.[12] Two strong π backbonds between the two occupied d_π orbitals of iron and the unoccupied π* orbital of NO^{+} explain the large Fe-NO force constant obtained for **2H-NO**. In an earlier study, similar values of 15.4 mdyn/Å for the N-O bond and 5.0 mdyn/Å for the Ru-NO bond in $[Ru(NH_3)_5(NO)]Br_3$ were obtained, which exhibits a similar bonding situation.[13]

Table 6.3.2. Comparison of Experimental and QCC-NCA Vibrational Frequencies (in cm^{-1}) and of QCC-NCA and Calculated (DFT) Force Constants (in mdyn/Å)

Mode	Exp. frequencies		QCC-NCA frequencies		Force Constants f	
	n.a.i.[a]	$^{15}N^{18}O$	n.a.i.	$^{15}N^{18}O$	QCC-NCA	Calcd.[b]
ν(N-O)	1850	n.a.	1850	1769	14.51	14.43
ν(Fe-NO)	550	535	550	535	3.56	4.31

[a] n.a.i. = natural abundance isotopes. [b] Calculated with BP86/TZVP and extracted from from the Gaussian output file using a modified version of the program Redong[8,9] (cf. Section 6.2).

Interestingly, ferric heme nitrosyls have larger Fe-NO force constants than the corresponding ferrous hemes nitrosyl complexes. For example, [Fe(TPP)(NO)] has an Fe-NO force constant of 2.975 mdyn/Å obtained from QCC-NCA.[9] In contrast, the binding constant for NO in ferric heme systems ($K_{eq} = 10^3$ to 10^5 M^{-1}) is much smaller than in ferrous hemes ($K_{eq} = 10^{11}$ to 10^{12} M^{-1}).[14] Hence, the Fe-NO bond is thermodynamically stronger in ferrous than in ferric heme nitrosyls. But why is the Fe-NO force constant significantly larger in ferric heme compounds, and how does this relates to the stability of these complexes? This very important question is further investigated using potential energy surface (PES) calculations on six-coordinate ferric heme NO model systems. The surprising results of the PES calculations are presented in Section 6.4.

6.4 Binding of NO to Ferric Hemes: Potential Energy Surface (PES) Calculations.

In the so-called Enemark-Feltham scheme, the Fe(III)-porphyrin NO adducts are classified as $\{FeNO\}^6$ complexes where the exponent "6" refers to the number of d electrons plus the unpaired electron of NO.[15] The electronic structure of the $\{FeNO\}^6$ heme complexes with axial N-donor coordination has in general been described as Fe(II)-NO^+ (cf., for example, ref.[12]) in agreement with $\{RuNO\}^6$ systems where this electronic structure was observed before and has extensively been studied.[13,16] Hence, the Fe-NO interaction in these complexes is dominated by π backbonding from two t_2 type d orbitals ('d_π') of low-spin iron(II) into the unoccupied π^* orbitals of NO^+. This bonding description is analogous to the isoelectronic Fe(II)-CO complexes. A few crystal structures of Fe(III)-porphyrin NO model complexes have been determined including five-coordinate (5C) [Fe(OEP)(NO)](ClO_4) (OEP = octaethylporphyrin),[17] six-coordinate (6C) [Fe(OEP)(L)(NO)](ClO_4) (L = neutral N-donor ligands), and related systems.[18] These complexes show linear Fe-N-O units and extremely short Fe-NO bond lengths of 1.63 - 1.65 Å in agreement with the Fe(II)-NO^+ description. In addition, the N-O stretching vibrations in these complexes are usually found in the 1900 cm^{-1} region as shown in Table 6.4.1, which also reflects the coordinated NO^+. Hence, it was believed for a long time that the bonding description of $\{FeNO\}^6$ is fully analogous to Fe(II)-CO. However, in recent DFT studies it was found that the N-O and Fe-N(O) stretching vibrations in different Fe(III)-porphyrin NO adducts do *not* show an inverse correlation upon porphyrin substitution as the Fe(II)-porphyrin CO complexes,[19] but a direct correlation where an increase in ν(N-O) goes along with an increase in ν(Fe-NO) and vice versa. Therefore, *additional contributions to the Fe-NO bond must exist in these complexes besides the strong π backbond*.[20] Related to this, axial thiolate (cys) coordination to $\{FeNO\}^6$ in heme proteins and model complexes is known to induce bent Fe-N-O units ($\angle$(Fe-N-O) = 161-165°),[21, 22, 23] and lower N-O stretching frequencies of 1800 - 1850 cm^{-1}. In the study presented in Section 6.2, these differences have been attributed to a *trans* effect of the thiolate on the bound NO, leading to the occupation of an Fe-N-O σ antibonding orbital, which is responsible for the bending of the Fe-N-O unit

and the weakening of the Fe-NO and N-O bonds (cf. Section 6.2 and ref[24]). Interestingly, the same Fe-N-O σ antibonding orbital had also been identified in one of the above mentioned DFT studies (ref. 20a) as the reason for Fe-N-O bending upon porphyrin ring substitution in five-coordinate $[Fe(porphyrin)(NO)]^+$ complexes. In addition to these slight variations in the 'classic' π backbonding electronic structure model for heme $\{FeNO\}^6$ systems, it has been pointed out by Walker in a recent review [25] that the $\{FeNO\}^6$ formalism leaves room for an even wider variation in electronic structure: the Fe(III)-porphyrin NO adducts could also exhibit an Fe(III)-NO(radical) electronic structure, where the unpaired electrons of low-spin iron(III) and NO are antiferromagnetically coupled leading to the experimentally observed diamagnetic ground state. This would be advantageous for the nitrophorins, because it would prevent the autoxidation reaction of Fe(II)-NO^+ complexes,[26] which ultimately leads to ferrous NO adducts and hence, deactivation of the proteins as NO carriers. In order to understand the functioning of the nitrophorins and the nature of ferric heme NO interactions in general, it is necessary to elucidate the electronic structures of the formed Fe(III)-porphyrin NO adducts in detail. The established Fe(II)-NO^+ and the elusive Fe(III)-NO(radical) electronic structures, for example, will lead to very different reactivities. In addition, the formation of an Fe(II)-NO^+ complex from ferric heme and NO requires an NO to Fe(III) electron transfer. However, not much is known about the energetics and the mechanism of complex formation in these systems.

In this study, the mechanism and energy landscape of NO binding to ferric hemes and the possible variation in electronic structure of the formed complexes is investigated in detail. The binding of NO to ferric hemes is investigated using potential energy surface (PES) calculations. These results provide insight into (a) the relative stabilities of Fe(II)-NO^+ vs. Fe(III)-NO(radical) electronic structures, (b) the NO to Fe(III) electron transfer upon coordination of NO, and (c) the surprisingly large Fe-NO force constant in ferric hemes. In particular, it is demonstrated that the elusive Fe(III)-NO(radical) complex appears as a minimum on the PES. The biological implications of these results are discussed.

Table 6.4.1. Vibrational properties of ferric heme NO adducts in proteins and model complexes

Complex	ν(N-O) [cm^{-1}]	ν(Fe-NO) [cm^{-1}]	Reference
P450cam-NO	1806	528	27
P450cam-NO + adamantone	1818	520	27
SR-NO [a]	1828	510	28
P450nor-NO	1851	530	27a
CPO-NO [a]	1868	538	27a/29
iNOS-NO		537	30
[Fe(OEP)(NO)](ClO_4) [b]	1868/1838	611/600	17/20a
HRP-NO [a]	1903	604	31
NorBC-NO [a]	1904	594	32
rNp1-NO	1917	591	33/34
hHO-1-NO [a]	1918	596	35
[Fe(OEP)(MI)(NO)](ClO_4)	1921	-	18a
Hb-NO [a]	1925	594	36/31b
Mb-NO [a]	1927	595	37/31b
[Fe(TPP)(HO-*i*-C_5H_{11})(NO)](ClO_4)	1935	-	18d

[a] SR = picket fence porphyrin model complex with axial thiolate ligand; CPO = chloroperoxidase; HRP = horseradish peroxidase; NorBC = bacterial NOR; hHO-1 = human heme oxygenase-1; Hb = hemoglobin; Mb = myoglobin
[b] Data for the chloroform solvate and the corresponding solvent free complex, respectively

Scheme 6.4.1

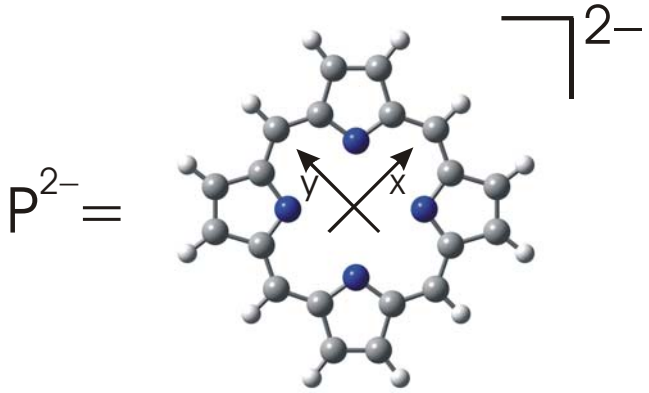

6.4.1 Density Functional Calculations. The structures of the models $[Fe(P)(MI)(NO)]^+$ ($\tilde{\mathbf{1}}$, S = 0), $[Fe(P)(MI)]^+$ (S = 1/2, 5/2) and [Fe(P)(MI)] (S = 0, 2) were fully optimized using BP86/TZVP. For these calculations, a simplified TPP ligand has been used where the four phenyl groups in *meso* position of the porphyrin ring have been replaced by hydrogen. The resulting porphine (P) ligand is shown in Scheme 6.4.1 along with the applied coordinate system. For the potential energy surface (PES) calculations, B3LYP/LanL2DZ geometry optimizations were applied using fixed Fe-NO distances. The Fe-N-O angle was fixed at 170° below 2.64 Å for the Fe(III)-NO(radical) (S = 0) PES. B3LYP/TZVP single points were also performed on the structures obtained from B3LYP/LanL2DZ. All these methods were used as implemented in Gaussian 03.[38] Orbitals were plotted using GaussView.

Electronic Structure of $[Fe(P)(MI)(NO)]^+$ ($\tilde{\mathbf{1}}$). In order to understand the PES results it is necessary to investigate the electronic structure of $\tilde{\mathbf{1}}$ and of the corresponding one electron reduced complex [Fe(TPP)(MI)(NO)] (Fe(II)-NO(radical)) first. As already mentioned above, this work is attributed to my colleague Praneeth V. K. K. and my supervisor Prof. Nicolai Lehnert. It is therefore included here as Appendix (vide infra), because these results are necessary for the understanding of the PES calculations.

6.4.2 Nitric oxide binding to ferrous and ferric porphyrin complexes. Calculations on the stability of the ferrous and the ferric NO complexes show that the formation of nitrosyl complexes is energetically more favorable for ferrous compared to ferric hemes by ~7.5 kcal/mol.[11] This number is equivalent to a difference in binding constant by a factor of 3×10^5. This is in excellent agreement with the experimentally determined trend in dissociation rate constants: for ferric heme systems, dissociation rate constants range from 0.65 to 40 s^{-1}, leading to a relatively small binding constant for NO ($K_{eq} = 10^3$ to 10^5 M^{-1}). In contrast, for Fe(II) systems, the dissociation rate constants are in the order of 10^{-4} s^{-1}, leading to very large binding constants for NO ($K_{eq} = 10^{11}$ to 10^{12} M^{-1}).[14] The calculated complex formation energies therefore show that the Fe-NO bond is thermodynamically stronger in ferrous compared to ferric heme NO adducts. This again

poses the question of why the Fe-NO force constant is so much larger in the ferric case, and how this relates to the complex stability.

6.4.3 Potential Energy Surface Calculations for the Interaction of NO with Ferric Heme. In order to obtain detailed insight into the mechanism of NO binding to five-coordinate ferric heme, we then performed potential energy surface (PES) calculations using model system $\tilde{\mathbf{1}}$ on (a) the closed-shell Fe(II)-NO^+ electronic state, and (b) the Fe(III)-NO(radical) electronic state, where the unpaired electrons of Fe(III) and NO are antiferromagnetically coupled (AFC). Since the five-coordinate reactant $[Fe(P)(MI)]^+$ can either be high-spin or low-spin, we have considered both of these spin states for the calculations: case (b) therefore corresponds to either a total spin of S = 0 (low-spin iron(III)) or S = 2 (high-spin iron(III)). Geometry optimizations have been performed on these three different electronic structures varying the Fe-NO distance in a systematic way between 1.5 and 5 Å. Since this endeavor requires a very large number of calculations, we employed the B3LYP/LanL2DZ method for these partial optimizations, since this method generates a fully-optimized structure for model system $\tilde{\mathbf{1}}$ that compares well with experiment and the BP86/TZVP structure (cf. Table 6.4.2). Figure 6.4.1 shows the PES obtained from these calculations. Importantly, B3LYP/LanL2DZ predicts that the Fe(III)-NO(radical) (S = 0) state is actually the ground state of the complex. Since this is not in agreement with experiment, we have then performed B3LYP/TZVP single-point calculations on the B3LYP/LanL2DZ structures for the two S = 0 states, because this method has shown to give better energies. The S = 2 surface has not been recalculated, but shifted in energy to reproduce the calculated NO dissociation energy of ~4 kcal/mol from the B3LYP/TZVP treatment (cf. Table 7 in ref[11]). Figure 6.4.2 shows the three potential energy surfaces obtained this way.

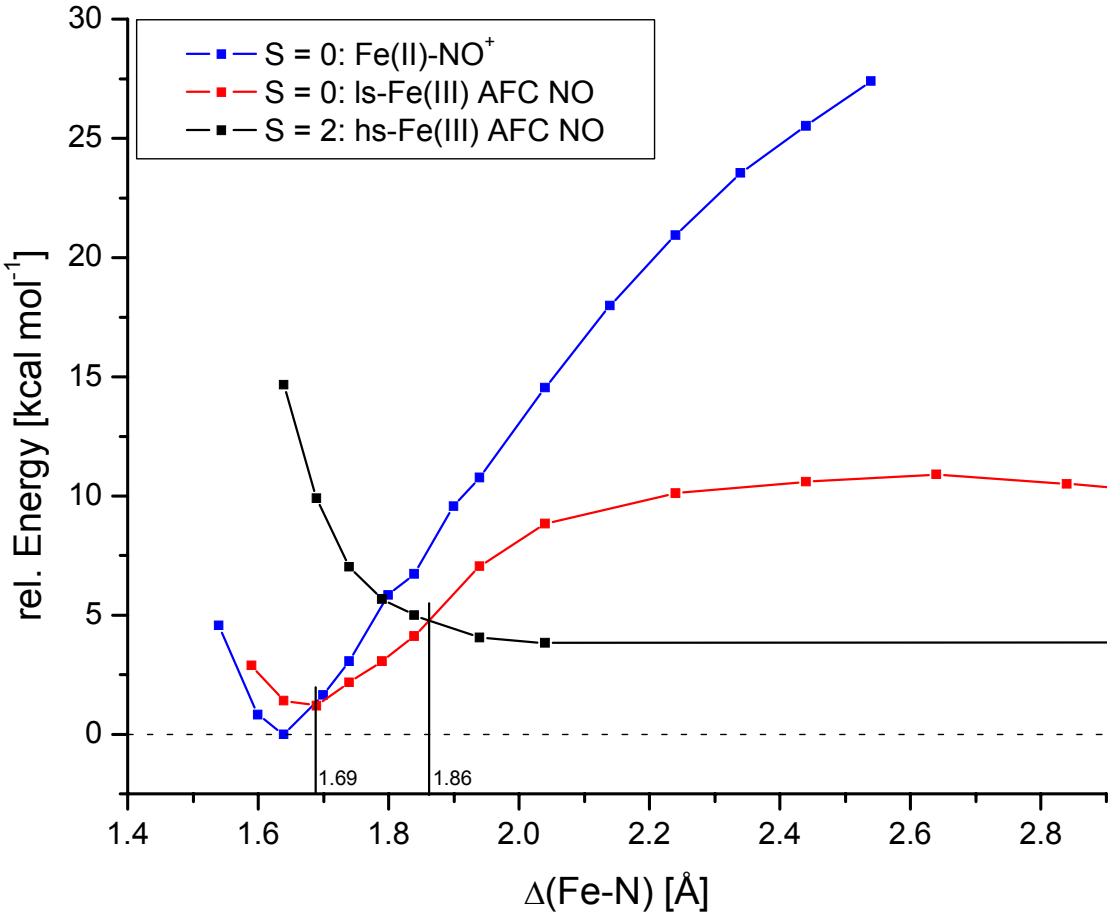

Figure 6.4.2. Potential energy surfaces for (a) closed shell Fe(II)-NO^+ (blue); (b) low-spin (ls) Fe(III) antiferromagnetically coupled (AFC) to NO (open shell S = 0; red); and (c) high-spin (hs) Fe(III) antiferromagnetically coupled (AFC) to NO (S = 2; black). Surfaces (a) and (b) were obtained using B3LYP/TZVP single point calculations on the B3LYP/LanL2DZ structures (cf. Figure 6.4.1). Surface (c) corresponds to the B3LYP/LanL2DZ result, but shifted to lower energy to resemble the calculated NO dissociation energy of 3.9 kcal/mol obtained with B3LYP/TZVP (cf. Table 7 in ref.[11]). All calculations were performed applying model $[Fe(P)(MI)(NO)]^+$ ($\tilde{\mathbf{1}}$).

Table 6.4.2. Geometric and vibrational properties of [Fe(P*)(L)(NO)] complexes (L = MI, Py, etc., or missing; P* = tetraphenylporphyrin or octaethylporphyrin type ligand)

Molecule [a]	*Geometric Parameters [Å]*					*Vibrational Frequencies [cm^{-1}]*		
	ΔFe-N(NO)	ΔN-O	∠Fe-N-O	ΔFe-L_{tr}	ΔFe-N_P	ν(N-O)	ν(Fe-NO)	δ(Fe-N-O)
Fe^{III} Complexes								
[Fe(OEP)(NO)](ClO_4) [b, c]	1.644	1.112	177		1.994	1868	611	
[Fe(OEP)(MI)(NO)](ClO_4) [b]	1.646	1.135	177	1.988	2.003	1921		
[Fe(OEP)(Py)(NO)]Cl [d]							602	
[Fe(SP-14)(Py)(NO)]Cl [d]							603	
[Fe(TPP)(NO)](BF_4)						1853		
[Fe(TPP)(MI)(NO)](BF_4)						1896		588
[Fe(TPP)(MI)($^{15}N^{18}O$)](BF_4)						1816		572
[Fe(P)(1-MI)(NO)]$^+$ – calc. BP86/TZVP {Fe^{II}-NO^+}	1.644	1.147	180	2.018	2.022	1933	639	606/598
[Fe(P)(1-MI)(NO)]$^+$ – calc. B3LYP/LanL2DZ {Fe^{II}-NO^+}	1.639	1.169	180	1.976	2.023	1908	657	613/601
[Fe(P)(1-MI)(NO)]$^+$ – calc. B3LYP/LanL2DZ {Fe^{III}-NO(rad.)}	1.689	1.178	180	1.967	2.021	1841	430	570/523
Fe^{II} Complexes								
[Fe^{II}(TPP)(MI)(NO)] [e]	1.750	1.182	138	2.173	2.008	1630	440	530(ip) 291(oop)
[Fe^{II}(P)(MI)(NO)] – calc. [e] BP86/TZVP	1.734	1.186	140	2.179	2.022	1662	609	482(ip) 317(oop)

[a] MI = 1-methylimidazole; P = Porphine ligand used for calculations; values for ΔFe-N_P are averaged. [b] Taken from refs.[18a,b]. [c] Chloroform solvate. [d] Taken from ref[39]. [e] Taken from ref.[9].

As shown in Figure 6.4.2, the B3LYP/TZVP calculations predict the Fe(II)-NO^+ state at lowest energy in agreement with experiment (vide infra). The corresponding energy surface of this state shown in blue is unusually steep for a metal-ligand bond, which is due to the fact that a dissociation of the complex into Fe(II) and NO^+ is energetically very unfavorable. The equilibrium Fe-NO distance for this state is predicted to be <1.65 Å (cf. Table 6.4.2), which is in excellent agreement with experiment (vide supra). The Fe-N-O unit in this state is linear. The PES for the S = 0 state where low-spin (ls) Fe(III) is antiferromagnetically coupled (AFC) to NO, termed ls-Fe(III)-NO(radical), is shown in red in Figure 6.4.2. To our great surprise, this state is energetically very close to the Fe(II)-NO^+ ground state, predicted about 1.0 kcal/mol higher in energy. In this case, a stable minimum is obtained, with a longer Fe-NO distance of 1.69 Å. Calculated spin densities for the fully optimized structure are +0.84 on Fe and -0.73 on NO, which resembles the antiferromagnetic coupling between the low-spin Fe(III) and NO. The two unpaired electrons are located in the d_{yz} and π^*_y orbitals in a rough approximation (see

below). Therefore, due to the small energetic separation between the two S = 0 states, the Fe(II)-NO^+ energy surface crosses the ls-Fe(III)-NO(radical) surface at an elongation of the Fe-NO bond of only ~0.05 Å from the equilibrium distance. In addition, *the crossing from the Fe(II)-NO^+ to the ls-Fe(III)-NO(radical) state does not go along with a bending of the Fe-N-O unit*: full geometry optimization of the ls-Fe(III)-NO(radical) state leads to an Fe-NO bond length of 1.69 Å, and a linear Fe-N-O unit. The electronic structure of this state is illustrated in Scheme 6.4.2. In this case, a strong polarization of the Fe-NO backbond is observed, where the α-spin interaction almost disappears. MO coefficients for the corresponding antibonding combinations show only 8% d orbital contribution, compared to 27% for the Fe(II)-NO^+ state. As mentioned above, the unpaired electrons in the ls-Fe(III)-NO(radical) case are primarily located in α-d_{yz} and β-π^*_y. The latter orbital is strongly mixed with β-d_{yz}, leading to a corresponding antibonding combination that consists of 47% π^*_y and 44% β-d_{yz}. This strong covalency quenches part of the spin density, leading to a distribution of roughly +0.5 on Fe and -0.5 on NO. The remaining backbond between β-d_{xz} and β-π^*_x is comparable to the Fe(II)-NO^+ state (cf. Scheme 6.4.2), and hence, shows a strong contribution to the total spin density, resulting in the calculated values listed above. In summary, although one of the β-backbonds is strengthened, this is not sufficient to compensate the loss of backbonding for α spin. This explains the distinctively weaker Fe-NO bond in the ls-Fe(III)-NO(radical) case, where ν(Fe-NO) is predicted at only 430 cm^{-1} as shown in Table 6.4.2 (Fe-NO force constant: 2.26 mdyn/Å). For ν(N-O), a shift of ~70 cm^{-1} to lower energy is predicted. The observation that the Fe-N-O unit is not bent in the ls-Fe(III)-NO(radical) state is due to the fact that the coupling of the ^2E state from $[d_{xz},d_{yz}]^3$ on iron with the ^2E state from $[\pi_x,\pi_y]^3$ on NO does only lead to non-degenerate states, even in an effective C_{4v} symmetry. This electronic state is therefore not Jahn-Teller active. In conclusion, a crossing from the Fe(II)-NO^+ ground to the ls-Fe(III)-NO(radical) state is induced by an elongation of the Fe-NO bond, and correspondingly, leads to a distinct weakening of the Fe-NO and N-O bonds. The closeness in energy of these states implies that there might be some ls-Fe(III)-NO(radical) admixture into the Fe(II)-NO^+ ground state. This mixing could even be dynamically mediated by the Fe-NO stretch, which means that the Fe(II)-

NO^+ ground and the ls-Fe(III)-NO(radical) state would become vibronically coupled. In C_{4v} symmetry, coupling between the $^1A_1$ ground state of Fe(II)-NO^+ with the $^1A_1$ component of ls-Fe(III)-NO(radical) could indeed be induced by ν(Fe-NO).[40]

Scheme 6.4.2

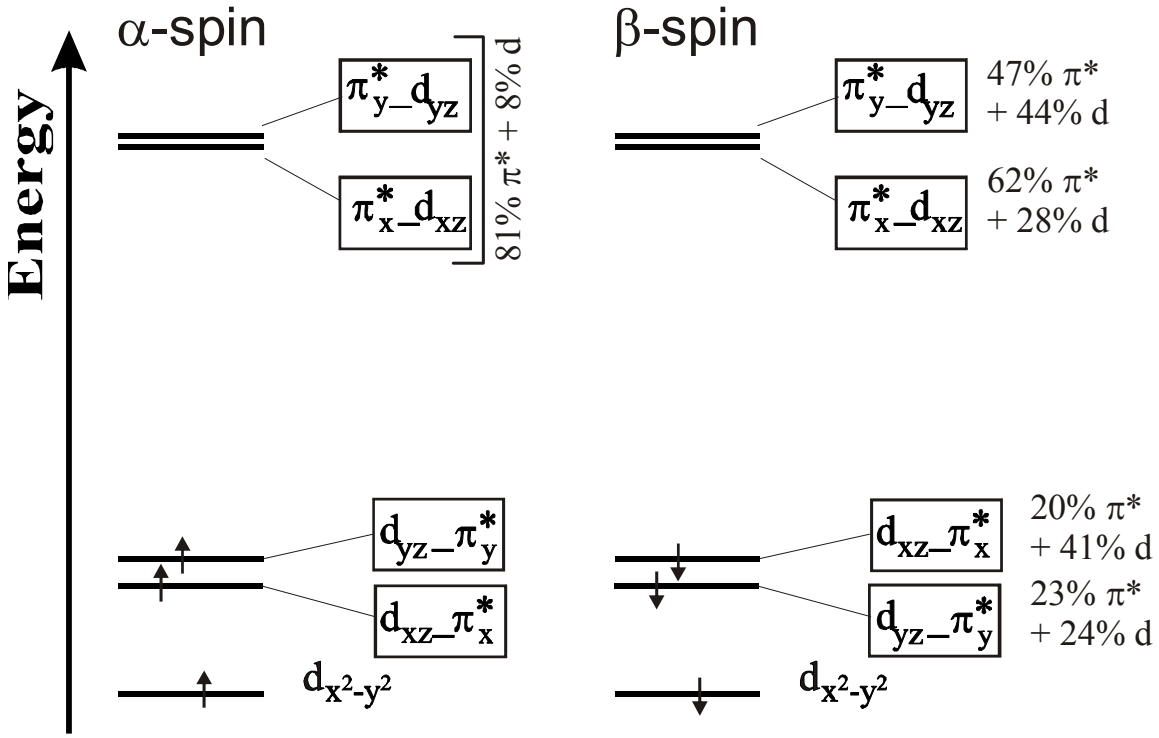

Based on these findings, the dissociation of NO from the iron center could be envisioned as follows: upon a small elongation of the Fe-NO bond to about 1.70 Å (cf. Figure 6.4.2), the critical electron transfer that leads from the Fe(II)-NO^+ to the ls-Fe(III)-NO(radical) electronic structure takes place, which is a symmetry-allowed process. If NO moves further away from the iron, the ls-Fe(III)-NO(radical) surface crosses the hs-Fe(III)-NO(radical) energy surface (shown in black in Figure 6.4.2), which corresponds to the electronic state where high-spin Fe(III) is antiferromagnetically coupled to the unpaired electron of NO. Hence, this process is identical with a spin crossover of the iron(III) center from low-spin to high-spin. The hs-Fe(III)-NO(radical) state corresponds to the product state that is obtained after complete dissociation of NO, because five-coordinate ferric heme is known to be high-spin. The crossing of these surfaces is roughly predicted

to occur around 1.9 Å, and hence, still at an Fe-NO distance below 2 Å. These two states cannot directly interact by spin-orbit coupling, so the intersystem crossing must be mediated by intermediate states of S = 1 total spin, but we have not further investigated this point. In summary, *the amazing finding of these PES calculations on six-coordinate ferric-heme NO adducts is that upon an elongation of the Fe-NO bond of only about 0.25 Å, the complex passes through at least four different electronic structures* (including at least one intermediate S = 1 state). The observed complexity of this energy landscape is unprecedented, even for transition metal nitrosyls, and rather unexpected.

There are a number of additional, important conclusions that derive from these findings. First, the large Fe-NO force constant actually resembles the Fe(II)-NO^+ state, and hence, the energetically very unfavorable dissociation of the complex into Fe(II) and NO^+. This explains the very steep energy surface for this state, leading to the large force constant and ν(Fe-NO) frequency of about 600 cm^{-1}. In contrary, the dissociation of NO from the iron center actually leads to Fe(III) and free NO, and therefore, corresponds to a completely different process. For this reason, the experimentally derived Fe-NO force constant is not a measure for the stability of the Fe-NO bond in this case. *These quantities are actually completely unrelated, because they depend on the properties of different electronic states*. Because of this, complex **1** has a large Fe-NO force constant but actually a quite weak Fe-NO bond in agreement with the small NO binding constant, and the observed rapid loss of NO from the iron center in solution. Therefore, it can be concluded that the ls-Fe(III)-NO(radical) state is characterized by both weaker Fe-NO and N-O bonds relative to the Fe(II)-NO^+ state. Experimentally, this would be manifested by a longer Fe-NO bond and a lower Fe-NO vibrational frequency as predicted by the calculations. The N-O frequency is also predicted to be lower in the ls-Fe(III)-NO(radical) case, because of the electron transfer from iron to the antibonding π* orbitals of NO that occurs upon changing the ground state from Fe(II)-NO^+ to ls-Fe(III)-NO(radical). Vice versa, the experimental data available for ferric heme NO adducts with axial N-donor coordination in proteins and model complexes clearly show that these complexes have the assumed Fe(II)-NO^+ ground state (from Fe-NO bond distances and the Fe-NO and N-O stretching frequencies). Finally, the hs-Fe(III)-NO(radical) surface is

dissociative, and the transition from ls-Fe(III)-NO(radical) to hs-Fe(III)-NO(radical) corresponds to a spin crossover. This means that once the system has entered the hs-Fe(III)-NO(radical) electronic state, the dissociative nature of this energy surface will actually drive the NO away from the metal center, which allows the NO to diffuse off and this way, inhibits its retention. This explains the surprisingly large rate constants for NO dissociation measured experimentally for ferric hemes.

6.4.4 Discussion. In order to obtain detailed insight into the iron-NO interaction in six-coordinate ferric heme nitrosyls, we have calculated the potential energy surfaces for three key electronic states as shown in Figure 6.4.2: (a) Fe(II)-NO^+ (S = 0, blue), which is the established ground state as described above; (b) the open shell singlet state ls-Fe(III)-NO(radical), where low-spin (ls) Fe(III) is antiferromagnetically coupled to NO (S = 0, red); and (c) the corresponding high-spin (hs) state hs-Fe(III)-NO(radical) (S = 2, black), which corresponds to the product state upon dissociation of NO. These results show that *the elusive ls-Fe(III)-NO(radical) state does in fact exist as an energy minimum, and that this state is surprisingly close in energy to the Fe(II)-NO^+ ground state* (DFT energy separation: only ~1 kcal/mol). The calculated energy difference between these states is likely underestimated by a few kcal/mol, at least for the case of axial N-donor coordination. This is evident from the vibrational properties, which do not show any indication for the presence of the ls-Fe(III)-NO(radical) state. From the calculated complex formation energies, a realistic error of 1 - 2 kcal/mol is estimated for the B3LYP/TZVP method. This would shift the crossing point of the two S = 0 surfaces to about 1.70 - 1.76 Å. In addition, the two states could be mixed, so the shape of the ground state energy surface around the crossing point is clearly not well defined from the DFT treatment. Scheme 6.4.3 shows the ground state PES with corrected energies as an illustration, including key energy parameters. Taking into account the small error in relative energies from DFT, it is estimated that an elongation of the Fe-NO bond of only 0.05 - 0.1 Å from the equilibrium position leads to a change of the ground state of the complex, i.e. the critical iron(II) to NO^+ electron transfer occurs at an Fe-NO distance of only 1.70 - 1.75 Å. Importantly, the properties of the two states, Fe(II)-NO^+ and ls-Fe(III)-NO(radical), are very different. From the calculations, the ls-Fe(III)-NO(radical)

state has a weaker (longer) Fe-NO bond, and hence, a lower Fe-NO stretching frequency. Due to the electron transfer from iron(II) into a π* orbital of NO, the N-O bond is also weaker giving rise to ν(N-O) at lower frequency. Hence, both the Fe-NO and the N-O bond become weaker in going from Fe(II)-NO^+ to ls-Fe(III)-NO(radical), which corresponds to a direct correlation of these bond strengths.

These results are very important, because *this implies that a small perturbation of the Fe-N-O unit, for example, due to interaction of the bound NO with a protein side chain, might be able to induce a change of the ground state from Fe(II)-NO^+ to ls-Fe(III)-NO(radical)*. This should be evident from the spectroscopic properties of the complex. However, no clear experimental proof for the existence of a ferric heme nitrosyl with the ls-Fe(III)-NO(radical) ground state is available so far. However, this finding offers an attractive explanation for the observed weaker Fe-NO and N-O bond strengths in ferric heme nitrosyls with axial thiolate coordination, which could be attributed to a change in ground state to ls-Fe(III)-NO(radical). However, this would not explain the observed bending of the Fe-N-O unit; our results clearly demonstrate that a bent Fe-N-O unit is not an intrinsic property of the ls-Fe(III)-NO(radical) state. On the other hand, our DFT results, shown in Section 6.2, show that these properties can also be explained within the Fe(II)-NO^+ ground state model (cf. Section 6.2 and ref.[24]). This point needs further investigation.

Scheme 6.4.3

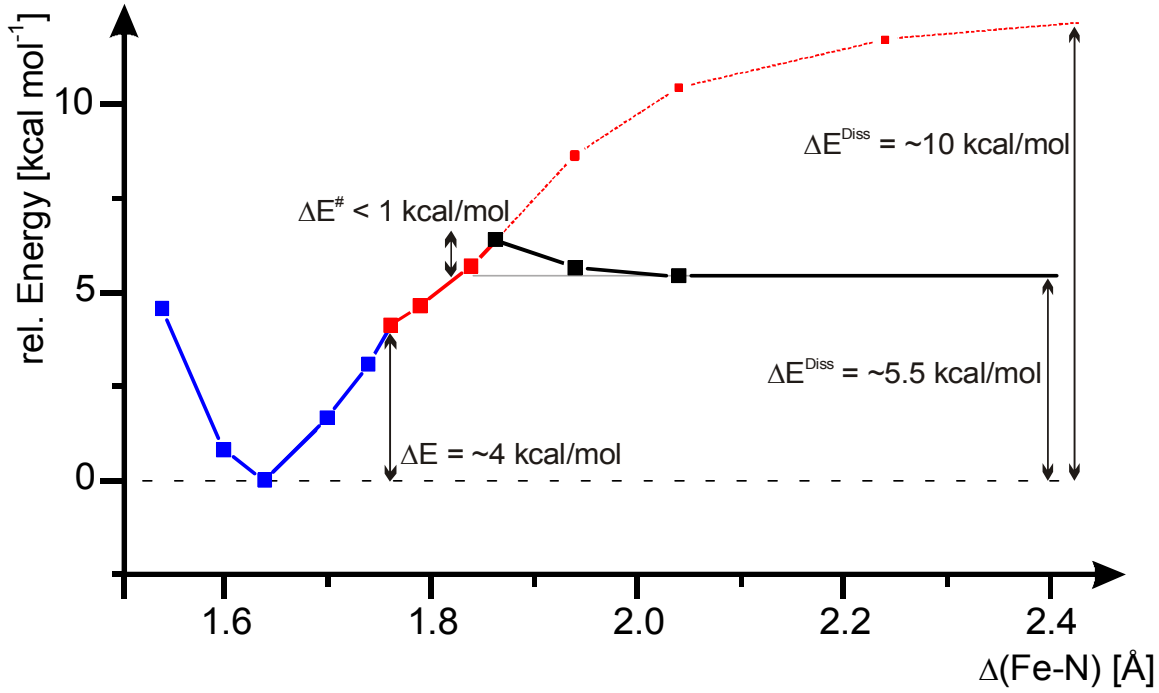

Upon a further elongation of the Fe-NO bond, the ls-Fe(III)-NO(radical) crosses the hs-Fe(III)-NO(radical) energy surface at a distance of ~1.9 Å (cf. Scheme 6.4.3). This transition corresponds to a spin crossover of the iron(III), and is related to the fact that the five-coordinate ferric heme product is actually high-spin. Importantly, *the hs-Fe(III)-NO(radical) PES is dissociative for the Fe-NO bond*. This generates a small kinetic barrier for the dissociation of NO, which, however, is <1 kcal/mol, and hence, negligible. More importantly, this dramatically lowers the thermodynamic stability of the Fe-NO bond, from about -10 kcal/mol on the ls surfaces to only about -4 kcal/mol (cf. Scheme 6.4.2). Therefore, *the properties of the hs-Fe(III)-NO(radical) energy surface determine the thermodynamic weakness of the Fe-NO bond in ferric heme nitrosyls, and the large dissociation rate constant of NO*. On the other hand, the large Fe-NO force constant and short Fe-NO distance in the ground state relate to the properties of the Fe(II)-NO^+ surface, which is very steep due to the fact that the dissociation of the complex into iron(II) and NO^+ is energetically very unfavorable. Altogether, a dissociation of NO from the iron center requires the system to pass through at least four different electronic states (including an S = 1 intermediate state, vide supra). *The observed complexity of this*

energy landscape is unprecedented, even for transition metal nitrosyls, and completely unexpected. The 'simple' Fe(II)-NO^+ electronic structure description of these complexes, and the analogies normally drawn to Fe(II)-heme CO complexes, do not in any way implicate such complexity as determined here.

Based on these properties of ferric-heme nitrosyls, the occurrence of ferric instead of ferrous hemes in the NO delivery proteins (nitrophorins) and enzyme-product complexes of cytochrome cd_1 NIR and NOS is not arbitrary. This is actually related to the weakness of the Fe-NO bond in these systems, which enables loss of NO. The corresponding rate constants k_{off} are approximately 4 to 8 orders of magnitude larger in ferric compared to ferrous hemes as discussed above.[41] Hence, formation of ferrous heme NO adducts has often been referred to as a 'dead-end' of protein activity, and would certainly impose a rather dramatic limit on the dissociation of NO from the NIR or NOS enzyme-product complexes or the nitrophorins.

Finally, it is interesting to compare the properties of ferric heme nitrosyls to those of the corresponding ruthenium(III) NO adducts. In the latter case, the electronic structure does also correspond to Ru(II)-NO^+, but no lability of the bound NO is observed. In contrary, these compounds are some of the most stable transition metal nitrosyls known. What is the reason for this substantial difference? Since ruthenium is a second-row transition metal, the tendency to form high-spin complexes is greatly reduced. Hence, five-coordinate Ru(III) products obtained upon dissociation of NO from the corresponding nitrosyl complexes have in general low-spin ground states, and therefore, no spin-crossover is observed upon loss of NO. Considering Figure 6.4.2, this would mean that the hs-metal(III)-NO(radical) energy surface (black) disappears (i.e. shifts to much higher energy) for Ru(III). Independently of how the energies of the S = 0 states play out, the removal of the hs-metal(III)-NO(radical) surface from the picture will automatically lead to a much more stable complex. This is another demonstration of how significant these results are for the detailed understanding of the electronic structures, thermodynamic stabilities, spectroscopic properties, and reactivities of group 8 metal(III) nitrosyls.

Conclusions.

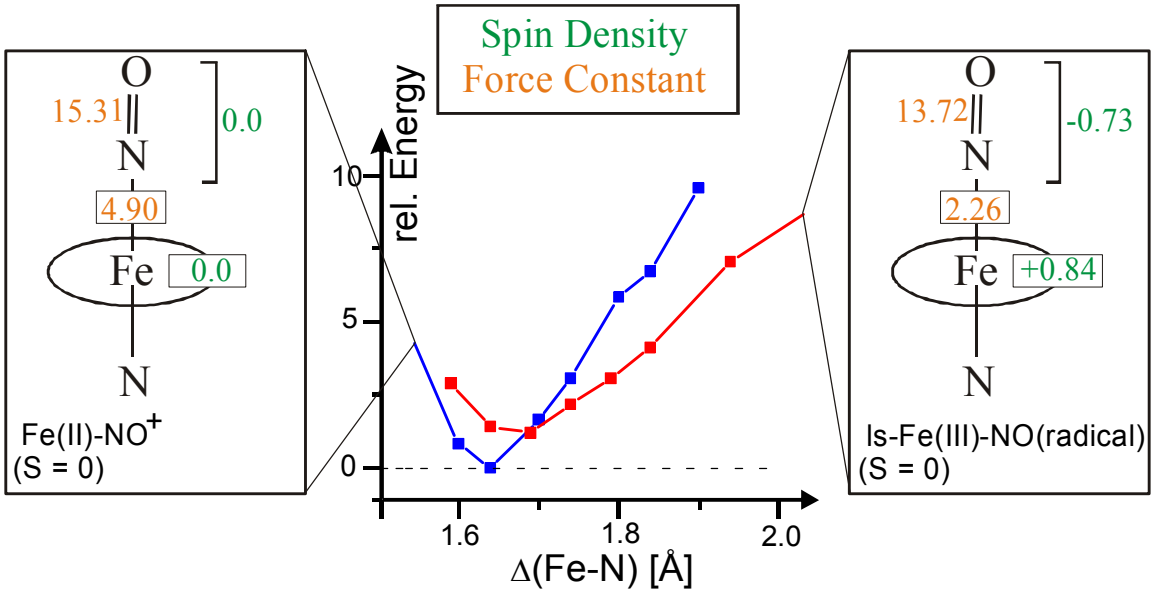

In this study, we have characterized the Fe(II)-NO^+ ground state of six-coordinate ferric heme nitrosyls in detail using the model complex [Fe(TPP)(MI)(NO)](BF_4) as example. Applying DFT calculations, the elusive low-spin Fe(III)-NO(radical) (S = 0) state has then been investigated. Surprisingly, this state is located just a few kcal/mol above the ground state. It is characterized by very different properties compared to Fe(II)-NO^+; in particular, the Fe-NO and N-O bond strengths are greatly reduced, which is related to a reduction of π backbonding. Upon a small elongation of the Fe-NO bond by 0.05 - 0.1 Å from the equilibrium position, the Fe(II)-NO^+ ground state energy surface crosses the low-spin Fe(III)-NO(radical) (S = 0) energy surface. Importantly, this shows that low-spin Fe(III)-NO(radical) (S = 0) could become the ground state of ferric heme nitrosyls upon small steric or electronic perturbations as they occur, for example, in protein active sites. This is especially true for axial thiolate (cysteinate) coordination, because thiolates tend to stabilize iron(III). On the other hand, the observed thermodynamic weakness of the Fe-NO bond in ferric heme nitrosyls is due to the properties of the high-spin Fe(III)-NO(radical) (S = 2) state, which is dissociative with respect to the Fe-NO bond, and which appears at very low energy. These potential energy surface calculations reveal an unexpectedly complex energy landscape for binding of NO to ferric heme.

6.4.5 Appendix: Electronic structure of [Fe(P)(MI)(NO)]$^{+}$ ($\tilde{\mathbf{1}}$). As already mentioned above, this work is attributed to my colleague Praneeth V. K. K. and my supervisor Prof. Nicolai Lehnert. It is included here, because these results are necessary for the detailed understanding of the PES calculations presented above. The electronic structure of the ferric six-coordinate complex [Fe(TPP)(MI)(NO)]$^{+}$ (**1**) is analyzed using the model [Fe(P)(MI)(NO)]$^{+}$ (P = porphine ligand). Geometry optimization has been performed on this system using BP86/TZVP and B3LYP/LanL2DZ. As shown in Table 6.4.2, both methods give a very good agreement with the crystal structure of the six-coordinate complex [Fe(OEP)(MI)(NO)](ClO_4).[18a] In particular, the very short Fe-NO bond < 1.65 Å and the linear Fe-N-O unit are reproduced by the DFT treatment. For the further analysis of the electronic structure of **1**, the BP86/TZVP optimized model [Fe(P)(MI)(NO)]$^{+}$ ($\tilde{\mathbf{1}}$) is used for consistency with earlier work on ferrous heme NO adducts.[42] The obtained structure of $\tilde{\mathbf{1}}$ is shown in Figure A.1. For the following evaluation of the MO diagram of $\tilde{\mathbf{1}}$, the applied coordinate system in Scheme 6.4.1 is used.

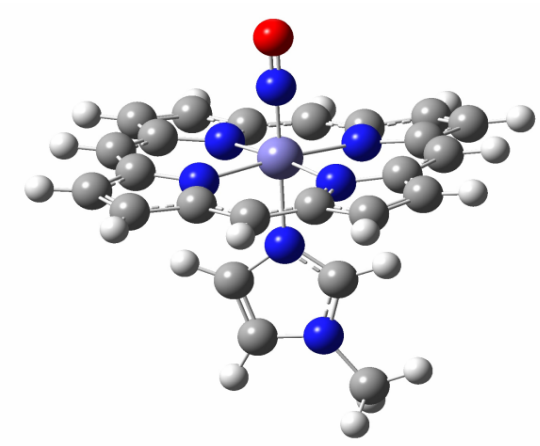

Figure A.1. Fully optimized structure of [Fe(P)(MI)(NO)]$^{+}$ ($\tilde{\mathbf{1}}$; P = porphine; MI = 1-methylimidazole) obtained with BP86/TZVP. Important structural parameters are given in Table 6.4.2.

Figure A.2 shows the obtained MO diagram of complex $\tilde{\mathbf{1}}$. Contour plots of important molecular orbitals are presented in Figure A.3. As evidenced by the N-O stretching frequency of ~1900 cm^{-1} (vide supra), the linear Fe-N-O unit, and in agreement with the literature [15,12a] and recent DFT results,[20] the electronic structure of complex **1** can in general be classified as Fe(II)-NO^+. Since iron is in the +II oxidation state and low-spin in these compounds (as evident from magnetic Mössbauer measurements), it has a $[d_{xz},d_{yz},d_{x^2-y^2}]^6 \approx [t_2]^6$ electron configuration. Both π* orbitals of the NO^+ ligand (isoelectronic to N_2) are empty and hence, undergo π backbonding interactions with the d_{xz} and d_{yz} orbitals of the metal in the applied coordinate system. The corresponding bonding combinations, d_{xz}_π_x* and d_{yz}_π_y*, are delocalized over several molecular orbitals. Major contributions are found in MO <111>, which has 55% d_{xz} and 19% π_x* character, and <110>, which corresponds to a mixture of 36% d_{yz} and 18% π_y* (cf. Table A.1). Hence, the strength of this backbond is better estimated from the corresponding antibonding combinations, π_x*_d_{xz} <123> and π_y*_d_{yz} <124>, which are the LUMOs of complex $\tilde{\mathbf{1}}$. Both have about 68% π* and 27% d orbital character, which corresponds to a very strong π backbonding interaction. Contour plots of these orbitals are shown in Figure A.3. The third t_2 type d orbital of iron, $d_{x^2-y^2}$ <118>, is practically non-bonding (cf. Table A.1). In summary, the calculated orbital coefficients are also in agreement with the Fe(II)-NO^+ description. Two very strong Fe-NO π backbonds lead to a transfer of a significant amount of electron density from the d_{xz} and d_{yz} orbitals of Fe to the π* orbitals of NO. The total donation corresponds to about one electron. In addition, there is a very weak σ interaction between σ_{nb} of NO^+ and d_{z^2} of Fe. The corresponding bonding combination, σ_{nb}_d_{z^2} <66>, has 51% σ_{nb} and 4% d contribution. Finally, the HOMO of complex $\tilde{\mathbf{1}}$ (MO <122>), which corresponds to the porphyrin A_{2u} <81> orbital (cf. Chapter 4 for porphyrin MO labels), shows a very small admixture of an Fe-N-O σ *antibonding* orbital (cf contour plot in Figure A.3). The charge contributions obtained here are 1% d_z^2 and 0.3% σ*, which is negligible for the total Fe-NO bond strength (cf. Table A.1).

Having elaborated a detailed electronic structure description of complex **1**, it is now interesting to make a comparison with the corresponding, one-electron reduced complex [Fe(P)(MI)(NO)] ($\widetilde{\mathbf{3}}$).[42b] This compound has been described as Fe(II)-NO(radical),[42a] and correspondingly, *the reduction in going from **1** to **3** is mostly ligand (NO) based*. A closer comparison of the electronic structures of these complexes reveals further differences. In the case of **3**, the Fe-N-O unit is bent, which leads to a strong Fe-NO σ bond between d_{z^2} of iron and the singly occupied in-plane π* orbital of NO. This explains the large stability of the Fe-NO bond in this case and the observed *trans* effect of the NO ligand on axially coordinated N-donor ligands, which induces long Fe(II)-N_L bond lengths compared to the corresponding bis(imidazole) ligated Fe(II)-porphyrins.[43] In contrast, the Fe-NO σ bond in **1** is very weak, because it is mediated by the σ_{nb} orbital of NO, which is located at very low energy and exhibits poor donor abilities. *The negligible σ bond in **1** leads to the observed very short Fe-NO bond and the lack of a trans-effect of NO on the bound MI ligand*. In fact, all Fe(II)-NO^+ complexes with *trans* N-donor ligands exhibit Fe-N_L bond lengths comparable to the corresponding $[Fe^{III}(porphyrin)(imidazole)_2]^+$ complexes.[18a] On the other hand, the Fe-NO π backbond is distinctively stronger for **1** compared to **3**. However, this does actually not relate to the observed π*_d mixing, but only to the fact that the number of backbonds is reduced from two in **1** to 1.5 in **3**. This is evident from the d orbital contributions to the corresponding π*_d antibonding orbitals, which are 27% for **1**, and 25% (average) for **3** for the π_v*_d_{yz} (α/β<126> in ref.[42b]) orbital. Surprisingly, this indicates that the linear Fe-N-O unit and the shorter Fe-NO bond by itself do *not* facilitate the π backbond in a noticeable fashion in **1** compared to **3**.

Table A.1. Charge contributions of important molecular orbitals of $[Fe(P)(MI)(NO)]^+$ ($\tilde{\mathbf{1}}$) calculated with BP86/TZVP

Nr.	label	**Energy** [Hartree]	Fe	N		O		N_{MI}	Σ MI
			D	s	P	s	p	s+p	
<125>	d_{z^2}_ σ_{nb} + Im(σ)	-0.23526	56	4	3	1	2	9	11
<124>	π_y*_ d_{yz}	-0.25401	27	0	42	0	26	0	1
<123>	π_x*_ d_{xz} (LUMO)	-0.25465	27	0	42	0	26	0	0
<122>	A_{2u}<81> + d_{z^2}_ σ^* (HOMO)	-0.29701	1	0.2	0.1	0	0	2	2
<121>	A_{1u}<79>	-0.30203	0	0	0	0	0	0	0
<120>	E_g<75/76> + d_{yz} _π_y*	-0.32744	10	0	2	0	2	0.5	1
<119>	E_g<75/76> + d_{xz} _π_x*	-0.32773	10	0	3	0	2	0	0
<118>	$d_{x^2-y^2}$	-0.33166	86	0	0	0	0	0	0
<117>	B_{2u}<74> + Im(π)	-0.33288	0	0.3	0.2	0	0	1	41
<116>	A_{2u}<72> + $d_{x^2-y^2}$	-0.34318	6	0.3	0.2	0	0	2	2
<114>	Im(π) + d_{yz} _π_y*	-0.36820	14	0	2	0	4	18	52
<112>	E_g<70/71>	-0.37193	2	0	0	0	0	5	13
<111>	d_{xz} _π_x*	-0.39427	55	0	6	0	13	1	1
<110>	d_{yz} _π_y* + Im(π)	-0.40249	36	0	5	0	13	5	14
<109>	E_u<77/78> + π_x*	-0.40746	1	0	1	0	4	0	0
<108>	B_{1u}	-0.41055	0	0	0	0	0	0	0
<107>	E_u<77/78> + Im(π)_ d_{yz}	-0.41102	4	0	0	0	0	5	21
<106>	B_{1g}<80>_ d_{xy}	-0.43033	19	0	0	0	0	0	0
<102>	Im(σ)_ d_{z^2} + σ_{nb}	-0.44589	13	1	1	0	1	36	67
<73>	π_x^b	-0.61229	2	0	41	0	47	0	0
<72>	π_y^b	-0.61271	3	0	43	0	48	0	0
<66>	σ_{nb}_ d_{z^2} + Im(σ)	-0.63694	4	2	14	9	26	2	7

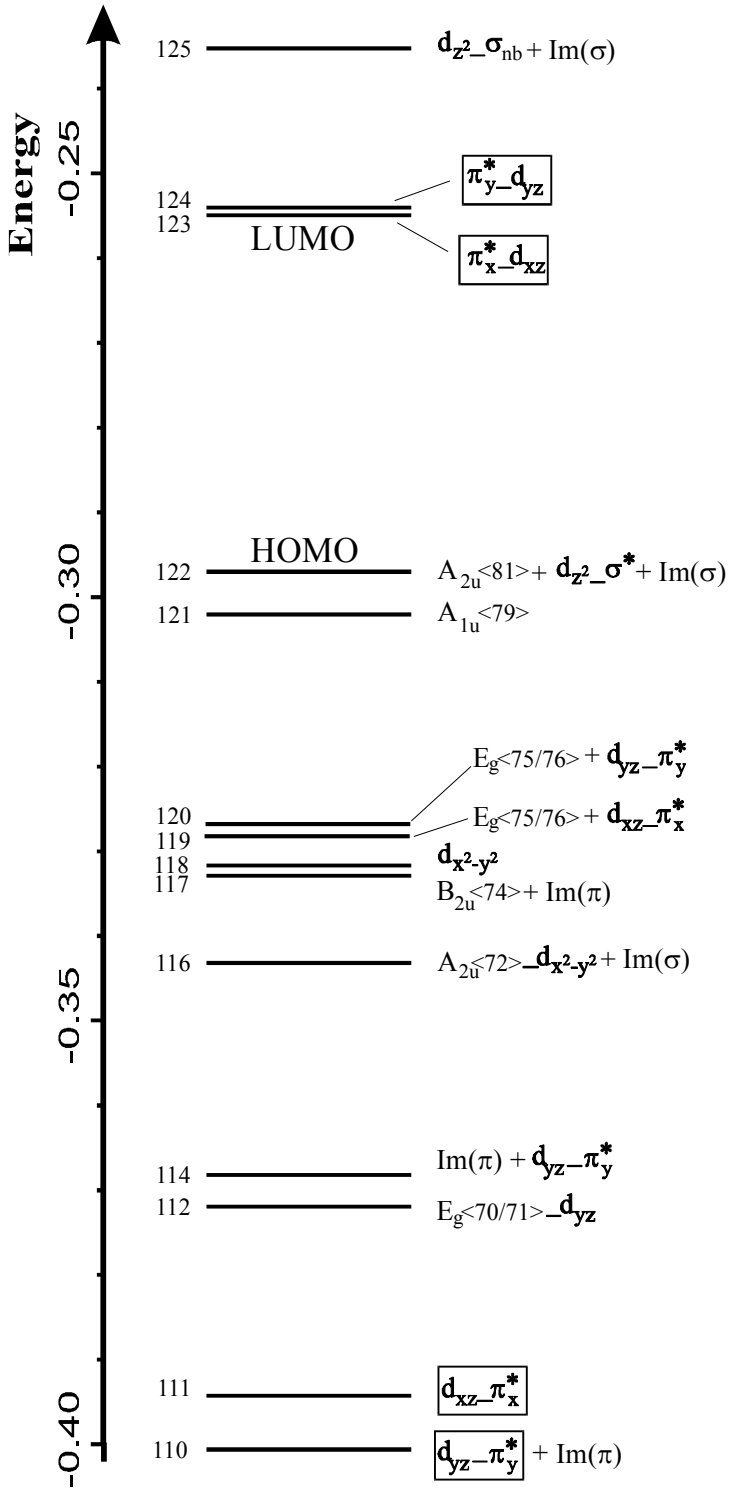

Figure A.2. MO diagram of $[Fe(P)(MI)(NO)]^+$ ($\widetilde{\mathbf{1}}$) calculated with BP86/TZVP. The applied coordinate system is shown in Scheme 6.4.1. A_{1u}, A_{2u} and E_g, etc. correspond to porphine orbitals.[42b] The nomenclature '*a*_*b*' indicates that orbital *a* interacts with *b* and that *a* has a larger contribution to the resulting MO.

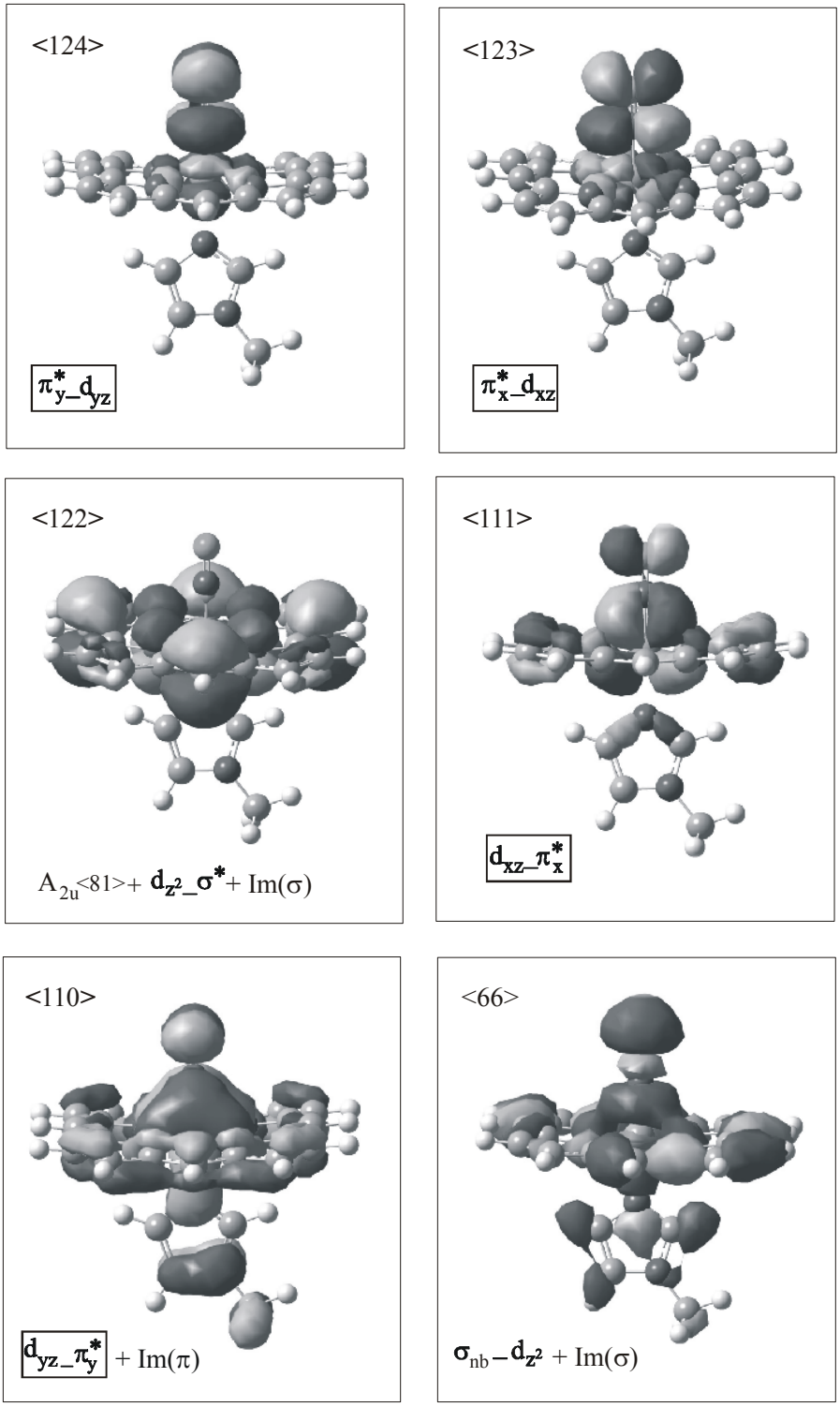

Figure A.3. Contour plots of important molecular orbitals of $[Fe(P)(MI)(NO)]^+$ ($\tilde{\mathbf{1}}$) calculated with BP86/TZVP. For labels see Figure A.2 and Table A.1.

References

[1] (a) Cooper, C. E. *Biochim. Biophys. Acta* **1999**, *1411*, 290-309. (b) Ford, P. C.; Laverman, L. E. *Coord. Chem. Rev.* **2005**, *249*, 391-403.
[2] Suzuki, N.; Higucji, T.; Urano, Y.; Kikuchi, K.; Uchida, T.; Mukai, M.; Kitagawa, T.; Nagano, T. *J. Am. Chem. Soc.* **2000**, *122*, 12059-12060.
[3] Xu, N.; Powell, D. R.; Cheng, L.; Richter-Addo, G. B. *Chem. Commun.* **2006**, 2030.
[4] Franke, A.; Srochel, G.; Suzuki, N; Higuchi, T.; Okuzono, K.; van Eldik, R. *J. Am. Chem. Soc.* **2005**, *127*, 5360-5375.
[5] Ellison, M. K.; Scheidt, W. R. *J. Am. Chem. Soc.* **1999**, *121*, 5210-5219.
[6] Lehnert, N. *Habilitationsschrift*, Christian-Albrechts-Universität zu Kiel, Germany, **2005**.
[7] Wolak, M.; Stochel, G.; Hamza, M.; van Eldik, R. *Inorg. Chem.* **2000**, *39*, 2018.
[8] Allouche, A.; Pourcin, J. *Spectrochim. Acta A* **1993**, *49*, 571.
[9] Praneeth, V. K. K.; Näther, C.; Peters, G.; Lehnert, N. *Inorg. Chem.* **2000**, *39*, 2352.
[10] Leu, B. M.; Zgierski, M. Z.; Wyllie, G. R. A.; Scheidt, W. R.; Sturhahn, W.; Alp, E. E.; Durbin, S. M.; Sage, J. T. *J. Am. Chem. Soc.* **2004**, *126*, 4211-4227.
[11] Praneeth, V. K. K.; Paulat, F.; Näther, C.; Lehnert, N. *Manuscript in preparation.*
[12] (a) Averill, B. A. *Chem. Rev.* **1996**, *96*, 2951-2964. (b) Enemark, J. H.; Feltham, R. D. *Coord. Chem. Rev.* **1974**, *13*, 339-406. (c) Wasser, I. M.; de Vries, S.; Moënne-Loccoz, P.; Schröder, I.; Karlin, K. D. *Chem. Rev.* **2002**, *102*, 1201-1234.
[13] Paulat, F.; Kuschel, T.; Näther, C.; Praneeth, V. K. K.; Sander, O.; Lehnert, N. *Inorg. Chem.* **2004**, *43*, 6979-6994.
[14] (a) Antonini, E.; Brunori, M.; Wyman, J.; Noble, R. W. *J. Biol. Chem* **1966**, 241, 3236-3238. (b) Traylor, T. G.; Sharma, V. S. Biochemistry. **1992**, 31, 2847-2849. (c) Sharma, V. S.; Traylor, T. G.; Gardiner, R.; Mizukami, H. Biochemistry. **1987**, 26, 3837-3843. (d) Hoshino, M.; Ozawa, K.; Seki, H.; Ford, P. C. *J. Am. Chem. Soc.* **1993**, *115*, 9568-9575.
[15] Enemark, J. H.; Feltham, R. D. *Coord. Chem. Rev.* **1974**, *13*, 339-406.
[16] Bottomley, F. *Coord. Chem. Rev.* **1978**, *26*, 7-32.
[17] Ellison, M. K.; Schulz, C. E.; Scheidt, W. R. *Inorg. Chem.* **2000**, *39*, 5102-5110.
[18] (a) Ellison, M. K.; Scheidt, W. R. *J. Am. Chem. Soc.* **1999**, *121*, 5210-5219. (b) Ellison, M. K.; Schulz, C. E.; Scheidt, W. R. *J. Am. Chem. Soc.* **2002**, *124*, 13833-13841. (c) Scheidt, W. R.; Lee, Y. J.; Hatano, K. *J. Am. Chem. Soc.* **1984**, *106*, 3191-3198. (d) Yi, G.-B.; Chen, L.; Khan, M. A.; Richter-Addo, G. B. *Inorg. Chem.* **1997**, *36*, 3876-3885.
[19] (a) Li, X.-Y.; Spiro, T. G. *J. Am. Chem. Soc.* **1988**, *110*, 6024. (b) Ray, G. B.; Li, X.-Y.; Ibers, J. A.; Sessler, J. L.; Spiro, T. G. *J. Am. Chem. Soc.* **1994**, *116*, 162 and ref. herein.
[20] (a) Linder, D. P.; Rodgers, K. R.; Banister, J.; Wyllie, G. R. A.; Ellison, M. K.; Scheidt, W. R. *J. Am. Chem. Soc.* **2004**, *126*, 14136-14148. (b) Linder, D. P.; Rodgers, K. R. *Inorg. Chem.* **2005**, *44*, 1367-1380.
[21] Pant, K.; Crane, B. R. *Biochemistry* **2006**, *45*, 2537.
[22] Shimizu, H.; Park, S.-Y.; Gomi, Y.; Arakawa, H.; Nakamura, H.; Adachi, S.-I.; Obayashi, E.; Iizuka, T.; Shoun, H.; Shiro, Y. *J. Biol. Chem.* **2000**, *275*, 4816.
[23] Xu, N.; Powell, D. R.; Cheng, L.; Richter-Addo, G. B. *Chem. Commun.* **2006**, 2030.
[24] Paulat, F.; Lehnert, N. *Inorg. Chem.* **2007**, *46*, 1547-1549.
[25] Walker, F. A. *J. Inorg. Biochem.* **2005**, *99*, 216-236.
[26] (a) Ehrenberg, A.; Szczepkowski, T. W. *Acta Chem. Scand.* **1960**, *14*, 1684-1692. (b) Hoshino, M.; Maeda, M.; Konishi, R.; Seki, H.; Ford, P. C. *J. Am. Chem. Soc.* **1996**, *118*, 5702-5707. (c) Fernandez, B. O.; Lorkovic, I. M.; Ford, P. C. *Inorg. Chem.* **2004**, *43*, 5393-5402. (d) Møller, J. K. S.; Skibsted, L. H. *Chem. Eur. J.* **2004**, *10*, 2291-2300. (e) Lim, M. D.; Lorkovic, I. M.; Ford, P. C. *J. Inorg. Biochem.* **2005**, *99*, 151-165.
[27] (a) Obayashi, E.; Tsukamoto, K.; Adachi, S.-I.; Takahashi, S.; Nomura, M.; Iizuka, T.; Shoun, H.; Shiro, Y. *J. Am. Chem. Soc.* **1997**, *119*, 7807-7816. (b) Hu, S.; Kincaid, J. R. *J. Am. Chem. Soc.* **1991**, *113*, 2843-2850.
[28] Suzuki, N.; Higuchi, T.; Urano, Y.; Kikuchi, K.; Uchida, T.; Mukai, M.; Kitagawa, T.; Nagano, T. *J. Am. Chem. Soc.* **2000**, *122*, 12059-12060.
[29] Hu, S.; Kincaid, J. R. *J. Biol. Chem.* **1993**, *268*, 6189-6193.
[30] Rousseau, D. L.; Li, D.; Couture, M.; Yeh, S.-R. *J. Inorg. Biochem.* **2005**, *99*, 306-323.

[31] (a) Tomita, T.; Haruta, N.; Aki, M.; Kitagawa, T.; Ikeda-Saito, M. *J. Am. Chem. Soc.* **2001**, *123*, 2666-2667. (b) Benko, B.; Yu, N. T. *Proc. Natl. Acad. Sci. USA* **1983**, *80*, 7042-7046.
[32] Pinakoulaki, E.; Gemeinhardt, S.; Saraste, M.; Varotsis, C. *J. Biol. Chem.* **2002**, 277, 23407-23413.
[33] Ding, X. D.; Weichsel, A.; Andersen, J. F.; Shokhireva, T. K.; Balfour, C.; Pierik, A. J.; Averill, B. A.; Montfort, W. R.; Walker, F. A. *J. Am. Chem. Soc.* **1999**, *121*, 128-138.
[34] Maes, E. M.; Walker, F. A.; Monfort, W. R.; Czernuszewicz, R. S. *J. Am. Chem. Soc.* **2001**, *123*, 11664-11672.
[35] Wang, J.; Lu, S.; Moënne-Loccoz, P.; Ortiz de Montellano, P. R. *J. Biol. Chem.* **2003**, 278, 2341-2347.
[36] (a) Sampath, V.; Zhao, X.; Caughey, W. S. *Biochem. Biophys. Res. Commun.* **1994**, *198*, 281-287. (b) Wang, Y.; Averill, B. A. *J. Am. Chem. Soc.* **1996**, *118*, 3972-3973.
[37] Miller, L. M.; Pedraza, A. J.; Chance, M. R. *Biochemistry* **1997**, *36*, 12199-12207.
[38] Frisch, M. J.; Trucks, G. W.; Schlegel, H. B.; Scuseria, G. E.; Robb, M. A.; Cheeseman, J. R.; Montgomery, J. A., Jr.; Vreven, T.; Kudin, K. N.; Burant, J. C.; Millam, J. M.; Iyengar, S. S.; Tomasi, J.; Barone, V.; Mennucci, B.; Cossi, M.; Scalmani, G.; Rega, N.; Petersson, G. A.; Nakatsuji, H.; Hada, M.; Ehara, M.; Toyota, K.; Fukuda, R.; Hasegawa, J.; Ishida, M.; Nakajima, T.; Honda, Y.; Kitao, O.; Nakai, H.; Klene, M.; Li, X.; Knox, J. E.; Hratchian, H. P.; Cross, J. B.; Adamo, C.; Jaramillo, J.; Gomperts, R.; Stratmann, R. E.; Yazyev, O.; Austin, A. J.; Cammi, R.; Pomelli, C.; Ochterski, J. W.; Ayala, P. Y.; Morokuma, K.; Voth, G. A.; Salvador, P.; Dannenberg, J. J.; Zakrzewski, V. G.; Dapprich, S.; Daniels, A. D.; Strain, M. C.; Farkas, O.; Malick, D. K.; Rabuck, A. D.; Raghavachari, K.; Foresman, J. B.; Ortiz, J. V.; Cui, Q.; Baboul, A. G.; Clifford, S.; Cioslowski, J.; Stefanov, B. B.; Liu, G.; Liashenko, A.; Piskorz, P.; Komaromi, I.; Martin, R. L.; Fox, D. J.; Keith, T.; Al-Laham, M. A.; Peng, C. Y.; Nanayakkara, A.; Challacombe, M.; Gill, P. M. W.; Johnson, B.; Chen, W.; Wong, M. W.; Gonzalez, C.; Pople, J. A. *Gaussian 03*, Gaussian, Inc.: Pittsburgh, PA, 2003.
[39] Lipscomb, L. A, Lee B-A, Yu, N-T. *Inorg. Chem.* **1993**, 32, 281-286.
[40] Note that the symmetry of six-coordinate ferric heme nitrosyls is lower than C_{4v}, which further diminishes symmetry-related restrictions. C_{4v} is the maximum possible symmetry of a corresponding five-coordinate $[Fe(porphyrin)(NO)]^+$ complex.
[41] (a) Cooper, C. E. *Biochim. Biophys. Acta* **1999**, *1411*, 290-309. (b) Ford, P. C.; Laverman, L. E. *Coord. Chem.Rev.* **2005**, *249*, 391-403.
[42] (a) Praneeth, V. K. K.; Neese, F.; Lehnert, N. *Inorg. Chem.* **2005**, *44*, 2570-2572. (b) Praneeth, V. K. K.; Näther, C.; Peters, G.; Lehnert, N. *Inorg. Chem.* **2006**, *45*, 2795-2811. (c) Praneeth, V. K. K.; Haupt, E.; Lehnert, N. *J. Inorg. Biochem.* **2005**, *99*, 940-948. Erratum: ibid, 1744. (d) Lehnert, N.; Praneeth, V. K. K.; Paulat, F. *J. Comp. Chem.* **2006**, *27*, 1338-1351. (e) Lehnert, N. "Electron Paramagnetic Resonance and Low-Temperature Magnetic Circular Dichroism Spectroscopy of Ferrous Heme Nitrosyls"; in: "The Smallest Biomolecules: Perspectives on Heme-Diatomic Interactions"; Ghosh, A., ed., Elsevier, Amsterdam, **2007**, in press
[43] Wyllie, G. R. A.; Schulz, C. A.; Scheidt, W. R. *Inorg. Chem.* **2003**, 42, 5722-5734.

7 Collaborative Investigations

7.1 Scope of this project

The collaborative investigations performed during my graduation (Promotion) focus on computational studies on the catalytic cycle of P450nor (Section 7.2), on copper-diazene type complexes (Section 7.3), on model studies for copper nitrite reductase (Section 7.4), on the complex $[Fe^{III}(tmdta)]^-$ (Section 7.5) and on studies on the N-N cleavage in Mo/W hydrazidium complexes with diphosphine coligands (Section 7.6). These studies resulted in several publications, which are included in this chapter. Since it is not obvious what my contribution to the individual publications is, I would like to clarify this in the following. In most cases, I have performed spectroscopic (Raman and MCD) or computational studies that were included in these papers.

Section 7.2 comprises the investigations on key intermediates of the catalytic cycle of P450nor using density functional theory calculations. This work has been mostly carried out by my supervisor Prof. Dr. Nicolai Lehnert, and is therefore included in this thesis in the collaborative chapter. As already mentioned in the Introduction (cf. Chapter 1), Fe(III) is part of the catalytic cycle of P450nor. In this case, the ferric form is catalytically active and binds NO forming the corresponding ferric nitrosyl adduct with *trans* cysteine coordination. This is followed by two-electron reduction leading to a formal Fe(I)-NO complex that reacts with a second molecule of NO forming nitrous oxide. I have optimized the structures of the intermediates of the catalytic cycle of P450nor using BP86/TZVP in the given spin states.

Sections 7.3 and 7.4 comprise studies on copper-diazene complexes and on CuNIR model systems, which have been performed in collaboration with Prof. Dr. Kiyoshi Fujisawa, University of Tsukuba, Japan. Note that not much is known about the coordination chemistry of copper(I) with dinitrogen, diazene, and hydrazine. To this end, we have investigated mononuclear and binuclear copper(I)-hydrazine and -diazene complexes using anionic hydrotris(pyrazolyl)borate (L–) and neutral tris(pyrazolyl)methane (L') coligands, as presented in Section 7.3. I have performed the resonance Raman

measurements on these compounds. The copper(I)-nitrosyl $\{CuNO\}^{11}$ adduct is a very important intermediate in the general reactions of copper proteins with biologically available nitric oxide. In particular, copper nitrite reductase (CuNIR) is involved in the generation (and presumably degradation) of NO in denitrifying bacteria. In the paper presented in Section 7.4, two new crystal structures of mononuclear end-on Cu(I)-NO complexes are presented, and the first detailed spectroscopic analyses (vibrational and electronic) of this type of complexes are provided. As already mentioned in Chapter 3, my contribution to this publication is the MCD spectroscopic investigation of [Cu{HB(3,5-*i*-$Pr_2pz)_3$}NO], also referred as [Cu(L1)(NO)]. Samples for MCD were recorded in silicone oil (DC 200) mulls.

Section 7.5 comprises studies on the equilibrium between the twist-boat (tb) and half-chair (hc) conformers of the central diamine chelate ring of $[Fe^{III}(tmdta)]^-$ in solids and aqueous solution. I have performed the resonance Raman measurements on these compounds.

Finally, Section 7.6 comprises experimental and theoretical studies on the N-N cleavage of the dialkylhydrazido complex [W(dppe)2(NNC5H10)] upon treatment with acid, leading to the nitrido/imido complex and piperidine. I have performed the potential energy surface (PES) calculations shown in Figure 4 of this publication.

7.2. Electronic Structure of Iron(II)-Porphyrin Nitroxyl Complexes: Molecular Mechanism of fungal Nitric Oxide Reductase (P450nor)

Nicolai Lehnert*, V. K. K. Praneeth, Florian Paulat

Published in: *J. Comp. Chem.* **2006**, *27*, 1338-1351.
(special issue: Computational Bioinorganic Chemistry)

Electronic Structure of Iron(II)–Porphyrin Nitroxyl Complexes: Molecular Mechanism of Fungal Nitric Oxide Reductase (P450nor)

NICOLAI LEHNERT, V. K. K. PRANEETH, FLORIAN PAULAT
Institut für Anorganische Chemie, Christian-Albrechts-Universität Kiel, Olshausenstrasse 40, D-24098 Kiel, Germany

Received 18 November 2005; Accepted 26 January 2006
DOI 10.1002/jcc.20400
Published online in Wiley InterScience (www.interscience.wiley.com).

Abstract: Density functional calculations are employed to investigate key intermediates of the catalytic cycle of fungal nitric oxide reductase (P450nor). The formal Fe(II)–nitroxyl species Fe(II)—NO/(−) can principally exist in the two spin-states S = 0 and S = 1. In the S = 0 case, a very covalent Fe—NO σ bond is present, which leads to an electronic structure description that is actually intermediate between Fe(I)—NO and Fe(II)—NO^-. In contrast, the S = 1 case shows a ferrous Fe(II)—NO complex with the extra electron being stored in the π system of the porphyrin ligand. Importantly, the Fe(II)—NO/(−) species are very basic. The electronic structures and spectroscopic properties of the corresponding N- and O-protonated forms are very different, and unequivocally show that the Mb–HNO adduct (Mb-Myoglobin) prepared by farmer and coworkers is in fact N-protonated. The presence of an axial thiolate ligand enables a second protonation leading to the corresponding Fe(IV)—$NHOH^-$ species, which is identified with the catalytically active intermediate *I* of P450nor. This species reacts with a second molecule of NO by initial electron transfer from NO to Fe(IV) followed by addition of NO^+ forming an N—N bond. This is accompanied by an energetically very favorable intramolecular proton transfer leading to the generation of a quite stable Fe(III)—N(OH)(NOH) complex. This way, the enzyme is able to produce dimerized HNO under very controlled conditions and to prevent loss of this ligand from Fe(III). The energetically disfavoured tautomer Fe(III)—$N(OH_2)$(NO) is the catalytically productive species that spontaneously cleaves the N—OH_2 bond forming N_2O and H_2O in a highly exergonic reaction.

 J Comput Chem 27: 1338–1351, 2006

Key words: electronic structure; iron(II)–porphyrin nitroxyl complex; P450nor

Introduction

Due to their tremendous significance in biology, much research has been focused on the geometric and electronic structures, spectroscopic properties, and reactivities of iron–porphyrin NO complexes.[1] Nitric oxide plays a central role in many important biological processes including nerve signal transmission, blood pressure control, and immune response with new functions of this molecule still being discovered.[2] Most of these tasks involve heme proteins. In addition, nitric oxide is an intermediate in assimilatory and dissimilatory denitrification.[3] Assimilatory nitrite reductases are usually found in plants, and reduce nitrite to ammonia. These enzymes contain an active site that consists of a siroheme with an axially bound 4Fe–4S iron–sulfur cluster.[4] The addition of nitrite to reduced, active enzyme leads to the immediate formation of a stable ferrous siroheme–nitrosyl complex, which is also the major species present upon enzyme turnover.[4c,d] This species then undergoes further reduction leading to a one-electron reduced Fe(II)—NO intermediate, labeled Fe(II)—NO/(−) in the following, which is readily protonated and ultimately becomes ammonia in the further course of the reaction. In contrast, the nitrite reductases in dissimilatory denitrification produce nitric oxide, which is then further reduced to nitrous oxide by a different class of enzymes, the nitric oxide reductases (NOR).[5] In the case of fungal NOR (P450nor), the active site consists of a heme center with axially coordinated cysteinate.[6] The proposed mechanism of this

Correspondence to: N. Lehnert; e-mail: nlehnert@ac.uni-kiel.de

Contract/grant sponsor: the Deutsche Forschungsgemeinschaft (DFG; contract/grant numbers: LE 1393/1 and 1393/1-2)

Contract/grant sponsor: the Fonds der Chemischen Industrie (FCI)

This article contains Supplementary Material available at http://www.interscience.wiley.com/jpages/0192-8651/suppmat

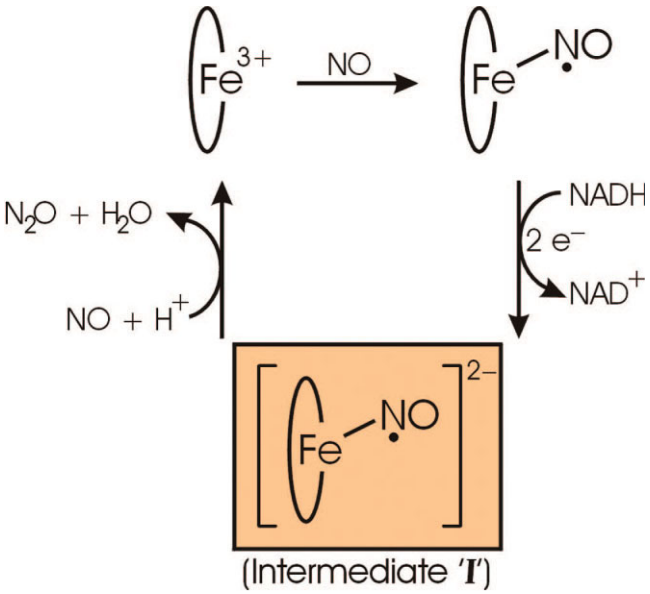

Scheme 1.

enzyme is shown in Scheme 1.[7] Initially, nitric oxide is bound to the ferric form of the enzyme, which is then reduced by two electrons from NADH to yield intermediate *I*, which therefore corresponds to a Fe(II)—NO/(−) species. This intermediate is characterized by a Soret band position of 444 nm compared to 434 nm for the ferrous NO complex.[7] Resonance Raman spectroscopy led to the identification of the Fe—NO stretch in *I* at 596 cm^{-1}. Importantly, this intermediate does not seem to undergo deuterium exchange, which indicates that *I* is not protonated.[8] The further course of the reaction is less clear, but leads to reaction with another molecule of NO to create nitrous oxide. In later work, a more detailed mechanism for this enzyme was proposed by Daiber et al.[9] based on kinetic studies, where intermediate *I* is again described as Fe(II)—NO/(−) species, but either singly or doubly protonated. The electronic structure of this intermediate has been proposed as either Fe(III) with a bound N(H)—OH radical (doubly protonated) or Fe(IV) with bound HNO and a cysteinyl radical (singly protonated), which is both counterintuitive. Hence, although Fe(II)—NO/(−) intermediates and/or corresponding protonated species are of great biological importance, not much is known about their detailed electronic structures and reactivities.

To gain more information about the properties of one-electron reduced ferrous nitrosyls, Fe(II)—NO/(−), a number of researchers have investigated corresponding model systems.[10] In a series of classic studies, Ryan and coworkers[11] used spectroelectrochemistry to investigate synthetic model complexes of type [Fe(P)(NO)] (P = tetraphenylporphyrin, octaethylporphyrin, and related porphyrinoids). One-electron reduction of these five-coordinate species led to only small changes of the Soret band position and intensity, which shows that the reducing equivalent is not stored in the π-system of the macrocyclic ligand.[11b] Hence, the electronic structure of the nonprotonated Fe(II)—NO/(−) species could either be of the Fe(II)—NO^- or of Fe(I)—NO type; that is, the one-electron reduction could either be ligand (NO) or metal centered. Based on the observed strong shift of the N—O stretching frequency down to 1496 cm^{-1}, it was claimed that the complex has to be described as low-spin Fe(II)—NO^- (S = 0), which is a ferrous "nitroxyl" species.[11b] Binding studies with N-donor ligands showed that upon reduction of the Fe(II)—NO complex, the axial pyridine, or amine ligand is lost.[11a] This indicates that nitroxyl has an even stronger *trans*-effect on coordinated axial ligands than NO.[12,13] It was also found that the Fe(II)—NO^- species reacts with weak acids, presumably forming corresponding Fe(II)—HNO and [Fe(II)—H_2NO]$^+$ species as reactive intermediates. However, such solutions are not stable and immediately led to the formation of hydroxylamine, ammonia and ferrous bis-ammonia complexes.[14] Information on corresponding protonated Fe(II)–nitroxyl complexes is available from the work of Farmer and coworkers[15] using myoglobin. Reduction of ferrous Mb–NO with Cr(II) salts led to the formation of a surprisingly stable Fe(II)–HNO complex as evidenced by ^{1}H-NMR spectroscopy. Only a small shift of the Soret band from 421 to 423 nm is observed in this reaction. The resulting species is diamagnetic and shows resonance Raman signals at 1385 cm^{-1} for ν(N—O) and 651 cm^{-1} for the Fe—NO stretch. Bond lengths from EXAFS measurements are 1.82 Å for Fe—NO and 2.09 Å for Fe—N(imidazole) as shown in Table 1.[8] Hence, this species corresponds to a six-coordinate complex with axial histidine coordination. An interesting question is then how an axial cysteinate as in P450nor would influence the reactivity of this intermediate. This question was addressed by Farmer and coworkers[16] investigating electrocatalytic nitrite reduction by myoglobin and P450 CYP119 in surfactant films. The results show a markely reduced current and a higher product specificity for the P450 enzyme in this reaction.[16b] The reduced activity of P450 CYP119 compared to myoglobin is somewhat surprising at the first glance, but can be explained by the known lower NO affinity of heme active sites with axial cysteinate coordination.[2h] In addition, the P450 enzyme also seems to exhibit a reduced rate of N–N coupling.[8]

At this point it should also be underlined that there is growing evidence for an independent biological significance of free nitroxyl itself.[17] This species might be created in vivo by nitric oxide synthase in the absence of its reduced pterin cofacor.[18] Results by Bartberger et al.[17b] show that free nitroxyl is protonated under physiological conditions, and that the redox potential of the HNO/NO couple is about −0.5 V, which means that free NO should not be largely reduced to HNO in cells. The pK_A of the free ^{1}HNO/$^3NO^-$ pair has been estimated to 11.4.[19] Therefore, NO and HNO do not seem to interconvert in vivo to a significant extend, which allows them to mediate different biological functions.[17] Free nitroxyl is easily trapped by ferric porphyrins (e.g., metmyoglobin and methemoglobin)[20] or thiols in vivo.[17a] In addition, free HNO converts rapidly to N_2O through dimerization followed by dehydration ($k \sim 2 \times 10^9$ $M^{-1}s^{-1}$).[17a]

In this study, density functional (DFT) calculations are used to define the electronic structures of the Fe(II)–nitroxyl complexes. For the calculations, six-coordinate species are chosen because the enzymatic species can be expected to be six-coordinate with either histidine or cysteinate present. These are modeled using porphine (P^{2-}; cf. Scheme 2) for the porphyrin ligand and 1-methylimidazole (MI) and methylthiolate (CH_3S^-) as axial ligands, respectively. Spectroscopic parameters are calculated and correlated with the known experimental

Table 1. Calculated Geometric Properties and Relative Energies of $[Fe(P)(L)(NO)]^{-/2-}$ Complexes and Corresponding Intermediates (L = MI or CH_3S^-) Compared to Experiment.

	Geometric parameters [Å]					Relative energies (kcal/mol)	
Molecule[a]	ΔFe—N	ΔN—O	∠Fe—N—O	ΔFe—L_{tr}	ΔN—N	BP86	B3LYP
[Mb-HNO] (ref. 8)	1.82	1.24	131	2.09	—	—	—
$[Fe(P)(MI)(NO)]^-$ (**1**, S = 0)	1.795	1.211	124	2.439	—	0	0
$[Fe(P)(MI)(NO)]^-$ (S = 1)	1.715	1.193	141	2.256	—	+3.9	−2.7
$[Fe(P)(CH_3S)(NO)]^{2-}$ (**2**, S = 0)	1.776	1.215	131	2.587	—	0	0
$[Fe(P)(CH_3S)(NO)]^{2-}$ (S = 1)	1.764	1.205	139	2.478	—	−0.4	−9.6
$[Fe(P)(CH_3S)(NHO)]^-$ (**3a**, S = 0)	1.824	1.252	133	2.354	—	0	0
$[Fe(P)(CH_3S)(NOH)]^-$ (**3b**, S = 0)	1.746	1.401	117	2.411	—	+25.4	+29.0
$[Fe(P)(CH_3S)(NHOH)]$ (**4**, S = 0)	1.810	1.397	125	2.230	—	—	—
$[Fe(P)(CH_3S)(N_2O_2)]^{2-}$ (**5**, S = 1/2)	1.957	1.238	125	2.437	1.549	—	—
$[Fe(P)(CH_3S)(N_2O_2H)]^-$ (**6a**, S = 1/2)	1.988	1.398	121	2.250	1.308	0	0
i-$[Fe(P)(CH_3S)(N_2O_2H)]^-$ (**6b**, S = 1/2)	2.080	1.269	123	2.293	1.793	+27.6	+33.1
$[Fe(P)(CH_3S)(N_2O_2H_2)]$ (**7b**, S = 1/2)	2.128	1.406	115	2.177	1.250	0	0
i-$[Fe(P)(CH_3S)(N_2O_2H_2)]$ (**7a**, S = 1/2)	1.988[c]	1.398	121	2.212	1.760	+16.5	+18.1
$[Fe^{II}(P)(NO)]$-calc[13]	1.705	1.179	146	—	—	—	—
$[Fe^{II}(P)(MI)(NO)]$-calc[13]	1.734	1.186	140	2.179	—	—	—
$[Fe^{II}(P)(CH_3S)(NO)]^-$-calc[26]	1.788	1.198	138	2.416	—	—	—
$[Fe^{II}(TPP)(NO)]$ (ref. 29)[b]	1.72	1.12	149	—	—	—	—
$[Fe^{II}(TPP)(MI)(NO)]$ (ref. 12)	1.750	1.182	138	2.173	—	—	—

[a]MI = 1-methylimidazole; P = Porphine (2−).
[b]Highly disordered structure.
[c]Fixed at the optimized distance obtained for **6a**. Otherwise, $N_2O_2H_2$ is lost from iron during the geometry optimization.

data described above. This allows for an identification of the key intermediate *I* in the catalytic cycle of P450nor. Comparison with the electronic structures of corresponding ferrous nitrosyls is also provided. Based on these results, the reaction mechanism of P450nor is investigated by optimization of key species and then application of frequency and solvent field calculations to obtain the corresponding free energies. From these results, pK_A values for the protonation of the initially formed Fe(II)—NO/(−) intermediate are also obtained. Finally, the biological implications of these results are discussed. Note that the mechanism of P450nor has been investigated before using DFT calculations.[21] Structures of the model system $[Fe(P)(CH_3S)(NO)]^{2-}$ and of corresponding protonated and nitrosylated systems have been calculated before by Silaghi–Dumitrescu,[21a] but no correlation with experimental data is given and the mechanism of P450nor is not quantitatively evaluated in this work. In a recent publication, Vincent et al.[21c] investigated key steps in the mechanism of P450nor using DFT. However, comparison of the calculated properties with experimental data is again limited in this article, the energies of the different protonation steps are not considered, and the entire scenario of the possible protonation equilibria of the different species involved is missing. Hence, the work presented here reaches far beyond the scope of these earlier studies.

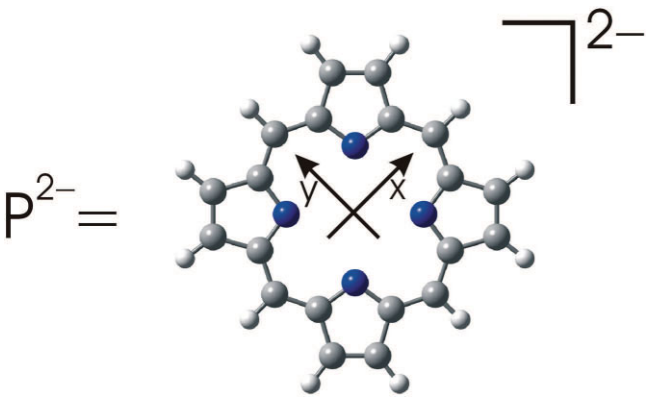

Scheme 2.

Table 2. Calculated Vibrational Properties and Force Constants of $[Fe(P)(L)(NO)]^{-/2-}$ Complexes and Corresponding Intermediates (L = MI or CH_3S^-) Compared to Experiment.

	Vibrational frequencies (cm^{-1})		Force constants (mdyn/Å)		
Molecule[a]	ν(N—O)	ν(Fe—NO)	N—O	Fe—NO	Fe—L_{tr}[c]
$[Fe(TPP)(NO)]^-$	1496		—	—	—
[Mb-HNO] (ref. 8)	1385	651	—	—	—
P450nor: intermediate *I*[7b]		596	—	—	—
$[Fe(P)(MI)(NO)]^-$ (**1**, S = 0)	1511	544/(435)	10.29	2.50	0.21
$[Fe(P)(MI)(NO)]^-$ (S = 1)	1630	616	11.63	3.52	0.47
$[Fe(P)(CH_3S)(NO)]^{2-}$ (**2**, S = 0)	1500	502	9.97	2.61	0.42
$[Fe(P)(CH_3S)(NO)]^{2-}$ (S = 1)	1567	573/453	10.77	2.73	0.61
$[Fe(P)(CH_3S)(NHO)]^-$ (**3a**, S = 0)	1386	601/430	8.67	2.52	1.07
$[Fe(P)(CH_3S)(NOH)]^-$ (**3b**, S = 0)	833	649	3.44	3.32	0.88
$[Fe(P)(CH_3S)(NHOH)]$ (**4**, S = 0)	952	609/544[b]	4.50	2.63	1.56
$[Fe^{II}(P)(NO)]$-calc[13]	1703	595	12.71	3.62	—
$[Fe^{II}(P)(MI)(NO)]$-calc[13]	1662	609	12.22	3.26	0.61
$[Fe^{II}(P)(CH_3S)(NO)]^-$-calc[29]	1599	531/440	11.26	2.38	0.81
$[Fe^{II}(TPP)(NO)]$ (ref. 13)	1697	532	12.53	2.98	—
$[Fe^{II}(TPP)(MI)(NO)]$ (ref. 13)	1630	440/530	11.55	2.55	—

[a]MI = 1-methylimidazole; P = $Porphine^{2-}$.
[b]Both modes at 609 and 544 cm^{-1} are strongly mixed with in-plane and out-of-plane Fe—N—H bends.

Computational Procedures

Density Functional Calculations

The structures of the models **1**–**8** listed in Tables 1–3 have been fully optimized using BP86/TZVP in the given spin states. For all these calculations, the simple porphine P^{2-} ligand as shown in Scheme 2 has been used. Axial histidine and cysteinate ligands have been modeled using 1-methylimidazole (MI) and methylthiolate (CH_3S^-), respectively. Vibrational frequencies have been calculated for all structures. Low-lying imaginary frequencies ($<25i$ cm^{-1}) have been obtained for **1** (S = 0; MI rotation), and **3a** and **3b** (rotation of the axial ligands along the z axis). The structure of $[Fe(P)(CH_3S)(NO)]^{2-}$ (S = 1) shows one imaginary frequency at $\sim 110i$ cm^{-1} that, however, corresponds to a rotation of the CH_3 group around the S—CH_3 axis of the thiolate ligand, and hence, is irrelevant. In addition, B3LYP/LanL2DZ* calculations have been performed on all these model systems to obtain accurate total energies for the determination of reaction energies. The LanL2DZ* basis set consists of LanL2DZ plus polarization functions (from TZVP) on all heavy atoms. Solvation effects were included in the calculations using the PCM model and water as the solvent. From these results, pK_A values can be calculated using the equation:

$$pK_A = \frac{\Delta G}{2.3026 \cdot R \cdot T}.$$

Surprisingly, the calculated value for the $^1HNO/^3NO^-$ pair of 23.5 shows significant deviation from the experimental value of ~11.4. Using B3LYP/TZVP instead of B3LYP/LanL2DZ* single-point calculations only leads to a small improvement of the theoretical result (calcd.: 19.1). Hence, the much more cost-efficient B3LYP/LanL2DZ* method is used for the calculations on the model complexes. All these methods were used as implemented in the Gaussian 98 package.[22] Force constants in internal coordinates were calculated using a modified version of the program Redong[23] (QCPE 628). Molecular orbitals were visualized using GaussView. S^2-expansion techniques have been applied on the ferrous nitrosyls using a program provided by Zilberberg and coworkers.[24]

Results and Analysis

Electronic Structure of $[Fe(P)(MI)(NO)]^-$ (1)

Figure 1(top) shows the optimized structure of $[Fe(P)(MI)(NO)]^-$ (**1**) for S = 0, and Table 1 lists important structural parameters for this model complex obtained from BP86/TZVP calculations. Bond lengths of 1.795 Å for Fe—NO and 1.211 Å for N—O are obtained. Corresponding force constants are 2.5 mdyn/Å for Fe—NO and 10.3 mdyn/Å for N—O as listed in Table 2. The Fe—N(imidazole) bond is very long at 2.439 Å, which is basically nonbonding. This is also reflected by the Fe—N(imidazole) force constant, which is only 0.2 mdyn/Å. The calculated value of 1511

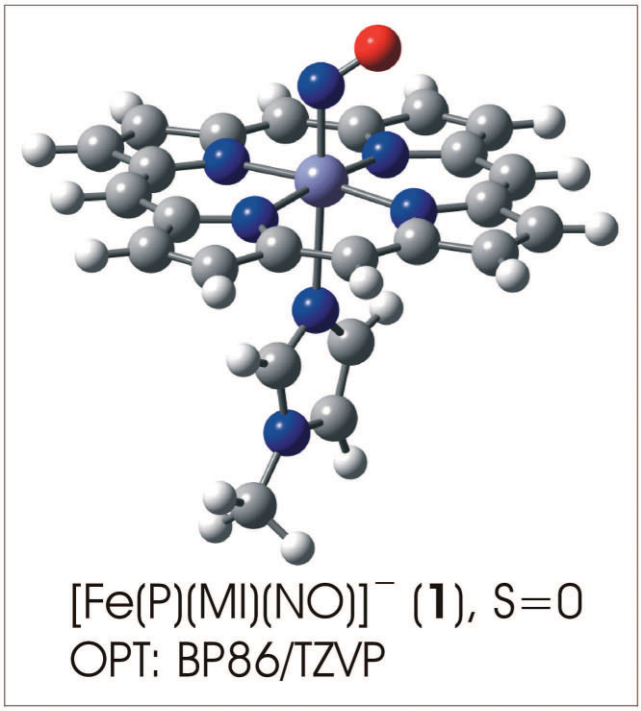

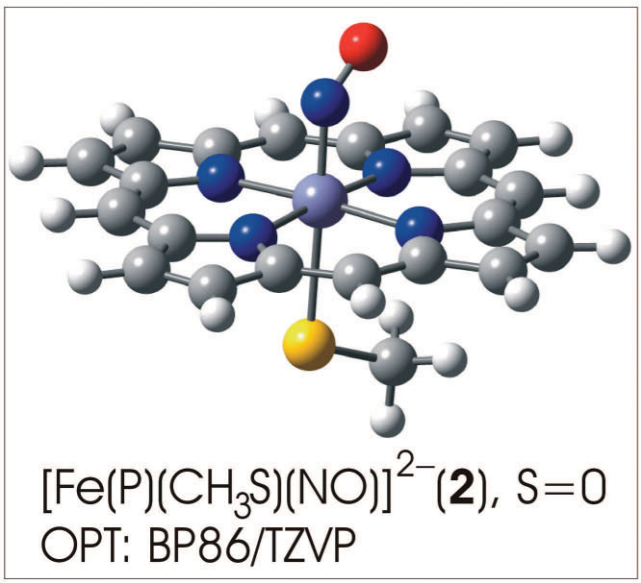

Figure 1. Figures of the fully optimized structures of [Fe(P)(MI)(NO)]$^-$ (**1**, S = 0; P = Porphine (2−); MI = 1-methylimidazole) and [Fe(P)(CH_3S)(NO)]$^{2-}$ (**2**, S = 0) obtained with BP86/TZVP. Structural parameters are given in Table 1.

cm^{-1} for the N—O stretch ν(N—O) of **1** is in excellent agreement with the experimentally determined N—O stretching frequency of 1496 cm^{-1} for one-electron reduced [Fe(TPP)(NO)] (TPP = tetraphenylporphyrine).[11b] This is additional strong evidence that [Fe(TPP)(NO)]$^-$ has an S = 0 ground state as has been proposed by Ryan and coworkers (see Introduction). Therefore, the electronic structure of the corresponding six-coordinate species [Fe(P)(MI)(NO)]$^-$ (**1**) in the relevant S = 0 state will be analyzed in the following. Note that from the calculations, the S = 0 and S = 1 states of [Fe(P)(MI)(NO)]$^-$ are very close in energy (within 5 kcal/mol), that is, the ground state is S = 0 with BP86 and S = 1 for B3LYP as listed in Table 1. The MO diagram of **1** (S = 0) is given in Figure S1, and contour plots of important orbitals are shown in Figure S2. The coordinate system used for the following discussion is shown in Scheme 2 where the Fe—N(O) bond is roughly oriented along the z axis. The HOMO of complex **1**, labeled π^*_h_d_{z^2}/d_{xz} ⟨123⟩, corresponds to an equal mixture of d_{z^2}/d_{xz} of iron and π^*_h of NO (h = horizontal; the π^* orbital within the Fe—NO plane). This MO is Fe—NO bonding and hence, constitutes a very strong Fe—NO σ bond. On the other hand, this orbital is σ antibonding with respect to MI, which explains the very weak Fe—N(imidazole) interaction in this complex, which has also been observed experimentally.[11] To lower energy, the three t_2 orbitals of iron, d_{xz}, d_{yz}, and $d_{x^2-y^{2*}}$ (in the given coordinate system) are found, which are fully occupied. An additional contribution to the Fe—NO bond corresponds to a backbonding interaction between d_{yz} and the π^*_v orbital of NO (v = vertical; the π^* orbital perpendicular to the Fe—NO plane). The strength of this interaction is estimated best from the corresponding antibonding combination, π^*_v_d_{yz} ⟨127⟩, which has 22% d and 67% π^* character as listed in Table S1. Based on this MO description, the Fe(II)—NO^- (ferrous-nitroxyl) classification of [Fe(TPP)(NO)]$^-$ as proposed by Ryan and coworkers[11b] is not entirely correct, because the two σ electrons occupying the π^*_h orbital of the bound $^1NO^-$ ligand are *fully delocalized* over the Fe—N—O unit by strong mixing with d_{z^2} of iron. Because of this, the NO bond is stronger and ν(NO) around 1500 cm^{-1} is higher in energy in **1** than in free NO^- (1290 cm^{-1}; cf. ref. 17a). On the other hand, a one-electron reduced Fe(II)—NO/(−) species has also been characterized for a nonheme iron complex using a tethered cyclam ligand.[25] In this case, ν(N—O) is observed at 1271 cm^{-1}, which shows that the NO ligand experiences a much stronger degree of reduction in this complex. This marks an important difference between heme vs. nonheme iron chemistry.

The electronic structure of [Fe(P)(MI)(NO)]$^-$ completely changes in the S = 1 state. As listed in Table 1, this complex has shorter Fe—N(O), N—O, and Fe—N(imidazole) bond lengths than **1** (S = 0). In fact, these bond distances are actually close to the values observed for the ferrous–nitrosyl complex [Fe(P)(MI)(NO)]. Correspondingly, the calculated N—O stretching frequency of 1630 cm^{-1} for the S = 1 complex matches the value of 1662 cm^{-1} calculated for [Fe(P)(MI)(NO)]. This shows that [Fe(P)(MI)(NO)]$^-$ with S = 1 has a ferrous–nitrosyl electronic structure, where the extra electron must then be stored in the porphyrin ligand by forming a P^{3-} radical anion. This description is confirmed by the calculated spin density of the S = 1 complex. As a consequence, the nature of the porphyrinoid macrocycle might play an important role in determining the ground state of [Fe(porphyrin)(L)(NO)]$^-$ type complexes. Because the spectroscopic properties of the S = 0 and S = 1 states are very different, it is obvious from the experimental data on [Fe(TPP)(NO)]$^-$ that this complex has an S = 0 ground state as discussed above.[11]

Electronic Structure of $[Fe(P)(CH_3S)(NO)]^{2-}$ (2)

Based on the electronic structure description of $[Fe(P)(MI)(NO)]^-$ (**1**, S = 0) elaborated above, it is interesting to explore how an axial thiolate ligand as observed in P450nor would alter the properties of the Fe—NO subunit. From previous work on ferrous nitrosyls it is known that this effect can be substantial (vide infra).[26] To this end, we have optimized the structure of the model system $[Fe(TPP)(CH_3S)(NO)]^{2-}$ (**2**, S = 0) using BP86/TZVP. As shown in Table 1, the obtained Fe—NO and N—O bond distances of 1.776 and 1.215 Å are very close to those of **1**. Correspondingly, the N—O stretching frequency of **2** calculated at 1500 cm^{-1} almost matches the value of 1511 cm^{-1} for **1**. The fact that **1** and **2** have overall similar properties is not surprising, because due to the strong *trans*-effect of the coordinated nitroxyl ligand, the axial imidazole in **1** and thiolate in **2** are only very weakly bound (force constants are 0.21 mdyn/Å for Fe—N and 0.42 mdyn/Å for Fe—S, respectively). Small differences in electronic structures are evident from the calculated force constants shown in Table 2, which can be explained based on the MO diagram of **2** shown in Figure S3 (contour plots are given in Fig. S4). Analysis of the MO scheme shows that the principal bonding interactions between iron(II) and NO^- are very similar in **1** and **2**, that is, a σ bond is formed between π^*_h of $^1NO^-$ and a mixed d_{z^2}/d_{xz} orbital of iron and a π backbond is present due to interaction of π^*_v and d_{yz}. Compared to **1**, the mixing between π^*_h and d_{z^2} is somewhat reduced, which leads to a slight weakening of the Fe—NO σ bond and a slight increase in the occupation of π^*_h in **2**. This corresponds to a slight *trans*-effect of the thiolate ligand on the coordinated NO (cf. ref. 26). In the case of the π backbond, analysis of the antibonding orbital π^*_v–d_{yz} shows a slight increase in metal contribution in the case of **2**, which corresponds to a slight strengthening of this interaction. Taken together, both effects lead to a slight increase of the occupation of the π^* orbitals of NO in **2**, which explains the observed reduction of the N—O force constant by 0.3 mdyn/Å from 10.29 mdyn/Å in **1** to 9.97 mdyn/Å in **2**. For the Fe—NO bond, these effects cancel, leaving the corresponding force constant almost unchanged, as shown in Table 2. In the S = 1 state of $[Fe(TPP)(CH_3S)(NO)]^{2-}$, a similar situation is encountered as in the case of $[Fe(P)(MI)(NO)]^-$, where the porphyrin ring is reduced leading to a P^{3-} radical anion. However, in the case of **2**, the stabilization of the S = 1 state relative to the S = 0 state is enhanced. Calculated energies are −0.4 kcal/mol with BP86 and −9.6 kcal/mol with B3LYP in favor of S = 1 as shown in Table 1.

From these results, the main effect of thiolate coordination in the Fe(II)–nitroxyl complexes seems to be a stabilization of the S = 1 state, whereas the electronic structure of the Fe—NO subunit is hardly altered. It is, of course, tempting to conclude that this is the actual reason for axial cysteinate coordination in P450nor, which researchers have speculated about for a long time.[8] An S = 1 ground state for intermediate *I* would be advantageous for the following reaction with the radical NO, which would otherwise be spin forbidden. However, as we will show below, we believe that intermediate *I* in P450nor is actually protonated, and therefore, the question of whether the Fe(II)–nitroxyl complex with thiolate coordination has an S = 0 or S = 1 ground state is not relevant for the mechanism of P450nor. At this point it should also be mentioned that electrocatalytic investigations of Farmer and coworkers on the nitrite and NO reduction by myoglobin and P450 CYP119 did not show any enhancement of NO reductase activity for the P450 enzyme in agreement with this conclusion.[16]

Comparison of the Electronic Structures of Fe(II)–Nitroxyl Complexes and Ferrous NO Adducts

The electronic structure of the ferrous six-coordinate complex [Fe(P)(MI)(NO)] has been described as Fe(II)—NO(radical) adduct.[13a] Analysis of the unrestricted single-determinantal wave function from the B3LYP calculation by expansion in the basis of Löwdin–Amos–Hall paired orbitals using the approach of Zilberberg and coworkers[27] again validates this description. From this analysis, the ground state of this complex has 88% Fe(II)—NO(radical) character with a 12% admixture of a ligand field excited state. The SOMO of this complex, which corresponds to a bonding combination of a mixed d_{z^2}/d_{xz} orbital of iron(II) and π^*_h of NO, reflects this electronic structure. Charge contributions to the SOMO of 42% Fe and 43% NO [13b] are basically identical with the HOMO of one-electron reduced $[Fe(P)(MI)(NO)]^-$ (**1**) in the S = 0 state as described above. This means that one-electron reduction of the ferrous nitrosyl simply leads to a double occupation of its SOMO, which strengthens the Fe—NO σ bond, whereas at the same time the Fe—N(imidazole) bond is further weakened in agreement with the experimental results.[11] Based on this large difference in σ bonding, one would expect that **1** exhibits a stronger Fe–NO bond than the ferrous nitrosyl complex. However, this is not the case, as is evident from the calculated Fe—NO force constants listed in Table 2. This is due to a reduction of π-backbonding, but also an increase of Coulomb repulsion, between d_{xz} and π^*_h in **1** compared to the ferrous nitrosyl complex. This is a very important result, because it indicates that the corresponding Fe—NO stretching vibration should be shifted to *lower energy* in **1** compared to [Fe(P)(MI)(NO)].

In the case of the corresponding complexes with axial thiolate coordination, a more complicated situation is encountered. This is due to the fact that the ferrous nitrosyls, $[Fe(P)(CH_3S)(NO)]^-$ and [Fe(P)(MI)(NO)], have different electronic structures, where axial thiolate coordination leads to a distinct weakening of the Fe—NO σ bond.[26] In addition, spin polarization effects are observed for the π-backbond in $[Fe(P)(CH_3S)(NO)]^-$, which leads to a large amount of positive spin density on the NO ligand (>1.0) and the occurrence of negative spin density on iron. We have now reevaluated this electronic structure using Löwdin–Amos–Hall paired orbitals, and we found that the observed spin-polarization effects are actually due to the admixture of a distinct amount of Fe(III)—NO^- character into the ground state of $[Fe(P)(CH_3S)(NO)]^-$, which has 74% Fe(II)—NO(radical) character with 18% admixture of Fe(III)—NO^- and 6% contribution from a ligand field excited state. This is due to a stabilization of Fe(III) by the thiolate ligand. These special features of the electronic structure of the ferrous nitrosyl are lost upon one electron reduction. Because the axial thiolate has a strong effect on the Fe—NO unit in the ferrous nitrosyl, but only a weak effect in $[Fe(P)(CH_3S)(NO)]^{2-}$ (**2**) in the S = 0 state (vide supra), the change of force constants and vibrational frequencies is distinctively smaller in this case compared to the complexes with axial

imidazole ligation. The Fe—NO force constant actually slightly increases from 2.38 mdyn/Å in ferrous $[Fe(P)(CH_3S)(NO)]^-$ to 2.61 mdyn/Å in **2**. The Fe—NO stretching frequency does not follow this trend and slightly drops to 502 cm^{-1} in **2**. This is due to a change in mode mixing of δ(Fe—N—O) with porphyrin vibrations, and hence, might be overestimated in the calculations. On the other hand, the N—O stretch follows the general trend and decreases by ~100 cm^{-1} upon one-electron reduction, reflecting the increase in the occupation of the π^* orbitals of NO in **2**. Importantly, the experimentally determined Fe—NO stretches in the ferrous P450cam and chloroperoxidase NO adducts are observed at 554 and 542 cm^{-1}, respectively,[28] which means that the one-electron reduced species must have a frequency at identical or lower energy. In contrast, the Fe—NO stretch in intermediate *I* has been reported at 596 cm^{-1} (cf. Table 2). Based on these results, we believe that the proposal of Daiber et al., following kinetic evidence, is correct, and that intermediate *I* is actually protonated. This aspect is further analyzed in the next section.

Protonation of $[Fe(P)(CH_3S)(NO)]^{2-}$ (2) and Nature of the [Mb–HNO] Adduct and Intermediate I

Based on the finding that intermediate *I* is most probably protonated, it is then important to investigate the resulting singly and doubly protonated ferrous-nitroxyl species. Note that the free $^1HNO/^3NO^-$ pair has a pK_A of approximately 11.4, which means that $^3NO^-$ is fully protonated in water yielding ^1HNO. Starting with the singly protonated case, the bound nitroxyl could either be protonated at the coordinating nitrogen or the terminal oxygen atom. The structures of both resulting complexes, $[Fe(P)(CH_3S)(NHO)]^-$ (**3a**, S = 0, N-protonated) and $[Fe(P)(CH_3S)(NOH)]^-$ (**3b**, S = 0, O-protonated), have been fully optimized using BP86/TZVP and are shown in Figure 2 [open-shell spin states (S = 1, 2) have not been considered in these cases, because the work of Silaghi–Dumitrescu has shown that these are at distinctively higher energies (>+15 kcal/mol)][21a]. Importantly, the electronic structures of these intermediates are very different. This is already indicated by the obtained bond distances as shown in Table 2. In the case of **3a**, protonation leads to an increase of both the Fe—N and N—O distances to 1.824 and 1.252 Å, respectively, compared to **2**. An inspection of the MO diagram of this complex shows that the added proton binds to the π^*_h orbital of the NO ligand leading to a planar Fe—N(H)O unit. This strongly decreases π^*_h in energy, and hence, decreases its interaction with d_{z^2} of iron compared to **2**. Because the resulting bonding orbital, $\pi^*_h\_d_{z^2}$, is distributed over several MOs (cf. ⟨106⟩ in Fig. 2), it is useful to analyze the corresponding antibonding (unoccupied) combinations, $d_{z^2}\_\pi^*_h$. In the case of **3a**, this orbital has 56% d_z2 and only 15% π^* character (cf. Fig. 2), whereas the corresponding orbital of **2** has 43% d_{z^2} and 33% π^* contribution (cf. Table S2). Hence, upon protonation of the coordinated NO in **2**, the two electrons occupying the σ bonding orbital $\pi^*_h\_d_{z^2}$ are shifted toward the generated HNO ligand and the metal–ligand covalency decreases. This weakens both the Fe—N σ bond and the N—O bond in **3a** compared to **2**. The backbond between π^*_v of NO and d_{yz} of iron is somewhat stronger in the case of **3a**, where the corresponding antibonding combination, $\pi^*_v\_d_{yz}$ ⟨117⟩ (cf. Fig. 2), has 60% π^*_v and 30% d_{yz} character. This somewhat compensates the loss in Fe—N σ bonding in **3a** compared to **2**. In addition, this further weakens the N—O bond, which explains the strongly reduced N—O force constant and stretching frequency in **3a** compared to **2** (cf. Table 2). In summary, the electronic structure of the intermediate **3a** can be described as a simple Fe(II)–HNO adduct with a quite strong π backbond.

Importantly, the electronic structure of the O-protonated tautomer **3b** is very different. In this case, the Fe—N distance is decreased to 1.746 Å, whereas the N—O bond length is strongly increased to 1.401 Å compared to **2**. As in the case of **3a**, the resulting Fe—NOH unit is planar, as shown in Figure 2, which indicates that the proton interacts with the π^*_h orbital of NO. This is confirmed by inspection of key MOs of **3b** shown in Figure 2. As in the case of **3a**, the addition of a proton to π^*_h lowers this orbital in energy, which leads to a distinct increase of its occupation and a decrease of its mixing with d_{z^2} of iron compared to **2**. The corresponding antibonding combination, $d_{z^2}\_\pi^*_h$ ⟨120⟩, has charge contributions of 52% d_{z^2} and 20% π^*_h, which is quite similar to **3a**. Hence, as in the case of **3a**, the two electrons occupying the $\pi^*_h\_d_{z^2}/d_{xz}$ HOMO in **2** are transferred to the NO ligand upon protonation. The π backbond between π^*_v and d_{yz} is further enhanced compared to **2** and **3a**. This is evident from the corresponding antibonding combination, $\pi^*_v\_d_{yz}$ ⟨117⟩ (cf. Fig. 2), which has 50% π^*_v and 37% d_{yz} character in the case of **3b**. Hence, this bonding description should give rise to a somewhat stronger Fe—N bond and a somewhat weaker N—O bond in **3b** compared to **3a**. However, this is not in agreement with the observed large difference in N—O bond lengths in these complexes. The strong elongation of the N—O distance to 1.401 Å in **3b** is actually due to a *polarization* of the out-of-plane π^*_v and π^b_v orbitals of NO leaving two p orbitals behind, N(p) and O(p), that only weakly interact. Hence, the out-of plane π bond has almost disappeared in **3b**, leading to an N—O single bond. Because O(p) is occupied and N(p) is empty, the latter forms a very strong π backbond with d_{yz}, which explains the distinct shortening (strengthening) of the Fe—N bond in **3b**. In summary, the electronic structure of this complex has to be described as Fe(II)—NOH with a very weak N—O bond. The remarkably different electronic structures of the N- and O-protonated tautomers of **2** are also reflected by their vibrational properties. In the case of **3a**, the N—O force constant of 8.67 mdyn/Å corresponds to a weak N—O double bond with a predicted N—O stretch of 1386 cm^{-1}. In contrast, the N—O force constant of 3.44 mdyn/Å in **3b** confirms the single bond character with a predicted ν(N—O) of only 833 cm^{-1}. Compared to the N—O stretch of **2** calculated at 1500 cm^{-1}, the position of ν(N—O) therefore allows to easily distinguish between the complexes **2**, **3a**, and **3b** experimentally. Whereas the Fe—N force constant of **3a** (2.52 mdyn/Å) is almost identical to that of **2**, the Fe—NO stretch in this complex is predicted to be ~600 cm^{-1}, and hence, about 100 cm^{-1} higher in energy than in **2**. This surprising result is due to an intrinsic admixture of the Fe—N—H bend into ν(Fe—NO), which increases the energy of this mode in the case of **3a**. Complex **3b** has the strongest Fe—N bond with a force constant of 3.32 mdyn/Å and a predicted Fe—NO stretch of 649 cm^{-1}.

Farmer and coworkers reported the synthesis of an HNO adduct of Mb, which turned out to be surprisingly stable.[8] Based on ^1H-NMR results it was proposed that this species is N-protonated.

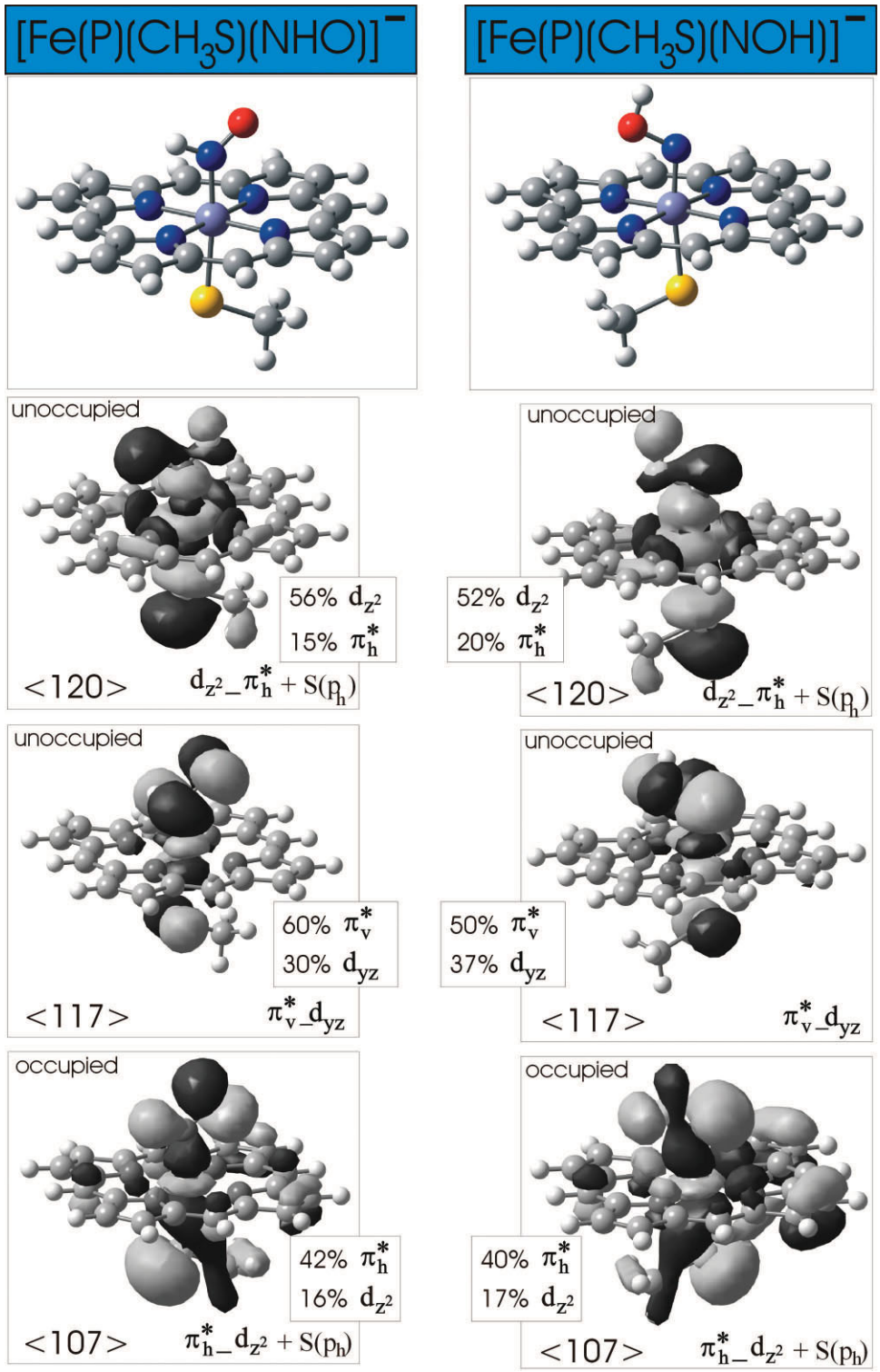

Figure 2. Optimized geometries (top) and contour plots of important molecular orbitals of $[Fe(P)(CH_3S)(NHO)]^-$ (**3a**, S = 0, left) and $[Fe(P)(CH_3S)(NOH)]^-$ (**3b**, S = 0, right) calculated with BP86/TZVP. Orbital decompositions are also included.

Table 3. Calculated Electronic Energies ε, and Free Energy and Solvation Corrections (G_{corr} and G_{SOLV}) for $[Fe(P)(CH_3S)(NO)]^{-/2-}$ Complexes and Corresponding Intermediates (P = Porphine(2−)) at T = 298.15 K. Calculated free reaction energies relative to **3a** (cf. Scheme 3) and pK_A values are also listed.

	Calculated energies (Hartree)					
Complex	ε	G_{corr}	G_{SOLV}	G_{SUM}[a]	ΔG (kcal/mol)	pK_A
$[Fe(P)(CH_3S)(NO)]^{2-}$ (**2**, S = 0)	−1291.92578	0.24907	−0.25048	−1291.92719	+46.64	—
$[Fe(P)(CH_3S)(NHO)]^{-}$ (**3a**, S = 0)	−1292.61334	0.26788	−0.07394	−1292.41940	**0.0**	34.2
$[Fe(P)(CH_3S)(NOH)]^{-}$ (**3b**, S = 0)	−1292.56709	0.26667	−0.07726	−1292.37768	+26.2	15.0
$[Fe(P)(CH_3S)(NHOH)]$ (**4**, S = 0)	−1293.10301	0.28044	−0.02837	−1292.85094	−8.6	6.3[b]
$[Fe(P)(CH_3S)(N_2O_2)]^{2-}$ (**5**, S = 1/2)	−1421.89651	0.25431	−0.25295	−1421.89515	+21.2	—
$[Fe(P)(CH_3S)(N_2O_2H)]^{-}$ (**6a**, S = 1/2)	−1422.58098	0.27005	−0.06977	−1422.38070	−21.3	31.1
i-$[Fe(P)(CH_3S)(N_2O_2H)]^{-}$ (**6b**, S = 1/2)	−1422.52818	0.26885	−0.08156	−1422.34089	+3.7	12.8
i-$[Fe(P)(CH_3S)(N_2O_2H_2)]$ (**7a**, S = 1/2)	−1423.07461	0.28490[c]	−0.00746	−1422.79717	−20.4	—
$[Fe(P)(CH_3S)(N_2O_2H_2)]$ (**7b**, S = 1/2)	−1423.10339	0.28505	−0.00486	−1422.82320	−36.9	—
Transition State (**7c**, S = 1/2); **estim.**[d]	−1423.04991		−0.00248	−1422.76734	(−1.8)	—
hs-$[Fe(P)(CH_3S)]$ (**8**)	−1162.00805	0.24826	−0.00437	−1161.76416	−89.6[e]	—
NO	−129.91377	−0.01574	0.00215	−129.92736	—	—
$^3NO^-$	−129.90481	−0.01751	−0.12263	−130.04495	0	—
^1HNO	−130.49584	−0.00830	−0.00975	−130.51389	32.03	23.5[f]
H^+ (see ref. 30)	0			−0.41789	—	—
N_2O	−184.69207	−0.01064	−0.00096	−184.70367	—	—
H_2O	−76.43112	0.00290	−0.01138	−76.43960	—	—

[a] $G_{SUM} = \varepsilon + G_{corr} + G_{SOLV}$; ε = electronic energy, G_{corr} = thermal and entropy correction to ε, G_{SOLV} = free energy of solvation. G_{corr} is taken from the BP86/TZVP frequency calculation, the other energies are calculated with B3LYP/LanL2DZ* (see Experimental Section).
[b] Relative to **3a**.
[c] The structure of **7a** has not been fully optimized (cf. Table 1). Hence, the calculated G_{corr} is only an estimate.
[d] We were not able to obtain the structure of the transition state from true transition state optimizations. The energy given here (using G_{corr} from **7b**) corresponds to a structure where the N—OH and both O—H distances have been fixed and the geometry was then optimized. This is only a crude approximation.
[e] Energy includes the formation of N_2O and H_2O.
[f] Experimental pK_A value for $^1HNO \rightarrow {}^3NO^- + H^+$: ∼11.4 (ref. 19a).

Vibrational energies of 1385 cm^{-1} for the N—O and 651 cm^{-1} for the Fe—NO stretch were reported for this complex. This N—O vibrational frequency is in very good agreement with the value of 1386 cm^{-1} calculated for **3a**, which nicely confirms that [Mb–HNO] is, in fact, N-protonated. The Fe—NO stretch of this species is at higher energy than the value of 601 cm^{-1} calculated for **3a**. This shift in energy could be due to the axial N- vs. S-donor ligands in [Mb–HNO] and **3a**, respectively. As shown in Table 2, bottom, the Fe—NO stretch in iron(II)–nitrosyls also shows a distinct shift to lower energy in the presence of an axial thiolate donor compared to the complex with axial imidazole ligation.[26]

The N- and O-protonated tautomers **3a** and **3b** also strongly differ with respect to their relative energies. As shown in Table 3, N-protonation of **2** leads to a gain of 47 kcal/mol in terms of free energy (including solvation effects), which corresponds to a calculated pK_A of 34. On the other hand, O-protonation only leads to a gain of free energy of 20 kcal/mol (pKA ∼15). Hence, *N-protonation is strongly favoured over O-protonation* in agreement with the experimental observation that [Mb–HNO] is also N-protonated. This result is further confirmed by calculated energies from an earlier DFT study.[21a] At this point it should be mentioned that the absolute values of the obtained free energies are probably overestimated. This can be seen from the pK_A of free HNO, which is calculated to be 23.5 compared to an experimental value of only 11.4. Nevertheless, as observed in many cases of pK_A calculations, trends are usually reproduced very well. Hence, the calculated pK_A values of **3a** and **3b** relative to that of HNO show that (a) coordination of HNO to Fe(II) increases the pK_A value of this species, and (b) that O-protonation is clearly less favourable.

Besides the two singly protonated tautomers **3a** and **3b**, intermediate *I* could also correspond to the doubly protonated intermediate $[Fe(P)(CH_3S)(NHOH)]$ (**4**) as proposed by Daiber et al.[9] Total free energy calculations show that **4** is, in fact, 8.6 kcal/mol lower in energy than **3a** in agreement with this idea. The predicted

vibrational properties of **4** show a weak N—O bond with ν(N—O) at 952 cm^{-1} similar to **3b** and, importantly, a predicted Fe—N stretch (mixed with Fe—N—H bends, cf. Table 2) at 609 cm^{-1} similar to **3a**. Therefore, considering the experimental Fe—N stretch in *I* observed at 596 cm^{-1}, these results are not conclusive whether this species is singly N- or doubly N,O-protonated. This could easily be decided from the N—O stretch, which, however, has not been observed experimentally. The optimized structure of **4** is shown in Figure 3. In this case, the NHOH ligand is planar, which means that both protons are bound to the former π^*_h orbital. This leads to a further decrease of this orbital in energy and, hence, a decrease of the strength of the Fe—N σ bond in **4**. The corresponding bonding combination, π^*_h_d_{z^2} ⟨95⟩, has 49% π^*_h and only 10% d_{z^2} character in agreement with this analysis (cf. Fig. 3). On the other hand, the binding of the second proton also has a profound effect on the π^*_v orbital, which decreases in energy and now becomes occupied. This is evident from the corresponding antibonding combination, d_{yz}_π^*_v ⟨115⟩ (cf. Fig. 3), which has 34% π^*_v and 40% d_{yz} character. In summary, the electronic structure of **4** is somewhat similar to **3b**, but the Fe—N σ bond is distinctively weakened in the doubly protonated species in agreement with the lower Fe—N force constant in this case (cf. Table 2). In addition, the π^*_v orbital now becomes occupied, which formally leads to a Fe(IV)—$NHOH^-$ electronic structure for complex **4**, although one has to keep in mind that the Fe—N bond is very covalent. Therefore, based on the spectroscopic and mechanistic significance, we propose that intermediate *I* is a doubly protonated Fe(IV)—$NHOH^-$ species.

In conclusion, the above analysis shows that the Fe(II)—NO/(−) species in myoglobin corresponds to a singly N-protonated complex, whereas the corresponding intermediate *I* in P450nor is doubly N,O-protonated. Therefore, we propose that the actual role of the axial thiolate ligand in P450nor is the stabilization of the formed Fe(IV)—$NHOH^-$ intermediate by strong donation of the thiolate to the iron center thus stabilizing the formal Fe(IV) oxidation state. In other words, the thiolate enables the double protonation of the Fe(II)—NO/(−) intermediate by lowering its pK_B values. As demonstrated in the next section, this intermediate leads to a clean formation of N_2O when reacted with one molecule of NO, thus avoiding the formation of potentially toxic NO_x species.

Molecular Mechanism of P450nor

From the work of Shoun and coworkers[6,7] it is known that P450nor is catalytically active in its ferric oxidation state, which binds one molecule of NO. The next step is the reaction with NADH leading to the formation of intermediate *I* as presented in Scheme 1. As shown by our analysis presented above and kinetic studies by Daiber et al.,[9] this step corresponds to a *direct hydride transfer* initially generating an Fe(II)—HNO species as shown in Scheme 3. This species is N-protonated, which is energetically strongly favoured over the O-protonated form. Hence, in the following mechanistic discussion all free energies will be related to this species **3a**, which is set to 0.0 kcal/mol in Scheme 3. This species is subsequently protonated leading to the fast formation of the corresponding Fe—NHOH species **4**, which therefore can be identified with intermediate *I* as observed spectroscopically in agreement with the proposal of Daiber et al.[9] It is stabilized by approx-

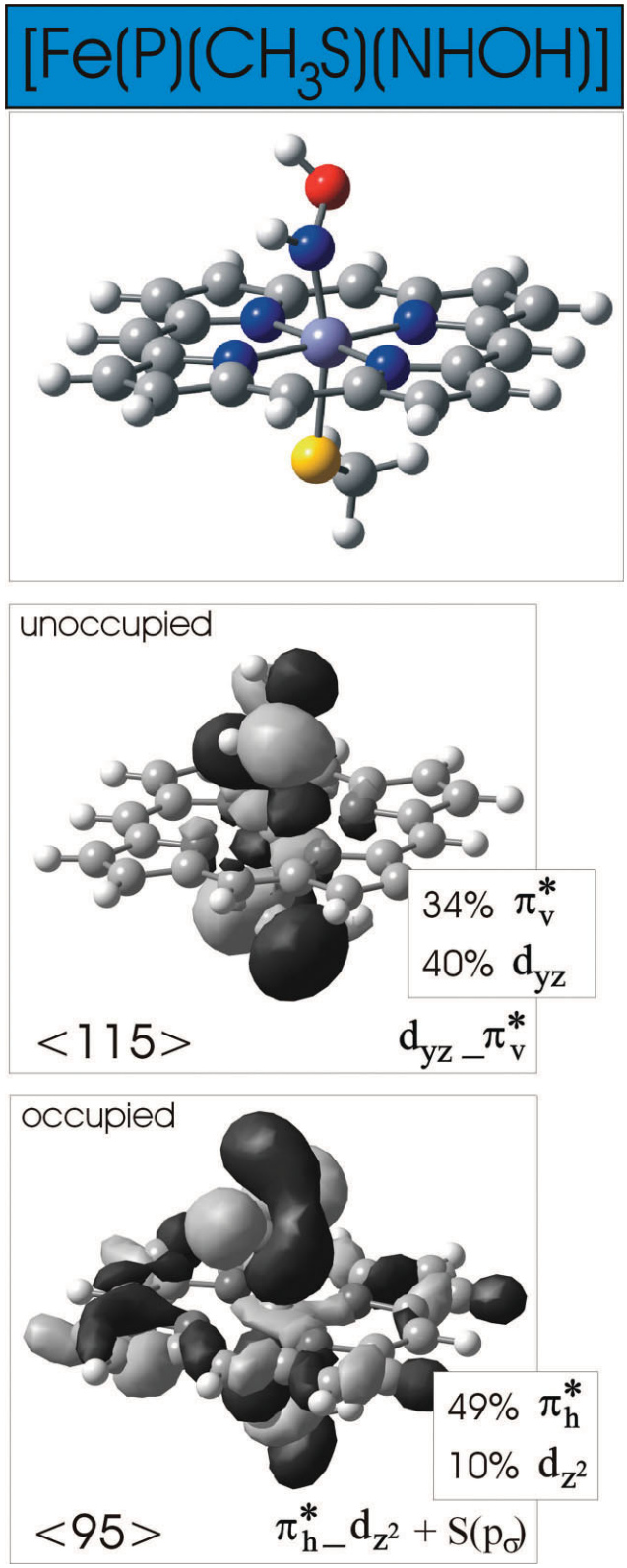

Figure 3. Optimized geometry (top) and contour plots of important molecular orbitals of [Fe(P)(CH_3S)(NHOH)] (**4**, S = 0) calculated with BP86/TZVP. Orbital decompositions are also included.

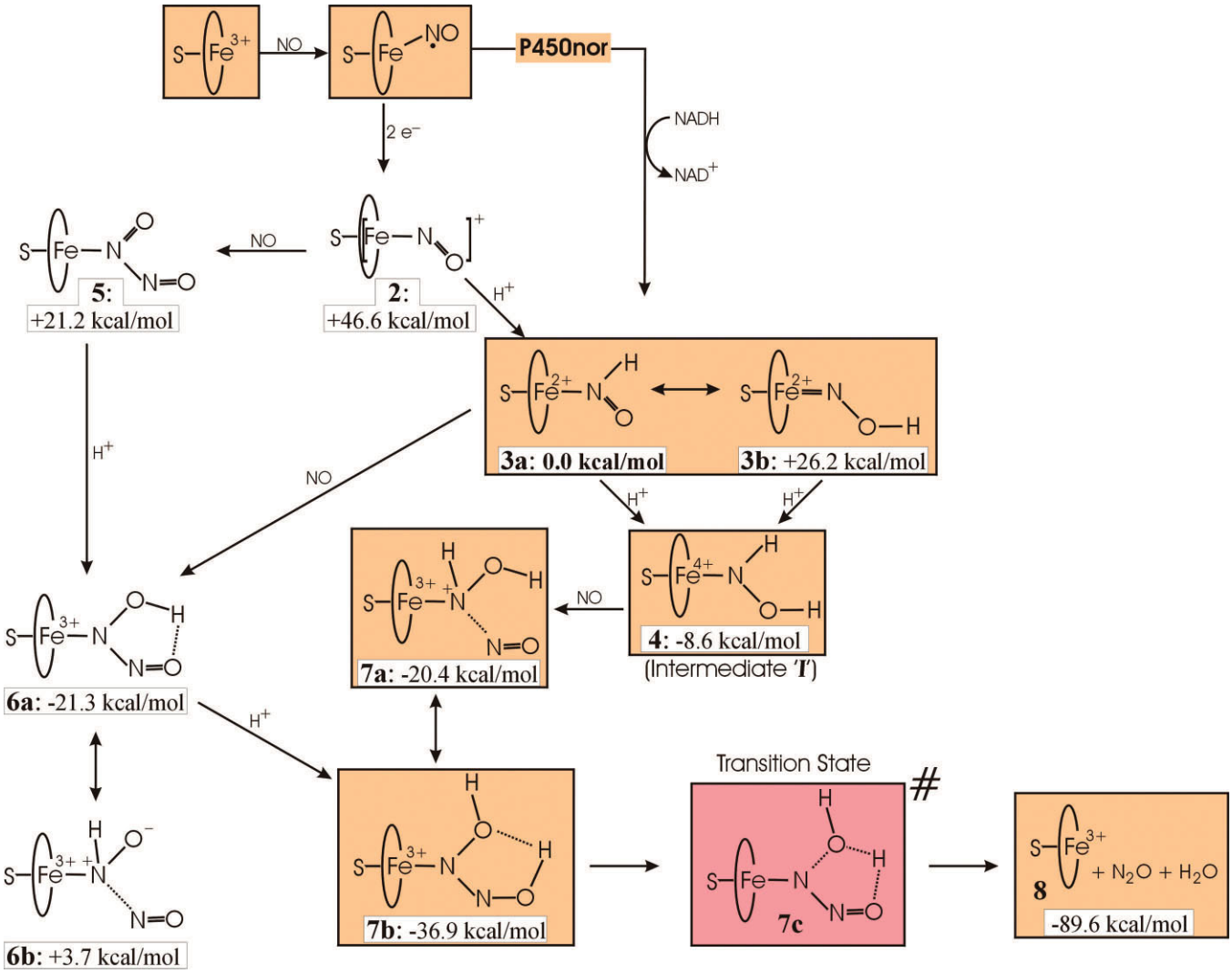

Scheme 3.

imately 9 kcal/mol relative to **3a**. The electronic structure of this intermediate is very interesting as described above and formally corresponds to an Fe(IV)—$NHOH^-$ complex. Intermediate **4** could be envisioned to react with NO by an outer sphere electron transfer to the iron center creating Fe(III) and NO^+, where the NO^+ then subsequently or concertedly attacks the lone pair on the nitrogen of the coordinated NHOH ligand. This process corresponds to a spin-allowed reaction. Importantly, the calculations show that the N-protonated Fe(III)—$N_2O_2H_2$ species formed this way is unstable and easily loses the generated $N_2O_2H_2$ ligand. However, proton transfer from the nitrogen atom of the former NHOH ligand to the oxygen of the incoming NO molecule leads to the generation of the stable O,O′-protonated Fe(III)—$N_2O_2H_2$ complex **7b** as shown in Scheme 3. The formation of **7b** from **4** and NO is highly exergonic by about 28 kcal/mol. This is a very important result, because it shows that the attack of NO on intermediate **4** is a three step process including (a) electron transfer to the formal iron(IV), (b) attachment of the resulting NO^+ forming an N—N bond, and (c) simultaneous proton transfer from the N atom of the former NHOH ligand to the O atom of the incoming NO. This mechanism explains why the anticipated radical reaction of NO with the coordinated HNO species is efficiently catalyzed by the heme center. Based on this reaction sequence, the N-protonated Fe(III)—$N_2O_2H_2$ species is an intermediate on the reaction coordinate leading to **7b**. To estimate the energy of this species, we have optimized its structure using a fixed Fe—N distance. This leads to intermediate **7a**, where NO is loosely attached to the NHOH ligand. The energy of this species is −12 kcal/mol relative to **4** and NO. Therefore, the subsequent proton transfer generating the tautomer **7b** is highly exergonic by −16 kcal/mol, and hence, should occur extremely fast in the actual enzymatic reaction. This ensures that the formed $N_2O_2H_2$ ligand stays bound to the iron(III) center. In addition, the structure of **7b** as shown in Scheme 3 is perfectly set up for proton transfer leading to the tautomer **7c**, where the oxygen of the former NHOH ligand is doubly protonated. Upon geometry optimization, this species

relaxes back to **7b**, which therefore corresponds to the most stable tautomer of the Fe(III)—$N_2O_2H_2$ complex. However, fixing the two O—H bonds in **7c** at 0.97 Å and geometry optimization leads to the spontaneous cleavage of the N—OH_2 bond and the formation of a five-coordinate Fe(III) complex, nitrous oxide and water. This reaction is highly exergonic, which shows that **7c** must corresponds to a transition state, because this species is higher in energy than both the reactant **7b** that it is formed from, and the products obtained after its decomposition. We therefore tried to optimize the structure of this transition state, but these calculations were not successful. To estimate the energy for proton transfer leading from **7b** to **7c**, a geometry optimization was performed were both O—H and the N—O bond distances were fixed at 0.97 and 1.41 Å, respectively. As shown in Table 3, this structure is 35 kcal/mol higher in energy than **7b**. This indicates that the transition state must have a significantly elongated N—O bond, which would lead to a substantial lowering of the barrier as evident from the strong thermodynamic driving force of the reaction. Because it is known from experiments that the five-coordinate ferric heme in P450nor is high spin, we therefore used the corresponding high-spin complex **8** to calculate the free energy for the reaction leading from **7b** to **8**, nitrous oxide and water. *This process is exergonic by about 53 kcal/mol, and therefore, thermodynamically highly favorable*. Note that the decay of **7c** initially generates an Fe(III)—N_2O complex, which loses the N_2O ligand in the calculations regardless whether the high-spin or low-spin state of the ferric heme is considered. This dissociation of nitrous oxide closes the catalytic cycle.

In model complex studies using organic solvens, Fe(II)—NO/(−) species could also potentially be generated in a proton-free environment. To investigate whether these intermediates would react with NO, we have also calculated the corresponding reaction energy. As shown in Scheme 3, this process leading from **2** to the Fe—N_2O_2 intermediate **5** is strongly exergonic by about 25 kcal/mol, and hence, this reaction should proceed smoothly. In addition, **5** is almost as basic as **2**, which indicates that this species could be doubly protonated upon addition of acid leading to **7b**, which then follows the reaction mechanism of P450nor as described above. This sequence certainly requires a protected binding site for the intermediate as present in the protein to exclude crossreactions of different species in solution or disproportionation reactions, etc.

In two very recent studies, alternative reaction mechanisms for P450nor have been also published based on DFT calculations.[21c,d] Importantly, Vincent et al.[21c] also concluded that intermediate *I* of P450nor corresponds to the doubly protonated species **4** as presented here, although this work does not explicitly consider the energies of the different protonation steps, which is of key importance as we have shown above. The further mechanism published in this article then differs from our results. This is due to the fact that upon reaction of **4** with NO, the initially formed, N-protonated species **7a** does lead to loss of $N_2O_2H_2$ from iron as discussed above. Because Vincent et al. did not consider the energetically favourable tautomer **7b**, which contains a stable Fe—$N_2O_2H_2$ bond, their further mechanism invokes decomposition of free $N_2O_2H_2$. However, we think that the tautomer **7b** is formed instantaneously from **7a** due to the strong thermodynamic driving force, and that a mechanism considering free $N_2O_2H_2$ is therefore not valid. As presented above, the iron center is actually assisting in the decomposition of the coordinated $N_2O_2H_2$ in **7b** by fixing the structure in a conformation that is ideally set up for proton transfer leading to the transition state **7c**. In a recent DFT study by Tsukamoto et al.,[27d] a completely different reaction mechanism is promoted where the ferric–heme NO adduct is only reduced by one electron by NADH, and the NO then dissociates from the generated ferrous heme. In the next step, a second electron transfer occurs from the $NADH^+$ radical to free NO generating free NO^-, which then reacts with NAD^+. Considering the known properties of ferric and ferrous heme nitrosyls,[2h] this scenario is very unlikely. First, NO is bound very strongly to ferrous heme nitrosyls, and hence, a fast dissociation of NO from the heme is unlikely. Vice versa, it can be envisioned that the two-electron reduction by NADH is actually performed to *avoid* the ferrous nitrosyl complex. Second, this mechanism cannot explain the experimentally observed properties of intermediate *I*, which contains a bound NO ligand but is clearly further reduced compared to a corresponding ferrous complex (cf. Introduction). This latter mechanism is therefore highly unrealistic.

Conclusions

The main conclusions that are drawn from the calculations presented in this work are:

1. the one-electron reduced ferrous nitrosyl species Fe(II)—NO/(−) can principally exist in the two spin states S = 0 and S = 1, which are isoenergetic in the calculations for N-donor *trans* ligands, whereas thiolate leads to a slight preference for the S = 1 state. So far, experimental evidence is only available for the S = 0 case;
2. the S = 0 ground state of Fe(II)—NO/(−) has an electronic structure that is intermediate between Fe(II)—NO^- and Fe(I)—NO. The effect of an axial thiolate ligand on the electronic structure is marginal. Importantly, this species is not part of the catalytic cycle of P450nor;
3. this is in contrast to the ferrous Fe(II)—NO complexes, where the axial thiolate has a profound effect on the electronic structure leading to an admixture of ~20% Fe(III)—NO^- character into the ground state wavefunction;
4. the Mb–HNO adduct prepared by Farmer and coworkers corresponds to the N-protonated Fe(II)–NHO tautomer, which is energetically strongly preferred over the O-protonated form;
5. in contrast, intermediate *I* of P450nor is doubly protonated and formally corresponds to an Fe(IV)–$NHOH^-$ complex. This species is perfectly set up for reaction with a second molecule of NO;
6. the role of the thiolate is then to stabilize the Fe(IV)–$NHOH^-$ species and to enable the double protonation of the reduced NO ligand in P450nor;
7. the Fe(IV)–$NHOH^-$ intermediate reacts with nitric oxide by initial electron transfer from NO to Fe(IV) followed by addition of NO^+ to the NHOH ligand forming an N—N bond. This process is accompanied by an intramolecular proton transfer. This reaction sequence ensures that nitrous oxide is the product of catalysis, and that no other NO_x species is formed;

8. the obtained Fe—$N_2O_2H_2$ intermediate is quite stable and corresponds to an Fe(III)—N(OH)(NOH) species. The doubly O-protonated tautomer Fe(III)—$N(OH_2)$(NO) is energetically unfavorable, but corresponds to the catalytically productive species that spontaneously decomposes to N_2O and water in a highly exergonic process;
9. this way, the enzyme produces dimerized HNO *under controlled conditions*, which, in its free form, also decomposes to N_2O and H_2O (see Introduction);
10. electrocatalytic work by Farmer et al.[16] shows that Mb forms hydroxylamine and ammonia from nitrite reduction, whereas P450 CYP119 is less reactive, but more selectively produces N_2O. One possible explanation for this difference is that in Mb, the N-protonated intermediate Fe(II)—NHO is catalytically active, and that this is the route leading to NH_2OH by additional proton and electron transfer, whereas in P450nor, the corresponding doubly-protonated species is the reactive intermediate leading to N_2O formation.

Supporting Information

MO diagrams and contour plots of **1** and **2** and tables with charge decompositions of important molecular orbitals of these species; tables with cartesian coordinates of the optimized structures of 1–7 are available from the Supporting Information.

References

1. (a) McCleverty, J. A. Chem Rev 2004, 104, 403; (b) J Inorg Biochem 2005, 99, issues 1 and 4; (c) Chem Rev 2002, 102, issue 4.
2. (a) Moncada, S.; Palmer, R. M.; Higgs, E. A. Pharmacol Rev 1991, 43, 109; (b) Snyder, S. H. Science 1992, 257, 494; (c) Culotta, E.; Koshland, D. E. Science 1992, 258, 1862; (d) Butler, A. R.; Williams, D. L. H. Chem Soc Rev 1993, 233; (e) Bredt, D. S.; Snyder, S. H. Annu Rev Biochem 1994, 63, 175; (f) Lancaster, J. R., Jr. In: Encyclopedia of Inorganic Chemistry; Bruce, R. B., Ed.; Wiley: Chichester, 1994; (g) Feelisch, M.; Stamler, J. S., Eds.; Methods in Nitric Oxide Research; Wiley: Chichester, 1996; (h) Cooper, C. E. Biochim Biophys Acta 1999, 1411, 290.
3. (a) Ferguson, S. J. Curr Opin Chem Biol 1998, 2, 182; (b) Richardson, D. J.; Watmough, N. J. Curr Opin Chem Biol 1999, 3, 207; (c) Moura, I.; Moura, J. J. G. Curr Opin Chem Biol 2001, 5, 168.
4. (a) Janick, P. A.; Rueger, D. C.; Krueger, R. J.; Barber, M. J.; Siegel, L. M. Biochemistry 1983, 22, 396; (b) Fry, I. V.; Cammack, R.; Hucklesby, D. P.: Hewitt, E. J. FEBS Lett 1980, 111, 377; (c) Christner, J. A.; Janick, P. A.; Siegel, L. M.; Münck, E. J Biol Chem 1983, 258, 11157; (d) Lancaster, J. R.; Vega, J. M.; Kamin, H.; Orme–Johnson, N. R.; Orme–Johnson, W. H.; Krueger, R. J.; Siegel, L. M. J Biol Chem 1979, 254, 1268; (e) Handbook of Metalloproteins; Wiley: Chichester; 2001, vol. 1.
5. (a) Ferguson, S. J. Curr Opin Chem Biol 1998, 2, 182; (b) Richardson, D. J.; Watmough, N. J. Curr Opin Chem Biol 1999, 3, 207; (c) Moura, I.; Moura, J. J. G. Curr Opin Chem Biol 2001, 5, 168.
6. (a) Nakahara, K.; Tanimoto, T.; Hatano, K.; Usuda, K. Shoun, H. J Biol Chem 1993, 268, 8350; (b) Obayashi, E.; Tsukamoto, K.; Adachi, S.-I.; Takahashi, S.; Nomura, M.; Iizuka, T.; Shoun, H.; Shiro, Y. J Am Chem Soc 1997, 119, 7807; (c) Park, S.-Y.; Shimizu, H.; Adachi, S.-I.; Nakagawa, A.; Tanaka, I.; Nakahara, K.; Shoun, H.; Obayashi, E.; Nakamura, H.; Iizuka, T.; Shiro, Y. Nat Struct Biol 1997, 4, 827; (d) Shimizu, H.; Park, S.-Y.; Gomi, Y.; Arakawa, H.; Nakamura, H.; Adachi, S.-I.; Obayashi, E.; Iizuka, T.; Shoun, H.; Shiro, Y. J Biol Chem 2000, 275, 4816.
7. (a) Shiro, Y.; Fujii, M.; Iizuka, T.; Adachi, S.-I.; Tsukamoto, K.; Nakahara, K.; Shoun, H. J Biol Chem 1995, 270, 1617; (b) Obayashi, E.; Takahashi, S.; Shiro, Y. J Am Chem Soc 1998, 120, 12964.
8. Farmer, P. J.; Sulc, F. J Inorg Biochem 2005, 99, 166.
9. Daiber, A.; Nauser, T.; Takaya, N.; Kudo, P.; Weber, P.; Hultschig, C.; Shoun, H.; Ullrich, V. J Inorg Biol Chem 2002, 88, 343.
10. (a) Olson, L. W.; Schaeper, D.; Lançon, D.; Kadish, K. M. J Am Chem Soc 1982, 104, 2042; (b) Lançon, D.; Kadish, K. M. J Am Chem Soc 1983, 105, 5610; (c) Fujita, E.; Fajer, J. J Am Chem Soc 1983, 105, 6743.
11. (a) Choi, I. K.; Ryan, M. D. Inorg Chim Acta 1988, 153, 25; (b) Choi, I. K.; Liu, Y.; Feng, D.; Paeng, K. J.; Ryan, M. D. Inorg Chem 1991, 30, 1832; (c) Choi, I. K.; Ryan, M. D. New J Chem 1992, 16, 591; (d) Liu, Y.; Ryan, M. D. Inorg Chim Acta 1994, 225, 57; (e) Liu, Y.; DeSilva, C.; Ryan, M. D. Inorg Chim Acta 1997, 258, 247.
12. Wyllie, G. R. A.; Schulz, C. E.; Scheidt, W. R. Inorg Chem 2003, 42, 5722.
13. (a) Praneeth, V. K. K.; Neese, F.; Lehnert, N. Inorg Chem 2005, 44, 2570; (b) Praneeth, V. K. K.; Näther, C.; Peters, G.; Lehnert, N. Inorg Chem 2006, 45, in press.
14. Liu, Y.; Ryan, M. D. J Electroanal Chem 1994, 368, 209.
15. (a) Lin, R.; Farmer, P. J. J Am Chem Soc 2000, 122, 2393; (b) Sulc, F.; Immoos, C. E.; Pervitsky, D.; Farmer, P. J. J Am Chem Soc 2004, 126, 1096.
16. (a) Lin, R.; Bayachou, M.; Greaves, J.; Farmer, P. J. J Am Chem Soc 1997, 119, 12689; (b) Immoos, C. E.; Chou, J.; Bayachou, M.; Blair, E.; Farmer, P. J. J Am Chem Soc 2004, 126, 4934.
17. (a) Stamler, J. S.; Singel, D. J.; Loscalzo, J. Science 1992, 258, 1898; (b) Bartberger, M. D.; Liu, W.; Ford, E.; Miranda, K. M.; Switzer, C.; Fukuto, J. M.; Farmer, P. J.; Wink, D. A.; Houk, K. N. Proc Natl Acad Sci USA 2002, 99, 10958; (c) Miranda, K. M.; Paolocci, N.; Katori, T.; Thomas, D. D.; Ford, E.; Bartberger, M. D.; Espey, M. G.; Kass, D. A.; Feelisch, M.; Fukuto, J. M.; Wink, D. A. Proc Natl Acad Sci USA 2003, 100, 9196.
18. Rusche, K. M.; Spiering, M. M.; Marletta, M. A. Biochemistry 1998, 37, 15503.
19. (a) Shafirovich, V.; Lymar, S. V. Proc Natl Acad Sci USA 2002, 99, 7340; (b) Lymar, S. V.; Shafirovich, V.; Poskrebyshev, G. A. Inorg Chem 2005, 44, 5212.
20. (a) Bazylinski, D. A.; Hollocher, T. C. J Am Chem Soc 1985, 107, 7982; (b) Bari, S. E.; Marti, M. A.; Amorebieta, V. T.; Estrin, D. A.; Doctorovich, F. J Am Chem Soc 2003, 125, 15272.
21. (a) Silaghi–Dumitrescu, R. Eur J Inorg Chem 2003, 1048; (b) Harris, D. L. Int J Quantum Chem 2002, 88, 183; (c) Vincent, M. A.; Hillier, I. H.; Ge, J. Chem Phys Lett 2005, 407, 333; (d) Tsukamoto, K.; Watanabe, T.; Nagashima, U.; Akiyama, Y. J Mol Struct (Theochem) 2005, 732, 87.
22. Frisch, M. J.; Trucks, G. W.; Schlegel, H. B.; Scuseria, G. E.; Robb, M. A.; Cheeseman, J. R.; Zakrzewski, V. G.; Montgomery, J. A., Jr.; Stratmann, R. E.; Burant, J. C.; Dapprich, S.; Millam, J. M.; Daniels, A. D.; Kudin, K. N.; Strain, M. C.; Farkas, O.; Tomasi, J.; Barone, V.; Cossi, M.; Cammi, R.; Mennucci, B.; Pomelli, C.; Adamo, C.; Clifford, S.; Ochterski, J.; Petersson, G. A.; Ayala, P. Y.; Cui, Q.; Morokuma, K.; Salvador, P.; Dannenberg, J. J.; Malick, D. K.; Rabuck, A. D.; Raghavachari, K.; Foresman, J. B.; Cioslowski, J.; Ortiz, J. V.; Baboul, A. G.; Stefanov, B. B.; Liu, G.; Liashenko, A.; Piskorz, P.; Komaromi, I.; Gomperts, R.; Martin, R. L.; Fox, D. J.; Keith, T.; Al-Laham, M. A.; Peng, C. Y.; Nanayakkara, A.; Challacombe, M.; Gill, P. M. W.; Johnson, B.; Chen, W.; Wong, M. W.; Andres, J. L.; Gonzalez, C.: Head–Gordon, M.; Replogle, E. S.; Pople, J. A. Gaussian 98 Rev. A.11; Gaussian, Inc.: Pittsburgh, PA, 2001.

23. Allouche, A.; Pourcin, J. Spectrochim Acta 1993, 49A, 571.
24. Zilberberg, I.; Ruzankin, S. Ph. Quantum Chemistry division; Boreskov Institute of Catalysis: Novosibirsk 630090, Russian Federation.
25. Serres, R. G.; Grapperhaus, C. A.; Bothe, E.; Bill, E.; Weyhermüller, T.; Neese, F.; Wieghardt, K. J Am Chem Soc 2004, 126, 5138.
26. Praneeth, V. K. K.; Haupt, E.; Lehnert, N. J Inorg Biochem 2005, 99, 940; Erratum: J Inorg Biochem 2005, 99, 1744.
27. (a) Zilberberg, I.; Ruzankin, S. Ph.; Malykhin, S.; Zhidomirov, G. M. Chem Phys Lett 2004, 394, 392; (b) Zilberberg, I.; Ruzankin, S. Ph. Chem Phys Lett 2004, 394, 165.
28. (a) Hu, S.; Kincaid, J. R. J Am Chem Soc 1991, 113, 9760; (b) Hu, S.; Kincaid, J. R. J Biol Chem 1993, 268, 6189.
29. Scheidt, W. R.; Frisse, M. E. J Am Chem Sco 1975, 97, 17.
30. Tawa, G. J.; Topol, I. A.; Burt, S. K.; Caldwell, R. A.; Rashin, A. A. J Chem Phys 1998, 109, 4852.

7.3. Mononuclear and Binuclear Copper(I)-Diazene Complexes: a New Chapter of Copper Coordination Chemistry

Florian Paulat, Nicolai Lehnert, Yoko Ishikawa, Ken-Ichi Okamoto and Kiyoshi Fujisawa

Published in: *Inorg. Chim. Acta* **2007**, *360*, asap
(special issue in honor of Edward I. Solomon)

Available online at www.sciencedirect.com
ScienceDirect
Inorganica Chimica Acta xxx (2007) xxx–xxx
Inorganica Chimica Acta
www.elsevier.com/locate/ica

Mononuclear and binuclear copper(I)–diazene complexes: A new chapter of copper coordination chemistry

Florian Paulat [a], Nicolai Lehnert [a,*], Yoko Ishikawa [b], Ken-Ichi Okamoto [b], Kiyoshi Fujisawa [b,*]

[a] Department of Chemistry, The University of Michigan, 930 N. University, Ann Arbor, MI 48109, USA
[b] Graduate School of Pure and Applied Sciences, Department of Chemistry, University of Tsukuba, Tsukuba 305-8571, Japan

Received 30 April 2007; accepted 15 May 2007

Dedicated to Professor Edward I. Solomon on the occasion of his 60th birthday.

Abstract

Starting from copper(II) hydrotris(pyrazolyl)borate precursors and substituted hydrazines, we were able to synthesize mononuclear and binuclear copper(I)–diazene complexes for the first time. The mechanism of these reactions corresponds to a simple hydrazine oxidation by the copper(II) centers. Binuclear diazene complexes contain the central Cu(I)–NR=NR–Cu(I) unit, which we have structurally and spectroscopically characterized. Interestingly, usage of a sterically demanding hydrotris(pyrazolyl)borate ligand that prevents the dimer formation, leads to decomposition of the diazene complex and the isolation of a copper(I)–hydrazine complex. The same is observed when a tris(pyrazolyl)methane ligand is applied. Finally, using 1,1-diphenylhydrazine or the corresponding monophenyl derivative, we were able to obtain mononuclear Cu(I)–diazene complexes. In this case, the phenyl substituent(s) prevent the dimerization, but also stabilize the diazene ligand. Mononuclear and binuclear Cu(I)–diazene complexes are characterized by their intense reddish to purple color, which is caused by an intense Cu-d to diazene-π^* transition in the visible region. Resonance Raman spectra of the diazene complexes show the Cu–N and N–N stretching vibrations in the 500 cm^{-1} and 1350–1400 cm^{-1} energy regions, respectively, in agreement with the diazene description of the complexes. The copper(I)–diazene bond in these complexes is dominated by π backbonding.

Keywords: Bioinorganic chemistry; Copper; Pyrazolylborate; Nitrogen ligand; Diazene; Raman spectroscopy; DFT calculations

1. Introduction

Small nitrogen-containing molecules in different oxidation states are not only important in biological systems in the global nitrogen cycle, and as the source of nitrogen in amino acids and nucleic acids, but also play an important role in chemical industry as the key substrates of fertilizers, drugs, and industrial products. In this respect, the conversion of atmospheric N_2 into NH_3 is one of the most important chemical processes. The large-scale transformation of N_2 and H_2 into NH_3 is performed in industry by the Haber–Bosch process at high temperature and pressure, employing transition metal-based catalysts to accelerate the thermodynamically feasible production of NH_3 [1,2]. In comparison, biological N_2-fixing systems (nitrogenases) can reduce N_2 to NH_3 under much milder conditions, but still require a significant energy input [3–5]. Nevertheless, the catalytic transformation of molecular nitrogen into nitrogenous compounds, such as ammonia and organonitrogen compounds, at ambient temperature and pressure is still one of the greatest challenges in chemistry. The active sites of the nitrogenases, which are the enzymes that catalyze N_2 fixation, consist of a cluster of Fe/Mo, Fe/V, or Fe metal ions only. The structure of this cluster has

* Corresponding authors. Tel.: +1 734 615 3673; fax: +1 734 615 3790 (N. Lehnert).
E-mail address: lehnertn@umich.edu (N. Lehnert).

0020-1693/$ - see front matter © 2007 Elsevier B.V. All rights reserved.
doi:10.1016/j.ica.2007.05.027

recently been improved to high resolution for the Fe/Mo type nitrogenase [6]. From X-ray analyses and spectroscopic data, HN=NH (1,2-diazene) has been postulated as a metal-bound intermediate in enzymatic N_2 fixation [6,7]. This molecule is extremely unstable in its free state, and undergoes a bimolecular decomposition above −150 °C to give N_2 and N_2H_4 [8]. The stability of diazene is greatly enhanced when its lone pairs are coordinated to transition metals. Corresponding complexes have been reported by Sellmann [9,10] and other chemists [11–14], using different types of supporting ligands.

Due to this biological and industrial relevance of reduced nitrogen species, many chemists have tried to make corresponding model complexes, which has led to the generation of a large number of transition metal dinitrogen, diazene, and hydrazine complexes [9–14]. In particular, V, Fe, and Mo were commonly used for the preparation of model complexes. Stable dinitrogen, diazene, or hydrazine complexes were also obtained with metal ions such as W, Ti, Zr, Cr, Mn, Tc, Re, Ru, Os, Co, Rh, Ir, Ni, Pd, Pt, Au, and Sm. The crystal structures for a number of these model complexes were determined. In addition, spectroscopic and physical methods were applied for the characterization of these compounds, and the redox properties and abilities of the complexes to activate N_2 for utilization were investigated. From these studies, various coordination modes of dinitrogen, diazene, and hydrazine to transition metal ions were discovered, summarized in Scheme 1. A significant number of these compounds were obtained from the reaction of corresponding transition metal precursors with hydrazine (N_2H_4), which leads to hydrazine oxidation yielding diazene or dinitrogen complexes [9]. In addition, alkyl-substituted hydrazine or hydrazido (diazenido), and diazene complexes have also been prepared, because alkyl substituents tend to stabilize coordinated hydrazine and diazene ligands [9–14].

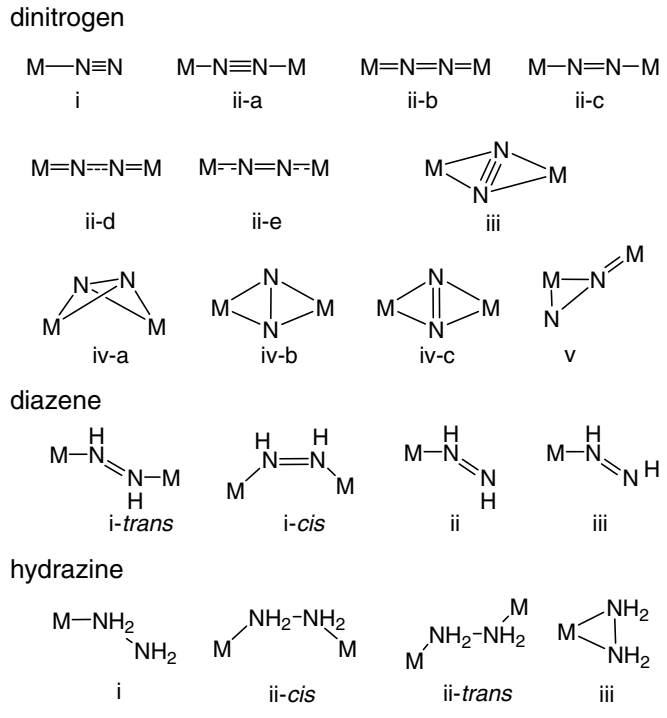

Scheme 1. Binding modes of dinitrogen, diazene, and hydrazine to transition metals.

The coordination chemistry of copper toward dinitrogen and its reduced species, although poorly defined, is also of biological relevance. Interestingly, the copper-containing active site of the enzyme nitrous oxide reductase (N_2OR) is **not** inhibited by dinitrogen [15], although studies on ruthenium complexes have shown that N_2 is in general a stronger ligand to transition metals than N_2O [16]. In terms of model complexes, not much is actually known about the interaction of copper with hydrazine, diazene, and especially dinitrogen. Previous to our studies, only three crystal structures of corresponding copper(I) compounds had been published: a 1,2-dimethyl substituted diazene complex, $[\{CuCl\}_2(\mu\text{-}N_2Me_2)]_n$ [17], and two hydrazine complexes, $[\{Cu(CN)\}_2(\mu\text{-}N_2H_4)]_n$ [18] and $[\{Cu(Cl)\}_2(\mu\text{-}N_2H_4)]_n$ [19]. However, these compounds correspond to inorganic polymers as indicated.

Because of this lack of knowledge about the coordination chemistry of copper(I) with dinitrogen, diazene, and hydrazine, we started a systematic investigation of this area using anionic hydrotris(pyrazolyl)borate (L^-) and neutral tris(pyrazolyl)methane (L') coligands. Our initial approach to this chemistry was to use hydrazine oxidation as described above. This way, we were able to obtain mononuclear and binuclear copper(I)–hydrazine and –diazene complexes for the first time. Interestingly, the exact nature of the reaction product depends on the charge and the bulkiness of the applied coligand (substituted L^- or L', respectively), and hence, represents a true ligand second-coordination sphere effect [20]. We have also applied substituted hydrazine substrates for these reactions. These results are summarized in this paper. Note that the syntheses, crystal structures, and spectroscopic characterization of the binuclear copper(I)–diazene complexes have been published in a preceding communication [21]. These results are briefly summarized below.

2. Experimental

2.1. Materials

Preparation and handling of all complexes was performed under an argon atmosphere by employing standard Schlenk line techniques. Dichloromethane was distilled from P_2O_5 prior to use. Heptane and pentane were carefully purified by refluxing/distilling under an argon atmosphere over sodium benzophenone ketyl. Hydrazine monohydrate (98%), 0.2 M NaOH(aq), anhydrous sodium sulfate, 1,1-diphenylhydrazine hydrochloride, phenylhydrazine and triethylamine were purchased from Wako Pure Chemical Ind. Ltd. ^{15}N-enriched hydrazine sulfate and 1,2-dimethylhydrazine dihydrochloride were obtained from ICON, NY and Tokyo Kasei Kogyo, Co., Ltd., respectively.

The deuterated solvent was obtained from Cambridge Isotope Laboratories, Inc. The precursors, [{Cu(L1)}$_2$-(μ-OH)$_2$] and [Cu(L3)(OH)] (L1 = HB(3,5-*i*Pr$_2$pz)$_3$ anion, L3 = HB(3-*t*Bu-5-*i*Prpz)$_3$ anion) were prepared according to literature methods [22,23]. The preparation of the precursor [{Cu(L1′)}$_2$(μ-OH)$_2$](ClO$_4$)$_2$ will be reported in the near future [24].

Caution! Although we have not encountered any problems during complex syntheses, it is noted that the perchlorate salts of metal complexes with organic ligands are potentially explosive and should be handled only in small quantities with appropriate precautions.

2.2. Preparation of complexes

2.2.1. [{Cu(L1)}$_2$(μ-HN=NH)] (1)

The precursor [{Cu(L1)}$_2$(μ-OH)$_2$] (310.9 mg, 0.285 mmol) was dissolved in dichloromethane (25 cm^3)/heptane (5 cm^3) at room temperature and cooled to −50 °C. Hydrazine monohydrate (0.035 cm^3, 0.71 mmol) was added using a microsyringe. The reaction mixture was stirred for 30 min at −50 °C, and for 30 min at −30 °C. During this time, the color of the solution changed from blue to dark purple. After cooling to −50 °C, the solvent was evaporated (remaining volume: 10 cm^3) and the solution was stored at −50 °C for one week. The obtained purple microcrystals (186.7 mg, 0.172 mmol, yield 60%) were filtered off and dried under vacuum at 0 °C for 5 min. IR (KBr, cm^{-1}): 3222 (*ν*N–H), 2964 (*ν*C–H), 2932 (*ν*C–H), 2868 (*ν*C–H), 2540 (*ν*B–H), 1534 (*ν*C=N), 1469, 1392, 1298, 1265, 1174, 1043, 787, 733. Far-IR (CsI, cm^{-1}): 643, 587, 517, 472, 397, 305, 287, 267, 226, 169. ^{1}H NMR (CD$_2$Cl$_2$, 600 MHz, −50 °C): *δ* 1.21 (d, *J* = 7 Hz, 36H, CH*Me*$_2$), 1.24 (d, *J* = 7 Hz, 36H, CH*Me*$_2$), 2.99 (sept, *J* = 7 Hz, 6H, C*H*Me$_2$), 3.45 (sept, *J* = 7 Hz, 6H, C*H*Me$_2$), 4.90 (s, 2H, NH (diazene)), 5.84 (s, 6H, Pz). UV–Vis (CH$_2$Cl$_2$, −50 °C, λ_{max}/nm (*ε*/cm^{-1} mol^{-1} dm^3)): 343 (1030), 439 (1250), 573 (3500). *Anal*. Calc. for C$_{54}$H$_{94}$N$_{14}$B$_2$Cu$_2$: C, 59.60; H, 8.71; N, 18.02. Found: C, 59.72; H, 8.54; N, 18.05%.

2.2.2. [{Cu(L1)}$_2$(μ-^{15}NH=^{15}NH)]

This complex was prepared analogous to [{Cu(L1)}(μ-N$_2$Me$_2$)] by using ^{15}N-enriched hydrazine sulfate.

2.2.3. [{Cu(L1)}(μ-NMe=NMe)] (2)

This complex was synthesized by two methods. (i) The precursor [{Cu(L1)}$_2$(μ-OH)$_2$] (222.9 mg, 0.204 mmol) and 1,2-dimethylhydrazine dihydrochloride (32.6 mg, 0.245 mmol) were dried under reduced pressure for a few minutes at room temperature and then cooled to −50 °C in a Schlenk tube. Then, cooled dichloromethane/pentane (20 cm^3) was added. After the [{Cu(L1)}$_2$(μ-OH)$_2$] was completely dissolved, the solution was treated with 0.2 M NaOH(aq) (2.45 cm^3, 0.490 mmol) using a syringe for neutralization of the 1,2-dimethylhydrazine dihydrochloride. The suspension was warmed to 0 °C and stirred for 30 min. During this time, the color of the solution changed from blue to red. Then, the water phase was removed and the organic phase was dried with anhydrous sodium sulfate. After the sodium sulfate was filtered off, the filtrate was concentrated and stored at −50 °C for several days. Red crystals (145.7 mg, 0.131 mmol, yield 64%) were collected by filtration and dried under vacuum at 0 °C for 5 min. (ii) This method is similar to (i) and was used to make samples for spectroscopy. Here, 1,2-dimethylhydrazine dihydrochloride was neutralized with triethylamine instead of 0.2 M NaOH(aq) at −50 °C. IR (KBr, cm^{-1}): 2964 (*ν*C–H), 2932 (*ν*C–H), 2868 (*ν*C–H), 2532 (*ν*B–H), 1537 (*ν*C=N), 1470, 1380, 1299, 1261, 1174, 1047, 785, 657. Far-IR (CsI, cm^{-1}): 631, 590, 519, 402, 305, 162. ^{1}H NMR (CD$_2$Cl$_2$, 600 MHz, −50 °C): *δ* 1.20 (d, *J* = 7 Hz, 36H, CH*Me*$_2$), 1.21 (d, *J* = 7 Hz, 36H, CH*Me*$_2$), 3.00 (sept, *J* = 7 Hz, 6H, C*H*Me$_2$), 3.44 (sept, *J* = 7 Hz, 6H, C*H*Me$_2$), 3.79 (s, 6H, N*Me* (diazene)), 5.84 (s, 6H, Pz). UV–Vis (CH$_2$Cl$_2$, −50 °C, λ_{max}/nm (*ε*/cm^{-1} mol^{-1} dm^3)): 357 (7000), 390 (sh, 5380), 407 (sh, 5110), 487 (5660). *Anal*. Calc. for C$_{56}$H$_{98}$N$_{14}$B$_2$Cu$_2$·C$_5$H$_{12}$·CH$_2$Cl$_2$: C, 58.48; H, 8.87; N, 15.40. Found: C, 58.58; H, 9.03; N, 15.42%.

2.2.4. [Cu(L3)(NH$_2$-NH$_2$)] (3)

The precursor [Cu(L3)(OH)] (214.7 mg, 0.365 mmol) was dissolved in dichloromethane (20 cm^3) at room temperature and cooled to −50 °C. Hydrazine monohydrate (0.020 cm^3, 0.41 mmol) was added using a microsyringe. The reaction mixture was stirred for 30 min at −50 °C, and for 30 min at 0 °C. During this time, the color of the solution changed from greenish yellow to colorless. The solution was then dried with anhydrous sodium sulfate and filtered over Celite. Cooled heptane (10 cm^3) was added to the filtrate, which was then concentrated. Colorless crystals (131.8 mg, 0.219 mmol, yield 60%) were collected by filtration and dried under vacuum at 0 °C for a few minutes. IR (KBr, cm^{-1}): 3398 (*ν*N–H), 3342 (*ν*N–H), 2962 (*ν*C–H), 2926 (*ν*C–H), 2864 (*ν*C–H), 2522 (*ν*B–H), 1605, 1532 (*ν*C=N), 1457, 1361, 1296, 1180, 1044, 787, 753, 643. Far-IR (CsI, cm^{-1}): 643, 574, 538, 517, 471, 416, 353, 331, 260, 175. ^{1}H NMR (CD$_2$Cl$_2$, 600 MHz, −50 °C): *δ* 1.23 (d, *J* = 7 Hz, 18H, CH*Me*$_2$), 1.38 (d, *J* = 7 Hz, 27H, C*Me*$_3$), 3.49 (sept, *J* = 7 Hz, 3H, C*H*Me$_2$), 3.75 (s, 2H, NH (coordinated)), 4.76 (s, 2H, NH (not coordinated)), 5.83 (s, 3H, Pz). *Anal*. Calc. for C$_{30}$H$_{56}$N$_8$BCu · 0.5CH$_2$Cl$_2$: C, 56.74; H, 8.90; N, 17.36. Found: C, 56.58; H, 8.42; N, 17.34%.

2.2.5. [{Cu(L1′)}$_2$(μ-NH$_2$-NH$_2$)](ClO$_4$)$_2$ (4)

The precursor [{Cu(L1′)}$_2$(μ-OH)$_2$](ClO$_4$)$_2$ (215.6 mg, 0.167 mmol) was dissolved in dichloromethane (20 cm^3) at room temperature and cooled to −50 °C. Hydrazine monohydrate (0.018 cm^3, 0.36 mmol) was then added using a microsyringe. The reaction mixture was stirred for 30 min at −50 °C, and for 60 min at 0 °C. During this time, the color of the solution changed from greenish brown to colorless. To complete the reaction, the solution was kept overnight at

room temperature, then dried with anhydrous sodium sulfate, and filtered over Celite. Heptane (10 cm^3) was added to the filtrate and the solution was concentrated. Colorless crystals (84.0 mg, 0.065 mmol, yield 39%) were obtained, collected by filtration, and dried under vacuum at 0 °C for a few minutes. IR (KBr, cm^{-1}): 3333 (*v*N–H), 3260 (*v*N–H), 3172 (*v*N–H), 2970 (*v*C–H), 2933 (*v*C–H), 2871 (*v*C–H), 1556 (*v*C=N), 1469, 1385, 1290, 1237, 1183, 1097 (*v*Cl–O), 827, 735, 623. *Caution!* Elemental analysis of this compound could not be obtained due to sample explosion during heating.

2.2.6. [Cu(L1)(N=NPh$_2$)] (5)

The precursor [{Cu(L1)}$_2$(μ-OH)$_2$] (215.1 mg, 0.197 mmol) and 1,1-diphenylhydrazine hydrochloride (105.5 mg, 0.478 mmol) were dried under reduced pressure for a few minutes at room temperature and then cooled to −50 °C in a Schlenk tube. Then, cold dichloromethane (20 cm^3) was added. After the [{Cu(L1)}$_2$(μ-OH)$_2$] was completely dissolved, the solution was treated with triethylamine (0.070 cm^3, 0.502 mmol) using a microsyringe for neutralization of the 1,1-diphenylhydrazine hydrochloride. After 10 min stirring at −50 °C, the reaction mixture was allowed to warm up to 0 °C, and then stirred for 5 min. During this time, the color of the solution changed from blue to reddish brown. The solution was then stirred for another 30 min at −50 °C. The solvent was evaporated to a remaining volume of 10 cm^3, and the solution was stored at −50 °C for one week. Reddish brown microcrystals (165.4 mg, 0.233 mmol, yield 59%) were obtained, filtered off, and dried under vacuum at 0 °C for 5 min. IR (KBr, cm^{-1}): 3063 (*v*C–H), 2962 (*v*C–H), 2933 (*v*C–H), 2866 (*v*C–H, aliphatic), 2531 (*v*B–H), 1589 (*v*C=C, (Ph)), 1535 (*v*C=N), 1459, 1390, 1298, 1264, 1173, 1042, 783, 762, 689, 655. Far-IR (CsI, cm^{-1}): 647, 627, 618, 594, 517, 487, 460, 422, 312, 267, 225, 169. ^{1}H NMR (CD_2Cl_2, 600 MHz, −50 °C): δ 1.16 (d, $J = 7$ Hz, 18H, CH*Me*$_2$), 1.18 (d, $J = 7$ Hz, 18H, CH*Me*$_2$), 2.57 (sept, $J = 7$ Hz, 3H, C*H*Me$_2$), 3.40 (sept, $J = 7$ Hz, 3H, C*H*Me$_2$), 5.77 (s, 3H, Pz), 7.38 (t, $J = 8$ Hz, 4H, Ph-3,5), 7.44 (t, $J = 8$ Hz, 2H, Ph-4), 7.69 (t, $J = 8$ Hz, 4H, Ph-2,6). UV–Vis (CH_2Cl_2, −50 °C, λ_{max}/nm (ε/cm^{-1} mol^{-1} dm^3)): 314 (6900), 407 (10400), 716 (390). *Anal.* Calc. for $C_{39}H_{56}N_8BCu \cdot 0.5CH_2Cl_2$: C, 61.72; H, 7.87; N, 15.36. Found: C, 62.13; H, 7.76; N, 14.64%.

2.2.7. [Cu(L1)(N=NHPh)] (6)

The precursor [{Cu(L1)}$_2$(μ-OH)$_2$] (212.3 mg, 0.194 mmol) was dissolved in dichloromethane (25 cm^3) at room temperature and cooled to −50 °C. Phenylhydrazine (0.050 cm^3, 0.508 mmol) was added using a microsyringe. The reaction mixture was stirred for 30 min at −50 °C, and for 30 min at −30 °C. During this time, the color of the solution changed from blue to dark purple. After cooling to −50 °C, the solvent was evaporated to a remaining volume of 10 cm^3, and the solution was stored at −50 °C for several months. ^{1}H NMR (CD_2Cl_2, 600 MHz, −50 °C): δ 1.12 (d, $J = 7$ Hz, 18H, CH*Me*$_2$), 1.14 (d, $J = 7$ Hz, 18H, CH*Me*$_2$), 2.86 (sept, $J = 7$ Hz, 3H, C*H*Me$_2$), 3.38 (sept, $J = 7$ Hz, 3H, C*H*Me$_2$), 5.78 (s, 3H, Pz), 6.74 (t, $J = 8$ Hz, 2H, Ph-3,5), 6.92 (t, $J = 8$ Hz, 1H, Ph-4), 7.18 (t, $J = 8$ Hz, 2H, Ph-2,6). UV–Vis (CH_2Cl_2, −50 °C, λ_{max}/nm (ε/cm^{-1} mol^{-1} dm^3)): 342 (sh, 2670), 430 (4750), 510 (4300), 625 (sh, 1540). We did not obtain a satisfactory elemental analysis due to fast decomposition of this complex at room temperature.

2.3. Measurements

IR spectra were recorded in the 4600–400 cm^{-1} region (MIR) using KBr pellets, and in the 650–100 cm^{-1} region (FIR) using CsI disks at room temperature. For this purpose, a JASCO FT/IR-550 spectrophotometer was applied. ^{1}H NMR spectra were obtained on a Bruker AVANCE-600 NMR spectrometer at −50 °C. Chemical shifts are reported versus the internal standard $(CH_3)_4Si$, or referenced to residual protons in the deuterated solvents. Electronic absorption spectra were measured on an Otsuka Electronics MCPD-2000 system with an optical fiber attachment (300–1100 nm) at −50 °C. The elemental analyses (C, H, N) were performed by the Department of Chemistry at the University of Tsukuba.

FT-Raman spectra were recorded on a Bruker IFS 66 interferometer with a Bruker FRA 106 Raman attachment using a Nd:YAG laser for excitation ($\lambda = 1064$ nm). Measurements were performed on pure compounds at room temperature. Resonance Raman spectra were obtained on a setup that consists of the following components: an Acton SpectraPro 500-i double monochromator with an attached PI-CCD camera (1100 × 330 pixel, back illuminated with UVAR coating), a Spectra-Physics Stabilite 2017 Ar^+ ion gas laser, and a Spectra-Physics 2080 Kr^+ ion gas laser. Measurements were performed on frozen solutions at liquid nitrogen temperature.

2.4. Density functional theory (DFT) calculations

Spin-restricted DFT calculations using the BP86 functional together with Ahlrich's TZVP basis set [25] were performed with the program package GAUSSIAN-03 [26]. The TZVP basis set has been applied as implemented in G03. The structures of the model complexes [Cu(L)(NNPh$_2$)], [Cu(L)(NN(H)Ph)], *trans*-[Cu(L)(N(H)NPh)], and *cis*-[Cu(L)(N(H)NPh)] were fully optimized using BP86/TZVP. For the calculations, the simplified hydrotris(pyrazolyl)borate ligand 'L' has been used where the pyrazolyl substituents are replaced by hydrogen. Frequency calculations for the obtained structures show no imaginary modes indicating that true energy minima have been obtained. Since B3LYP/LanL2DZ calculations had been applied to binuclear copper(I)–diazene complexes in a preceding communication [21], we evaluated the applicability of this method to copper(I)–diazene complexes. For this purpose, full geometry optimizations with B3LYP/LanL2DZ were

conducted for the four mononuclear diazene model systems listed above. Importantly, the calculated structures and vibrational properties from this method are similar to those obtained with BP86/TZVP (cf. Table 4). Finally, in order to investigate the energy differences between the different isomers of [Cu(L)(N_2HPh)], B3LYP/TZVP single point calculations have been performed on the BP86/TZVP optimized structures of the corresponding model systems. Orbitals were plotted with the program GAUSSVIEW.

2.5. Crystal structure determination

The structures of [{Cu(L1)}$_2$(μ-N_2H_2)] (**1**) (CCDC-235558) and [{Cu(L1)}(μ-N_2Me_2)] (**2**) (CCDC-235559) have been reported in Ref. [21].

For [Cu(L3)(N_2H_4)] (**3**) and [{Cu(L1′)}$_2$(μ-N_2H_4)](ClO_4)$_2$ (**4**), the single crystals for X-ray structural determination were obtained by recrystallization from dichloromethane/heptane solutions at −30 °C. Crystal data and refinement parameters for these compounds are given in Table 1. The diffraction data for [Cu(L3)(N_2H_4)] were measured on an AFC 5S diffractometer at −80 °C, and a Rigaku/MSC Mercury CCD system at −69 °C was used for [{Cu(L1′)}$_2$(μ-N_2H_4)](ClO_4)$_2$. Graphite-monochromated Mo Kα ($\lambda = 0.71070$ Å) radiation was applied in these experiments. All crystals were mounted on the tip of a glass fiber using heavy weight oil. For [Cu(L3)(N_2H_4)], the unit cell parameters of each crystal were obtained from a least-squares refinement based on 20 reflections. The intensities of three representative reflections monitored every 100 reflections did not show any decay, and therefore, no decay correction was applied. All data were corrected for Lorentz and polarization effects. The structure was solved by direct methods (SAPI-91) [27] and expanded using Fourier techniques. The non-hydrogen atoms were refined anisotropically. Hydrogen atoms were located at their calculated positions. Refinement was carried out by a full-matrix least-squares method on *F*. All calculations were performed using the teXsan crystallographic software package [28]. For [{Cu(L1′)}$_2$(μ-N_2H_4)](ClO_4)$_2$, the unit cell parameters of each crystal were determined using CRYSTALCLEAR [29] from six images. The crystal to detector distance was about 45 mm in each case. Data were collected using 0.5° intervals in ϕ and ω for 40 s/frame to a maximum 2θ value of 55.0°. A total of 744 oscillation images were collected. The highly redundant data sets were reduced using CRYSTALCLEAR and corrected for Lorentz and polarization effects. An empirical absorption correction was applied for each crystal. Structures were solved by direct methods using the program SIR-92 [30]. The positions of the metal atoms and their first coordination sphere were located from the *E*-map; other non-hydrogen atoms were found in alternating difference Fourier syntheses. Least-squares refinement cycles were refined anisotropically (CRYSTALSTRUCTURE) [31,32]. Hydrogen atoms were placed in calculated positions. Crystallographic data and structure refinement parameters including the final discrepancies (*R* and R_w) are listed in Table 1.

Table 1
Summary of crystallographic data of [Cu(L3)(N_2H_4)] (**3**) and [{Cu(L1′)}$_2$(μ-N_2H_4)](ClO_4)$_2$ (**4**)

Complex	[Cu(L3)(N_2H_4)] · 2(CH_2Cl_2)	[{Cu(L1′)}$_2$(μ-N_2H_4)](ClO_4)$_2$ · (CH_2Cl_2 · 2H_2O)
Formula	$C_{32}H_{60}BCl_4CuN_8$	$C_{57}H_{102}Cl_4Cu_2N_{14}O_{10}$
Formula weight	637.60	1412.42
Crystal system	monoclinic	monoclinic
Space group	$P2_1/n$ (#14)	$P2_1/c$ (#14)
a (Å)	19.968(8)	12.527(4)
b (Å)	12.970(6)	30.216(9)
c (Å)	16.165(8)	20.900(7)
β (°)	99.64(3)	109.647(4)
V (Å^3)	4127(3)	7450(4)
Z	4	4
D_{calc} (g/cm^3)	1.244	1.259
μ(Mo Kα) (cm^{-1})	8.20	7.724
Reflections collected	7949	60 343
Unique reflections	7630	16 927
R_{int}	0.122	0.052
Number of observations	5469 ($I > 3\sigma(I)$)	7282 ($I > 5\sigma(I)$)
Number of variables	415	886
R[a]	0.0619	0.0905
R_w[a]	0.0827	0.1141
Maximum/minimum peak (e/Å^3)	0.80/−0.65	2.24/−0.91

[a] $R = \sum\|F_o| - |F_c\|/\sum|F_o|$; $R_w = [\sum w(|F_o| - |F_c|)^2/\sum w(F_o^2)]^{1/2}$, $w = 1/\sigma^2(|F_o|)$.

3. Results and analysis

3.1. Binuclear Cu(I)–diazene complexes

Reaction of the copper(II) precursor [{Cu(L1)}$_2$(μ-OH)$_2$] having the isopropyl-substituted borate coligand $L1^-$ ($L1^-$ = hydrotris(3,5-diisopropyl-1-pyrazolyl)borate anion) with hydrazine or 1,2-dimethylhydrazine leads to the clean formation of bridging copper(I) diazene complexes of type [{Cu(L1)}$_2$(μ-RN=NR)] (R = H: **1**; R = Me: **2**) in about 60% yield as shown in Eq. (1). Crystal structures of compounds **1** and **2** have been reported in a recent publication [21].

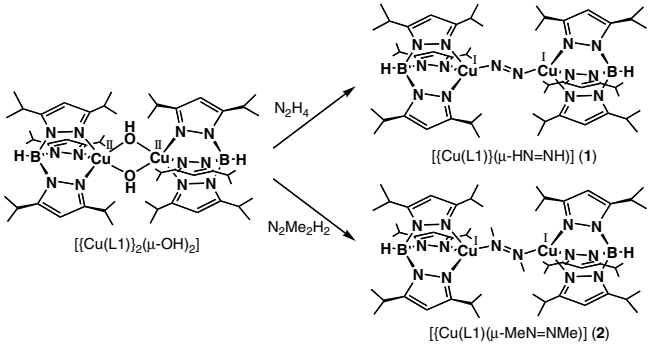

(1)

These diazene complexes are stable in solution or the solid state at low temperature under an argon atmosphere. Mechanistically, the formation of these complexes correspond to a simple redox reaction where two Cu(II) ions oxidize hydrazine to diazene:

$$2(L)Cu(II)–OH + H_2N–NH_2 \rightarrow 2(L)Cu(I) + HN{=}NH + 2H_2O \quad (2)$$

The formed diazene is then stabilized by coordination to the generated Cu(I) species. The resulting binuclear diazene complexes are characterized by a strong absorption band in the visible region at ~570 (**1**) and ~485 nm (**2**), respectively. These features correspond to Cu(I)-d to diazene-π^* CT transitions as evident from resonance Raman measurements. A simple representation of the electronic structure of this class of compounds is shown in Scheme 2. The Cu(I)–diazene bond is dominated by π backdonation from the filled d_{xz} orbitals of copper (in the given coordinate system) into the empty π_v^* orbital (v = vertical: the π^* orbital orthogonal to the Cu–N=N–Cu plane; cf. Scheme 2) of diazene. The Cu(I) to diazene CT transition can then be assigned as indicated in Scheme 2. This transition is responsible for the deep colors of complexes **1** and **2**, which are very unusual for Cu(I) compounds.

Bridging diazene complexes also show characteristic resonance Raman spectra upon excitation into the metal to diazene CT transition as has been demonstrated before for Fe(II)-diazene complexes [33,34]. Table 2 summarizes the obtained band positions from these experiments. Surprisingly, whereas the N–N stretching frequencies for all three compounds are similar (1350–1380 cm^{-1}) in agreement with the diazene formulation of the N_2R_2 ligand, the metal–N stretching vibrations show strongly diverting properties. For **1**, this mode is strongly resonance enhanced and observed at 523 cm^{-1}. Surprisingly, the similar compounds **2** and $[\{Fe'N_HS'_4\}_2(N_2H_2)]$ do not show any comparable features. In addition, the DFT calculations predict ν_S(Cu–N) at much lower energy for **2**. What is the reason for this apparent lack of resonance enhancement for ν_S(metal–N) in **2** and $[\{Fe'N_HS'_4\}_2(N_2H_2)]$, and the appearance of this mode at much lower energy in these compounds compared to **1**? This difference can be understood based on the calculated atomic displacements of ν_S(Cu–N) in **1** and **2**. As shown in Scheme 3, the symmetric Cu–N stretch in compound **1** corresponds to *a rotation of*

Table 2
Raman assignments of bridging diazene complexes

Mode	Cu–N_2R_2–Cu (Ref. [21])		$[\{Fe'N_HS'_4\}_2(N_2H_2)]$
	1: R = H[a]	**2**: R = Me[a]	(Ref. [34])
ν_S(Cu–N)	**523** (512)	not obs. (251)	not obs.
γ_S(N–H)	not obs. (603)		667/659
ν(N–N)	**1358** (1421)	**1365** (1416)	**1382**
δ_S(N–N–H)	**1547** (1573)		**1480**

[a] 'not obs.' = not observed; calculated band positions from DFT are given in brackets.

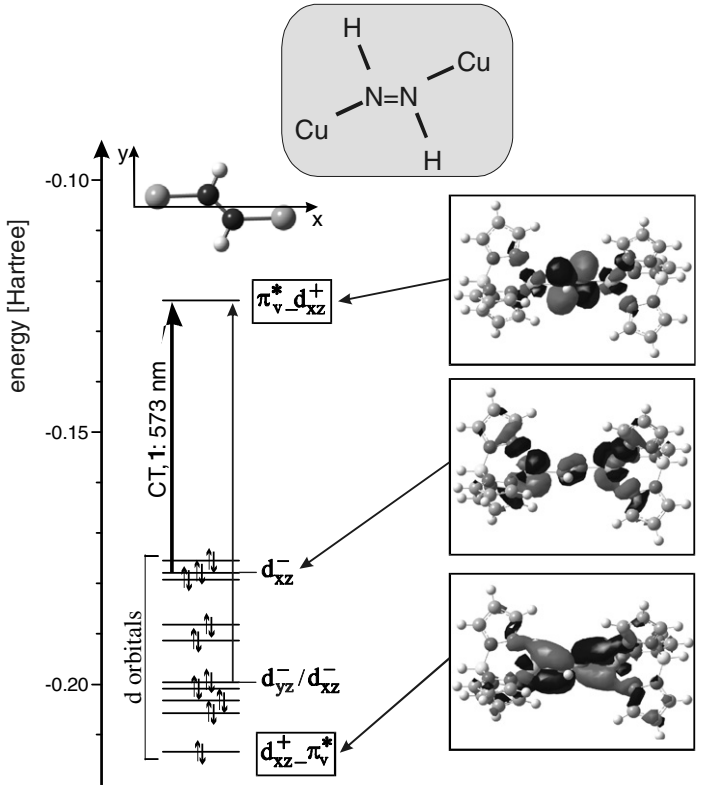

Scheme 2. MO diagram of the binuclear Cu(I)–diazene complex **1** (recalculated for the B3LYP/LanL2DZ structure from Ref. [21] using BP86/TZVP).

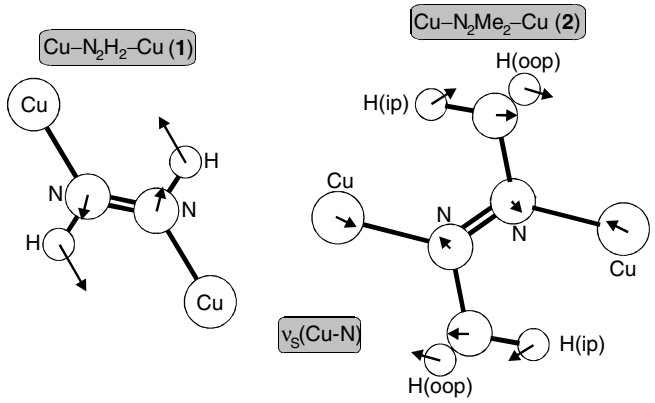

Scheme 3. Atomic displacement vectors for ν_S(Cu–N) in **1** (calculated: 512 cm^{-1}; observed: 523 cm^{-1}; left) and **2** (calculated: 251 cm^{-1}; not observed; right).

the N_2H_2 group between the two copper centers, where the copper atoms essentially do not show any displacement. Therefore, the increased mass of the CH_3 groups compared to H shifts this mode to much lower energy in **2** (below 300 cm^{-1} from the calculation). Moreover, this increase in effective mass of the diazene unit changes the nature of ν_S(Cu–N) in **2**, which does not correspond to a pure rotation of the diazene unit anymore, but also contains a significant amount of copper displacement. Hence, although the Cu–N force constants can be expected to be similar for **1** and **2**, the corresponding symmetric Cu–N stretches are at very different energies due to the very different nature of the actual motions associated with them. A very similar effect can be expected for $[\{Fe'N_HS'_4\}_2(N_2H_2)]$: in this case, the diazene protons undergo strong hydrogen bridges with adjacent thiolate donors [35,36], which fixes their position and prevents the rotation of the diazene group in ν_S(metal–N) as compared to **1**. This will again induce a change in effective mass, and shift ν_S(metal–N) to much lower energy compared to **1**. Besides this frequency shift, the different nature of ν_S(metal–N) in **1** and **2** will also affect the resonance enhancement of this mode, since this lowers its mixing with ν(N–N) in **2** and induces mixing with other core vibrations.

3.2. Cu(I)–hydrazine complexes

In order to obtain mononuclear copper(I)–diazene complexes, we used the precursor [Cu(L3)(OH)] with the sterically demanding ligand $L3^-$ ($L3^-$ = hydrotris(3-*tert*-butyl-5-isopropyl-1-pyrazolyl)borate anion) for the complex synthesis. Due to the presence of the bulky *tert*-butyl groups in the 3rd positions of the pyrazolyl rings, complexes with $L3^-$ are always mononuclear.[1] Importantly, the product obtained from the reaction of [Cu(L3)(OH)] and hydrazine was diamagnetic and colorless. From the reaction mixture, the mononuclear copper(I)–hydrazine complex [Cu(L3)-(NH_2-NH_2)] (**3**) was isolated as

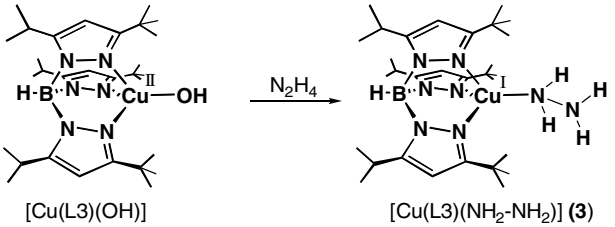

(3)

indicated in Eq. (3) and structurally characterized. In this complex, Cu is tetrahedrally coordinated by four nitrogen atoms as shown in Fig. 2, top. Because of the bulky

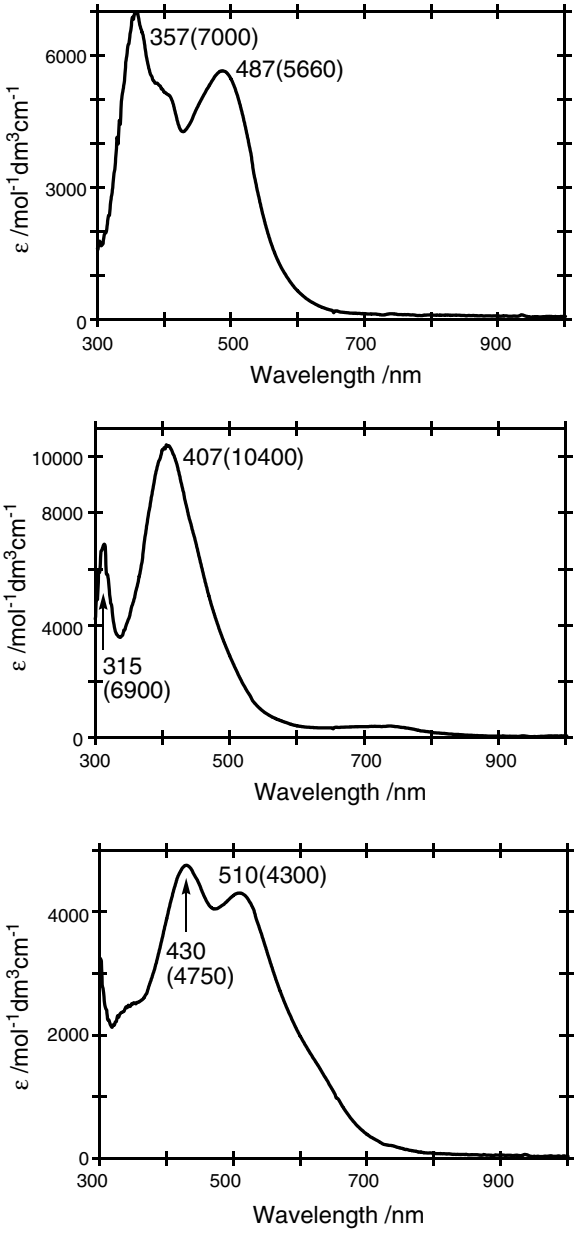

Fig. 1. Absorption spectra of the reaction mixtures of 1,2-dimethylhydrazine (top), 1,1-diphenylhydrazine (middle), and 1-phenylhydrazine (bottom) with $[\{Cu(L1)\}_2(\mu\text{-}OH)_2]$.

[1] This is already evident from the copper(II)-hydroxo precursor, which is dinuclear for ligand $L1^-$, but mononuclear for $L3^-$ in Ref. [23].

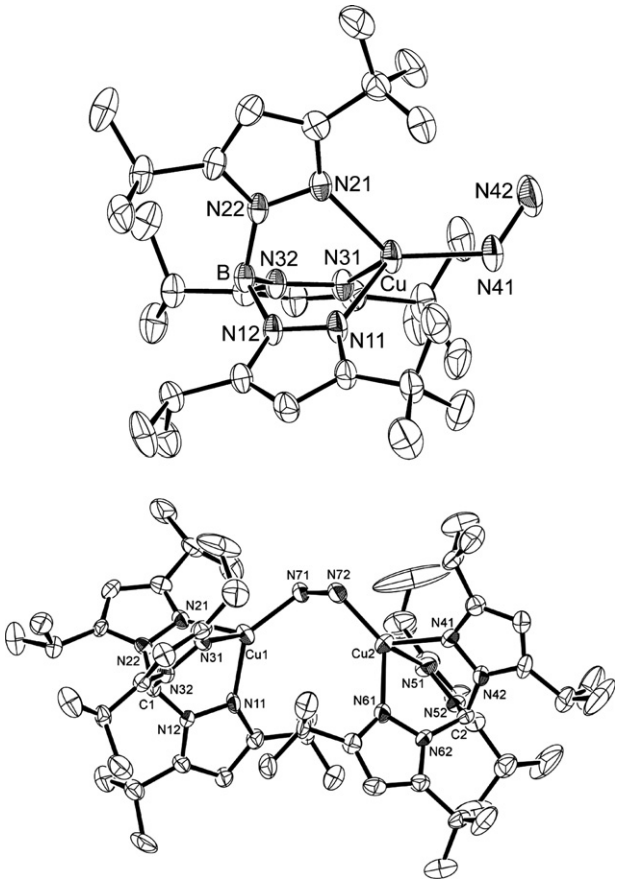

Fig. 2. Molecular structures of mononuclear and binuclear copper(I)–hydrazine complexes, $[Cu(L3)(N_2H_4)]$ (**3**, top) and $[\{Cu(L1')\}_2(\mu\text{-}N_2H_4)]^{2+}$ ($\mathbf{4}^{2+}$, bottom).

tert-butyl groups of $L3^-$, hydrazine is unable to bridge two Cu(I) ions, leading to the mononuclear structure of **3**. The N41–N42 distance of 1.434(6) Å in this complex is consistent with a single bond between the two nitrogen atoms, and is close to the value obtained for free hydrazine (1.447 Å), or other monodentate hydrazine complexes (1.439–1.46 Å) [11]. The Cu1–N41–N42 angle of 123.5(3)° is also typical for monodentate hydrazine complexes (115–121°) [14]. Interestingly, this angle is comparable with those of the binuclear diazene complexes **1** and **2**, which have an N=N double bond.

The fact that copper is in the oxidation state +I in complex **3** shows that the formation of this complex is more complicated than just a simple coordination of hydrazine to the precursor [Cu(L3)(OH)]. Since the precursor corresponds to copper(II), a redox reaction must have taken place. We propose that initially, the same reaction as in the case of **1** occurs, i.e. the reduction of copper(II) to copper(I) and the concomitant formation of diazene as shown in Eq. (2). However, due to the bulky nature of $L3^-$, a stable, binuclear copper(I)–diazene complex cannot form. We propose that the corresponding mononuclear species, [Cu(L3)(HN=NH)], is unstable and facilitates diazene disproportionation

$$2[Cu(L3)(HN{=}NH)] \rightarrow 2[Cu(L3)] + N_2 + N_2H_4 \qquad (4)$$

leading to the copper(I) complex [Cu(L3)], which readily reacts with excess hydrazine present in the reaction mixture to form **3**. Further experiments are necessary to prove either the formation of the intermediate [Cu(L3)(HN=NH)] or the generation of N_2.

In order to investigate second coordination sphere effects on the formation of the diazene complexes, we also applied the neutral ligand L1′ (L1′ = tris(3,5-diisopropyl-1-pyrazolyl)methane), which is otherwise similar to $L1^-$. Reaction of the binuclear precursor $[\{Cu(L1')\}_2(\mu\text{-}OH)_2](ClO_4)_2$ with hydrazine again efforts a colorless solution of a diamagnetic complex. We were able to crystallize the reaction product, which corresponds to the binuclear copper(I)–hydrazine complex $[\{Cu(L1')\}_2(\mu\text{-}N_2H_4)](ClO_4)_2$ (**4**) as shown in Eq. (5). In this case, reduction of the copper(II) precursor to copper(I) is observed, but no diazene complex is obtained.

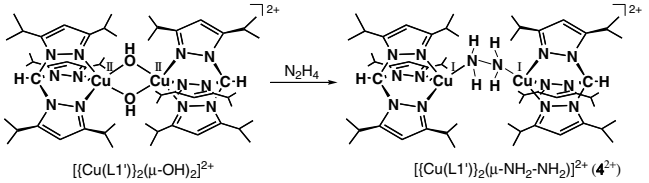

(5)

Again, we believe that the isolation of the hydrazine complex has to be explained by an instability of the corresponding diazene complex. However, the formation of a binuclear structure is possible here, due to the reduced steric demand of L1′ compared to $L3^-$. Therefore, we feel that the fact that no diazene complex is obtained relates to an electronic effect in this case. Previous work has shown that tris(pyrazolyl)methane ('methane') ligands lead to copper(I) complexes that are somewhat electron-deficient compared to the corresponding complexes with hydrotris(pyrazolyl)borate ('borate') ligands with identical substituents on the pyrazolyl rings [20]. This can nicely be probed by comparison of the properties of the corresponding carbonyl complexes [20,37]. Our spectroscopic studies have shown that the copper(I) borate complexes lead to stronger Cu(I)–CO backbonds than corresponding methane complexes [20]. Since the Cu(I)–diazene interaction in **1** is dominated by backdonation, we feel that the weaker backbond in the case of the coligand L1′ renders the binuclear diazene complexes unstable, again leading to decomposition and formation of the free copper(I) complex $[Cu(L1')]^+$. This species then reacts readily with excess hydrazine to form **4**. Further work is necessary to prove the proposed mechanism for the generation of **4** under these reaction conditions.

The crystal structure of **4** is shown in Fig. 2, bottom. The overall structure of this complex resembles that of **1** or **2**. However, the torsion angle of the N–N bond (Cu1–N71–N72–Cu2) is only 78.2(7)° indicative of a *cis* arrangement of the copper ions, in contrast to the torsion angles of

1 and **2** (180°), where the metals show a *trans* arrangement. The N71–N72 distance of **4** (1.440(9) Å) is much longer than those of **1** (1.13(1) Å) and **2** (1.27(2) Å) and similar to that of **3** (1.434(6) Å) (cf. Table 3). From this observation and the number of counter ions present in the unit cell, it is evident that **4** corresponds to a hydrazine bridged copper(I) complex. The Cu···Cu′ distance (4.0125(16) Å) is slightly shorter than those of **1** (4.709(1) Å) or **2** (4.786(5) Å) in agreement with the *cis*-Cu–N–N–Cu structure.

3.3. Mononuclear Cu(I)–$NNPh_2$ complex

In order to finally synthesize a mononuclear diazene complex, reaction of the precursor $[\{Cu(L1)\}_2(\mu\text{-}OH)_2]$ with 1,1-diphenylhydrazine at low temperature was then conducted. In this case, we anticipated that the bulky phenyl substituents would prevent a dimerization of the complex, and would add to the stabilization of the diazene ligand.

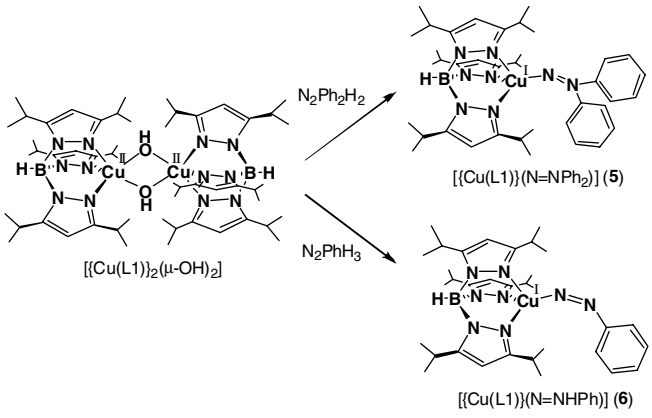

(6)

After addition of 1,1-diphenylhydrazine, the reaction mixture turned reddish brown indicative of the formation of a diazene complex as shown in Eq. (6), top. Fig. 1, middle shows the corresponding absorption spectrum, which is in agreement with this conclusion. We were able to determine a preliminary crystal structure of the reaction product $[Cu(L1)(NNPh_2)]$ (**5**), shown in Figs. S1 and 3, left. The structure shows that, to our knowledge, we were in fact able to isolate the first isodiazene complex of copper. We were not able to complete the structure refinement due to low crystal quality (cf. Supplementary material). However, it is evident from the preliminary structure that this complex is mononuclear. Two independent molecules are found in the unit cell as shown in Fig. S1. The N71–N72 (1.20(2) Å) and N81–N82 (1.28(2) Å) distances are consistent with a double bond between the two nitrogen atoms in comparison with the N–N distances of **1** and **2** (cf. Table 3). The Cu1–N71–N72 (139.1(15)°) and Cu2–N81–N82 (134.6(12)°) angles are also typical for diazene complexes.

Fig. 3, right shows the fully optimized structure on the BP86/TZVP level of a simplified model for **5** that lacks the side chains of the borate ligand $L1^-$. The overall structure of this model $\tilde{\mathbf{5}}$ is very similar to the crystal structure of **5**. Geometric parameters obtained from the calculation are listed in Table 4, which show excellent agreement with experiment. As already mentioned in Section 3.1, (resonance) Raman spectroscopy is a very powerful tool to obtain insight into the electronic structures of metal–diazene complexes. Fig. 4 shows the non-resonance Raman spectrum of **5** in comparison to the calculated spectrum for $\tilde{\mathbf{5}}$, which show very good agreement. In general, the prediction of non-resonance Raman spectra with DFT methods is a good method to achieve detailed spectral assignments as demonstrated recently [38]. Based on the calculation, most peaks in the Raman spectrum of **5** can be assigned as listed in Table 5. The intense bands observed at 1587 and 1460 cm^{-1} correspond to C–C stretching vibrations of the phenyl rings. Importantly, the two peaks at 1401 and 1389 cm^{-1} are assigned to the N–N stretch ν(N–N). This splitting pattern is not reproduced by the calculations, which show only one band for ν(N–N). However, the calculations predict that ν(N–N) is mixed with C–N stretching modes of the pyrazolyl rings. Since the isopropyl substituents of the pyrazolyl rings are missing in the model system $\tilde{\mathbf{5}}$, the resulting small shifts of the pyrazolyl ring stretching modes might be significant enough to induce this error. To lower energy, bands at 1309 and 1202 cm^{-1} correspond to additional pyrazolyl ring modes. These bands are predicted by the calculations at 1285 and 1193 cm^{-1}, which shows that the neglect of the isopropyl side chains in $\tilde{\mathbf{5}}$ only has a limited effect on the pyrazolyl ring stretching modes. To lower energy, a number of phenyl vibrations are observed in the 1000–1200 cm^{-1} region (cf. Table 5). The agreement between experiment and calculations is in general good, except for the intense 1123 cm^{-1} feature. In this case, the calculations predict two intense bands at 1136 and 1097 cm^{-1}, which correspond to the antisymmetric and symmetric C–N stretching modes of the diphenylisodiazene unit, respectively. The fact that only one of them is observed experimentally is quite puzzling, and prevents a clean assignment of the 1123 cm^{-1} feature. A similar situation is encountered for the 731 cm^{-1} feature: this band could either be assigned to the symmetric B–N stretch of the borate ligand (calc.:

Table 3
Structural comparison of copper(I)–diazene and –hydrazine complexes

	1[a]	2[a]	3	4	5
Cu–N_{pz}[b] (Å)	2.05	2.08	2.13	2.11	2.13
N–N[c] (Å)	1.13(1)	1.27(2)	1.434(6)	1.440(9)	1.24[e]
Cu–N[c] (Å)	1.841(8)	1.92(1)	2.055(4)	1.965(9)[e]	1.88[e]
Cu–N–N[c] (°)	151.6(8)	132(1)	123.5(3)	119.7(6)[e]	136.9[e]
Cu···Cu (Å)	4.709(1)	4.786(5)		4.0125(16)	
Cu–N–N–Cu[d] (°)	180	180		78.2(7)	

[a] Ref. [21].
[b] Pyrazolyl ring nitrogens, averaged values.
[c] Diazene or hydrazine nitrogens.
[d] Torsion angles.
[e] Averaged values.

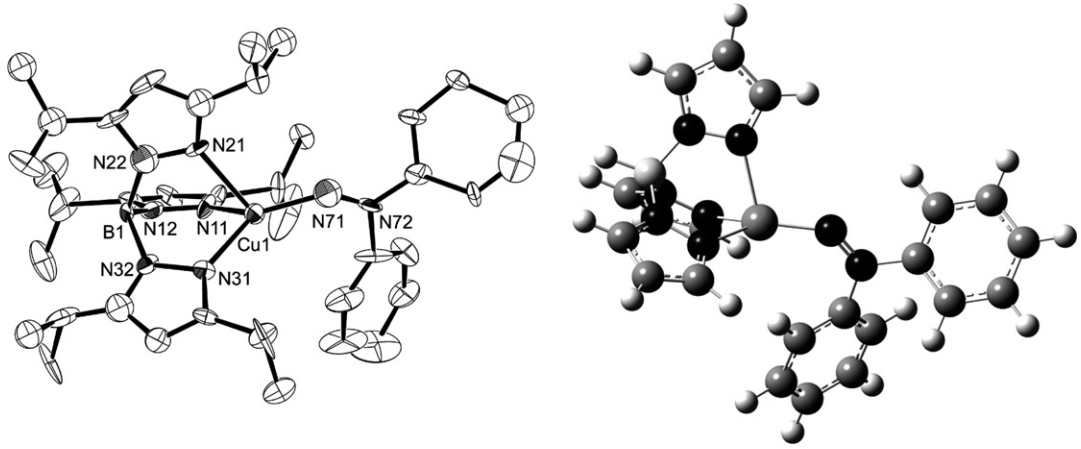

Fig. 3. Left: preliminary structure of [Cu(L1)(NNPh$_2$)] (**5**). Right: fully optimized structure of model [Cu(L)(NNPh$_2$)] (**$\tilde{5}$**) using BP86/TZVP. Structural parameters are given in Table 4.

Table 4
Calculated geometric and vibrational properties of mononuclear Cu(I)–diazene complexes

Complex	Geometric parameters in (Å) and (°)				Vibrational frequencies (cm^{-1})[a]			
	d(Cu–N)	*d*(N–N)	*d*(N–C(av))	∠(Cu–N–N)	δ(N–N–H)	*v*(N–N)	*v*(Cu–N)	δ(Cu–N–N)
BP86/TZVP								
[CuL(NNPh$_2$)]	1.840	1.259	1.471(av)	135		1386	593/**496**	419
[CuL(NN(H)Ph)]	1.837	1.252	1.451	136	1510	1478/1413	504	427
trans-[CuL(N(H)NPh)]	1.897	1.281	1.412	143	1481	1445/**1398**	480	448
cis-[CuL(N(H)NPh)]	1.879	1.278	1.415	130	1449	1439/**1405**	521	374
B3LYP/LanL2DZ								
[CuL(NNPh$_2$)]	1.875	1.282	1.476(av)	138		1415	621/**506**	432
[CuL(NN(H)Ph)]	1.873	1.277	1.456	138	1573	1495/1452	492	419
trans-[CuL(N(H)NPh)]	1.933	1.295	1.429	141	1523	1487/**1437**	481	442
cis-[CuL(N(H)NPh)]	1.912	1.293	1.439	130	1486/1478	**1454**/1449	528	372

[a] If two energies are listed for a certain vibration, then the feature with the larger contribution of this vibration is given in bold (if applicable).

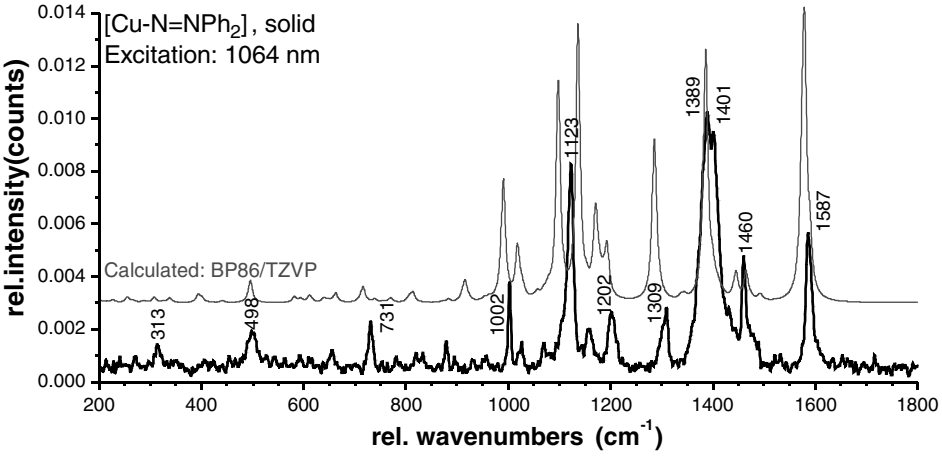

Fig. 4. Non-resonance Raman spectrum of solid [Cu(L1)(NNPh$_2$)] (**5**) recorded at an excitation wavelength of 1064 nm (bold), and calculated spectrum (thin) using BP86/TZVP. For a color version of this figure, see Fig. S7.

770 cm^{-1}), or a mixed phenyl mode (calc.: 755 cm^{-1}). Based on intensity considerations, we prefer the former assignment, but this is only tentative. Finally, at 498 cm^{-1}, the Cu–N stretch of the Cu–diazene unit is observed. Further vibrational assignments are available from the resonance Raman spectra of **5** shown in Fig. 5. Importantly, strong resonance enhancement is observed for the Cu–N(diazene) stretch, which allows for the obser-

Table 5
Non-resonance (nr) and resonance (r) Raman assignments of [Cu(L1)(NNPh$_2$)] (**5**), taken from Figs. 4 and 5, top (514 nm excitation)

Experimental (cm^{-1})		BP86/TZVP	Assignment[a]
nr Raman	r Raman	(cm^{-1})	
1587	1590	1590–1574	$\nu(Ph)_{24} + \nu(Ph)_{25}$: $\nu_{sym}(C–C) + \nu_3(C–C)$
	1552		?
1460	1462	1465/1445	$\nu(Ph)_{23}$: $\delta(C–C–H) + \nu_{asym4}(C–C)$
1401	1403	1386	ν(N–N) mixed with
1389	1390	(1385/1380)	pyrazole: ν_{asym}(C–N)
1309		1285	pyrazole: ν_{sym}(C–N)/ν(N–N)
1202		1193	pyrazole: ν(N–N)
1156		1171	$\nu(Ph)_{19}$: $\delta_{sym}(C–C–H) + \nu_{asym}(C–N)^{Ph}$
1123	1128	1136 or 1097 ?	$\nu_{asym}(C–N)^{Ph} + \delta_{sym}$ (C–C–H); $\nu_{sym}(C–N)^{Ph} + \nu(Ph)_{16}$: ν_1(C–C)
1026		1018	$\delta_{asym}(C–C–C)^{Ph}$
1002		990	$\nu(Ph)_{12}$: δ_{sym}(C–C–C)
	936		?
	782	770 or 755 ?	pyrazole: ν_{sym}(B–N); $\nu(Ph)_9$: $\gamma_1(H) + \delta_{sym}(C–N–C)^{Ph}$
731	735	716	$\nu(Ph)_9$: $\gamma_1(H) + \nu_{sym}(C–N)^{Ph}$
	659[b]	662/647 ?	$\nu(Ph)_7$: $\delta_2(C–C–C) + \gamma(H) + \delta(C–N–N)^{Ph}$
	629[b]	639 ?	$\gamma(H)^{Ph} + \gamma(N)^{Ph}$
	608[b]	615/593 ?	$\delta(C–C–C)^{Ph} + \nu$(Cu–N)
498	504	496	ν(Cu–N)
	427[b]	419	δ_{ip}(Cu–N–N)
313		307	$\delta_{oop}(Cu–N–N) + \delta(C–N–N)^{Ph}$
	275	269/267/255[b]	pyrazole: ν(Cu–N) + δ(B–N–N)

[a] Phenyl modes $\nu(Ph)_{xx}$ are labeled according to Fig. 3 in Ref. [38] using bromobenzene as model. Phenyl modes not listed in this reference are labeled as $\nu/\delta/\gamma()^{Ph}$.
[b] Resonance enhancement due to small ν(Cu–N) admixture.

vation of a number of low-energy vibrations that are mixed with this mode as listed in Table 5. Most prominently, the band at 427 cm^{-1}, which is absent in the non-resonance Raman spectra, is assigned to the Cu–N–N bending vibration of the isodiazene unit (calc.: 419 cm^{-1}). In summary, very good agreement between the calculations and experiment is observed for the Raman spectra. These results also show that the magnitude of the experimentally observed bands is due to phenyl vibrations.

Comparison of the resonance Raman spectra of **5** in Fig. 5 shows that both the Cu–N and N–N vibrations are strongly resonance enhanced upon laser excitation into the intense absorption band at 407 nm. Resonance Raman profiles shown in Figs. S2–S6 further stress this observation. This proves that the absorption feature at 407 nm corresponds to a copper(I) to diazene CT transition, similar to the observation made for the bridging complexes **1** and **2** (cf. Fig. 1, top). The exact nature of this transition can be understood from the electronic structure of **5**, which is schematically shown in Scheme 4, left. The d_{xz} orbital (in the given coordinate system) of copper(I) undergoes a quite strong π backbond with the π^*_v orbital of isodiazene. Since the occupied d orbitals of copper are strongly mixed as indicated, the strength of this interaction is estimated best from the corresponding antibonding combination, π^*_v—d_{xz}, shown in Scheme 4, which has about 15% copper-d_{xz} contribution. Since the phenyl rings are tilted with respect to the Cu–N–N plane of isodiazene, the admixture of phenyl orbitals into π^*_v is limited as can be seen from the orbital plot of π^*_v—d_{xz}. Two of the occupied d-orbitals of copper(I) have a d_{xz} contribution, which could potentially give rise to two CT transitions. The more intense one is predicted at higher energy as indicated with the thicker arrow in Scheme 4.

3.4. Mononuclear Cu(I)–N_2HPh complex

In addition to the reaction with 1,1-diphenylhydrazine, we have also applied 1-phenylhydrazine for the reaction with the copper(II) precursor [{Cu(L1)}$_2$(μ-OH)$_2$] as shown in Eq. (6), bottom. The corresponding reaction was performed at low temperature. After addition of 1-phenylhydrazine to the reaction mixture, the solution turned dark purple, indicative of the formation of a diazene complex. The UV–Vis spectrum of the obtained complex is shown in Fig. 1, bottom. Due to the presence of the phenyl substituent, we believe that again a mononuclear diazene complex of the formula [Cu(L1)(N$_2$HPh)] (**6**) has formed, although no crystal structure could have been obtained to prove this point. DFT calculations indicate that **6** can exist in the form of three different isomers, the fully optimized structures (using BP86/TZVP) of which are shown in Fig. 6. Total energy calculations predict that the isodiazene isomer of the complex (Fig. 6, left) is unstable by ~10–15 kcal/mol (cf. Table 6) with respect to the corresponding diazene tautomers. The corresponding *cis* and *trans* forms have quite similar energies, and might co-exist in solution. The ground state should be the *trans* isomer shown in Fig. 6, middle. Accordingly, it is possible that the absorption spectrum of **6** in Fig. 1, bottom actually corresponds to a mixture of these two isomers, which would explain the broad appearance of the absorption bands. We have also performed resonance Raman measurements on the reaction mixtures of **6** as shown in Fig. 7. Unfortunately, the resonance enhancement is weak compared to **5**, and the spectra contain much less features. Calculated key vibrational energies of the three isomers of **6** are listed in Table 4 (the predicted non-resonance Raman spectra are shown in Fig. S8). The spectra obtained at 647 nm upon pre-resonance excitation are dominated by four features at 459, 509, 1299, and 1345 cm^{-1}. These features all disappear upon resonance excitation close to the maximum of the intense absorption band at 510 nm of **6**. Main features are now found at 488, 521, and 1453 cm^{-1}. Interestingly, whereas the region around 500 cm^{-1} in the resonance Raman spectra only contains one intense band for complex **5** corresponding to the Cu–N stretch, there are two peaks observed for **6** at 488 and 521 cm^{-1}. Compared to the

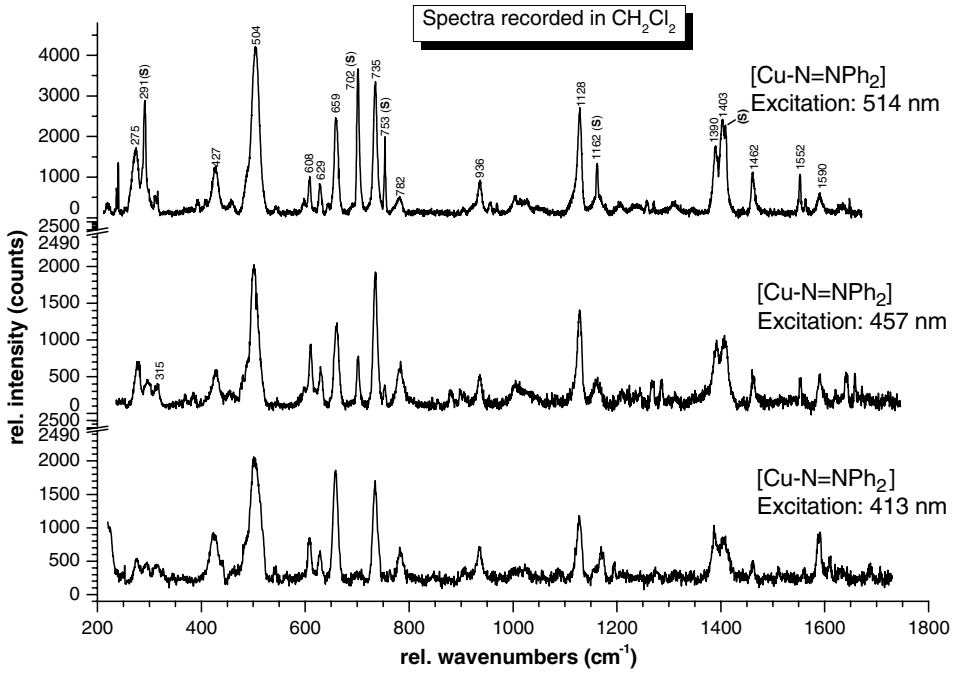

Fig. 5. Resonance Raman spectra of [Cu(L1)(NNPh$_2$)] (**5**) in frozen CH_2Cl_2 solutions recorded at excitation wavelengths of 514 nm (top), 457 nm (middle), and 413 nm (bottom). Solvent peaks are marked as '(**S**)' in the top panel.

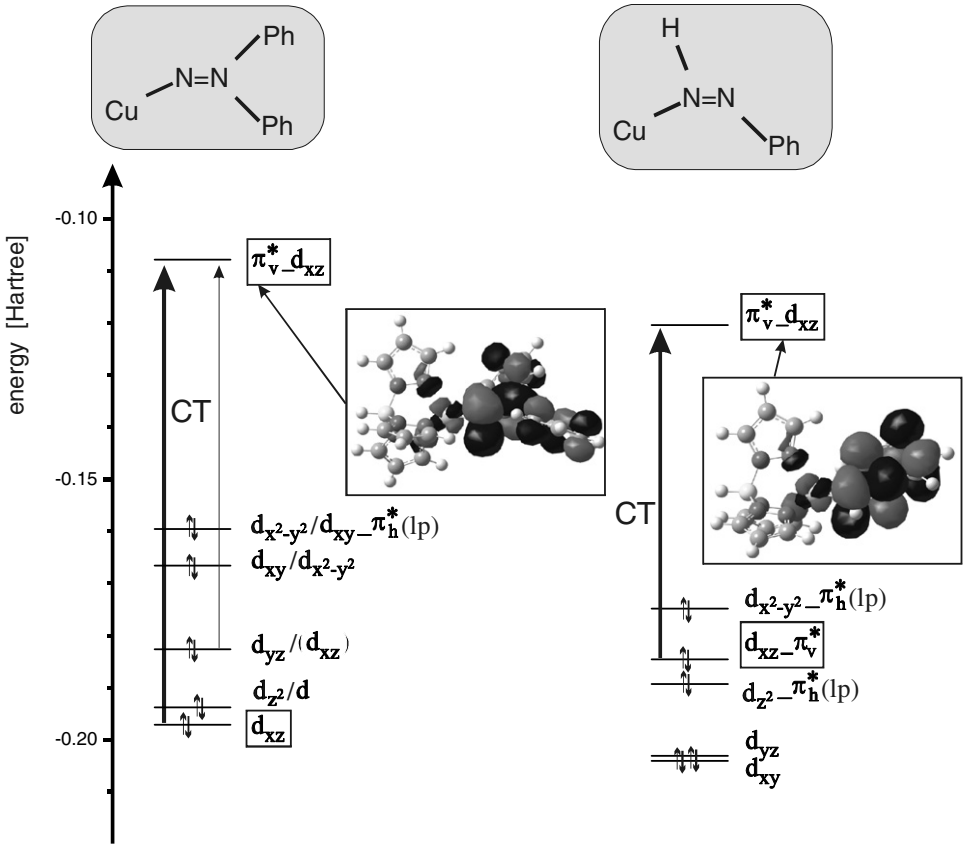

Scheme 4.

calculated vibrational energies listed in Table 4, the feature at higher energy could be assigned to ν(Cu–N) of the *cis* isomer (calc.: 521 cm^{-1}), whereas the band at lower energy could correspond to ν(Cu–N) of the *trans* tautomer (calc.: 480 cm^{-1}). This indicates a mixture of species in solution, in agreement with the calculated small energy difference

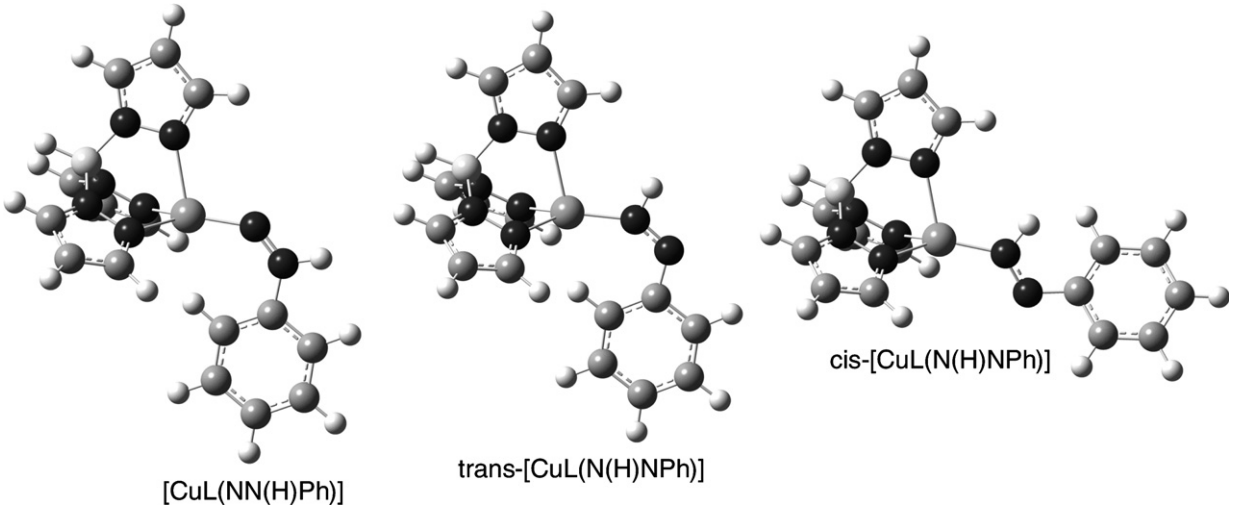

Fig. 6. Fully optimized structures of three different isomers of [Cu(L)(N_2HPh)] (model $\tilde{\mathbf{6}}$) using BP86/TZVP. Structural parameters are given in Table 4.

Table 6
Relative energies of Cu–N_2HPh complex isomers

Complex	Relative energy (kcal/mol)	
	BP86/TZVP	B3LYP/TZVP[a]
[CuL(NN(H)Ph)]	+14.3	+14.7
trans-[CuL(N(H)NPh)]	0	0
cis-[CuL(N(H)NPh)]	+3.8	+4.3

[a] Calculated for the BP86/TZVP structures.

between these isomers. The feature at 1453 cm^{-1} could then correspond to the N–N stretch of either the *cis* or *trans* isomer. The other ν(N–N) is most likely hidden under the solvent peak around 1400 cm^{-1}. The calculations also show that the positions of ν(Cu–N) and δ(N–N–H) are the best experimental signatures to spectroscopically distinguish between the three isomers of **6**. Excitation at 413 nm again shows enhancement of the same features as the 514 nm enhancement.

The formation of the mononuclear diazene complexes **5** and **6** can be rationalized by a reaction similar to Eq. (2), where, due to the presence of the phenyl substituents, the coordination of the formed diazene is only possible to one copper(I) center (R′ = Ph, H):

$$(L)Cu(II)–OH + H_2N–NRR' \rightarrow (L)Cu–NH–NRR' + H_2O$$

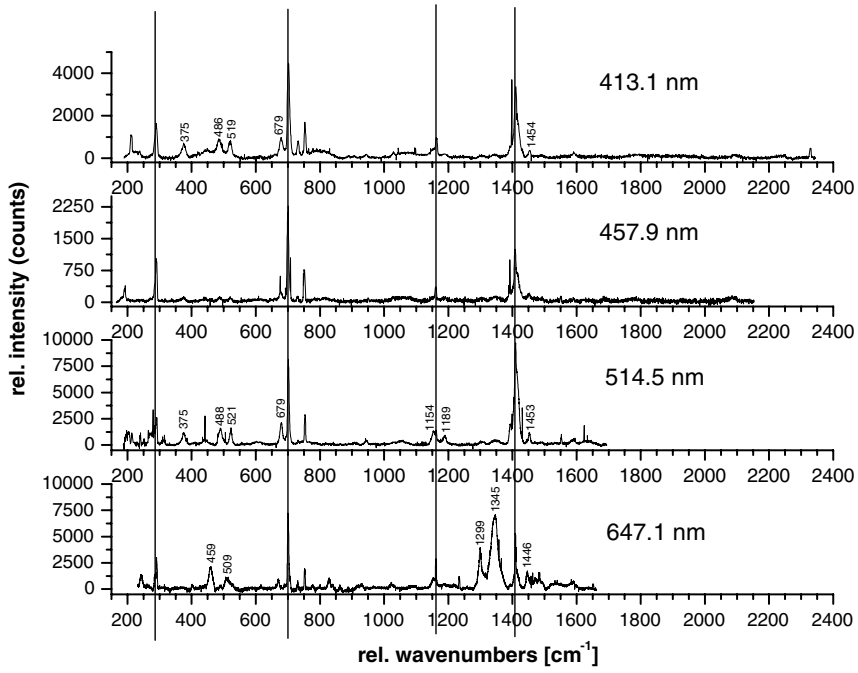

Fig. 7. Resonance Raman spectra of [Cu(L1)(N_2HPh)] (**6**) in frozen CH_2Cl_2 solutions recorded at the indicated excitation wavelengths. Major solvent peaks are marked with vertical lines.

$$(L)Cu–NH–NRR' + (L)Cu(II)–OH \rightarrow (L)Cu(I)–N_2RR' + (L)Cu(I) + H_2O \quad (7)$$

where the first step corresponds to the complexation of the substituted hydrazine to copper(II), followed by a fast outer sphere electron transfer to form the diazene complex.

Scheme 4, left shows a simplified MO diagram of the electronic structure of the *trans*-diazene isomer of **6**, which is very similar to **5**. Again, a quite strong π backbond between d_{xz} of copper and π_v^* of diazene is present. Shown in Scheme 4 is the corresponding antibonding combination, π_v^*–d_{xz}, which has about 13% Cu-d character in agreement with **5**. In this case, the d orbitals are relatively clean, and correspondingly, only one CT band is predicted from the calculations as indicated. From the simple MO consideration, this CT is predicted at lower energy for **6** compared to **5**, which would be in agreement with experiment. This is due to the fact that in the case of **6**, the phenyl ring is coplanar to the Cu–N–N plane, which increases interaction of π_v^* with phenyl orbitals, and this way, shifts π_v^* to lower energy in **6** compared to **5**.

4. Summary and conclusions

In this paper and a preceding communication [21], we have systematically explored the coordination chemistry of copper(I) towards diazene and hydrazine for the first time. For these syntheses, we have started from copper(II) precursors and added hydrazine, which subsequently becomes oxidized to diazene concomitant to the formation of copper(I). Using tridentate hydrotris(pyrazolyl)-borate anionic ligands (L^-) with low steric demand, binuclear, bridging copper(I) diazene complexes are formed, which we have structurally and spectroscopically characterized. This way, diazene is optimally stabilized by backbonding to two copper(I) centers. Using such a borate ligand with large steric demand that prevents the formation of the binuclear unit, only a hydrazine complex can be isolated, which we rationalize with a decomposition of an intermediate mononuclear diazene complex. Mononuclear copper(I) diazene complexes are accessible when 1,1-diphenylhydrazine or phenylhydrazine are used for the reactions. Here, the phenyl ring(s) offer stabilization for the formed diazene ligand and, at the same time, prevent a second copper(I) from binding to the phenyl-substituted nitrogen due to steric strain. The stabilization of the diazene ligand by the phenyl substituents is evident from the increased stability of the 1,1-diphenyldiazene complex as compared to the monophenyl analogue. We characterized these complexes spectroscopically, and structurally in the former case. Finally, we explored the effect of the negative charge of the borate ligand on the properties of the complexes by performing reactions with a corresponding tris(pyrazolyl)methane ligand of low steric demand. In this case, a binuclear hydrazine complex is the only isolable product. This is probably due to the somewhat electron-poorer copper(I) center in this case, which reduces backbonding from Cu(I) to diazene and this way, renders the diazene complex unstable toward decomposition.

Acknowledgements

This research was supported in part by the Japan Society of the Promotion of Science (Grant-in-Aid for Scientific Research (B), Nos. 14350471 and 17350043) to K.F. and the Fonds der Chemischen Industrie (FCI) to F.P. and N.L. We thank Ms. Ursula Cornelissen, University of Kiel, Germany, for the measurement of the non-resonance Raman spectrum of **5**.

Appendix A. Supplementary material

CCDC 644539 and 644540 contain the supplementary crystallographic data for $[Cu(L3)(N_2H_4)]$ and $[\{L1'Cu\}_2(\mu\text{-}N_2H_4)](ClO_4)_2$. These data can be obtained free of charge via http://www.ccdc.cam.ac.uk/conts/retrieving.html, or from the Cambridge Crystallographic Data Centre, 12 Union Road, Cambridge CB2 1EZ, UK; fax: (+44) 1223-336-033; or e-mail: deposit@ccdc.cam.ac.uk. The preliminary crystal structure of **5**, selected bond distances and angles, resonance Raman profiles of **5**, and calculated non-resonance Raman spectra of **6** are available. Supplementary data associated with this article can be found, in the online version, at doi:10.1016/j.ica.2007. 05.027.

References

[1] M. Appl, Ammonia, Wiley–VCH, Weinheim, 1999.
[2] J.R. Jennings, Catalytic Ammonia Synthesis: Fundamentals and Practice, Plenum Press, New York, 1991.
[3] J.B. Howard, D.C. Rees, Chem. Rev. 96 (1996) 2965.
[4] G.J. Leigh, Nitrogen Fixation at the Millennium, Elsevier, Amsterdam, 2002.
[5] F. Studt, F. Tuczek, Angew. Chem., Int. Ed. 44 (2005) 5639.
[6] O. Einsle, F.A. Tezcan, S.L.A. Andrade, B. Schmid, M. Yoshida, J.B. Howard, D.C. Rees, Science 297 (2002) 1696.
[7] B.M. Barney, T.-C. Yang, R.Y. Igarashi, P.C. Dos Santos, M. Laryukhin, H.-I. Lee, B.M. Hoffman, D.R. Dean, L.C. Seefeldt, J. Am. Chem. Soc. 127 (2005) 14960.
[8] N. Wiberg, H. Bachuber, G. Fisher, Angew. Chem., Int. Ed. 11 (1972) 829.
[9] D. Sellmann, J. Sutter, Acc. Chem. Res. 30 (1997) 460.
[10] D. Sellmann, A. Hille, A. Rösler, F.W. Heinemann, M. Moll, G. Brehm, S. Schneider, M. Reiher, B.A. Hess, W. Bauer, Chem. Eur. J. 10 (2004) 819.
[11] B.T. Heaton, C. Jacob, P. Page, Coord. Chem. Rev. 154 (1996) 193.
[12] D. Sutton, Chem. Rev. 93 (1993) 995.
[13] M. Hidai, Y. Mizobe, Chem. Rev. 95 (1995) 1115.
[14] B.A. Mackay, M.D. Fryzuk, Chem. Rev. 104 (2004) 385.
[15] J.K. Kristjansson, T.C. Hollocher, J. Biol. Chem. 255 (1980) 704.
[16] F. Paulat, T. Kuschel, C. Näther, V.K.K. Praneeth, O. Sander, N. Lehnert, Inorg. Chem. 43 (2004) 6979.
[17] I.D. Brown, J.D. Dunitz, Acta Crystallogr. 13 (1960) 28.
[18] D.T. Cromer, A.C. Larson, R.B. Roof Jr., Acta Crystallogr. 20 (1966) 279.
[19] D. Cheng, C. Feng, S. Xia, Transition Met. Chem. 25 (2000) 635.
[20] K. Fujisawa, T. Ono, Y. Ishikawa, N. Amir, Y. Miyashita, K.-I. Okamoto, N. Lehnert, Inorg. Chem. 45 (2006) 1698.

[21] K. Fujisawa, N. Lehnert, Y. Ishikawa, K.-I. Okamoto, Angew. Chem., Int. Ed. 43 (2004) 4944.
[22] K. Fujisawa, T. Kobayashi, K. Fujita, N. Kitajima, Y. Moro-oka, Y. Miyashita, Y. Yamada, K.-I. Okamoto, Bull. Chem. Soc. Jpn. 73 (2000) 1797.
[23] N. Kitajima, K. Fujisawa, C. Fujimoto, Y. Moro-oka, S. Hashimoto, T. Kitagawa, K. Toriumi, K. Tatsumi, A. Nakamura, J. Am. Chem. Soc. 114 (1992) 1277.
[24] K. Fujisawa (in preparation).
[25] A. Schaefer, H. Horn, R. Ahlrichs, J. Chem. Phys. 97 (1992) 2571.
[26] M.J. Frisch, G.W. Trucks, H.B. Schlegel, G.E. Scuseria, M.A. Robb, J.R. Cheeseman, J.A. Montgomery Jr., T. Vreven, K.N. Kudin, J.C. Burant, J.M. Millam, S.S. Iyengar, J. Tomasi, V. Barone, B. Mennucci, M. Cossi, G. Scalmani, N. Rega, G.A. Petersson, H. Nakatsuji, M. Hada, M. Ehara, K. Toyota, R. Fukuda, J. Hasegawa, M. Ishida, T. Nakajima, Y. Honda, O. Kitao, H. Nakai, M. Klene, X. Li, J.E. Knox, H.P. Hratchian, J.B. Cross, C. Adamo, J. Jaramillo, R. Gomperts, R.E. Stratmann, O. Yazyev, A.J. Austin, R. Cammi, C. Pomelli, J.W. Ochterski, P.Y. Ayala, K. Morokuma, G.A. Voth, P. Salvador, J.J. Dannenberg, V.G. Zakrzewski, S. Dapprich, A.D. Daniels, M.C. Strain, O. Farkas, D.K. Malick, A.D. Rabuck, K. Raghavachari, J.B. Foresman, J.V. Ortiz, Q. Cui, A.G. Baboul, S. Clifford, J. Cioslowski, B.B. Stefanov, G. Liu, A. Liashenko, P. Piskorz, I. Komaromi, R.L. Martin, D.J. Fox, T. Keith, M.A. Al-Laham, C.Y. Peng, A. Nanayakkara, M. Challacombe, P.M.W. Gill, B. Johnson, W. Chen, M.W. Wong, C. Gonzalez, J.A. Pople, GAUSSIAN-03, Gaussian, Inc., Pittsburgh, PA, 2003.
[27] H.-F. Fan, Structure Analysis Programs with Intelligent Control (SAPI-91), Rigaku Corporation: Tokyo, Japan, 1991.
[28] teXsan: Single Crystal Structure Analysis Package, Version 1.10b, Molecular Structure Corporation, The Woodlands, TX, 1999.
[29] J.W. Pflugrath, Acta. Crystallogr., Sect. D 55 (1999) 1718.
[30] A. Altomare, G. Cascarano, C. Giacovazzo, A. Guagliardi, J. Appl. Crystallogr. 26 (1993) 343.
[31] CRYSTALSTRUCTURE 3.81: Crystal Structure Analysis Package, Version 3.81, Rigaku and Rigaku/MSC, 2006.
[32] D.J. Watkin, C.K. Prout, J.R. Carruthers, B.P.W., Crystal Issue 10, Chemical Crystallography Laboratory, Oxford, UK, 1996.
[33] N. Lehnert, B.E. Wiesler, F. Tuczek, A. Hennige, D. Sellmann, J. Am. Chem. Soc. 119 (1997) 8869.
[34] N. Lehnert, B.E. Wiesler, F. Tuczek, A. Hennige, D. Sellmann, J. Am. Chem. Soc. 119 (1997) 8879.
[35] D. Sellmann, W. Soglowek, F. Knoch, M. Moll, Angew. Chem. Int. Ed. 28 (1989) 1271.
[36] D. Sellmann, H. Friedrich, F. Knoch, M. Moll, Z. Naturforsch. B 49 (1994) 76.
[37] J.L. Schneider, S.M. Carrier, C.E. Ruggiero, V.G. Young Jr., W.B. Tolman, J. Am. Chem. Soc. 120 (1998) 11408.
[38] F. Paulat, V.K.K. Praneeth, C. Näther, N. Lehnert, Inorg. Chem. 45 (2006) 2835.

7.4. Structural and Spectroscopic Characterization of Mononuclear Copper(I) Nitrosyl Complexes: End-on versus Side-on Coordination of NO to Copper(I)

Kiyoshi Fujisawa*, Akira Tateda, Yoshitaro Miyashita, Ken-ichi Okamoto, Florian Paulat, V. K. K. Praneeth, Anna Merkle, Nicolai Lehnert*

Submitted for publication

Structural and Spectroscopic Characterization of Mononuclear Copper(I) Nitrosyl Complexes: End-on versus Side-on Coordination of NO to Copper(I)

Kiyoshi Fujisawa*[1], Akira Tateda[1], Yoshitaro Miyashita[1], Ken-ichi Okamoto[1], Florian Paulat[2], V. K. K. Praneeth[2], Anna Merkle[2], Nicolai Lehnert*[2]

Graduate School of Pure and Applied Sciences, University of Tsukuba, Tsukuba 305-8571, Japan
Department of Chemistry, University of Michigan, Ann Arbor, Mi 48109, USA

In memory of Swiatoslaw (Jerry) Trofimenko, the pioneer of scorpionate ligands.

Abstract.

Two crystal structures of the mononuclear copper(I)-nitrosyl complexes [Cu(L3)(NO)] (**1**) and [Cu(L3')(NO)](ClO_4) (**2**) with the related coligands $L3^-$ (hydrotris(3-tertiary-butyl-5-isopropyl-1-pyrazolyl)borate) and L3' (tris(3-tertiary-butyl-5-isopropyl-1-pyrazolyl)methane) are presented. These compounds are then investigated in detail using a variety of spectroscopic methods. Vibrational spectra show ν(N-O) at 1698 cm^{-1} and ν(Cu-NO) split at 365/338 cm^{-1} for **1**, which translates to force constants of 12.53 (N-O) and 1.31 mdyn/Å (Cu-NO), respectively. The weak Cu-NO force constant is in agreement with the observed instability of the Cu-NO bond. Interestingly, complex **2** with the neutral coligand L3' shows a stronger N-O bond, evident from ν(N-O) at 1742 cm^{-1}. This difference is attributed to a true second coordination sphere effect, where the covalency of the Cu(I)-NO bond is not altered. The EPR spectrum of **1** is in agreement with the Cu(I)-NO(radical) electronic structure of the complexes, as obtained from density functional theory (DFT) calculations. In addition, an interesting trend between $g_{//}$ (g_z) and the Cu-N-O angle is established. Finally, high-quality MCD spectra of **1** are presented and assigned using TD-DFT calculations. Based on the in-depth spectroscopic characterization of end-on

[1] University of Tsukuba, Tsukuba 305-8571, Japan. Email: kiyoshif@chem.tsukuba.ac.jp
[2] University of Michigan, Ann Arbor, MI 48109, USA. Email: lehnertn@umich.edu

bound NO to copper(I) presented in this work, it is possible to determine the binding mode of the Cu-NO intermediate of Cu Nitrite Reductase studied by Scholes and coworkers (Usov, O. M.; Sun, Y.; Grigoryants, V. M.; Shapleigh, J. P.; Scholes, C. P., *J. Am. Chem. Soc.* **2006,** 128, 13102-13111) in solution as strongly bent (~135^{o}), but likely not side-on.

1. Introduction

The copper(I)-nitrosyl {CuNO}^{11} adduct[1, 2] is a very important intermediate in the general reactions of copper proteins with biologically available nitrogen monoxide (commonly referred to as nitric oxide, NO).[3, 4] For example, NO is believed to be a mediator of copper protein activity,[5] and might also play a role in neurodegenerative diseases.[6] In particular, Cu nitrite reductase (CuNIR) is involved in the generation (and presumably degradation) of NO in denitrifying bacteria.[7, 8] Crystal structures of a large number of CuNIR's have been determined, which show great similarities for the enzymes obtained from different organisms.[9] CuNIR's are homotrimers where each subunit contains one copper type 1 center for electron transfer. The catalytically active type 2 centers are located at the respective interfaces of two subunits of the enzyme. In oxidized CuNIR, the type 2 centers are tetrahedrally coordinated by three histidines and a water molecule, where two histidines are provided by one subunit, whereas the third one comes from the adjacent subunit.[10-15] The observed coordination mode of nitrite to the oxidized active site is asymmetric η^2-O,O corresponding to the formation of a copper(II)-nitrito intermediate.[11, 13, 16, 17] This binding mode is also observed in a large number of corresponding model complexes.[8, 18] After completion of the catalytic cycle, NO (presumably coordinated to copper(II)) and water are generated. The exact mechanism for this conversion is still under discussion.[7, 8, 19] Interestingly, under anaerobic conditions with limited reductant and nitrite present, CuNIR is also able to act as an NO reductase by converting NO to N_2O,[20, 21] a reaction that has also been observed for corresponding model complexes.[22] In this latter function, a {CuNO}^{11} complex is most likely the catalytically active species.

In a recent study by Murphy and coworkers, a Cu(I)-NO intermediate of CuNIR, which was generated by exposing crystals of fully reduced CuNIR to NO

saturated buffer, has been structurally characterized.[23] *Surprisingly, this species shows an unprecedented side-on coordination of nitric oxide to copper(I)*, which corresponds to a new intermediate in the biological chemistry of NO. The authors also tried to generate this species in solution by treatment of ascorbate reduced CuNIR with NO under anaerobic conditions. From electron paramagnetic resonance (EPR) measurements on these solutions, the crystallograpically obtained $\{CuNO\}^{11}$ species was proposed to have a Cu(II)-NO^- electronic structure. These spectacular results, and in particular the unusual binding mode of nitric oxide to the copper(I) active site of CuNIR, has sparked the interest in the coordination chemistry of copper(I) and NO, and the spectroscopic properties of corresponding species.[24-26] Recently, Scholes and Solomon and coworkers have demonstrated spectroscopically that the solution species obtained by Murphy and coworkers is in fact a Cu(II)-NO_2^- complex.[21] Based on these results, these authors concluded that the crystallographycally observed side-on $\{CuNO\}^{11}$ species is most likely not relevant for the catalytic cycle of the enzyme, because it is only generated in the crystal, but not in solution in the presence of excess NO. In addition, density function theory (DFT) calculations clearly indicate that the side-on $\{CuNO\}^{11}$ intermediate should have a Cu(I)-NO(radical) electronic structure.[21, 26] Independent of these studies, Scholes and coworkers have shown by EPR and electron-nuclear double resonance (ENDOR) spectroscopy that a $\{CuNO\}^{11}$ species can in fact be generated for CuNIR in solution by using fully reduced enzyme in the presence of limited amounts of NO.[25] From these studies, however, it is not clear whether the obtained $\{CuNO\}^{11}$ species shows end-on or side-on coordinated NO. Based on the crystal structure of a corresponding model complex (vide infra), some researchers favor the end-on binding mode of NO for this species.[21] On the other hand, the CuNIR crystal structure by Murphy and coworkers points toward a side-on coordination of NO.[23] The question whether a side-on bound $\{CuNO\}^{11}$ species can exist is therefore of high significance for the understanding of the NO reductase activity of CuNIR, but also of fundamental interest for the coordination chemistry of copper(I) and NO.

In the light of this biological and medicinal significance of copper-nitrosyls, it is surprising that the biomimetic coordination chemistry of copper and NO and the investigation of the properties of these systems are not very developed. In fact, only one crystal structure of a mononuclear copper nitrosyl model complex has been reported so far by Tolman and coworkers, using $[HB(3\text{-}t\text{Bupz})_3]^-$ ($Tp^{t\text{-Bu}}$) as coligand.[27] Key spectroscopic data of this complex including the N-O stretch, EPR parameters, and electronic spectra were reported. Based on these data and unrestricted Hartree-Fock (UHF) calculations, the electronic structure of copper(I) NO complexes was described as Cu(I)-NO(radical). Besides this, a dinuclear copper-nitrosyl has been synthesized by Karlin and coworkers.[28]

In this work, two mononuclear copper nitrosyl complexes with anionic $[HB(3\text{-}t\text{Bu-}5\text{-}i\text{Prpz})_3]^-$ ($L3^-$)[18,29,30] and neutral $[HC(3\text{-}t\text{Bu-}5\text{-}i\text{Prpz})_3]$ (L3')[30] coligands have been synthesized, and structurally and spectroscopically characterized in detail. For this purpose, vibrational (IR), UV-Vis absorption, EPR, and magnetic circular dichroism (MCD) spectroscopies have been applied. In correlation to DFT calculations, these data are analyzed in detail, and key insight about the nitrosyl binding to copper(I) is obtained. In addition, the effect of the total charge of the coligands on the properties of the Cu(I)-nitrosyls is discussed. Based on the detailed spectroscopic signature of end-on bound NO to copper(I) elaborated here, the spectroscopic data obtained by Scholes and coworkers for the Cu(I)-NO complex of CuNIR in solution can be used to determine the binding mode of NO in this case. The conclusions drawn this way are further supported by DFT calculations.

2. Experimental Section

Materials.

Preparation and handling of all complexes was performed under an argon atmosphere using standard Schlenk tube techniques or in an inert atmosphere glovebox. Anhydrous dichloromethane and chloroform were purchased from Aldrich Chemical Company and stored in a glovebox. $^{15}N^{18}O$ gas was obtained

from Shoko Co., Ltd and Aldrich Chemical Company. Other reagents are commercially available and were used without further purification. [Cu{HB(3-*t*Bu-5-*i*Prpz)$_3$}(NCMe)] ([Cu(L3)(NCMe)]) and [Cu{HC(3-*t*Bu-5-*i*Prpz)$_3$}($OClO_3$)] ([Cu(L3')($OClO_3$)]) were prepared by published methods.[30] *Caution: Although we have not encountered any problems, it is noted that the perchlorate salts of metal complexes with organic ligands are potentially explosive and should be handled only in small quantities with appropriate precautions.* The elemental analyses (C, H, N) were performed by the Department of Chemistry at the University of Tsukuba.

Complex Syntheses.

[Cu(L3)(NO)] (1). [Cu(L3)(NCMe)] [30] (0.0616 g, 0.127 mmol) was dissolved in dichloromethane (2.0 mL) in a glovebox. The solution was cooled to –78 °C under an argon atmosphere, and argon was then replaced by NO. The solution was stirred for 1 h at –50 °C. The solution was kept at –30 °C for 1 day. The solution was then cooled down to –50 °C again. Crystallization from dichloromethane at –50 °C yielded red crystals. Elemental analysis (%) calcd for $C_{30}H_{52}N_7BCuO \cdot CH_2Cl_2$: C, 54.27; H, 7.93; N, 14.29; found: C, 54.87; H, 8.14; N, 14.19. IR (KBr, cm^{-1}): 2965 ν(CH), 2564 ν(BH), 1698 $\nu(^{14}N^{16}O)$, [$\nu(^{15}N^{18}O)$ = 1627]. UV-Vis λ/nm (ε/$mol^{-1}dm^3cm^{-1}$) (dichloromethane), 506(960).

[Cu(L3')(NO)](ClO_4) (2). [Cu(L3')($OClO_3$)] [30] (0.1290 g, 0.192 mmol) was dissolved in chloroform (8.0 mL) in a glovebox. The solution was cooled to –50 °C under an argon atmosphere, and argon was then replaced by NO. The solution was stirred for 1 h allowing the temperature to reach about –4 °C. The solution was further kept at –30 °C for 1 day. The solution was then cooled to –50 °C. Crystallization from chloroform at –50 °C yielded orange crystals. Elemental analysis (%) calcd for $C_{31}H_{52}N_7CuO_5Cl \cdot CHCl_3$: C, 46.81; H, 6.51; N, 11.94; found: C, 47.18; H, 6.46; N, 11.48. IR (KBr, cm^{-1}): 2970 ν(CH), 1742 $\nu(^{14}N^{16}O)$, [$\nu(^{15}N^{18}O)$ = 1710/1666]. UV-Vis λ/nm (ε/$mol^{-1}dm^3cm^{-1}$) (chloroform), 458(1140).

Labeled nitrosyl complexes, [Cu(L3)($^{15}N^{18}O$)] and [Cu(L3')($^{15}N^{18}O$)](ClO_4), were synthesized by using $^{15}N^{18}O$ in the same manner as complexes **1** and **2**, respectively.

We did not perform detailed decomposition kinetic measurements. 15 h after MIR measurements in solid KBr disks (exposed to air for 15 h), the ν(N-O) peak of **2** had almost disappeared, whereas that of **1** just became somewhat weaker (Figure S5). Therefore, the stability of **1** is clearly much larger than that of **2**.

Crystal Structure Determination.

The detailed crystal data, data collection, and structural refinement parameters for **1** and **2** are given in Table S1. Complete atomic labels are shown in Figures S1 and S2. The diffraction data were measured on a Rigaku/MSC Mercury CCD system with graphite monochromated Mo Kα (λ = 0.71069 Å) radiation at low temperature. All crystals were mounted on glass fiber using epoxy glue. The unit cell parameters of each crystal were obtained using Rigaku Daemon software and refined using CrystalClear on all observed reflections.[31] Data using 0.5° intervals in ϕ and ω for 35 s/frame (**1**) and for 30 s/frame (**2**) were collected with a maximum resolution of 0.77 Å (744 oscillation images). The highly redundant data sets were reduced using CrystalClear and corrected for Lorentz and polarization effects. An empirical absorption correction was applied for each complex.[32, 33] Structures were solved by direct methods using the program *SIR*92.[34] The position of the metal atoms and their first coordination sphere were located from a direct method *E*-map; other non-hydrogen atoms were found in alternating difference Fourier syntheses[35] and least-squares refinement cycles. These were refined anisotropically during the final cycles (CrystalStructure).[32, 33] Hydrogen atoms were placed in calculated positions. Higher *R* and GOF values are due to one disordered dichloromethane for **1**, and disordered methyl carbons of the isopropyl groups of L3 as well as disordered chloroform and perchlorate molecules for **2** in the unit cell. The O atoms (O41) and N atoms (N41) of the NO molecules in both structures show

somewhat large thermal ellipsoids. This phenomenon has also been observed in Tolman's structure reported before.[27] This is probably due to the fact that even at low temperature, the low energy motions of NO (rotation, etc.) are not fully frozen. Moreover, we observed these problems in Cu(I)-CO complexes even at low temperature.[30] Therefore, this is a common observation for Cu-X-O complexes with tris(pyrazolyl)borate and tris(pyrazolyl)methane coligands. Crystallographic data and structure refinement parameters including the final discrepancies (R and R_w) are listed in Table S1. Crystallographic data have been deposited at the CCDC, 12 Union Road, Cambridge CB2 1EZ, UK and copies can be obtained on request, free of charge, by quoting the publication citation and the deposition numbers: CCDC-615640 for **1** and CCDC-615641 for **2**.

Spectroscopic Measurements.

UV-Vis absorption data were recorded with an Ostuka Electronics MCPD-2000 system with an optical fiber attachment in the 300−1100 nm region at low temperature. The magnetic circular dichroism (MCD) setup consists of a JASCO J-810 spectropolarimeter and an Oxford Instruments SPECTROMAG SM4000 magnetocryostat. Samples for MCD were recorded in silicone oil (DC 200) mulls. EPR spectra were recorded on a Bruker EMX EPR spectrometer in frozen solution (CH_2Cl_2/{CH_2Cl}$_2$(1:1)) in quartz tubes (diameter 5 mm) at 5−10 K with an Oxford Instruments liquid helium cryostat in the 2000−4200 G region. The spectrum of **1** shown in Figure 3 in red was measured at a frequency of 9.341 GHz and a microwave power of 20 mW. IR data were obtained with a JASCO FT/IR-550 spectrometer in the 4000−400 cm^{-1} region for MIR (middle infrared) and 650−150 cm^{-1} for FIR (far infrared) measurements.

Normal Coordinate Analysis.

Normal coordinate calculations were performed using the QCPE computer program 576 by M.R. Peterson and D.F. McIntosh. The calculations are based on a general valence force field; force constants are refined with a non-linear

simplex algorithm. The simplex optimization was used to refine only *selected* force constants according to the quantum-chemical centered normal coordinate analysis (QCC-NCA) scheme.[36] Here, a force field from DFT calculations is used as a starting point to generate initial force constants and a subset of these is fit to reproduce the known experimental frequencies. Force constants are extracted from the Gaussian output using a modified version of the program Redong (QCPE 628).[37]

For the QCC-NCA treatment, the BP86/TZVP optimized structure of model system [Cu(L0)(NO)] (see DFT part) has been used, but the Cu-N-O angle has been adjusted to 180^{o} for simplification, which is very close to the experimentally determined value of 172^{o}. The calculated force field for [Cu(L0)(NO)] (BP86/TZVP) has been applied. For the QCC-NCA, the Cu-NO and N-O force constants as well as the Cu-NO/N-O non-diagonal element have been fitted to reproduce the experimentally observed vibrational energies of the Cu-N-O unit. Importantly, the QCC-NCA treatment reproduces the split appearance of the Cu-NO stretch. In order to refine the vibrational energies of the two split components, the diagonal elements of the C-C-CH_3 bending coordinates of the pyrazolyl rings have been slightly adjusted (lowered by 0.04 mdyn/Å) compared to the DFT-predicted values. From these results, the Cu-NO stretch is mixed with a [Cu(L3)] skeletal bending mode, which is shown in Figure S8. This mode is predicted at 350 cm^{-1} in the calculations. The mixing between this core bending mode and ν(Cu-NO) is reproduced accurately in the QCC-NCA, which means that the [Cu(L3)] core modes are well described in the calculation. In the QCC-NCA fit, the component at lower energy has more Cu-NO character (from the potential energy distribution (PED)), and correspondingly, a larger $^{15}N^{18}O$ isotope shift. Experimentally, this trend is reversed, as apparent from the inverse trend in the isotope shifts. The Cu-N-O bends are found in the 200–250 cm^{-1} region, with small isotope shifts of 2–4 cm^{-1}. They are strongly mixed with [Cu(L3)] skeletal modes.

Density Functional Theory (DFT) Calculations.

The structures of the model complexes [Cu(L0)(NO)] (L0 = hydrotris(3,5-dimethyl-1-pyrazolyl)borate) and $[Cu(L0')(NO)]^+$ (L0' = tris(3,5-dimethyl-1-pyrazolyl)methane) were fully optimized with BP86/TZVP using the program package Gaussian 03.[38] For these calculations, the TZVP basis set [39] has been applied as implemented in G03. For method calibration, the structures of these models have also been fully optimized using B3LYP/LanL2DZ, which applies Becke's three parameter hybrid functional with the correlation functional of Lee, Yang, and Parr (B3LYP [40-42]). The LanL2DZ basis set consists of Dunning/Huzinaga full double zeta (D95) basis functions [43] on first row and Los Alamos effective core potentials plus DZ functions on all other atoms.[44, 45] However, the obtained structures are in general inferior to the ones calculated with BP86/TZVP. In order to investigate whether B3LYP calculations can help improving the deviations in the Cu-N-O angle between the calculation and experiment, model [Cu(L0)(NO)] has also been fully optimized with B3LYP/TZVP and B3LYP/6-311G*. However, no improvement is observed as shown in Table S2. Calculated vibrational frequencies for all these geometry optimizations included in Table S2 show no imaginary modes, which shows that true energy minima have been obtained in all cases. Relative energies in Table 3 were either taken from BP86/TZVP calculations ('BP86'), or from B3LYP/TZVP calculations ('B3LYP') on the BP86/TZVP optimized structures. EPR parameter (BP86/TZVP) and TD-DFT (B3LYP/TZVP) calculations were performed using the program package ORCA.[46] For Figure 4, the BP86/TZVP optimized structure of model [Cu(L0)(NO)] was used, and the Cu-N-O angle was adjusted correspondingly. For the geometry optimization of CuNIR models (cf. Figure 7), the crystal structure with bound NO (PDB :1SNR) from ref. 23 was used together with the BP86/TZVP method. The histidines were fixed in space by freezing their anchor C atoms of the protein backbone, which where transformed into CH_3 groups for the calculations.

EPR Spectral Simulations.

EPR spectra were simulated using the program SpinCount (Version 2.2.40), written by Prof. Michael Hendrich, Carnegie Mellon University. EPR parameters are listed in the caption of Figure 3. The best fit is obtained with g_z around 1.79–1.80. The error bars for the hyperfine values are larger, around 5–10%.

3. Results and Discussion

3.1 Synthesis and Structural Characterization

The nitrosyl complexes [Cu(L3)(NO)] (**1**) and [Cu(L3')(NO)](ClO_4) (**2**) were obtained from the reaction of [Cu(L3)(NCMe)] and [Cu(L3')($OClO_3$)][30] with NO in good yield as shown in Eq. 1.

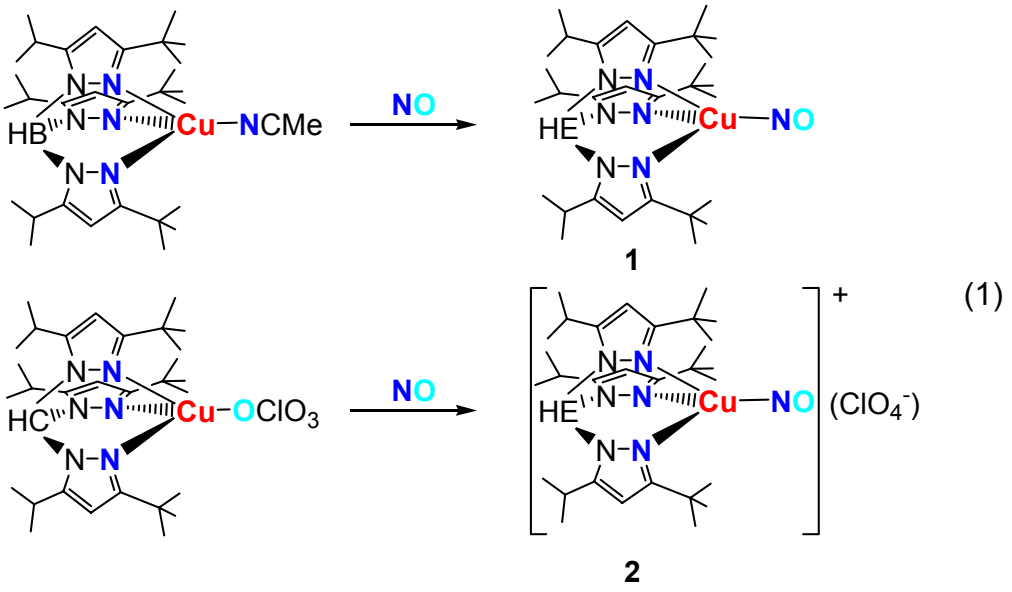

(1)

Detailed procedures are given in the Experimental Section. Complex **2** is very unstable toward NO loss (Figure S5). The structures of **1** and **2** determined by X-ray crystallography indicate that both complexes are mononuclear. As mentioned above, these compounds constitute only the second and third examples for mononuclear Cu(I)-NO model complex structures ever obtained in the literature.

The perspective drawings of their structures are shown in Figures 1 and 2, respectively. In the copper nitrosyl complexes **1** and **2,** the copper ions have distorted tetrahedral coordination geometries. Cu-NO distances of **1** (1.779(4) Å) and **2** (1.7836(5) Å) are similar, and comparable to Tolman's compound [Cu(Tp$^{t\text{-}Bu}$)(NO)] (**3**, 1.759(6) Å; cf. Table 1). On the other hand, the N-O distance of **1** (1.083(7) Å) is distinctively longer than that of **2** (1.035(8) Å), indicating a potential differences in π backbonding (vide infra). Because of the difference in the total charge of the ligands (L3$^-$: anion, L3': neutral), it is expected from previous work that π-backdonation in **1** is stronger than in **2**,[30] which would be in agreement with the experimental trend. The copper ions are almost linearly ligated by NO in both cases (Cu-N-O angle = 171.9(5)^o for **1** and 176.4(10)^o for **2**). Although electronic effects usually predominate among the factors that induce nitrosyl bending,[27] the possibility that there are steric influences on the Cu-N-O angle is suggested by the observed orientation of the nitrosyl oxygen atom away from one of the *tert*-butyl groups and toward the open space between two pyrazolyl substituents in **3**. In this complex, the Cu-N-O angle is 163.4(6)^o,[27] which is different from **1** and **2** reported here.

3.2 Vibrational Spectroscopy and Normal Coordinate Analysis

Tolman and coworkers reported the N-O stretching vibrations ν(N-O) for a number of [Cu(Tp)(NO)] type complexes (Tp$^-$ = substituted hydrotris(pyrazolyl)-borate),[27, 47] but the critical Cu-NO stretch ν(Cu-NO) could not be identified. Clearly, the instability of the complexes renders the determination of high-quality vibrational data difficult. Figures S3 and S6 show the IR data of **1**, which show ν(N-O) at 1698 cm^{-1}, and ν(Cu-NO) at 365 and 338 cm^{-1}. These bands shift to 1627, 358, and 332 cm^{-1} upon $^{15}N^{18}O$ substitution (cf. Table 1), respectively. To determine quantitative measures for the N-O and Cu-NO bond strengths and to explore the reason for the split appearance of ν(Cu-NO), a quantum-chemistry-centered normal-coordinate analysis (QCC-NCA)[36] was performed. As shown in Table 2, excellent agreement with experiment has been achieved, and the

[Cu(L3)] skeletal mode that interacts with ν(Cu-NO) has been identified (see Figure S8). Obtained force constants are 12.53 (N-O) and 1.31 mdyn/Å (Cu-NO), where the latter value corresponds to a weak Cu-NO bond in agreement with the labile attachment of NO. In comparison, **2** exhibits ν(N-O) at 1742 cm^{-1}, and ν(Cu-NO) is tentatively assigned to the bands at 369 and 344 cm^{-1} (cf. Figures S4 and S7). Due to the poor quality of the far infrared (FIR) data of this very labile complex, a QCC-NCA was not attempted. In previous studies of Cu(I)-carbonyl complexes, we determined that anionic 'borate' type ligands like $L3^-$ lead to more electron-rich copper centers compared to analogous neutral 'methane' ligands like L3'.[30] Hence, the borate complexes give rise to distinctively stronger π-backbonding interactions with CO, which is reflected by stronger Cu-CO and weaker C-O bonds. CO is therefore the perfect probe to measure the electronic properties of Cu(I).[30, 47] *This trend is not followed by NO*: as evident from the vibrational data on **1** and **2**, and calculations on corresponding models as shown in Table 1, there is only a slight increase in the strength of the backbond in **1** compared to **2**. Correspondingly, the difference in (calculated) Cu-NO force constants is < 0.1 mdyn/Å, and ν(Cu-NO) are similar. This small change in backbonding can only account for part of the observed large difference in the N-O bond strengths of **1** and **2**. The further weakening of the N-O bond in **1** is actually due to a stronger polarization of the π orbitals of NO, and hence, a true second coordination sphere effect in the case of **1**, due to the presence of the extra negative charge on the $L3^-$ ligand. This is evident from an inspection of the corresponding molecular orbitals from the DFT calculations (vide infra). Importantly, the calculations reproduce the difference in vibrational properties very well (compare Δ(L3'-L3) and Δ(L0'-L0) in Table 1). Interestingly, the experimental trend in ν(N-O) itself,

$[HB(3\text{-}CF_3\text{-}5\text{-}CH_3pz)_3]^- \geq L3' > [HB(3,5\text{-}Ph_2pz)_3]^- > [HB(3\text{-}t\text{-}Bupz)_3]^- > L3^-$,

is similar to the trend observed for ν(C-O) in the carbonyl complexes.[30, 47]

3.3 EPR Spectroscopy and Electronic Structure

Copper-nitrosyl {CuNO}[11] adducts afford an *S* = 1/2 ground state with characteristic EPR spectra: complex **3** exhibits $g_{\perp}$ = 1.99 and $g_{//}$ = 1.83, and a large ^{14}N hyperfine coupling $^{N}A_{\perp}$ = 81 MHz as published by Tolman and coworkers.[27] In comparison, **1** shows $g_{//}$ = 1.79 - 1.80, and $^{N}A_{\perp}$ = 98 MHz as shown in Figure 3.[48] Comparison with the calculated g values in Table 3 reveals an interesting trend for the g values of Cu(I)-nitrosyls, where $g_z = g_{//}$ (z points along the Cu-N(O) bond as indicated in Figure 5) is very sensitive to the Cu-N-O angle. In order to investigate this further, g values were calculated for model [Cu(L0)(NO)] varying the Cu-N-O angle, and these results are shown in Figure 4. Using the known Cu-N-O angle of 163° for **3**, g_z = 1.833 is predicted from Figure 4, which is in excellent agreement with the experimental value of 1.83 for this compound. In comparison, the Cu(I)-NO adduct of CuNIR shows very different g values as listed in Table 3,[25] indicative of a different coordination geometry (see Discussion). The obtained hyperfine parameters $^{N}A_{\perp(x)}$ > 80 MHz for **1** and **3** are very large and indicate *significant radical character on the bound NO ligand*. Scheme 1, top shows the binding scheme for **1** obtained from the DFT calculations. For the theoretical treatment, simplified model systems [Cu(L0)(NO)] and [Cu(L0')(NO)](ClO_4) have been applied for **1** and **2**, respectively, as described in the Experimental Section. Different functional/basis set combinations have been used for the geometry optimizations as listed in Table S2. In general, good agreement with the experimental structures has been obtained, with exception of the Cu-N-O angle. In fact, none of the methods applied was able to reproduce the experimental value for this parameter. For the further discussion, the BP86/TZVP results are used (cf. Tables 1 – 3). As indicated in Scheme 1, the singly-occupied π^* orbital of NO (α-π^*_h) is located in the Cu-N-O plane. Due to the fact that all copper(I) d orbitals are fully occupied, the overlap of this orbital with d_{xz} is actually repulsive for α-spin. This is compensated by the backbond between d_{xz} and the empty β-π^*_h orbital. The strength of this interaction is best estimated from the corresponding antibonding combination, π^*_h_d_{xz}, which has 10% metal d character. Altogether, this leads to a spin density distribution of +0.9 on NO and +0.1 on copper, in agreement with

earlier calculations.[26] Hence, the calculations clearly favor the Cu(I)-NO(radical) over the Cu(II)-NO^- electronic description in agreement with EPR and MCD (vide infra) results. The other π^* orbital, π^*_v (located perpendicular to the Cu-N-O plane), is unoccupied and undergoes further backbonding interactions. The corresponding antibonding combinations show about 15–20% d admixture, which corresponds to a quite strong interaction. However, comparison of the calculated Cu-NO force constant of 2.215 mdyn/Å with the experimental value of 1.310 mdyn/Å shows that the strength of this interaction is clearly overestimated in the calculations, which is not unusual.[36] The π^*_v - d_{yz} backbond shows small spin-polarization effects (where the β-spin interaction is stronger), which somewhat lowers the total spin density on copper. This effect depends strongly on the applied DFT functional, which makes the prediction of very accurate total spin densities difficult. This bonding scheme is in agreement with the observed, large $^{N}A_{\perp(x)}$ value, and also explains the observed strong dependence of g_z on the Cu-N-O angle (cf. Figure 4). This relates to the spin-orbit coupling matrix element $2\lambda\langle\pi^*_h\_d_{xz}|l_z|\pi^*_v\_d_{yz}\rangle/\Delta E$ in the theoretical equation for the g shifts from perturbation theory,[49]

$$g_i = g_e - 2\lambda \sum_{n\neq 0} \frac{\langle \Psi_0 | L_i | \Psi_n \rangle \langle \Psi_n | L_i | \Psi_0 \rangle}{E_n - E_0},$$

which maximizes at 180° when $\pi^*_h\_d_{xz}$ and $\pi^*_v\_d_{yz}$ become almost degenerate ($\Delta E \approx 0$).

3.3 Electronic Spectra

In previous work,[27] UV-Vis absorption and MCD data above 300 nm have been presented for **3**, but no detailed analysis of the data has been provided. The characteristic absorption band at 494 nm for **3** has been loosely assigned to a Cu(I)-d to NO-π^* transition, but no further details are provided. As shown in Figure S9, this feature is observed at 506 nm (ε = 960 M^{-1} cm^{-1}) for **1**, and at 458 nm (ε = 1140 M^{-1} cm^{-1}) for **2**. We have re-investigated complex **1** using low-temperature MCD spectroscopy in silicone mulls, which allows for the

measurement of high-quality data. Based on the spectrum obtained shown in Figure 6, five electronic transitions can actually be identified in the electronic spectra of the Cu(I)-NO complex (bands 2–6), and an additional weak feature is identified at 810 nm. These transitions can be assigned for the first time with the help of TD-DFT calculations. Application of B3LYP/TZVP and the experimental Cu-N-O angle of 172^{o} reproduces the general shape of the electronic spectra well, but all transitions appear shifted to lower energy by ~4000 cm^{-1} (cf. Figure 6). This is due to the fact that all bands observed in the visible region correspond to CT transitions of type d $\rightarrow \pi^*$, which are usually obtained too low in energy by TD-DFT. The tentative assignments as shown in Figure 6 are further supported by the appearance of pseudo-**A** term signals in the spectra (pairs of bands 2-3 and 4-5/6; see Table S3), which are in agreement with the calculated polarizations of these transitions. In order for a pseudo-**A** term to arise, two electronic transitions with orthogonal electric transition dipole moments are needed, which are coupled by spin-orbit coupling. These requirements are fulfilled by the given assignment (see Table S3). Based on these results, the medium strong absorption band of the Cu(I)-NO complexes in the visible region around 500 nm is due to d $\rightarrow \pi^*_v$ type CT transitions into the unoccupied π^*_v orbital of NO (bands 2 – 5, cf. Figure 6). The observed transition energies allow for the determination of the relative energies of the corresponding four d orbitals of highest energy, as included in Scheme 1, bottom. The fifth d orbital, d_{xz}, is probably located at lowest energy in these complexes, due to a strong interaction with the singly occupied π^*_h orbital of NO. Since the corresponding CT transition is of d $\rightarrow \pi^*_h$ type (band 6, cf. Figure 6), the relative energy of this orbital cannot exactly be scaled to the other four d-orbitals as indicated in Scheme 1. Importantly, *the lack of intense (low-energy) d-d bands in the MCD spectra of **1** is a further indication that copper has a d^{10} electron configuration, in agreement with the Cu(I)-NO(radical) description of the end-on coordinated {CuNO}^{11} complexes* elaborated above. This is further supported by the TD-DFT results. Note that band 1 in Figure 6 corresponds to an impurity of [Cu^{II}(L3)(ONO)], which shows a very intense MCD transition in this area.[18] The

observation of a very small amount of Cu(II) impurity is in agreement with corresponding, very weak features in the EPR spectra that account for about 5% of the total copper concentration.

Discussion

In this paper, two new crystal structures of mononuclear end-on Cu(I)-NO complexes are presented, and the first detailed spectroscopic analyses (vibrational and electronic) of this type of complexes are provided. Experimental force constants for [Cu(L3)(NO)] are 12.53 mdyn/Å (N-O) and 1.31 mdyn/Å (Cu-NO); the latter value is in agreement with the very labile Cu-NO bond in these systems. In comparison, the corresponding complex with a tris(pyrazolyl)methane ligand has a stronger N-O bond due to a second coordination sphere effect. The EPR spectrum of [Cu(L3)(NO)] is indicative of the Cu(I)-NO(radical) electronic structure of the complexes in agreement with the DFT results. Interestingly, the g_z value correlates very well with the geometric structure of the Cu-N-O unit, and decreases upon increase of the Cu-N-O angle. Finally, high-quality MCD spectra of [Cu(L3)(NO)] are presented, and assigned using TD-DFT calculations. These results provide the first in-depth assignment of the electronic spectra of the end-on $\{CuNO\}^{11}$ species. In particular, the observed CT absorption band in the visible region is due to $d \rightarrow \pi^*_v$ type transitions. Based on the MCD results, an approximate determination of the d-orbital energy scheme for [Cu(L3)(NO)] is possible. Importantly, the lack of intense low-energy d-d bands in the MCD spectra is a further indication that copper has a d^{10} electron configuration, in agreement with the Cu(I)-NO(radical) description of the complexes.

In summary, based on the experimentally calibrated electronic structure description of end-on Cu(I)-NO complexes elaborated here, and in agreement with results published previously,[26,27] it is therefore now proven beyond any doubt that the Cu(I)-NO unit has to be described as Cu(I)-NO(radical).

The detailed spectroscopic characterization of end-on bound Cu(I)-NO complexes provided in this work allows to draw further conclusions about the Cu(I)-NO intermediate observed by Scholes and coworkers for CuNIR in solution.[25] From their EPR and ENDOR results, it is not clear whether this species has end-on or side-on coordinated NO. Although the crystal structure of Murphy and coworkers shows side-on bound NO,[23] others have speculated that this structure is an 'artifact' observed in the crystal, but that this binding mode does not exist in solution. This opinion is supported by recent DFT calculations on the CuNIR active site, which predict that the end-on geometry is more stable by about 7 kcal/mol compared to the side-on bound species.[21] These contradictory findings pose the important question whether the side-on coordination mode of NO to Cu(I) is feasible or not. As we have demonstrated in this paper, the EPR g_z value of the Cu(I)-NO species shows a strong correlation with the Cu-N-O angle. Hence, *our EPR results in comparison with the data obtained by Scholes and coworkers for the Cu(I)-NO complex of CuNIR (cf. Figure 4) do in fact support a strongly bent, or even side-on coordination of NO in the enzyme*. As shown in Table 3, the end-on bound Cu(I)-NO model complexes show g_z around 1.83, whereas in the case of CuNIR, g_z is found at 1.93. Based on this, we believe that the Cu(I)-NO intermediate of CuNIR generated in the presence of low concentrations of NO does in fact show a strongly bent to side-on binding mode of NO. How is it possible, though, that the enzyme behaves so differently than the model complexes studied so far? A first indication as to why this is in fact possible comes from recent DFT results of Wasbotten et al.,[26] which show that the type of coligand bound to copper actually has a large influence on the relative energies of the end-on and side-on coordinated species. In order to further investigate this point, we have performed DFT geometry optimizations on the CuNIR active site with bound NO, where the three histidines are held in position by fixing their anchor C atoms (of the CH_3

groups) in space. As shown in Figure 7, the obtained Cu(I)-NO geometry from this calculation shows a Cu-N-O angle of 136° (cf. Figure 7, bottom left), which is intermediate between end-on (> 160°; from the model complexes) and side-on (71°; from Murphy's structure). We have further generated end-on and side-on bound structures for CuNIR by fixing the Cu-N-O angle at 170° and 67°, respectively, and reoptimization of the structures. The resulting geometries are shown in Figure 7 top and bottom right. To test whether these three structures also follow the trend in g_z values as described above, we have then calculated the g tensors for the three binding modes. Importantly, as shown in Figure 7, *the general trend in g values is in fact followed by the CuNIR models*. Based on these results, two important conclusions can be drawn:

(a) the side-on coordination of NO to copper(I) is reasonable, and depends on the coligand(s) bound to copper;

(b) the EPR parameters of the Cu(I)-NO species of CuNIR as determined by Scholes and coworkers [25] do in fact reflect a strongly bent or side-on coordination of NO to copper(I).

Comparison of the calculated g tensors with the g values obtained by Scholes and coworkers shows in fact the best agreement between the fully optimized structure (Cu-N-O angle = 136°; cf. Figure 7, bottom left) and the experimental data. However, the calculated difference in g values between this structure and the side-on bound species is relatively small, so it would be unjustified to claim that the fully optimized structure exactly reflects the Cu(I)-NO geometry present in the enzymatic species detected in solution. Nevertheless, the results clearly indicate that the Cu(I)-N-O unit is strongly bent in the enzyme in solution, but likely not side-on.

In summary, the geometry of the Cu(I)-NO subunit in proteins and model complexes has a much larger flexibility in terms of the coordination mode of NO and the Cu-N-O angle than previously anticipated from model complex studies. These results are also in agreement with the crystal structure of NO bound amine

oxidase, which shows a Cu(I)-N-O angle of 117^{o} (assuming that this species corresponds to a Cu(I)-NO complex, which, however, is somewhat unclear in this case).[50]

Acknowledgement

This work was supported by the Grant-in-Aid for Scientific Research (B) (No. 17350043) from the Japan Society of the Promotion of Science (to KF) and the Fonds der Chemischen Industrie (FCI) (to FP and NL).

Supporting Information

Complete ref. 38, crystallographic data (Table S1), complete atomic labels (Figures S1-S2), vibrational (IR) and electronic absorption spectra for **1** and **2** (Figures S3-S7, S9), Table of DFT geometry optimized structures and vibrational frequencies for models of **1** and **2** using different combinations of functionals and basis sets (see Experimental Section) (Table S2), Table of the results of TD-DFT calculations for **1** (Table S3). This material is available free of charge via the Internet at http://pubs.acs.org.

Table 1. Comparison of experimental and calculated properties of Cu(I)-NO complexes.

Complex	Geometric Parameters [Å]			Vibrations [cm^{-1}]		Force Constants [b]	
	Cu-NO	N-O	Cu-N-O [a]	ν(N-O)	ν(Cu-NO)	f(N-O)	f(Cu-NO)
[Cu($Tp^{t\text{-}Bu}$)(NO)] [c]	1.759(6)	1.108(7)	163.4(6)	1712			
[Cu(L3)(NO)]	1.779(4)	1.083(7)	171.9(5)	1698	365/(338)	12.53	1.31
[Cu(L3')(NO)](ClO_4)	1.786(5)	1.035(8)	176.4(10)	1742	369/(344)		
Δ(L3'-L3)	**0.007**	**-0.048**	**4.5**	**44**	**4**		
BP86/TZVP: full opt							
[Cu(L0)(NO)]	1.812	1.188	148	1707	456/(458)	12.72	2.22
[Cu(L0')(NO)]$^+$	1.818	1.178	147	1758	453	13.56	2.14
Δ(L0'-L0)	**0.006**	**-0.010**	**-1**	**51**	**-3**	**0.84**	**-0.07**

[a] In degrees.
[b] In [mdyn/Å].
[c] Ref. [27]

Table 2. Comparison of experimental and QCC-NCA vibrational frequencies [cm^{-1}] and of QCC-NCA and calculated (DFT) force constants [mdyn/Å].

mode	exp.		QCC-NCA		Force constants f	
	n.a.i. [a]	$^{15}N^{18}O$	n.a.i. [a]	$^{15}N^{18}O$	QCC-NCA	Calculated [b]
[Cu(L3)(NO)] (**1**)						
ν(N-O)	1698	1627	1700	1625	12.530	12.72
ν(Cu-NO)[c]	365	358	366	363	1.310	2.22
	338	332	335	330		

[a] n.a.i. = natural abundance isotopes.
[b] Calculated with BP86/TZVP.
[c] The Cu-NO stretch is mixed with a [Cu(L3)] core bending mode, see Experimental Section. Free NO: ν(N-O) = 1876 cm^{-1}; $f_{N\text{-}O}$ = 15.49 mdyn/Å[51]

Table 3. Calculated and observed EPR parameters of Cu(I)-NO adducts.

Complex	EPR parameters		Cu-N-O angle	ΔE [kcal/mol]	
	$g_{\perp}$	$g_{//}$		BP86	B3LYP
Cu(I)-NO in CuNIR [a]	2.046 1.998	1.926	**?**		
[Cu(Tp$^{t\text{-Bu}}$)(NO)] [b]	1.99	1.83	163		
[Cu(L3)(NO)]	~1.97	~1.80	172		
[Cu(L0)(NO)] - calc.	2.019 2.012	1.902	154	0	0
[Cu(L0)(NO)] - 172^{o} [c]	2.019 1.999	1.783	172	+0.8	+2.7
[Cu(L0')(NO)]$^{+}$ - calc.	2.015 2.012	1.907	155	0	0
[Cu(L0')(NO)]$^{+}$ - 174^{o} [c]	2.016 1.998	1.786	174	+0.8	+0.7

[a] Ref. [25]
[b] Ref. [27]
[c] Obtained from the fully optimized structure (BP86/TZVP) by changing the Cu-N-O angle as indicated.

Legends for Figures and Schemes

Figure 1 ORTEP view of [Cu(L3)(NO)] (**1**) showing 50% thermal ellipsoids and the atom labeling scheme. For clarity, hydrogen atoms were omitted. Selected bond distances (Å) and angles (deg): Cu1-N41 1.779(4), Cu1-N11 2.053(2), Cu1-N21 2.064(3), Cu1-N31 2.051(3), N41-O41 1.083(7), B1-N12 1.557(5), B1-N22 1.540(5), B1-N32 1.541(4); Cu1-N41-O41 171.9(5), N41-Cu1-N11 123.66(17), N41-Cu1-N21 122.81(18), N41-Cu1-N31 122.32(17), N11-Cu1-N21 91.85(12), N11-Cu1-N31 92.28(13), N21-Cu1-N31 95.61(14), N12-B1-N22 108.9(3), N12-B1-N32 109.8(3), N22-B1-N32 110.9(2).

Figure 2 ORTEP view of the cation of [Cu(L3')(NO)](ClO_4) (**2**) showing 50% thermal ellipsoids and the atom labeling scheme. For clarity, hydrogen atoms were omitted. Selected bond distances (Å) and angles (deg): Cu1-N41 1.786(5), Cu1-N11 2.070(3), Cu1-N21 2.058(4), N41-O41 1.035(8), C1-N12 1.451(4), C1-N22 1.448(7); Cu1-N41-O41 176.4(10), N41-Cu1-N11 125.09(14), N41-Cu1-N21 125.2(2), N11-Cu1-N21 90.68(12), N11-Cu1-N11' 89.16(12), N12-C1-N22 112.2(2), N12-C1-N12' 111.3(3). Symmetry code: x, -y + 1/2, z.

Figure 3 EPR spectrum of **1** at 5 K (red) including simulations (green). Top: for this simulation, the Cu hyperfine values determined by Tolman and coworkers (see ref. [25,27]) were used ($^{Cu}A_{\perp}$ = 187 MHz; $^{Cu}A_{//}$ = 320 MHz). However, the central region of the spectrum could not be fit this way. Bottom: alternative simulation, where the Cu hyperfine was allowed to vary stronger. Fit: g_x = 1.962, g_y = 1.972, g_z = 1.8; $^{Cu}A_x$ = 100 MHz, $^{Cu}A_y$ = 105 MHz, $^{Cu}A_z$ = 270 MHz; ^{14}N hyperfine (NO): $^{N}A_x$ = 98 MHz, $^{N}A_y$ = 19 MHz, $^{N}A_z$ = 17 MHz. Note that g_z could not exactly be determined due to lack of spectral resolution. The value of g_z is around 1.79–1.80.

Figure 4 Calculated g values (BP86/TZVP) as a function of the Cu-N-O angle. Indicated are the predicted g values for **3**.

Figure 5 Calculated g tensor orientation for [Cu(L0)(NO)] with the Cu-N-O angle set to 172° (BP86/TZVP). In this case, g_z ($g_{//}$) equals g_{min}

exactly, whereas g_{mid} and g_{max} approximately correspond to g_x and g_y in the coordinate system shown in Scheme 1, top.

Figure 6 UV-Vis (top) and MCD spectrum (bottom) of **1** including Gaussians obtained from a correlated fit, and TD-DFT based assignments. The TD-DFT calculated spectrum is shown in orange (shifted by 4000 cm^{-1} to higher energy).

Figure 7 Geometry optimized (BP86/TZVP) structures of Cu(I)-NO species in CuNIR. For these calculations, the anchor atoms (C atoms of the artificial CH_3 groups) of the three histidines were frozen at their crystallographic positions. Top: optimized structure with frozen Cu-N-O angle at the crystallographically determined value.[23] Bottom, left: fully optimized structure. Bottom, Right: optimized structure with frozen Cu-N-O angle at a value typical for the model complexes. Listed are relative energies with respect to the fully optimized structure, and calculated g values for the three structures.(BP86/TZVP).

Scheme 1 Frontier orbitals of the fully optimized model [Cu(L0)(NO)] obtained from BP86/TZVP (upper part, spin unrestricted). The relative d-orbital energies are obtained from MCD (lower part, paired electrons).

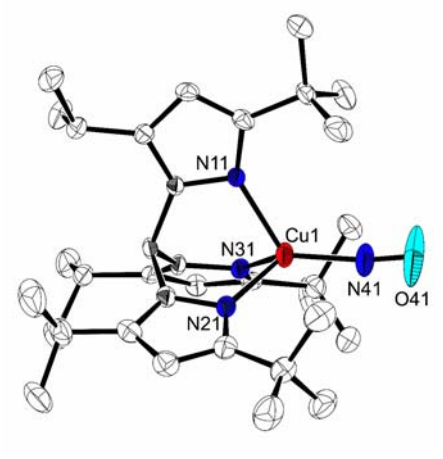

Figure 1. ORTEP view of [Cu(L3)(NO)] (**1**) showing 50% thermal ellipsoids and the atom labeling scheme. For clarity, hydrogen atoms were omitted. Selected bond distances (Å) and angles (deg): Cu1-N41 1.779(4), Cu1-N11 2.053(2), Cu1-N21 2.064(3), Cu1-N31 2.051(4), N41-O41 1.083(7), B1-N12 1.557(5), B1-N22 1.540(5), B1-N32 1.541(4); Cu1-N41-O41 171.9(5), N41-Cu1-N11 123.66(17), N41-Cu1-N21 122.81(18), N41-Cu1-N31 122.32(17), N11-Cu1-N21 91.85(12), N11-Cu1-N31 92.28(13), N21-Cu1-N31 95.61(14), N12-B1-N22 108.9(3), N12-B1-N32 109.8(3), N22-B1-N32 110.9(2).

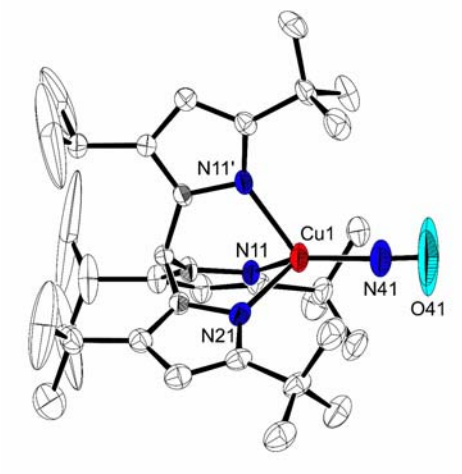

Figure 2. ORTEP view of the cation of [Cu(L3')(NO)](ClO_4) (**2**) showing 50% thermal ellipsoids and the atom labeling scheme. For clarity, hydrogen atoms were omitted. Selected bond distances (Å) and angles (deg): Cu1-N41 1.786(5), Cu1-N11 2.070(3), Cu1-N21 2.058(4), N41-O41 1.035(8), C1-N12 1.451(4), C1-N22 1.448(7); Cu1-N41-O41 176.4(10), N41-Cu1-N11 125.09(14), N41-Cu1-N21 125.2(2), N11-Cu1-N21 90.68(12), N11-Cu1-N11' 89.16(12), N12-C1-N22 112.2(2), N12-C1-N12' 111.3(3). Symmetry code: x, -y + 1/2, z.

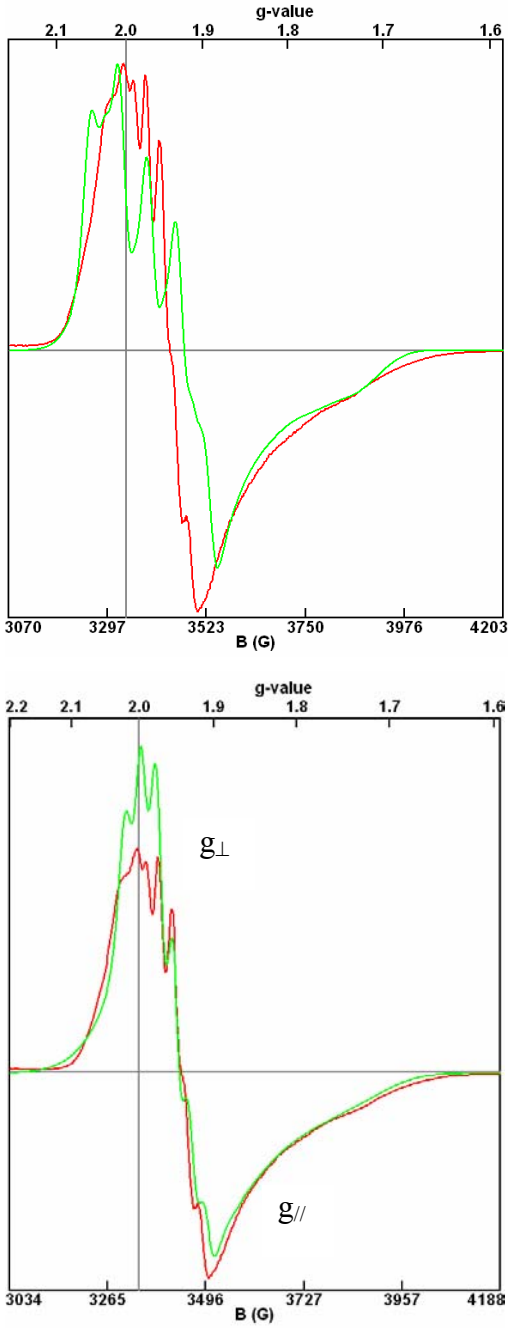

Figure 3. EPR spectrum of **1** at 5 K (red) including simulations (green). Top: for this simulation, the Cu hyperfine values determined by Tolman and coworkers (see ref. [25, 27]) were used ($^{Cu}A_{\perp}$ = 187 MHz; $^{Cu}A_{//}$ = 320 MHz). However, the central region of the spectrum could not be fit this way. Bottom: alternative simulation, where the Cu hyperfine was allowed to vary stronger. Fit: g_x = 1.962, g_y = 1.972, g_z = 1.8; $^{Cu}A_x$ = 100 MHz, $^{Cu}A_y$ = 105 MHz, $^{Cu}A_z$ = 270 MHz; ^{14}N hyperfine (NO): $^{N}A_x$ = 98 MHz, $^{N}A_y$ = 19 MHz, $^{N}A_z$ = 17 MHz. Note that g_z could not exactly be determined due to lack of spectral resolution. The value of g_z is around 1.79–1.80.

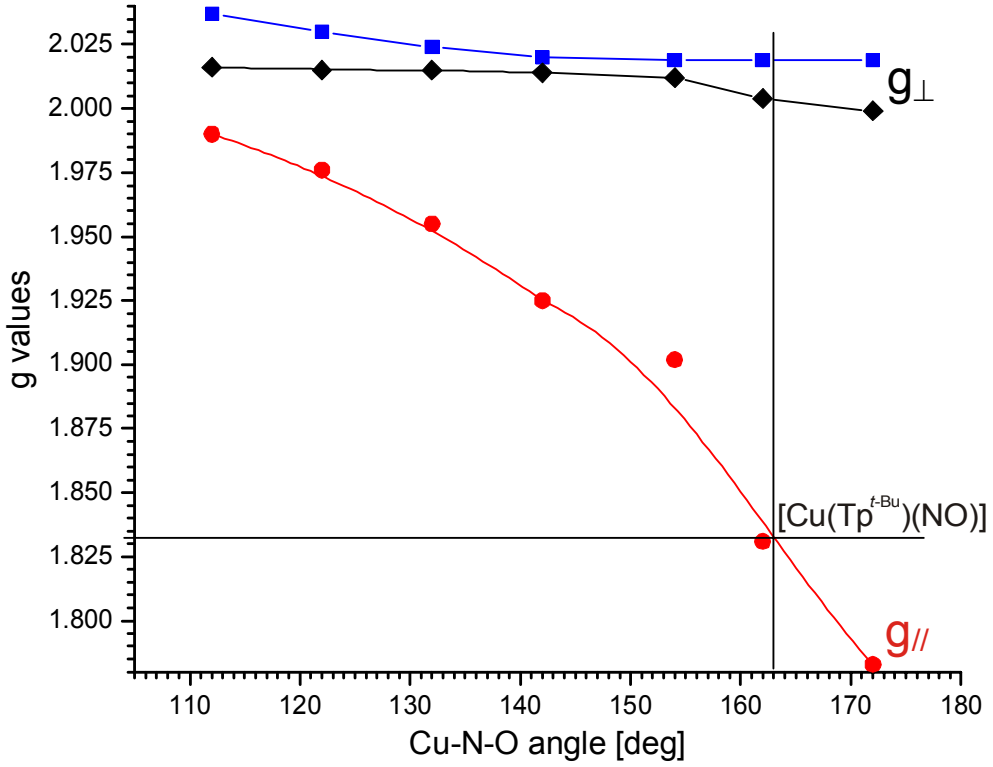

Figure 4. Calculated g values (BP86/TZVP) as a function of the Cu-N-O angle. Indicated are the predicted g values for **3**.

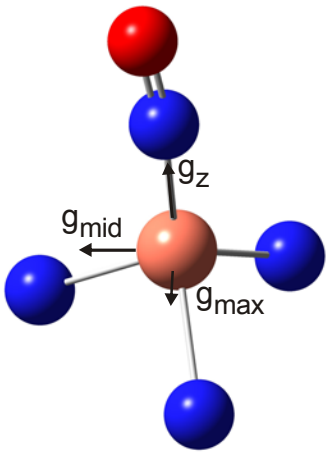

Figure 5. Calculated g tensor orientation for [Cu(L0)(NO)] with the Cu-N-O angle set to 172° (BP86/TZVP). In this case, g_z ($g_{//}$) equals g_{min} exactly, whereas g_{mid} and g_{max} approximately correspond to g_x and g_y in the coordinate system shown in Scheme 1, top.

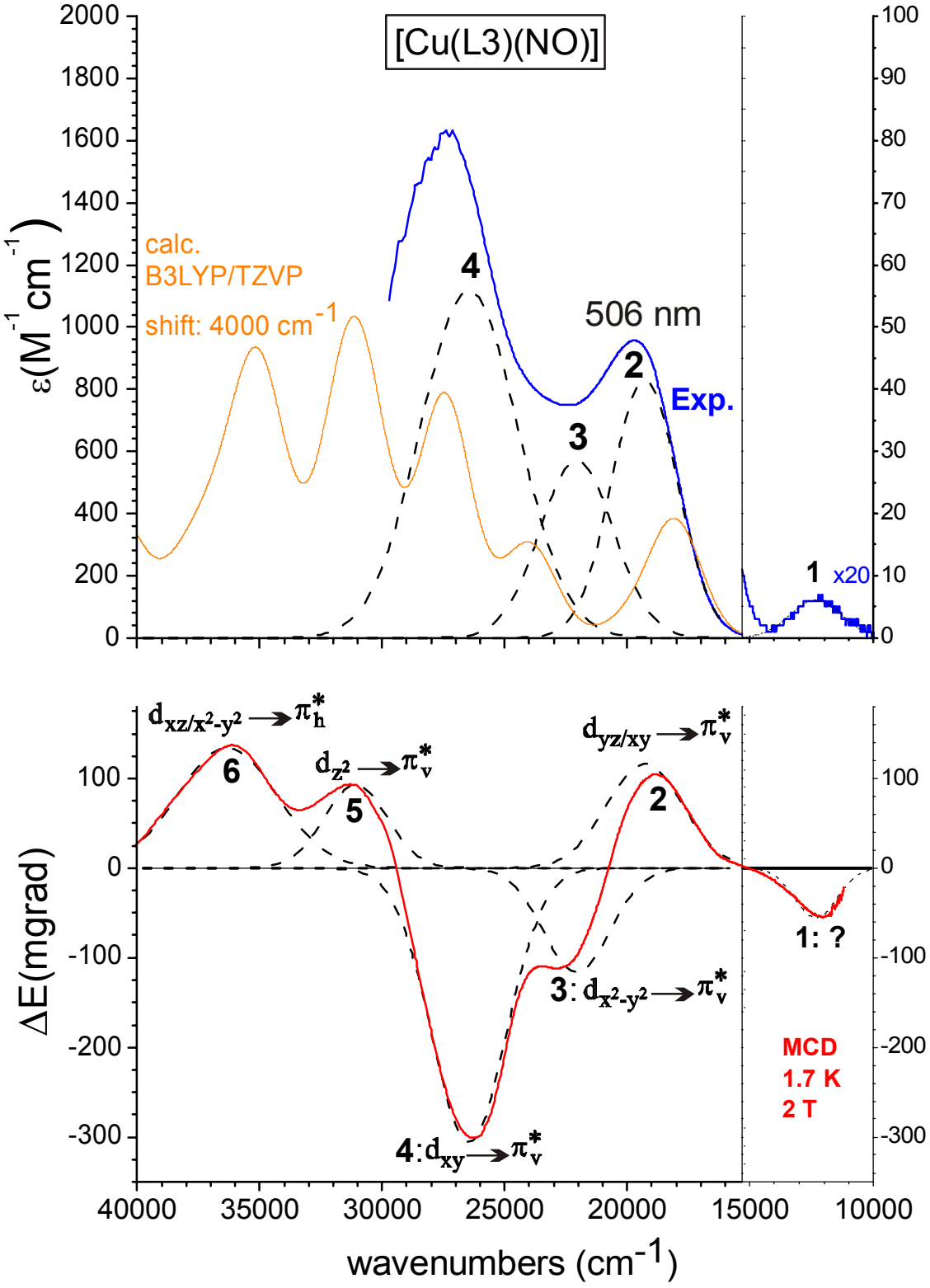

Figure 6. UV-Vis (top) and MCD spectrum (bottom) of **1** including Gaussians obtained from a correlated fit, and TD-DFT based assignments. The TD-DFT calculated spectrum is shown in orange (shifted by 4000 cm^{-1} to higher energy).

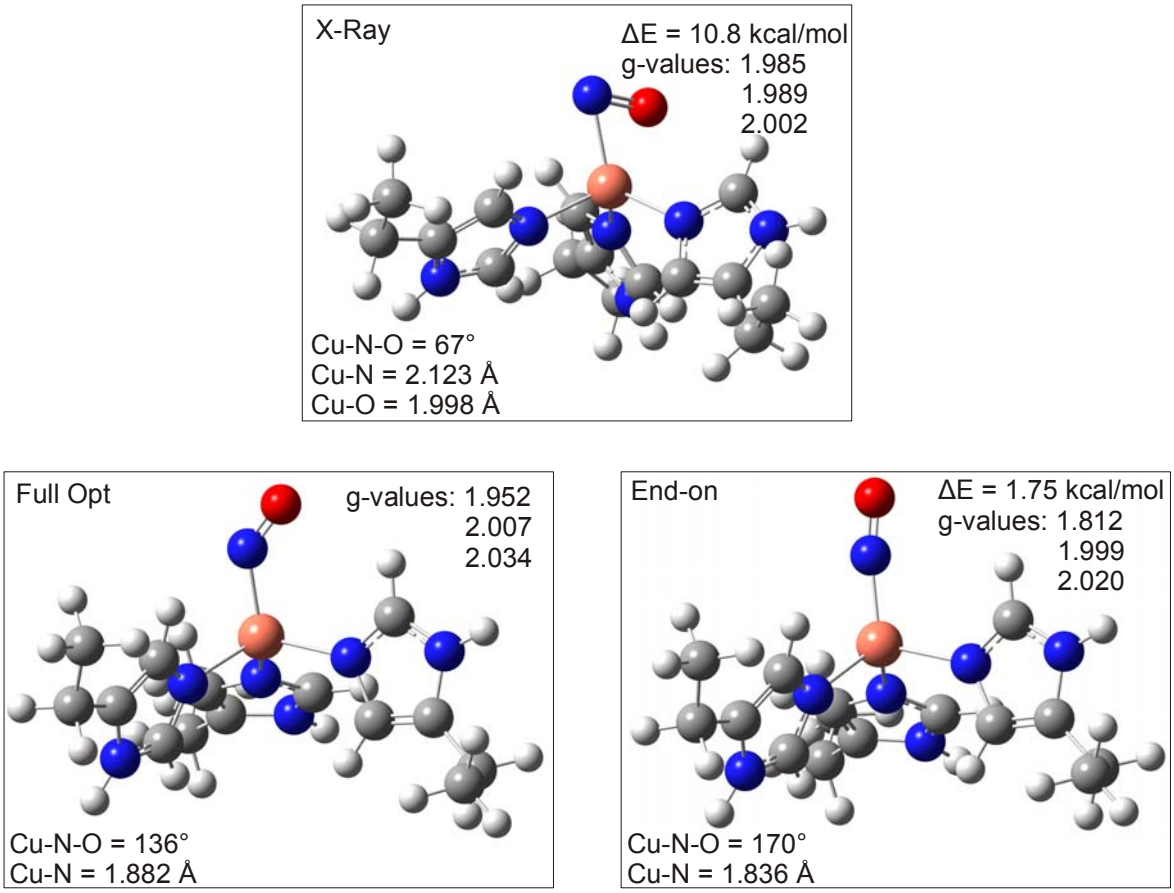

Figure 7. Geometry optimized (BP86/TZVP) structures of Cu(I)-NO species in CuNIR. For these calculations, the anchor atoms (C atoms of the artificial CH_3 groups) of the three histidines were frozen at their crystallographic positions. Top: optimized structure with frozen Cu-N-O angle at the crystallographically determined value.[23] Bottom, left: fully optimized structure. Bottom, Right: optimized structure with frozen Cu-N-O angle at a value typical for the model complexes. Listed are relative energies with respect to the fully optimized structure, and calculated g values for the three structures.

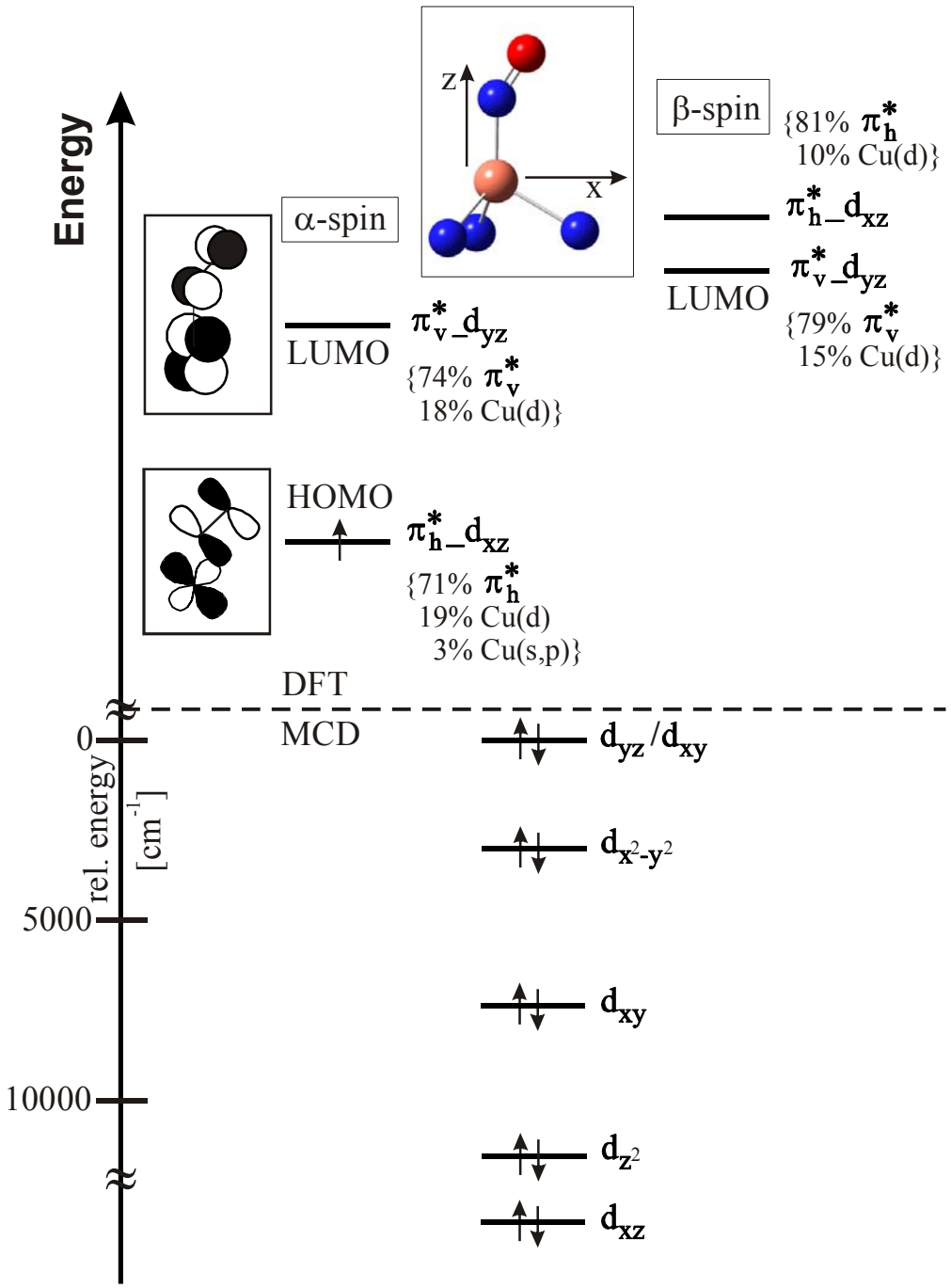

Scheme 1. Frontier orbitals of the fully optimized model [Cu(L0)(NO)] obtained from BP86/TZVP (upper part, spin unrestricted). The approximate relative d-orbital energies are obtained from MCD (lower part, paired electrons).

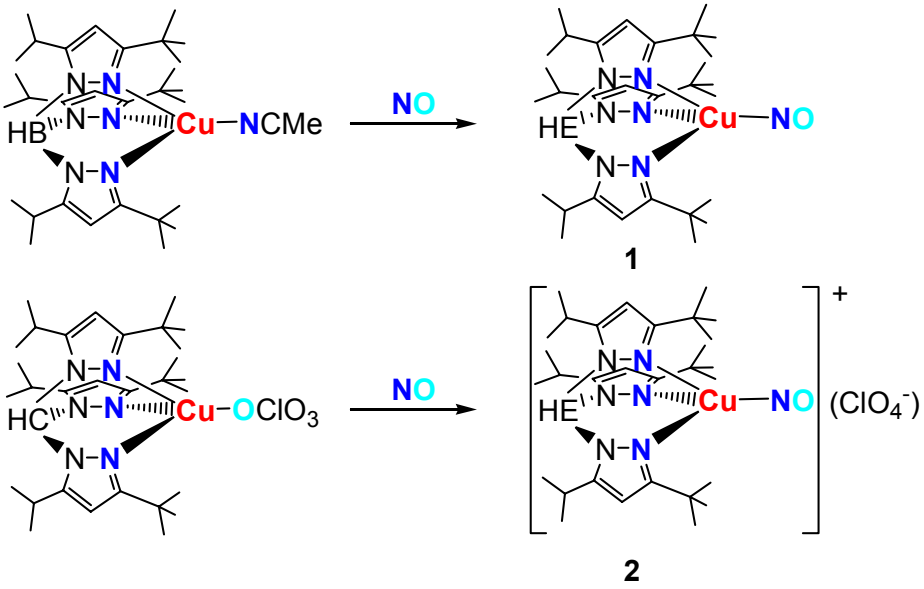

Equation 1.

References

1. In the Enemark-Feltham notation[2], the number of d electrons of the metal plus the unpaired electron of NO are added up and then used as a superscript (here: 11). This allows for a classification of transition metal nitrosyls, in the case of which the assignment of metal and NO oxidation states is sometimes very difficult.
2. Enemark, J. H.; Feltham, R. D., *Coord. Chem. Rev.* **1974,** 13, 339-406.
3. Shiva, S.; Wang, X.; Ringwood, L. A.; Xu, X.; Yuditskaya, S.; Annavajjhala, V.; Miyajima, H.; Hogg, N.; Harris, Z. L.; Gladwin, M. T., *Nature Chem. Biol.* **2006,** 2, 486-493.
4. Bryan, N. S.; Fernandez, B. O.; Bauer, S. M.; Garcia-Saura, M. F.; Milsom, A. B.; Rassaf, T.; Maloney, R. E.; Bharti, A.; Rodriguez, J.; Feelisch, M., *Nature Chem. Biol.* **2005,** 1, 290-297.
5. Torres, J.; Svinstunenko, D.; Karlsson, B.; Cooper, C. E.; Wilson, M. T., *J. Am. Chem. Soc.* **2002,** 124, 963-967.
6. Sorenson, J. R. J., *J. Inorg. Biochem.* **2001,** 87, 125-127.
7. Averill, B. A., *Chem. Rev.* **1996,** 96, 2951-2964.
8. Wasser, I. M.; de Vries, S.; Moënne-Loccoz, P.; Schröder, I.; Karlin, K. D., *Chem. Rev.* **2002,** 102, 1201-1234.
9. Suzuki, S.; Kataoka, K.; Yamaguchi, K., *Acc. Chem. Res.* **2000,** 33, 728-738.
10. Godden, J. W.; Turley, S.; Teller, D. C.; Adman, E. T.; Liu, M. Y.; Payne, W. J.; LeGall, J., *Science* **1991,** 253, 438-442.
11. Adaman, E. T.; Godden, J. W.; Turley, S., *J. Biol. Chem.* **1995,** 270, 27458-27474.
12. Murphy, M. E. P.; Turley, S.; Kukimoto, M.; Nishiyama, M.; Horinouchi, S.; Sasaki, H.; Tanokura, M.; Adman, E. T., *Biochemistry* **1995,** 34, 12107-12117.
13. Murphy, M. E. P.; Turley, S.; Adman, E. T., *J. Biol. Chem.* **1997,** 45, 28455-28460.
14. Dodd, F. E.; Van Beeumen, J.; Eady, R. R.; Hasnain, S. S., *J. Mol. Biol.* **1998,** 282, 369-382.
15. Inoue, T.; Gotowda, M.; Deligeer; Kataoka, M.; Yamaguchi, K.; Suzuki, S.; Watanabe, H.; Gohow, M.; Kai, Y., *J. Biochem.* **1998,** 124, 876-879.
16. Strange, R. W.; Dodd, F. E.; Abraham, Z. H. L.; Grossmann, J. G.; Brüser, T.; Eady, R. R.; Smith, B. E.; Hasnain, S. S., *Nature Struct. Biol.* **1995,** 2, 287-292.
17. Howes, B. D.; Abraham, Z. H. L.; Lowe, D. J.; Brüser, T.; Eady, R. R.; Smith, D. E., *Biochemistry* **1994,** 33, 3171-3177.
18. Lehnert, N.; Cornelissen, U.; Neese, F.; Ono, T.; Noguchi, Y.; Okamoto, K.; Fujisawa, K., *Inorg. Chem.* **2007,** 46, 3916-3933.
19. Kataoka, K.; Furusawa, H.; Takagi, K.; Yamaguchi, K.; Suzuki, S., *J. Biochem.* **2000,** 127, 345-350.
20. Casella, S.; Shapleigh, J. P.; Toffanin, A.; Basaglia, M., *Biochem. Soc. Trans.* **2006,** 34, 130-132.
21. Ghosh, S.; Dey, A.; Usov, O. M.; Sun, Y.; Grigoryants, V. M.; Scholes, C. P.; Solomon, E. I., *J. Am. Chem. Soc.* **2007,** 129, 10310-10311.
22. Ruggiero, C. E.; Carrier, S. M.; Tolman, W. B., *Angew. Chem. Int. Ed. Engl.* **1994,** 33, 895-897.
23. Tocheva, E. I.; Rosell, F. I.; Mauk, A. G.; Murphy, M. E. P., *Science* **2004,** 304, 867-870.
24. Antonyuk, S. V.; Strange, R. W.; Sawers, G.; Eady, R. R.; Hasnain, S. S.,

Proc. Natl. Acad. Sci. USA **2005,** 102, 12041-12046.
25. Usov, O. M.; Sun, Y.; Grigoryants, V. M.; Shapleigh, J. P.; Scholes, C. P., *J. Am. Chem. Soc.* **2006,** 128, 13102-13111.
26. Wasbotten, I. H.; Ghosh, A., *J. Am. Chem. Soc.* **2005,** 127, 15384-15385.
27. Ruggiero, C. E.; Carrier, S. M.; Antholine, W. E.; Whittaker, J. W.; Cramer, C. J.; Tolman, W. B., *J. Am. Chem. Soc.* **1993,** 115, 11285-11298.
28. Paul, P. P.; Tyeklar, Z.; Farooq, A.; Karlin, K. D.; Liu, S.; Zubieta, J., *J. Am. Chem. Soc.* **1990,** 112, 2430-2432.
29. Fujisawa, K.; Kobayashi, T.; Fujita, K.; Kitajima, N.; Moro-oka, Y.; Miyashita, Y.; Yamada, Y.; Okamoto, K., *Bull. Chem. Soc. Jpn.* **2000,** 73, 1797-1804.
30. Fujisawa, K.; Ono, T.; Ishikawa, Y.; Amir, N.; Miyashita, Y.; Okamoto, K.; Lehnert, N., *Inorg. Chem.* **2006,** 45, 1698-1713.
31. Pflugrath, J. W., CrystalClear Ver. 1.3. *Acta. Cryst.* **1999,** D55, 1718-1725.
32. *CrystalStructure 3.70: Crystal Structure Analysis Package*, Version 3.70; Rigaku and Rigaku/MSC: 2005.
33. Watkin, D. J.; Prout, C. K.; Carruthers, J. R.; W., B. P. *Crystal Issue 10*, Chemical Crystallography Laboratory: Oxford, UK, 1996.
34. Altomare, A.; Cascarano, G.; Giacovazzo, C.; Guagliardi, A.; Burla, M.; Polidori, G.; Camalli, M., SIR 92. *J. Appl. Crystallogr.* **1994,** 27, 435.
35. Beurskens, P. T.; Admiraal, G.; Beurskens, G.; Bosman, W. P.; de Gelder, R.; Israel, R.; Smits, J. M. M. *The DIRDIF-99 program system*, Technical Report of the Crystallography Laboratory, University of Nijmegen, The Netherlands: 1999.
36. Praneeth, V. K. K.; Näther, C.; Peters, G.; Lehnert, N., *Inorg. Chem.* **2006,** 45, 2795-2811.
37. Allouche, A.; Pourcin, J., *Spectrochim. Acta* **1993,** 49A, 571-580.
38. Frisch, M. J. et al., *Gaussian 03*, Gaussian, Inc.: Pittsburgh, PA, 2003.
39. Schäfer, A.; Horn, H.; Ahlrichs, R., *J. Chem. Phys.* **1992,** 97, 2571-2577.
40. Becke, A. D., *Phys. Rev. A* **1988,** 38, 3098-3100.
41. Becke, A. D., *J. Chem. Phys.* **1993,** 98, 1372-1377.
42. Becke, A. D., *J. Chem. Phys.* **1993,** 98, 5648-5652.
43. Dunning, T. H., Jr.; Hay, P. J.; Schaefer, H. F., III., *Modern Theoretical Chemistry*. Plenum: New York, 1976.
44. Hay, P. J.; Wadt, W. R., *J. Chem. Phys.* **1985,** 82, 270-283 and 299-310.
45. Wadt, W. R.; Hay, P. J., *J. Chem. Phys.* **1985,** 82, 284-290.
46. Neese, F. *ORCA*, Version 2.2; Max-Planck Institut für Bioanorganische Chemie, Mülheim/Ruhr, Germany, 2004.
47. Schneider, J. L.; Carrier, S. M.; Ruggiero, C. E.; Young, J., V. G.; Tolman, W. B., *J. Am. Chem. Soc.* **1998,** 120, 11408-11418.
48. Unfortunately, we did not obtain good EPR data for **2**, due to decomposition.
49. Lever, A. B. P.; Solomon, E. I., Ligand Field Theory and the Properties of Transition Metal Complexes. In *Inorganic Electronic Structure and Spectroscopy*, Solomon, E. I.; Lever, A. B. P., Eds. Wiley: New York, 1999; Vol. Volume 1.
50. Wilmot, C. M.; Hajdu, J.; McPherson, M. J.; Knowles, P. F.; Phillips, S. E. V., *Science* **1999,** 286, 1724-1728.
51. Fadini, A.; Schnepel, F.-M., *Schwingungsspektroskopie*. Thieme Verlag: Stuttgart, 1985.

7.5. $[Fe^{III}(tmdta)]^-$-twist-boat/half-chair conformer ratio reliably deduced from DFT-calculated Raman spectra

Roland Meier, Joachim Maigut, Bernd Kallies, Nicolai Lehnert, Florian Paulat, Frank W. Heinemann, Gernot Zahn, Martin P. Feth, Harald Krautscheid and Rudi van Eldik

Published in: *Chem. Commun.* **2007**, *38*, 3960-3962.

$[Fe^{III}(tmdta)]^-$–twist-boat/half-chair conformer ratio reliably deduced from DFT-calculated Raman spectra†

Roland Meier,*[a] Joachim Maigut,[a] Bernd Kallies,*[b] Nicolai Lehnert,*[c] Florian Paulat,[c] Frank W. Heinemann,[a] Gernot Zahn,[d] Martin P. Feth,[e] Harald Krautscheid[f] and Rudi van Eldik[a]

Received (in Cambridge, UK) 4th June 2007, Accepted 10th August 2007
First published as an Advance Article on the web 20th August 2007
DOI: 10.1039/b708437d

The equilibrium between the twist-boat (tb) and half-chair (hc) conformers of the central diamine chelate ring of $[Fe^{III}(tmdta)]^-$ in solids and aqueous solution has been studied by Raman spectroscopy, supported by calculated Raman spectra using Density Functional Theory.

Monitoring changes in the coordination sphere around iron centers that result from the dissolution of solid complex salts in water is of high importance for the elucidation of structure–activity relationships,[1] a critical target in many industrial and academic applications of iron chelates.[2] The complex investigated here, $[Fe^{III}(tmdta)]^-$ (tmdta = trimethylenediamine tetraacetate), is used in the bleaching of photographic films and paper.[3] The conformational equilibria of chelate complexes are often very difficult to monitor, especially in the cases of complexes with paramagnetic metal centers. Here, the use of NMR for structural elucidation fails. In this study, we demonstrate how Raman spectroscopy coupled to density functional theory (DFT) calculations can be successfully applied for this purpose.

Upon coordination to tmdta, metal centers like Fe^{III} can form half-chair (**hc**) or twist-boat (**tb**) conformational isomers (see Scheme 1).[4–6] The half-chair conformer was found in the crystal structure of $Li[Fe(tmdta)]\cdot 3H_2O$ (**1a**),[3] whereas the twist-boat form was encountered during structural studies of $NH_4[Fe(tmdta)]\cdot H_2O$ (**1b**)[4] and $Na[Fe(tmdta)]\cdot 3H_2O$ (**1c**).[5]

Various salts of $[Fe^{III}(tmdta)]^-$ have been studied in the past by solid-state Raman spectroscopy,[7] followed by the analysis of the Raman spectra of their corresponding aqueous solutions.[8] In the latter study, the predominance of the **hc** form in solution was suggested, based on the evaluation of bands in the 600–300 cm^{-1} wavenumber region. Here, Fe–N and Fe–O valence stretching, as well as skeletal vibrations of the coordination polyhedron, are expected to appear.[7,8] However, this analysis remained on an empirical level and was strongly impaired by the fact that the vibrational assignments of the bands used to identify the species found in solution were not known.

A major revision of these findings is presented in the current Communication. We have re-investigated the solid-state Raman spectra of the two isomers of $[Fe^{III}(tmdta)]^-$ in detail and correlated the experimental data to Raman spectra calculated by DFT. For this purpose, the structures of the two conformers were fully optimized in the gas phase using B3LYP/6-31+G* (*cf.* Computational aspects in the ESI†). The computed spectra were then used to simulate the composite spectra of conformer mixtures, which were correlated to the experimental Raman spectra of aqueous solutions of $[Fe^{III}(tmdta)]^-$ salts.

In the structural studies reported to date,[4–6] it was not clearly determined which of the two conformers (**tb** or **hc**) was preferred in the solid-state. In order to broaden the knowledge basis for this purpose, we have investigated the crystal structures of two new Fe^{III}–tmdta salts, *i.e.* $K[Fe^{III}(tmdta)]$ (**1d**) and $\{C(NH_2)_3\}[Fe^{III}(tmdta)]\cdot 2H_2O$ (**1e**).‡ In both cases, the **tb** conformation is found in the solid-state. Interestingly, the structure of **1e** also contains 6% of the **hc** conformer, leading to disorder in the crystal (further details are presented in the ESI†). The latter finding motivated us to re-determine the structures of $Li[Fe^{III}(tmdta)]\cdot 3H_2O$ (**1a**)[4] and $NH_4[Fe^{III}(tmdta)]\cdot 0.5H_2O$ (**1b**) at high resolution in order to explore the possibility of conformational mixtures in these salts.§[5] From the literature, fractional coordinates are available for **1a**.[4] This is not the case for **1b**, where only the lattice constants have been published.[5] It was again surprising that—while **1b** contains solely the **tb** form—salt **1a**, which was originally considered to be purely **hc**, in fact shows a similar disorder to that encountered for **1e**, but with a distribution of 91% **hc** *vs.* 9% **tb**. Our results now show rather clearly that the **tb**

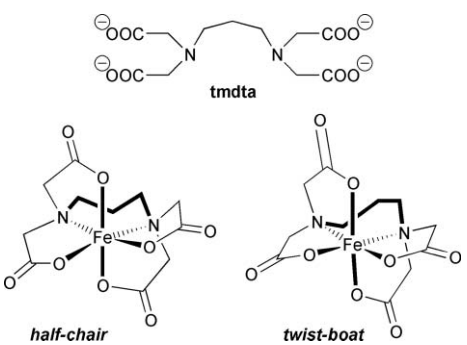

Scheme 1 The ligand tmdta, and the half-chair and twist-boat conformational isomers of $[Fe^{III}(tmdta)]^-$.

[a]*Institute for Inorganic Chemistry, University of Erlangen-Nürnberg, Egerlandstraße 1, 91058 Erlangen, Germany*
[b]*Zuse Institute Berlin, Takustraße 7, 14195 Berlin, Germany*
[c]*Department of Chemistry, The University of Michigan, 930 N. University, Ann Arbor, MI 48109-1055, USA*
[d]*MPI für Chemische Physik fester Stoffe, Nöthnitzer Straße 40, 01187 Dresden, Germany*
[e]*ALTANA Pharma AG, A Member of the NYCOMED Group, Physicochemical Research, Byk-Gulden-Straße 2, 78467 Konstanz, Germany*
[f]*Institute of Inorganic Chemistry, University of Leipzig, Johannisallee 29, 04103 Leipzig, Germany*

† Electronic supplementary information (ESI) available: Preparation of complexes, X-ray structure analysis and crystallographic details, Raman spectra details and computational aspects. See DOI: 10.1039/b708437d

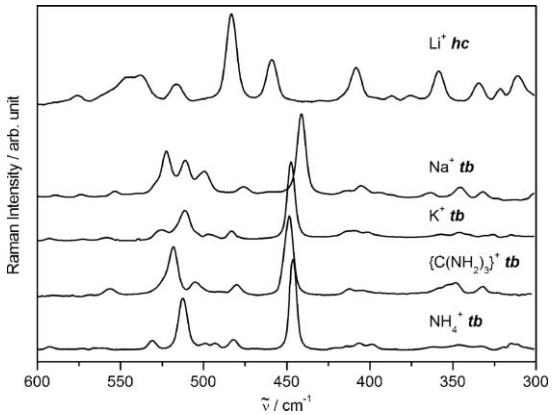

Fig. 1 Solid-state Raman spectra of $[Fe^{III}(tmdta)]^-$ salts **1a–e**. The counterion and dominating conformer found in the corresponding crystal structure (**hc** or **tb**) are indicated.

form is favoured in solid salts of $[Fe^{III}(tmdta)]^-$. Crystallization of the **hc** conformer seems only to be possible in the lithium salt.[9] However, one should take into account that the isomer distribution in the solid-state is a result of the counterbalancing solid-state forces in the crystal and does not reflect the intrinsic **tb** or **hc** arrangement characteristics of the metal complexes in the chelate backbone that is valid for solution- or gas-phase conditions.

As mentioned before,[8] in the 600–300 cm^{-1} wavenumber range, Fe–N and Fe–O valence stretching, as well as skeletal vibrations of

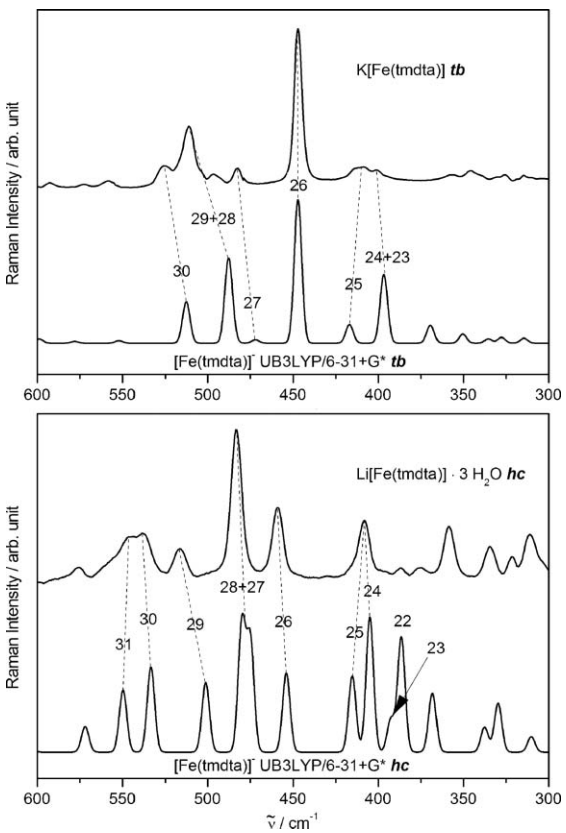

Fig. 2 Comparison of solid-state Raman spectra of the potassium (**1d**, top) and lithium (**1a**, bottom) salts of $[Fe^{III}(tmdta)]^-$ with calculated spectra of the twist-boat (top) and half-chair (bottom) conformers. Band numbering follows the entries in Table 1 and Table 2.

Table 1 Bands of the solid-state Raman spectrum of **1d** (**tb** conformer)

		Wavenumber/cm^{-1}			
No.	Sym.[a]	Exp'l[b]	Calc'd[c]	Intensity[d]	Description
23	A	401	396.3	11.8	Gly rock (eq.)
24	B		398.3	0.1	Gly rock (eq.)
25	B	409	416.5	3.2	Gly rock (all)
26	A	447	446.8	25.1	Ring twist
27	B	483	471.5	0.6	Gly rock (ax.)
28	B	511	485.5	2.1	ν_{as}(Fe–N)
29	A		487.5	13.3	ν_{s}(Fe–N)
30	A	525	512.2	7.1	Ring bend

[a] Irreducible representation in the C_2 point group. [b] *cf.* Fig. 2, top. [c] Calculated wavenumbers scaled by a factor of 1.027. [d] Calculated Raman intensity.

the coordination polyhedron, appear. Correspondingly, this is the most suitable wavenumber range to study the spectral differences between the **hc** and **tb** conformers. Thus, solid-state Raman spectra of the five salts, **1a–e**, of $[Fe^{III}(tmdta)]^-$ have been measured, as shown in Fig. 1 for the 600–300 cm^{-1} wavenumber range. The most prominent bands were assigned based on an analysis of the corresponding DFT-calculated spectra. These results are presented in Fig. 2, and in Table 1 and Table 2.

The most significant difference between the spectra of the two conformers is the presence of a very intense band at ~440 cm^{-1} in all **tb** spectra, whereas the Raman intensity of the **hc** spectrum is virtually zero in this region (*cf.* Fig. 1). Our DFT computations show (*cf.* band 26 in Fig. 2 (top) and Table 1) that this band corresponds to a ring-twist motion of the linearly-arranged CH_2–CH_2–CH_2 fragment in the central diamine chelate ring. The related vibration of the **hc** conformer appears at 460 cm^{-1} in the spectrum of Li[Fe(tmdta)]·$3H_2O$ (**1a**) and at 454 cm^{-1} in the scaled, computed spectrum of the geometry-optimized **hc** conformer (*cf.* band 26 in Fig. 2 (bottom) and Table 2). This vibration belongs to a rocking motion of the central methylene group in the diamine chelate ring. No significant Raman intensity is observed in the **tb** spectrum between 460 and 450 cm^{-1} (*cf.* Fig. 1). The most intense band in the 600–300 cm^{-1} region of the **hc** conformer appears at 480 cm^{-1} (*cf.* bands 27 and 28 in Fig. 2 (bottom) and Table 2). This feature is assigned to rocking motions of the axial glycinate rings, which are motions unique to this conformer.

The assignments of the remaining bands are presented in Table 1 and Table 2. The results show that the experimental and calculated

Table 2 Bands of the solid-state Raman spectrum of **1a** (**hc** conformer)

		Wavenumber/cm^{-1}			
No.	Sym.[a]	Exp'l[b]	Calc'd[c]	Intensity[d]	Description
24	A	408	404.6	8.9	Ring bend
25	A		414.9	5.0	Ring bend
26	A	459	453.6	5.2	Ring rock
27	A	483	474.5	7.3	Gly rock (ax1)
28	A		479.5	8.5	Gly rock (ax2)
29	A	516	500.7	4.6	ν(Fe–N_1) + ring twist
30	A	538	532.9	5.6	ring rock
31	A	544	549.1	4.1	ν(Fe–N_2) + ring twist

[a] Irreducible representation in the C_1 point group. [b] *cf.* Fig. 2, bottom. [c] Calculated wavenumbers scaled by a factor of 1.027. [d] Calculated Raman intensity.

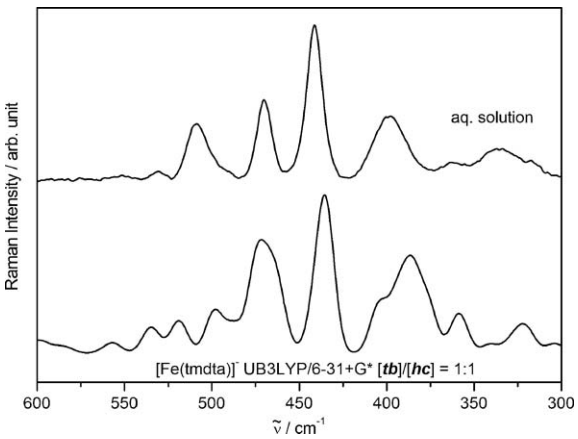

Fig. 3 Comparison of the unique Raman spectrum of aqueous solutions of **1a–e** and a computed spectrum generated by mixing pure computed **hc** and **tb** spectra in the ratio 1 : 1. Calculated wavenumbers are scaled by a factor of 1.012.

Raman spectra for the **hc** and **tb** conformers agree reasonably well. Deviations in vibrational energies might be due to (a) solid-state packing effects (size difference between counter-cations), (b) electrostatic interactions of the metal-bound and free carboxylato oxygen atoms of $tmdta^{4-}$ with counter-cations and (c) hydrogen bonds between these oxygens and protons of the crystal water molecules. All of these might affect the vibrational energies.

It can therefore be concluded that differences between the Raman spectra of the two conformers in the 500–400 cm^{-1} range represent a crucial tool that allows aqueous solutions of $[Fe(tmdta)]^-$ salts to be analysed in terms of being (i) a pure solution of either conformer or (ii) a mixture of both conformers. The decision between (i) and (ii), followed by quantification of a possible equilibrium, can thus be based on the absolute intensities of the Raman signals of each conformer. In order to achieve this, and to avoid the tedious calibration of experimental Raman spectra, we have used the calculated absolute Raman intensities of the different bands, which are obtained directly from calculated molecular polarizabilities by means of theoretical methods. Comparison of the calculated and experimental spectra shows a good agreement between the relative Raman intensities, justifying this approach. Thus, linear combinations of the calculated spectra of pure species with varying **[tb]/[hc]** ratios were generated until a best fit of the experimental solution spectrum with the theoretical composite spectrum was achieved.

Since the calculated energies of the **tb** and the **hc** conformers in the gas phase are nearly equal ($\Delta H_{\mathbf{hc-tb}} = -0.13$ kJ mol^{-1}, $\Delta G_{\mathbf{hc-tb}} = 0.54$ kJ mol^{-1}), and since their calculated dipole moments ($\mu_{\mathbf{hc}} = 10.56$ Debye, $\mu_{\mathbf{tb}} = 10.54$ Debye) suggest a nearly identical electrostatic contribution to their free solvation energy, one would expect a **[tb]/[hc]** ratio of about 1 : 1 in aqueous solutions of $[Fe(tmdta)]^-$ on the basis of DFT calculations.

Fig. 3 shows the simulated spectrum that gives the best agreement with the experimental solution spectrum. In fact, this is the theoretical composite Raman spectrum with a 1 : 1 **[tb]/[hc]** ratio, as predicted by thermodynamic considerations. Importantly, with the help of the band assignments obtained for the pure conformers, it is now possible to fully understand the solution spectrum and to interpret the solution as an *equal* mixture of both forms. The most intense band near 440 cm^{-1} in the simulated solution spectrum (Fig. 3) corresponds to vibration **tb** 26 (ring twist), slightly broadened by the less intense band **hc** 26 (ring rock). The band at 470 cm^{-1} is a mixture of **tb** bands 28 and 29 (Fe–N stretch), and **hc** features 27 and 28 (gly rock). The remaining broad bands above 500 and below 400 cm^{-1} are mixtures of various normal modes of both conformers. Thus, the spectrum of the 1 : 1 **[tb]/[hc]** equilibrium mixture in the 600–300 cm^{-1} region is dominated by contributions of the **tb** conformer because of its more intense Raman vibrations. However, the presence of the band at 470 cm^{-1} clearly indicates the presence of the **hc** conformer at a significant concentration; in a pure **tb** solution spectrum, the band next to the ring twist would be expected to occur at a higher wavenumber (around 500 cm^{-1}).

This report is the first demonstration of how the combined application of Raman spectroscopy and quantum chemical methods can be used to quantify the equilibrium species involved in the interconversion of labile coordination isomers. The two new crystal structures of the $[Fe^{III}(tmdta)]^-$ salts, **1d** (inorganic counter-cation) and **1e** (organic counter-cation), reveal that the **tb** conformation is generally preferred in the solid-state. The detailed vibrational band assignments obtained for the Raman spectra of pure solids of both conformers allowed a revision of the previously incorrectly determined **[tb]/[hc]** ratio[8] of aqueous $[Fe^{III}(tmdta)]^-$ solutions, where the **hc** fraction was assumed to be present in a large excess. On the contrary, our analysis of the Raman spectrum of $[Fe(tmdta)]^-$ in aqueous solution reveals a **[tb]/[hc]** ratio of about 1 : 1. We are currently investigating the mechanistic details of the **[tb]/[hc]** interconversion and the possible influence of the $[Fe^{III}(tmdta)]^-$ water exchange reaction on the dynamics of this process. Furthermore, work is in progress to apply our approach of DFT-supported Raman studies to elucidation of the dynamics in solution of related metal–tmdta complexes in order to evaluate the role of the central metal ion in the conformational equilibrium.

Notes and references

‡ Coordinates for the structures of four monomeric complexes have been deposited with the CCDC. Deposition numbers: CCDC 649049 (**1a**), 649050 (**1b**), 649047 (**1d**) and 649048 (**1e**). For crystallographic data in CIF or other electronic format see DOI: 10.1039/b708437d

§ We are grateful to N. Burzlaff (Erlangen) for solving the X-ray structure of **1b**.

1 R. Meier, *Habilitation Thesis*, University of Leipzig, Leipzig, 2003.
2 W. L. Howard and D. A. Wilson, Chelating Agents, in *Kirk–Othmer Encyclopedia of Chemical Technology*, ed. J. I. Kroschwitz and M. Howe-Grant, John Wiley & Sons, New York, 4th edn, 1993, vol. **5**, pp. 764–795.
3 T. Egli, *J. Biosci. Bioeng.*, 2001, **92**, 89; C. K. Schmidt and H.-J. Brauch, Aminopolycarboxylate Complexing Agents in *Organic Pollutants in the Water Cycle*, ed. T. Reemtsma and M. Jekel, Wiley-VCH, 2006, pp. 155–180.
4 T. Yamamoto, K. Mikata, K. Miyoshi and H. Yoneda, *Inorg. Chim. Acta*, 1988, **150**, 237.
5 H. P. Bommeli, G. Anderegg and W. Petter, *Z. Kristallogr.*, 1986, **174**, 23; H. P. Bommeli, *Dissertation Thesis*, ETH Zürich, Zürich, 1992.
6 K.-I. Okamoto, K. Kanamori and J. Hikada, *Acta Crystallogr., Sect. C: Cryst. Struct. Commun.*, 1990, **46**, 1640.
7 K. Kanamori, H. Dohniwa, N. Ukita, I. Kanesaka and K. Kawai, *Bull. Chem. Soc. Jpn.*, 1990, **63**, 1447.
8 K. Kanamori, N. Ukita, K. Kawai, S. Taguchi, K. Goto, T. Eguchi and M. Kishita, *Inorg. Chim. Acta*, 1991, **186**, 205.
9 Crystallographic data and refinement details of **1a**, **1b**, **1d** and **1e** are summarized in Table S1. Important bond lengths and angles are given in Table S2‡.

7.6. Reduction Pathway of End-on Terminally Coordinated Dinitrogen. V. N-N Bond Cleavage in Mo/W Hydrazidium Complexes with Diphosphine Coligands. Comparison with Triamidoamine Systems

Klaus Mersmann, Kay H. Horn, Natascha Böres, Nicolai Lehnert, Felix Studt, Florian Paulat, Gerhard Peters, Ivana Ivanovic-Burmazovic, Rudi van Eldik,* and Felix Tuczek*

Published in: *Inorg. Chem.* **2005**, *44*, 3031-3045.

Inorg. Chem. **2005**, *44*, 3031–3045

Reduction Pathway of End-On Terminally Coordinated Dinitrogen. V. N–N Bond Cleavage in Mo/W Hydrazidium Complexes with Diphosphine Coligands. Comparison with Triamidoamine Systems

Klaus Mersmann,[†] Kay H. Horn,[†] Natascha Böres,[†] Nicolai Lehnert,[†] Felix Studt,[†] Florian Paulat,[†] Gerhard Peters,[†] Ivana Ivanovic-Burmazovic,[‡] Rudi van Eldik,*[,‡] and Felix Tuczek*[,†]

Institut für Anorganische Chemie, Christian-Albrechts-Universität Kiel, Otto Hahn Platz 6/7, 24098 Kiel, Germany, and Institut für Anorganische Chemie, Friedrich-Alexander Universität Erlangen-Nürnberg, Egerlandstrasse 1, 91058 Erlangen, Germany

Received September 22, 2004

N–N cleavage of the dialkylhydrazido complex $[W(dppe)_2(NNC_5H_{10})]$ ($\mathbf{B}^W$) upon treatment with acid, leading to the nitrido/imido complex and piperidine, is investigated experimentally and theoretically. In acetonitrile and at room temperature, $\mathbf{B}^W$ reacts orders of magnitude more rapidly with $HNEt_3BPh_4$ than its Mo analogue, $[Mo(dppe)_2(NNC_5H_{10})]$ ($\mathbf{B}^{Mo}$). A stopped-flow experiment performed for the reaction of $\mathbf{B}^W$ with $HNEt_3BPh_4$ in propionitrile at −70 °C indicates that protonation of $\mathbf{B}^W$ is completed within the dead time of the stopped-flow apparatus, leading to the primary protonated intermediate $\mathbf{B}^WH^+$. Propionitrile coordination to this species proceeds with a rate constant $k_{obs(1)}$ of $1.5 \pm 0.4\ s^{-1}$, generating intermediate RCN–$\mathbf{B}^WH^+$ (R = Et) that rapidly adds a further proton at N_β and then mediates N–N bond splitting in a slower reaction ($k_{obs(2)} = 0.35 \pm 0.08\ s^{-1}$, 6 equiv of acid). $k_{obs(1)}$ and $k_{obs(2)}$ are found to be independent of the acid concentration. The experimentally observed reactivities of $\mathbf{B}^{Mo}$ or $\mathbf{B}^W$ with acids in nitrile solvents are reproduced by DFT calculations. In particular, geometry optimization of models of solvent-coordinated, N_β-protonated intermediates is found to lead spontaneously to separation into the nitrido/imido complexes and piperidine/piperidinium, corresponding to activationless heterolytic N–N bond cleavage processes. Moreover, DFT indicates a spontaneous cleavage of nonsolvated $\mathbf{B}^W$ protonated at N_β. In the second part of this article, a theoretical analysis of the N–N cleavage reaction in the Mo(III) triamidoamine complex $[HIPTN_3N]Mo(N_2)$ is presented (HIPTN$_3$N = hexaisopropylterphenyltriamidoamine). To this end, DFT calculations of the $Mo^{III}N_2$ triamidoamine complex and its protonated and reduced derivatives are performed. Calculated structural and spectroscopic parameters are compared to available experimental data. N–N cleavage most likely proceeds by one-electron reduction of the Mo(V) hydrazidium intermediate $[HIPTN_3N]Mo(NNH_3)^+$, which is predicted to have an extremely elongated N–N bond. From an electronic-structure point of view, this reaction is analogous to that of Mo/W hydrazidium complexes with diphos coligands. The general implications of these results with respect to synthetic N_2 fixation are discussed.

I. Introduction

Because of the triple bond present in N_2, N−N cleavage of this molecule is highly endothermic in the gas phase. The corresponding bond dissociation enthalpy (225 kcal mol^{-1})[1] can be dramatically lowered if dinitrogen is coordinated to transition-metal centers. In some dinitrogen complexes, N−N bond splitting is even possible under ambient conditions. Thus, spontaneous N−N cleavage has been detected for dinitrogen coordinated in an end-on or side-on bridging geometry to two transition-metal centers.[2] Alternatively, N−N cleavage is facilitated if the bond order has been reduced through protonation and/or alkylation.[3,4] This reaction mode also applies to the reduction pathway of N_2 coordinated end-on terminally to mononuclear transition-metal complexes.[5] Importantly, the latter pathway is considered to apply to the reduction and protonation of N_2 in

* To whom correspondence should be addressed. E-mail: ftuczek@ac.uni-kiel.de (F.T.), vaneldik@chemie.uni-erlangen.de (R.v.E.).
† Christian-Albrechts-Universität Kiel.
‡ Friedrich-Alexander Universität Erlangen-Nürnberg.

(1) Cotton, F. A.; Murillo, C. A.; Bochmann, M.; Wilkinson G. *Advanced Inorganic Chemistry*, 6th ed.; John Wiley & Sons: New York, 1999.

10.1021/ic048674o CCC: $30.25
Published on Web 03/29/2005

the enzyme nitrogenase, which catalyzes the biological process of nitrogen fixation.[6]

If N_2 is coordinated end-on terminally to Mo/W complexes with diphosphine coligands, N−N cleavage requires two-electron reduction at the level of NNH_2 intermediates.[7] For practical reasons, these reactions have been studied using alkylated derivatives.[3] Thus, two-electron reduction of the Mo(IV) dialkylhydrazido(2−) complex $[MoBr(NNC_5H_{10})(dppe)_2]Br$ (compound $\mathbf{A}^{Mo}$) with BuLi or electrochemically has been found to generate under reductive elimination of the trans bromo ligand the five-coordinate, two-electron-reduced intermediate $[Mo(NNC_5H_{10})(dppe)_2]$ (compound $\mathbf{B}^{Mo}$), protonation of which with HBr in THF leads to formation of HNC_5H_{10} (piperidine) and the imido complex $[MoBr(NH)(dppe)_2]Br$ under cleavage of the N−N bond. The kinetics of this process has been studied in detail by Henderson et al. using nitrile solvents RCN and the weak acid $HNEt_3BPh_4$ (R = Me, Et, Ph).[8] Under these conditions, the observed rate constant of the overall splitting reaction, k_{obs}, is greatly decreased, and the nitrido and imido compounds $[(RCN)Mo(N)(dppe)_2]BPh_4$ and $[(RCN)Mo(NH)(dppe)_2](BPh_4)_2$, respectively, are obtained as final products (Scheme 1).

On the basis of the kinetic data, the alkylhydrazidium species $[Mo(NNHC_5H_{10})(dppe)_2]^+$ ($\mathbf{B}^{Mo}H^+$) has been postulated as the primary product resulting from protonation of $\mathbf{B}^{Mo}$. In nitriles, addition of a solvent molecule RCN to $\mathbf{B}^{Mo}H^+$ then was hypothesized to generate the six-coordinate intermediate $[(RCN)Mo(NNHC_5H_{10})(dppe)_2]^+$ ($RCN-\mathbf{B}^{Mo}H^+$), which subsequently rearranges to a bent alkylhydrazidium structure (R = Me, Et, Ph). This species either directly decays to the nitrido complex and piperidine with a rate constant k_4 or adds another proton at N_α to generate a doubly protonated species that subsequently undergoes N−N splitting with a rate constant k_5. The direct (k_4) and proton-assisted (k_5) decay channels of the primary intermediate $\mathbf{B}^{Mo}H^+$ both contribute to a N−N cleavage rate constant k_{obs} on the order of 1−60 s^{-1}, much smaller than that found for the reaction of compound $\mathbf{B}^{Mo}$ with HBr in THF ($k_{obs} > 300\ s^{-1}$).

Scheme 1. Mechanism of Reaction between $\mathbf{B}^{Mo}$ and Acid (Henderson et al.[8])

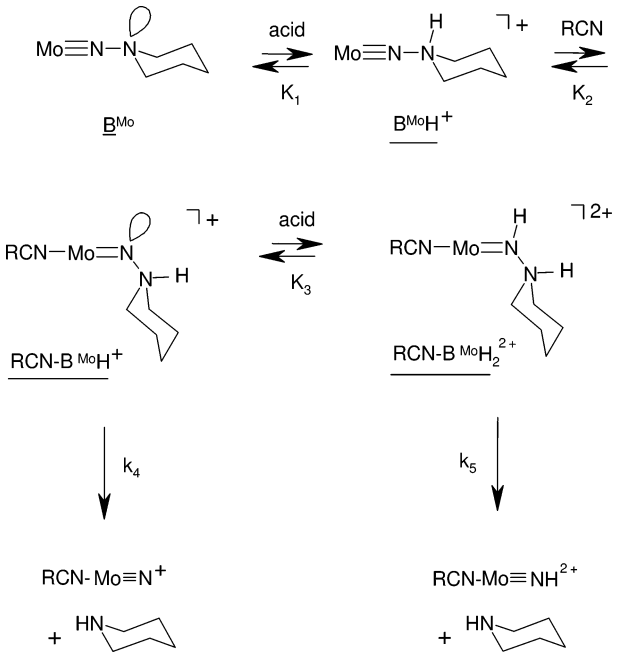

In the accompanying article,[9] compounds $\mathbf{A}^{Mo}$ and $\mathbf{B}^{Mo}$ and their tungsten counterparts $\mathbf{A}^{W}$ and $\mathbf{B}^{W}$ are characterized by X-ray structure analysis, spectroscopy, and DFT calculations on the model complex $[Mo(NNC_5H_{10})(PH_2C_2H_4PH_2)_2]$ ($\tilde{\mathbf{B}}$).[9] On the basis of these results, the N−N splitting of compound $\mathbf{B}^{W}$ is investigated spectroscopically and theoretically in the present study with the goal of elucidating the contributions of electronic structure to this process. Particular attention is thereby directed toward correlating the results of the theoretical treatment to the available kinetic and spectroscopic data and understanding the influence of the solvent and the acid on the mechanism of this reaction. To this end, the N−N cleavage process of $\mathbf{B}^{W}$ is monitored at various temperatures in different solvents (THF, acetonitrile, propionitrile, benzonitrile), employing $HNEt_3BPh_4$ and $HLutBPh_4$ as acids (Lut = 2,6-lutidine). Importantly, the reaction of $\mathbf{B}^{W}$ with $HNEt_3BPh_4$ in acetonitrile at room temperature is found to be much faster than the corresponding reaction of $\mathbf{B}^{Mo}$. A stopped-flow experiment and corresponding kinetic analysis are therefore performed for the protonation of $\mathbf{B}^{W}$ with $HNEt_3BPh_4$ in propionitrile at −70 °C. The two-electron-reduced compounds $\mathbf{B}^{Mo}$ and $\mathbf{B}^{W}$ contain three potentially Lewis-basic centers, i.e., N_α, N_β, and the metal. DFT calculations are employed to obtain information on the protonation processes at these different sites and to understand the reactivities of the corresponding protonated intermediates.

(2) (a) Laplaza, C. E.; Johnson, A. R.; Cummins, C. C. *J. Am. Chem. Soc*. **1996**, *118*, 709 and references therein. (b) Clentsmith, G. K. B.; Bates, V. M.; Hitchcock, P. B.; Cloke, F. G. N. *J. Am. Chem. Soc.* **1996**, *118*, 709. (c) Caselli, A.; Solari, E.; Scopelliti, R.; Floriani, C.; Re, N.; Rizzoli, C.; Chiesi-Villa, A. *J. Am. Chem. Soc.* **2000**, *122*, 709. (d) Fryzuk, M. D.; Kozak, C. M.; Bowdridge, M. R.; Patrick, B. O.; Rettig, S. J. *J. Am. Chem. Soc.* **2002**, *124*, 8389. (e) Fryzuk, M. D.; MacKay, B. A.; Johnson, S. A.; Patrick, B. O. *Angew. Chem., Int. Ed.* **2002**, *41*, 3709. (f) Fryzuk, M. D.; MacKay, B. A.; Patrick, B. O. *J. Am. Chem. Soc.* **2003**, *125*, 3234.

(3) (a) Pickett, C. J.; Leigh, G. J. *J. Chem. Soc., Dalton* **1981**, 1033. (b) Hussain, W.; Leigh, G. J.; Pickett, C. J. *J. Chem. Soc., Chem. Commun*. **1982**, 747.

(4) (a) Fryzuk, M. D.; Love, J. B.; Rettig, S. J.; Young, V. G. *Science* **1997**, *275*, 1445. (b) Pool, J. A.; Lobkovski, E.; Chirik, P. J. *Nature* **2004**, *427*, 527. (c) Smith, J. M.; Lachicotte, R. J.; Holland, P. L. *J. Am. Chem. Soc.* **2003**, *125*, 15752. (d) Le Grand, N.; Muir, K. W.; Pétillon, F. Y.; Pickett, C. J.; Schollhammer, P.; Talarmin, J. *Chem. Eur. J.* **2002**, *8*, 3115 and references therein. (e) Ishino, H.; Tokunaga, Sh.; Seino, H.; Ishii, Y.; Hidai, M. *Inorg. Chem.* **1999**, *38*, 2489. (f) Schrock, R. R.; Glassman, T. E.; Vale, M. G.; Kol, M. *J. Am. Chem. Soc*. **1993**, *115*, 1760 and references therein.

(5) (a) MacKay, B. A.; Fryzuk, M. D. *Chem. Rev.* **2004**, *104*, 385. (b) Fryzuk, M. D.; Johnson, S. A. *Coord. Chem. Rev.* **2000**, *200*−*202*, 379. (c) Hidai, M. *Coord. Chem. Rev.* **1999**, *185*−*186*, 99. (d) Hidai, M.; Mizobe, Y. *Chem. Rev.* **1995**, *95*, 1115.

(6) Thorneley, R. N. F.; Lowe, D. J. In *Molybdenum Enzymes*; Spiro, T. G., Ed.; Wiley-Interscience: New York, 1985.

(7) Chatt, J.; Pearman, A. J.; Richards, R. L. *J. Chem. Soc., Dalton Trans.* **1977**, 1852.

(8) Henderson, R. A.; Leigh, G. J.; Pickett, C. J. *J. Chem. Soc., Dalton Trans.* **1989**, 425.

(9) Horn, K. H.; Böres, N.; Lehnert, N.; Mersmann, K.; Näther, C.; Peters, G.; Tuczek, F. **2005**, *44*, 3016−3030.

Chart 1. [$HIPTN_3N$]MoN_2 Complex

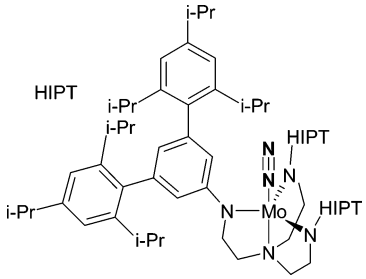

Whereas the protolytic N−N cleavage process of the alkylated compounds $\mathbf{B}^{Mo}$ and $\mathbf{B}^{W}$ provides considerable insight into the mechanistic features of this elementary reaction, the analogous step in the conversion of N_2 to NH_3 at Mo/W complexes with diphosphine ligands is complicated by cross reactions between NNH_2 species and their two-electron-reduced derivatives according to the simplified reaction

$$Mo^{IV}(NNH_2)^{2+} + Mo^{II}(NNH_2) \rightarrow Mo^{0}(N_2) + Mo^{IV}(NH)^{2+} + NH_3 \quad (1)$$

(where Mo = Mo(diphos)$_2$).[10] These problems have been overcome by using a Mo(III) complex with the novel triamidoamine ligand $[HIPTN_3N]^{3-}$ (hexaisopropylterphenyltriamidoamine), which provides a sterically shielded site for the conversion of N_2 to ammonia (Chart 1).[11] Insight into details of this process was obtained from the characterization of a number of intermediates. Specifically, protonation of the dinitrogen complex [$HIPTN_3N$]$Mo(N_2)$ (**1**) was found to lead to the NNH and NNH_2 complexes [$HIPTN_3N$]Mo(NNH) (**1-H**) and [$HIPTN_3N$]$Mo(NNH_2)^+$ (**2**), which could be isolated and characterized.[11a,b] N−N cleavage of **2** was hypothesized to proceed via the further reduced and protonated intermediates [$HIPTN_3N$]$Mo(NNH_2)$ (**3**) and [$HIPTN_3N$]-$Mo(NNH_3)^+$ (**5**), generating NH_3 and the nitrido complex [$HIPTN_3N$]MoN (**6**), which could be isolated and characterized as well. By protonation and reduction of **6**, the Mo(IV) ammine complex [$HIPTN_3N$]$Mo(NH_3)^+$ is formed, which, upon one-electron reduction, is able to rebind N_2 under release of NH_3, closing the reactive cycle. Importantly, the catalytic conversion of N_2 to NH_3 has been demonstrated for this system, achieving six turnovers with a yield of 65%. This represents a significant improvement over the Mo/W diphosphine systems for which a conversion of N_2 to NH_3 in three cycles could be achieved, however, with a total yield of only 0.75 NH_3 per metal complex.[10]

As two paradigms are thus available for the cyclic conversion of N_2 to NH_3, it is of significant interest to compare the reactive properties of these two systems from an electronic structure point of view, particularly with respect to the question of how N−N cleavage is mediated. To this end, DFT calculations on models **I** and **II** of the N_2 complex [$HIPTN_3N$]$Mo(N_2)$ (**1**) and its protonated/reduced derivative [$HIPTN_3N$]$Mo(NNH_2)^+$ (**2**) are presented here; Scheme 2 shows the corresponding calculated structures. For investigation of the subsequent N−N splitting, model **II** is first reduced by one electron, generating model **III** of neutral NNH_2 species [$HIPTN_3N$]$Mo(NNH_2)$ (**3**). Then, one proton is added to **III**, generating model **V** of the postulated hydrazidium intermediate [$HIPTN_3N$]$Mo(NNH_3)^+$ (**5**), which cleaves the N−N bond upon further one-electron reduction (Scheme 2). Alternatively, addition of one electron to **III** is considered, generating model **IV** of the negatively charged hydrazido(2−) intermediate [$HIPTN_3N$]$Mo(NNH_2)^-$ (**4**), which cleaves the N−N bond upon further protonation. These reactions are compared to the analogous protolytic N−N splitting reactions of compounds $\mathbf{B}^{Mo}$ and $\mathbf{B}^{W}$ (vide supra). Moreover, the electronic structures of the various Mo triamidoamine N_2, NNH_2, and NNH_3 species **I**−**V** are

Scheme 2. Possible Mechanisms of N−N Cleavage at a [$HIPTN_3N$]Mo Center

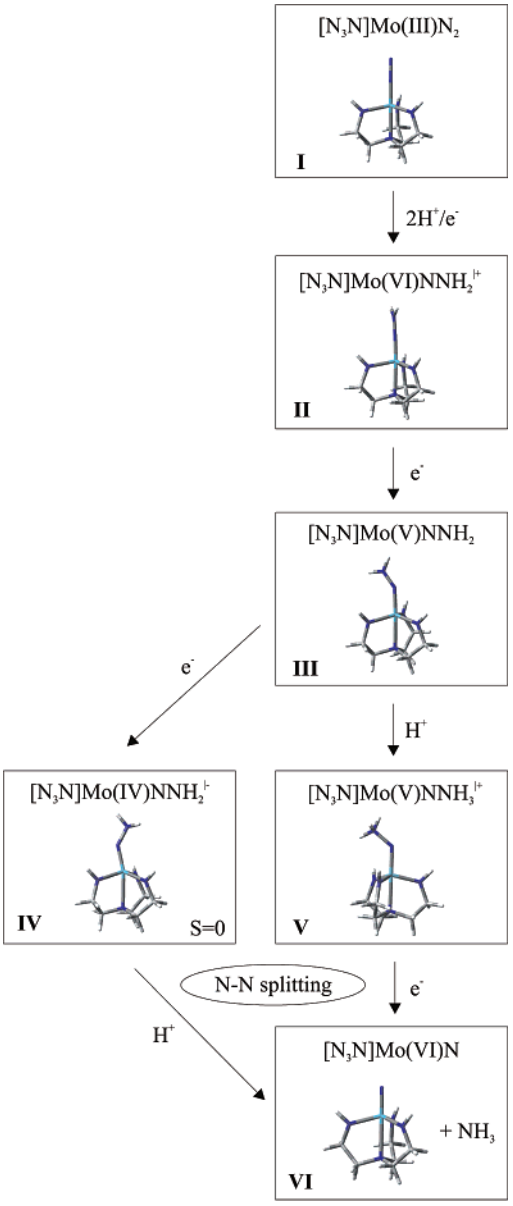

(10) Pickett, C. J.; Talarmin, J. *Nature (London)* **1985**, *317*, 652.
(11) (a) Yandulov, D. V.; Schrock, R. R. *J. Am. Chem. Soc.* **2002**, *124*, 6252. (b)Yandulov, D. V.; Schrock, R. R. *Science* **2003**, *301*, 76. (c) Yandulov, D. V.; Schrock, R. R.; Rheingold, A. L.; Ceccarelli, C.; Davis, W. M. *Inorg. Chem.* **2003**, *42*, 796. (d) Ritleng, V.; Yandulov, D. V.; Weare, W. W.; Schrock, R. R.; Hock, A. S.; Davis W. M. *J. Am. Chem. Soc.* **2004**, *126* (19), 6150.

determined. Metal−N and N−N distances as well as metal−N and N−N stretching frequencies are calculated, and theoretical predictions are compared to the available experimental data. The effects of the coligands and the d-electron configurations on the activation of the N_2 and NNH_x ligands are evaluated on the basis of electronic charges on the N_2 and NNH_x ligands. The theoretical results are correlated to the observed reactivities, and the implications on the transition-metal-mediated conversion of N_2 to NH_3 are discussed.

II. Experimental and Computational Procedures

Sample Preparation. $[W(NNC_5H_{10})(dppe)_2]$ (compound $\mathbf{B}^W$) was prepared as described in the accompanying article.[9] The ^{15}N-labeled compound was synthesized from the corresponding isotope-labeled dinitrogen complex $[W(^{15}N)_2(dppe)_2]$. All sample preparations were performed under a nitrogen or argon atmosphere using Schlenk techniques. All solvents were dried under argon. 2,6-Lutidine was purchased from Lancaster. Lutidine·$HBPh_4$ was synthesized from a metathesis reaction between lutidine·HCl and $NaBPh_4$ according to the method described in ref 12.

NMR Spectroscopy. ^{15}N NMR spectra were recorded on a Bruker Avance 400 Pulse Fourier transform spectrometer operating at a ^1H frequency of 400.13 MHz using a 5-mm inverse triple-resonance probe head. The reference as a substitutive standard was neat CH_3NO_2, $\delta(^{15}N) = 0$ ppm.

Stopped-Flow Measurements. Low-temperature kinetic data were obtained by recording time-resolved UV/vis spectra using a modified Bio-Logic stopped-flow module μSFM-20 instrument combined with cryo-stopped-flow accessory (Huber CC90 cryostat) and equipped with a J & M TIDAS high-speed diode array spectrometer with combined deuterium and tungsten lamp (200−1015 nm bandwidth). Isolast O-rings were used for all sealing purposes. Concentration-dependent measurements were performed by mixing different concentrations of $[HNEt_3]^+$ with at least 6 times lower concentrations of complex ([complex] = 0.053 mM) in a 1:1 volume ratio and also by using the same acid solution ($[[HNEt_3]^+]$ = 3.2 mM) and applying the option of a variable mixing volume ratio. During the measurements, nitrogen was flashed through the system. Data were analyzed using the integrated Bio-Kine software version 4.23 and also the Specfit/32 program.

DFT Calculations. Spin-restricted DFT calculations were performed for the model complex $[Mo(NNC_5H_{10})(PH_2C_2H_4PH_2)_2]$ ($\tilde{\mathbf{B}}$) and its solvent-coordinated and/or protonated derivatives using Becke's three-parameter hybrid functional with the correlation functional of Lee, Yang, and Parr (B3LYP).[13] The LANL2DZ basis set was used for the calculations. It applies the Dunning/Huzinaga full double-ζ (D95)[14] basis functions on the first row atoms and the Los Alamos effective core potentials plus DZ functions on all other atoms.[15] All computational procedures are used as they are implemented in the Gaussian 98 package.[16] Wave functions are plotted with the visualization program GaussView. Judging from the fact that the geometric and spectroscopic properties of $\mathbf{B}^W$ are well reproduced by $\tilde{\mathbf{B}}$, we refrained from carrying out parallel calculations on a W model system. Spin-restricted DFT calculations (B3LYP/LANL2DZ) were performed for the singlet ground state of model complexes $[N_3N]Mo^{VI}NNH_2^+$ (**II**) and $[N_3N]Mo^{IV}NNH_2^-$ (**IV**). In the case of model complexes $[N_3N]Mo^{III}N_2$ (**I**), $[N_3N]Mo^{V}NNH_2$ (**III**), $[N_3N]Mo^{IV}NNH_2^-$ (**IV**), and $[N_3N]Mo^{V}NNH_3^+$ (**V**), corresponding spin-unrestricted DFT calculations were performed for the doublet (**I**, **III**, **V**) and triplet (**IV**) states.

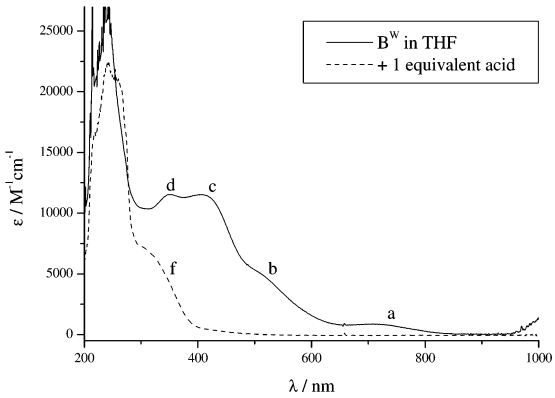

Figure 1. UV/vis spectrum of $\mathbf{B}^W$ and of protonation products in THF.

III. Results and Analysis

A. Protolytic N−N Cleavage of the W(dppe)$_2$ Dialkylhydrazido Complex $\mathbf{B}^W$. 1. Protonation of $\mathbf{B}^W$ with HLutBPh$_4$ in THF. The UV/vis absorption spectrum of $\mathbf{B}^W$ in THF is presented in Figure 1. Above 300 nm, it exhibits four bands at 720, 520, 412, and 350 nm that are denoted a−d. Upon protonation of $\mathbf{B}^W$ in THF at room temperature with 1 equiv of 2,6-lutidine·$HBPh_4$ (HLutBPh$_4$), bands a−d disappear within about 15 min, leaving a final spectrum (f) with an absorption feature at 320 nm.[17] Quantitative formation of piperidine in this reaction was demonstrated by GC. The 320-nm band in spectrum f is therefore associated with the nitrido complex $[W(dppe)_2(N)]^+$.

2. Protonation of $\mathbf{B}^W$ with HNEt$_3$BPh$_4$ in Propionitrile. To study the protolytic N−N cleavage of $\mathbf{B}^W$ in coordinating solvents, various nitriles were employed. Reaction of $\mathbf{B}^W$ with $HNEt_3BPh_4$ in acetonitrile was so fast that its kinetics could not be monitored, even with the stopped-flow technique at −35 °C. This indicates that the reaction of $\mathbf{B}^W$ with $HNEt_3BPh_4$ in this solvent is much faster than the corresponding reaction of $\mathbf{B}^{Mo}$, for which a stopped-flow study at room temperature has been performed.[8] Therefore, the reaction of $\mathbf{B}^W$ was investigated in propionitrile at −70 °C. UV/vis absorption spectra of $\mathbf{B}^W$ before and after protonation (Figure S1) are very similar to the corresponding spectra in THF

(12) Malinak, S. M.; Simeonov, A. M.; Mosier, P. E.; McKenna, C. E.; Coucouvanis, D. *J. Am. Chem. Soc*. **1997**, *119*, 1662.
(13) Becke, A. D. *J. Chem. Phys.* **1993**, *98*, 5648.
(14) Dunning, T. H., Jr.; Hay, P. J. In *Modern Theoretical Chemistry*; Schaefer, H. F., III, Ed.; Plenun: New York, 1976.
(15) (a) Hay, P. J.; Wadt, W. R. *J. Chem. Phys.* **1985**, *82*, 270 and 299. (b) Wadt, W. R.; Hay, P. J. *J. Chem. Phys.* **1985**, *82*, 284.
(16) Frisch, M. J.; Trucks, G. W.; Schlegel, H. B.; Scuseria, G. E.; Robb, M. A.; Cheeseman, J. R.; Zakrzewski, V. G.; Montgomery, J. A., Jr.; Stratmann, R. E.; Burant, J. C.; Dapprich, S.; Millam, J. M.; Daniels, A. D.; Kudin, K. N.; Strain, M. C.; Farkas, O.; Tomasi, J.; Barone, V.; Cossi, M.; Cammi, R.; Mennucci, B.; Pomelli, C.; Adamo, C.; Clifford, S.; Ochterski, J.; Petersson, G. A.; Ayala, P. Y.; Cui, Q.; Morokuma, K.; Malick, D. K.; Rabuck, A. D.; Raghavachari, K.; Foresman, J. B.; Cioslowski, J.; Ortiz, J. V.; Baboul, A. G.; Stefanov, B. B.; Liu, G.; Liashenko, A.; Piskorz, P.; Komaromi, I.; Gomperts, R.; Martin, R. L.; Fox, D. J.; Keith, T.; Al-Laham, M. A.; Peng, C. Y.; Nanayakkara, A.; Gonzalez, C.; Challacombe, M.; Gill, P. M. W.; Johnson, B.; Chen, W.; Wong, M. W.; Andres, J. L.; Gonzalez, C.; Head-Gordon, M.; Replogle, E. S.; Pople, J. A. *Gaussian 98*, revision A.7; Gaussian, Inc.: Pittsburgh, PA, 1998.
(17) Reaction conditions: 15 mL of solvent, $[\mathbf{B}^W] = 1.5$ mmol/L, 1 equiv of acid, room temperature, oxygen- and moisture-free conditions.

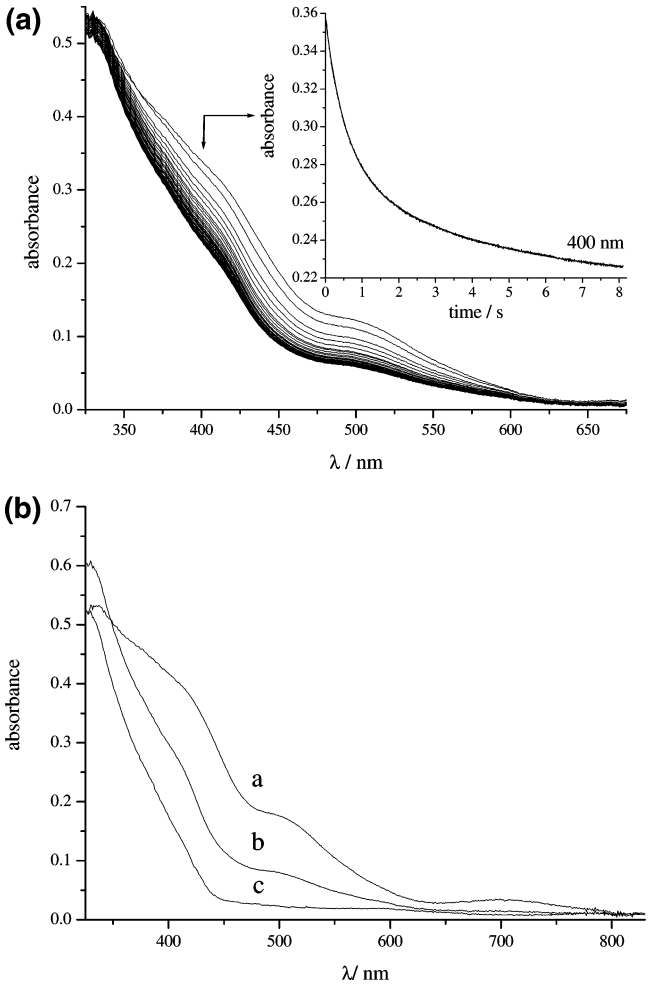

Figure 2. (a) Time evolution of the UV/vis spectra recorded at time intervals of 0.22 s. Experimental conditions: [$\mathbf{B}^{W}$] = 0.053 mM, [$HNEt_3BPh_4$] = 0.32 mM in propionitrile at −70 °C. Inset: Absorbance/time plot showing the evolution of absorbance at 400 nm. (b) Spectra of (a) starting, (b) intermediate, and (c) product species calculated from the rapid-scan measurements in Figure 2a.

(Figure 1), indicating that protonation of $\mathbf{B}^{W}$ in propionitrile also leads to the nitrido complex and piperidine.

Time-dependent spectra of the protonation of $\mathbf{B}^{W}$ (0.053 mM) with $HNEt_3BPh_4$ (0.32 mM) at −70 °C in propionitrile are shown in Figure 2a. The decay of the absorbance at 400 nm exhibits a biphasic character for which $k_{obs(1)} = 1.5 \pm 0.4\ s^{-1}$ and $k_{obs(2)} = 0.35 \pm 0.08\ s^{-1}$. It should be noted, however, that the first spectrum recorded immediately after mixing (see Figure 2b, spectrum a) in comparison to the spectrum of $\mathbf{B}^{W}$ (0.053 mM) and $HNEt_3BPh_4$ (0.32 mM) before mixing (cf. Figure S1, solid line) exhibits about 50% lower absorbance in the spectral range of 350−650 nm. This clearly shows that a fast reaction, which is ascribed to the rapid protonation of $\mathbf{B}^{W}$, has already occurred within the dead time of the stopped-flow instrument. In agreement with Scheme 1, the faster process ($k_{obs(1)}$) is attributed to solvent attack on the protonated intermediate $\mathbf{B}^{W}H^{+}$ and the slower process ($k_{obs(2)}$) to the N−N cleavage reaction of the corresponding solvent-coordinated intermediate EtCN−$\mathbf{B}^{W}H^{+}$. For a 10-fold higher acid concentration, the corresponding values of $k_{obs(1)}$ and $k_{obs(2)}$ are almost identical, i.e., 1.6 ± 0.4 and $0.36 \pm 0.09\ s^{-1}$, respectively. The option of

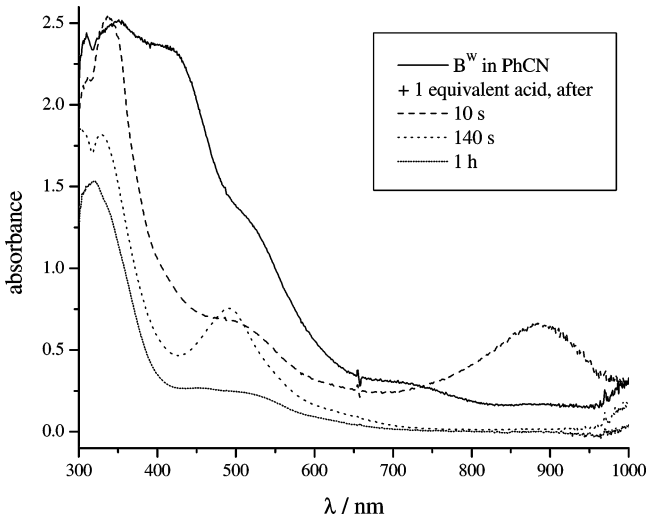

Figure 3. UV− vis spectrum of $\mathbf{B}^{W}$ and of time-dependent protonation products in benzonitrile.

a variable mixing volume ratio was applied for concentrations of $HNEt_3BPh_4$ up to 6 mM, and no changes in the $k_{obs(1)}$ and $k_{obs(2)}$ values could be observed. The independence of $k_{obs(1)}$ from the H^{+} concentration reflects the fact that protonation of $\mathbf{B}^{W}$ to the primary intermediate $\mathbf{B}^{W}H^{+}$ is much faster than solvent attack and already complete upon addition of 6 equiv of acid during the mixing time. A propionitrile solution of $\mathbf{B}^{W}$ was titrated with $HNEt_3BPh_4$, and it was observed that just a small excess of acid is required for complete protonation. The saturation of the initial protonation equilibrium at acid concentrations slightly in excess of the complex concentration has also been established for $\mathbf{B}^{Mo}$.[8] The fact that $k_{obs(2)}$ is also independent of the H^{+} concentration differs from the protonation of $\mathbf{B}^{Mo}$ for which the overall rate constant for N−N cleavage (k_{obs}) was found to depend on the acid concentration.[8]

Calculated spectra for the decay process of compound $\mathbf{B}^{W}$ are given in Figure 2b. It is clearly seen that the spectrum of the solvent-coordinated, protonated intermediate (**b**) observed after the first phase of the decay ($k_{obs(1)}$) has a higher absorbance in the UV region than both the nonsolvated, protonated species observed at "$t = 0$" (i.e., after the dead time of the apparatus) and the final product (**c**). The intermediate in spectrum b is a W(II) complex that is bent at N_α. Its electronic structure (orbital occupancy) is different from that of compound **B** (see below); in particular, the HOMO has changed from a metal-type dσ orbital to a metal-type dπ orbital. Hence, its absorption spectrum is different from that of compound **B** and its protonated derivative. The final product (**c**) (see Figure 2b and spectrum f in Figure 1) is a W(IV) nitrido or imido complex, with a low absorption at 400 nm.

3. Protonation of $\mathbf{B}^{W}$ with $HNEt_3BPh_4$ in Benzonitrile. In benzonitrile, the protolytic N−N cleavage of $\mathbf{B}^{W}$ with $HNEt_3BPh_4$ is dramatically slowed, rendering it possible to follow this process at room temperature. UV/vis spectroscopic monitoring of the reaction course, however, reveals characteristic differences from the results described above (Figure 3). The spectrum of unprotonated $\mathbf{B}^{W}$ in benzonitrile

Scheme 3. Formation of a Dialkylisodiazene Intermediate

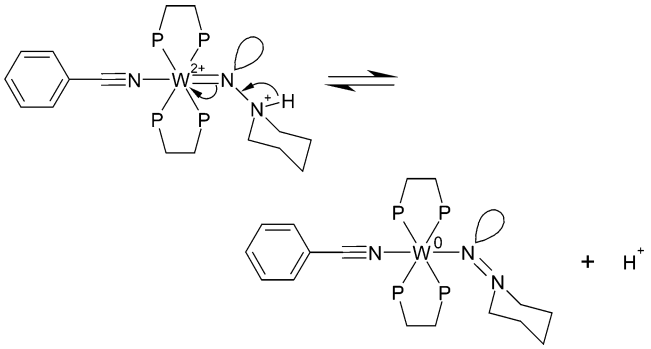

is almost identical to that in propionitrile (Figure S1) or THF (Figure 1). Upon protonation with 1 equiv of acid, an intense band appears at 900 nm that is not observable in propionitrile or in THF. This band subsequently shifts to 500 nm and then, in a much slower process, disappears upon conversion to the final spectrum. These observations obviously reflect changes in the electronic structure of the solvent-coordinated intermediate(s) that are caused by the replacement of propionitrile by benzonitrile. Because benzonitrile is more π-accepting than acetonitrile and propionitrile, we attribute the intermediate with the unusual 900-nm band to a benzonitrile-coordinated, bent W(0) dialkylisodiazene complex (Scheme 3). In this intermediate, which is stabilized by two π-back-bonding interactions to the benzonitrile ligand, the protonated hydrazidium ligand has transferred two electrons to the metal center, possibly under loss of its proton; at the same time, the N−N interaction is enhanced to a double bond. This explains why N−N cleavage is dramatically slowed. A charge-transfer (CT) transition could occur in this intermediate from the metal center to the π^* orbital of the bent isodiazene ligand, in analogy to the low-energy CT band observed in Fe-diazene complexes.[18]

The spectrum of the second intermediate already is very similar to that of the final product, except for the more pronounced absorption band around 500 nm. The intensity of this band has decreased in the spectrum of the final product (after 1 h). Interestingly, this band is not present in the spectrum of the benzonitrile nitrido complex $[W(N)(PhCN)(dppe)_2]^+$ prepared independently (cf. Figure S2). Only after several hours does this band disappear and the spectrum of the reaction mixture approach that of $[W(N)(PhCN)(dppe)_2]^+$. We therefore attribute the 500-nm band to a benzonitrile-coordinated, bent dialkylhydazidium intermediate with a very long N−N bond where complete N−N cleavage appears to be hindered by the electron-withdrawing effect of the coordinated benzonitrile ligand.

To confirm that N−N splitting of $\mathbf{B}^W$ takes place in benzonitrile, ^{15}N NMR spectroscopy was employed. The spectrum of $\mathbf{B}^W$ in benzonitrile exhibits a doublet at −18 ppm that is assigned to N_β, split by coupling with N_α (Figure S3). The signal of N_α is not observed, presumably because of broadening effects. Upon addition of $HLutBPh_4$, the signal at −18 ppm disappears, and two signals at −341.17 and −352.8 ppm are detected. These are assigned to piperidine and piperidinium, respectively (Figure S4).[19] It thus can be concluded that N−N splitting takes place in benzonitrile as well, but at a strongly decreased rate as compared to acetonitrile and propionitrile.

4. Theoretical Treatment. To obtain further insight into the mechanism of the protolytic N−N bond cleavage of compound $\mathbf{B}^W$, DFT was employed. As described in the accompanying article,[9] geometry optimization of a slightly simplified model $\tilde{\mathbf{B}}$ was found to closely match the experimentally observed geometry of $\mathbf{B}^W$. The HOMO of $\tilde{\mathbf{B}}$ containing two additional electrons compared to its precursor $\tilde{\mathbf{A}}$ corresponds to a linear combination of the metal d_σ orbital with a ligand orbital having N−N σ^* character, inducing a weakening of the N−N bond. Protonation of $\mathbf{B}^W$ was then simulated by attaching a proton to the N_β atom of the dialkylhydrazido(2−) ligand of $\tilde{\mathbf{B}}$ in a geometry derived from that of piperidine (HNC_5H_{10}). This generates structure $\tilde{\mathbf{B}}H^+$, which is a model for the alkylhydrazidium species $\mathbf{B}^WH^+$ (cf. Scheme 1). Importantly, global geometry optimization of this structure leads to separation into piperidine and the nitrido complex, corresponding to an exothermic (−41 kcal/mol) and spontaneous N−N cleavage process of $\mathbf{B}^W$ after protonation at N_β (Scheme 4). Figure 4a displays a relaxed potential energy surface (rPES) for the N−N splitting process of $\tilde{\mathbf{B}}H^+$, demonstrating that this reaction occurs without a barrier. The HOMO of $\tilde{\mathbf{B}}H^+$ containing a N−N antibonding interaction (cf. the accompanying article[9]) thereby evolves to the lone pair of piperidine. The five-coordinate nitrido complex will coordinate a solvent molecule after completion of the N−N cleavage process. The N−N bond-splitting reaction of $\tilde{\mathbf{B}}H^+$ thus can be considered as an orbital- and symmetry-allowed, heterolytic cleavage process that is associated with an oxidation of the metal center from +II to +IV. Note that this process occurs without significant bending of $\tilde{\mathbf{B}}H^+$ at N_α.

So far, the solvent has not been included in the calculation. However, as shown experimentally, solvent attack on the protonated derivatives of the bialkylated complexes $\mathbf{B}^{Mo}$ and $\mathbf{B}^W$ plays an important role in the N−N splitting reaction, at least in nitrile solvents. To obtain further information on this reaction mode, bonding of acetonitrile (R = Me) to the protonated intermediate $\mathbf{B}^WH^+$ was simulated by DFT, leading to the model MeCN−$\tilde{\mathbf{B}}H^+$. Attachment of the MeCN ligand to the linear molecule $\tilde{\mathbf{B}}H^+$ initially leads to an increase of energy (+16 kcal/mol; Scheme 4). Then, this structure bends at N_α, causing a change of one of the in-plane p-donor orbitals of the NNR_2 group (π_h^*) to a lone pair at N_α and a conversion of the HOMO of $\tilde{\mathbf{B}}H^+$ from a d_σ- to a d_π-type metal orbital. Importantly, this HOMO contains an antibonding contribution of the lone pair at N_α and a p orbital at N_β that is directed along the N−N axis and is antibonding with respect to the lone pair at N_α (Chart 2). Further geometry optimization of structure MeCN−$\tilde{\mathbf{B}}H^+$ leads to separation into the nitrido complex and piperidine,

(18) Lehnert, N.; Wiesler, B.; Tuczek, F.; Hennige, A.; Sellmann, D. *J. Am. Chem. Soc.* **1997**, *119*, 8869−8878.

(19) Duthaler, R. O.; Roberts, J. D. *J. Am. Chem. Soc.* **1978**, *100* (12), 3882.

Scheme 4. Protonation Pathways and Product Energies in Relation to $\tilde{\mathbf{B}}H^+$ (kcal/mol; *partial optimization; N−N distance fixed at 1.5 Å)

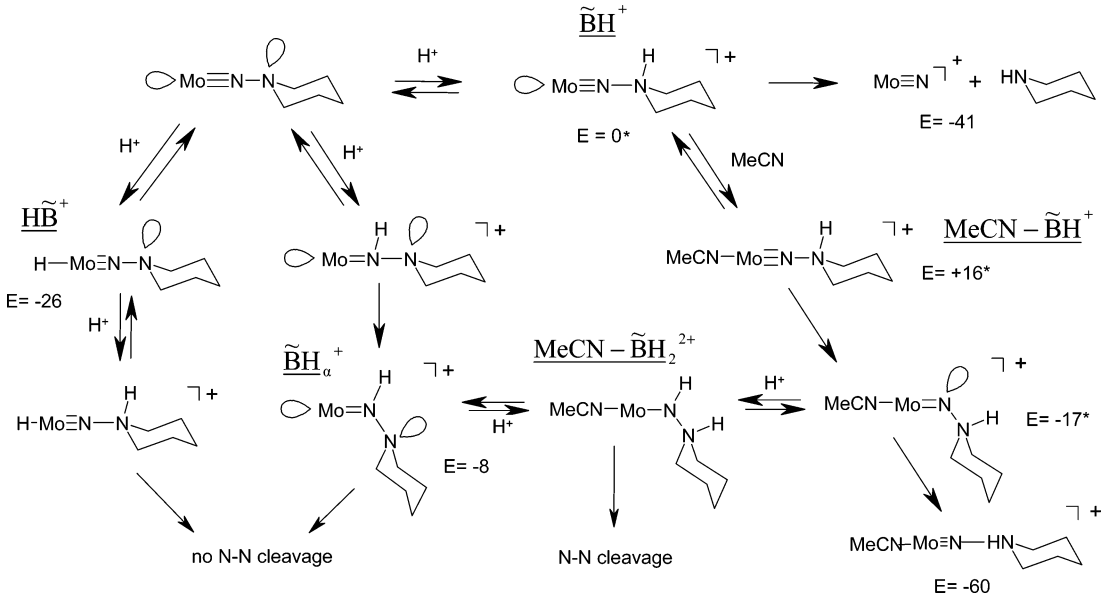

indicating that the nitrile-coordinated intermediates RCN−$\mathbf{B}^{W}H^+$ spontaneously cleave the N−N bond just as their nonsolvated counterpart does (Scheme 4). In analogy to the N−N cleavage process of this intermediate, the HOMO of structure MeCN−$\tilde{\mathbf{B}}H^+$ is thereby converted to the N lone pair of piperidine. Again, the N−N antibonding interaction in the HOMO of the doubly reduced, protonated intermediate is essential for this spontaneous, heterolytic N−N cleavage process.

With respect to the retardation of the N−N splitting reaction of $\mathbf{B}^{W}$ in benzonitrile (cf. section III.A.3), it also appeared of interest to treat the benzonitrile-coordinated, N_β-protonated intermediate PhCN−$\mathbf{B}^{W}H^+$ by DFT. Geometry optimization of the corresponding model MeCN−$\tilde{\mathbf{B}}H^+$ initially leads to bending at *both* N_α of the NNR_2 group *and* the nitrogen atom of the nitrile ligand, indicating some charge transfer to the benzonitrile ligand. Further DFT geometry optimization leads to N−N cleavage, suggesting that spontanous N−N splitting occurs in benzonitrile as well. This is in agreement with the ^{15}N NMR spectroscopic evidence for N−N cleavage of $\mathbf{B}^{W}$ in this solvent (vide supra) and the similar findings of Henderson et al. for $\mathbf{B}^{Mo}$.[8] The observed decrease of the N−N splitting rate of $\mathbf{B}^{W}$ in benzonitrile as compared to the rates in acetonitrile and propionitrile must be a consequence of the delocalization of electron density into the π^* orbitals of the benzonitrile ligand, which is also evident from the unusual features detected by UV/vis spectroscopic monitoring of the protonation reaction (Figure 3). Back-bonding into the benzonitrile ligand acts to decrease the basicity on N_β, possibly causing a partial deprotonation of PhCN−$\tilde{\mathbf{B}}H^+$ (cf. Scheme 3), and introduces a barrier for N−N cleavage (which is not evident in the calculation based on the simplified model); both factors effectively slow the N−N cleavage process.

Reduced basicity of the benzonitrile-coordinated species PhCN−$\mathbf{B}^{Mo}H^+$ (however, at N_α) has also been invoked by Henderson et al.[8] to explain that, for this solvent, no acid-assisted N−N cleavage of $\mathbf{B}^{Mo}H^+$ could be detected. This pathway was hypothesized to involve a second protonation at N_α, leading to the doubly protonated species RCN−$\mathbf{B}^{Mo}H_2^{2+}$ (R = Me, Et), which undergo N−N splitting with a rate constant k_5 (Scheme 1). Geometry optimization of the corresponding doubly protonated, acetonitrile-coordinated structure MeCN−$\tilde{\mathbf{B}}H_2^{2+}$, however, was found to leave the N−N bond intact. To obtain more information on the energetics of N−N cleavage, a relaxed potential energy scan (rPES) along the N−N coordinate was performed (Figure 4b). Interestingly, the rPES shows an exothermic splitting process of the N−N bond (approximately −45 kcal/mol) with a very small activation barrier (∼1 kcal/mol). Upon elongation of the N−N bond, the N_α proton first flips into a position between N_α and N_β. Then proton transfer from N_α to N_β occurs.[20] This theoretical result supports the presence of an alternative, acid-assisted N−N cleavage pathway for the intermediates RCN−$B^{M}H^+$ (M = Mo, W), associated with the rate constant k_5 in Scheme 1. Experimentally, the second protonation (at N_α) is characterized by an equilibrium constant K_3, making the overall rate of this decay path effectively dependent on the product k_5K_3. The fact that no dependence of the N−N cleavage rate on the acid concentration is observed for the protolytic N−N cleavage of $\mathbf{B}^{W}$ in propionitrile can then be explained in two ways: (i) K_3 is already saturated by a small excess of acid (exactly as for the protonation equilibrium at N_β), and the observed N−N cleavage process is dominated by the k_5 pathway; (ii) K_3 is so small that the k_5 route is unimportant in comparison to the k_4 pathway. On the basis of the observation that the N−N cleavage reaction of $\mathbf{B}^{W}$ is much faster than of that $\mathbf{B}^{Mo}$, we assume that alternative i is correct. This would be in agreement with the general rule that tungsten complexes are easier to protonate than their molybdenum counterparts.[21]

(20) Of course, the resulting nitrido complex will be protonated in the presence of an excess of acid.
(21) Henderson, R. A.; Leigh, G. J.; Pickett, C. *Adv. Inorg. Chem. Radiochem.* **1983**, *27*, 197−292.

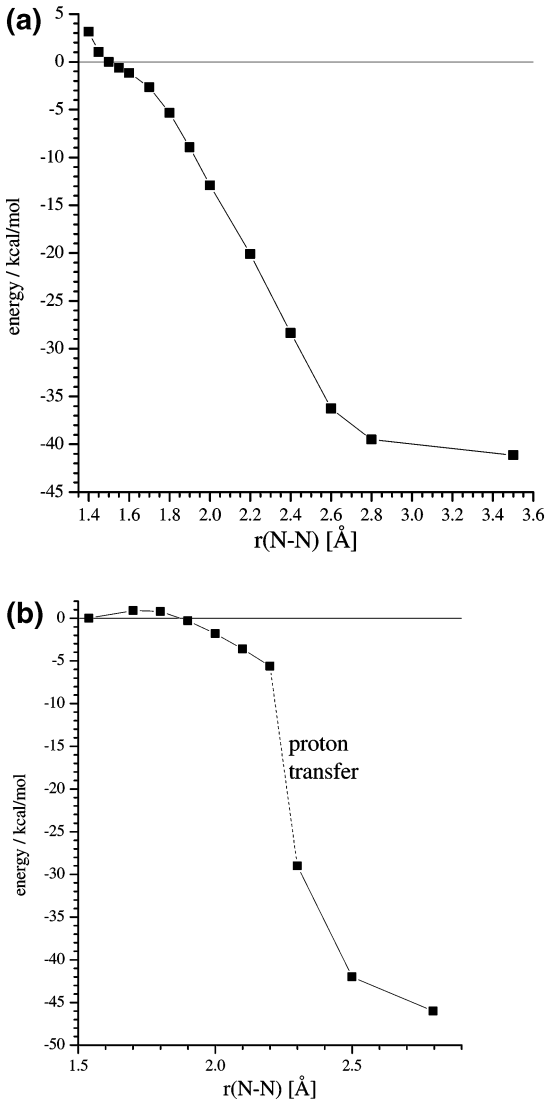

Figure 4. rPES for N−N splitting reactions of (a) $\tilde{\mathbf{B}}H^+$ and (b) MeCN−$\tilde{\mathbf{B}}H_2^{2+}$.

Chart 2. Contour Plot of HOMO from MeCN−BH^+

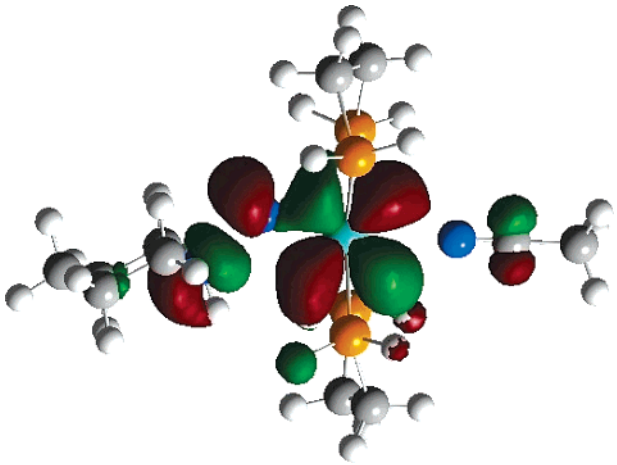

With respect to further mechanistic scenarios for the N−N splitting of $\mathbf{B}^W$, initial protonation at the metal has to be considered. As shown in the accompanying article,[9] the HOMO of this molecule exhibits a large lobe toward the open side of the complex, making this a potential site for attack by H^+ as well. For this reason, bonding of a proton to $\tilde{\mathbf{B}}$ was simulated by DFT, leading to the *metal*-protonated species $H\tilde{\mathbf{B}}^+$. After geometry optimization, the energy of this structure was found to be 26 kcal/mol lower than that of the N_β-protonated species $\tilde{\mathbf{B}}H^+$ (Table 1), and the N−N bond was left intact. In this case, however, N−N cleavage (even after further protonation at N_β) is prevented by formation of a hydrido group trans to the NNR_2 ligand that consumes the electrons in the HOMO of $\mathbf{B}^W$ necessary for N−N cleavage. Metal protonation thus would correspond to a thermodynamically favorable, but nonproductive step in the overall reaction scheme, lowering the observed N−N splitting rate. It must be taken into account, on the other hand, that protonation of $\mathbf{B}^W$ proceeds by proton transfer from undissociated acid or protonated solvent,[8] imposing some steric requirements on this process. A space-filling representation of the structure of $\mathbf{B}^W$ shows that the metal is highly shielded by the phenyl groups of the dppe ligands (Figure 5). Moreover, upon protonation at N_β, solvent attack on $\mathbf{B}^W$ is rapid in coordinating solvents (vide supra). Both effects would act to kinetically disfavor protonation at the metal center.

Table 1. Energies of Protonated Intermediates

intermediate	energy (a.u.)	relative energy (kcal/mol)
$\tilde{\mathbf{B}}H^{+\,a}$	−561.878083	0
$H\tilde{\mathbf{B}}^{+\,b}$	−561.920119	−26
$\tilde{\mathbf{B}}H_\alpha{}^{+\,b}$	−561.890336	−8
MeCN−Mo≡N^+ + $C_5H_{11}N^b$	−561.9743466	−60
Mo≡N^+ + $C_5H_{11}N^b$	−561.943661	−41

[a] N−N distance fixed at 1.50 Å, partially optimized. [b] Fully optimized.

Judging from the finding that N_α is more negative than N_β in $\mathbf{B}^W$,[22] initial protonation of $\mathbf{B}^W$ should be possible at N_α as well. DFT geometry optimization of the corresponding intermediate $\tilde{\mathbf{B}}H_\alpha{}^+$ leads to bending of the NNR_2 group at N_α, leaving the N−N bond intact (relative energy = −8 kcal/mol). As evidenced by a DFT PES, elongation of the N−N bond by 3 Å from the optimized value is endothermic by 70 kcal/mol (Figure S5); protonation at N_α therefore does not lead to N−N splitting under ambient conditions. This corresponds to the fact that heterolytic cleavage after protonation at N_α would lead to a negatively charged (piperidide) fragment and the imido complex, which energetically is highly unfavorable. To mediate N−N cleavage, the proton therefore has to shift from N_α to N_β, which can be effected by a combination of deprotonation/reprotonation steps (Scheme 4).

To conclude, protonation at N_β is found by DFT to induce an exothermic and activationless N−N cleavage process, in both the unsolvated and the solvent-coordinated primary intermediate $\mathbf{B}^WH^+$ and RCN−$\mathbf{B}^WH^+$. From the literature data and our own experimental results, solvent attack on the primary intermediate $\mathbf{B}^WH^+$ is faster than N−N splitting of the solvated intermediate RCN−$\mathbf{B}^WH^+$. The same probably holds for the N−N cleavage process of the unsolvated intermediate $\mathbf{B}^WH^+$; i.e., this direct decay channel also

(22) cf. Table 11 of the accompanying article.[9]

Table 2. Comparison of Calculated Structures **I**−**VI** with Experimental Results

complex[a]		data source[b]	bond lengths (Å) N−N	Mo−N	Mo−N_{AD}[c,d]	MoN_{AM}[e]	angles (deg) MoNN	N_{AM}MoN
$[N_3N]Mo^{III}N_2$ $S = 1/2$	**I**	X-ray	1.06	1.96	1.98	2.19	179.2	179.8
		opt	1.17	1.97	1.99	2.25	178.5	178.5
$[N_3N]Mo^{VI}NNH_2^+$	**II**	opt	1.32	1.78	1.96	2.31	177.0	177.6
$[N_3N]Mo^{V}NNH_2$	**III**	opt	1.35	1.86	1.99	2.34	142.0	176.6
$[N_3N]Mo^{IV}NNH_2^-$ $S = 0$	**IV**	opt	1.42	1.82	2.03	2.49	141.0	159.8
$[N_3N]Mo^{V}NNH_3^+$	**V**	opt	1.57	1.85	1.96	2.35	128.9	179.2
$[N_3N]Mo^{IV}N$	**VI**	X-ray	−	1.65	2.00	2.40	−	179.1
		opt	−	1.70	1.98	2.56	−	175.2

[a] $[N_3N] = (HNCH_2CH_2)_3N^{3-}$. [b] opt = optimized structure, X-ray data taken from ref 11c. [c] Data are averaged for simplification. [d] N_{AD} is the nitrogen atom of the Amides. [e] N_{AM} is the nitrogen atom of the amine.

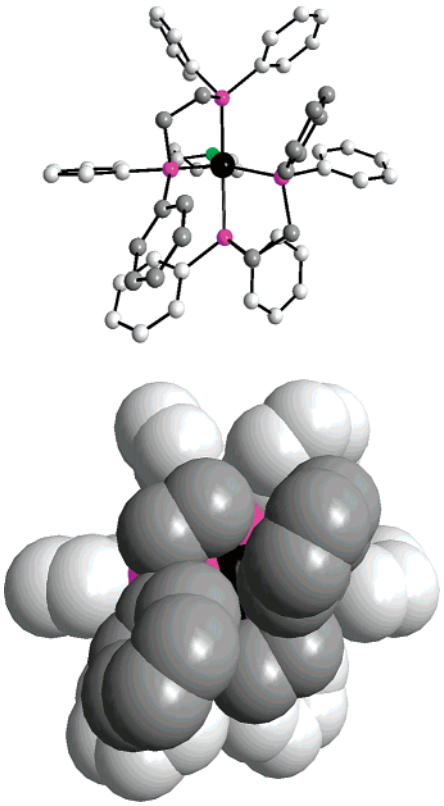

Figure 5. Structure of $\mathbf{B}^{W}$: view of the shielded metal side.

appears to be slower than solvent attack on the protonated intermediate $\mathbf{B}^{W}H^+$. Direct N−N cleavage of $\mathbf{B}^{W}H^+$ thus appears to be intercepted by solvent attack in coordinating solvents. N−N cleavage of the doubly protonated intermediate (at N_α *and* N_β), finally, is theoretically predicted to occur in an almost activationless fashion as well. In contrast to $\mathbf{B}^{Mo}$, the protonation preequilibrium of this decay channel appears to be saturated for $\mathbf{B}^{W}$ in the presence of an excess of acid. Under such conditions, the observed N−N cleavage process of $\mathbf{B}^{W}$ is therefore dominated by the decay of the doubly protonated intermediate.

B. Protonation, Reduction, and N−N Cleavage of Dinitrogen in [$Mo^{III}(N_2)$(triamidoamine)]. 1. Introductory Remarks. DFT calculations and geometry optimizations have been performed for the complexes $[N_3N]Mo^{III}(N_2)$ (**I**) and $[N_3N]Mo^{VI}(NNH_2)^+$ (**II**), which are models for the respective N_2 and NNH_2 intermediates of the [$HIPTN_3N$]-Mo fragment (Chart 1). Moreover, DFT calculations have been performed on the hypothetical intermediates $[N_3N]$-$Mo^{V}(NNH_2)$ (**III**), $[N_3N]Mo^{IV}(NNH_2)^-$ (**IV**), and $[N_3N]$-$Mo^{V}(NNH_3)^+$ (V) ([N_3N] = triamidoamine; the terphenyl substitutents of $HIPTN_3N$ have been replaced by hydrogen atoms in these calculations). A comparison between calculated bond distances/angles and experimentally determined structural data is given in Table 2. Calculated frequencies are compared with available spectroscopic data in Table 3. NPA charges for the calculated structures are given in Table 4; energies and decompositions for important orbitals of **I**, **III**, and **V** are collected in Tables 5−7.

Table 3. Comparison of Calculated and Observed Frequencies of Complexes **1**, **2**, and **6** with Models **I**, **II**, **V**, and **VI**

complex		mode	experimental[a,b] ^{14}N	experimental[a,b] ^{15}N	B3LYP[a] ^{14}N	B3LYP[a] ^{15}N
$[N_3N]Mo^{III}N_2$ $S = 1/2$	**I**	ν(N−N)	1990	1924	1911	1844
$[N_3N]Mo^{VI}NNH_2^+$	**II**	$\nu(N-H)_{as}$	3379	3370	3691	3679
		$\nu(N-H)_{s}$	3274	3270	3542	3538
		ν(N−N)	−	−	1487	1443
$[N_3N]Mo^{V}NNH_3^+$	**V**	ν(N−N)	−	−	467	455
		ν(Mo−N)	−	−	712	700
$[N_3N]Mo^{IV}N$	**VI**	ν(Mo−N)	1013	986	1090	1059

[a] In cm^{-1}. [b] Data taken from ref 11c.

Table 4. NPA Charges of Model Complexes **I**−**VI**

complex[a]		atom Mo	Nα	Nβ	H[b]	N_{AD}[b,c]	N_{AM}[d]
$[N_3N]Mo^{III}N_2$ $S = 1/2$	**I**	1.10	−0.18	−0.05	−	−0.90	−0.56
$[N_3N]Mo^{VI}NNH_2^+$	**II**	1.26	−0.17	−0.57	0.43	−0.82	−0.58
$[N_3N]Mo^{V}NNH_2$	**III**	1.19	−0.37	−0.65	0.38	−0.91	−0.58
$[N_3N]Mo^{IV}NNH_2^-$ $S = 0$	**IV**	0.87	−0.49	−0.71	0.33	−0.94	−0.57
$[N_3N]Mo^{V}NNH_3^+$	**V**	1.31	−0.49	−0.67	0.45	−0.86	−0.58
$[N_3N]Mo^{IV}N$	**VI**	1.23	−0.42	−	−	−0.89	−0.60

[a] $[N_3N] = (HNCH_2CH_2)_3N^{3-}$. [b] Charge for each H atom. [c] N_{AD} is the nitrogen atom of the amides. [d] N_{AM} is the nitrogen atom of the amine.

2. N_2 Complex (I). As a starting point for the investigation of the N−N cleavage process in the Mo triamidoamine system, the electronic structure of the dinitrogen complex $[N_3N]Mo^{III}(N_2)$ (**I**) is determined. A DFT study on **I** has been presented before.[23] The d-orbital energy level scheme of **I** is typical for a trigonal-bipyramidal complex (Figure 6 and Table 5). The $d_{x^2-y^2}$ and d_{xy} orbitals are shifted to high energy by strong σ- and π-antibonding interactions of the amide p-donor orbitals within the trigonal plane. At lower energy are found the degenerate d_{xz} and d_{yz} orbitals, which are

(23) Cui, Q.; Musaev, D. G.; Svensson, M.; Sieber, S.; Morokuma, K. *J. Am. Chem. Soc.* **1995**, *117*, 12366.

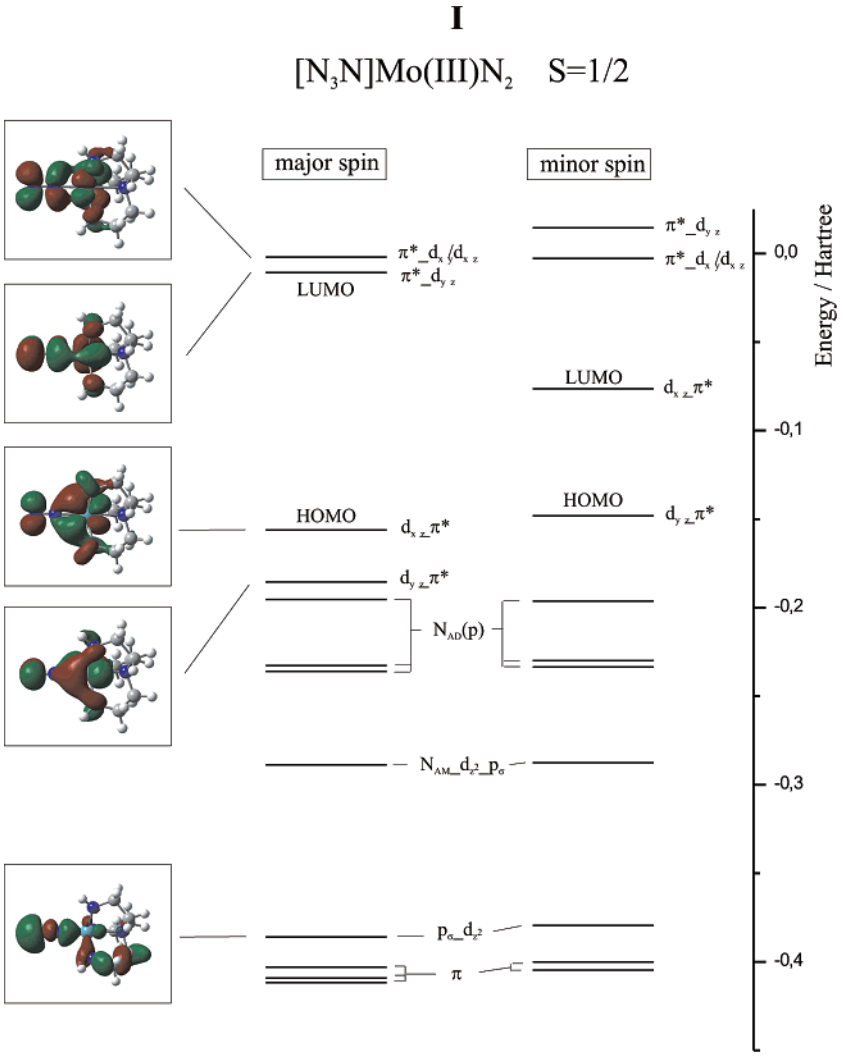

Figure 6. MO diagram and contour plots of important molecular orbitals of **I**.

Table 5. Charge Contribution of Model Complex **I**

orbital	label	energy (hartree)	α spin charge decomposition				
			Nα	Nβ	Mo	N_{AD}	N_{AM}
π^*–d_{xy}/d_{xz}	56	−0.00191	19	19	29	12	1
π^*–d_{z^2}/d_{yz}	55	−0.01069	27	26	21	8	1
d_{xz}–π^*	54	−0.15617	2	19	61	9	0
d_{yz}–π^*	53	−0.18548	1	15	65	10	0
N_{AD}	52	−0.19524	0	0	2	78	1
N_{AD}	51	−0.23272	0	0	22	56	1
N_{AD}	50	−0.23589	0	0	17	62	0
N_{AM}–p_σ–d_{z^2}	49	−0.28873	4	2	7	2	55
p_σ–d_{z^2}	40	−0.38605	19	53	6	6	1
π	39	−0.40297	50	34	3	1	0
π	38	−0.40916	15	15	2	21	7
π	37	−0.41176	33	26	3	10	3

nonbonding with respect to the amide orbitals but back-bonding with respect to the dinitrogen orbitals. Population of these orbitals with the three electrons of Mo(III) gives rise to a ^{2}E ground state. NBO charge analysis indicates a charge of −0.18 at N_α and −0.05 at N_β, comparable to those of Mo/W dinitrogen complexes with diphosphine coligands.[24] At 1.17 Å, the calculated N−N bond length is larger than experimentally determined (1.06 Å), indicating that the activation of this ligand predicted by the calculation is too large. Correspondingly, the N−N stretching frequency is calculated at 1911 cm^{-1}, lower than experimentally observed (1990 cm^{-1}).

3. Mo(VI) NNH_2 Complex (II). Bonding of two protons to the dinitrogen complex **I** along with one-electron reduction gives the NNH_2 complex $[N_3N]Mo(NNH_2)^+$ (**II**). The HOMO of this species is a nonbonding linear combination of amide lone pairs (Figure S6). As described earlier, the planar NNH_2 ligand has an in-plane π_h^* orbital that mostly corresponds to a p-donor orbital at N_α, whereas the out-of plane orbital π_v^* has N−N π^* character.[24] Below the HOMO are the bonding combinations of Mo d_{yz} and d_{xz}/d_{xy} with the NNH_2 π_v^* and π_h^* orbitals, respectively, which are primarily of *ligand* character (Table S1); LUMO and LUMO + 1 are formed by the corresponding metal−ligand anti-bonding combinations. The electrons associated with metal−ligand π-bonding can therefore be assigned to the ligand, corresponding to a Mo(VI)/hydrazido(2−) formulation. However, NBO charge analysis indicates that the total charge on the NNH_2 ligand is slightly positive. This indicates a strong donation of the 2− ligand charge back to the Mo(VI) metal center, effectively leading to a neutral bound isodiazene

(24) Lehnert, N.; Tuczek, F. *Inorg. Chem.* **1999**, *38*, 1671.

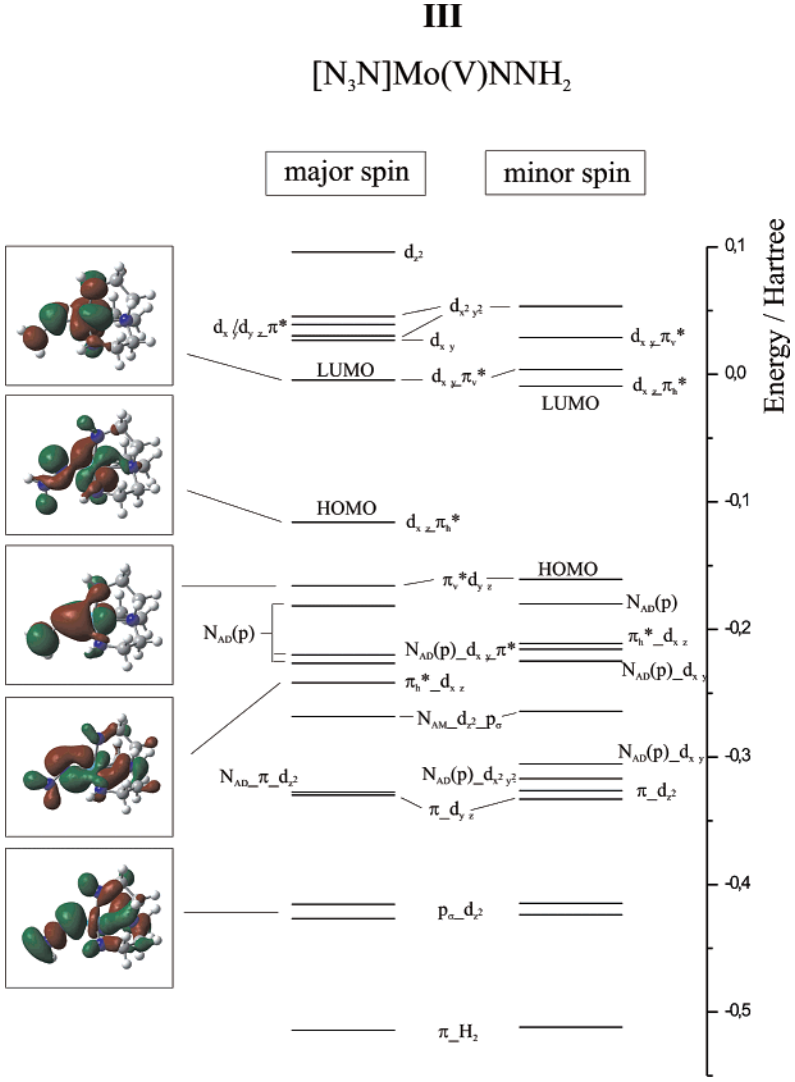

Figure 7. MO diagram and contour plots of important molecular orbitals of **III**.

species. This also agrees with the N−N bond length of 1.32 Å and the N−N stretching frequency of 1487 cm^{-1}, which both are indicative of a N−N double bond.[18,24] Complex **II** therefore corresponds to a Mo(VI) hydrazido(2−) species that is subject to large ligand → metal charge donation because of the highly positive charge on the metal center.

4. Mo(V) NNH_2 Complex (III). Transfer of one electron to **II** gives the putative neutral $S = {}^1/_2$ Mo(V) species $[N_3N]$-Mo(NNH_2) (**III**). DFT geometry optimization of this structure reveals bending of the NNH_2 group at N_α in the NH_2 plane, causing conversion the π_h^* p-donor orbital to a lone pair at N_α (for simplicity, we retain the π_h^* formulation for this orbital). The SOMO of **III** is a metal d_{xz} orbital with an antibonding contribution from the lone pair at N_α (d_{xz}–π_h^*, Figure 7 and Table 6). The corresponding antibonding combination with π_v^*, d_{xy}–π_v^*, is unoccupied. Because of population of the SOMO that is metal−ligand antibonding but N−N nonbonding, the metal−N bond of **III** is elongated by 0.08 Å with respect to that in **II**, whereas the N−N bond length is increased by only 0.03 Å.

5. Mo(IV) NNH_2 Complex (IV) and Its Protolytic N−N Cleavage. Addition of one electron to **III** generates the doubly reduced NNH_2 complex $[N_3N]Mo^{IV}(NNH_2)^-$ (**IV**), which, upon protonation, cleaves the N−N bond. The two electrons of the Mo(IV) configuration give rise to $S = 0$ and $S = 1$ states, the former being found at lower energy

Table 6. Charge Contribution of Model Complex **III**

orbital	label	energy (hartree)	α spin charge decomposition					
			Nα	Nβ	Mo	H	N_{AD}	N_{AM}
d_{z^2}	63	0.09590	9	3	27	3	5	13
$d_{x^2-y^2}$	61	0.04551	4	1	57	1	18	0
d_{xy}/d_{yz}–π^*	60	0.03909	7	3	60	1	12	0
$d_{x^2-y^2}$	59	0.03026	0	0	79	0	6	0
d_{xy}	58	0.02681	0	1	79	0	6	0
d_{xy}–π_v^*	56	−0.00448	19	8	40	0	11	1
d_{xz}–π_h^*	55	−0.11599	18	5	49	5	9	1
π_v^*–d_{yz}	54	−0.16575	13	30	42	0	8	0
N_{AD}(p)	53	−0.18145	0	0	1	0	77	1
N_{AD}(p)	52	−0.21997	4	0	13	1	61	1
N_{AD}(p)	51	−0.22645	4	1	17	1	56	1
π_h^*–d_{xz}	50	−0.24180	34	2	30	7	4	13
N_{AM}–d_{z^2}–p_σ	49	−0.26819	12	1	9	2	2	46
N_{AD}–π–d_{z^2}	46	−0.32755	6	10	12	0	39	3
π–d_{yz}	45	−0.32986	25	43	7	0	11	1
p_σ	37	−0.41564	12	6	4	1	11	14
p_σ–d_{z^2}	36	−0.42684	40	20	13	2	6	5
π–H_2	29	−0.51441	6	65	1	26	0	0

V

$[N_3N]Mo(V)NNH_3^{|+}$

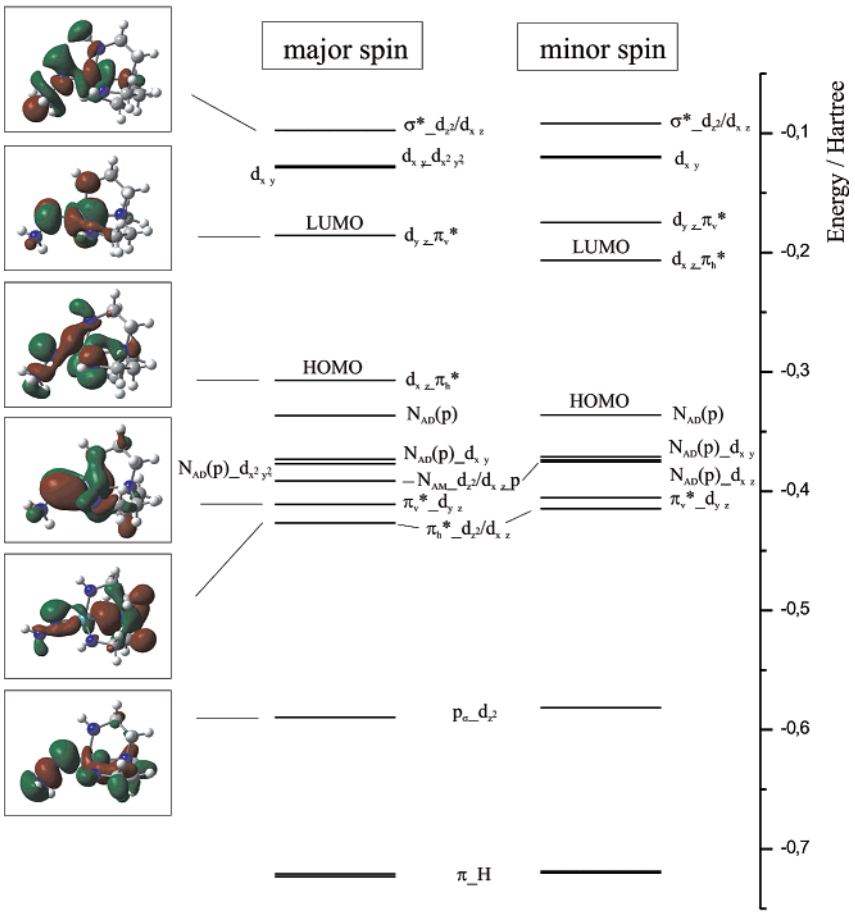

Figure 8. MO diagram and contour plots of important molecular orbitals of **V**.

(9.39 kcal mol^{-1}). Geometry optimization of the $S = 0$ complex leads to a doubly bent NNH_2 ligand (Scheme 2). The HOMO of **IV** is an antibonding combination of a metal d_{xz} orbital with the lone pair at N_α derived from π_h^*. Moreover, this orbital contains a contribution of a N_β p orbital along the N−N bond that is antibonding to the lone pair at N_α (Figure S7). At lower energy is found the bonding combination of the out-of-plane π_v^* with the metal d_{yz} orbital, which is of primarily ligand character (Table S2). This bonding description would correspond to a Mo(IV) hydrazido(2−) formulation for **IV**. This is supported by a N−N bond length of 1.42 Å, indicative of N−N single bond character. NBO charge analysis gives a negative charge of −0.6 for the NNH_2 group, corresponding to back-donation of −1.4 charge units from this ligand to the Mo(IV) metal center.

If a proton is added to model **IV** at N_β, spontaneous N−N cleavage takes place upon geometry optimization and the separate components ammonia and nitrido complex are obtained. Judging from the above bonding description, this corresponds to a heterolytic N−N cleavage process proceeding by two-electron transfer from the HOMO of the protonated derivative of **IV** to the lone pair of NH_3, which is preformed in the HOMO of **IV**. The triplet state of **IV** has not been included in this treatment because it is higher in energy than the singlet state (vide supra) and requires an intersystem crossing along the N−N cleavage path to give the diamagnetic products.

6. Mo(V) NNH_3 Complex (V) and Its Reductive N−N Cleavage. As an alternative to the protolytic N−N cleavage process described above, one proton can be added to **III**, leading to the NNH_3 complex $[N_3N]Mo^V(NNH_3)^+$ (**V**; Scheme 2). Exactly as for **III**, structure **V** has a NNH_3 ligand bent at N_α. The single d electron is contained in the SOMO ⟨55⟩ of **V**, which, as in the case of **III**, is an antibonding combination of a metal orbital with the lone pair at N_α derived from π_h^* (Figure 8, Table 7). Importantly, this orbital also contains a p orbital at N_β directed along the N−N bond, effectively leading to a N−N antibonding interaction with the lone pair at N_α. This is relevant to the N−N splitting process considered below. The other p-donor orbital at N_α of the NNH_3 group that is derived from the out-of-plane orbital π_v^* is involved in a π-bonding fashion with d_{yz} in MO ⟨50⟩.

As indicated by the calculated bond distances, both the N−N and the metal−N bonds are greatly elongated in this

Table 7. Charge Contribution of Model Complex **V**

orbital	label	energy (hartree)	α spin charge decomposition					
			Nα	Nβ	Mo	H	N_{AD}	N_{AM}
$\sigma^*-d_{z^2}/d_{xz}$	60	−0.09762	33	17	32	3	5	3
$d_{xy}/d_{x^2-y^2}$	59	−0.12755	5	14	47	9	17	0
d_{xy}	58	−0.12888	3	2	46	2	30	0
$d_{yz}/d_{xy}-\pi_v^*$	56	−0.18574	19	1	52	3	13	0
$d_{xz}-\pi_h^*$	55	−0.30706	18	14	43	1	12	4
$N_{AD}(p)$	54	−0.33664	3	1	4	1	75	1
$N_{AD}(p)-d_{xy}$	53	−0.37326	18	0	12	1	51	2
$N_{AD}(p)d_{x^2-y^2}$	52	−0.37691	8	0	13	1	51	6
$N_{AM}-d_{xz}$	51	−0.39143	14	2	24	1	7	33
$\pi_v^*-d_{yz}$	50	−0.41104	38	1	35	2	11	0
$\pi_h^*-d_{z^2}/d_{xz}$	49	−0.42665	37	2	20	2	4	16
$p_\sigma-d_{z^2}$	36	−0.58954	32	32	12	1	7	0
$\pi-H_2$	29	−0.72094	1	74	0	24	0	0
$\pi-H_3$	28	−0.72307	2	73	0	24	0	0

intermediate (1.85 and 1.57 Å, respectively), corresponding to population of the metal−N and N−N antibonding SOMO. This is also reflected by the extremely low N−N and metal−N stretching frequencies predicted by the calculation (467 and 712 cm^{-1}, respectively; Table 3). The extreme weakening of the N−N bond in **V** is further evidenced by the fact that the σ^* orbital ⟨60⟩ of **V** is at 0.20 au above the SOMO, significantly lowered in energy with respect to that in complex **II** where σ^* was found at 0.26 a.u. above the SOMO.

Single-electron transfer to **V** leads to double occupancy of its HOMO. Upon geometry optimization of the corresponding structure, the N−N bond is cleaved, and the separate components NH_3 and nitrido complex are obtained. It can therefore be concluded that both pathways are in principle effective in the conversion of N_2 to NH_3 on Mo triamidoamine systems, i.e., protolytic cleavage of the hydrazido(2−) complex **IV** and reductive cleavage of the hydrazidium complex **V**. Importantly, both pathways involve an intermediate Mo(IV) hydrazidium species that spontaneously cleaves the N−N bond.

IV. Discussion

In the preceding sections, the mechanism of N−N cleavage in Mo and W hydrazidium complexes with diphos and triamidoamine ligands (diphos = dppe, depe) was evaluated. The N−N splitting process in the Mo/W−NNH_2 and −NNH_3 systems with diphos coligands was investigated on the basis of the dialkylated, doubly reduced, five-coordinate complex [W(dppe)$_2$(NNC_5H_{10})] (compound $\mathbf{B}^W$) a full characterization of which is presented in the accompanying article.[9] As known for the analogous molybdenum complex (compound $\mathbf{B}^{Mo}$), protonation of $\mathbf{B}^W$ in various solvents leads to cleavage of the N−N bond under generation of the nitrido complex and piperidine, providing a prototypical example for the N−N splitting step in the transition-metal-mediated conversion of N_2 to NH_3.

In acetonitrile and at room temperature, compound $\mathbf{B}^W$ reacts much more rapidly with acids than its molybdenum counterpart. A stopped-flow experiment for the reaction of $\mathbf{B}^W$ with $HNEt_3BPh_4$ was therefore performed in propionitrile at −70 °C. As reported in the Results and Analysis section, protonation of $\mathbf{B}^W$ is complete within the dead time of the stopped-flow apparatus, leading to the primary protonated intermediate $\mathbf{B}^WH^+$. Propionitrile coordination to this species proceeds with a rate constant $k_{obs(1)}$ of 1.5 ± 0.4 s^{-1}, generating the intermediate RCN−$\mathbf{B}^WH^+$ (R = Et) that subsequently mediates N−N bond splitting in a slower reaction ($k_{obs(2)} = 0.35 \pm 0.08$ s^{-1}, 6 equiv of acid). A much slower reaction was observed upon treatment of $\mathbf{B}^W$ with $HLutBPh_4$ in benzonitrile at room temperature, proceeding via intermediates that could not be observed in acetonitrile, propionitrile, and THF.

Geometry optimization of a model of the solvent-coordinated, N$_\beta$-protonated intermediate RCN−$\mathbf{B}^WH^+$ was found to spontaneously lead to separation into the nitrido complex and piperidine, corresponding to an activationless heterolytic cleavage of the N−N bond. The much slower N−N cleavage reaction of $\mathbf{B}^W$ in benzonitrile along this pathway was attributed to the delocalization of electronic charge into the aromatic ring of the coordinated solvent molecule. Importantly, DFT also indicates the possibility of activationless N−N cleavage of *unsolvated* intermediate $\mathbf{B}^W$, initiated by protonation at N$_\beta$. In coordinating solvents such as nitriles, this process appears to be intercepted by solvent attack, in agreement with the literature. Nevertheless, this direct reaction path might be relevant to the protolytic N−N cleavage process in non- or weakly coordinating solvents.

For the N−N cleavage reaction of the molybdenum dialkylhydrazido complex $\mathbf{B}^{Mo}$ in acetonitrile, a second, acid-assisted pathway had been observed.[8] This is based on further protonation of RCN−$\mathbf{B}^{Mo}H^+$ at N$_\alpha$ with an equilibrium constant K_3, generating the doubly protonated species RCN−$\mathbf{B}^{Mo}H_2^{2+}$ that subsequently decays to the imido complex and piperidine with a rate constant k_5. The overall rate of this process depends on the product k_5K_3 and thus becomes dependent on the acid concentration. For the protonation of the tungsten complex $\mathbf{B}^W$ in propionitrile at −70 °C, however, no dependence of the reaction rate on the acid concentration could be observed. On the basis of the easier protonability of tungsten as compared to molybdenum NNH_x complexes (x = 0, 1, 2)[21] it was concluded that the equilibrium associated with K_3 is saturated in the presence of an excess of acid. Theoretical simulation of the N−N cleavage process of the doubly protonated intermediate revealed an exothermic process (−45 kcal/mol) with a very small activation barrier (∼1 kcal/mol). Judging from the large value of K_3 for $\mathbf{B}^W$, this must be the dominant pathway for the N−N cleavage reaction of this molecule in the presence of an excess of acid.

In competition with the direct N−N cleavage process triggered by protonation at N$_\beta$, unsolvated $\mathbf{B}^W$ can also be protonated at the metal. As the electron pair in the HOMO of $\mathbf{B}^W$ is consumed for hydride formation, N−N splitting does not occur in this case, even after further protonation at N$_\beta$. Metal protonation therefore would correspond to a nonproductive step in the overall reaction scheme. Judging from the rapid solvent attack on the N$_\beta$-protonated intermediate and from steric considerations, however, this process does not appear to be important. Initial protonation of $\mathbf{B}^W$ at N$_\alpha$, finally, was found to lead to an intermediate that requires

70 kcal/mol to cleave the N−N bond. Nevertheless, N−N cleavage can be induced in this intermediate by transfer of the proton from N_α to N_β, probably via a deprotonation−reprotonation sequence of reactions or by an additional protonation at N_β (cf. Scheme 4).

As a result of the theoretical treatment, protonation of $\mathbf{B}^W$ thus does not allow N−N cleavage (single protonation at N_α), inhibits further protolytic N−N cleavage (protonation at the metal), or induces N−N cleavage as an allowed process (protonation at N_β, along with or without protonation at N_α). This qualitatively agrees with the results of the experimental data available for $\mathbf{B}^W$ and supports the kinetic scheme originally established by Henderson et al.[8] for $\mathbf{B}^{Mo}$ (Scheme 1). So far, the calculations do not indicate the presence of significant activation barriers in the allowed N−N cleavage pathways of $\mathbf{B}^W$ and $\mathbf{B}^{Mo}$. Although activation parameters have not been experimentally determined for this reaction, the fact that the N−N cleavage rate of $\mathbf{B}^W$ becomes slow at low temperature appears to indicate the presence of a barrier in this process. Possibly, our theoretical picture of initial proton transfer to compound **B** is too simple, and the primary interaction of the acid with compound **B** is more in the form of an H-bonded acid−base complex.[25] In this complex, the actual proton transfer might occur only after elongation of the N−N bond, i.e., concomitant with the N−N cleavage process, introducing a barrier along the N−N coordinate.

Solvent coordination to the primary protonated intermediate $\mathbf{B}H^+$ appears to be associated with a barrier as well. The fact that nitrile does not coordinate to the starting complex has already been noted by Henderson et al.[8] The reason for this finding is the lone pair at the metal pointing into the vacant site. Compound **B** thus is not Lewis acidic but rather *Lewis basic* and will not easily accept a solvent. Coordination of nitriles to the monoprotonated form is slow because this intermediate does not bend at N_α after initial protonation and thus still has a lone pair at the metal. This only changes upon bending of $\mathbf{B}H^+$ at N_α, thus giving a Lewis acidic character to this species and allowing coordination of solvent. Moreover, bending is associated with an orbital redistribution, shifting two electrons from a dσ- to a dπ-type metal orbital. Solvent coordination to $\mathbf{B}H^+$, therefore, is associated with an activation barrier; the calculation gives +16 kcal/mol. In particular, it becomes slower at low temperatures than observed in the room-temperature experiment of Henderson et al.[8] where it was complete within the dead time of the stopped-flow apparatus. Alternatively, initial protonation at N_α or initial double protonation at N_α and N_β should lead to an intermediate that is bent at N_α and thus readily would accept a solvent molecule. Judging from the slow solvent coordination observed for $\mathbf{B}^W$ at low temperature, these scenarios appear less probable.

In the second part of this article, a theoretical analysis of the reduction and protonation of N_2 in the Mo(III) triamidoamine system up to the point of N−N cleavage and generation of the first molecule of NH_3 is presented. To this end, DFT calculations of the $Mo^{III}N_2$ complex and its diprotonated, one-electron-reduced NNH_2 derivative **II** were performed. Calculated structural and spectroscopic parameters were compared to available experimental data. Moreover, the postulated one-electron-reduced derivative of **II**, intermediate **III**, was treated by DFT. For the cleavage of the N−N bond, two scenarios were considered: (i) one-electron reduction of the Mo^V-NNH_2 complex **III** leading to a $Mo^{IV}-NNH_2$ complex, followed by protonation, and (ii) protonation of the Mo^V-NNH_2 complex **III** to a Mo^V-NNH_3 species, followed by one-electron reduction. In both cases, geometry optimization of the intermediate Mo(IV) hydrazidium species leads to the separated nitrido complex and ammonia; i.e., both reaction modes mediate a spontaneous N−N cleavage process. Judging from the lower-lying LUMO for **V** as compared to **III**, pathway ii appears more favorable than pathway i; i.e., protonation of the NNH_2 group of **III** to a hydrazidium species before electron transfer to induce N−N cleavage helps to make the necessary reduction potential less negative. On the other hand, the terminal NH_2 group of **III** is still slightly positive (+0.11), in contrast to that of its one-electron-reduced counterpart **IV** (−0.05, cf. Table 3). Therefore, **IV** is easier to protonate than **III**. The actual pathway will thus depend on the applied reduction potential and the pK_a value of the acid effective in the protonation.

What are the implications of the geometric and electronic structures on the reactivities of the Mo/W diphos and the Mo triamidoamine systems? Most notably, the diphos systems bind dinitrogen at the zerovalent stage (d^6 configuration), whereas N_2 binding of the triamidoamine ligands occurs at the Mo(III) level. Judging from N−N distances, N−N stretching frequencies, and calculated charges, the activation of N_2 is comparable in both systems. Importantly, the three negatively charged equatorial amido groups in the trigonal triamidoamine system are both strong σ and strong π donors, pushing the $d_{xy}/d_{x^2-y^2}$ orbitals to high energy by σ/π-antibonding interactions such that they become unoccupied. Thus, only the amide nonbonding d_{xz} and d_{yz} orbitals are populated and interact with the dinitrogen π^* orbitals. In contrast, the neutral, equatorial phosphine groups of the Mo/W diphos systems are σ donors and π acceptors, generating (along with the axial ligands) a set of two d_σ orbitals and a set of three d_π orbitals. At the zerovalent level of the metal center, the d_π orbitals are occupied by six electrons. However, whereas the two electrons in the nonbonding d_{xy} orbital are not involved in the reduction of N_2 to NH_3 on Mo(0) or W(0) complexes at any stage, all three metal d_π electrons are needed for this process in the Mo triamidoamine system. The latter system therefore is more economical in the use of reduction equivalents.

A second important difference between the two systems relates to fact that the ligand in the trans position to the N_2 coordination site is fixed in the triamidoamine complex. In contrast, this ligand is exchangeable in Mo/W diphos complexes and lost upon two-electron reduction at the NNH_2 and NNR_2 stage, forming five-coordinate species. However, a solvent molecule or the conjugate base of the employed acid can coordinate to the empty coordination site just after

(25) Golubev, N. S.; Shenderovich, I. G.; Smirnov, S. N.; Denisov, G. S.; Limbach, H.-H. *Chem.—Eur. J.* **1999**, *5*, 492.

protonation of the reduced intermediate, re-forming a six-coordinate complex. *The actual N−N cleavage process of this solvent-coordinated intermediate is entirely analogous to that described for the triamidoamine system.* In both cases, the reactive species—a Mo(IV)/W(IV) complex in that and a Mo(II) complex in the diphos system—exhibits a hydrazidium group which is bent at N_α, forming a lone pair at this position. The HOMO of this intermediate is an in-plane metal d_π orbital with an antibonding contribution of the lone pair at N_α. Moreover, it contains a p-orbital at N_β that is directed along the N−N bond and is antibonding with respect to the lone pair at N_α. Upon N−N cleavage, this HOMO evolves to the lone pair of ammonia, and the two-electron-oxidized metal nitrido species is left behind.

Acknowledgment. The authors gratefully acknowledge financial support from Deutsche Forschungsgemeinschaft (SFB 583 and TU58/12-1) and Fonds der Chemischen Industrie.

Supporting Information Available: Charge contributions of models **II** and **IV**; UV/vis absorption spectra of compound $\mathbf{B}^{W}$ in propionitrile (with and without acid) and in benzonitrile (with acid); UV/vis absorption spectrum of $[W(N)(NCPh)(dppe)_2]BPh_4$ in benzonitrile; ^{15}N NMR spectra of compound $\mathbf{B}^{W}$ in benzonitrile, with and without acid; PES for the N−N cleavage reaction of the α-protonated intermediate. This material is available free of charge via the Internet at http://pubs.acs.org.

IC048674O

8 Summary and Outlook

In this thesis, syntheses, and detailed spectroscopic and quantum-chemical investigations on transition metal complexes (including iron, manganese and cobalt) in the field of bioinorganic chemistry are presented. The preceding chapters comprise research that relates to a vide variety of different fields in chemistry, such as inorganic coordination chemistry (transition metal complexes), physical chemistry (spectroscopy: mainly MCD and rRaman), synthetic organic chemistry (porphyrin syntheses), computational chemistry, and biochemistry (model systems with relevance to heme proteins). However, approximately 75 % of the work presented here deal with the syntheses, MCD, and Raman spectroscopic, and quantum-chemical investigations of ferric heme model complexes and their reaction with NO. In the following, the most important results in this area are summarized.

Heme proteins have impressively diversified biological functions, which are mediated by the versatile electronic structures of iron porphyrins. Therefore, it is important to investigate the electronic structures as well as the electronic and vibrational spectra of heme proteins and their corresponding model complexes in detail to understand their roles in biology. Magnetic Circular Dichroism (MCD) and resonance Raman (rRaman) spectroscopies are extremely powerful techniques to investigate the electronic structures and spectra of transition metal complexes. To this end, and in order to have unlimited access to these important methods, I have built two MCD and one rRaman spectrometer together with my supervisor Prof. Dr. Nicolai Lehnert. Note that the MCD spectrometer built in Kiel is only the third one in the field of chemistry in Germany. The MCD spectrometer consists of a JASCO CD spectropolarimeter, an Oxford Spectromag^{4000} cryostat with incorporated superconducting magnet, and a head-on photomultiplier tube as detector covering the wavelength range of 163 – 1100 nm. Typical experimental conditions for low-temperature MCD measurements are temperatures between 1.5 – 30 K using liquid helium and magnetic fields of 0-7 T. The rRaman spectrometer built in Ann Arbor, USA, consists of an argon/krypton ion mixed gas laser BeamLok 2060 from Spectra-Physics, which allows to perform measurements at 647.1, 568.2, 530.9, 514.5, 488.0, 476.5, 457.9, 413.1, 406.7 and 351.0 nm excitation wavelengths, and a PI Acton TriVista DM 55 double monochromator with an attached SPEC 10 400B liquid-nitrogen cooled CCD detector.

Five-coordinate hs ferric heme centers occur in the catalytic or redox cycles of many metallo proteins, including P450 type enzymes, horseradish peroxidase (HRP), haemoglobin (Hb) and myoglobin (Mb), Cytochromes, bacterial nitric oxide reductase (NorBC), and in nitrophorins (Np) and therefore, play an important role in enzymology. However, high-spin (hs) ferric hemes exhibit very complicated MCD and UV-Vis absorption spectra and therefore, detailed assignments of the MCD spectra of these species are missing, and thus, the nature of the different transitions observed is unknown. To this end, the vibrational and electronic spectra (MCD and UV-Vis) of five-coordinate ferric [Fe(TPP)(Cl)] are analyzed in detail in this work. For the first time, complete assignments for both the vibrational and electronic spectra of this complex have been obtained. In combination with TD-DFT calculations, we are able to explain a number of puzzling observations in the absorption spectra of [Fe(TPP)(Cl)], which include (a) the nature of the intense broad band to higher energy of the Soret band, (b) the broad appearance of the Soret band, (c) the position of Q and Q_v, (d) the assignment of the ~640 nm feature, (e) the position of Cl → Fe CT transitions, and (f) porphyrin → d_π CT transitions. Thus, all of the open questions with respect to the electronic spectra of [Fe(TPP)(Cl)] are now solved.

A correlated fit of the absorption and low-temperature MCD spectra of [Fe(TPP)(Cl)] was performed first, which allowed for the identification of at least 20 different electronic transitions. In order to obtain further insight into the nature of the different transitions, we measured VTVH **C**-term saturation curves, which allow for the determination of the polarizations of the MCD bands. An accurate theoretical description of [Fe(TPP)(Cl)] was obtained from TD-DFT calculations on the B3LYP/LanL2DZ* level. These calculations are not sufficient enough by themselves to assign the spectra, but they supply a number of important pieces to solve the puzzle. The TD-DFT results provide a list of important transitions and their relative energies and intensities with good accuracy, and this way, define the "active space" of electronic transitions that are relevant. Finally, the occurrence of pseudo **A**-terms in the MCD **C**-term spectra is very useful to locate E_u excited states, split in the lower symmetry of [Fe(TPP)(Cl)] (vide infra). The Soret band in [Fe(TPP)(Cl)] is split into three components, which is evident from the saturation behavior and the TD-DFT results. This is due to the fact that the Soret band is mixed with the porphyrin A_{2u}<72> → E_g<82/83> ($\pi \rightarrow \pi^{*(1)}$) transition. Importantly, there is no additional A_{1u} → E_g<82/83> transition present in the porphyrin that corresponds to $\pi \rightarrow \pi^{*(1)}$. Note that this assignment could further be confirmed by rRaman spectroscopy. However, from the low-

temperature MCD data, the Q and Q_v bands could not clearly be identified due to their low intensities in both MCD and UV-Vis. For the identification of Q and Q_v in metalloporphyrins, rRaman spectroscopy is a powerful tool. Both Q and Q_v lead to Raman **B**-term enhancement, which is related to vibronic coupling and is manifested in the enhancement of anomalous polarized A_{2g} modes. The rRaman spectrum of [Fe(TPP)(Cl)] excited at 568.2 nm shows weak and the data obtained at 514.5 nm show medium intense anomalous polarized bands indicating vibronic coupling. In addition, overtones are enhanced upon excitation into the absorption band at 510 nm, which indicates that this band actually corresponds to Q_v. This latter assignment is in very good agreement with the high-temperature MCD data, which reveals Q_v at 20202 cm^{-1}. A closer inspection of the **C**-term MCD spectrum then identifies one component of Q_v at 20150 cm^{-1} showing the expected in-plane polarization. It is known from the literature that irradiation into the near-ultraviolet band at 379 nm in [Fe(TPP)(X)] (X = F^-, Cl^-, Br^-, I^- and N_3^-) leads to photoreduction of the iron atom and dissociation of a halid radical. The band at 25577 cm^{-1} in MCD indeed shows z-polarization and is therefore, in agreement with the photoreduction experiments, assigned to the $CT^{(Cl,\pi,\sigma)}$ transition mixed with $CT^{(5)}$. The A_{1u}<79> → d_π transition ($CT^{(1)}$) is assigned to the bands at 15000 and 15600 cm^{-1}, which give rise to a pseudo **A**-term in MCD due to the E_u symmetry of the excited state. In the course of the $CT^{(1)}$ excitation, one electron is transferred from the A_{1u}<79> HOMO of the porphyrin into the d_π orbitals of iron, which generates a porphyrin π-cation radical electronic structure in the excited state. Note that crystallographic data obtained on the π-cation radical complex [Zn(TPP)(ClO_4)] show a strongly ruffled porphyrin core, where the Zn atom is moved out of the porphyrin plane towards the axial perchlorate ligand. The enhancement of the low-lying porphyrin deformation modes upon excitation at 647.1 nm, which is observed in the rRaman spectra of [Fe(TPP)(Cl)], is therefore in excellent agreement with the assignment to $CT^{(1)}$.

In addition, ferric heme nitrosyls have been investigated in this thesis. Ferric heme nitrosyls with *trans* thiolate coordination show a bent structure in both proteins and their corresponding model complexes, which demonstrates an intrinsic bending of the Fe-N-O moiety due to electronic effects. Another interesting feature of thiolate-coordinated ferric heme nitrosyls is the low ν(N-O) stretching frequency of 1800-1850 cm^{-1}. In order to determine the role of thiolate for the functions of the above-mentioned proteins, we explored the electronic effect of the thiolate on the Fe-NO unit using quantum-chemical calculations. These results demonstrated that the difference

between axial N- and S-donor-coordinated ferric heme nitrosyls is due to a σ-*trans* effect of the coordinated thiolate on the bound NO mediated by an NO σ* orbital. In this way, the Fe-N and N-O bonds are weakened, and the Fe-N-O unit is bent in the S-coordinated case. This is reflected by lower ν(N-O) and ν(Fe-N) stretching frequencies in the presence of thiolate coordination. Besides this computational study, I have investigated the complex [Fe(OEP)(NO){S-2,6-$(CF_3CONH)_2C_6H_3$}] (**2H-NO**, OEP = octaethylporphyrin and S-2,6-$(CF_3CONH)_2C_6H_3$ = SR'), and the corresponding compound with only one hydrogen bond (**1H-NO**) using in-situ UV-Vis absorption and rRaman spectroscopies. Note that these complexes are extremely unstable. They react with smallest amounts of dioxygen under formation of [Fe(OEP)(NO)(NO_2)]. Upon warming up, these complexes immediately lose NO. The reactions of **2H** and **1H** with one equivalent of NO lead to the formation of the corresponding NO complexes (**2H-NO** and **1H-NO)** with absorption maxima observed at 430, 536 and 567 nm, respectively. However, the reaction of **1H** with one equivalent of NO leads only to a few percent of the NO complex and therefore, no rRaman data could be obtained for this compound. After addition of another equivalent of NO or excess NO, the nitrosyl complexes decomposed in both cases to form the complex [Fe(OEP)(NO)(NO_2)], which relates to the presence of higher NO_x (for example N_2O_3) impurities, which are always present in nitric oxide even after rigorous purification procedures as has been shown by van Eldik and coworkers. In the rRaman spectrum of **2H-NO** in a frozen CH_2Cl_2 solution, ν(N-O) is observed at 550 cm^{-1}, which shifts to 535 cm^{-1} in the isotopically labeled complex **2H-^{15}N^{18}O**. The observed isotopic shift of 15 cm^{-1} is in excellent agreement with the calculated shift of 17 cm^{-1}. The vibrational assignments have been further investigated using Normal Coordinate analysis (NCA) leading to force constants of 14.51 and 3.56 mdyn $Å^{-1}$ for the N-O and Fe-NO bond, respectively. Interestingly, ferric heme nitrosyls exhibit larger Fe-NO force constants than the corresponding ferrous hemes nitrosyl complexes. For example, [Fe(TPP)(NO)] has an Fe-NO force constant of 2.975 mdyn/Å obtained from QCC-NCA. In contrast, the binding constant for NO in ferric heme systems (K_{eq} = 10^3 to 10^5 M^{-1}) is much smaller than in ferrous hemes (K_{eq} = 10^{11} to 10^{12} M^{-1}). Hence, the Fe-NO bond is thermodynamically stronger in ferrous than in ferric heme nitrosyls. But why is the Fe-NO force constant significant larger in ferric heme compounds, and how does this relate to the stability of these complexes? I have further investigated this very important question using potential energy surface (PES) calculations on six-coordinate ferric heme NO model systems with different electronic states: (a) Fe(II)-NO^+ (S = 0), which is the established ground state, (b) the open shell

singlet state ls-Fe(III)-NO(radical), where low-spin (ls) Fe(III) is antiferromagnetically coupled to NO (S = 0), and (c) the corresponding high-spin (hs) state hs-Fe(III)-NO(radical) (S = 2, black), which corresponds to the product state upon dissociation of NO. These results show that the elusive ls-Fe(III)-NO(radical) state does in fact exist as an energy minimum, and that this state is surprisingly close in energy to the Fe(II)-NO^+ ground state (DFT energy separation: only ~1 kcal/mol). It is estimated that an elongation of the Fe-NO bond of only 0.05 - 0.1 Å from the equilibrium position leads to a change of the ground state of the complex, i.e. the critical iron(II) to NO^+ electron transfer occurs at an Fe-NO distance of only 1.70 - 1.75 Å. Importantly, the properties of the two states, Fe(II)-NO^+ and ls-Fe(III)-NO(radical), are very different. From the calculations, the ls-Fe(III)-NO(radical) state has a weaker (longer) Fe-NO bond, and hence, a lower Fe-NO stretching frequency. Due to the electron transfer from iron(II) into a π^* orbital of NO, the N-O bond is also weaker giving rise to ν(N-O) at lower frequency. Hence, both the Fe-NO and the N-O bond become weaker in going from Fe(II)-NO^+ to ls-Fe(III)-NO(radical), which corresponds to a direct correlation of these bond strengths. These results are very important, because this implies that a small perturbation of the Fe-N-O unit, for example, due to interaction of the bound NO with a protein side chain, might be able to induce a change of the ground state from Fe(II)-NO^+ to ls-Fe(III)-NO(radical). This finding also offers an attractive explanation for the observed weaker Fe-NO and N-O bond strengths in ferric heme nitrosyls with axial thiolate coordination (compared to axial N-donor coordination) as discussed above, which could be attributed to a change in ground state to ls-Fe(III)-NO(radical). However, this would not explain the observed bending of the Fe-N-O unit (vide supra); our results clearly demonstrate that a bent Fe-N-O unit is not an intrinsic property of the ls-Fe(III)-NO(radical) state. On the other hand, our DFT results also show that these properties can be explained within the Fe(II)-NO^+ ground state model. This point needs further investigation. The observed thermodynamic weakness of the Fe-NO bond in ferric heme nitrosyls is due to the properties of the high-spin Fe(III)-NO(radical) (S = 2) state, which is dissociative with respect to the Fe-NO bond, and which appears at very low energy. These potential energy surface calculations reveal an unexpectedly complex energy landscape for binding of NO to ferric heme.

In addition to the studies on ferric heme model complexes and their reaction with NO, the synthesis of cofacial bisporphyrin model complexes has been carried out in this thesis. Two synthetic routes have been applied, the so-called direct and the rational synthetic route. The

synthesis of the cofacial bisporphyrin H_4DPA (anthracene linker unit) corresponds to a multi-step synthesis starting from 1,8-dichloroanthraquinone. The corresponding complex $[Co_2(DPA)(NO)_2]$ has been synthesized and spectroscopically characterized using UV-Vis absorption, IR- and rRaman spectroscopies. The obtained spectroscopic data are similar to the data obtained for the monoporphyrins [Co(TMP)(NO)] and [Co(TPP)(NO)]. The UV-Vis absorption spectrum of $[Co_2(DPA)(NO)_2]$ shows the Soret band at 414 nm, the Q band at 545 nm and the Q_v band at 594 nm. The N-O stretching vibration is observed as strong band at 1685 cm^{-1} in IR and as weak band at 1686 cm^{-1} in rRaman ($\lambda_{exc.}$ = 457.9 nm), respectively. In order to investigate these systems in more detail, quantum-chemical calculations have also been performed. The reaction of the cofacial metalloporphyrins with nitric oxide can theoretically lead to three different isomers depending on whether the NO is bound outside or inside the pocket formed by the two porphyrins: a) both NO molecules are bound inside (i/i), b) one NO binds outside and the other one inside (i/o), and c) both NO molecules bind outside (o/o). From the calculations on $[Co_2(DPA)(NO)_2]$ (S = 0), the o/o isomer is lowest in energy, the i/o form is 0.32 kcal mol^{-1} higher in energy, and the i/i isomer is predicted 1.79 kcal mol^{-1} higher in energy, respectively, which is very close. Correspondingly, in $[Fe_2(DPA)(NO)_2]$ (S = 1), the o/o isomer is lowest in energy, and the i/i isomer is found 1.56 kcal mol^{-1} higher in energy. Hence, not much driving force is needed to direct the NO molecules to bind inside the pocket. In addition, the geometries of the intermediates relevant for the *trans* mechanism of NorBC have been optimized for DPA and DPB (biphenylene linker), including the nitrosyl complexes as shown above, the M-N_2O_2-M intermediate (bridged hyponitrite), and the μ-oxo dimer. These calculations lead to the following conclusions: a) no interaction of the NO molecules is observed in the i/i isomer as reflected by the large N_{NO}-N_{NO} distance in $[M_2(DPA)(NO)_2]$, b) the coordination of imidazole did not lead to any improvement in the N_{NO}-N_{NO} distance, c) the cobalt complex stabilizes the Co-N_2O_2-Co intermediate as evident from the obtained N_{NO}-N_{NO} distance of 1.27 Å in $[Co_2(DPA)(N_2O_2)]$, whereas in the corresponding iron complex the N_{NO}-N_{NO} distance is distinctively larger (calculated: 1.79 Å), d) the protonation of the Fe-N_2O_2-Fe intermediate leads to an decrease in the N_{NO}-N_{NO} bond length, for example 1.42 Å in $[Fe_2(DPA)(N_2O_2H)]^+$ ($[Fe_2(DPA)(N_2O_2)]$: 1.79 Å), and e) the μ-oxo dimer is stabilized in the biphenylene bridged cofacial porphyrin ($[\{Fe_2(DPA)\}_2O]$ could not be optimized due to the large Fe-Fe distance). Importantly, these results indicate that the coupling and reduction of NO using cofacial porphyrins as a platform should be feasible.

9 Curriculum Vitae (Lebenslauf)

Persönliche Daten:

Geburtstsdatum	16.07.1979
Geburtsort	Köln
Familienstand	Ledig
Nationalität	Deutsch

Ausbildung:

08/2004 – 12/2007	Promotionsstudent an der Christian-Albrechts-Universität (C.A.U.) zu Kiel in der Sektion Anorganische Chemie
Thema:	"Synthesis, MCD- and Raman- Spectroscopic, and Quantum-Chemical Investigations of Ferric Heme Model Complexes and their Reaction with NO"
Leitung:	Prof. Dr. Nicolai Lehnert und Prof. Dr. Felix Tuczek
08/2006 – 11/2007	Auslandsaufenthalt zu Forschungszwecken an der University of Michigan in Ann Arbor, Michigan, USA (Arbeitsgruppe von Prof. Dr. Nicolai Lehnert).
10/1999 - 06/2004	Chemiestudium an der Christian-Albrechts-Universität zu Kiel
10/2001	Diplomchemiker-Vorprüfung (Note: sehr gut)
06/2004	Diplomchemiker-Hauptprüfung (Note: sehr gut)
Thema:	„Synthese und spektroskopische Charakterisierung von Modellsystemen für die NO-Reduktase und MCD-spektroskopische Untersuchung relevanter Vorstufen"
Leitung:	Prof. Dr. Nicolai Lehnert und Prof. Dr. Felix Tuczek
25.02.2002 - 30.03.2002	Werkstudent bei DyStar Textilfarben GmbH & Co. Deutschland KG im Bereich Produktion & Technik BRU Synthesebetrieb in Brunsbüttel
1990 - 1999	Gymnasium Marne, Schleswig-Holstein
06/1999	Abitur

Preise und Auszeichnungen

01/2005 – 12/2006	Chemiefonds-Stipendium für Doktoranden gestiftet vom Fonds des Verbandes der Chemischen Industrie (FCI)
2004	Otto-Diels-Preis für die Diplomarbeit und die hervorragende Leistung während des Studiums
1999	Buchpreis des Fonds der chemischen Industrie für den besten Chemie-Abiturienten am Gymnasium Marne

Lehrtätigkeit

2004	Studentische Hilfskraft in verschiedenen Praktika (Grundpraktikum Chemie und Biochemie, Chemisches Praktikum für Zahnmediziner und anorganisch-chemisches Praktikum für Fortgeschrittene I)
2004 – 2006	Wissenschaftlicher Assistent im anorganisch-chemischen Praktikum für Fortgeschrittene I & II und Grundpraktikum für Chemie und Biochemie mit Abnahme von Prüfungen. Außerdem Betreuung und Anleitung zum wissentschaftlichen Arbeiten von mehreren Praktikanten im anorganisch-chemischen Praktikum für Fortgeschrittene III.
2006	Vorlesungsvertretungen für Prof. Dr. Felix Tuczek bzw. Prof. Dr. Nicolai Lehnert bei der zweistündigen „Koordinationschemie“ Vorlesung für fortgeschrittene Studenten mit Vordiplom
2006 – 2007	Betreuung und Anleitung zum wissenschaftlichen Arbeiten von „undergraduate“ und einer „graduate“ Studentin an der University of Michigan.

Poster

10/2004	7. Norddeutsches Doktoranden-Kolloquium der anorganisch-chemischen Institute in Hamburg
08/2005	12th International Conference on Biological Inorganic Chemistry (ICBIC), University of Michigan, Ann Arbor, Michigan, USA

Vorträge

12/2004	Otto-Diels-Preis Verleihung im Rahmen des Weihnachtskolloquiums der Sektion Chemie (Kiel)
10/2005	8. Norddeutsches Doktoranden-Kolloquium der anorganisch-chemischen Institute in Warnemünde
03/2006	Stipendiatentreffen des Fonds der Chemischen Industrie in Berlin

10 Publication List (Publikationsliste)

1) **F. Paulat**, T. Kuschel, C. Näther, V. K. K. Praneeth, O. Sander, N. Lehnert „Spectroscopic Properties and Electronic Structure of Pentammineruthenium(II) Dinitrogen Oxide and corresponding Nitrosyl Complexes: Binding Mode of N_20 and Reactivity“
Inorg. Chem. **2004**, *43*, 6979-6994.

2) K. Mersmann, K. H. Horn, N. Böres, N. Lehnert, F. Studt, **F. Paulat**, G. Peters, I. Ivanovic-Burmazovic, R. van Eldik, F. Tuczek
“Reduction Pathway of End-on Terminally Coordinated Dinitrogen. V. N-N Bond Cleavage in Mo/W Hydrazidium Complexes with Diphosphine Coligands. Comparison with Triamidoamine Systems”
Inorg. Chem. **2005**, *44*, 3031-3045.

3) **F. Paulat**, V. K. K. Praneeth, N. Lehnert
„Quantum Chemistry based Analysis of the Vibrational Spectra of five- coordinate Metalloporphyrins [M(TPP)(Cl)]”
Inorg. Chem. **2006**, *45*, 2835-2856.

4) N. Lehnert, V. K. K. Praneeth, **F. Paulat**
„Electronic Structure of Fe(II)-Porphyrin Nitroxyl Complexes: Molecular Mechanism of fungal Nitric Oxide Reductase (P450nor)”
J. Comput. Chem. **2006**, *27*, 1338-1351.
(special issue: Computational Bioinorganic Chemistry)

5) **F. Paulat**, N. Lehnert
„Electronic Structure of Ferric Heme Nitrosyl Complexes with Thiolate Coordination“
Inorg. Chem. **2007**, *46*, 1547-1549.

6) R. Meier, J. Maigut, B. Kallies, N. Lehnert, **F. Paulat**, F. W. Heinemann, G. Zahn, M. P. Feth, H. Krautscheid, R. van Eldik
„$[Fe^{III}(tmsta)]^-$ twist-boat/half-chair conformer ratio reliably deduced from DFT-calculated Raman spectra“
Chem. Commun. **2007**, 3960-3962.

7) **F. Paulat**, N. Lehnert, Y. Ishikawa, K. Okamoto, K. Fujisawa

„Mononuclear and Binuclear Copper(I)-Diazene Complexes: a New Chapter of Copper Coordination Chemistry"

Inorg. Chim. Acta **2007**, *360*, in press (Available online 26 May 2007).

(special issue in honor of Edward I. Solomon)

8) **F. Paulat**, N. Lehnert

„First Detailed Assignment of the Magnetic Circular Dichroism and UV-Vis Spectra of Five-Coordinate High-Spin Ferric [Fe(TPP)(Cl)]"

Submitted for publication.

9) K. Fujisawa, A. Tateda, Y. Miyashita, K. Okamoto, **F. Paulat**, V. K. K. Praneeth, A. Merkle, N. Lehnert

„Structural and Spectroscopic Characterization of Mononuclear Copper(I) Nitrosyl Complexes: End-on versus Side-on Coordination of NO to Copper(I)"

Submitted for publication.

10) V. K. K. Praneeth, **F. Paulat**, C. Näther, N. Lehnert

„Electronic Structure of Six-Coordinate Iron(III)-Porphyrin NO Adducts: the Elusive Iron(III)-NO(radical) State and its Influence on the Properties of these Complexes"

Manuscript in preparation.

11 Acknowledgment (Danksagung)

In erster Linie möchte ich mich herzlich bei Herrn Prof. Dr. Nicolai Lehnert für die interessante Aufgabenstellung, die ausgiebigen Fachgespräche und die vielen Hilfestellungen (Anregungen) bedanken. Ausserdem möchte ich mich herzlich bei Herrn Prof. Dr. Felix Tuczek für die freundliche Unterstützung während meiner Doktorandenzeit und die vielfältigen Anregungen bedanken. Darüber hinaus möchte ich mich bei Nicolai, seiner Frau Shannon und Tochter Sophia für die freundliche Atmosphäre und die Unterstüzung während der letzten vier Jahre bedanken.

Mein grösster Dank gilt meinen lieben Eltern und Geschwistern, die immer für mich da waren und mich in jeglicher Hinsicht unterstützt haben.

Darüber hinaus möchte in mich bei meinen Kollaborationspartnern für die Bereitstellung der interessanten Komplexverbindungen bedanken, insbesondere bei Herrn Prof. Dr. Kiyoshi Fujisawa, Herrn Prof. Dr. George B. Richter-Addo und Herrn Dr. Roland Meier.

Mein Dank gilt auch den Mitgliedern der Arbeitgruppen Lehnert und Tuczek für die freundliche Arbeitsatmosphäre. Herzlich sei an dieser Stelle meinen Kollegen und Freunden Gerald, Bengt, Jan B., Rainer, Jan S., Praneeth V. K. K., Corinne und Anna für den Spass und die fachlichen Gespräche gedankt. Insbesondere möchte ich mich auch bei Frau Uschi Cornelissen, Frau Stephanie Pehlke, Frau Marianne Karbstein, Herrn Dr. Gerhard Peters und Frau Helga Ofterdinger für die technische Unterstützung bedanken. Weiterer Dank gebührt den Werkstätten in Kiel und in Ann Arbor für den Bau der MCD-Tische, insbesondere Herrn Kim F. Firestone.

Für die finanzielle Unterstützung in Form eines Chemiefonds-Stipendiums möchte ich mich bei dem Fonds der Chemischen Industrie bedanken.

Eidesstattliche Erklärung

Hiermit erkläre ich an Eides statt, dass die vorliegende Abhandlung –abgesehen von der Beratung durch meine Betreuer Herrn Prof. Dr. Nicolai Lehnert und Herrn Prof. Dr. Felix Tuczek- nach Inhalt und Form meine eigene Arbeit ist.

Diese Arbeit hat weder in Auszügen noch in ganzer Form in anderen Prüfungsverfahren vorgelegen.

_____

Florian Paulat